

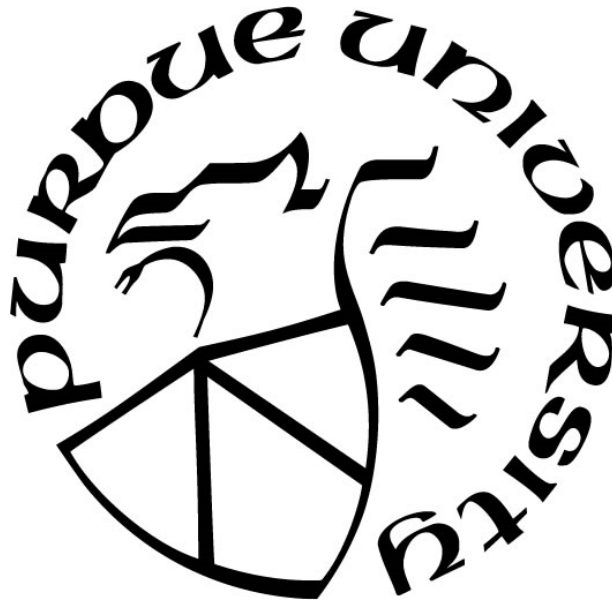
**BEHAVIOR AND DESIGN OF CONCRETE FRAME CORNERS:
STRUT-AND-TIE METHOD APPROACH**

by
Hwa-Ching Wang

A Dissertation

*Submitted to the Faculty of Purdue University
In Partial Fulfillment of the Requirements for the degree of*

Doctor of Philosophy



Lyles School of Civil Engineering
West Lafayette, Indiana
December 2020

THE PURDUE UNIVERSITY GRADUATE SCHOOL
STATEMENT OF COMMITTEE APPROVAL

Dr. Christopher S. Williams, Chair

Lyles School of Civil Engineering

Dr. Arun Prakash

Lyles School of Civil Engineering

Dr. Donald F. Meinheit

Wiss, Janney, Elstner Associates, Inc.

Dr. Robert J. Frosch

Lyles School of Civil Engineering

Approved by:

Dr. Dulcy M. Abraham

For my grandparents

ACKNOWLEDGMENTS

Being able to complete my dissertation, I have received considerable support and assistance. I would like to show my great appreciation here.

I would like to thank my advisor, Dr. Chris Williams, for guiding me through this journey. Your insights and detail-oriented attitude always inspired me to be precise in work and to elaborate in writing and presentation. Your encouragement motivated me to step forward.

I would like to thank my advisory committee members, Dr. Arun Prakash, Dr. Donald Meinheit, and Dr. Robert Frosch, for providing me with precious suggestions on the project so that I was able to improve the design and obtained valuable results.

I would like to thank the project supervisor, Mr. Gray Klein, for bringing the research to attention. The research has contributed to the field because of your effort.

I would like to thank lab technicians, Harry and Kevin, for dealing with heavy-duty equipment. Without you, I could not move even one small specimen.

I would like to thank my labmates, Ahmed, Andi, Becky, Bobby, David, Eric, Ryan, Ting-Wei and Will for the great help with fabrication and tests. Thank you for dirtying your clothes with concrete with me.

I would like to thank my friends Chen-Lin, Meng-Ju, Tzu-Chun, Wan-Chih, and Yu-Chun, for the kindly friendship. You created a family-like atmosphere when we experienced foreign lives.

I would like to thank Yelin, for being with me and supporting me during the stressful period. Your accompanying was my great support.

I would like to thank my aunt, Yu-Chen, my uncle, Ing-Hui, who always have my back. I could release my worries with your generous efforts for our home.

I would like to thank my brother Hwa-Chun for nothing and everything. Just want to show that I did not forget you.

I would like to thank my grandparents for your selfless sacrifice for me. You raised me up and gave me everything. You took care of me and supported me. All my achievements belong to you.

TABLE OF CONTENTS

| | |
|---|----|
| LIST OF TABLES | 10 |
| LIST OF FIGURES | 12 |
| ABSTRACT..... | 19 |
| 1. INTRODUCTION | 20 |
| 1.1 Overview..... | 20 |
| 1.2 Project Objectives | 22 |
| 1.3 Organization..... | 22 |
| 2. BACKGROUND | 24 |
| 2.1 Overview of Knee Joints..... | 24 |
| 2.2 Experimental Studies on Knee Joints under Closing Moments..... | 28 |
| 2.2.1 Early Studies | 28 |
| 2.2.2 Studies on Reinforcement Details | 30 |
| 2.2.3 Code Provisions Related to Closing Knee Joints | 40 |
| 2.2.4 Summary..... | 41 |
| 2.3 Introduction to the Strut-and-Tie Method..... | 42 |
| 2.3.1 Background..... | 42 |
| 2.3.2 Fundamental Concepts of the Strut-and-Tie Method | 43 |
| 2.3.3 Isolate D-Regions | 47 |
| 2.3.4 Determine Forces Acting at Interface between B- and D-Regions | 47 |
| 2.3.5 Develop Strut-and-Tie Model and Solve for Member Forces | 48 |
| 2.3.6 Proportion Ties | 50 |
| 2.3.7 Sizing Nodal Zones and Struts | 50 |
| 2.3.8 Checking Nodal Strength and Strut Strength..... | 55 |
| 2.3.9 Providing Distributed Reinforcement for Struts..... | 57 |
| 2.3.10 Providing Anchorage for Ties | 57 |
| 2.3.11 Summary | 58 |
| 2.4 Current Design Methodologies for Curved-Bar Nodes | 58 |
| 2.5 Strength Coefficients for Nodal Zones and Struts | 63 |
| 2.5.1 Nodal Zone Coefficient for CTT nodes..... | 63 |

| | | |
|-------|--|-----|
| 2.5.2 | Strut Coefficient for Interior Struts..... | 64 |
| 2.6 | Research Need | 65 |
| 3. | EXPERIMENTAL PROGRAM..... | 67 |
| 3.1 | Overview..... | 67 |
| 3.2 | Test Specimens | 67 |
| 3.2.1 | Series I: Single-Layer Longitudinal Bars | 67 |
| 3.2.2 | Series II: Double-Layer Longitudinal Bars | 72 |
| 3.2.3 | Series III: Reduced Clear Side Cover..... | 74 |
| 3.2.4 | Series IV: Adjoining Members with Different Cross-Sections | 77 |
| 3.2.5 | Series V: Multiple Purposes | 80 |
| 3.3 | Fabrication of Specimens..... | 83 |
| 3.3.1 | Concrete Mixture Design..... | 83 |
| 3.3.2 | Formwork | 84 |
| 3.3.3 | Steel Reinforcement..... | 85 |
| 3.3.4 | Casting and Curing of Concrete | 88 |
| 3.4 | Test Frame | 89 |
| 3.5 | Instrumentation | 92 |
| 3.5.1 | Load | 92 |
| 3.5.2 | Displacement and Rotation..... | 92 |
| 3.5.3 | Strain in Reinforcing Bars | 94 |
| 3.5.4 | Digital Image Correlation System | 97 |
| 3.6 | Test Procedure | 97 |
| 3.7 | Material Test | 99 |
| 3.7.1 | Compressive Strength of Concrete | 99 |
| 3.7.2 | Modulus of Elasticity of Concrete..... | 100 |
| 3.7.3 | Splitting tensile strength of Concrete | 100 |
| 3.7.4 | Modulus of rupture of Concrete | 101 |
| 3.7.5 | Tensile Strength of Reinforcing Bars | 102 |
| 3.8 | Summary..... | 103 |
| 4. | EXPERIMENTAL RESULTS AND DISCUSSION | 104 |
| 4.1 | Overview..... | 104 |

| | | |
|-------|---|-----|
| 4.2 | Series I: Single-Layer Longitudinal Bars (S-Series) | 104 |
| 4.2.1 | Overall Behavior..... | 104 |
| 4.2.2 | Visual Observations..... | 109 |
| 4.2.3 | Strain in the Reinforcing Bars | 114 |
| 4.2.4 | Stress Transmission and Failure Mechanisms..... | 117 |
| 4.2.5 | Summary..... | 122 |
| 4.3 | Series II: Double-Layer Longitudinal Bars (D-Series)..... | 123 |
| 4.3.1 | Overall Behavior..... | 123 |
| 4.3.2 | Visual Observations..... | 127 |
| 4.3.3 | Strain in the Reinforcing Bars | 134 |
| 4.3.4 | Summary..... | 138 |
| 4.4 | Series III: Reduced Clear Side Cover (C-Series)..... | 139 |
| 4.4.1 | Overall Behavior..... | 139 |
| 4.4.2 | Visual Observations..... | 141 |
| 4.4.3 | Strain in the Reinforcing Bars | 145 |
| 4.4.4 | Summary..... | 147 |
| 4.5 | Series IV: Different Cross-Sections (B-Series) | 148 |
| 4.5.1 | Overall Behavior..... | 149 |
| 4.5.2 | Visual Observations..... | 150 |
| 4.5.3 | Strain in the Reinforcing Bars | 153 |
| 4.5.4 | Summary..... | 154 |
| 4.6 | Series V: Multiple Purposes (M-Series) | 155 |
| 4.6.1 | Overall Behavior..... | 155 |
| 4.6.2 | Visual Observations..... | 159 |
| 4.6.3 | Strain in the Reinforcing Bars | 161 |
| 4.6.4 | Summary..... | 164 |
| 4.7 | Closing Remarks..... | 165 |
| 5. | ANALYSIS OF THE EXPERIMENTAL RESULTS..... | 166 |
| 5.1 | Overview..... | 166 |
| 5.2 | Categorization of Specimens | 166 |
| 5.3 | Evaluation of the Design Expression for Radial Stress at the Bar Bend | 170 |

| | | |
|-------|--|-----|
| 5.4 | Evaluation of the Effect of Clear Side Cover | 172 |
| 5.4.1 | Comparison of Overall Behavior | 172 |
| 5.4.2 | Evaluation of the Modification Factor for Reduced Clear Side Cover | 175 |
| 5.5 | Evaluation of the Effect of a Strut Angle not Equal to 45 Degrees | 178 |
| 5.5.1 | Evaluation | 178 |
| 5.6 | Performance of Knee Joints with Transverse Reinforcement..... | 181 |
| 5.6.1 | Comparison of Overall Behavior | 182 |
| 5.6.2 | Evaluation of Commonly Used Joint Details | 184 |
| 5.7 | Stress Analysis of Diagonal Strut and Curved-Bar Node | 185 |
| 5.8 | Summary | 189 |
| 6. | STRUT-AND-TIE MODEL AND DATABASE ANALYSIS | 191 |
| 6.1 | Overview | 191 |
| 6.2 | Database | 192 |
| 6.3 | Sectional Analysis and Joint Shear Capacity | 198 |
| 6.4 | Development of the Strut-and-Tie Model | 202 |
| 6.4.1 | Strut-and-Tie Models for Various Loading Configurations | 202 |
| 6.4.2 | Calculation of Internal Forces | 206 |
| 6.4.3 | Sizing the CTT node and the CCC node | 209 |
| 6.4.4 | Determination of Load Capacity | 211 |
| 6.4.5 | Parameters for the Strut-and-Tie Model | 213 |
| 6.5 | Results and Discussion | 214 |
| 6.5.1 | Evaluation of ACI Sectional Analysis and Joint Shear Capacity | 214 |
| 6.5.2 | Evaluation of the Strut-and-Tie Method..... | 219 |
| 6.6 | Summary | 224 |
| 7. | FINITE ELEMENT ANALYSIS | 226 |
| 7.1 | Overview | 226 |
| 7.2 | Modeling Parameters | 227 |
| 7.2.1 | Material..... | 227 |
| 7.2.2 | Configuration..... | 234 |
| 7.2.3 | Mesh | 237 |
| 7.2.4 | Solver Parameters | 238 |

| | | |
|-------|---|-----|
| 7.3 | Model Validation | 238 |
| 7.3.1 | Effect of various material parameters..... | 239 |
| 7.3.2 | Results from different mesh types | 240 |
| 7.3.3 | Comparison of damage patterns at different load steps..... | 242 |
| 7.3.4 | Summary of Model Validation | 246 |
| 7.4 | Analytical Investigation..... | 246 |
| 7.5 | Results and Discussion of the Numerical Investigation | 255 |
| 7.5.1 | Evaluation of the Strength of Numerical Specimens with Identical Adjoining Members | 255 |
| 7.5.2 | Evaluation of the Strength of Numerical Specimens with Various Strut Angles.... | 277 |
| 7.6 | Summary | 291 |
| 8. | CONCLUSIONS | 293 |
| | APPENDIX A. MEASUREMENT OF BEND RADII | 297 |
| | APPENDIX B. DETERMINATION OF INTERNAL FORCES FOR STRUT-AND-TIE MODELS | 298 |
| | APPENDIX C. LIST OF EVALUATION DATABASE | 309 |
| | APPENDIX D. LIST OF NUMERICAL SPECIMENS | 313 |
| | APPENDIX E. FULL-FIELD STRAIN MAP FROM DIGITAL IMAGE CORRELATION MEASUREMENT | 315 |
| | APPENDIX F. STRESS-STRAIN CURVES OF LONGITUDINAL REINFORCEMENT | 329 |
| | REFERENCES | 332 |

LIST OF TABLES

| | |
|---|-----|
| Table 2-1 Nodal zone coefficient (adapted from ACI 318-19 ¹) | 56 |
| Table 2-2 Strut coefficient (adapted from ACI 318-19 ¹)..... | 56 |
| Table 2-3 Minimum distributed reinforcement (adapted from ACI 318-19 ¹) | 57 |
| Table 2-4 CTT-nodal zone coefficients in the literature..... | 64 |
| Table 3-1 Summary of specimens..... | 69 |
| Table 3-2 Concrete mixture designs | 84 |
| Table 3-3 Summary of bends..... | 87 |
| Table 4-1 Summary of test results, joint efficiency, and ductility of S-Series specimens | 107 |
| Table 4-2 Summary of test results, joint efficiency, and ductility of D-Series specimens..... | 125 |
| Table 4-3 Summary of test results, joint efficiency, and ductility of C-Series specimens | 140 |
| Table 4-4 Summary of test results, joint efficiency, and ductility of B-Series specimens | 149 |
| Table 4-5 Summary of test results and joint efficiency of M-Series specimens | 157 |
| Table 5-1 Summary of specimens and test variables..... | 168 |
| Table 5-2 Categorization of S-Series and D-Series specimens | 170 |
| Table 5-3 Summary of test results of S-Series and C-Series specimens | 174 |
| Table 5-4 Categorization of C-Series specimens..... | 175 |
| Table 5-5 Categorization of B-Series specimens..... | 178 |
| Table 5-6 Categorization of M-Series specimens..... | 184 |
| Table 5-7 Stress acting on concrete under bar bend for..... | 186 |
| Table 5-8 Stress analysis of bars for specimens in the Strength Compromised category | 189 |
| Table 6-1 Collected knee joints tested with closing moments from the literature..... | 194 |
| Table 6-2 Relationship between applied load, internal axial force, and bending moment at the joint face | 200 |
| Table 6-3 Magnitudes of tie forces | 207 |
| Table 6-4 Magnitudes of resultant strut forces | 208 |
| Table 6-5 Orientations of resolved struts..... | 208 |
| Table 6-6 Parameters for the strut-and-tie model | 213 |

| | |
|--|-----|
| Table 6-7 Summary of analysis results using sectional analysis for specimens in the current study | 216 |
| Table 6-8 Summary of analysis results using the strut-and-tie method for specimens in the current study | 220 |
| Table 7-1 Concrete material model..... | 228 |
| Table 7-2 FEA numerical specimens with identical adjoining members | 248 |
| Table 7-3 FEA numerical specimens with different adjoining members (FEM-B-Series) | 249 |
| Table 7-4 Concrete material model used in the parametric analysis | 253 |
| Table 7-5 Parameters defining bond-slip relationship | 254 |
| Table 7-6 FEA results and calculated strengths of FEM-S-Series and FEM-D-Series specimens | 256 |
| Table 7-7 FEA results and calculated strengths of FEM-C-Series specimens | 264 |
| Table 7-8 Evaluation of cover effect based on FEA results | 265 |
| Table 7-9 Evaluation of cover effect based on both FEA and experimental results..... | 266 |
| Table 7-10 FEA results and calculated strengths of FEM-TR-Series specimens..... | 269 |
| Table 7-11 Evaluation of the effect of transverse reinforcement based on both FEA and experimental results | 271 |
| Table 7-12 Comparison of FEA results and STM results..... | 274 |
| Table 7-13 FEA results and calculated strengths of FEM-B-Series specimens | 278 |

LIST OF FIGURES

| | |
|---|----|
| Figure 1-1 Examples of knee joints | 20 |
| Figure 1-2 Knee joints under moments in different directions | 21 |
| Figure 2-1 Extension of D-region of a knee joint | 25 |
| Figure 2-2 Linear and non-linear stress distribution of knee joints under closing moments..... | 25 |
| Figure 2-3 Example of strut-and-tie model for knee joints..... | 26 |
| Figure 2-4 Proportioning CTT node at outer corner of knee joints | 27 |
| Figure 2-5 Curved-bar node (adapted from Klein ²² and ACI 318-19 ¹) | 27 |
| Figure 2-6 Specimen and loading configuration of Richart et al. ² (adapted from Richart et al. ²) | 29 |
| Figure 2-7 Reinforcement details investigated in the literature (adapted from Swann, ⁴ Mayfield et al., ⁵ and Johansson ¹³) | 31 |
| Figure 2-8 Schematic of test setup for cantilever beam and knee joint | 32 |
| Figure 2-9 Additional reinforcement details investigated in the literature (adapted from Zouzou et al. ⁷ and Marchetto et al. ¹⁶) | 32 |
| Figure 2-10 Details with and without splices (adapted from Plos ⁹) | 33 |
| Figure 2-11 Schematic of test setup used by Plos ⁹ | 34 |
| Figure 2-12 Splice details (adapted from Lundgrn ¹¹) | 34 |
| Figure 2-13 Additional splice details (adapted from Yuan et al. ⁶) | 35 |
| Figure 2-14 Schematic of test setup used by Yuan et al. ⁶ | 35 |
| Figure 2-15 Complex reinforcement details (adapted from Luo et al. ⁸ and Bai et al. ²⁶) | 36 |
| Figure 2-16 Schematic of test setup used by Luo et al. ⁸ | 37 |
| Figure 2-17 Reinforcement details (adapted from Stroband and Kolpa ²³) | 38 |
| Figure 2-18 Schematic of test setup used by Stroband and Kolpa ²³ | 39 |
| Figure 2-19 Shear force in closing knee joint | 40 |
| Figure 2-20 Effective joint area (adapted from ACI 318-19 ¹)..... | 41 |
| Figure 2-21 Examples of D-regions (adapted from Schlaich et al. ¹⁹ and ACI 318-19 ¹)..... | 43 |
| Figure 2-22 Components of a strut-and-tie model..... | 45 |
| Figure 2-23 Example of stress trajectory near the end of a deep beam (adapted from Williams et al. and Birrcher et al. ^{47,54}) | 45 |

| | |
|--|----|
| Figure 2-24 Types of nodes | 46 |
| Figure 2-25 Steps for implementing the strut-and-tie method ^{17,47} | 46 |
| Figure 2-26 Geometry of a D-region | 47 |
| Figure 2-27 Example of loads at interface between B-Region and D-Region | 48 |
| Figure 2-28 Example strut-and-tie model of cantilever beam and joint | 49 |
| Figure 2-29 Stresses on hydrostatic and non-hydrostatic node (adapted from Brown et al. ⁵⁵) | 51 |
| Figure 2-30 Hydrostatic node | 51 |
| Figure 2-31 Example of the typical geometry of a CCC node (adapted from Brown et al. ⁵⁵) | 52 |
| Figure 2-32 Example of the typical geometry of a CCT node (adapted from Brown et al. ⁵⁵) | 53 |
| Figure 2-33 Example of different CTT nodes in strut-and-tie model ⁵⁶ | 54 |
| Figure 2-34 Example of the typical geometry of a CCT node located at a load or bearing plate (adapted from ACI 318-19 ¹) | 54 |
| Figure 2-35 Available length for anchorage (adapted from ACI 318-19 ¹)..... | 58 |
| Figure 2-36 Typical strut-and-tie model for closing knee joints | 59 |
| Figure 2-37 Stress state at curved-bar node ²² assumed by ACI 318-19 ¹ | 61 |
| Figure 2-38 Stress state at curved-bar node in CEP-fib ⁵⁴ | 62 |
| Figure 3-1 Typical specimen details for Series I | 71 |
| Figure 3-2 Nomenclature for Series I | 72 |
| Figure 3-3 Typical specimen details for Series II..... | 73 |
| Figure 3-4 Nomenclature for Series II | 74 |
| Figure 3-5 Typical specimen details for Series III..... | 76 |
| Figure 3-6 Nomenclature for Series III..... | 77 |
| Figure 3-7 Typical specimen details for Series IV | 79 |
| Figure 3-8 Nomenclature for Series IV | 80 |
| Figure 3-9 Typical specimen details for Group TR in Series V | 81 |
| Figure 3-10 Typical specimen details for Group LS in Series V..... | 82 |
| Figure 3-11 Nomenclature for Series V..... | 83 |
| Figure 3-12 Formwork..... | 85 |
| Figure 3-13 Reinforcing bar bending table | 86 |
| Figure 3-14 Measurement of bend radius | 87 |

| | |
|---|-----|
| Figure 3-15 Construction of reinforcement cages | 88 |
| Figure 3-16 Slump test..... | 88 |
| Figure 3-17 Casting and curing..... | 89 |
| Figure 3-18 Test Frame..... | 91 |
| Figure 3-19 Load cells | 92 |
| Figure 3-20 Hydraulic cylinders and T-connector with pressure transducer..... | 92 |
| Figure 3-21 Instrumentation for displacement and rotation | 93 |
| Figure 3-22 Linear potentiometer | 93 |
| Figure 3-23 Inclometers..... | 94 |
| Figure 3-24 Installation of strain gauge | 94 |
| Figure 3-25 Strain gauge with full protection..... | 95 |
| Figure 3-26 Strain gauge arrangement..... | 96 |
| Figure 3-27 Digital image correlation system | 97 |
| Figure 3-28 Crack marking and measuring | 98 |
| Figure 3-29 Concrete compressive strength test..... | 99 |
| Figure 3-30 Test for modulus of elasticity test of concrete | 100 |
| Figure 3-31 Test for splitting tensile strength of concrete..... | 101 |
| Figure 3-32 Test for modulus of rupture of concrete..... | 102 |
| Figure 3-33 Test for tensile strength of reinforcement | 103 |
| Figure 4-1 Load-displacement curves of knee joint specimens: (a) Group S-1, (b) Group S-2, (c) Group S-3..... | 106 |
| Figure 4-2 Anchorage failure of Specimen S-27-R11-L | 107 |
| Figure 4-3 Crack maps and photos of Group S-1 specimens..... | 110 |
| Figure 4-4 Crack maps and photos of Group S-2 specimens..... | 111 |
| Figure 4-5 Crack maps and photos of Group S-3 specimens..... | 112 |
| Figure 4-6 Typical crack formation and propagation in joints of S-Series specimens | 113 |
| Figure 4-7 Measured strains in the reinforcing bars | 115 |
| Figure 4-8 Stress transmission mechanism within a joint | 118 |
| Figure 4-9 Stress flow in a joint as bars yield..... | 119 |

| | |
|--|-----|
| Figure 4-10 Load-displacement curves of knee joint specimens: (a) Group D-1, (b) Group D-2 | 124 |
| Figure 4-11 Relationship between C and displacement ductility factor μ for S-Series and D-Series specimens | 127 |
| Figure 4-12 Crack maps and photos of Group D-1 specimens | 128 |
| Figure 4-13 Crack maps and photos of Group D-2 specimens | 129 |
| Figure 4-14 Typical crack formation and propagation in joints of D-Series specimens | 130 |
| Figure 4-15 Damage on the top face of each D-Series specimen | 133 |
| Figure 4-16 Measured strains in the reinforcing bars of Group D-1 | 136 |
| Figure 4-17 Measured strains in the reinforcing bars of Group D-2 | 137 |
| Figure 4-18 Load-displacement curves of C-Series knee joint specimens | 140 |
| Figure 4-19 Crack maps and photos of C-Series specimens (Part 1) | 142 |
| Figure 4-20 Crack maps and photos of C-Series specimens (Part 2) | 143 |
| Figure 4-21 Typical crack formation and propagation in joints of C-Series specimens | 144 |
| Figure 4-22 Damage patterns on top surfaces of C-Series specimens | 145 |
| Figure 4-23 Measured strains in the reinforcing bars of C-Series specimens | 146 |
| Figure 4-24 Load-displacement curves of B-Series knee joint specimens | 150 |
| Figure 4-25 Crack maps and photos of B-Series specimens | 151 |
| Figure 4-26 Typical crack formation and propagation in joints of B-Series specimens | 151 |
| Figure 4-27 Damage patterns on top surfaces of B-Series specimens | 153 |
| Figure 4-28 Strain readings along reinforcing bars of B-Series specimens | 154 |
| Figure 4-29 Load-displacement curves of M-Series knee joint specimens | 156 |
| Figure 4-30 Damage patterns of specimens in M-Series (No.8 reinforcement) | 159 |
| Figure 4-31 Damage patterns of specimens in M-Series (No.8 reinforcement) | 160 |
| Figure 4-32 Damage patterns on top surfaces of M-Series specimens | 161 |
| Figure 4-33 Strain readings along reinforcing bars of Group TR specimens | 162 |
| Figure 4-34 Strain readings along reinforcing bars of Group LS specimens | 163 |
| Figure 5-1 Categorization of specimens | 169 |
| Figure 5-2 Relationship between joint efficiency and bend radius ratio for S-Series and D-Series specimens | 171 |
| Figure 5-3 Comparison of load-displacement behaviors of S-Series and C-Series specimens .. | 173 |

| | |
|---|-----|
| Figure 5-4 Relationship between joint efficiency and bend radius ratio for C-Series and S-Series specimens | 177 |
| Figure 5-5 Relationship between joint efficiency and bend radius ratio for B-Series and S-Series specimens | 179 |
| Figure 5-6 Calculation of θ_c for B-Series specimens | 180 |
| Figure 5-7 Comparison of load-relative displacement behaviors of S-Series, Group LS, and Group TR specimens | 183 |
| Figure 5-8 Relationship between joint efficiency and bend radius ratio for Group LS, Group TR, D-Series, and S-Series specimens | 185 |
| Figure 5-9 Relationship between measured bend radius and strut width | 188 |
| Figure 6-1 Schematics of loading configurations for specimens in the evaluation database | 195 |
| Figure 6-2 Number of specimens with each loading configuration in the evaluation database | 196 |
| Figure 6-3 Histograms of primary variables in the evaluation database | 197 |
| Figure 6-4 Notation for sectional analysis at nominal flexural strength | 199 |
| Figure 6-5 Structural analysis for Portal system | 200 |
| Figure 6-6 Notation for sectional analysis if longitudinal reinforcement has not yielded | 201 |
| Figure 6-7 Modified Hognestad model (adapted from Hognestad ^{80,79} and Wight et al. ¹⁷) | 202 |
| Figure 6-8 Selected strut-and-tie models for different loading configurations | 205 |
| Figure 6-9 Resolved struts and resulting orientations | 207 |
| Figure 6-10 Geometry of the CCC node as a hydrostatic node | 210 |
| Figure 6-11 Geometry of the CTT node when headed bars were used | 210 |
| Figure 6-12 Strength ratio based on sectional analysis versus diagonal strut width ratio for specimens in the current study | 215 |
| Figure 6-13 Strength ratio based on sectional analysis versus diagonal strut width ratio for specimens in the evaluation database | 218 |
| Figure 6-14 Strength ratio based on the strut-and-tie method versus diagonal strut width ratio for specimens in the current study | 219 |
| Figure 6-15 Strength ratio based on the strut-and-tie method versus diagonal strut width ratio for specimens in the evaluation database | 222 |
| Figure 7-1 Crack opening (adapted from Cervenka et al. ⁶⁷) | 229 |
| Figure 7-2 Stress-strain curve of concrete (adapted from Cervenka et al. ⁸⁴) | 230 |
| Figure 7-3 Critical compressive displacement (adapted from Cervenka et al. ⁸⁴) | 231 |

| | |
|--|-----|
| Figure 7-4 Reduction of compressive strength of concrete due to cracks (adapted from Cervenka et al. ⁸⁴)..... | 231 |
| Figure 7-5 Material models for reinforcement and steel plates | 233 |
| Figure 7-6 Modeling specimen components in ATENA for validation | 234 |
| Figure 7-7 Load cases | 236 |
| Figure 7-8 Mesh types (adapted from Cervenka et al. ⁸⁴)..... | 237 |
| Figure 7-9 Mesh types and sizes used for validation..... | 238 |
| Figure 7-10 Validation of FE models with various material parameters..... | 240 |
| Figure 7-11 Validation of FE models with various element types and sizes..... | 242 |
| Figure 7-12 Comparison between actual and predicted damage patterns for Specimen S-18-R3 | 243 |
| Figure 7-13 Comparison between actual and predicted damage patterns for Specimen S-18-R6 | 244 |
| Figure 7-14 Comparison between actual and predicted damage patterns for Specimen S-18-R6 | 245 |
| Figure 7-15 Nomenclature for numerical specimens..... | 247 |
| Figure 7-16 Configuration of numerical specimens (with identical adjoining members) | 251 |
| Figure 7-17 Different adjoining member depths of numerical specimens in FEM-B-Series | 252 |
| Figure 7-18 Bond-slip relationship used in ATENA 3D (adapted from ATENA 3D ⁸⁴ and CEB-FIP model code ²⁵)..... | 254 |
| Figure 7-19 Load-displacement curves of FEM-S-Series and FEM-D-Series specimens | 259 |
| Figure 7-20 Stress along longitudinal reinforcement from analytical results for Group FEM-DD-21 specimens | 260 |
| Figure 7-21 Relationship between P_{FEA}/P_{calc} and bend radius ratio for FEM-S-Series and FEM-D-Series specimens | 261 |
| Figure 7-22 Load-displacement curves of FEM-C-Series specimens | 263 |
| Figure 7-23 Load-displacement curves of Group FEM-C-13 specimens..... | 264 |
| Figure 7-24 Relationship between P_{FEA}/P_{calc} and bend radius ratio for FEM-C-Series | 267 |
| Figure 7-25 Load-displacement curves of FEM-TR-Series specimens..... | 270 |
| Figure 7-26 Relationship between P_{FEA}/P_{calc} and bend radius ratio for specimens with minimum distributed reinforcement in the joint..... | 272 |
| Figure 7-27 Strength ratio P_{FEA}/P_{STM} versus the bend radius ratio | 275 |
| Figure 7-28 Load-displacement curves of Group FEM-B-17 specimens | 280 |

| | |
|--|-----|
| Figure 7-29 Load-displacement curves of Group FEM-BD-18 specimens | 281 |
| Figure 7-30 Relationship between strength ratio based on various strength predictions and diagonal strut angle for FEM-B-Series specimens with a bend radius larger than a standard bend | 284 |
| Figure 7-31 Load-displacement curves of FEM-B-Series specimens with a standard bend | 286 |
| Figure 7-32 Relationship between strength ratio based on various strength predictions and diagonal strut angle for FEM-B-Series specimens with a bend radius of a standard bend | 288 |
| Figure 7-33 Relationship between strength ratio P_{FEA}/P_{calc} and bend radius ratio for FEM-B-Series specimens | 290 |

ABSTRACT

Reinforced concrete frame corners (that is, knee joints) subjected to closing moments plays an important role of transmitting stress between the two adjoining members. Being categorized as geometric discontinuity regions (D-regions), knee joints cannot be correctly analyzed and designed using traditional sectional analysis procedures. Instead, the strut-and-tie method is particularly suitable for such joints. Although strut-and-tie models provide the means to represent the distribution of stresses within a closing knee joint, questions arise when a curved-bar node is used to model the bar bend of the longitudinal reinforcement at the outer corner. The code-specified design expressions for curved-bar nodes have not been experimentally verified; therefore, the accuracy and conservativeness of the expressions remain unknown. This research project is aimed to provide insights to the proper application of the strut-and-tie method, through the concept of curved-bar nodes, to knee joints under closing moments.

An experimental program consisting of 24 specimens was conducted to investigate the effect of curved-bar nodes on knee joints under closing moments. An evaluation of the code-specified design expressions was included. The results demonstrate that the minimum code-specified bend radius is appropriate. The current requirements related to bond along the bar bend and clear side cover are shown to be conservative. Based on the test results, a procedure for constructing proper strut-and-tie models for closing knee joints is proposed and verified using an evaluation database consisting of 116 knee joint tests from the literature. Compared to other strength predictive methods and the code-specified strut-and-tie method, the proposed strut-and-tie method mitigates unconservativeness and delivers improved accuracy.

In addition to the experimental program and the proposed procedure, non-linear finite element analysis (FEA) using the software ATENA-3D was employed to conduct a parametric analysis as a supplement to the experimental data. Seventy-two numerical models were analyzed to further evaluate the code-specified expressions and the proposed strut-and-tie method. The FEA results are in a good agreement with the experimental observations and corroborate the conclusions from the experimental program regarding current code requirements. Moreover, the parametric analysis further supports the application of the proposed strut-and-tie methodology to knee joints under closing moments.

1. INTRODUCTION

1.1 Overview

Reinforced concrete (RC) frame corners (that is, knee joints) are formed when two structural concrete members (beams/columns) oriented perpendicular to each other are joined together at a joint as shown in Figure 1-1. Depending on the direction of the resisted moments, knee joints are primarily categorized into two types: closing corners and opening corners, as shown in Figure 1-2. Knee joints transfer moments and shear between adjoining members, directly affecting the safety of the assembly. The design of closing knee joints has long relied on “good practice.” Commonly applied detailing methods for closing knee joints are empirical. Common details in the field lack the support of analytical methods. Simple calculations have not been available to predict the efficiency of closing knee joints.

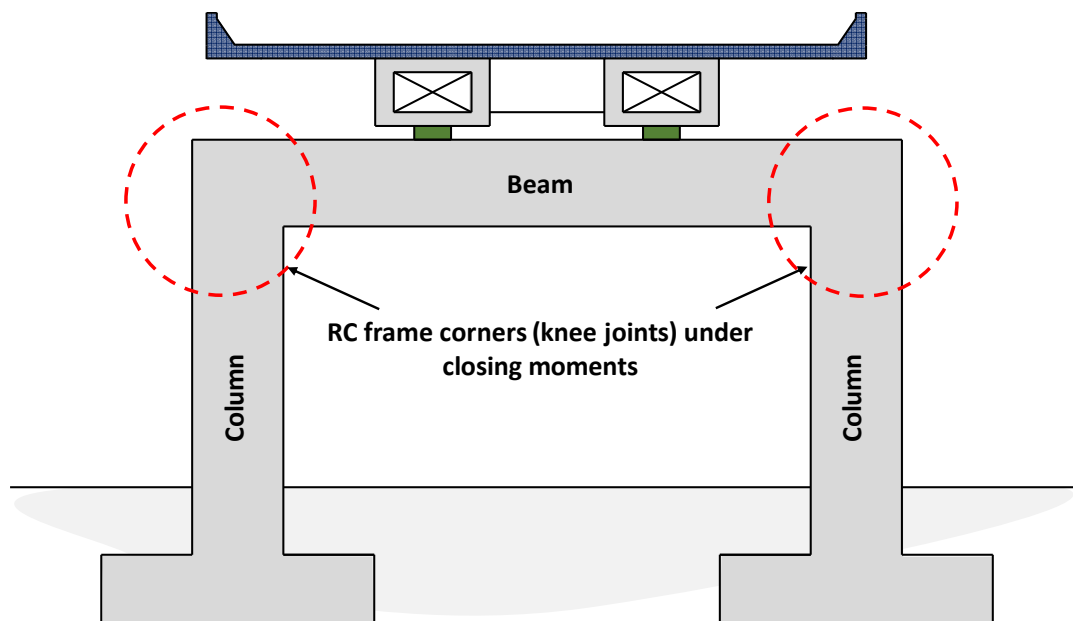


Figure 1-1 Examples of knee joints

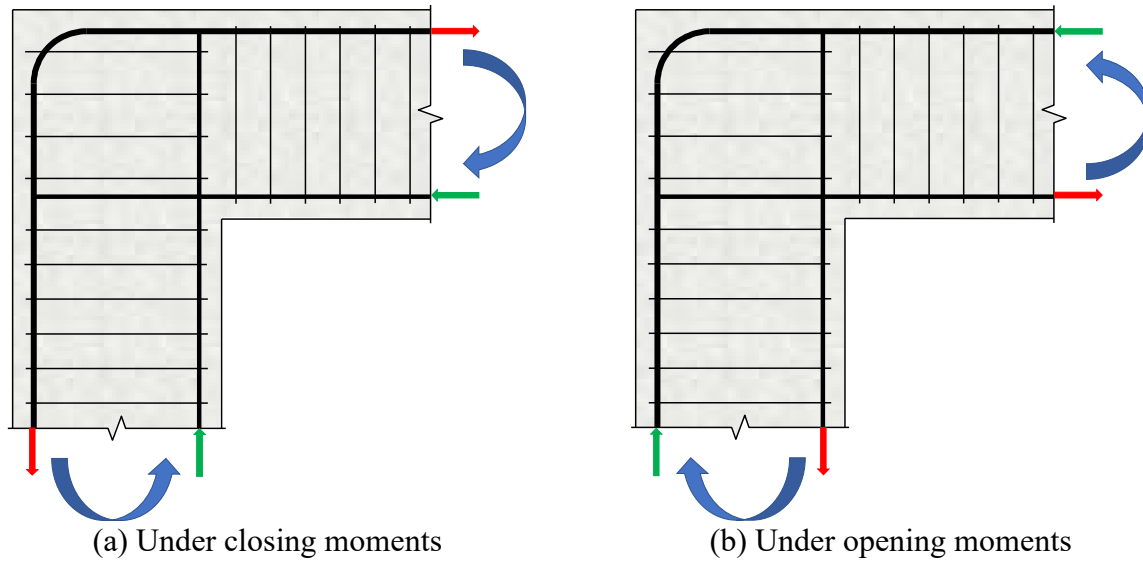


Figure 1-2 Knee joints under moments in different directions

The geometric discontinuity at closing knee joints creates a discontinuity region (D-region), and the application of the strut-and-tie method (STM) is therefore particularly suitable for such regions. Within the strut-and-tie model of a knee joint under closing moments, a unique CTT node forms at the outside of the joint. As the design code suggests, the CTT node can be modeled as a curved-bar node. Design expressions for curved-bar nodes were recently included in the 2019 edition of ACI 318.¹ The equations, however, have not been experimentally verified. The accuracy and the conservativeness remain unclear. Moreover, it is unknown if there are other factors that affect the design of closing knee joints. In other words, the domain of application is also uncertain. Research is needed to verify the appropriateness of the current design provisions.

As part of this research project, an experimental program consisting of 24 closing knee joint specimens was conducted to investigate the behavior of curved-bar nodes and potential influential factors. This research included the first experimental program that particularly focused on curved-bar nodes, providing a better understanding of the failure mechanism and stress transmission within the joint. Modifications to the code-specified design equations based on this research result in a more accurate design method.

Along with the experimental investigation, an evaluation database that includes a total of 116 closing knee joint tests was established. The evaluation database was used to verify proposed modifications to current code provisions. Furthermore, a procedure for constructing appropriate

strut-and-tie models for closing knee joints was verified using the evaluation database. The applicability of sectional analysis and joint shear analysis was also evaluated.

In addition to the database analysis, as a supplement to the experimental program, a parametric analysis was conducted using the finite element method software ATENA-3D. After calibrating material properties and mesh size based on three specimens from the experimental program used on benchmarks, 72 numerical models with a larger domain of parameters were analyzed to evaluate the code-specified design expressions.

1.2 Project Objectives

The primary research objective was to refine/verify the design expressions specified in the current design code through an experimental program, a database analysis, and a finite element parametric analysis. The following additional objectives were also achieved as a part of the research:

1. Investigate the effects of the bend radius of continuous longitudinal reinforcing bars on the overall behavior of frame corners as predicted by the curved-bar node design method.
2. Assess the curved-bar node design method and provide suggestions for refining the procedure.
3. Evaluate the ability of the strut-and-tie method to predict the strength and failure mechanisms of knee joints subjected to closing moment.
4. Compare the behavior of closing knee joints with continuous longitudinal bars and those with other details (bar splices).
5. Establish an evaluation database of closing knee joints and provide experimental data to enrich the database.
6. Develop a modeling technique using non-linear finite element analysis.
7. Conduct a non-linear finite element parametric analysis as a supplement to further evaluate the proposed design expressions.

1.3 Organization

The historical development of design and analysis method for knee joints subjected to closing moments is first introduced in Chapter 2 through the presentation of a thorough literature

review. The details of the experimental program are presented in Chapter 3, including test specimens, fabrication of the specimens, test setup, instrumentation, and material tests. In Chapter 4, the test results are presented. The discussion includes the effect of the bend radius on the behavior, failure mode, and stress transmission of closing knee joints. In Chapter 5, based on the test results, a detailed discussion is presented about the effect of other factors on the behavior of curved-bar nodes and closing knee joints, including multiple layers of longitudinal reinforcement, reduced clear side cover, transverse reinforcement, lap-spliced longitudinal reinforcement, and diagonal strut angles. Evaluation/refinement of the design expressions is also discussed in this chapter. In Chapter 6, a procedure for constructing appropriate strut-and-tie models is introduced and verified using an established evaluation database. The method is also compared to other strength predicting methods in this chapter. Non-linear finite element analysis of closing knee joints using the software ATENA-3D is introduced in Chapter 7. Lastly, in Chapter 8, conclusions and design recommendations for curved-bar nodes and closing knee joints are presented.

2. BACKGROUND

In this chapter, the development of design and analysis methods for reinforced concrete (RC) frame corners (that is, knee joints) is presented. First, past experiments on knee joint under closing moments and various design expressions from the literature are introduced, and current design code provisions for knee joints are described. Second, the strut-and-tie method (STM), as a rational and unified design method, is presented. Next, justification for applying the STM to knee joint is provided. Lastly, research needs are presented on the basis of current uncertainties when using the STM to design knee joints subjected to closing moments.

2.1 Overview of Knee Joints

From a safety standpoint, knee joints should be designed and constructed to be at least as strong as the adjoining members. That is, knee joints shall not fail before the adjoining members reach their maximum moment capacities. To achieve this requirement, several detailing methods²⁻¹⁶ have been proposed and experimentally verified to be effective. These methods, however, are empirical; no design guidelines based on simple analytical models are available. Moreover, these methods were proposed with consideration of a limited number of variables. The moment capacity ratio, which is defined as the ratio of the experimental moment capacity of knee joints to the smaller calculated moment capacity of the two adjoining members, cannot be systematically guaranteed to be greater than one.

Knee joints are classified as discontinuity regions (D-regions) because of the presence of a geometric discontinuity.^{1,17} According to Saint Venant's principle, the D-region of a knee joint extends from each joint face for a distance of one member depth as shown in Figure 2-1. Unlike regions of structural members following the Bernoulli hypothesis or beam theory (classified as B-regions), which assumes that plane sections remain plane, these regions have a non-linear strain profile as well as a nonlinear stress distribution in the joint as shown in Figure 2-2. Theoretically, knee joints should not be designed based on flexural analysis. Nevertheless, one common method to address knee joints under closing moments is to employ flexural analysis and joint shear analysis.^{1,18}

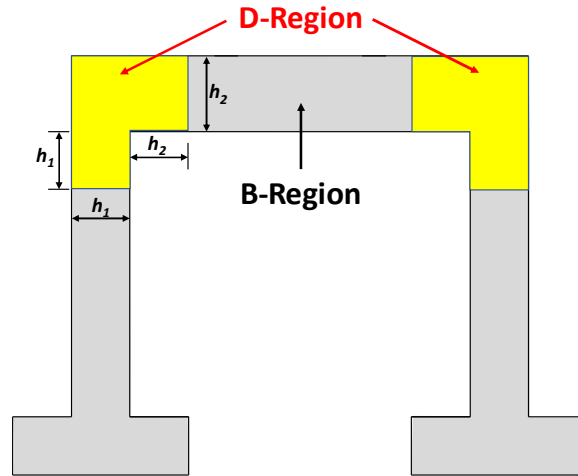


Figure 2-1 Extension of D-region of a knee joint

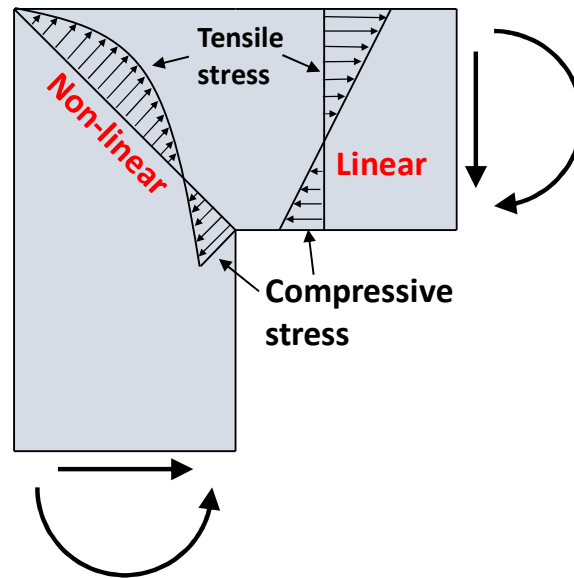


Figure 2-2 Linear and non-linear stress distribution of knee joints under closing moments

Relying on incorrect assumptions, the application of traditional sectional design methods to knee joints is questionable in regard to their predictive ability. Thus, a method is needed to ensure the consistent design of safe and serviceable knee joints. Because knee joints are classified as D-regions, the strut-and-tie method (STM)^{19–21} can be used to design such joints. STM is a powerful design tool in which the stress flow within a knee joint is represented by compression members (struts) and tension members (ties) joined at nodes (Figure 2-3). Accordingly, reinforcement can be proportioned, and the capacities of struts and nodes can be evaluated.

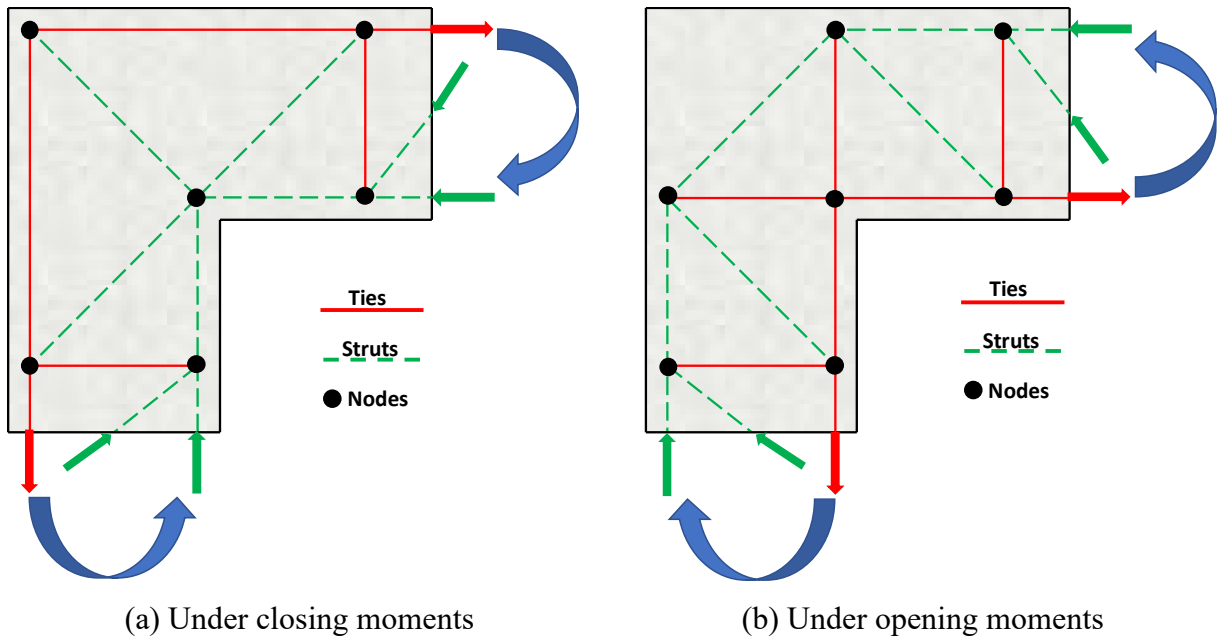


Figure 2-3 Example of strut-and-tie model for knee joints

For a knee joint subjected to closing moments, a CTT node forms at the outside of the joint. In this case, the two ties represent continuous reinforcing bars passing through the corner with a 90-degree bar bend. From the strut-and-tie model, it is implied that the strut force acts at the region defined by the bar bend as shown Figure 2-4. The concept was introduced in studies by Schlaich and Schafer^{19,20}. Nevertheless, not until 2008 did Klein²² propose an analytical method for this type of node. As explained by Klein,²² the CTT node can be modeled as a curved-bar node. In addition to the radial stress that acts on the inner bar bend, Klein²² suggested that the difference in force between the two ties develops through circumferential bond stress along the bar bend as shown in Figure 2-5. Also, the clear side cover has to be large enough to prevent potential splitting.

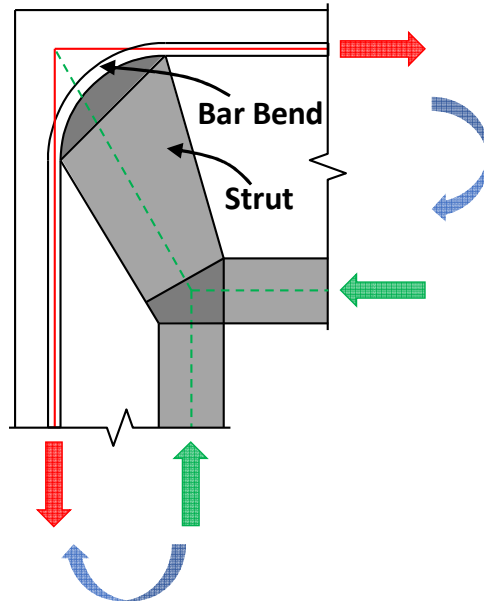


Figure 2-4 Proportioning CTT node at outer corner of knee joints

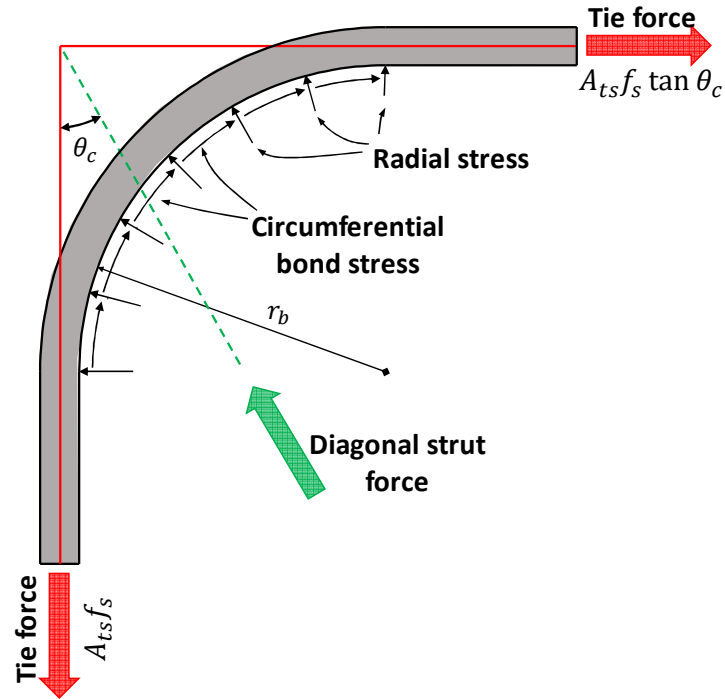


Figure 2-5 Curved-bar node (adapted from Klein²² and ACI 318-19¹)

Several experimental studies^{3,4,8,14,23} investigating closing frame corners with continuous bars along the outside of the joint have shown that the moment capacity ratio is related to the bend radius, the clear side cover, and the mechanical reinforcement ratio of the longitudinal bars. Finite element analyses²⁴ have also indicated that significant stress is transmitted between the bar bend and the concrete strut, implying that the radial stress at the bar bend is a critical factor in design. The proportioning method for curved-bar nodes is incorporated in the current ACI 318-19¹ code. However, very limited tests directly relevant to the evaluation of curved-bar nodes are presented in the literature.

In addition to the curved-bar node, another crucial element that determines the capacity of knee joints under closing moments is the diagonal strut. The diagonal strut plays the role of transmitting force between the CTT node at the outer corner and the CCC node at the re-entrant corner. That is, the capacity of the diagonal strut also affects the load-carrying capacity of knee joints. Located in a beam-column joint, the diagonal strut is classified as an interior strut in accordance with definitions within ACI 318-19.¹ According to ACI 318-19,¹ a strut coefficient of 0.75 is applied to calculate the effective compressive strength of concrete for an interior strut. Further discussion on this factor for interior struts is provided in Section 2.5.2.

2.2 Experimental Studies on Knee Joints under Closing Moments

A review of past studies on the behavior of knee joints under closing moments is presented in this section. Most past studies explored detailing methods for such knee joints and proposed empirical design expressions. Studies that incorporated finite element analysis and analytical analysis are included.

2.2.1 Early studies

The earliest study on knee joints under closing moments identified in the literature is from the year 1938. Richart et al.² conducted an experimental program to investigate the moment capacity and elastic properties of knee joints under closing moments. It was believed that high stress concentration occurred at the re-entrant corner of knee joints under closing moments. The authors therefore tested knee joint specimens with different types of fillets and chamfers at the re-entrant corner and outer corner, respectively (see Figure 2-6). In addition to the varying

geometries, the effects of rapidly applied load and sustained load were investigated. The specimens were loaded vertically to create closing moments in the joints as shown in Figure 2-6. The load-carrying capacity of each specimen was measured and compared to that of the specimens without fillets or chamfers. For the tests incorporating sustained loads, approximately one-third of the peak load was first applied and held for either one year or five months, and then the specimen was loaded until failure.

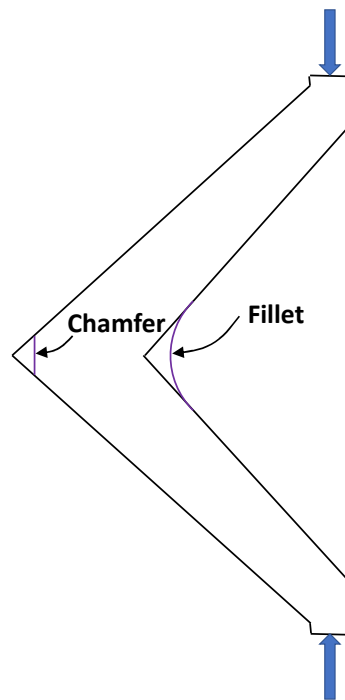


Figure 2-6 Specimen and loading configuration of Richart et al.² (adapted from Richart et al.²)

When applying loads monotonically, filleted corners increased strengths by 26 percent to 30 percent compared to specimens without a fillet at the re-entrant corner. The chamfering at the outer corner, however, had negligible effect on strength. The authors attributed this observation to a reduction in the moment arm of the applied load and a reduction of the concentrated stress at the inner corner. Another important finding was that specimens subjected to sustained load were able to achieve the same strength level as their counterparts subjected to rapidly applied loads. Overall, the study provided insights into the advantages of fillets as an effective use of material.

2.2.2 Studies on reinforcement details

After the earliest study on closing knee joints, which addressed the stress concentration at the inner corner, the primary focus was shifted toward reinforcement details in knee joints that lead to the ability to effectively resist closing moments. These studies were developed to experimentally verify if the proposed detailing methods can prevent the joint from failing before the failure of the adjoining members.

2.2.2.1 Continuous longitudinal reinforcing bars and headed reinforcing bars

Several studies in the literature included tests on knee joint specimens with continuous longitudinal tension reinforcement passing through the joint. Swann⁴ investigated the joint efficiency of a conventional detail (see Figure 2-7(a)) for closing knee joints, and compared the results to four other details shown in Figure 2-7(b) to (e). For each specimen, one adjoining member stood vertically and was fixed to the floor, while the other adjoining member was a cantilever beam. A load was vertically applied near the end of the beam to create closing moments at the joint (as shown schematically in Figure 2-8). The results revealed that the first four details, including the conventional detail, resulted in strengths less than predicted based on calculated flexural strength using the Hognestad stress block. Only the fifth detail (see Figure 2-7(e)), which had diagonal bars welded to the longitudinal reinforcement, was capable of resisting a load higher than expected. The author attributed the compromised strengths to the bearing failure of concrete in the diagonal compression zone at the bar bend. The diagonal welded bars of the fifth detail reduced stress in this region, resulting in a higher strength.

In contrast to the viewpoints proposed by Swann,⁴ Mayfield et al.⁵ believed that the strength of closing knee joints is not sensitive to reinforcement details. In other words, regardless of the reinforcement details that are chosen, the researchers stated that closing knee joints are able to reach a joint efficiency of 1.0. The authors supported the statement with an experimental program consisting of 15 knee joint specimens made of lightweight concrete. The details included six patterns as shown in Figure 2-7(a), (c), (d), (f), and (g). The detail of Figure 2-7(f) had two different stirrup spacings. The specimens were L-shaped and tested using a test setup similar to the setup used in Swann's study.⁴ All six specimens reached a load-carrying capacity higher than predicted based on flexural strength of the horizontal leg analyzed based on the method of stress block.

Similar details as presented in Figure 2-7(a) and (c) were experimentally investigated by Johansson.¹³ Unlike Swann⁴ and Mayfield et al.⁵, each L-shaped specimen was stood vertically and the load was applied from the top, similar to the setup used by Richart et al.² (see Figure 2-6). By comparing the test results to other studies, the author supported the point that the particular reinforcement details are not important to the capacity of closing knee joints.

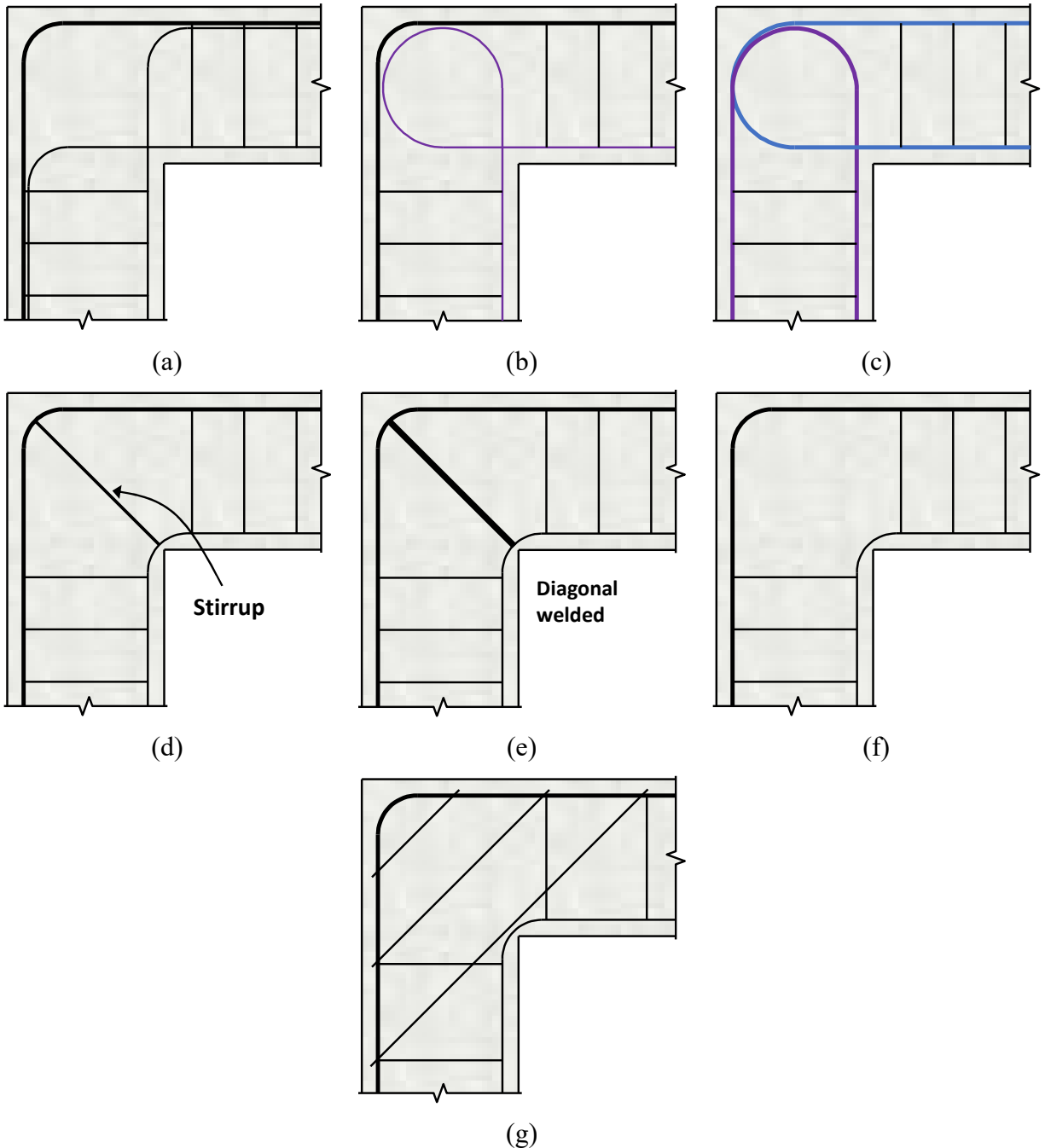


Figure 2-7 Reinforcement details investigated in the literature (adapted from Swann,⁴ Mayfield et al.,⁵ and Johansson¹³)

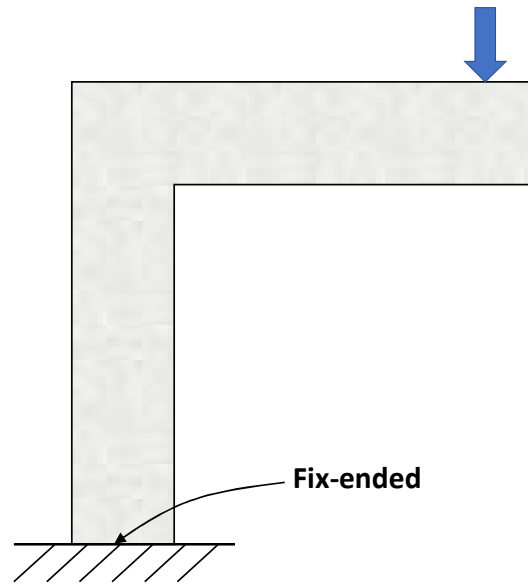


Figure 2-8 Schematic of test setup for cantilever beam and knee joint

Zouzou et al.⁷ introduced a detail that confines the potential zone of concentrated diagonal stresses with closed stirrups perpendicularly intersecting the diagonal as shown in Figure 2-9(b). To evaluate the effect of the confinement, the authors included another specimen without the confinement (see Figure 2-9(a)). The results demonstrated that the confined specimens exhibited a ductile behavior while the conventional one failed in a brittle manner.

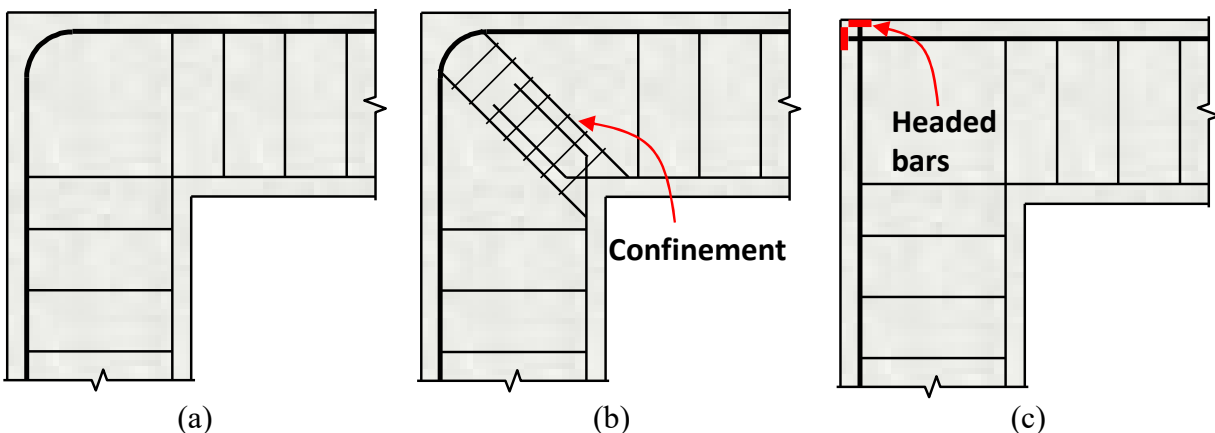


Figure 2-9 Additional reinforcement details investigated in the literature (adapted from Zouzou et al.⁷ and Marchetto et al.¹⁶)

Different from all of the above mentioned reinforcement details, Marchetto et al.¹⁶ proposed a detail that uses headed longitudinal reinforcing bars anchored at the outside corner of the joint (see Figure 2-9(c)). The authors tested four specimens using a loading system similar to the setup used by Johansson.¹³ The behavior of closing knee joints with headed bars was compared to those with continuous bars passing through the outer corner (see Figure 2-9(a)). The study concluded that properly designed headed bars were feasible as a replacement to conventional bent bars.

2.2.2.2 Lap-spliced longitudinal reinforcing bars

In addition to the previously described details, the effect of longitudinal reinforcing bars lap-spliced in knee joints is also a popular topic in the literature. Plos⁹ tested a closing knee joint with spliced reinforcement (see Figure 2-10(a)) and compared the test result to a specimen with continuous bars (see Figure 2-10(b)). Portal frame specimens were used for the research, and load was applied at the midspan of the beam as shown in Figure 2-11. It was observed that the ultimate strengths were similar for the two specimens. The author further concluded that no disadvantages were found with the use of spliced longitudinal reinforcing bars in closing knee joints.

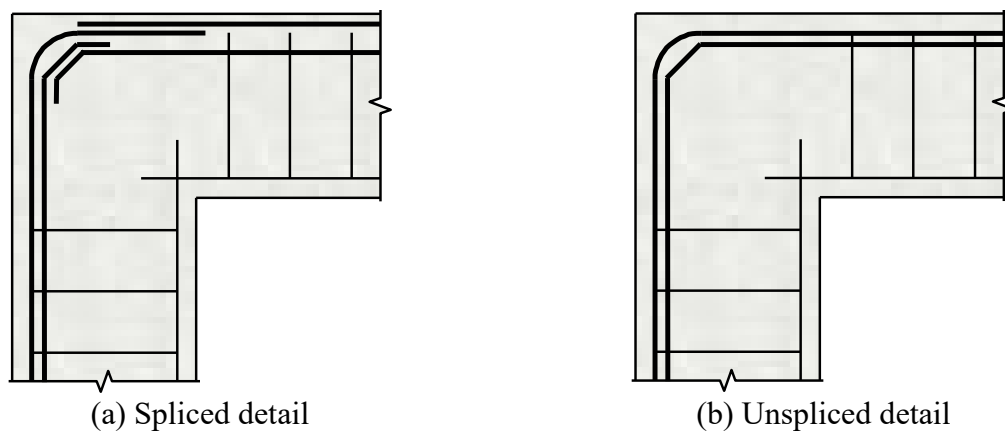


Figure 2-10 Details with and without splices (adapted from Plos⁹)

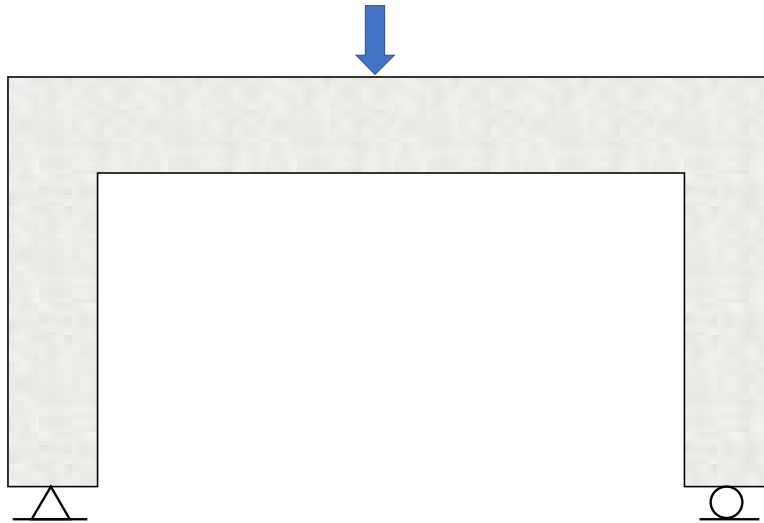


Figure 2-11 Schematic of test setup used by Plos⁹

The viewpoint that lap splices do not compromise the strength of closing knee joint was supported by Lundgrnen.¹¹ In the study, specimens with three different lap splice lengths illustrated in Figure 2-12 were tested and compared to a specimen with continuous bars. The author pointed out that one of the specimens with a short splice length (see Figure 2-12(c)) demonstrated slightly less flexural capacity compared to the other specimens and failed after an inclined crack appeared. However, the other test with a symmetrical short splice length failed due to fracture of the splice, demonstrating only 50% of the strength of the specimen with continuous bars. However, the behavior of the frame corner with a long splice was similar to that of the specimen with continuous bar. The author concluded that providing splice lengths based on code expressions²⁵ has no disadvantages compared to providing continuous bars.

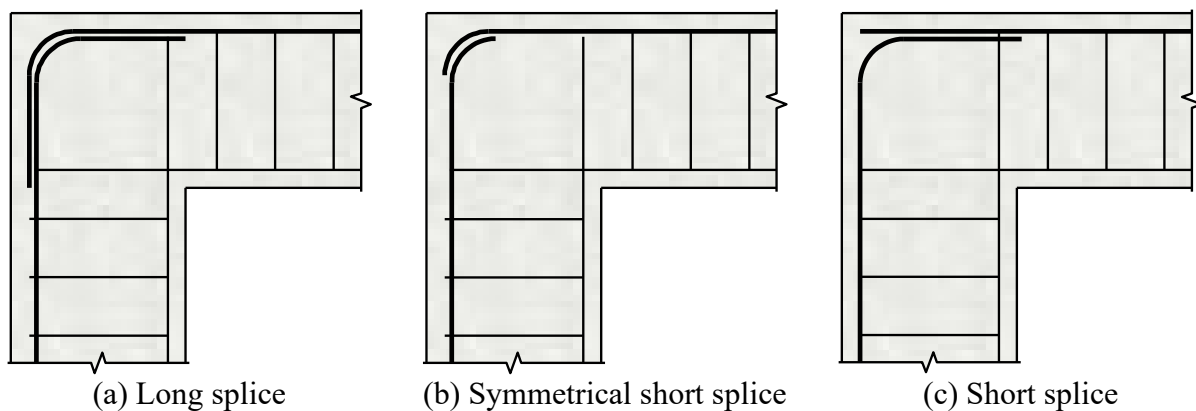


Figure 2-12 Splice details (adapted from Lundgrnen¹¹)

Yuan et al.⁶ developed details of lap-spliced bars and continuous bars with extra reinforcement in the joint as shown in Figure 2-13 to investigate the behavior of closing knee joints with and without initial cracks at the diagonal of the joint. A specimen with continuous reinforcement through the joint was tested for the purpose of comparison. Specimens used in this study were C-shaped, and load was applied as shown in Figure 2-14. The test results showed that initially uncracked specimens failed at sections away from the corner with yielding of the reinforcement, while initially cracked specimens failed due to splitting or bond failure of the cover concrete at a lower load than the uncracked specimens. Adding extra tension reinforcement (see Figure 2-13(b)) in the joint increased the capacity of closing knee joints.

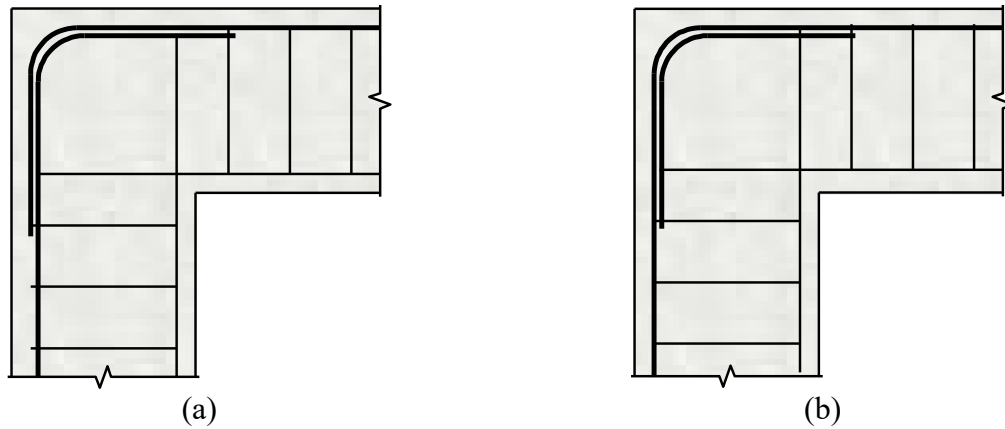


Figure 2-13 Additional splice details (adapted from Yuan et al.⁶)

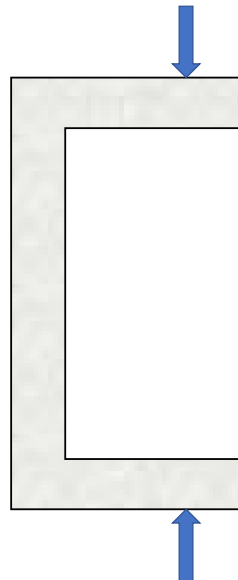


Figure 2-14 Schematic of test setup used by Yuan et al.⁶

Luo et al.⁸ conducted an extensive experimental program in which 27 closing knee joint specimens with complex reinforcement patterns with various lap-splice details were investigated. The reinforcement details used in this study include those shown in Figure 2-15(a) to (d). In addition to these four details with various lap-splice configurations, the authors considered the effect of the bend radius of the longitudinal reinforcement at the outer corner as well as the mechanical longitudinal reinforcement ratio ($\rho f_y / f'_c$). Load was applied horizontally to both legs of the specimens as shown in Figure 2-16. The authors suggested that lap length of the bent bars be longer than at least the minimum lengths required for straight bars to reach the flexural capacities of the frame corners.

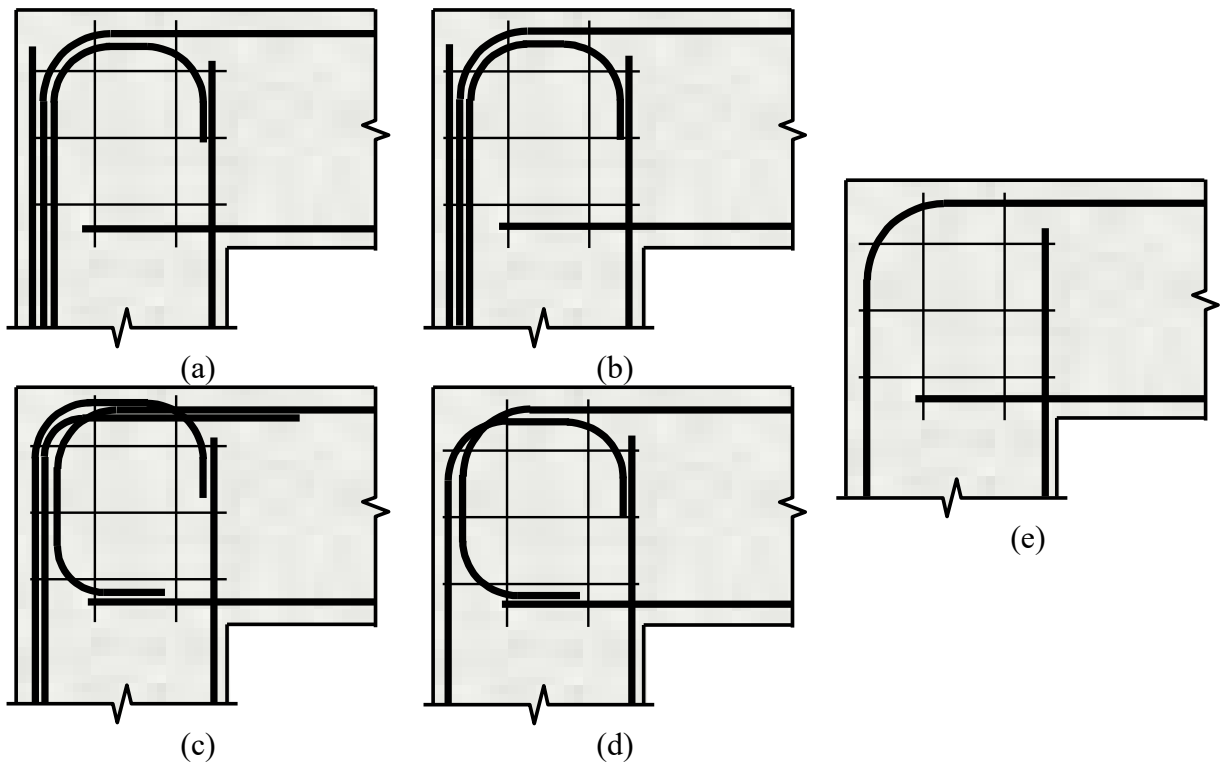


Figure 2-15 Complex reinforcement details (adapted from Luo et al.⁸ and Bai and Luo²⁶)

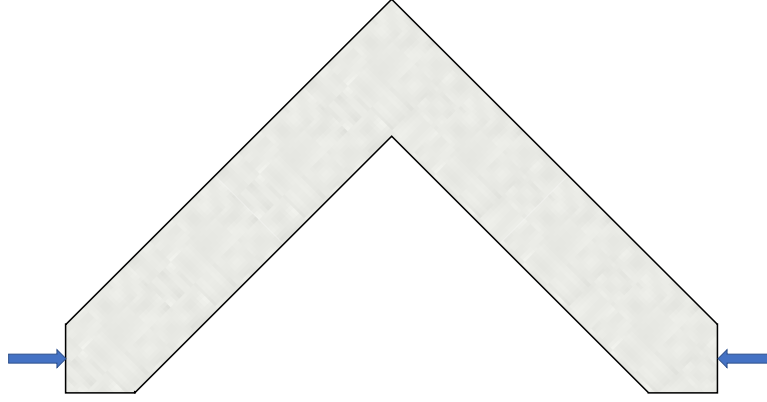


Figure 2-16 Schematic of test setup used by Luo et al.⁸

2.2.2.3 Effects of other factors

The research performed by Luo et al.⁸ demonstrated that the strength of knee joints was related to the bend radius of the longitudinal bars and the mechanical reinforcement ratio. This observation was investigated by Bai and Luo²⁶ as part of the same experimental program. In Bai and Luo,²⁶ 14 closing knee joint specimens detailed as shown in Figure 2-15(e) with various bend radii and mechanical longitudinal reinforcement ratios were tested. It was revealed that these two factors affected the capacity and the failure mode. For example, for specimens had a relatively high reinforcement ratio (1.09% and 1.53%) and a small bend radius of twice the bar diameter, it was observed that the failure occurred due to crushing of concrete under the bar bend or due to spalling of concrete in the diagonal strut. The failure occurred prior to the load reaching the calculated capacity. The authors maintained that for such arrangement, the compressive stress exhausted the capacity of the diagonal strut before or after the longitudinal reinforcement yielded. The failure mode might result in compromised strength. Based on the observation, the authors provided two design charts as part of the conclusion for the experimental program. One of the design charts⁸ correlated failure modes of closing knee joint with combinations of bend radius and mechanical reinforcement ratio, while the other design chart^{26,27} provided limitation of the bend radius, r_b , and the reinforcement ratio, ρ , to achieve satisfactory behavior, as formulated as the following equations.^{26,27}

$$\rho \leq 0.5 + 0.15 \frac{r_b}{d_b} \text{ for } 2 \leq \frac{r_b}{d_b} \leq 6 \quad 2-1$$

$$\rho \leq \frac{1.3}{30} \text{ for } 6 \leq \frac{r_b}{d_b} \leq 12 \quad 2-2$$

In Eqs. 2-1 and 2-2, d_b is the bar diameter of the bar bend.

Another extensive experimental study on closing knee joints was conducted by Stroband and Kolpa.²³ The authors believed that relatively large radial stresses concentrate at the bar bend and may cause bearing failure or concrete splitting at the bar bend. To investigate stresses in knee joints, the bend radius and mechanical reinforcement ratio were taken into consideration along with the clear side cover of concrete. Moreover, the effect of transverse reinforcement and lap-splice in the joint was also investigated. Thirty-three specimens with the details illustrated in Figure 2-17 and Figure 2-12(c) were tested. To create closing moments, the portal frame specimens were fabricated and tested using a statically indeterminant setup as shown in Figure 2-18. The specimens had a cross-sectional width of 2.8 in. and a height of 4.7 in. Based on the test results, the authors formulated a design expression, presented as Eq. 2-3, to limit the minimum bend radius of the longitudinal bars in order to obtain desired behavior of closing knee joints.

$$r_b \geq \frac{1}{20} \frac{f_y}{f'_c} \sqrt{\frac{1}{c_c/d_b + \frac{1}{2}}} d_b \quad 2-3$$

In the equation, c_c is the concrete cover to reinforcement and d_b is the diameter of the longitudinal reinforcement. In addition to this requirement for the bend radius, the authors suggested the clear side cover to the longitudinal reinforcement be greater than 1.5 times the longitudinal bar diameter. Additional hairpin reinforcement placed transversely across the joint was also recommended to prevent splitting in the joint.

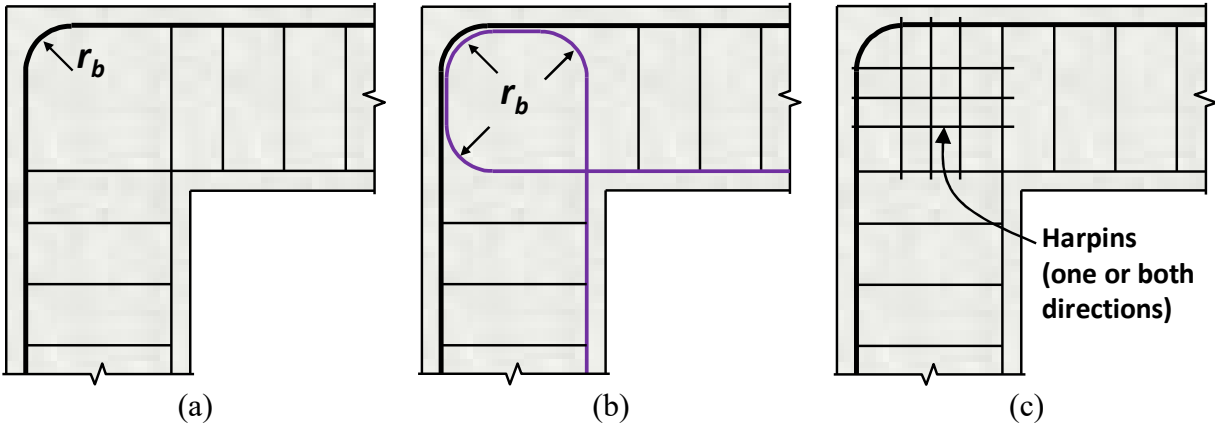


Figure 2-17 Reinforcement details (adapted from Stroband and Kolpa²³)

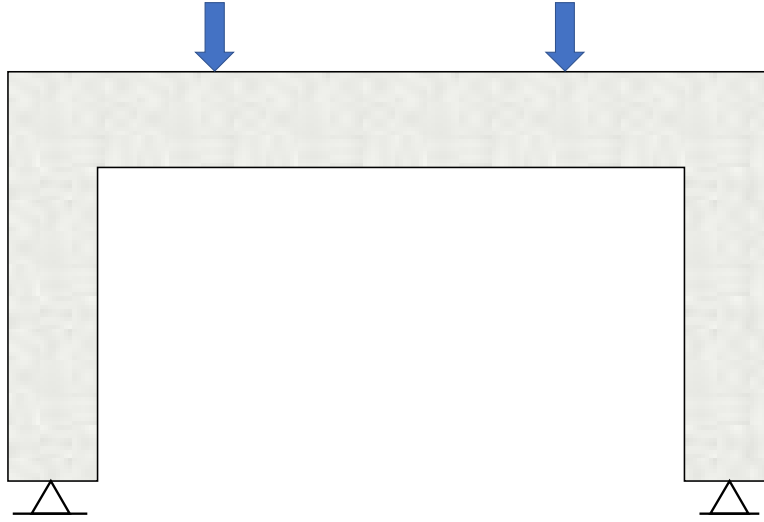


Figure 2-18 Schematic of test setup used by Stroband and Kolpa²³

The effect of the bend radius on closing knee joints were also investigated in a study by Hotta et al.¹⁴ The authors tested three L-shaped knee joint specimens, which had a cross-sectional width of 2.0 in. or of 3.1 in. and a height of 7.9 in., using a similar test setup as illustrated in Figure 2-16. The test results supported the observation that small bar bends caused bearing failure of the concrete to occur under the bar bend. The author used an empirical equation suggested by Fuji et al.³⁰ to calculate the anchorage strength, P_u , of the 90-degree bar bend at the outer corner of the specimens. The equation, presented as Eq. 2-4, includes consideration of the bend radius, clear side cover, spacing of bars, development length of hooked bars, location of the bar bend, and transverse reinforcement in the joint.

$$P_u = k_0 k_1 k_2 k_3 k_4 k_5 f_{b0} d_b r_b \quad 2-4$$

In Eq. 2-4, k_0 reflects concrete strength; k_1 reflects the ratio of the bend radius to the effective depth; k_2 reflects side cover thickness; k_3 is a coefficient for the position of the 90-degree bar bend; k_4 is related to the development length of hooked bars, l_{dh} ; k_5 reflects the effect of transverse reinforcement; and f_{b0} is the bearing strength at the bar bend.

The importance of the bend radius at the outer corner for designing closing knee joints was also pointed out in finite element studies. Bai et al.²⁶ stressed that small bend radii led to high compressive strains in the concrete under the bar bend. Finite element analyses conducted by Ingham²⁴ also maintained that high stress concentration occurred at this location.

2.2.3 Code provisions related to closing knee joints

Prior to the introduction of curved-bar node design procedures in ACI 318-19¹ (see Section 2.4), no provisions particularly for closing knee joints appeared in the code. Knee joints could be designed for joint shear in accordance with ACI 352R.¹⁸ Recently, the design procedures for joint shear in ACI 352R¹⁸ were adapted into Section 15.4 of ACI 318-19.¹

According to Section 15.4.1 of ACI 318-19,¹ for a knee joint, the joint shear force V_u should be assumed to equal the bar force $A_s f_y$ as illustrated in Figure 2-19. The nominal joint shear strength V_n is given in Table 15.4.2.3 of ACI 318-19.¹ It should be noted that closing knee joints are not framed with transverse beams that satisfy the requirements of Section 15.2.8 of ACI 318-19.¹ nor are they framed with continuous columns. Furthermore, continuous beams do not exist in the direction of joint shear. Therefore, according to Table 15.4.2.3 of ACI 318-19¹, Eq. 2-5 applies.

$$V_n = 12\lambda\sqrt{f'_c}A_j \quad 2-5$$

where A_j is the effective cross-sectional area within a joint as illustrated in Figure 2-20. In addition to the requirements for capacity and demand as mentioned above, detailing of joints is specified in Section 15.3 of ACI 318-19,¹ where transverse reinforcement is required to be provided in knee joints.

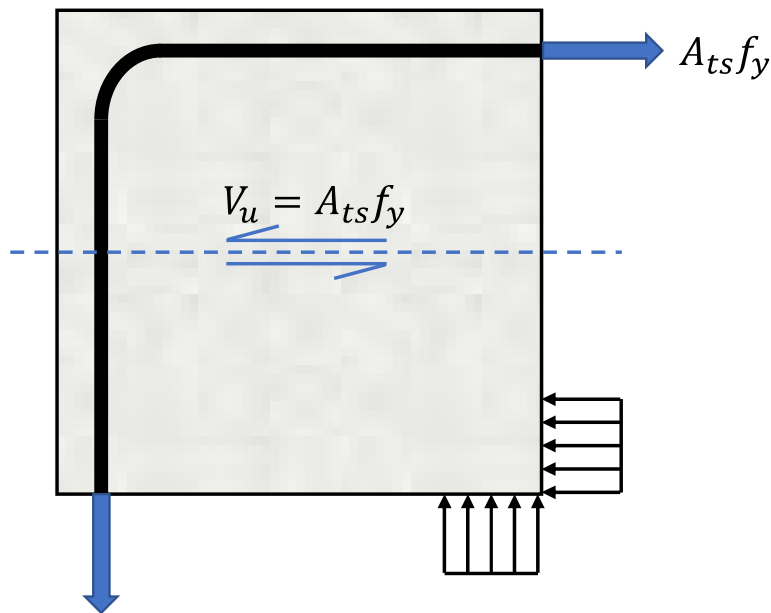


Figure 2-19 Shear force in closing knee joint

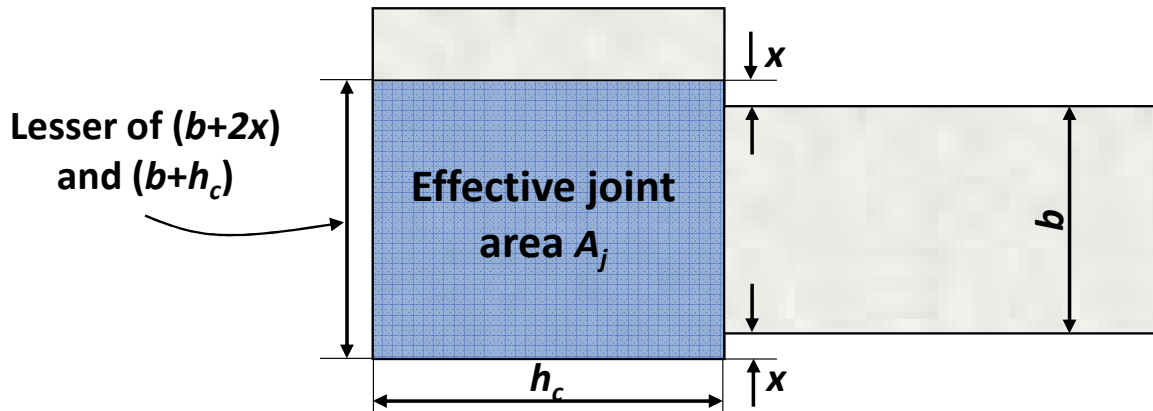


Figure 2-20 Effective joint area (adapted from ACI 318-19¹)

It should be noted that traditional design methods for knee joints, including the code provisions of Chapter 15 of ACI 318-19,¹ do not take the bend radius of longitudinal bars into consideration. This disagrees with the observations of past studies.

2.2.4 Summary

In Section 2.2, past experimental programs were reviewed. Several details of the reinforcement in closing knee joints were proposed and experimentally verified to be effective. However, no unified design guidelines based on a rational approach can be identified from the test results. Other studies identified factors that potentially affect the behavior of closing knee joints. The factors include the bend radius, mechanical reinforcement ratio, clear side cover, and transverse reinforcement in the joint. The observations were supported by finite element analyses. Based on the findings, several empirical equations were proposed, but the equations were derived from limited experimental data and might have limited applicability. Traditional design procedures for closing knee joints do not include the effect of the bend radius, which has been shown to affect joint behavior in past tests.

It is important to find a rational method to design knee joints under closing moments. Being categorized as geometric discontinuity regions (D-regions), such joints are suitable to be designed using the strut-and-tie method. Although not explicitly mentioned, the concept of the strut-and-tie method was incorporated into several past studies with discussions of the diagonal compression zone across the joint and the bearing strength under the bar bend. The strut-and-tie method is introduced in the next section.

2.3 Introduction to the Strut-and-Tie Method

An introduction to the strut-and-tie method (STM) is provided in this section. The background of the STM is first included, followed by a review of the procedures for applying the STM. Furthermore, the current code method for proportioning elements of strut-and-tie models is reviewed.

2.3.1 Background

The strut-and-tie method^{19,20} is a rational, analytical, and unified tool that is used to design discontinuity regions (D-Regions) in reinforcement concrete members. Unlike B-regions (the letter “B” referring to Bernoulli or beam theory) where a linear strain distribution is assumed over the section, D-regions have a more complex strain profile over the section. For this reason, traditional sectional design procedures are invalid. The strut-and-tie method, however, uses idealized load paths to represent the flow of stresses in D-regions.^{19–21,29} Struts are used along directions of compressive stress, ties are used along directions of tensile stress, and nodes are used to represent abrupt re-direction of stresses. Based on the lower-bound theory of plasticity, under the condition of equilibrium, structures are considered safe when all elements have adequate strength and sufficient deformability. Accordingly, designers are able to proportion ties with reinforcing bars and check if struts and nodes are capable of resisting applied stresses.^{19–21,29}

The development of the strut-and-tie method can be traced back to the “truss analogy,” which was introduced by Ritter³⁰ and Mörsch.³¹ The truss analogy was originally used to model shear forces in concrete beams as vertical steel members carrying load. The method was then refined; more sophisticated applications were proposed in the following decades.^{32–35} The method was generalized by the work of Schlaich et al.¹⁹, who proposed a general approach to model various D-regions based on stress trajectories. The proportioning method of each element was introduced. Schlaich et al.¹⁹ helped the strut-and-tie method to become a more unified and consistent design method.

The strut-and-tie method was verified to be effective for more and more complex structures. For example, Chen et al.³⁶ tested end regions of dapped beams with an opening, and Kuchma et al.³⁷ used tests on complex regions to validate the strut-and-tie method. Implementation of the strut-and-tie method has been demonstrated for the design of corbels, deep beams, pile caps,

beam-column joints, and other D-regions.^{38–48} The ACI 318 design code incorporated the strut-and-tie method as part of the main body of the code in 2014,⁴⁹ and refinements and additions to the provisions were introduced in ACI 318-19.¹

2.3.2 Fundamental Concepts of the Strut-and-Tie Method

2.3.2.1 B-Regions versus D-Regions

Reinforced concrete structures can be separated into B-regions and D-regions.^{17,19–21} B-regions, as mentioned above, follow the assumption that plane sections remain plane. That is, strain is linearly distributed over sections of the member. Under the assumption, when a beam is under a bending moment, the curvature of the deformed beam is related to the linear strain distribution at a section under consideration.

Unlike B-regions, D-regions violate the assumption that plane sections remain plane so that beam theory cannot be applied to relate stress flow to external loads. D-regions exist at locations near concentrated loads, reactions, or geometric discontinuities. D-regions extend from such discontinuities a distance equal to approximately the overall depth of the member;^{17,19–21} St. Venant's principle indicates that stresses become linear at this distance from a discontinuity. Examples of D-regions are illustrated in Figure 2-21.^{1,19}

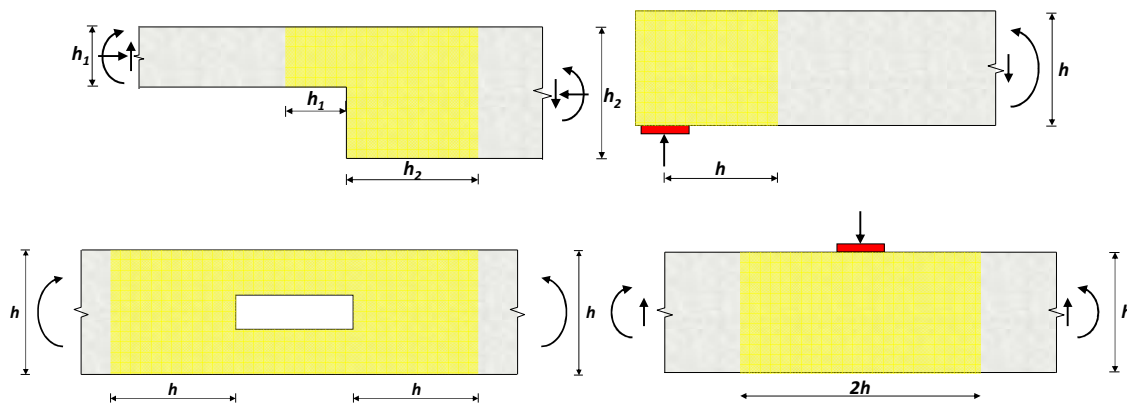


Figure 2-21 Examples of D-regions (adapted from Schlaich et al.¹⁹ and ACI 318-19¹)

2.3.2.2 Basic Principles

Based on the lower-bound theory of plasticity, the strut-and-tie method results in conservative structural designs when the following principles are satisfied: 1) the strut-and-tie model is in equilibrium with external forces and/or forces from the adjacent B-regions; 2) elements possess adequate strength; and 3) elements have sufficient deformation capacity. In addition, reinforcement needs to be properly anchored and developed.^{17,19–21}

The first principle can be achieved by properly selecting strut-and-tie models and enforcing equilibrium. Struts and ties should be placed approximately along the actual direction of stress flow in the D-region under consideration. This can be assisted by elastic finite element analysis or crack propagation during actual load tests. Concerning the second principle, ties can be proportioned easily with a sufficient amount of reinforcement. For struts and nodes, compressive strength of concrete is reduced by appropriate factors to reflect the efficiency of the concrete to resist compression. The efficiency factors, or strength reduction factors, are related to transverse strain and cracks, which are considered detrimental to the concrete.^{19,50} As compressive stresses flow through a non-confined strut, the stress disperses and develops tensile stress in the lateral direction.^{51,52} Also, diagonal tensile stress flows transversely through interior struts.⁵³ The transverse tensile stress eventually splits the strut as the compression increases, limiting the deformation capacity of the strut, as well as the efficiency.⁵⁴ To avoid such situations, providing distributed reinforcement through a strut mitigates the transverse strain and increases the efficiency of the concrete. The concrete must have sufficient capacity to resist the forces in struts or at nodes.¹⁹

2.3.2.3 Components

Components used in the strut-and-tie method include struts, ties, and nodes (see Figure 2-22). As explained previously, struts represent the idealized resultant of compressive stresses, ties are used to model resultant tensile stresses, and nodes reflect abrupt direction changes of stress.

For the design purpose, struts are modelled as idealized prismatic members. If a strut has the area of one end different from that of the other end, the strut is modeled as a uniformly tapered member.^{1,47} Concerning the stress state, struts are classified as two types: 1) boundary struts, and 2) interior struts¹ as illustrated in Figure 2-22. Boundary struts are not subjected to transverse

tensile stress, while interior struts develop tension in the transverse direction,^{47,55} as illustrated in Figure 2-23.

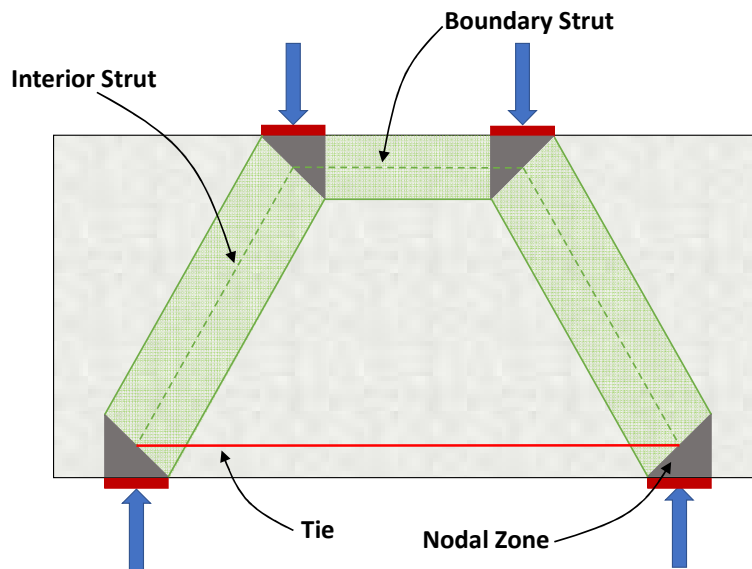


Figure 2-22 Components of a strut-and-tie model¹

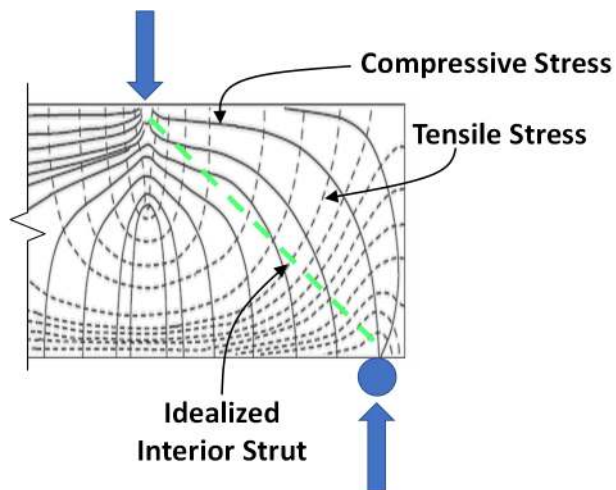


Figure 2-23 Example of stress trajectory near the end of a deep beam (adapted from Williams et al. and Birrcher et al.^{47,55})

Nodes exist at the intersections of struts and ties and can be categorized into three types: 1) CCC nodes, 2) CCT nodes, and 3) CTT nodes as illustrated in Figure 2-24. The letter “C” represents a compressive force, and the letter T represents a tensile force. The number of “T’s” indicate the number of ties that frame into the node regardless of the number of struts that intersect

at the node. For example, if two ties frame into a node, the node is a CTT node, even if two struts also frame into the same node. In addition, nodes can be classified as curved-bar nodes as described further in Section 2.4.

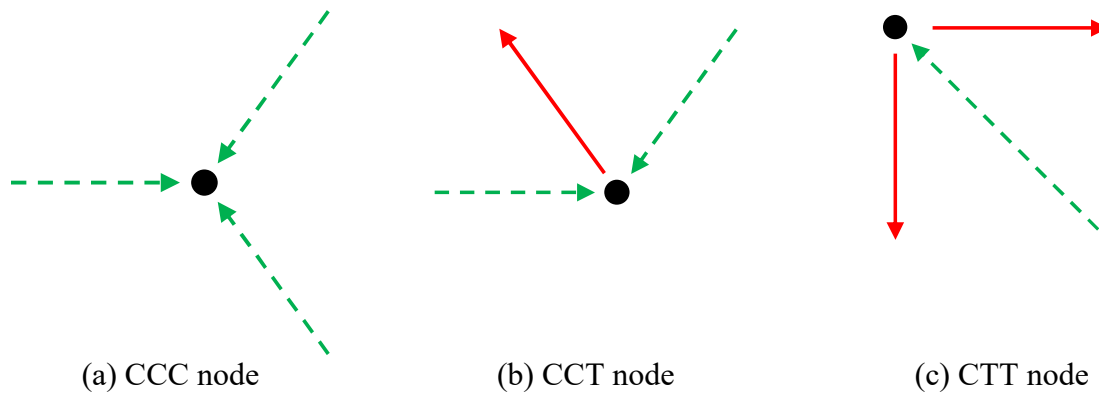


Figure 2-24 Types of nodes

2.3.2.4 Procedures

The procedure as described in the following sections is based on guidance and details in ACI 318-19¹ and corresponding descriptions are based on Williams et al.⁴⁷ and Brown et al.⁵⁶

The basic procedure^{17,47} for implementing the strut-and-tie method is summarized in the flow chart presented in Figure 2-25. Each step is introduced in the following sections.

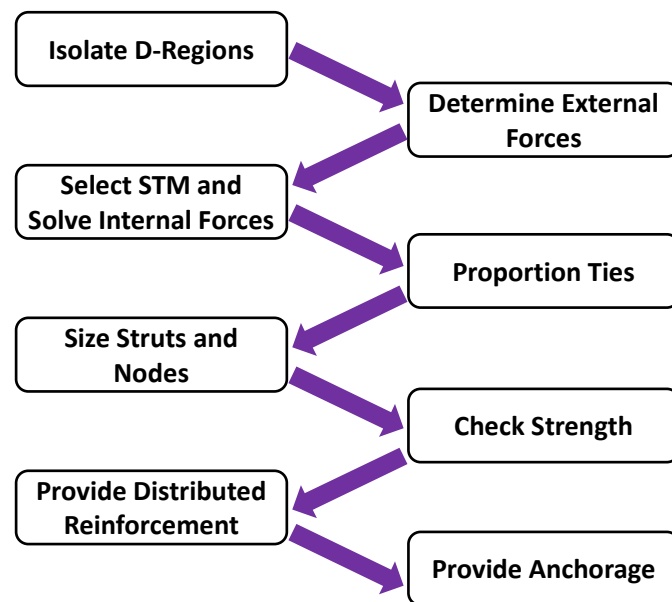


Figure 2-25 Steps for implementing the strut-and-tie method^{17,47}

2.3.3 Isolate D-Regions

The first step for using the strut-and-tie method is to define D-regions in a structure under consideration according to St. Venant's principle. That is, identify load and geometric discontinuities and assume a D-region extends a distance of the overall section depth from each discontinuity. As an example, every point within the region shaded in yellow in Figure 2-26 is within a distance h from a load or geometric discontinuity (that is, the frame corner). Therefore, it is appropriate to design the yellow shaded region using the strut-and-tie method.

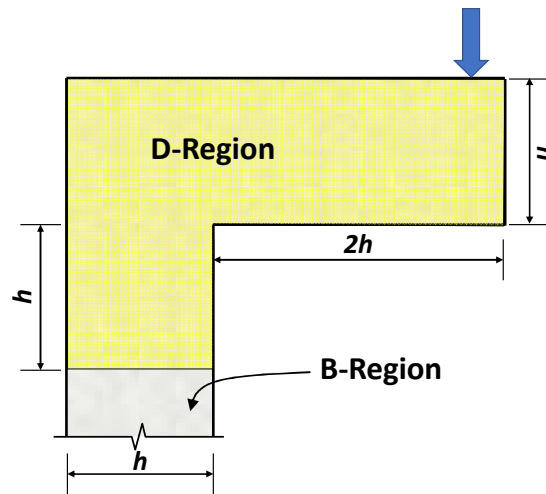


Figure 2-26 Geometry of a D-region

2.3.4 Determine Forces Acting at Interface between B- and D-Regions

The second step is to define loads that act on the interfaces between the D-region to be designed and adjacent B-regions. It should be noted that code-defined factored loads and load cases should be considered in design. Structural analysis should be conducted to determine support reactions and internal stresses at B-region/D-region interfaces. As illustrated in Figure 2-27, the internal stress distribution over the section at a B-region/D-region interface can be determined simply using elastic stress analysis. The distributed stress is then divided such that the resultant of each subdivision is treated as concentrated load acting at the interface as shown in Figure 2-27.

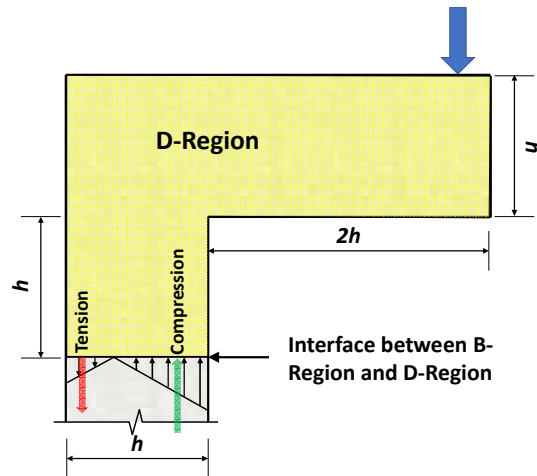


Figure 2-27 Example of loads at interface between B-Region and D-Region

2.3.5 Develop Strut-and-Tie Model and Solve for Member Forces

It is suggested that the strut-and-tie model reflect the actual stress flow in the D-region.^{17,19-21} As previously mentioned, this can be assisted by observed crack patterns from load tests or elastic stress analysis (such as finite element analysis) of the structure. The load path method^{17,19-21} can be also applied to construct a proper strut-and-tie model. It should be mentioned that the angle between struts and the ties framing into a node is required to be greater than or equal to 25 degrees in the current ACI 318-19¹ code. The limitation avoids incompatibilities between the shortening of the strut and the lengthening of the tie in nearly the same direction.¹ A valid example of a strut-and-tie model of the cantilever beam and joint shown in Figure 2-27 is presented in Figure 2-28.

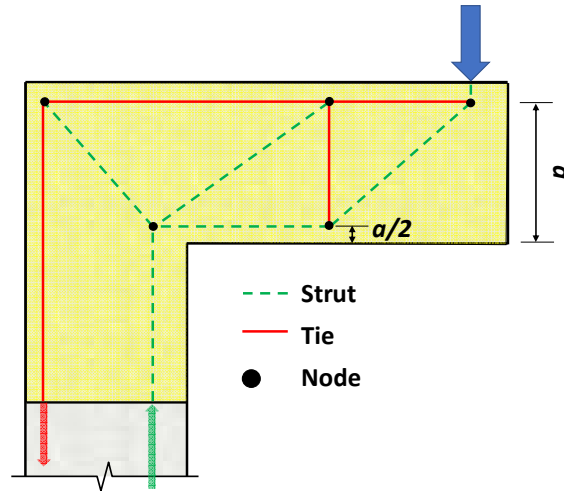


Figure 2-28 Example strut-and-tie model of cantilever beam and joint

Once the flow of stresses within the structural component is understood, the geometry of the struts and the ties should be determined. Longitudinal ties should be placed to coincide with the longitudinal reinforcing bars to be placed in the structure, which is at a distance of an effective depth away from the compression face as shown in Figure 2-28. Struts should follow the general flow (that is, direction) of compressive stresses. It is recommended that boundary struts be placed close to the edge of the member to maximize the moment arm for greater efficiency, but the strut should be of adequate width to allow it to carry the strut force.^{47,56} For this reason, it is common to place the strut at the middle of the rectangular stress block in accordance with the nominal flexural strength condition, which is $a/2$ away from the edge⁴⁷ as shown in Figure 2-28.

There is not a single way to construct a strut-and-tie model for many D-regions. Instead, several valid layouts may exist.^{19,47} The basic principles stated in Section 2.3.2.2 should be satisfied and the model should reasonably match the actual flow of forces in the member to ensure a conservative result and serviceable behavior. The constructed strut-and-tie model can be either internally statically determinant or internally statically indeterminate.^{47,56} However, statically determinant models are preferable in most cases as explained by Brown et al.⁵⁶ because member stiffnesses are not needed to solve for the internal force of each member.

2.3.6 Proportion Ties

After all internal member forces are calculated, the next step is to proportion the ties. That is, an adequate area of reinforcement should be provided to carry the corresponding tie force. The reinforcement can be non-prestressed or prestressed in accordance with Section 23.7 of ACI 318-19.¹ Therefore, the nominal strength (F_{nt}) of a tie is calculated as

$$F_{nt} = A_{ts}f_y + A_{tp}\Delta f_p \quad 2-6$$

where A_{ts} is the area of non-prestressed reinforcement in the tie; A_{tp} is the area of prestressing reinforcement in the tie; f_y is specified yield strength for non-prestressed reinforcement; and Δf_p is increased stress of prestressing reinforcement due to factored loads. The design strength should be greater than the tie force as stated in Eq. 2-7.

$$\phi F_{nt} \geq F_{ut} \quad 2-7$$

2.3.7 Sizing Nodal Zones and Struts

The geometries and sizes of the nodes must be determined to calculate their capacities. For struts, the capacity at the ends of the strut where the strut is connected to a node typically governs. Therefore, once the size of a node is determined, the corresponding strut width is simultaneously obtained.

Nodes are categorized as hydrostatic nodes or non-hydrostatic nodes (see Figure 2-29) as explained in Brown et. al.⁵⁶ For a hydrostatic node, all nodal faces are subjected to a stress with the same magnitude. The stress state reduces to a point if expressed by Mohr's circle. In this case, no shear stress develops in any direction within the node, and each force is perpendicular to the surface on which it is acting as shown in Figure 2-30.⁵⁶ The widths of the three faces is proportional to the magnitude of the corresponding forces as expressed in Eq. 2-8.

$$w_{n1}:w_{n2}:w_{n3} = C_1:C_2:C_3 \quad 2-8$$

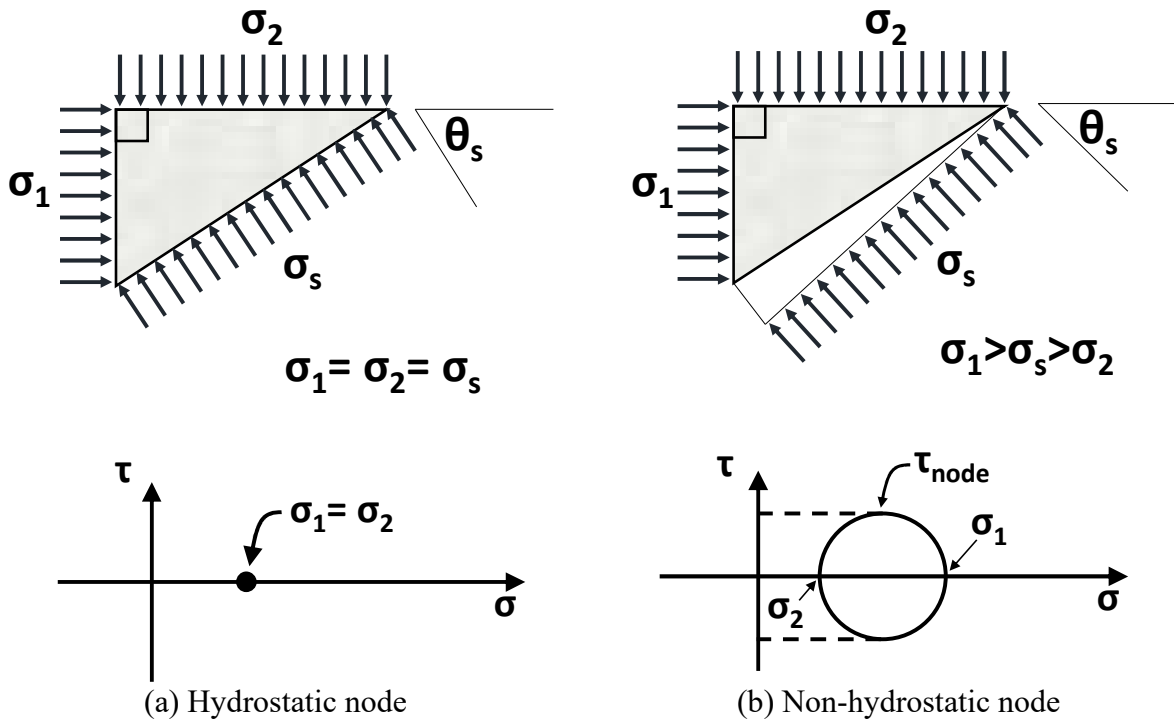


Figure 2-29 Stresses on hydrostatic and non-hydrostatic node (adapted from Brown et al.⁵⁶)

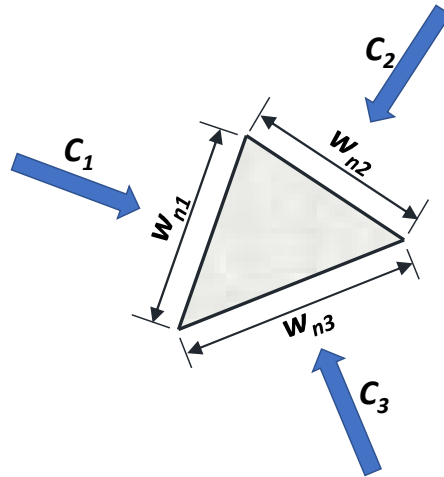


Figure 2-30 Hydrostatic node

Many studies,^{21,45,47} however, suggest that it is unrealistic or even impossible to achieve hydrostatic nodes; therefore, most strut-and-tie models use non-hydrostatic nodes. For a non-hydrostatic node, the forces do not have to be perpendicular to the faces on which they are acting (see Figure 2-29(a)). The stresses on the faces are not equal, and shear stress develops within the

node. To size each face of a non-hydrostatic node, Section 23.9.4 of ACI 318-19¹ states the following:

“The area of each face of a nodal zone, A_{nz} , shall be taken as the smaller of (a) and (b):

- (a) Area of the face of the nodal zone perpendicular to the action of F_{us}*
- (b) Area of a section through the nodal zone perpendicular to the line of action of the resultant force on the section”*

Methods for sizing different types of nodes described in the following sections are based on ACI 318-19¹ and corresponding descriptions are based on Williams et al.⁴⁷ and Brown et al.⁵⁶

1. CCC nodes

To size a CCC node, it is convenient to resolve struts connected to the node together so that a total of three compressive forces act on the node. If the CCC node is treated as a hydrostatic node as shown in Figure 2-30, Eq. 2-8 can be applied.¹ Otherwise, for non-hydrostatic nodes (see Figure 2-31), the width of the back face, a , and the size of the bearing plate or strut width, w_b , is typically known, and the width of the interface between the node and the diagonal strut, w_s , can be expressed as

$$w_s = w_b \sin \theta_s + a \cos \theta_s \quad 2-9$$

Figure 2-31 is a typical example of the geometry of a CCC node.^{47,56}

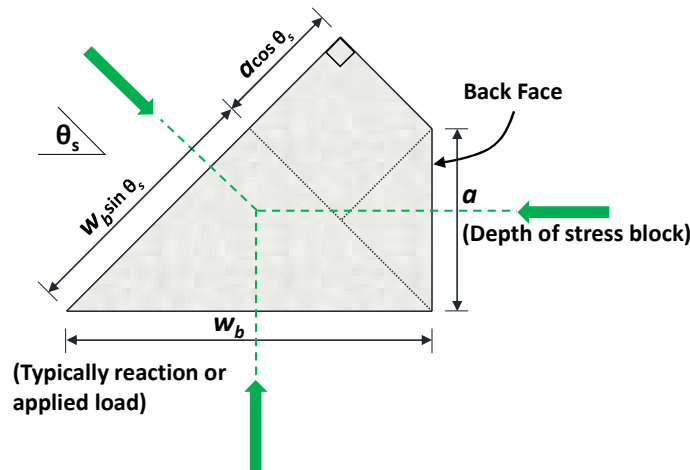


Figure 2-31 Example of the typical geometry of a CCC node (adapted from Brown et al.⁵⁶)

2. CCT nodes

A CCT node exists where one tie intersects with two or more compressive forces from struts or applied loads/reactions.^{1,47,56} Because only three forces acting in different directions are required for equilibrium, if more than two compressive forces intersect at the node, struts are often first resolved together so that the node consists of the intersection of the tie and two compressive forces as shown in Figure 2-32.^{47,56} The width of the back face can be considered twice the distance from the centroid of reinforcing bars to the edge of the member. With the width of the back face, w_t , and a known size of the bearing plate or strut width, w_b , the width of the interface between the diagonal strut and the CCT node, w_s , is determined using Eq. 2-10 (see Figure 2-32).

$$w_s = w_b \sin \theta_s + w_t \cos \theta_s \quad 2-10$$

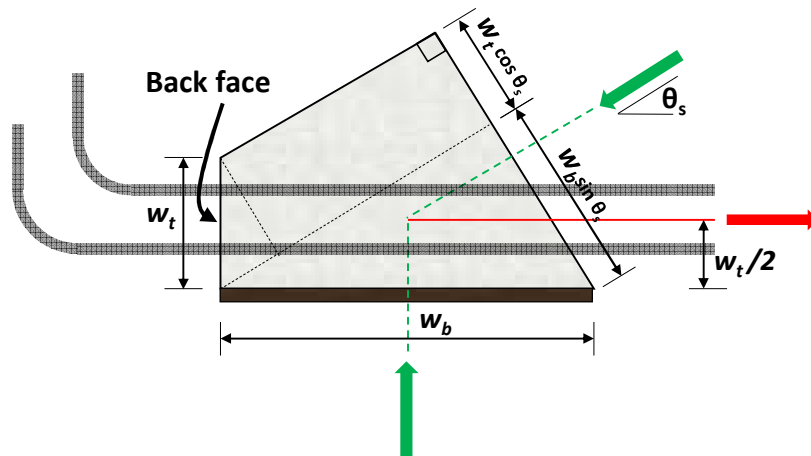


Figure 2-32 Example of the typical geometry of a CCT node (adapted from Brown et al.⁵⁶)

3. CTT nodes

A CTT node exists where two or more ties and one or more compressive forces intersect. There are two common types of CTT node: 1) a node with a defined geometry and 2) a smeared node with a geometry^{19,47,56} that is not clearly defined, as shown in Figure 2-33. The first type usually corresponds with the location of a load or support plate (that is, load or reaction area), as shown in Figure 2-34, or at a region in a member where the member geometry provides natural dimensions for the node.^{47,56} In this case, the nodal width at the interface between the node and the

strut, w_s , can often be determined in a manner similar to that introduced for CCC and CCT nodes, as given by Eq. 2-11 (see Figure 2-34).

$$w_s = w_{t1} \cos \theta_s + w_{t2} \sin \theta_s \quad 2-11$$

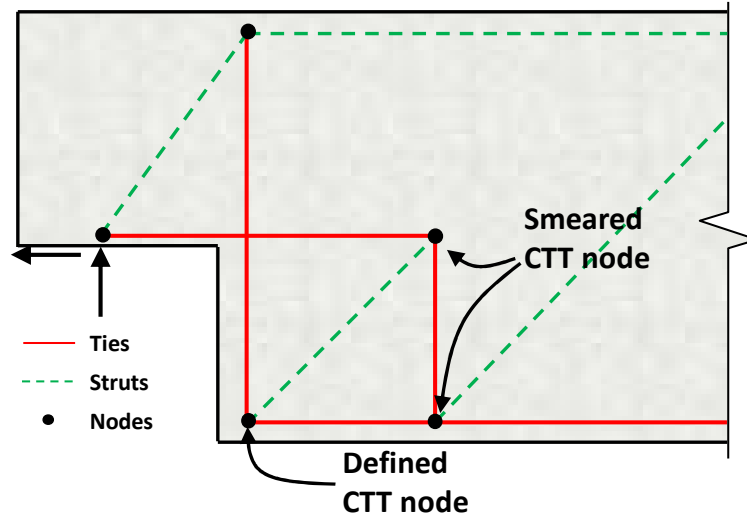


Figure 2-33 Example of different CTT nodes in strut-and-tie model⁵⁷

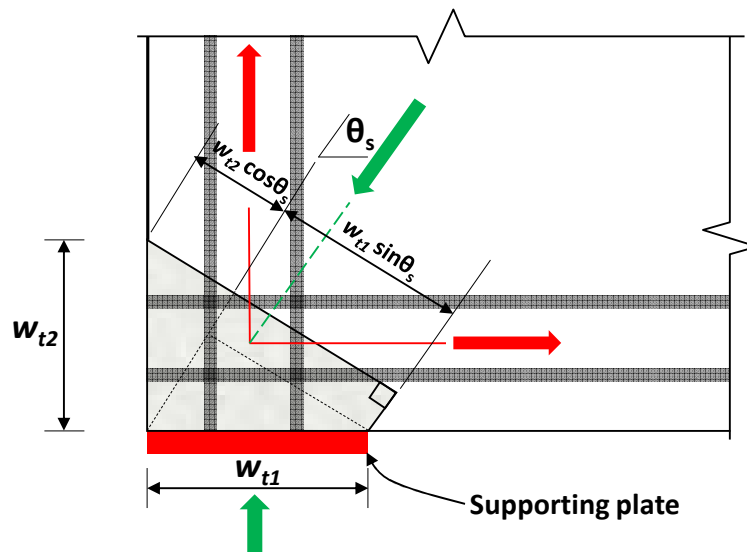


Figure 2-34 Example of the geometry of a CCT node located at a load or bearing plate (adapted from ACI 318-19¹)

The other frequently encountered CTT node appears away from the ends of a member (see Figure 2-33). For this type of CTT nodes, Birrcher et al.⁵⁵ and design codes¹ suggest that the

strength is not critical. Furthermore, CCC nodes and CCT nodes can be smeared. The details of smeared nodes are beyond the scope of the current discussion.

2.3.8 Checking Nodal Strength and Strut Strength

To ensure that nodes have sufficient strength, Eq. 2-12 must be satisfied for each nodal face.¹

$$\phi F_{nn} \geq F_{us} \quad 2-12$$

where ϕF_{nn} is the factored nominal strength of a nodal face and F_{us} is the force acting on the face as a result of factored loads applied to the structure. Similarly, struts must satisfy Eq. 2-13.¹

$$\phi F_{ns} \geq F_{us} \quad 2-13$$

where ϕF_{ns} is the factored nominal strength of a strut and F_{us} is the factored force in a strut.

1. Nodal strength

In accordance with Section 23.9 of ACI 318-19,¹ the nominal strength of a nodal zone can be expressed as

$$F_{nn} = f_{ce} A_{nz} \quad 2-14$$

where f_{ce} is the effective compressive strength of concrete, which is expressed as

$$f_{ce} = 0.85 \beta_c \beta_n f'_c \quad 2-15$$

and where A_{nz} is the area of the nodal face, which is, for example, equal to the width of the face under consideration multiplied by the dimension of the node perpendicular to the plane of the two-dimensional strut-and-tie model.

In Eq 2-15, the factor β_c reflects the condition of confinement in accordance with Table 23.4.3(b) of ACI 318-19.¹ As stated in Section R23.9.2 of the commentary to the code,¹ the nodal zone coefficient β_n reflects disruption of the nodal zone caused by the incompatibility of tensile strains and compressive strains. The disruption is higher when more ties frame into a node, resulting in a lower nodal coefficient. Based on the level of the disruption, the values of the nodal zone coefficient are summarized in Table 2-1 in accordance with Section 23.9.2 of ACI 318-19.¹

Table 2-1 Nodal zone coefficient (adapted from ACI 318-19¹)

| Node type | Nodal zone coefficient, β_n |
|-----------|-----------------------------------|
| CCC | 1.0 |
| CCT | 0.8 |
| CTT | 0.6 |

2. Strut strength

The strength of a strut can be calculated in accordance with Section 23.4 of ACI 318-19¹ as

$$F_{ns} = f_{ce}A_{cs} + A'_sf'_s \quad 2-16$$

where f_{ce} is expressed as

$$f_{ce} = 0.85\beta_c\beta_sf'_c \quad 2-17$$

and where A_{cs} is the cross-sectional area of the end of the strut. The term $A'_sf'_s$ is the contribution of compression reinforcement if provided along the length of the strut. In Eq. 2-17, the strut coefficient β_s reflects the reduced strength of struts caused by tensile stresses transverse to the strut. The strength of boundary struts does not need to be reduced because no transverse tensile stress exists at the strut.¹ In addition, the strut coefficient is related to the presence of distributed reinforcement and the location of the strut as summarized in Table 2-2.

Table 2-2 Strut coefficient (adapted from ACI 318-19¹)

| Strut location | Strut Type | Criteria | Strut Coefficient, β_s |
|---------------------------|----------------|--|------------------------------|
| Tension zones and members | Any | All cases | 0.4 |
| Other cases | Boundary strut | All cases | 1.0 |
| | Interior strut | With minimum distributed reinforcement | 0.75 |
| | | Diagonal tension failure is precluded | 0.75 |
| | | Beam-column joints | 0.75 |
| | | Other cases | 0.4 |

3. Curved-bar nodes

A unique node called a curved-bar node²² was introduced into ACI 318 in 2019.¹ In Section R23.10.1 of the commentary to ACI 318-19,¹ the following definition of a curved-bar node is given:

“A curved-bar node is formed by the bend region of a continuous reinforcing bar (or bars) where two ties extending from the bend region are intersected by a strut or the resultant of two or more struts (Fig. R23.10.5), or where a single tie is anchored by a 180-degree bend (Fig. R23.10.2)”

Design considerations for curved-bar nodes are provide in detail in Section 2.4.

2.3.9 Providing Distributed Reinforcement for Struts

As previously introduced, interior struts are subject to transverse tensile stresses that develop, leading to a reduced strength.¹ To limit tensile strain, a minimum amount of distributed reinforcement is required in accordance with Section 23.5 of ACI 318-19¹ as summarized in Table 2-3.

Table 2-3 Minimum distributed reinforcement (adapted from ACI 318-19¹)

| Reinforcement configuration | Minimum distributed reinforcement ratio |
|---|---|
| Orthogonal grid | 0.0025 in each direction |
| In one direction crossing strut at angle α_1 | $\frac{0.0025}{\sin^2 \alpha_1}$ |

In addition to the requirements in the table, the spacing of distributed reinforcement must not exceed 12 in. and the angle α_1 must not be less than 40 degrees. The minimum distributed reinforcement is not required if struts under consideration are laterally restrained. The conditions for lateral restraint are provided in Section 23.5.3 of ACI 318-19.¹

2.3.10 Providing Anchorage for Ties

Reinforcement that is used to carry tie forces must be appropriately developed at the critical section. According to Section 23.8.3 of ACI 318-19,¹ the critical section of a node is at the point where the tie exits the extended nodal zone as illustrated in Figure 2-35. With a defined critical

section, the available length, l_{anc} , can also be defined. Therefore, the reinforcing bars can be fully developed if the required development length is less than the available length.

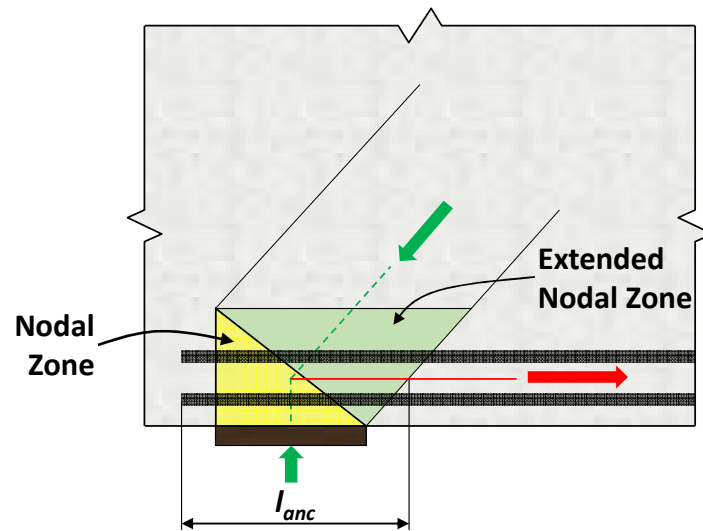


Figure 2-35 Available length for anchorage (adapted from ACI 318-19¹)

2.3.11 Summary

The procedure for applying the strut-and-tie method was presented in this section. The contents include the introduction of each step: 1) isolate D-regions, 2) determine design forces, 3) develop the strut-and-tie model, 4) proportion ties, 5) size nodal zones and struts, 6) check strength of nodes and strut, 7) provide distributed reinforcement for struts, and 8) provide anchorage for ties.^{17,47}

Current design procedures for curved-bar nodes are presented in the following section. Following the introduction of these design procedures, it is important to further discuss nodal zone coefficients as well as strut coefficients. This discussion is provided in Section 2.5

2.4 Current Design Methodologies for Curved-Bar Nodes

In this section, current design procedures for curved-bar nodes are presented. A typical strut-and-tie model for closing knee joints is presented in Figure 2-36, which can also be seen in Schlaich¹⁹ and El-Metwally et al.²¹ The CTT node located at the outer corner meets the definition for curved-bar nodes presented in Section 2.3.8. The current design methodology for such nodes

addresses observations from past research²² that the bend radius of the longitudinal bars affects joint behavior.

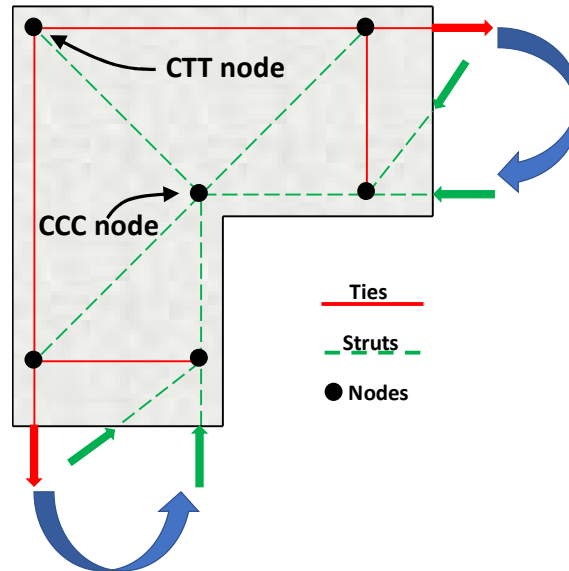


Figure 2-36 Typical strut-and-tie model for closing knee joints

Consistent with the definition in Section 2.3.8.3, the curved-bar node in Figure 2-36 is formed by the bend region of continuous longitudinal reinforcing bars, the tensile force in which is represented by the perpendicular ties, and the ties are equilibrated by one or more struts (one strut in this case). As outlined in Section 23.10 of ACI 318-19,¹ special treatment of the node is needed to deal with the radial stress on the bar bend and the circumferential bond stress that develops along the bar bend as shown previously in Figure 2-5. The current design expressions for curved-bar nodes in ACI 318-19¹ were adopted from recommendations introduced by Klein.²² Klein²² developed the expressions based on existing code provisions, such as the strength requirements for CTT and CCT nodes.

Before the bar stress at each side of the bar bend of a curved-bar node reaches the yield stress, it should be ensured that the concrete under the bar bend will not experience a stress greater than its effective compressive strength. For this reason, the bend radius should be large enough to provide adequate bearing area to control the magnitude of the radial stress shown in Figure 2-37(a). As shown in this figure, for a strut angle of 45 degrees, a bend radius of r_b provides a bearing area of $b_s\sqrt{2}r_b$, where b_s is the out-of-plane width of the strut. The strut force acting on the bearing area

should be in equilibrium with the two tie forces at yielding, which are equal to $\sqrt{2}A_{ts}f_y$. The average stress on the concrete can be determined by dividing the force by the bearing area, as stated in Eq. 2-18.

$$f_c = \frac{A_{ts}f_y}{b_s r_b} \quad 2-18$$

The stress f_c should be less than the effective compressive strength f_{ce} . Moving the term r_b to the left-hand side gives

$$r_b \geq \frac{A_{ts}f_y}{b_s f_{ce}} \quad 2-19$$

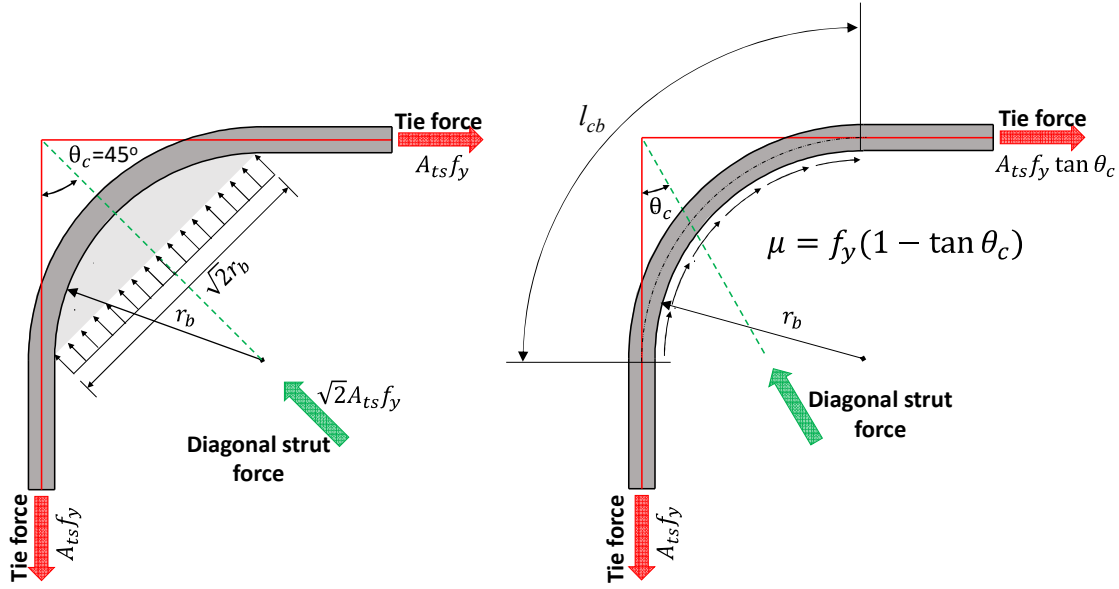
Here, Klein²² used the nodal zone coefficient, β_n , for CTT node to calculate f_{ce} , which results in $(0.6)(0.85)(f'_c)$, or $0.51f'_c$. Therefore, a conservative approximation of Eq. 2-20 is

$$r_b \geq \frac{2A_{ts}f_y}{b_s f'_c} \quad 2-20$$

This expression is given as Eq. 23.10.2a in ACI 318-19¹ and applies to curved-bar nodes with bar bends that are less than 180 degrees. If a 180-degree bar bend is used to anchor a single tie (refer to the definition given in Section 2.3.8), the resulting curved-bar node incorporates the nodal zone coefficient for a CCT node, and the required bend radius is given as Eq. 23.10.2b in ACI 318-19.¹ This equation is presented as Eq. 2-21 below.

$$r_b \geq \frac{1.5A_{ts}f_y}{w_t f'_c} \quad 2-21$$

Because closing knee joints are the focus herein, curved-bar nodes governed by Eq. 2-21 do not receive attention within this dissertation.



(a) Radial stress

(b) Circumferential bond stress

Figure 2-37 Stress state at curved-bar node²² assumed by ACI 318-19¹

If the two ties that intersect at a curved-bar node have different tie forces, Section 23.10.6 of ACI 318-19¹ requires that the length of the bend region of the reinforcing bars (measured along the bar centerline), l_{cb} , be sufficient to develop the difference in bar force between the straight portions of the bars extending from the bend. Considering the curved-bar node in a closing knee joint, circumferential bond stress develops along the bar bend due to the different tie forces if the diagonal strut angle is not equal to 45 degrees as shown in Figure 2-37(b). The centerline of the bar along the bar bend should be long enough to develop the difference in the tie forces at each end of the bend. Because the stress in the bar is assumed to vary from $f_y \tan \theta_c$ to f_y , the total circumferential bond stress to be developed is $f_y (1 - \tan \theta_c)$. As Klein²² suggested, for a 90-degree bend, the length (measured along the centerline of the bar) needed to develop the stress is proportional to the development length of straight bars by a factor of $(1 - \tan \theta_c)$ as expressed by Eq. 2-22.

$$l_{cb} > l_d (1 - \tan \theta_c) \quad 2-22$$

where, for a 90-degree bend, l_{cb} can be expressed in terms of r_b as

$$l_{cb} = \left(r_b + \frac{d_b}{2} \right) \frac{\pi}{2} \quad 2-23$$

Substituting l_{cb} into Eq. 2-23 and rearranging, the following equation results.

$$r_b > \frac{2l_d(1 - \tan \theta_c)}{\pi} - \frac{d_b}{2} \quad 2-24$$

In the FIP⁵⁸ requirements, any difference in force carried by the ties is not addressed in terms of circumferential bond stress. Rather, the design recommendation uses a different bearing area for the diagonal strut. The width of the strut at the bar bend is equal to $2r_b \sin \theta_c$ as shown in Figure 2-38. When the reinforcing bars yield, the force in the diagonal strut is $A_{ts}f_y / \cos \theta_c$ under equilibrium, resulting in an average stress on the bearing area of

$$f_c = \frac{A_{ts}f_y}{2r_b b_s \sin \theta_c \cos \theta_c} \quad 2-25$$

where the stress of concrete f_c should be limited to the effective compressive strength of concrete. Referring to ACI 318-19¹ provisions, The effective compressive strength, f_{ce} , is taken as $(0.6)(0.85)(f'_c)$. Moving r_b in the denominator to the left side of the equation and taking a conservative approximation give the minimum bend radius as presented in Eq. 2-26. It is noted that when θ_c is equal to 45 degrees, Eq. 2-26 is equivalent to Eq. 2-20.

$$r_b \geq \frac{A_{ts}f_y}{f'_c b_s \sin \theta_c \cos \theta_c} \quad 2-26$$

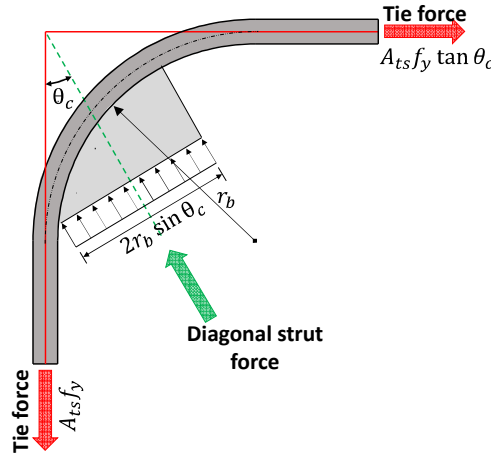


Figure 2-38 Stress state at curved-bar node in CEP-fib⁵⁴

To prevent splitting failure, Klein²² also suggested that clear side cover to the bar bend in knee joints be at least two times the longitudinal bar diameter. Otherwise, Klein²² recommended that the required bend radius in Eq. 2-20 be further enlarged by a factor of $2d_b/c_c$, where c_c is the

thickness of clear side cover to the longitudinal reinforcement. This recommendation by Klein²² was adopted into Section 23.10.3 of ACI 318-19.¹ Other than the requirements for the clear side cover, the code provisions¹ include guidelines in Section 23.10.4 of ACI 318-19¹ if multiple layers of reinforcement are used for curved-bar nodes. In this case, the bend radius of the inner layer should be used for design. In addition, in accordance with Section 23.10.5 of ACI 318-19,¹ the center of the bar curvature should be within the joint of a frame corner.

The methods proposed by Klein²² and FIP⁵⁴ are in agreement with past studies on closing knee joint. That is, the behavior of knee joints under closing moments is affected by the bend radius, mechanical reinforcement ratio, and clear side cover. Nevertheless, the design expressions lack experimental verification; the accuracy and the conservativeness remain unclear. It is still uncertain if the nodal zone factor for CTT nodes is applicable for the derivation of the expression for the required bend radius in closing knee joints. In addition, using the development length of straight bars to obtain the needed length of the bar bend is not well-supported. The effect of reduced clear side cover is also yet to have been thoroughly evaluated.

2.5 Strength Coefficients for Nodal Zones and Struts

For the assumed strut-and-tie model for a closing knee joint (see Figure 2-36), it is critical to check the strength of the CTT node at the outer corner, the diagonal strut, and the CCC node at the re-entrant corner. Although the design code has specified coefficients to reduce the strength of each element, values recommended in the literature for these coefficients vary.

2.5.1 Nodal Zone Coefficient for CTT nodes

It is important to review the nodal zone coefficient for CTT nodes because the compressive strength at the CTT node located at the outer corner of a closing knee joint determines if the longitudinal bars are able to fully develop their yield stress prior to concrete failure. ACI 318-19¹ specifies the nodal zone coefficient, β_n , for CTT nodes to be 0.6 as introduced in Table 2-1. Nevertheless, different values of the coefficient have been proposed in the past decades.

In a landmark report detailing the strut-and-tie method, Schlaich et al.¹⁹ proposed that the effective compressive strength of nodes is 80% of the concrete compressive design strength if tension bars are anchored in the nodes. If it is assumed that the uniaxial compressive strength has

a value of $0.85f'_c$, the nodal zone coefficient (for the purpose of comparison to β_n in ACI 318-19¹) is then equivalent to 0.8. Rogowsky and MacGregor⁵⁹ used the strut-and-tie method to design reinforced concrete deep beams, and the effective compressive strength was taken as $0.6f'_c$ for the nodal regions in the design. Therefore, the nodal zone coefficient is 0.71 if normalized by the factor 0.85. Jirsa et al.⁶⁰ suggested a higher value of the coefficient in an experimental study which particularly investigated the strength of nodes. The authors concluded the effective compressive strength can be taken as $0.8f'_c$ for CTT nodes, corresponding to a nodal zone coefficient of 0.94. All the aforementioned nodal coefficients are summarized in Table 2-4.

Table 2-4 CTT-nodal zone coefficients in the literature

| Reference | Nodal zone coefficient for CTT nodes |
|-------------------------------|--------------------------------------|
| ACI 318-19 ¹ | 0.6 |
| Schlaich et al. ¹⁹ | 0.8 |
| Rogowsky et al. ⁵⁹ | 0.71 |
| Jirsa et al. ⁶⁰ | 0.94 |

From the comparison among the proposed nodal zone coefficients for CTT nodes, the value ranges from 0.6 to 0.94. These will lead to different results when using the strut-and-tie method to design the same closing knee joint.

2.5.2 Strut Coefficient for Interior Struts

The strut that extends across the joint region is also a critical element that may control the capacity of closing knee joints. Being categorized as an interior strut located in a beam-column joint, the capacity of the diagonal strut should be reduced by a strut coefficient of 0.75 according to ACI 318-19.¹ Indeed, all other cases of interior struts have a strut coefficient less than 1.0 (see Table 2-2). It can be seen that the current code reflects that interior struts have reduced strength compared to boundary struts. As stated in Section 2.3.2.3, interior struts are weaker than boundary struts because tension develops transverse to the strut.¹ For example, as explained in the study by Rezaei,⁵³ interior struts in a deep beam are weaker than boundary struts due to tensile strain caused by bending.

Interior struts were previously named bottle-shaped struts as ACI 318-14 indicates.⁴⁹ Some researchers have argued that bottle-shaped struts are not necessarily weaker in terms of compressive strength. Furthermore, researchers have argued that the strength of bottle-shaped struts might not be related to the transverse reinforcement as the code implies. Brown et al.⁵² conducted an experimental program that included tests on 26 panel specimens with various types of transverse reinforcement and/or node reinforcement. The results revealed that the failure initiated at the interface where load was applied regardless of the pattern of the reinforcement. That is, the transverse reinforcement had little effect on the strut strength. In addition, the experimental data provided an average strut coefficient of 1.14 with a minimum value of 0.62. These values imply that the suggested strut coefficient in the current code is conservative.

Higher values for strut coefficients were obtained in a study conducted by Sahoo et al.⁶¹ The authors tested 14 specimens that consisted of panels and prisms without transverse reinforcement. The results showed that the average strut coefficient based on the experimental results is 1.07 with a minimum value of 0.95. The authors then concluded that unreinforced bottle-shaped struts are not as weak relative to prismatic struts as widely believed. Laughery et al.⁶² and Pujol et al.⁶³ also conducted tests on panels and prisms to study bottle-shaped struts. Furthermore, the authors collected data from the literature to perform a database analysis. Based on the results, bottle-shaped struts are not necessarily weaker than prismatic struts as the design code¹ implies.

In summary, researchers have suggested values that are in contrast to the strut coefficients in the current code.¹ The appropriateness of applying the current code-specified strut coefficient to closing knee joints should be evaluated.

2.6 Research Need

Despite past research on knee joints under closing moments, limited tests directly relevant to the evaluation of curved-bar nodes are presented in the literature. Among the collected data, the majority assessed different detailing patterns of reinforcement within RC frame corners. Little attention, however, was given to quantifying the effect of the bend radii, the concrete cover, and the longitudinal mechanical reinforcement ratio ω , all of which are expected to impact behavior as suggested by the current curved-bar node design procedure in ACI 318-19.¹ In addition, the cross-sections of the specimens in past experiments are generally smaller than realistic RC frame corners. Most tests in the evaluation database (which will be introduced in Chapter 6) have effective depths

less than 12 in., and only eight specimens have effective depths greater than 24 in. Additional specimens with sizes representative of frame corners in the field and detailed to evaluate curved-bar nodes should be designed and tested to verify the relevant design expressions.

It is necessary to evaluate the design procedure to ensure the STM code provisions result in efficient, safe, and serviceable knee joints. This research project aims to study the behavior of curved-bar nodes and develop an analytical, consistent method for detailing knee joints. The study is expected to provide results that relate directly to code provisions regarding the design of knee joints using the strut-and-tie method.

3. EXPERIMENTAL PROGRAM

3.1 Overview

The experimental program of this study is presented in this chapter. Twenty-four knee joint specimens were tested. The detailed design of the specimens is first introduced, followed by descriptions of specimen fabrication, instrumentation, the test procedure, and corresponding material tests.

3.2 Test Specimens

As mentioned in the previous chapter, when designing knee joints under closing moments using the strut-and tie method, the CTT node at the outer corner can be modeled by a curved-bar node, which significantly affects the behavior of the knee joint. Based on past research, details incorporated into the current design provisions for curved-bar nodes in ACI 318-19,¹ and other factors that may impact the behavior of closing knee joints, seven variables were identified and categorized as follows: (a) bend radii of longitudinal reinforcement, (b) longitudinal mechanical reinforcement ratio, (c) one versus two layers of longitudinal reinforcement, (d) concrete clear side cover, (e) presence of circumferential bond stress, (f) continuous versus lap-spliced longitudinal reinforcing bars, and (g) presence of distributed reinforcement.

To investigate the effect of the variables mentioned above, 24 specimens were developed as summarized in Table 3-1. The specimens were divided into five distinct series: (a) single-layer longitudinal bars, (b) double-layer longitudinal bars, (c) reduced clear side cover, (d) adjoining members with different cross sections, and (e) multiple-purpose. It should be noted that the values for material properties and bend radii, r_b , in Table 3-1 are measured values, and the mechanical longitudinal reinforcement ratio was calculated using the measured values from material tests (introduced in Section 3.7). The detailed design of the specimens is introduced in the following sections.

3.2.1 Series I: Single-Layer Longitudinal Bars

The purpose of Series I was to investigate the effect of the bend radius on the behavior of closing knee joints as predicted by the model for curved-bar nodes. More specifically, the

requirement for r_b expressed in Eq. 2-20 was evaluated. The variables to be investigated were the bend radius and the longitudinal mechanical reinforcement ratio, which is defined as Eq. 3-1.

$$\omega = \frac{f_y}{f'_c} \frac{A_{ts}}{bd} \quad 3-1$$

where b is the cross-sectional width and d is the effective depth. Eight specimens were included in Series I.

Table 3-1 Summary of specimens

| Series | Group ID | Specimen ID | Material | | Cover and Longitudinal Reinforcement | | | | | | Criterion for Bend Radii |
|---|--|-------------|-----------------|----------------|--------------------------------------|---------|---------------------------------|----------------|----------------|-------------------|--------------------------|
| | | | f'_c (ksi) | f_y (ksi) | c (in.) | Pattern | A_{ls} (in. ²) | r_b (in.) | d_b (in.) | ω (%) | |
| I: S-Series Single-Layer Longitudinal Bars | S-1 | S-27-R3-L | 3.45 | 69.8 | 2.0 | 6-No. 8 | 4.74 | 3.9 | 1.0 | 27.9 | Standard hook |
| | | S-27-R11-L | 3.49 | | | | | 10.8 | | 27.6 | Eq. 2-20 |
| | S-2 | S-18-R3 | 5.17 | 67.1 | | 6-No. 8 | 4.74 | 3.3 | 1.0 | 17.9 | Standard hook |
| | | S-18-R6 | 5.02 | | | | | 6.5 | | 18.4 | In between |
| | | S-18-R9 | 5.08 | | | | | 9.8 | | 18.2 | Eq. 2-20 |
| | S-3 | S-13-R3 | 5.15 | 66.1 | | 6-No. 7 | 3.60 | 3.3 | 0.875 | 13.4 | Standard hook |
| | | S-13-R5 | 5.28 | | | | | 4.7 | | 13.1 | In between |
| | | S-13-R8 | 5.35 | | | | | 8.1 | | 12.9 | Eq. 2-20 |
| | II: D-Series Double-Layer Longitudinal Bars | D-1 | D-20-R2 | 5.04 | | 69.1 | 2.0 | 8-No. 7 | 4.80 | 2.7 | 0.875 |
| D-20-R6 | | | 5.14 | 6.5 | 19.8 | | | | | In between | |
| D-20-R9 | | | 4.99 | 9.9 | 20.4 | | | | | Eq. 2-20 | |
| D-2 | | D-16-R2 | 5.38 | 62.6 | 10-No. 6 | 4.40 | | 2.4 | 0.625 | 15.6 | Standard hook |
| | | D-16-R5 | 4.94 | | | | | 5.9 | | 17.0 | In between |
| | | D-16-R10 | 5.29 | | | | | 10.2 | | 15.9 | Eq. 2-20 |
| III: C-Series Reduced Clear Side Cover | | C-1 | C-17-R3 | 5.29 | 66.3 | 1.25 | | 6-No. 8 | 4.74 | 3.3 | 1.0 |
| | C-17-R6 | | 5.33 | 6.5 | | | 17.1 | | | In between | |
| | C-17-R9 | | 5.04 | 9.2 | | | 18.1 | | | Eq. 2-20 | |
| | C-17-R12 | | 5.16 | 11.5 | | | 17.7 | | | Factored Eq. 2-20 | |
| IV: B-Series Different Cross-Sections | B-1 | B-16-R3 | 5.20 | 66.3 | 2.0 | 4-No. 8 | 3.16 | 3.2 | 1.0 | 11.7 | Standard hook |
| | | B-16-R6 | 5.20 | | | | | 6.5 | | 16.2 | Eq. 2-20 |
| V: M-Series Multiple Purposes | LS | LS-S-18-R3 | 5.04 | 66.3 | 2.0 | 6-No. 8 | 4.74 | 3.3 | 1.0 | 18.1 | Standard hook |
| | | LS-S-13-R3 | 4.76 | 64.7 | | 6-No. 7 | 3.60 | 2.8 | 0.875 | 14.2 | Standard hook |
| | TR | TR-S-18-R3 | 4.84 | 66.3 | | 6-No. 8 | 4.74 | 3.3 | 1.0 | 18.9 | Standard hook |
| | | TR-S-13-R3 | 4.66 | 64.7 | | 6-No. 7 | 3.60 | 2.7 | 0.875 | 14.5 | Standard hook |

3.2.1.1 Specimen details

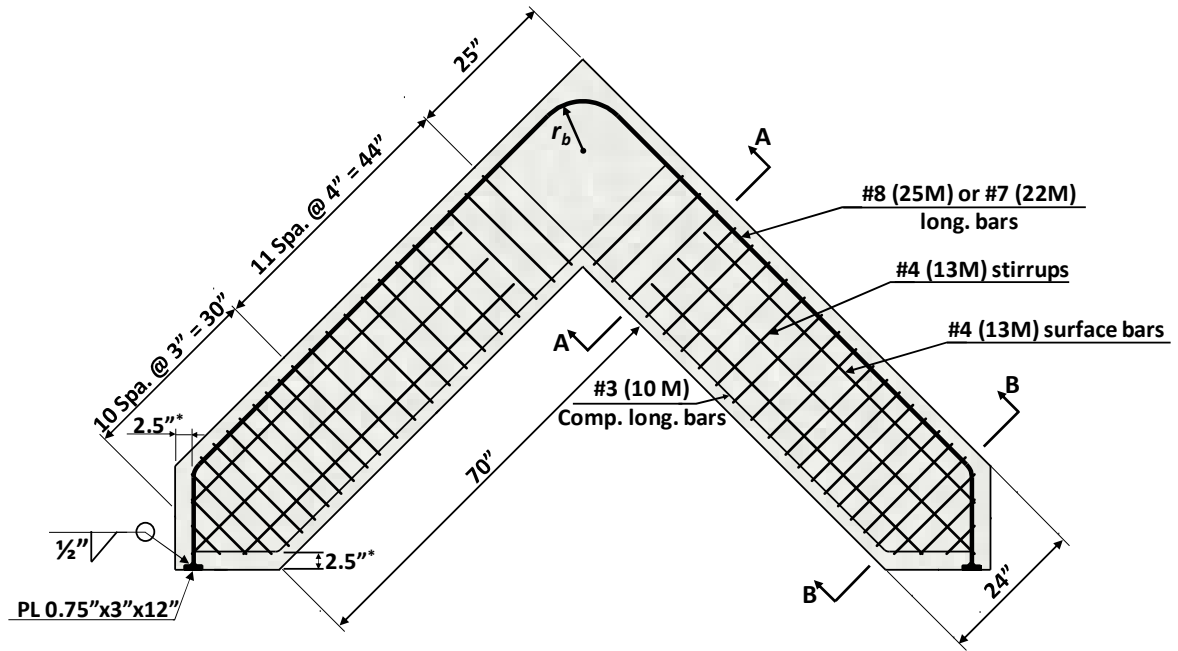
The eight specimens in this series were classified into three groups based on the longitudinal mechanical reinforcement ratio (13%, 18%, and 28%). These three values of ω resulted from three different combinations of concrete compressive strengths and reinforcing bar patterns. As indicated in Table 3-1, the concrete compressive strengths were approximately 3.5 ksi, 5.1 ksi, and 5.3 ksi. The longitudinal reinforcement consisted of either six No. 8 bars or six No. 7 bars. All the reinforcing bars were Grade 60 (ASTM A615⁶⁴).

Each group had two or three different values of r_b based on the following criteria: 1) the minimum inside bend diameter for standard hooks required by ACI 318-19,¹ 2) the bend radius satisfying Eq. 2-20, and 3) a bend radius between these two other radii. Group S-1 did not include a specimen with a bend radius satisfying criterion (3) because this group was used as an initial group to preliminarily examine the model for curved-bar nodes and ensure the test frame facilitated the tests properly. It should be noted that the measured bend radius of the second specimen in Group S-1 was slightly smaller than that required to meet Eq. 2-20 due to unpredictable variations in material properties. That is, the yield strength of the reinforcing bars was higher than expected. The clear side cover to the longitudinal bars was chosen to be 2.0 in., which requires no modification to the bend radius according to ACI 318-19.¹

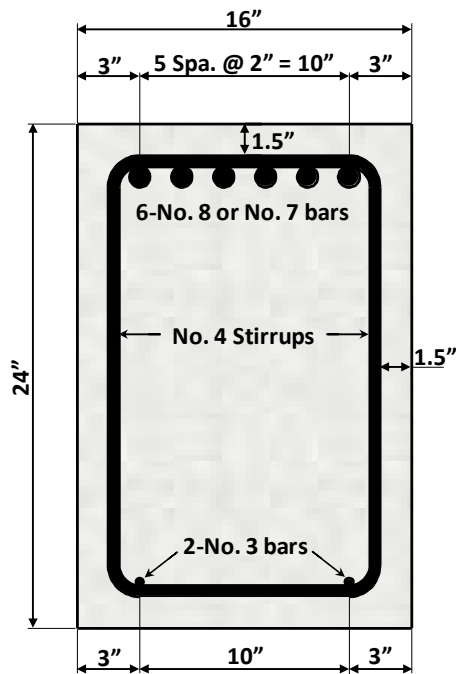
The typical details for the specimens in Series I are shown in Figure 3-1. Each knee joint specimen consisted of a joint and two perpendicular adjoining members (that is, legs) that framed into the joint. Each of the legs had a length of 70 in. At the end of each leg, a vertical surface was provided to facilitate the application of horizontal force than produced closing moments in the joint, while a horizontal surface was provided to place the specimen on roller supports. The two legs had identical cross-sections with a width of 16 in. and a depth of 24 in.

Both legs were provided with No. 4 stirrups spaced at 4 in. as shear reinforcement to prevent shear failure outside of the joint region. In addition, the stirrups were tightened to a spacing of 3 in. near the ends of the legs to improve anchorage (see Figure 3-1). No stirrups were provided in the joint for this series in order to investigate the strength and behavior without the influence of transverse reinforcement. The compression reinforcement in the legs consisted of two No. 3 bars and was anchored in the joint. Each end of the longitudinal bars was welded to a steel plate to prevent an anchorage failure except for specimens in Group S-1. The steel plate had dimensions

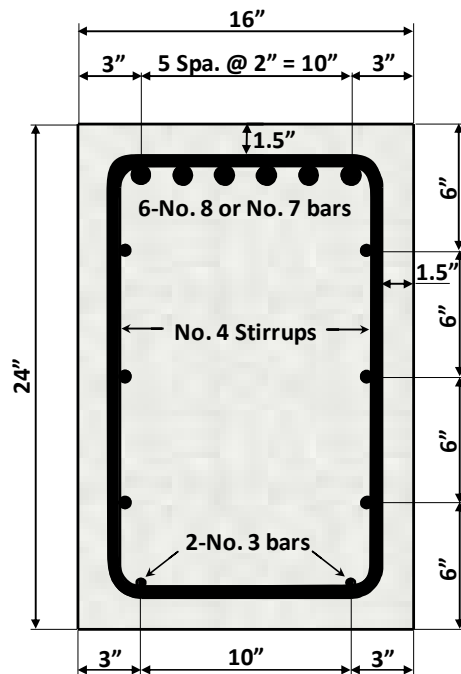
of 0.75 in. by 3 in. by 12 in., and the weld for each longitudinal bar had an effective throat depth of 0.5 in. Moreover, three No. 4 surface bars were provided as skin reinforcement longitudinally along each leg to further decrease the risk of failure in the leg.



*Cover to longitudinal reinforcement



Section A-A



Section B-B

Figure 3-1 Typical specimen details for Series I

3.2.1.2 Nomenclature

A nomenclature was developed to identify the specimens in Series I as shown in Figure 3-2. The letter “S” indicates the series code “Single,” the number after the series code indicates the approximate mechanical reinforcement ratio, the letter “R” followed by a value indicates the approximate bend radius, and the letter “L” is included for the specimens with relatively low concrete strength.

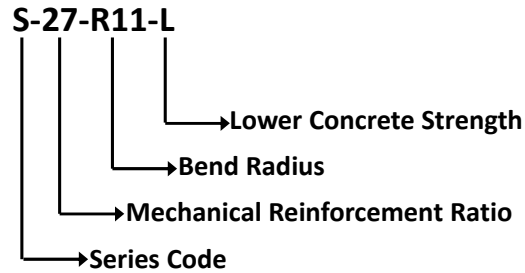


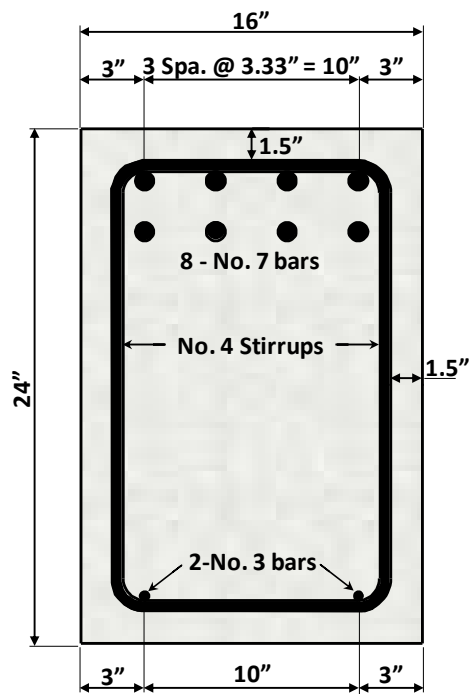
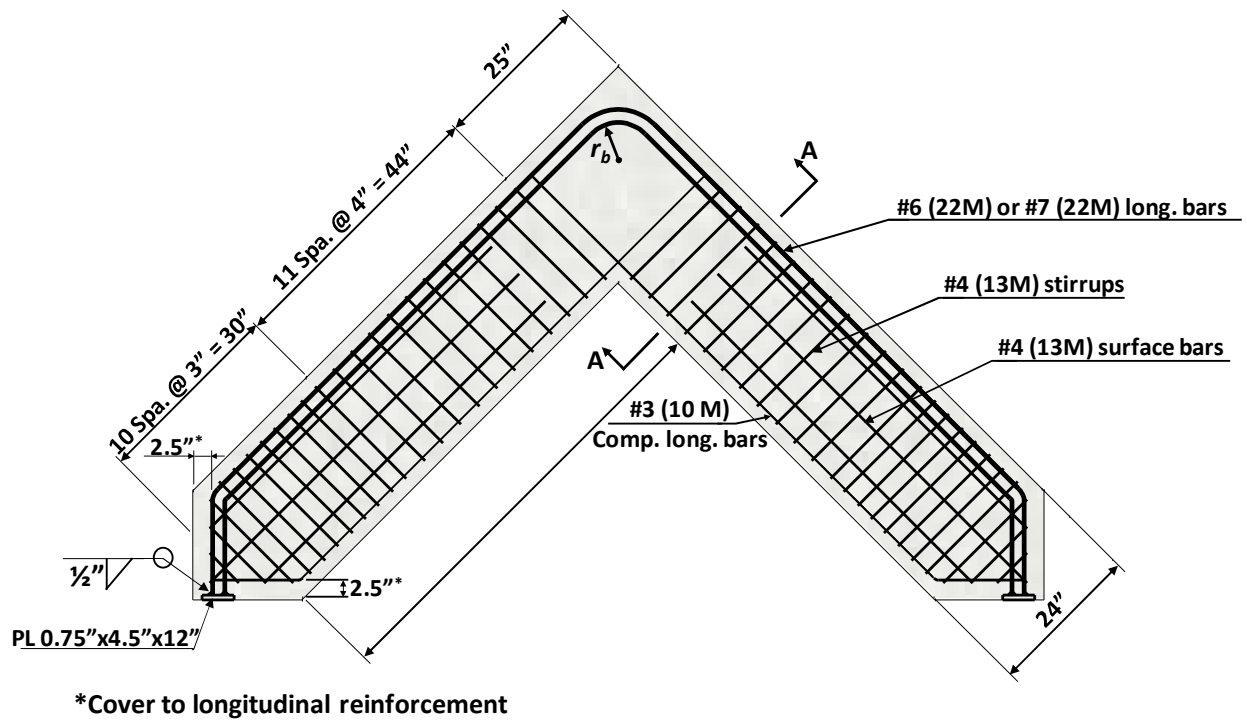
Figure 3-2 Nomenclature for Series I

3.2.2 Series II: Double-Layer Longitudinal Bars

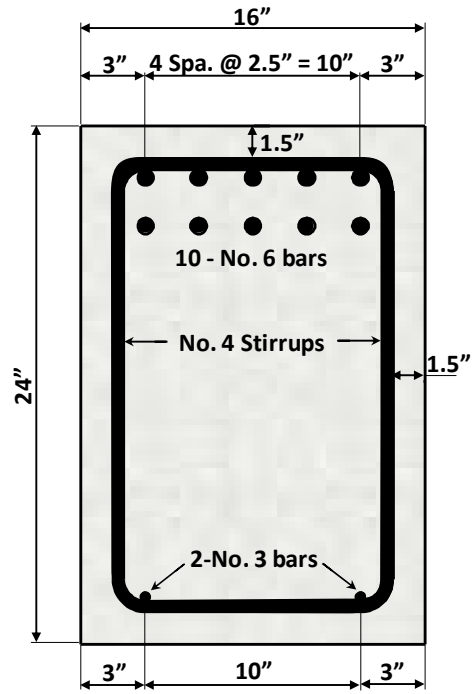
Similar to Series I, Series II was developed to investigate the effect of the bend radius on the behavior of knee joints under closing moments. However, the longitudinal reinforcement was arranged in two layers. As with Series I, the bend radius and longitudinal mechanical reinforcement ratio were again investigated. Six specimens classified into two groups were included in the series as summarized in Table 3-1.

3.2.2.1 Specimen details

The typical details of the Series II specimens are illustrated in Figure 3-3. Two different patterns of longitudinal reinforcing bars positioned in two layers were designed for this series: eight No. 7 bars (four in each layer) and ten No. 6 bars (five in each layer). The clear spacing between layers was 1.5 in. All the reinforcing bars were Grade 60 (ASTM A615⁵⁶). The concrete compressive strengths were approximately 5 ksi. The mechanical reinforcement ratio of Group D-1 and Group D-2 was approximately 20% and 16%, respectively. For Series II, the same criteria for the bend radius introduced for Series I was again used, and no modification factor was applied to the bend radius because a concrete clear side cover of 2.0 in. was used.



Section A-A
Specimens with No. 7 bars



Section A-A
Specimens with No. 6 bars

Figure 3-3 Typical specimen details for Series II

Like the Series I specimens, each specimen in Series II consisted of a joint and two perpendicular legs, each with a length of 70 in. A vertical surface and a horizontal surface were also provided at the end of each leg to apply loads and allow the specimen to be supported. The two legs had identical cross-sectional dimensions of 16 in. by 24 in. In each leg, No. 4 stirrups were provided with a spacing of 4 in. and with a closer spacing of 3 in. near the ends of the legs to prevent a shear failure or an anchorage failure. No. 4 surface reinforcement was also provided as in Series I. In addition, each end of the longitudinal reinforcement was welded to a steel plate to provide more anchorage. The plate had dimensions of 4.5 in. by 12 in. to allow the two layers of longitudinal reinforcing bars to be welded. The thickness of the plate was 0.75 in. No stirrups were provided in the joint. The compression reinforcement consisted of two No. 3 bars.

3.2.2.2 Nomenclature

A nomenclature was developed to identify the specimens in Series II as shown in Figure 3-4. The letter “D” indicates the series code “Double,” the number following the series code is the approximate mechanical reinforcement ratio, and the letter “R” followed by a value indicates the approximate bend radius.

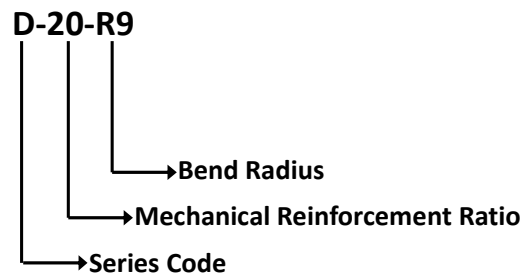


Figure 3-4 Nomenclature for Series II

3.2.3 Series III: Reduced Clear Side Cover

Series III was developed to investigate potential effects resulting from a clear concrete side cover less than two times the longitudinal bar diameter. Evidence of the effect of clear side cover on specimen behavior has been shown in past research,²³ and consideration of side cover is included in the design procedure required in ACI 318-19.¹ For this series, a clear side cover of 1.25 in. was selected. To make a direct comparison, specimens from Group S-2 in Series I were

selected as the control group. That is, specimens in Series III had the same target mechanical reinforcement ratio and a single layer of longitudinal reinforcing bars. Four specimens were included in the series.

3.2.3.1 Specimen details

The four specimens were each detailed with a different bend radius. In addition to the three previously used criteria for the bend radius (see Section 3.2.1.1), one more criterion for the bend radius, referred to as criterion (4), was used for this series: enlarged bend radius due to thin side cover. As previously introduced and based on the current requirement in ACI 318-19,¹ a factor of 2.0 in. divided by 1.25 in. was multiplied by the bend radius calculated using criterion (2) (that is, Eq. 2-20). The resulting target bend radius was 14.5 in. It should be noted that the actual bend radius was slightly smaller than the target value due to the difficulty in estimating the springback (introduced later in Section 3.3.3) of the reinforcement when bending the bars.

The typical details of the specimens in Series III are shown in Figure 3-5. The target compressive strength of concrete was 5 ksi for the Series III specimens. Furthermore, six Grade 60 (ASTM A615⁶⁴) No. 8 bars were arranged in one layer to create the same mechanical reinforcement ratio as the Group S-2 specimens. The overall dimensions were the same as the previous two series. The closed stirrups, the surface reinforcement, and the compression reinforcement were also arranged in the same pattern. To provide a reduced clear side cover, the longitudinal reinforcing bars were placed with a wider spacing over the cross-sectional width compared to the specimens in the other test series. The transverse reinforcement was, in turn, designed to be wider for the specimens in Series III as well. Based on the positions of the longitudinal bars, the end anchoring steel plate had dimensions of 3 in. by 13.5 in.

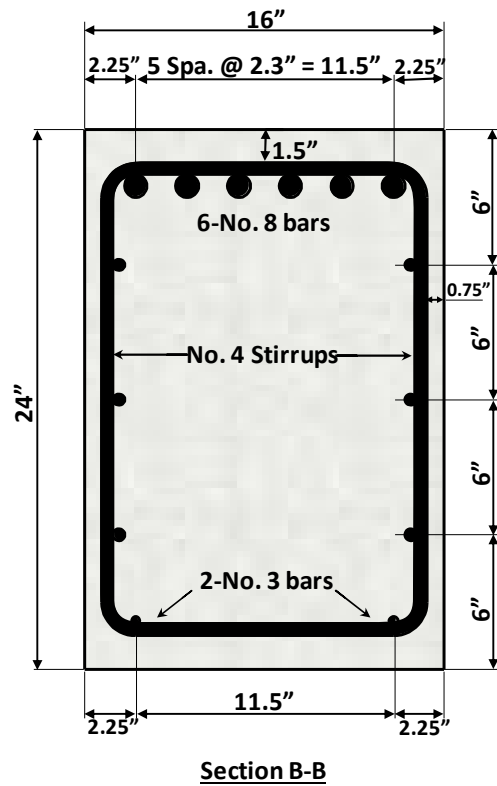
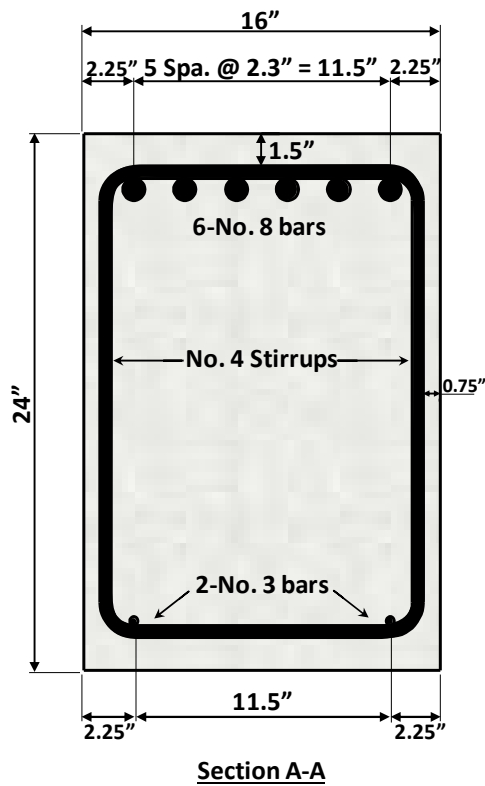
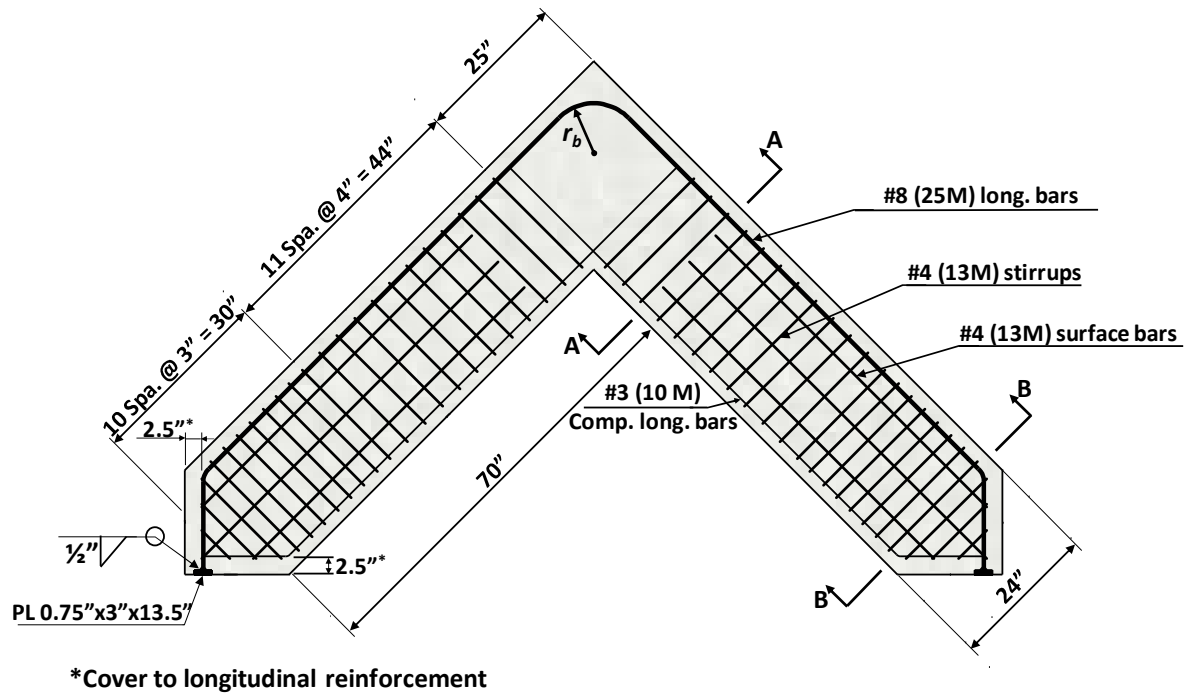


Figure 3-5 Typical specimen details for Series III

3.2.3.2 Nomenclature

The nomenclature developed to identify the specimens in Series III is shown in Figure 3-6. The letter “C” indicates the series code “Cover,” the number following the series code indicates the approximate mechanical reinforcement ratio, and the letter “R” following by a value indicates the approximate bend radius.

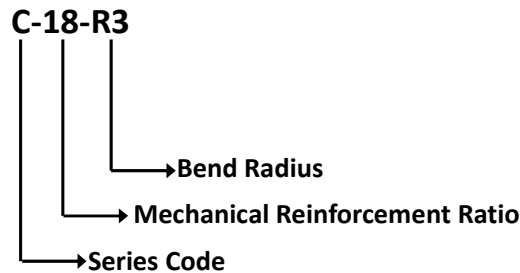


Figure 3-6 Nomenclature for Series III

3.2.4 Series IV: Adjoining Members with Different Cross-Sections

Series IV was developed to investigate curved-bar nodes for which the ties intersecting at the node have different forces, resulting in the presence of circumferential bond stress at the curved-bar node. In this case, the angle of the diagonal strut is not equal to 45 degrees.

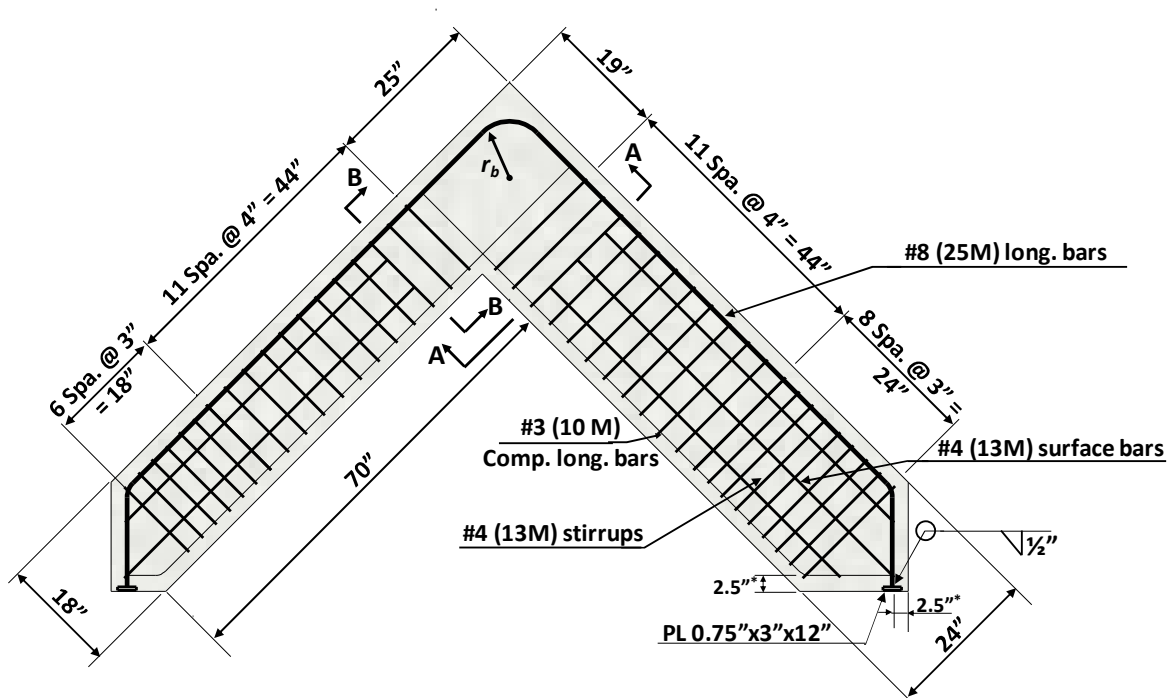
3.2.4.1 Specimen details

To create the desired stress distribution, the two adjoining members were designed to have different depths. One leg was 16 in. in width and 24 in. in depth, while the other was 16 in. in width and 18 in. in depth, as shown in Figure 3-7. With this arrangement, when the longitudinal bars yield within the leg with a shallower depth, the bars in the deeper leg do not reach the yield stress. Therefore, the bar stresses at each end of the bar bend are expected to be different, causing the angle of the diagonal strut θ_c (refer to Figure 2-5) to not equal 45 degrees. Reinforcement in the legs was similar to the details used in the other series. A steel plate was also welded to the end of the longitudinal reinforcing bars as shown in Figure 3-7.

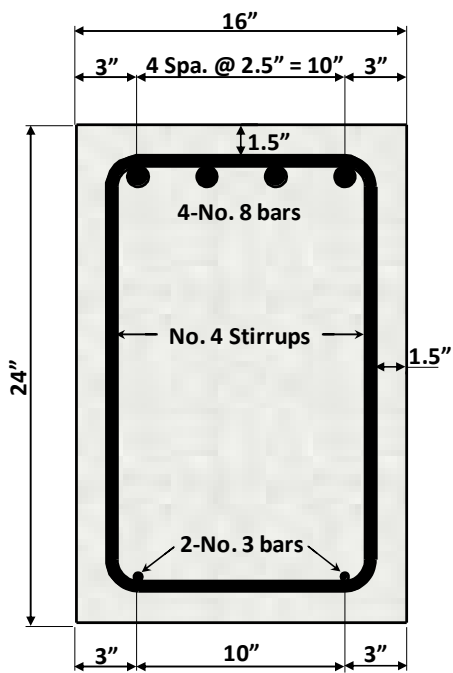
The criteria for the bend radii of the specimens were based on 1) the minimum inside bend diameter of standard hooks required by ACI 318-19,¹ 2) the bend radius satisfying Eq. 2-20, and a

new criterion based on the bend radius satisfying Eq. 2-24. Based on test results of other specimens, a specimen meeting the requirement of Eq. 2-24 was eliminated from the test program. Further details are given in Chapter 5.

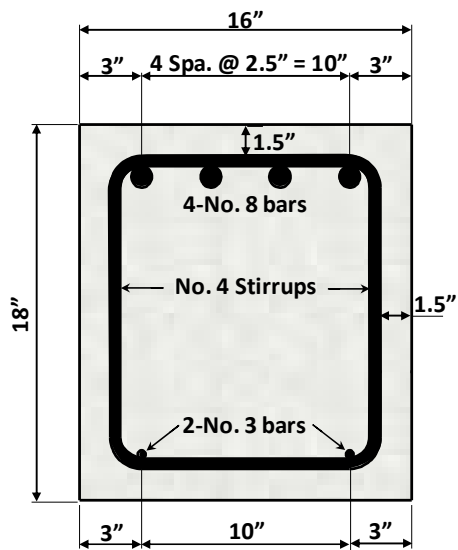
The target compressive strength of concrete was 5 ksi for the Series IV specimens. Four Grade 60 (ASTM A615⁶⁴) No. 8 bars were arranged in one layer. Therefore, the expected longitudinal mechanical reinforcement ratios for the shallow and deep legs were 19.0% and 13.7%, respectively, and the actual values were 16.2% and 11.7%, respectively, for both specimens. Both of these values of ω are provided in Table 3-1.



*Cover to longitudinal reinforcement



Section A-A



Section B-B

Figure 3-7 Typical specimen details for Series IV

3.2.4.2 Nomenclature

The nomenclature developed to identify the specimens in Series IV is shown in Figure 3-8. The letter “B” indicates the series code “Bond,” the number following the series code indicates the approximate mechanical reinforcement ratio for the shallow leg, and the letter “R” followed by a value indicates the approximately bend radius.

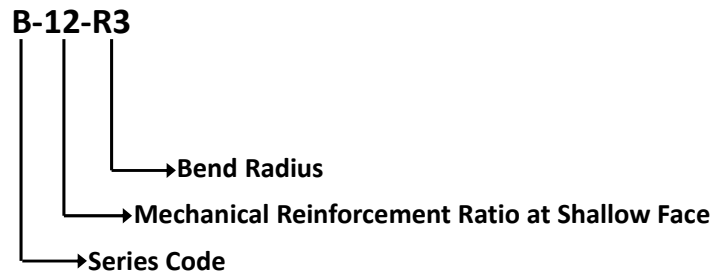


Figure 3-8 Nomenclature for Series IV

3.2.5 Series V: Multiple Purposes

Series V was developed to achieve two primary purposes. One purpose was to investigate the performance of knee joints with typical details in which the longitudinal bars are spliced within the joint region. The second purpose was to investigate if transverse reinforcement provided within the joint would aid in delaying the failure of closing knee joints. This series was planned to directly compare to specimens in Group S-2 and Group S-3 in Series I and therefore had similar cross sections and mechanical reinforcement ratios. Four specimens were included, all of which had a bend radius based on the minimum inside bend diameter of standard bends required by ACI 318-19.¹

3.2.5.1 Specimen details

The typical details of specimens in this series are shown in Figure 3-9 (Group TR) and Figure 3-10 (Group LS). As shown in Figure 3-9, to investigate the effect of transverse reinforcement, two specimens were constructed with the minimum amount of distributed reinforcement in accordance with Section 23.5 of ACI 318-19¹ provided in the joint. This transverse reinforcement consisted of No. 4 bars with a spacing of 5 in. The mechanical reinforcement ratio and reinforcement in the legs of the two specimens were designed to be the

same as those in Group S-2 and Group S-3 in Series I. The longitudinal bars were continuous through the joint.

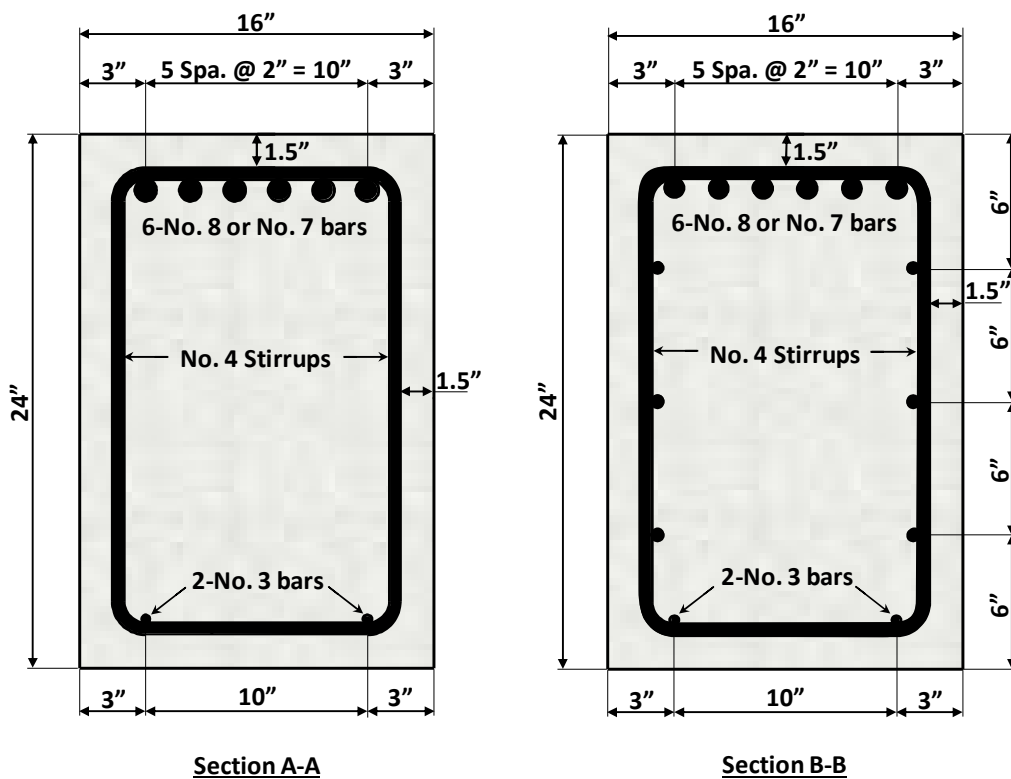
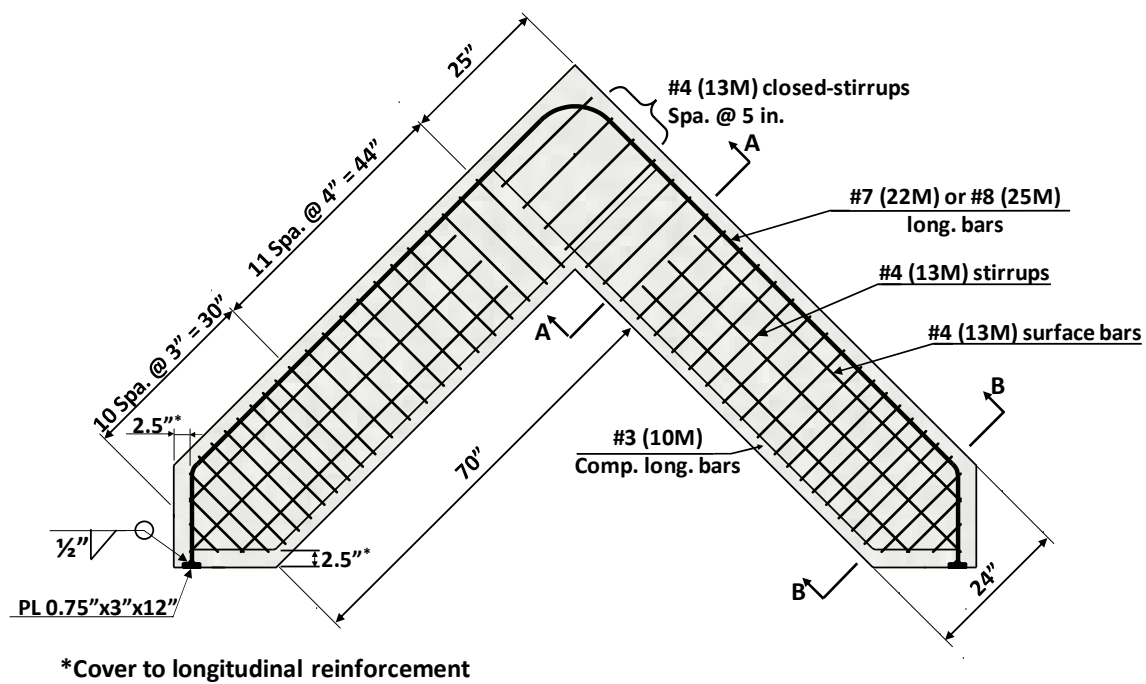
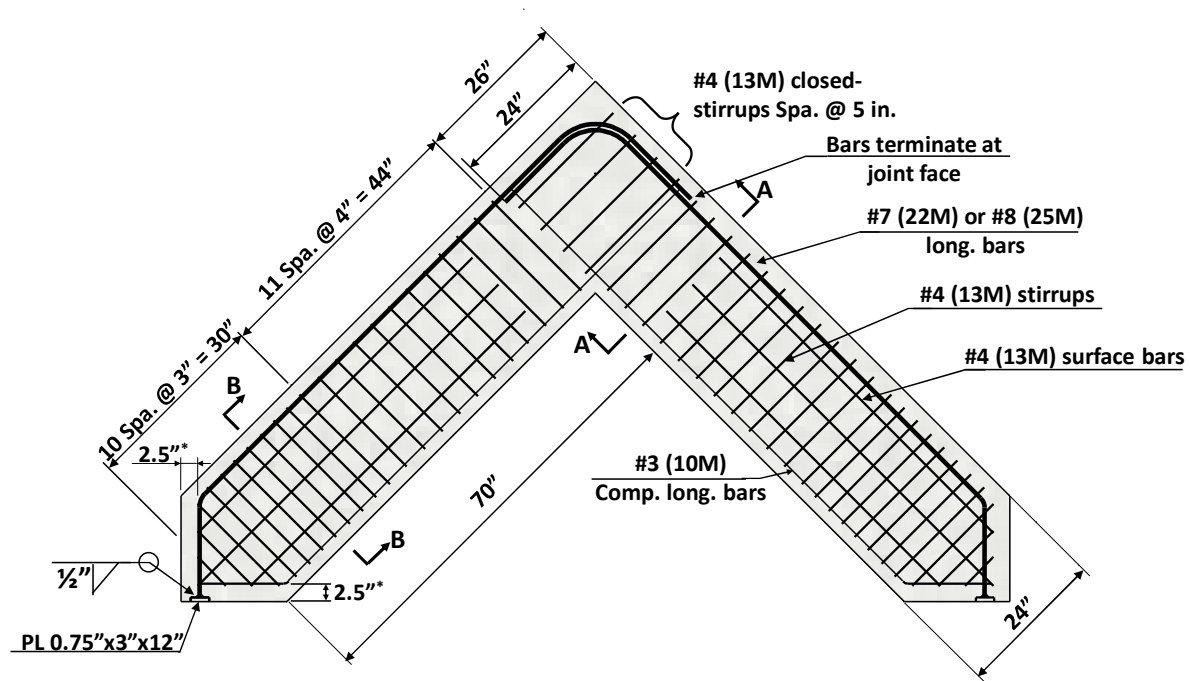
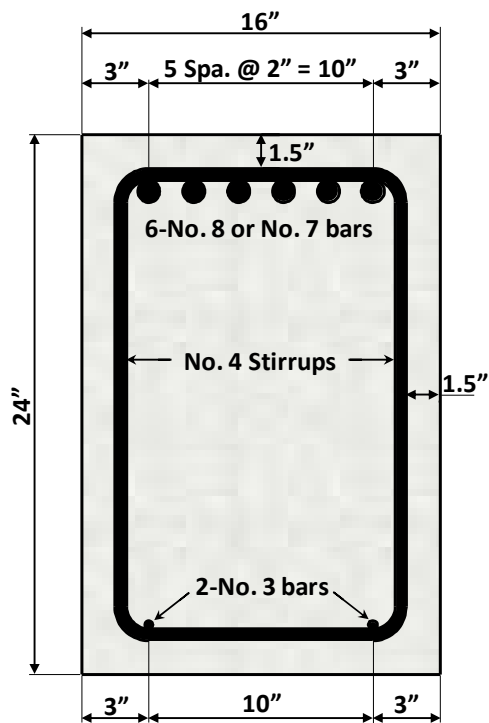


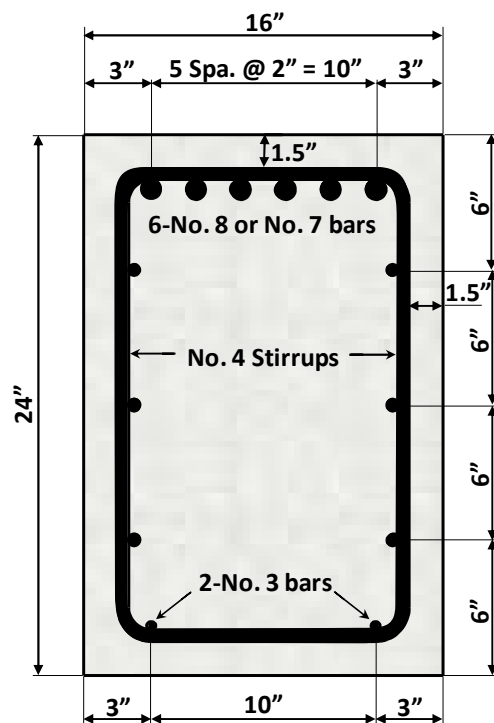
Figure 3-9 Typical specimen details for Group TR in Series V



*Cover to longitudinal reinforcement



Section A-A



Section B-B

Figure 3-10 Typical specimen details for Group LS in Series V

To represent a commonly used detail, the longitudinal reinforcing bars of the two other specimens in Series V were individually anchored in the joint with a 90-degree bend and a tail as shown in Figure 3-10. That is, the bars were lap-spliced within the joint. Terminated in alignment with the joint face, the tail had a length longer than the code¹ required extension for a 90-degree hook, $12d_b$ or 12 in. The development length, l_{dh} , also complied with the code requirement.¹ The minimum amount of distributed reinforcement was also provided in the joint, consisting of No. 4 bars with a spacing of 5 in. as for the specimens in Group TR. Furthermore, the mechanical reinforcement ratio and reinforcement details in the legs of the two specimens were designed to match those of Group S-2 and Group S-3 in Series I to facilitate direct comparisons.

3.2.5.2 Nomenclature

The nomenclature developed to identify the specimens in Series V is shown in Figure 3-11. The letter “LS” indicates the series code “Lap-Splice,” and the letter “TR” indicates the series code “Transverse Reinforcement.” The letter “S” indicates the arrangement of longitudinal reinforcing bars in a single layer within the legs. The number following the series code indicates the approximate mechanical reinforcement ratio and the letter “R” followed by a value indicates the approximate bend radius.

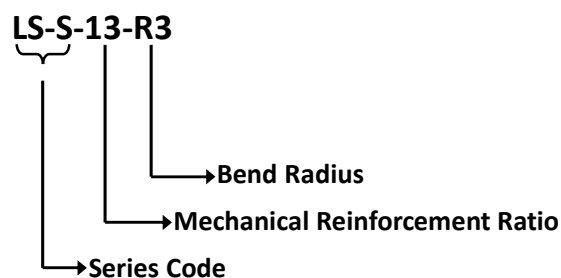


Figure 3-11 Nomenclature for Series V

3.3 Fabrication of Specimens

3.3.1 Concrete Mixture Design

Two concrete mixtures were developed to provide two different compressive strengths of concrete, as shown in Table 3-2. Having a water-cement ratio of 0.57 and an air-entraining

admixture, Mixture 1 has a target strength of 3.5 ksi and was used for Group S-1 in Series I. Mixture 2 was developed for the rest of the specimens and had a target compressive strength of 5.0 ksi. Mixture 2 had a water-cement ratio of 0.62 and no air-entraining admixture. Both mixture designs used Type I cement and river gravel for the coarse aggregate. The river gravel had a nominal maximum size of 0.75 in., which was specified to fit the requirement of minimum spacing of longitudinal reinforcement in accordance with Section 25.2 of ACI 318-19.¹

Table 3-2 Concrete mixture designs

| Material | Mixture 1 | Mixture 2 | Units |
|-----------------------------------|-----------|-----------|--------------------|
| Type I cement | 340 | 423 | lb/yd ³ |
| River gravel (3/4 in. nominal) | 1850 | 1900 | |
| Sand | 1375 | 1456 | |
| Class C fly ash | 100 | 0 | |
| Water | 250.5 | 263.5 | |
| Air-entraining Admixture | 1.2 | 0 | oz/100 lb CM |
| Slump | 5 to 7 | 5 to 7 | in. |
| Water-cement ratio | 0.57 | 0.62 | |

3.3.2 Formwork

As shown in Figure 3-12, the formwork for the specimens consisted of two major parts: a platform and side forms. The platform was made of phenolic plywood supported on 2-in. by 4-in. dimensional lumber spaced at 12 in. The platform was large enough to contain two sets of concrete forms.

After the platforms were placed, two sets of side forms were built on the platform. The casting surface of the side forms was made of phenolic plywood. Each set consisted of two outer walls, two inner walls, and two end assemblies, as shown in Figure 3-12. Each component included vertical studs cut from 2-in. by 4-in. dimensional lumber and spaced at 12 in. or less. Moreover, diagonal braces were installed on the inner walls to resist outward pressure when casting. Two

0.25-in. threaded rods passed through each leg of the specimens and were anchored at the inner and the outer walls using nuts and omni wedges to prevent expansion of the forms during casting. All joints in the formwork were caulked before placing the reinforcement to prevent concrete leakage.

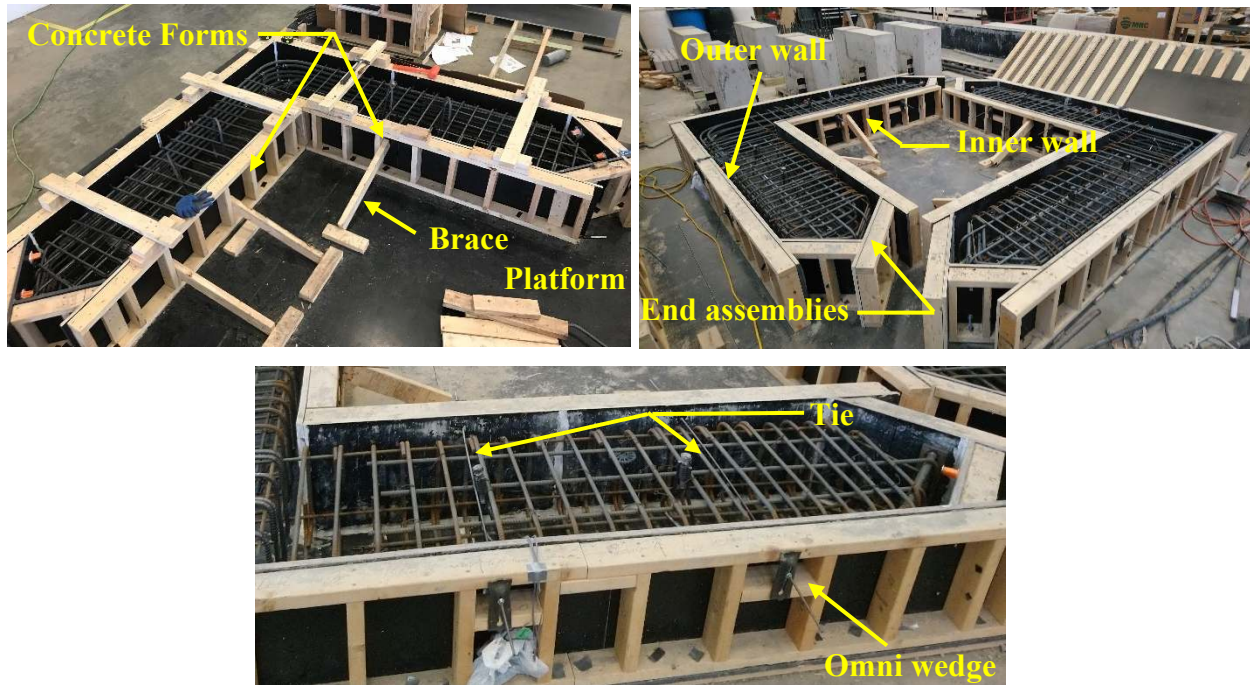


Figure 3-12 Formwork

3.3.3 Steel Reinforcement

All reinforcement (including tension and compression longitudinal reinforcement, closed stirrups, and surface reinforcement) was Grade 60 steel meeting ASTM A615.⁶⁴ Most of the reinforcement was pre-bent and delivered to Bowen Laboratory at Purdue University. Some reinforcing bars were delivered with extra length to be trimmed or bent in the lab to best meet the actual need.

Because most of the bend radii were not standard bends, special considerations were needed. In other words, typical center pins (as shown in Figure 3-13) used for bending a specific bar size did not provide the bend diameters needed in this study. According to the reinforcement fabricator, available pin diameters at the fabrication facility included 2 in. through 11 in. with increments of 0.5 in. in addition to pins with diameters of 12 in., 16 in., and 24 in. Secondly, the

springback phenomena that occurs when bending reinforcing bars needed to be taken into account. Springback resulted in actual bend diameters that were 10% to 30% larger than the center pin used to bend the bars. The amount of springback might be related to bending speed, size of the reinforcing bars, and size of the center pin. Considering the available pin diameters and the potential springback, the pin that would provide the closest bend diameter to the target diameter was selected. The target bend diameters and selected pin diameters are summarized in Table 3-3

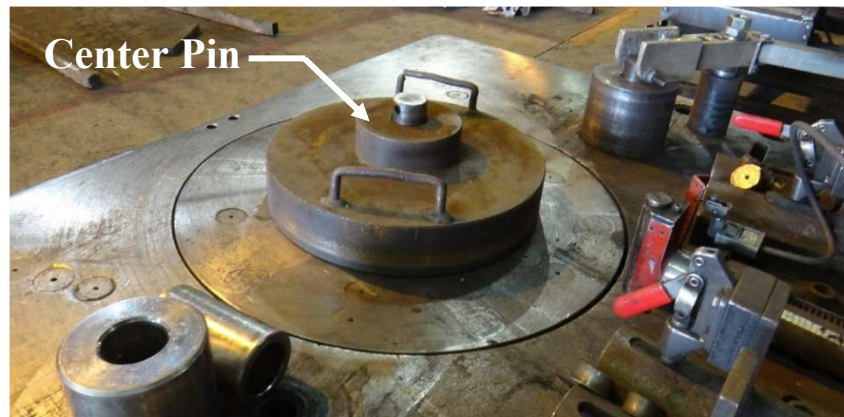


Figure 3-13 Reinforcing bar bending table

Following reinforcing bar fabrication, measurement of the actual bend diameters was conducted at the lab and assisted by the software Adobe Photoshop®. The bar bend to be measured was first placed on a grid paper and a photo was taken as shown in Figure 3-14. The image was then imported into the software. With a known grid size, the size of the bar bend was determined by the number of pixels counted by the program. Detailed procedures and calculations for this process are presented in Appendix A. The measured bend radii are summarized in Table 3-1.

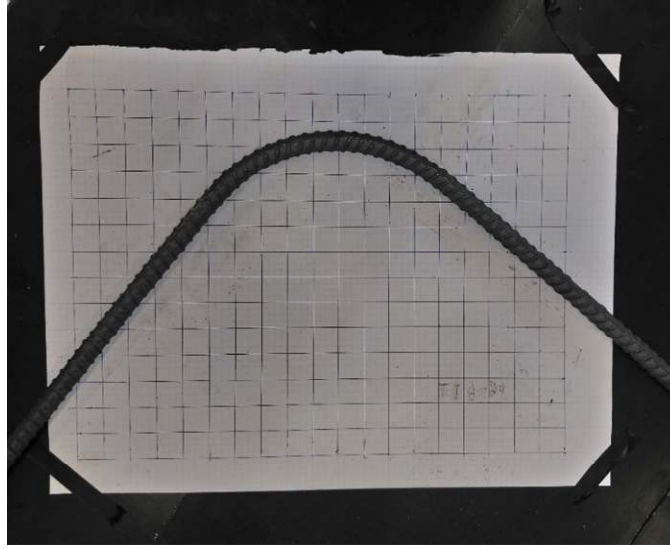


Figure 3-14 Measurement of bend radius

Table 3-3 Summary of bends

| Series | Specimen ID | Target bend diameter (in.) | Used pin diameter (in.) | Actual bend radius (in.) |
|----------|-------------|----------------------------|-------------------------|--------------------------|
| S-Series | S-27-R3-L | 6 | 6 | 3.9 |
| | S-27-R11-L | 20.5 | 16 | 10.8 |
| | S-18-R3 | 6 | 5.5 | 3.3 |
| | S-18-R6 | 12 | 10.5 | 6.5 |
| | S-18-R9 | 18 | 16 | 9.8 |
| | S-13-R3 | 5.25 | 5 | 3.3 |
| | S-13-R5 | 9.25 | 8 | 4.7 |
| | S-13-R8 | 13.5 | 12 | 8.1 |
| D-Series | D-20-R2 | 5.25 | 4.5 | 2.7 |
| | D-20-R6 | 12 | 10.5 | 6.5 |
| | D-20-R9 | 18 | 16 | 9.9 |
| | D-16-R2 | 4.5 | 4 | 2.4 |
| | D-16-R6 | 11 | 9.5 | 5.9 |
| | D-16-R10 | 16.5 | 16 | 10.2 |
| C-Series | C-17-R3 | 6 | 5.5 | 3.3 |
| | C-17-R6 | 12 | 10.5 | 6.5 |
| | C-17-R9 | 18 | 16 | 9.2 |
| | C-17-R12 | 29 | 24 | 11.5 |
| B-Series | B-16-R3 | 6 | 5.5 | 3.2 |
| | B-16-R6 | 12 | 10.5 | 6.5 |
| M-Series | LS-S-18-R3 | 6 | 5.5 | 3.3 |
| | LS-S-13-R3 | 5.25 | 4.5 | 2.8 |
| | TR-S-18-R3 | 6 | 5.5 | 3.3 |
| | TR-S-13-R3 | 5.25 | 4.5 | 2.7 |



Figure 3-15 Construction of reinforcement cages

3.3.4 Casting and Curing of Concrete

The concrete was ordered from a local ready-mix concrete supplier. A maximum of six specimens were cast at one time. When more than one concrete truck was required, concrete from two trucks were never combined within a single specimen. Upon the arrival of each concrete truck, a slump test was immediately conducted in accordance with ASTM C143⁵⁷ (see Figure 3-16) to check if the slump was satisfactory (5 in. to 7 in.).



Figure 3-16 Slump test

The concrete cast began after the slump test (see Figure 3-17(a)). Concrete was cast using two lifts, and internal immersion vibrators were used for each lift to ensure proper consolidation. During the cast, concrete was sampled according to ASTM C94⁵⁸ for material tests and was cast

into cylinder molds as well as beam molds (see Figure 3-17(b)). The cylinder molds were 4 in. by 8 in., and the beam molds had cross-sectional dimensions of 6 in. by 6 in.

Approximately three hours after casting, burlap were placed on the top of the concrete. The concrete was then watered with the burlap in place and was then covered with a plastic sheet to prevent water evaporation (Figure 3-17(c)). On the seventh day after casting, the concrete forms were removed, and the samples for material tests were demolded. The concrete was exposed to air until the specimen was tested (see Figure 3-17(d)).



(a) Cast



(b) Cylinder and beam samples



(c) Curing



(d) Demolded

Figure 3-17 Casting and curing

3.4 Test Frame

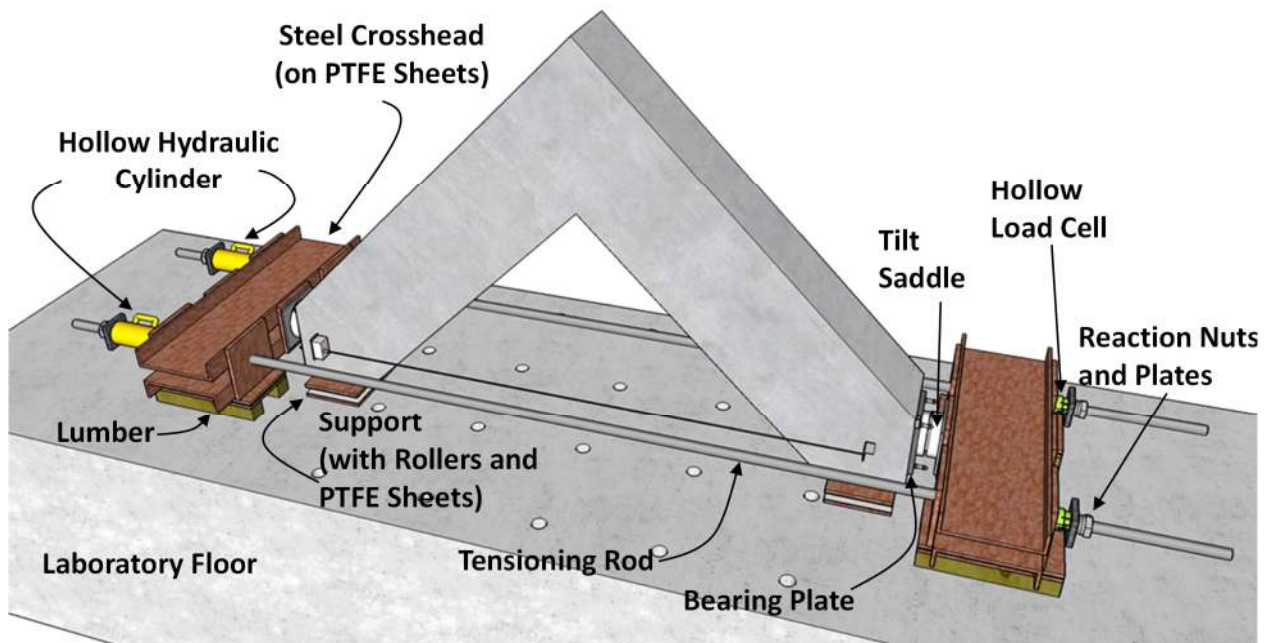
The test frame used to apply load to the specimens was a self-reacting system consisting of two steel crossheads and two tensioning rods as presented in Figure 3-18. Each steel crosshead was made from two steel channels. At the point of load application to the specimen, a tilt saddle was mounted to each crosshead to accommodate rotation of the loaded surface of the specimen.

Stiffeners on the channel sections (see Figure 3-18(b)) ensured the crossheads had sufficient capacity.

The steel crossheads rested on supports consisting of two steel plates between which two polytetrafluoroethylene (PTFE) sheets were placed. Similarly, underneath each of the legs of the specimen, a support consisting of two steel plates between which two polytetrafluoroethylene (PTFE) sheets and steel rollers was provided. These precautions were conducted to eliminate friction between the floor and the load frame and between the floor and the specimen.

The tensioning rods used to transfer load between the two crossheads had diameters of 1-7/8 in. At one end of each tensioning rod, a hollow hydraulic cylinder was installed to apply loads, while at the other end, a hollow load cell was mounted to measure the applied load. The hydraulic cylinder and the load cell were anchored with nuts and steel plates. Two different types of hydraulic cylinders were used in the experimental program. For Series I, the hydraulic cylinders had a capacity of 120 kip and a stroke limit of 3 in. For the other tests of the experimental program, the hydraulic cylinders were replaced with a model that had a capacity of 200 kip and a stroke limit of 6 in. because of higher anticipated displacements.

In addition to the loading system, two steel columns were placed on each side of the specimen being tested to act as a bracing system to prevent overturning (see Figure 3-18 (b)). The columns were installed using post-tensioned rods that passed through the strong floor. A turnbuckle was connected between the top of each column and the top surface of the specimen using steel shackles. The turnbuckles were loosened sufficiently in order to ensure they did not carry any load during the test.



(a) Components of test setup



(b) Specimen in test setup prior to testing

Figure 3-18 Test Frame

3.5 Instrumentation

The instrumentation used during the experimental program included load cells, pressure transducers, linear potentiometers, inclinometers, and strain gauges. In addition, a digital image correlation system was used to capture the full-field surface strains at the joints. Detailed descriptions of the instrumentation are provided in the following sections.

3.5.1 Load

Applied loads were measured using two load cells with a capacity of 110 kip during the tests. As shown in Figure 3-19, each of the two load cells was anchored with a nut and a steel plate on the end of each tensioning rod. The total load acting on the specimen was, therefore, the summation of the readings from the two load cells.

In addition to the load cells, two pressure transducers were used to measure the pressure in hydraulic cylinders. The measured pressure was converted to load by multiplying by the effective area of the hydraulic cylinders. Each pressure transducer was installed using a T-connector that was connected to the input port on the hydraulic cylinder, as shown in Figure 3-20. The total load measured using the pressure transducers was used to verify the loads indicated by the load cells, which acted as the primary sensors for measuring load.



Figure 3-19 Load cells



Figure 3-20 Hydraulic cylinders and T-connector with pressure transducer

3.5.2 Displacement and Rotation

Two linear string potentiometers were used to monitor relative displacement between the two legs of each specimen. As shown in Figure 3-21 and Figure 3-22, one linear potentiometer was mounted and centered on each side face of a leg using concrete-metal epoxy. An aluminum

bracket was epoxied and centered on each side face of the other leg as a reference point. In addition, two inclinometers were used to measure rotations as shown in Figure 3-23. One of the inclinometers was epoxied to the center of the loaded surface at the end of a leg to measure rotation near the point of load application. The other inclinometer was epoxied to the top surface of the joint at the joint face to measure rotation at the joint.

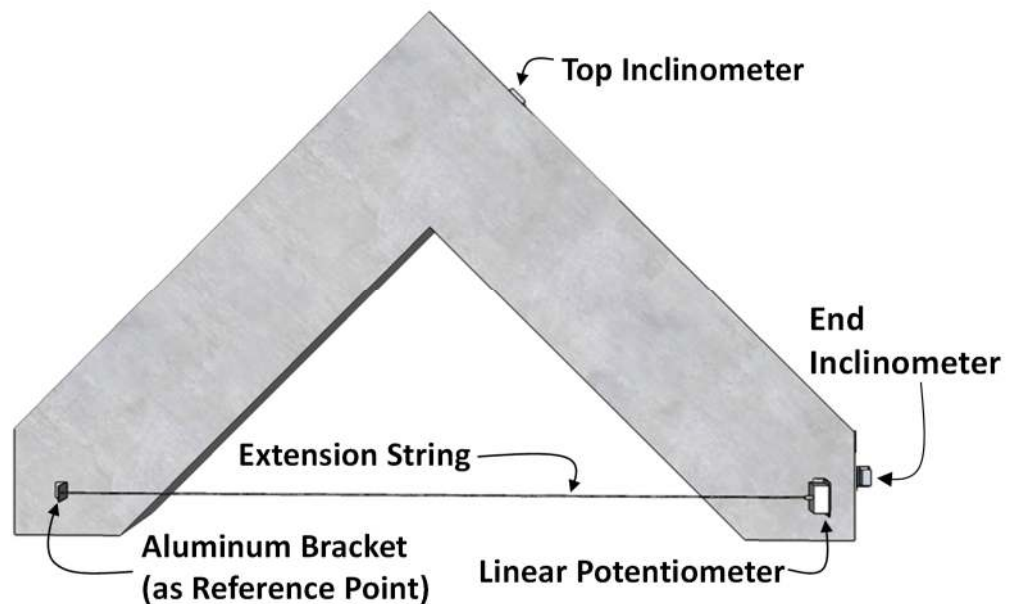


Figure 3-21 Instrumentation for displacement and rotation



Figure 3-22 Linear potentiometer



Figure 3-23 Inclinometers

3.5.3 Strain in Reinforcing Bars

Strain gauges were installed on the longitudinal reinforcing bars at several positions to measure the strain during the tests. The strain gauges were manufactured by Tokyo Sokki Ltd, and the model number of the gauges was FLA-05-11. The model had a gauge length of 5 mm and a resistance of 120 Ω . The installation of the strain gauges (see Figure 3-24) is described in the following paragraphs.

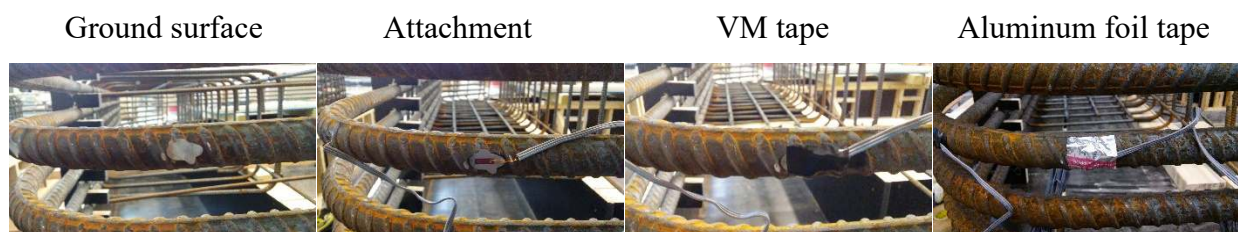


Figure 3-24 Installation of strain gauge

To ensure the strain gauges functioned properly during the tests, a specific installation procedure was followed. Surface preparation of the steel reinforcing bar was first conducted. The bar deformation at the desired position of the gauge was first ground down using 80-grit sandpaper. Then, the surface was finely ground using 200-grit sandpaper to create a smooth surface. The ground surface was located between the two longitudinal ribs of the bar to avoid reducing the cross section of the bar. The ground surface was then cleaned using acetone.

After the surface was prepared, a strain gauge was then installed, and protection was applied. The strain gauge was attached to the treated ground surface using CN adhesive from Tokyo Measuring Instruments Lab. To make the strain gauge waterproof, M-Coat A epoxy from Micro-Measurements was spread over the top of the strain gauge. After the coating was set, VM tape from 3M® was placed to isolate the lead wires from the bar and to cover the strain gauge. Then, aluminum foil tape was placed as a vapor barrier, and electrical tape was used to wrap the whole assembly to provide electrical insulation. Finally, Epoweld 8173 epoxy from Royal Adhesives & Sealants LLC® was applied to coat the assembly and provide another layer of protection. Strain gauges with complete protection are presented in Figure 3-25

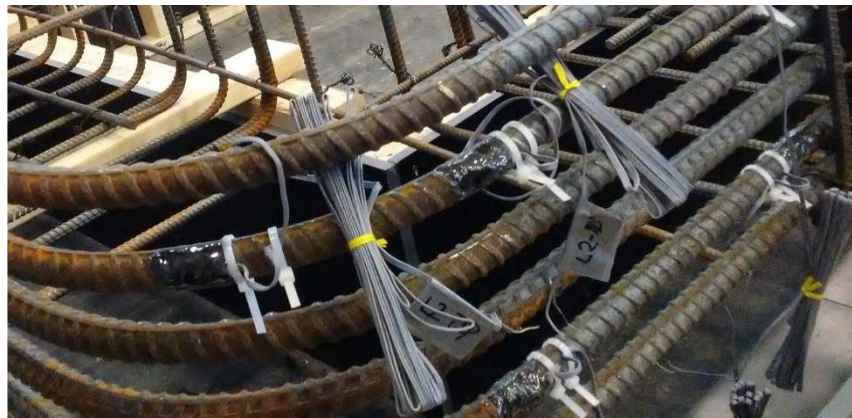


Figure 3-25 Strain gauge with full protection

Strain gauges were distributed along the longitudinal reinforcing bars typically at three positions: (1) at the joint face, (2) at the beginning of the bar bend, and (3) at the center of the bar bend. Six strain gauges were used for Series I and Series III: three strain gauges were installed on both the second bar and the fifth bar as illustrated in Figure 3-26(a). Because the specimens of Series II had two layers of longitudinal reinforcement, twelve strain gauges were used: six gauges were distributed on the inner layer and the other six were on the outer layer. In addition, the number of bars was different between Groups D-1 and D-2. Three gauges were installed on both the second bar and the third bar in each bar layer for Group D-1, while three gauges were installed on both the second bar and the fourth bar of each layer for Group D-2, as illustrated in Figure 3-26(b).

Because the focus of specimens in Series IV was the development of the circumferential bond stress along the bend region of the bars, the B-Series specimens had five strain gauges

distributed along the second longitudinal bar in a manner that allowed strain to be measured throughout the bend. The positions included the points corresponding to both joint faces, the two ends of the bend region of the bar, and the center of the bar bend, as illustrated in Figure 3-26(c).

Similar to the Series IV specimens, specimens of Group TR in Series V had five strain gauges distributed along a longitudinal reinforcing bar. The strain gauges were installed at the two ends of the bend region of the bar, at the points corresponding to both joint faces, and at the center of the bar bend. For the Group LS specimens, a single bar in both the inner and outer bar layers had gauges installed at the two ends of the bend region of the bar, at the point corresponding to the joint face, and at the center of the bar bend (see Figure 3-26(d)).

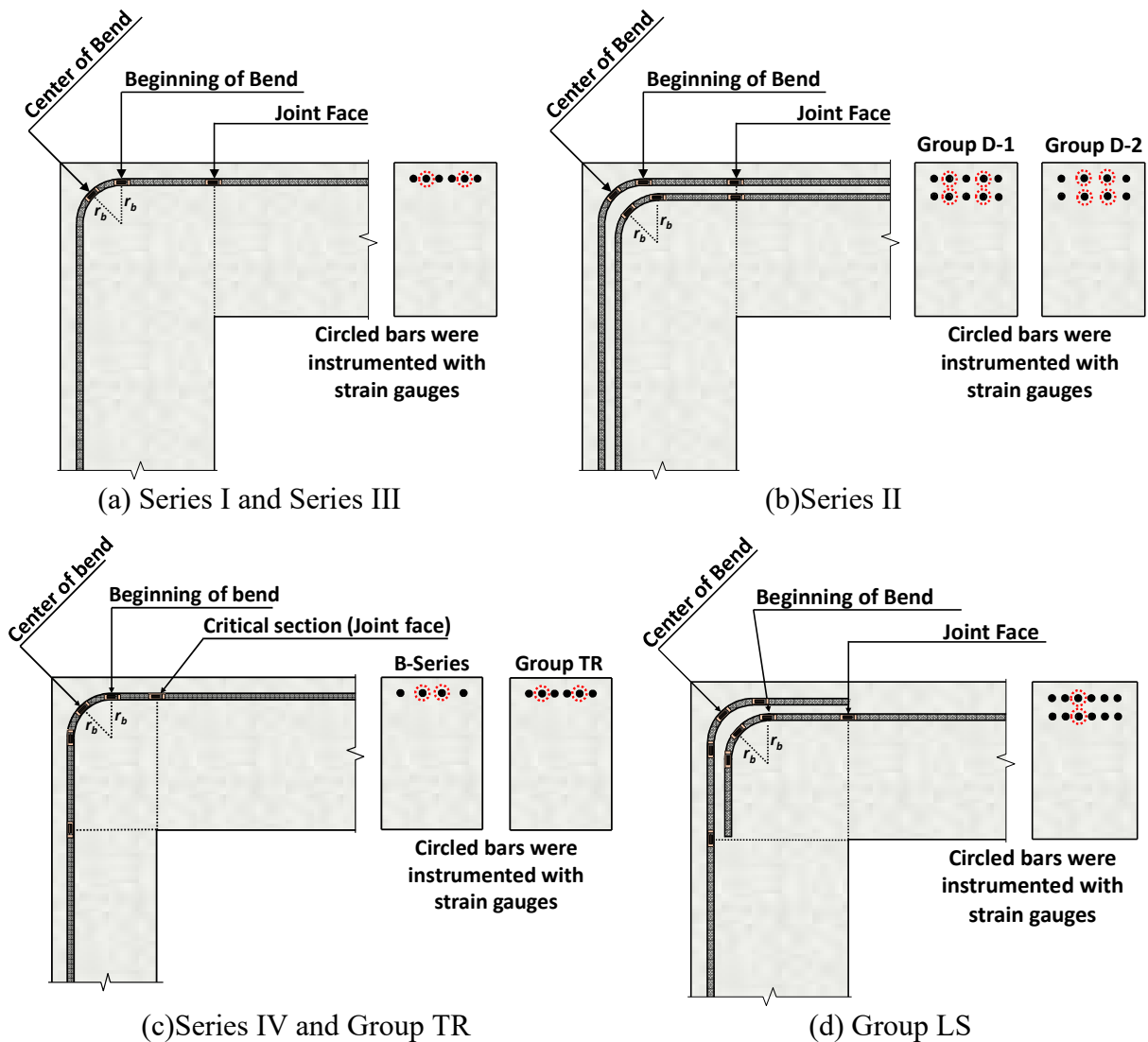


Figure 3-26 Strain gauge arrangement

3.5.4 Digital Image Correlation System

A 3D digital image correlation (DIC) system was employed to measure the full-field strain map on one of the joint surfaces for the specimens of Group D-1, Series III, Series IV, and Series V. The system consisted of two cameras, a speckle pattern on the joint region, and an algorithm used to correlate images, as presented in Figure 3-27. During the test, the two cameras collected images of the speckle pattern to capture three-dimensional coordinates of the speckles. By comparing an arbitrary set of images with a set of reference images, the displacement of any two speckles can be determined. Furthermore, the full-field strain map can be developed from the displacement information.

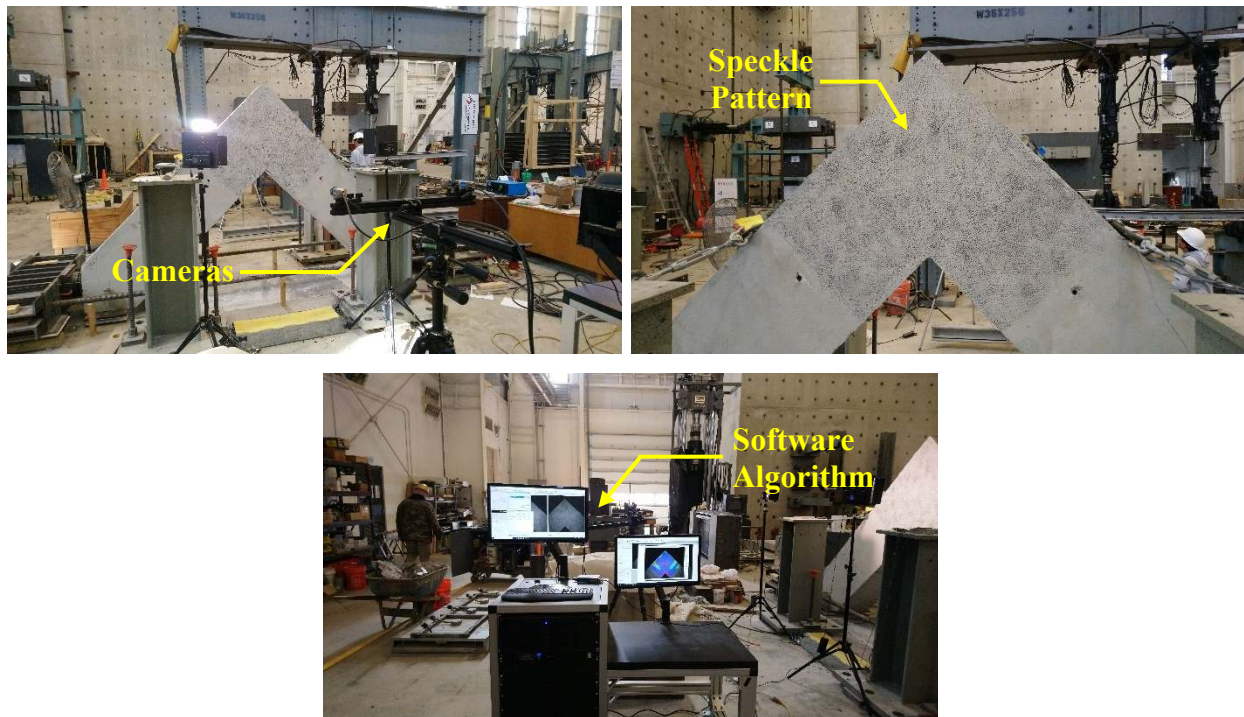


Figure 3-27 Digital image correlation system

3.6 Test Procedure

For the first tests of the experimental program (Specimen S-27-R3-L and Specimen S-27-R11-L), the specimens were first loaded to 15 kip in order to check if the test setup and the instrumentation were functioning correctly. After this, the specimens were loaded at increments of 15 kip. At each load step, cracks were marked on the side of the specimens without the speckle

pattern (see Figure 3-28). The widths of the cracks were measured after the load reached approximately 50% of the anticipated peak load. The crack mapping was discontinued after the load reached approximately 80% of the anticipated peak load. Once the applied load reached a plateau (that is, remained relatively constant with increasing deflection), the displacement was increased continuously until the specimen failed. The test was discontinued when the load dropped to 50% of the peak load or the stroke limit was reached.

To better capture the propagation of cracks, more load steps were added for the other tests of the research program. As with the first two specimens, a load of 15 kip was first applied during the tests on the S-Series, D-Series, C-Series, and M-Series specimens. Then, the load was increased to 20 kip as the second load step. After this, load was applied with increments of 10 kip. At each load step, cracks were marked. The widths of the cracks were measured at each load step between approximately 50% and 80% of the anticipated peak load. After the applied load reached a plateau, displacement was increased continuously until the load dropped to 50% of the peak load or the stroke limit was reached.

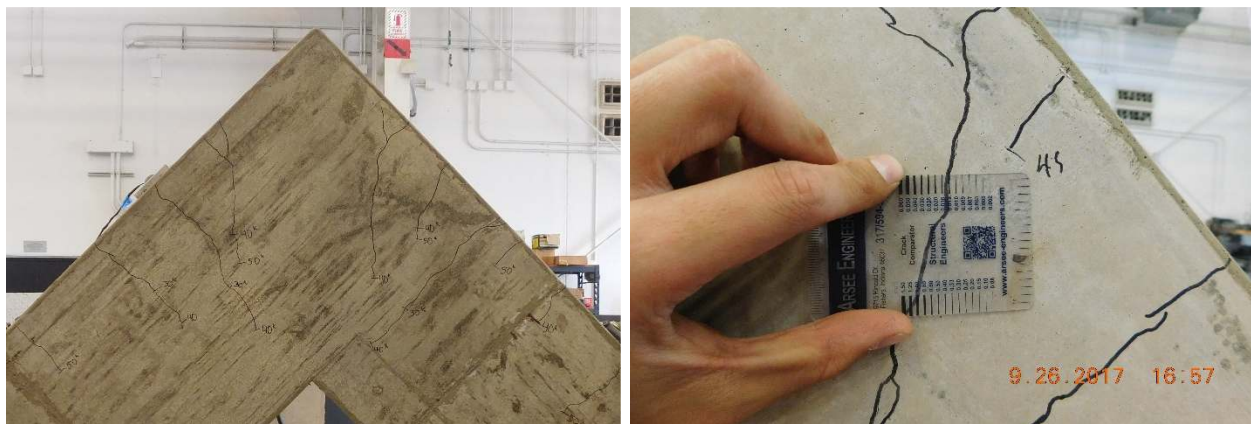


Figure 3-28 Crack marking and measuring

The procedure was slightly different for the B-Series specimens due to their lower anticipated strengths. A load of 5 kip was first applied to the specimen to examine the test frame. After this, the load was increased in increments of 5 kip until the applied load reached a plateau. Then, the load was continuously applied to the specimen until the load dropped to 50% of the peak load or the stroke limit was reached.

3.7 Material Test

Material tests were conducted in order to estimate the mechanical properties of concrete and steel reinforcing bars. For concrete, compressive strength, modulus of elasticity, splitting tensile strength, and modulus of rupture were measured. For reinforcing bars, tests to measure the tensile strength of the longitudinal bars were conducted. The measured properties were used to estimate the strengths of the knee joint specimens.

3.7.1 Compressive Strength of Concrete

Compressive strength tests of concrete was conducted in accordance with the procedure in ASTM C39⁶⁷ at Bowen Laboratory, as shown in Figure 3-29. Concrete cylinders of 4 in. by 8 in. were cast in accordance with ASTM C31⁶⁸ while casting test specimens. The diameter and height of each cylinder were measured before testing. The compression testing machine was programmed to stop when the load dropped to more than 50% of the peak strength. After the test, the peak strength was recorded as well as the break type.

Three cylinders were tested and the average of the three results was taken to represent the strength on a certain day. Typically, a test was conducted on the third day, seventh day, 14th day, and the 28th day after casting. A knee joint specimen was ready to test if the average result exceeded the design concrete compressive strength (3.5 ksi or 5.0 ksi). Compression tests were also conducted on the day of testing each knee joint specimen.



Figure 3-29 Concrete compressive strength test

3.7.2 Modulus of Elasticity of Concrete

The test for the modulus of elasticity of concrete was conducted at Bowen Laboratory in accordance with ASTM C469,⁶⁹ as shown in Figure 3-30. The tests were conducted on 4 in. by 8 in. concrete cylinders cast with each knee joint specimen. For the modulus of elasticity test, the cylinder was placed in a loading jig that contained two LDVTs. One of the LVDTs measured length change, and the other measured the change in diameter. The loading jig had a gauge length of 5.4 in. Each test consisted of three loading cycles to 40% of the expected cylinder strength, and the modulus of elasticity of the cylinder was taken as the average of the results from the two cycles. Three modulus of elasticity tests were conducted on the day of testing a knee joint specimen. The average of the results of the three tests was taken to represent the modulus of elasticity of the concrete of the knee joint specimen.

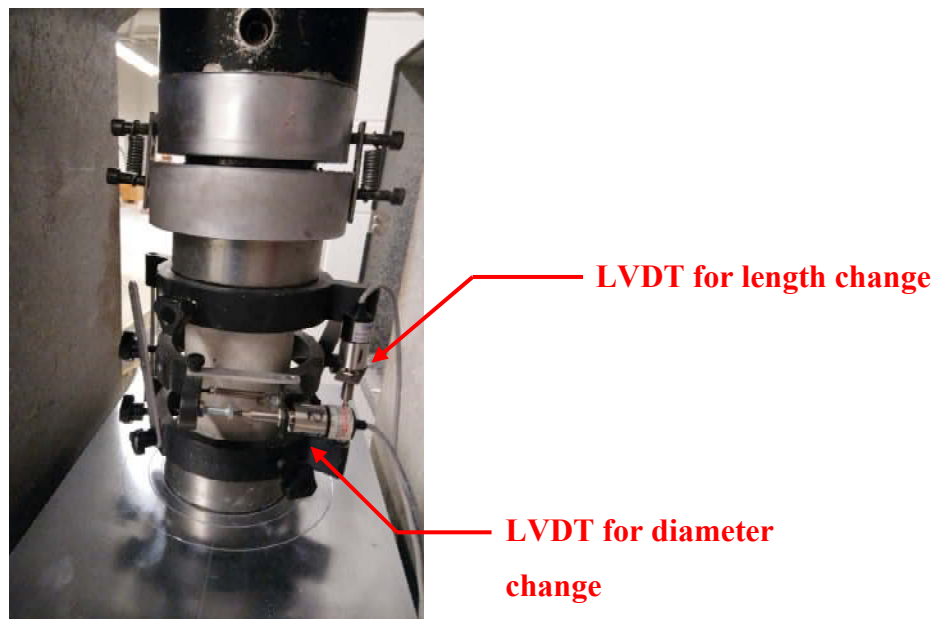


Figure 3-30 Test for modulus of elasticity test of concrete

3.7.3 Splitting Tensile Strength of Concrete

Splitting tensile tests were conducted in accordance with ASTM C496⁷⁰ at Bowen Laboratory, as shown in Figure 3-31. Again, 4 in. by 8 in. cylinders cast with each knee joint specimen were tested. Three cylinders were tested on the day of each test on a knee joint specimen.

The average of the three results was taken to represent the splitting tensile strength of the concrete in the specimen.



Figure 3-31 Test for splitting tensile strength of concrete

3.7.4 Modulus of Rupture of Concrete

Modulus of rupture tests were conducted at Bowen Laboratory in accordance with ASTM C78,⁷¹ as shown in Figure 3-32. Beam samples with cross-sectional dimensions of 6 in. by 6 in. were used. The lengths of the beam samples were 24 in. or 21 in, and the test span was according to ASTM C78.⁷¹ Three modulus of rupture tests were conducted on the day between two consecutive knee joint tests. The average of the three tests was taken as the modulus of rupture of the two knee joint specimens.



Figure 3-32 Test for modulus of rupture of concrete

3.7.5 Tensile Strength of Reinforcing Bars

Tensile tests on reinforcing bars were conducted in accordance with ASTM A370.⁷² Test coupons were directly sampled from the steel reinforcement delivered to Bowen Laboratory for the experimental program. Three coupons were taken for each size of the steel reinforcing bars used in the knee joint specimens. All bars of the same size used in the experimental program were taken from the same heat of steel. Each test coupon had a length of 36 in. The test setup is shown in Figure 3-33. At least 6 in. at each end of the coupon were gripped within the top and bottom crossheads of the test frame. A linear extensometer with a gauge length of 8 in. was placed at the mid-height of the coupon to measure the length change. Tensile load was applied until the coupon ruptured. The stress-strain data was recorded during the test. The tensile strength for a particular bar size was taken as the average of three tests on coupons of that same bar size.



Figure 3-33 Test for tensile strength of reinforcement

3.8 Summary

This chapter provided details of the experimental program on closing knee joints. To investigate the effect of curved-bar nodes on the behavior of knee joints, 24 specimens categorized into five series were tested: (1) single-layer longitudinal bars, (2) double-layer longitudinal bars, (3) reduced clear side cover, (4) adjoining members with different cross sections, and (5) multiple-purpose. The details of the specimens in each series were introduced along with the details of specimen fabrication and materials.

The instrumentation and test procedure were then described. The instrumentation included load cells, linear potentiometers, inclinometers, and strain gauges. In addition, a 3D digital image correlation system was employed to capture full-field strain maps. After a specimen was instrumented, load was applied following the procedure previous described until the specimen failed. During the tests, cracks were inspected and marked on the joint surface.

Along with each knee joint test, material tests were conducted to determine the properties of the material in each knee joint specimen. The measured concrete properties included compressive strength, modulus of elasticity, splitting tensile strength, and modulus of rupture. Furthermore, the tensile strength of the longitudinal reinforcing bars was measured.

4. EXPERIMENTAL RESULTS AND DISCUSSION

4.1 Overview

The experimental results are presented and discussed in this chapter. The test results of each series are presented separately in each section, including visual observations, load-relative-displacement relationships, and strain distribution along the longitudinal reinforcing bars. A discussion on stress development and transmission in knee joints under closing moments is also included.

4.2 Series I: Single-Layer Longitudinal Bars (S-Series)

This section describes the experimental results of the S-Series specimens. This series consisted of eight closing knee joint specimens and was developed to investigate the effect of the bend radius of the longitudinal bars on joint behavior. The design expression for curved-bar nodes based on radial stress (Eq. 2-20) when a single layer of longitudinal bars is provided in knee joints was evaluated. The effect of the mechanical longitudinal reinforcement ratio was also studied.

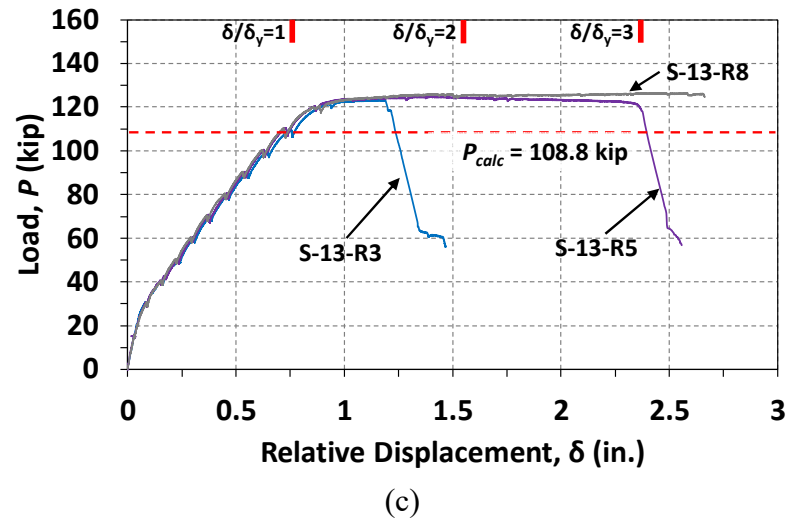
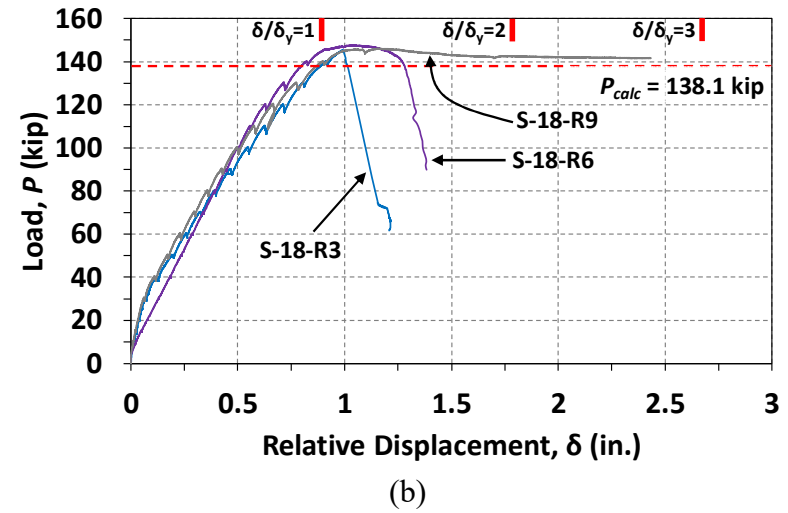
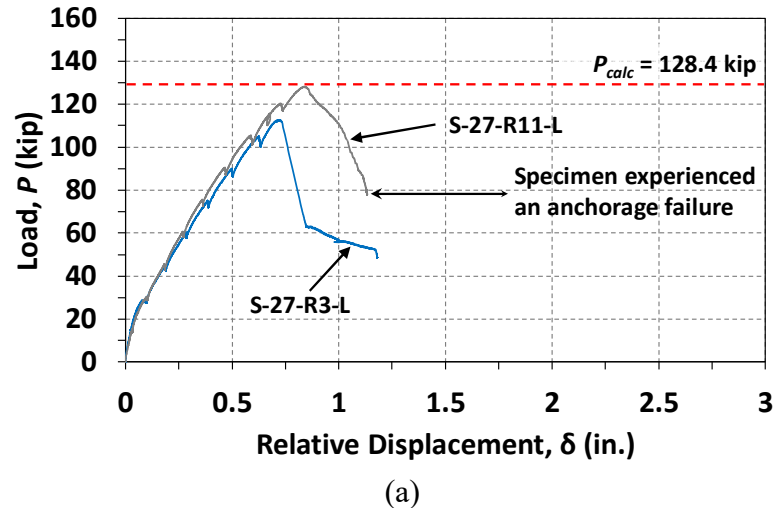
4.2.1 Overall Behavior

Plots that demonstrate the load-displacement relationship of the S-Series specimens are presented in Figure 4-1. The applied load, P , is the force acting horizontally on the specimen. The measured force was taken as the sum of the readings from both load cells described in the previous chapter. The relative displacement, δ , is the distance change between the two legs, taken as the average of the readings from the two linear potentiometers attached to both sides of one of the legs.

The calculated load capacity, P_{calc} , is indicated in the plots of Figure 4-1 as dashed red lines. The value of P_{calc} is defined as the applied load corresponding with the calculated nominal flexural strength, M_{calc} , at the section corresponding with the joint face. The nominal flexural strength, M_{calc} , is calculated in accordance with Section 22.2 of ACI 318-19¹ using the measured compressive strength of the concrete and the measured tensile strength of the longitudinal bars. It should be noted that because the values of P_{calc} are slightly different among the specimens in a particular group due to differences in measured material properties, only the greatest value of P_{calc}

for the specimens represented in each plot in Figure 4-1 is shown in order to improve readability. Values of P_{calc} and M_{calc} for each specimen are summarized in Table 4-1.

In addition to the experimental and calculated strengths of each specimen, the displacement ductility factor, μ , is also presented in Table 4-1 for Group S-2 and Group S-3. The displacement ductility factor is the ratio of the maximum displacement, δ_{max} , to the yield displacement, δ_y . The value of δ_{max} corresponds to the ultimate failure condition of the specimen or the end of the test if the stroke limit of the hydraulic cylinders was reached. The ultimate failure condition was defined as a sudden and substantial drop of the load-carrying capacity (approximately 50% or greater). The value of δ_y is defined as the yield moment M_y divided by the slope of a line drawn from the origin to a moment of $0.75M_y$ on the moment-relative displacement curve for that specimen. The moment-relative displacement curves have identical shapes to the load-relative displacement curves shown in Figure 4-1. The value of M_y is based on the actual load-displacement behavior of the specimens as presented in Figure 4-1(b) and (c). For simplicity, a single value of M_y was selected for each group of specimens (Group S-2 and Group S-3) to correspond with the point on the load-relative displacement curves where the slope becomes nearly zero. For Group S-2, M_y is 7197 kip-in., corresponding to a load P of 145 kip. For Group 3, M_y is 6138 kip-in., corresponding to a load P of 124 kip. Integer values of δ/δ_y are shown in Figure 4-1(b) and (c). Again, to improve readability, the ratios of δ/δ_y labeled on the plots are based on the specimen in each group with the largest value of δ_y . A value of μ was not calculated for Specimen S-27-R11-L because an anchorage failure occurred.



Legend

- Criterion (1)
- Criterion (2)
- Criterion (3)

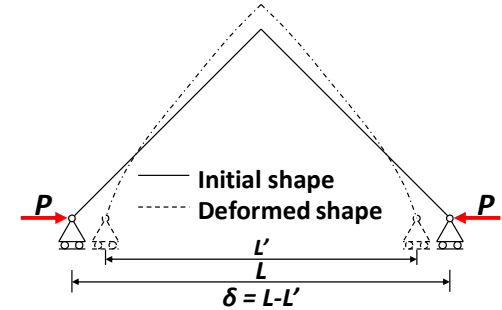


Figure 4-1 Load-displacement curves of knee joint specimens: (a) Group S-1, (b) Group S-2, (c) Group S-3

Table 4-1 Summary of test results, joint efficiency, and ductility of S-Series specimens

| Specimen ID | P_{test} (kip) | M_{test} (kip-in.) | P_{calc} (kip) | M_{calc} (kip-in.) | M_{test}/M_{calc} | δ_{max} (in.) | δ_y (in.) | μ | C |
|-------------|------------------|----------------------|------------------|----------------------|---------------------|----------------------|------------------|--------|------|
| S-27-R3-L | 113 | 5593 | 128.0 | 6336 | 0.88 | 0.72 | - | - | 0.66 |
| S-27-R11-L* | 128 | 6336 | 128.4 | 6356 | 1.00 | 0.84 | - | - | 1.85 |
| S-18-R3 | 145 | 7177 | 138.1 | 6836 | 1.05 | 1.02 | 0.85 | 1.20 | 0.86 |
| S-18-R6 | 148 | 7326 | 137.3 | 6796 | 1.08 | 1.30 | 0.73 | 1.77 | 1.64 |
| S-18-R9 | 146 | 7227 | 137.6 | 6811 | 1.06 | 2.45 | 0.85 | 2.87** | 2.50 |
| S-13-R3 | 123 | 6088 | 108.3 | 5361 | 1.14 | 1.27 | 0.77 | 1.64 | 1.14 |
| S-13-R5 | 125 | 6187 | 108.7 | 5380 | 1.15 | 2.37 | 0.76 | 3.12 | 1.67 |
| S-13-R8 | 127 | 6286 | 108.8 | 5385 | 1.16 | 2.67 | 0.75 | 3.58** | 2.91 |

*An anchorage failure occurred.

**Value based on relative displacement δ when stroke of hydraulic cylinders was reached.

Test results of the specimens in Group S-1 are shown in Figure 4-1(a). Specimen S-27-R3-L, which had a bend radius based on a standard hook, did not reach the calculated load-carrying capacity. The specimen failed at a load of 113 kip. The joint efficiency, defined as the ratio M_{test}/M_{calc} , was 0.88. For Specimen S-27-R11-L, the maximum applied load was approximately equal to the calculated load. The specimen, however, experienced an anchorage failure as shown in Figure 4-2). After the test on Specimen S-27-R11-L, a steel plate was welded to both ends of the longitudinal reinforcing bars of the remaining test specimens to prevent anchorage failures.



Figure 4-2 Anchorage failure of Specimen S-27-R11-L

As indicated in Figure 4-1(b), all specimens in Group S-2 achieved a load resistance greater than the calculated load. The displacement ductility factor, however, varied significantly among the specimens. Specimen S-18-R3, which had the smallest bend radius, exhibited a sudden load drop after reaching the peak load of 145 kip. Specimen S-18-R6 demonstrated some post-yield

behavior. That is, after reaching the peak load of 148 kip, the specimen continued to deform until a displacement ductility factor of 1.77 was reached. Then, a sudden drop in the load-carrying capacity occurred. It should be noted that the testing of Specimen S-18-R6 was temporarily stopped because an issue with the test frame was observed at a load of 90 kip. One of the steel crossheads was rotating due to the eccentricity of the tensioning bars relative to the point of load application to the specimens. The specimen was unloaded and then reloaded after the issue was resolved. For this reason, a reduced initial stiffness was observed upon reloading as shown in Figure 4-1(b). Specimen S-18-R9, which had a bend radius satisfying the ACI-required bend radius for curved-bar nodes, exhibited the highest displacement ductility factor. After the load reached 146 kip, the displacement continued to be increasing until the hydraulic cylinders reached their stroke limit. When the test was stopped, the relative displacement between the two legs was 2.45 in., corresponding to a displacement ductility factor of 2.87 (see Table 4-1).

In general, the specimens in Group S-3 behaved similarly to those in Group S-2. All three specimens exhibited load-carrying capacities greater than the calculated values. The displacement ductility factor was also related to the size of the bend radius. That is, a larger bend radius led to a higher displacement ductility factor. Specimen S-13-R3 had a μ -value of 1.64, while Specimen S-13-R5 and Specimen S-13-R8 achieved μ -values of 3.12 and 3.58, respectively. It should be noted that Specimen S-13-R8 did not reach the ultimate failure condition because the stroke limit of the hydraulic cylinders was reached. In general, the displacement ductility factors for the specimens in Group S-3 were greater than those of the specimens in Group S-2.

The experimental load capacity, P_{test} , defined as the maximum load resisted by a specimen, along with the joint efficiency M_{test}/M_{calc} is summarized for each specimen in Table 4-1. For specimens with relatively high mechanical longitudinal reinforcement ratio (that is, the specimens in Group S-1), the larger bend radius of Specimen S-27-R11-L resulted in a higher joint efficiency than the bend radius of a standard hook provided in Specimen S-27-R3-L. Of course, the value of M_{test}/M_{calc} may have been greater for Specimen S-27-R11-L if the anchorage failure had not occurred. For all specimens with lower values of ω (that is, the specimens in Group S-2 and Group S-3), the values of M_{test}/M_{calc} were greater than unity even when the radius of a standard hook was used. Nevertheless, for this scenario, a larger bend radius resulted in an increase in the displacement ductility factor.

The impact of the bend radius and the mechanical longitudinal reinforcement ratio can be better understood by rearranging Eq. 2-20 and substituting ω to develop Eq. 4-1. It should be noted that the strut width b_s was taken as the width of the joint b because the longitudinal reinforcing bars were distributed over the width of the cross section, which was consistent with Klein.²²

$$\frac{r_b}{d} \geq 2\omega \quad 4-1$$

To describe any bar bend radii of the specimens of the experimental program, the parameter C can be substituted into Eq. 4-1 as follows

$$\frac{r_b}{d} = C\omega \quad 4-2$$

Eq. 4-2 represents a simple relationship between the bend radius r_b and the mechanical longitudinal reinforcement ratio ω . To satisfy the ACI requirement for the bend radius (without modification for reduced side cover), the parameter C in Eq. 4-2 must be greater than or equal to 2.0. For each specimen, a value of C was calculated using the measured material properties as summarized in Table 4-1. It was found that a greater C -value corresponded with improved strength and/or ductility of the specimens. To be specific, with a relatively high value of ω , Specimen S-27-R3-L had a C -value of 0.66, resulting in a joint efficiency less than 1.0. Although the bend radius for Specimen S-18-R3 was similar to that of Specimen S-27-R3-L, a lower mechanical reinforcement ratio resulted in a value of C equal to 0.86, corresponding with improved strength and an M_{test}/M_{calc} value greater than 1.0. All other specimens had a C -value greater than 0.86 and achieved a strength greater than the calculated flexural capacity of the adjoining members (that is, $M_{test}/M_{calc} > 1.0$), with the exception of Specimen 1-2 which experienced an anchorage failure. As the value of C increased beyond 0.86, the specimens exhibited improved ductility.

4.2.2 Visual Observations

The crack patterns within the joint region of the S-Series specimens after each test are shown in Figure 4-3, Figure 4-4, and Figure 4-5. The hatched regions represent spalled or crushed concrete. The red lines shown on the figures indicate cracks that formed when the ultimate failure condition of the specimens was reached and correspond with a sudden loss of load-carrying capacity. The general trends of crack formation and propagation observed during the tests are illustrated in Figure 4-6. The numbers in the figure indicate the sequence of crack development.

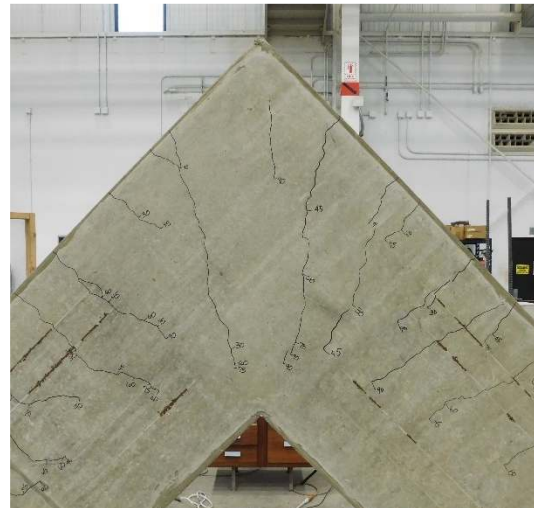
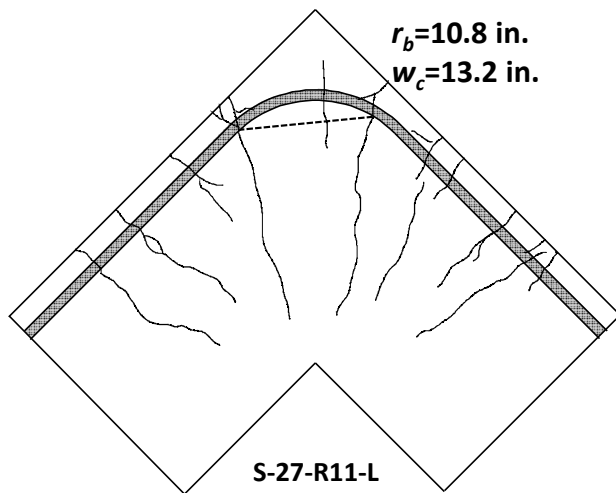
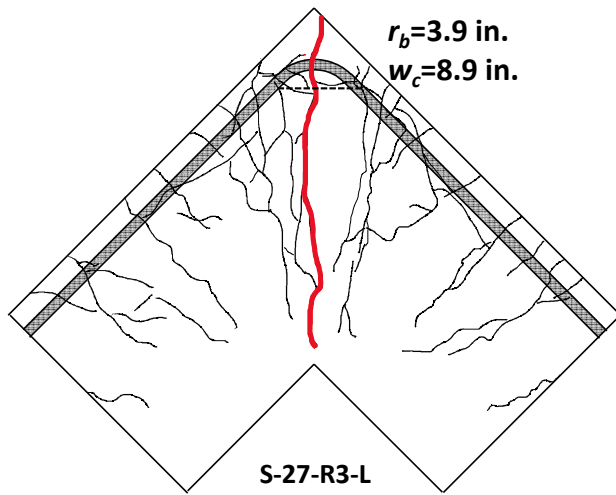


Figure 4-3 Crack maps and photos of Group S-1 specimens

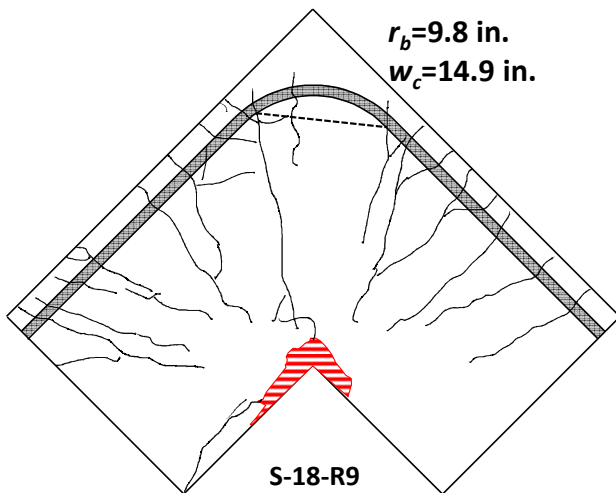
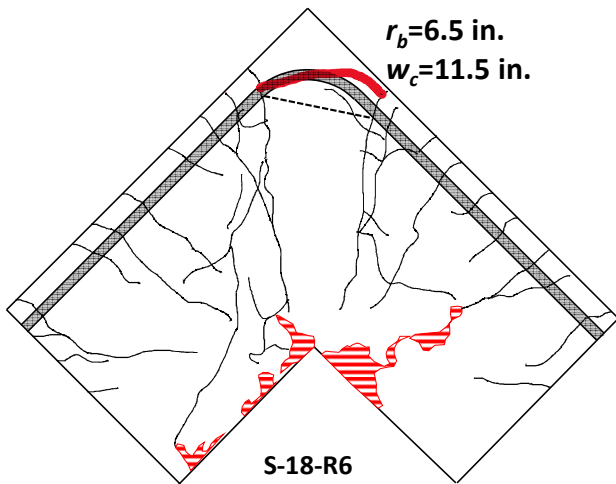
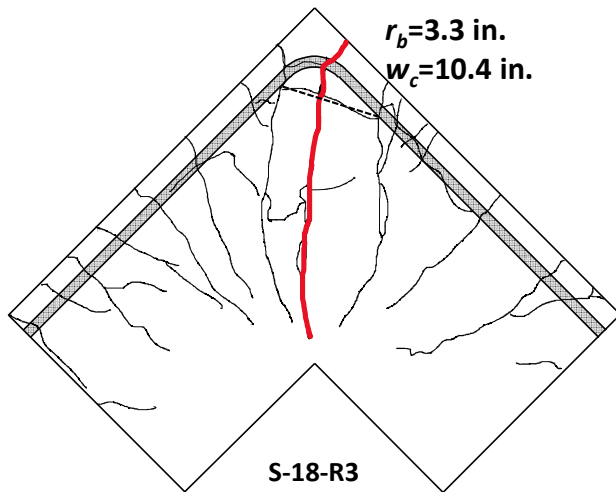


Figure 4-4 Crack maps and photos of Group S-2 specimens

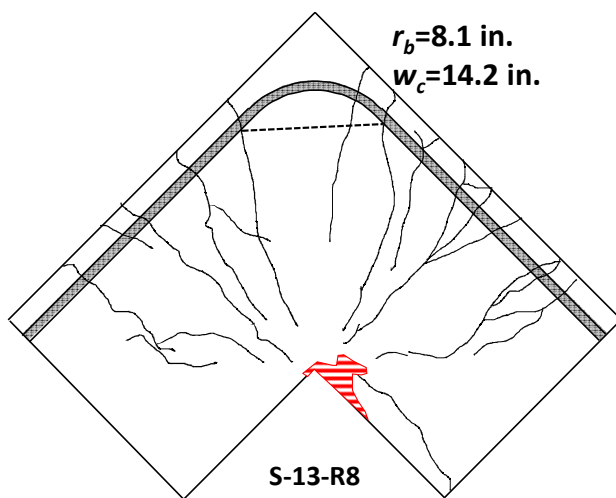
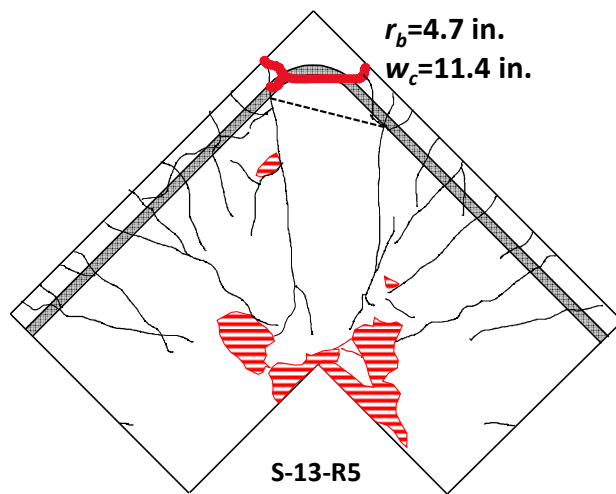
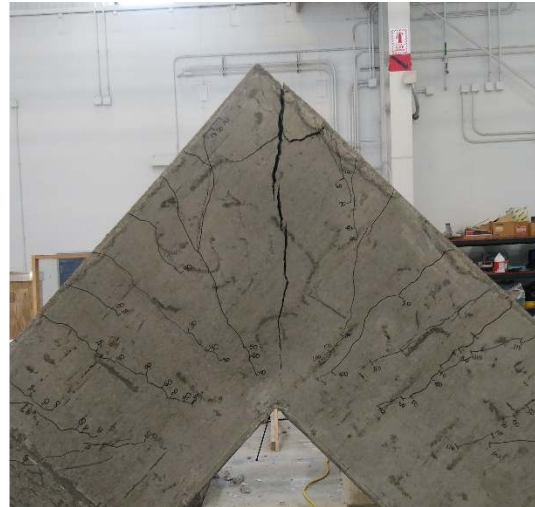
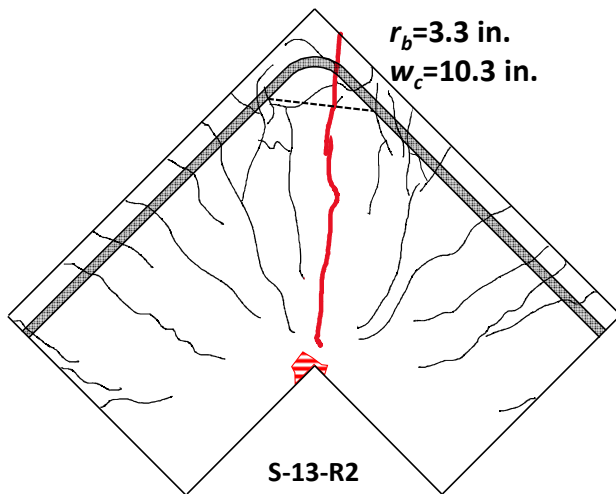


Figure 4-5 Crack maps and photos of Group S-3 specimens

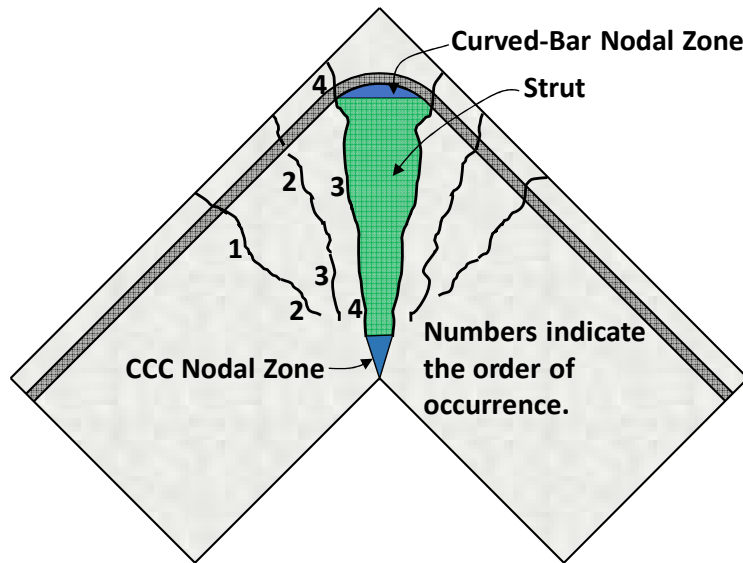


Figure 4-6 Typical crack formation and propagation in joints of S-Series specimens

Typically, the first cracks observed during the tests were flexural cracks that developed at both joint faces (that is, the critical sections for flexure) at approximately 30 kip (denoted by number 1 in Figure 4-6). As the applied load increased, the cracks at the joint faces propagated toward the re-entrant corner while new cracks formed in the joint (denoted by number 2). Note that these new cracks that formed in the joint did not necessarily initiate from the edge of the member (that is, the extreme tension fiber). Upon further loading, the existing cracks propagated, and additional cracks initiated closer to the bend region of the longitudinal bars (denoted by numbers 3 and 4 in Figure 4-6). Prior to ultimate failure, the area enclosed by the innermost cracks corresponded to the largest concentration of compressive stresses in the joint. The width of this region, w_c , was measured along the dashed line shown below the bar bend within each joint in Figure 4-3, Figure 4-4, and Figure 4-5. Comparing the magnitudes of the bend radii r_b and the measured widths w_c provided for each specimen in Figure 4-3, Figure 4-4, and Figure 4-5, a clear relationship between the values is evident.

After the development of the basic crack pattern illustrated in Figure 4-6, the visual distress experienced by the specimens and the ultimate failure mechanism differed based on the bend radius of the longitudinal reinforcement, as suggested by the crack patterns and concrete crushing indicated in Figure 4-3, Figure 4-4, and Figure 4-5. For the specimens with the bend radius of a standard hook (Specimens S-27-R3-L, S-18-R3, and S-13-R3), the ultimate failure condition was

characterized by the sudden development of a splitting crack within the joint along the strut. For Specimens S-27-R3-L and S-18-R3, this strut splitting crack developed prior to a yield plateau on the load-displacement plot (see Figure 4-1(a)). Specimen S-13-R3 experienced some ductility ($\mu=1.64$) prior to the splitting of the strut, but the ductility was less than that of the specimens with bar bend radii larger than that of a standard hook. Therefore, the failure mechanism of Specimens S-27-R3-L, S-18-R3, and S-13-R3 was defined by premature splitting of the strut.

Unlike the specimens with the bar bend radius of a standard hook, the specimens with bend radii between that of a standard hook and the radii required by Eq. 2-20 (Specimens S-18-R6 and S-13-R5) did not experience a premature failure due to the splitting of the strut. Instead, the specimens exhibited a failure characterized by concrete crushing near the CCC nodal zone (see Figure 4-6) and concrete splitting at the bar bend. As the load approached the ultimate failure condition, the crushing of concrete initiated at the re-entrant corner (CCC nodal zone). Upon further deformation of the specimen, a crack suddenly formed approximately along the bar bend, as indicated by thick red lines in Figure 4-4 and Figure 4-5, accompanied by a large loss in load-carrying capacity. At the same time, the crushing of concrete spread within the compression zone.

Specimens with bar bends satisfying Eq. 2-20 that did not experience a premature anchorage failure (Specimens S-18-R9 and S-13-R8) demonstrated behavior superior to that of the other specimens. These specimens did not exhibit splitting of the strut that extended across the joint nor horizontal cracking at the curved-bar node. As the end of each test was approached, crushing of concrete at the re-entrant corner initiated. Due to the stroke limit of the hydraulic cylinders, however, both specimens did not reach their ultimate failure conditions as previously described.

4.2.3 Strain in the Reinforcing Bars

The relationships between the applied load and the strains measured by the strain gauges installed along the longitudinal reinforcing bars are shown in Figure 4-7. The strain readings are plotted until ultimate failure or until the end of the test if failure did not occur (applicable to Specimens S-18-R9 and S-13-R8). It should be noted that the strains for Specimen S-18-R6 exhibit a different behavior compared to the other specimens due to the specimen being reloaded during the test, as previously described.

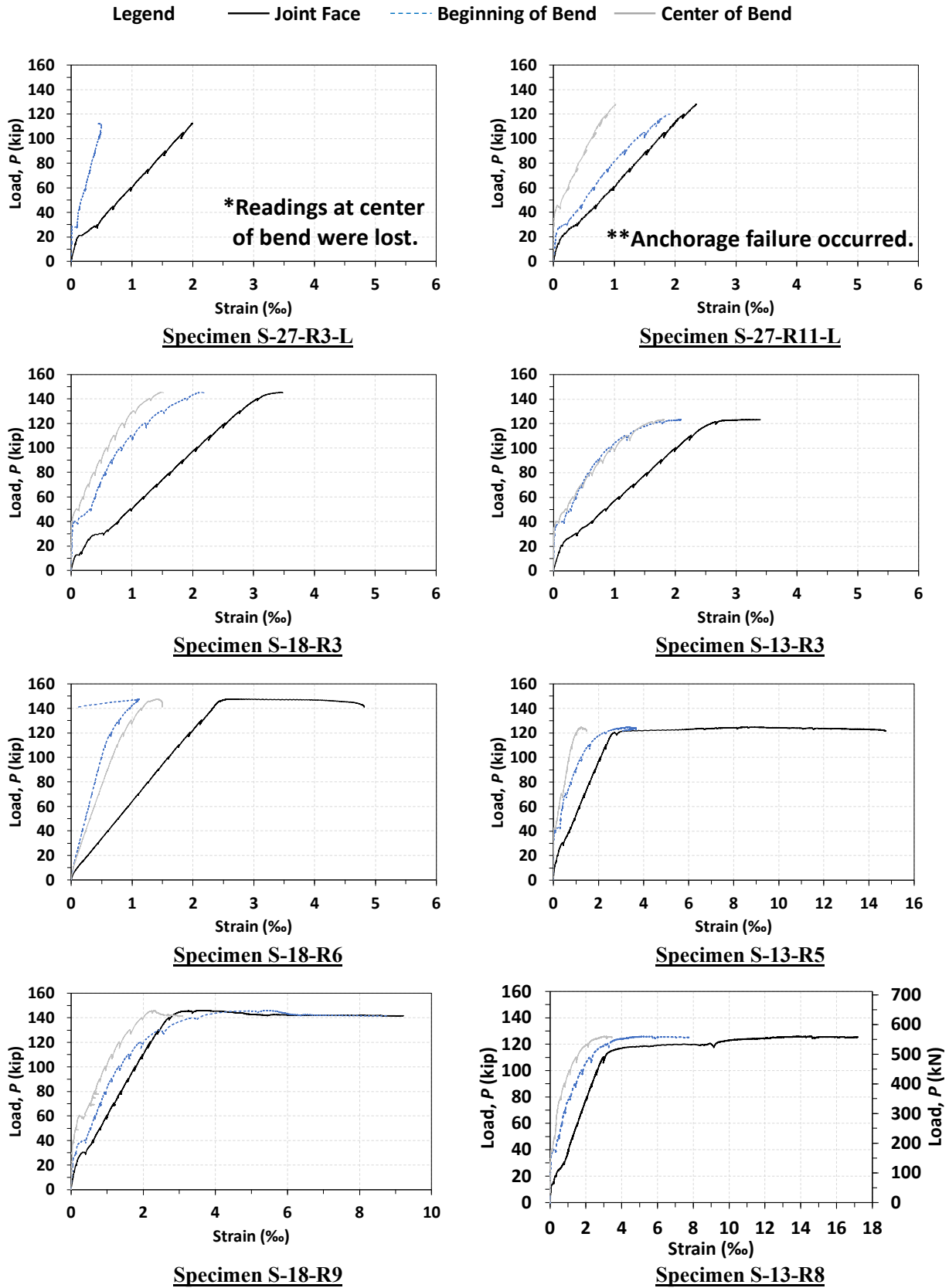


Figure 4-7 Measured strains in the reinforcing bars

In general, at the beginning of the test prior to the formation of flexural cracks, only the strain gauges located at the face of the joint show noticeable readings on the plots of Figure 4-7. At the same time, the measured strains at the beginning and center of the bar bends were nearly zero, indicating that the portion of the bars within the joint carried little tensile stress. The strain at these two locations began to increase as flexural cracks developed within the joint between approximately 20 and 50 kip. Sudden increases in the measured strains along the ascending branches of the plots in Figure 4-7 indicate the formation of cracks in the joint region.

After cracking and before the longitudinal bars experienced any yielding, the largest strain readings were measured at the joint face, as expected. Generally, the lowest strains were measured at the center of the bar bend, and the strain at the beginning of the bar bend fell between the strains measured at the two other gauge locations. The increase in strain from the joint face to the beginning of the bend and from the beginning of the bend to the center of the bend indicates that bond stress existed along the bars within the joint.

The data from the strain gauges also indicate that the bend radius affected the extent of yielding of the reinforcement within the joint prior to ultimate failure of the specimens. For example, the bars in the specimens with the bend radius of a standard hook and relatively low mechanical reinforcement ratios (Specimens S-18-R3 and S-13-R3) reached the yield strain of 0.0023 (calculated by dividing the measured yield stress of the bars by 29,000 ksi) at the face of the joint. However, the strain in the reinforcement at both the beginning and center of the bar bends did not reach the yield strain prior to the sudden loss in the load-carrying capacity of the specimens. The behavior of these specimens was characterized by splitting of the strut extending across the joint, indicating that the effective compressive strength of the concrete f_{ce} within the joint was reached before the yielding of the longitudinal bars extended into the bend region. With a relatively large mechanical reinforcement ratio, Specimen 1-1 experienced failure prior to any yielding of the reinforcement.

Because Specimen S-18-R6 was reloaded during testing, the discussion of strain measurements for knee joints with a bend radius between that of a standard hook and the requirement of Eq. 2-20 should focus on the data from Specimen S-13-R5. Prior to the initiation of ultimate failure, the measured strain in the bars of Specimen S-13-R5 at the beginning of the bar bend exceeded the yield strain. Yielding of the reinforcement, however, did not extend to the center of the bend, indicating that circumferential bond stress existed along the bend as the

specimen approached failure (see Figure 4-7). Although the strain readings from Specimen S-18-R6 may contain inaccuracies due to reloading, the specimen exhibited the same failure mode as Specimen S-13-R5.

For the specimens with a bend radius satisfying Eq. 2-20, except for Specimen S-27-R11-L, which had a relatively large mechanical reinforcement ratio and experienced an anchorage failure, the reinforcing bars yielded at all three strain gauge locations along the bend regions prior to the end of the test. In this case, the bond stress along the bars within the joint diminished, and only radial stresses acted at the bend region of the bars (see Figure 4-7).

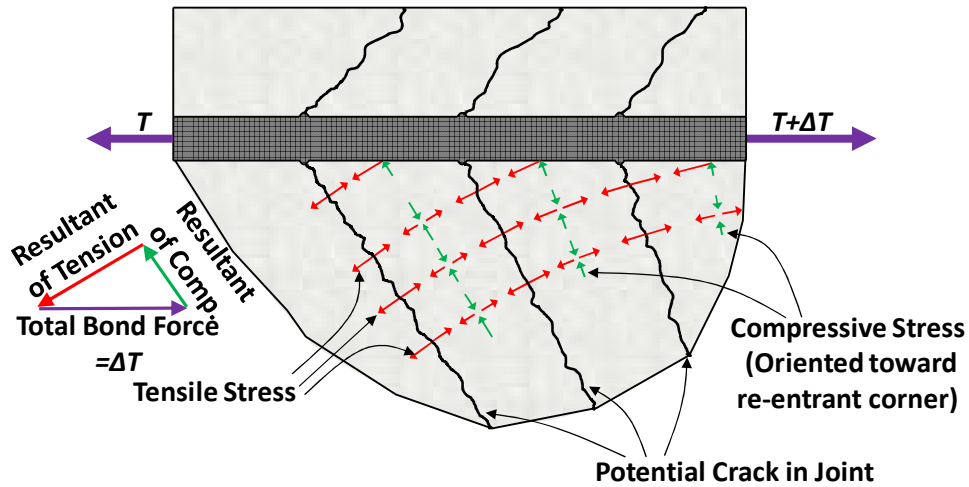
Previously, the value of C in Eq. 4-2 was related to the strength and ductility of the test specimens. The value of C also corresponds with the extent of yielding along the longitudinal bars within the joints of the specimens. With a relatively low C -value of 0.66, the bars of Specimen S-27-R3-L did not yield within the joint prior to failure. With lower values of ω , Specimens S-18-R3 and S-13-R3 had larger C -values of 0.86 and 1.14, respectively, which corresponded with yielding of the bars at the face of the joint and M_{test}/M_{calc} values exceeding 1.0. As the values of C increased due to larger bend radii, yielding of the bars extended farther into the joint. Specimens S-18-R9 and S-13-R8 had relatively large C -values of 2.50 and 2.91, respectively, and experienced yielding of the reinforcement through the entire joint along with improved ductility.

4.2.4 Stress Transmission and Failure Mechanisms

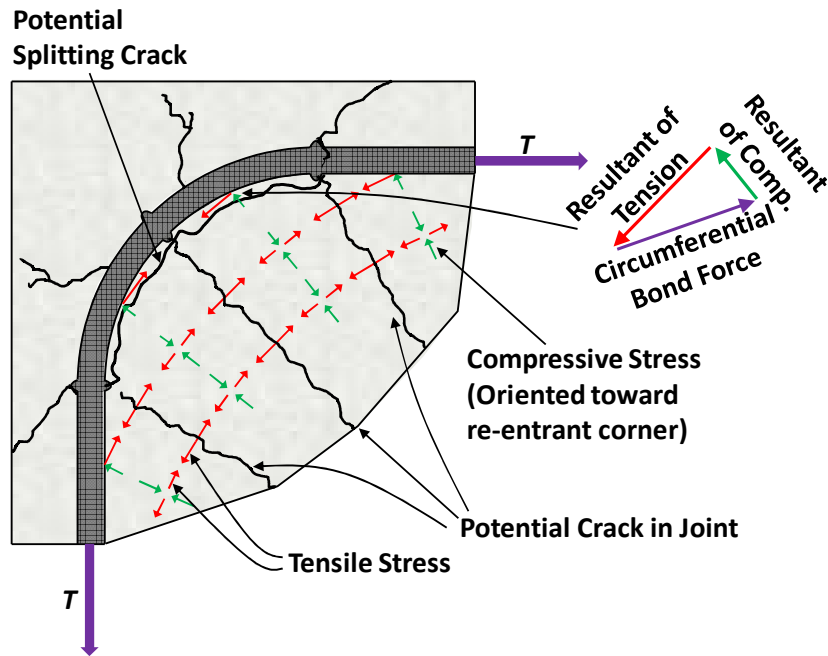
From the crack patterns and strain distributions described in the previous sections, the stress transmission mechanism in the joints can be inferred and the effect of the bend radius on the failure behavior can be better understood.

As previously noted, a difference in strain of the longitudinal bars between the face of the joint and the beginning of the bend indicates the presence of bond stress along the straight portion of the bars. The resultant of the bond stress is represented by the force ΔT in Figure 4-8(a). The force ΔT must be equilibrated by stresses within the joint region. These stresses can be represented by a fan-shaped strut that transmits compressive stresses (see Figure 4-9(a)) coupled with tensile stresses that develop perpendicular to the compressive stresses. The compressive stresses are oriented toward the re-entrant corner and are greatest along the diagonal that extends from the bend region of the bars to the re-entrant corner. The combination of the resultant compressive and tensile forces equilibrates the force ΔT in the bars, as illustrated in Figure 4-8(a). As indicated by

the orientation of cracks observed during the knee joint tests, the tensile stresses perpendicular to the fan-shaped strut lead to the formation of cracks within the joint region. A finite element analysis conducted by Ingham²⁴ also demonstrated the same stress flow pattern.



(a) Along the straight portion of the bars (adapted from Ingham²⁴)



(b) At the bar bend

Figure 4-8 Stress transmission mechanism within a joint

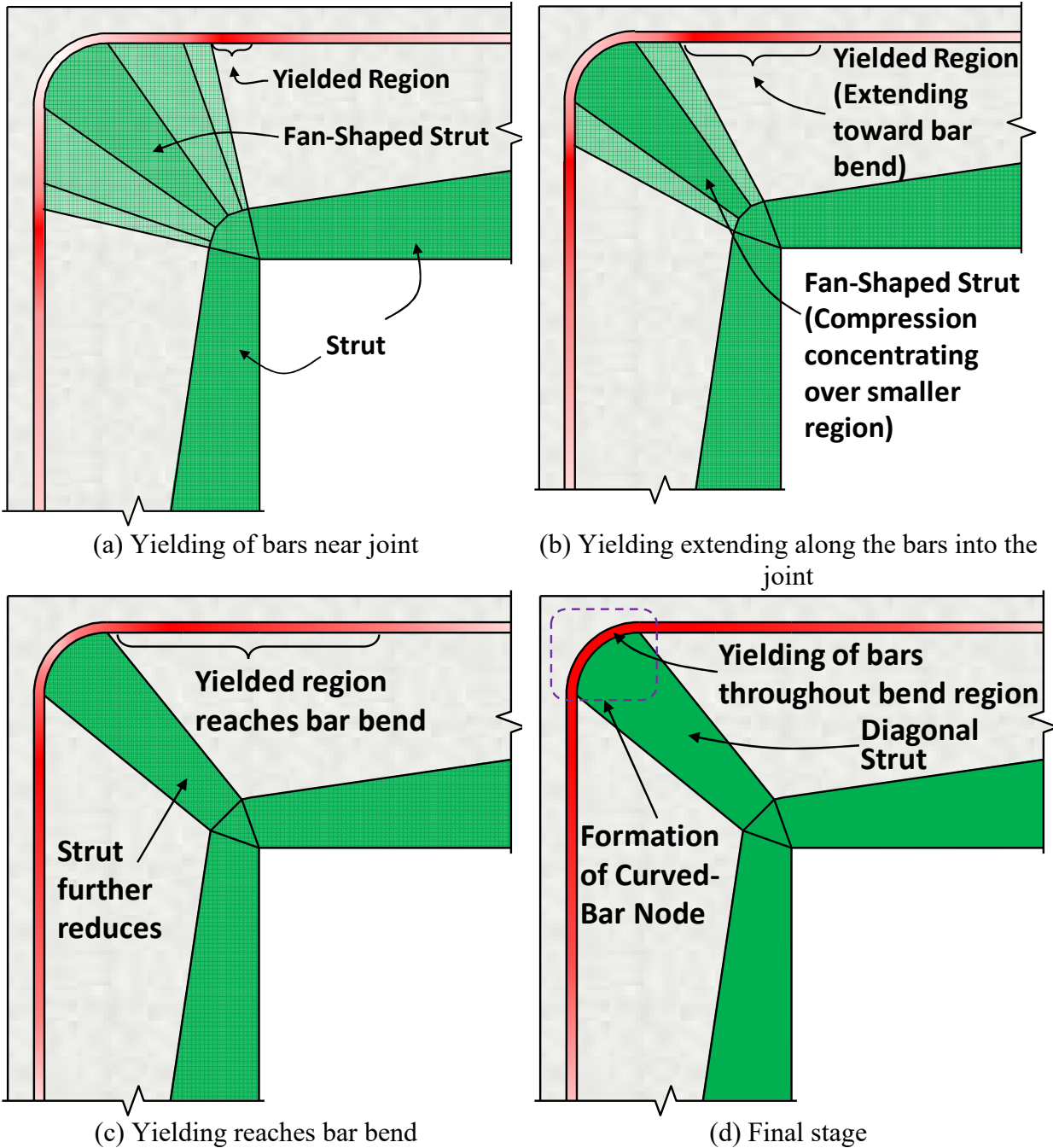


Figure 4-9 Stress flow in a joint as bars yield

A similar distribution of stress occurs along the bend region of the reinforcing bars before the yielding of the steel extends to the center of the bar bend (see Figure 4-8(b)). The difference of tensile stress between the beginning of the bend and the center of the bend corresponds with the existence of circumferential bond stress. The circumferential bond stress acting along the bend region develops due to the compressive stresses in the fan-shaped strut and the perpendicular

tensile stresses, as indicated in Figure 4-8(b). The compressive stresses are again oriented toward the re-entrant corner, while the tensile stresses result in the potential for the formation of diagonal cracks in the direction of the fan-shaped strut.

As the magnitude of a closing moment applied to a knee joint is increased, the stress transmission mechanism within the joint region experiences important changes once the longitudinal bars yield at the face of the joint. As the bars yield at the location of the joint face, the bond stress along the bars within the joint is transmitted by the mechanism previously described and illustrated in Figure 4-8. This state of stress is also represented in Figure 4-9(a). As the load applied to the specimen is increased further, yielding of the steel extends along the bars toward the outside corner of the specimen (that is, toward the bar bend), as illustrated in Figure 4-9(b). Bond stress is no longer present along the yielded portion of the bars because a force differential no longer exists along the bars within this region. Furthermore, because the bond stress is directly related to the existence of the compressive stresses in the fan-shaped strut and the corresponding perpendicular tensile stresses (see Figure 4-8), the elimination of bond stress along the yielded portion of the bars corresponds to a change in the area over which the fan-shaped strut is spread. In other words, the compressive stresses carried within the strut concentrate over a smaller region, as indicated in Figure 4-9. Upon further loading of the specimen, if it has not yet experienced failure, yielding of the bars continues to extend toward the center of the bar bend until the entire length of the bars within the joint region experiences yielding (see Figure 4-9(d)). At the same time, the fan-shaped strut reduces to a single diagonal strut that imposes highly concentrated compressive stresses on the curved-bar node located at the outside corner of the specimen. The strut-and-tie model of a frame corner (see Figure 2-3(a)) represents this state of stress. It should be noted that the two additional inclined struts in Figure 2-3(a) developed due to the shear force imposed on the legs of the knee joint specimens and had no significant effect on the general behavior of the joint regions.

The stress transmission mechanism within the joints as ultimate failure was approached was directly related to the bend radius of the longitudinal reinforcement. For the specimens with the bend radius of a standard hook (Specimens S-27-R3-L, S-18-R3, and S-13-R3), a fan-shaped strut developed within the joint region. Prior to extensive yielding of the reinforcement, and prior to any yielding of the bars in Specimen S-27-R3-L, the compressive stress in the concrete near the inside of the bar bend reached its effective compressive strength f_{ce} because of the small bend

radius of the bars, resulting in a brittle failure due to splitting of the strut. At the failure of Specimen S-27-R3-L, the extent of the fan-shaped strut had not yet started to reduce within the joint region. For Specimens S-18-R3 and S-13-R3, the longitudinal bars yielded at the face of the joint, and the yielded portion of the bars began to extend toward the beginning of the bar bend. At the failure of Specimens S-18-R3 and S-13-R3, the extent of the fan-shaped strut had begun to reduce within the joint region, culminating with the state illustrated in Figure 4-9(a).

The behavior of the specimens with the bend radius between that of a standard hook and the requirement of Eq. 2-20 (Specimens S-18-R6 and S-13-R5) suggests that the concrete in the bar bend could not effectively resist the circumferential bond stress that developed, leading to the formation of a bond splitting crack that extended between the points corresponding to the beginning and end of the bend region of the bars, as labeled in Figure 4-8(b). The yielded portion of the bars, however, extended into the bend region, resulting in the state illustrated in Figure 4-9(c) when failure occurred.

Unlike the other specimens, the stress transmission mechanism of the specimens with the bend radius satisfying Eq. 2-20 that did not experience a premature anchorage failure (Specimens S-18-R9 and S-13-R8) was able to achieve the final stage illustrated in Figure 4-9(d). As the applied load on the specimens increased, the bend region of the bars sustained the presence of the circumferential bond stress without the splitting of surrounding concrete experienced by other specimens. Eventually, the stress distribution within the joint corresponded to the strut-and-tie model (see Figure 2-3(a)). The strain readings indicated that the bars experienced yielding along their entire length within the joint. The force along the length of the reinforcement was constant, consistent with the ties of the strut-and-tie model. Furthermore, the bend radius was sufficient to allow the radial stress at the bend region to be resisted. Therefore, considering the specimens of the test program, only the specimens with a bend radius r_b satisfying the requirements of Eq. 2-20 (that is, specimens designed with a CTT node at the outer corner that was proportioned appropriately) achieved a stress distribution consistent with the assumed strut-and-tie model. As a result, the specimens exhibited ductile behavior.

4.2.5 Summary

The tests on the eight S-Series knee joint specimens provided the means to investigate the effect of the bend radius of longitudinal reinforcement arranged in a single layer and allowed a preliminary evaluation of the validity of Eq. 2-20, which must be satisfied in accordance with ACI 318-19,¹ to be conducted. The behavior of the specimens was described in terms of the transmission mechanism of stresses in the joint and the strut-and-tie method. The primary observations and conclusions from the tests on the S-series specimens are summarized as follows:

1. The bend radii of the longitudinal bars had a significant effect on the strength ratio M_{test}/M_{calc} and displacement ductility of the knee joint test specimens. Enlarging the size of the bend radius increased M_{test}/M_{calc} for low values of the mechanical longitudinal reinforcement ratio ($\omega = 0.27$). If a specimen with a relatively small bend radius resulted in an M_{test}/M_{calc} that reached unity, providing a larger bend radius resulted in improved ductility. This can be described using the parameter $C = \frac{r_b}{\omega d}$. Specimens with a value of C greater than 0.86 resulted in M_{test}/M_{calc} values greater than one. As the value of C increased beyond 0.86, ductility of the specimens as defined by the displacement ductility factor, μ , increased in a seemingly linear relationship with C .
2. The bend radii of the longitudinal bars influenced the observed behaviors of the specimens, as evidenced by the damage patterns at the end of the tests. The specimens with bend radii based on a standard hook experienced brittle failure characterized by splitting of the strut that extended across the joint. The specimens with bend radii satisfying the design equation for curved-bar nodes (Eq. 2-24) exhibited ductile behavior superior to the other specimens if anchorage failure did not occur. Bend radii between that of a standard hook and the requirement of the design equation resulted in failures characterized by the development of bond splitting cracks near the bar bend with concrete crushing at the re-entrant corner.
3. The extent of yielding of the longitudinal bars within the joints was related to the bar bend radius. For a bar bend satisfying the design equation for curved-bar nodes, the bars experienced yielding throughout the entire joint. For all other cases, the yielded region of the bars did not extend throughout the joint region prior to failure of the specimen.
4. The assumed strut-and-tie model for RC knee joints under closing moments was only achieved for the specimens with a CTT node at the outside of the joint proportioned using

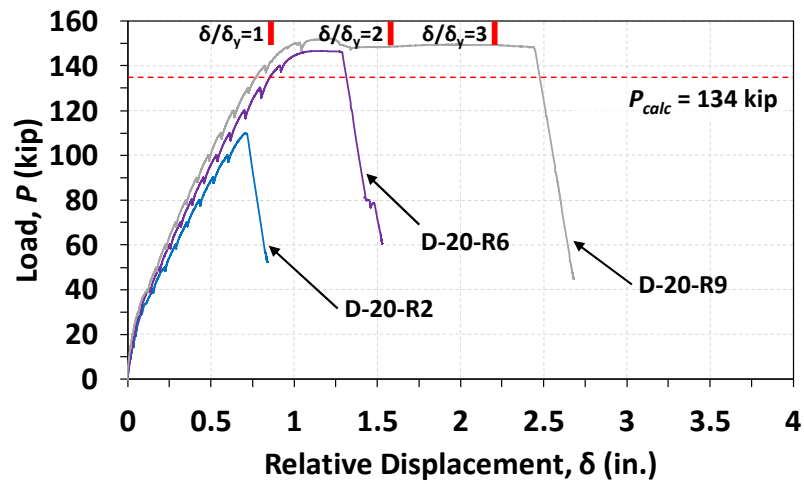
the design equation for curved-bar nodes (Eq. 2-20). As a result, the specimens exceeded M_{calc} and exhibited ductile behavior.

4.3 Series II: Double-Layer Longitudinal Bars (D-Series)

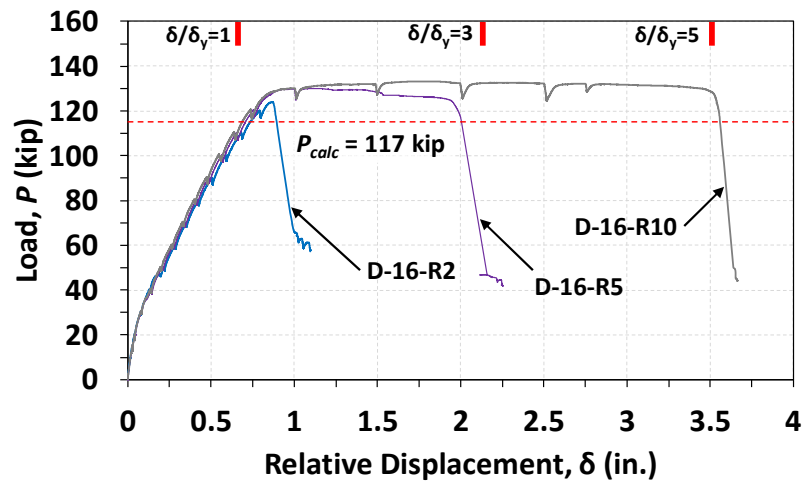
This section describes the experimental results of the six D-Series specimens. Like the S-Series specimens, the D-Series specimens were also developed to investigate the effect of the bend radius and the mechanical reinforcement ratio on the behavior of knee joints under closing moments. However, the specimens were detailed with two layers of longitudinal reinforcement. Section 23.10.4 of ACI 318-19¹ states that the value of r_b should be “taken as the bend radius of the innermost layers” when multiple layers of bars are present. Furthermore, the provision defines A_{ts} , which is input into Eq. 2-20, as the total area of reinforcement. It should be noted that the longitudinal bars in both layers of the D-Series specimens were detailed with the same bend radii. That is, the same pin was used on the reinforcing bar bending table to bend all the bars within a particular specimen.

4.3.1 Overall Behavior

Plots that demonstrate the relationship of applied load and relative displacement of each D-Series specimen are presented in Figure 4-10. The parameters in the plots are defined as they were for the S-Series specimens. Again, the horizontal dashed red lines in Figure 4-10 indicate the value of P_{calc} for each specimen group. Only the greatest P_{calc} for each group is shown in the plots to improve readability. Detailed test results are summarized in Table 4-2.



(a)



(b)

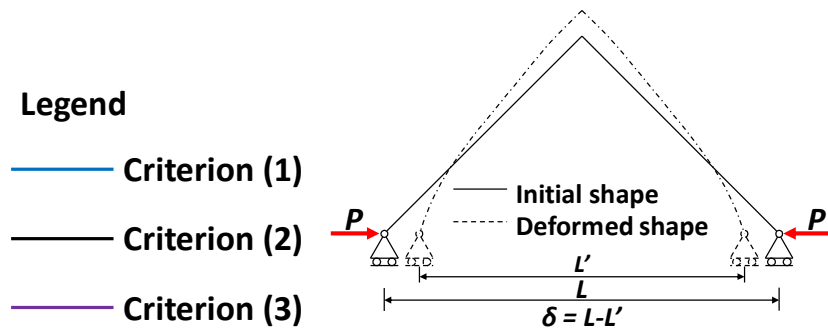


Figure 4-10 Load-displacement curves of knee joint specimens: (a) Group D-1, (b) Group D-2

Table 4-2 Summary of test results, joint efficiency, and ductility of D-Series specimens

| Specimen ID | P_{test} (kip) | M_{test} (kip-in.) | P_{calc} (kip) | M_{calc} (kip-in.) | M_{test}/M_{calc} | δ_{max} (in.) | δ_y (in.) | μ | C |
|-------------|------------------|----------------------|------------------|----------------------|---------------------|----------------------|------------------|-------|------|
| D-20-R2 | 110 | 5445 | 133.7 | 6618 | 0.82 | 0.71 | - | - | 0.66 |
| D-20-R6 | 149 | 7375 | 134.2 | 6642 | 1.11 | 1.29 | 0.77 | 1.67 | 1.61 |
| D-20-R9 | 152 | 7524 | 133.4 | 6603 | 1.14 | 2.45 | 0.83 | 2.93 | 2.38 |
| D-16-R2 | 124 | 6138 | 117.0 | 5791 | 1.06 | 0.89 | 0.75 | - | 0.67 |
| D-16-R5 | 130 | 6438 | 114.8 | 5682 | 1.13 | 2.00 | 0.72 | 2.77 | 1.49 |
| D-16-R10 | 133 | 6591 | 116.7 | 5776 | 1.14 | 3.56 | 0.70 | 5.08 | 2.84 |

The test results for the Group D-1 specimens are shown in Figure 4-10(a). Specimen D-20-R2, which had the bend radius of a standard hook, failed prematurely at a P_{test} value of 110 kip, reaching a joint efficiency, M_{test}/M_{calc} , of only 0.82. A significant loss in load-carrying capacity suddenly occurred, and no ductility was observed. Different from Specimen D-20-R2, the other two specimens of Group D-1 reached a joint efficiency greater than 1.0 and exhibited ductile behavior. Specimen D-20-R9, which had a bend radius satisfying the requirement of Eq. 2-20, reached a maximum load of 152 kip, and the specimen achieved relatively large deformations. Prior to the ultimate failure condition, Specimen D-20-R9 had a relative displacement of 2.45 in., corresponding to a displacement ductility factor of 2.93. Having a bend radius that fell in between that of the other two specimens, Specimen D-20-R6 was able to avoid premature failure prior to reaching a load plateau, but the displacement ductility factor was not as high as that of Specimen D-20-R9, reaching a value of 1.29.

The specimens in Group D-2 behaved similarly to their companion specimens in Group D-1. That is, larger bend radii resulted in higher joint efficiency and/or ductility. Specimen D-16-R2, which had the bend radius of a standard hook, reached a joint efficiency of 1.06. After reaching the peak load, a sudden drop in load-carrying capacity was observed. The specimen reached a displacement of 0.89 in. at failure. Both of the other Group D-2 specimens demonstrated an obvious load plateau, again indicating that a larger bend radius led to greater deformability. Prior to the ultimate failure condition, Specimen D-16-R10 experienced a relative displacement of 3.56 in., corresponding to a displacement ductility factor of 5.08, while Specimen D-16-R5 reached a relative displacement of 2.00 in., corresponding to a μ -value of 2.77.

It can be observed that the overall behavior of the D-Series specimens was similar to that of the S-Series specimens. For specimens with smaller longitudinal reinforcement ratios ω (Group

D-2), all specimens were able to reach joint efficiencies greater than 1.0. For this scenario, a larger bend radius resulted in an increased displacement ductility factor. For specimens with higher longitudinal reinforcement ratios ω (Group D-1), a bend radius larger than that of a standard hook resulted in increased joint efficiency. When the bend radius was further increased relative to a radius resulting in a joint efficiency greater than 1.0, the displacement ductility factor increased.

C -values, as defined previously, were also calculated based on measured material properties for the D-Series specimens as summarized in Table 4-2. It can be observed that specimens with a C -value greater than or equal to 0.67 were able to achieve a load-carrying capacity greater than the calculated value. For the S-Series specimens, a C -value greater than or equal to 0.86 corresponded with a joint efficiency greater than or equal to 1.0. Although this value is greater than that of the D-Series specimens, it should be noted that the S-Series did not include a specimen with a C -value between 0.66 and 0.86. Furthermore, the D-Series specimen with a C -value of 0.67 (that is, Specimen D-16-R2) was not able to reach a strength as high as other specimens in Group D-2. In other words, Specimen D-16-R2 exhibited strength that was slightly compromised.

The relationship between C and the displacement ductility factor μ for the S-Series and D-Series specimens is shown in Figure 4-11. Specimen D-20-R2 is not included due to its premature failure and relatively low joint efficiency. The plot seems to indicate that two layers of longitudinal reinforcement provide a similar relationship to that of one layer of longitudinal reinforcement. The application of Eq. 2-20 to specimens with two layers of reinforcing bars is addressed in Chapter 5 along with more detailed analysis.

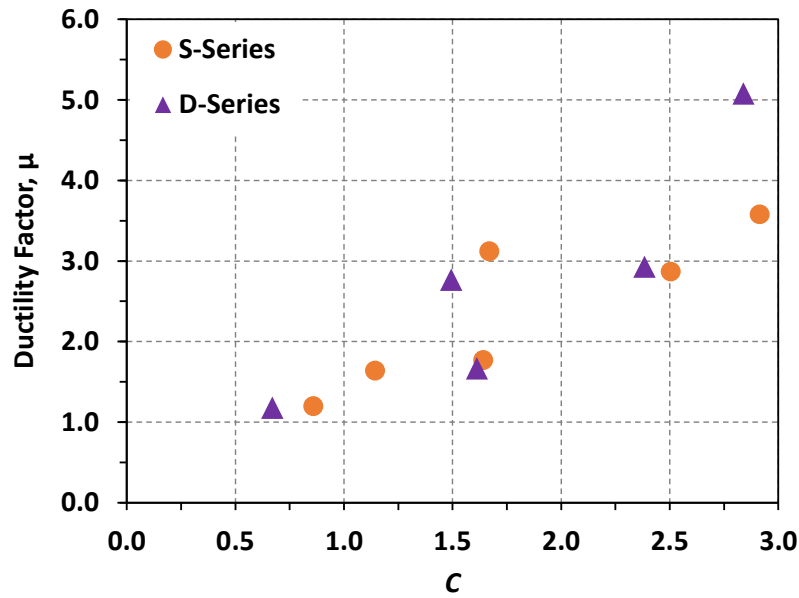


Figure 4-11 Relationship between C and displacement ductility factor μ for S-Series and D-Series specimens

4.3.2 Visual Observations

The crack pattern and a photograph of each D-Series specimen after being tested are presented in Figure 4-12 and Figure 4-13. Again, red lines shown on the figures indicate cracks that are believed to have appeared when the ultimate failure condition was reached. That is, the cracks formed at the same time as a substantial drop in load-carrying capacity. Hatched regions indicate the areas where crushing or spalling of concrete occurred. The observed formation and propagation of cracks during the tests are illustrated in Figure 4-14.

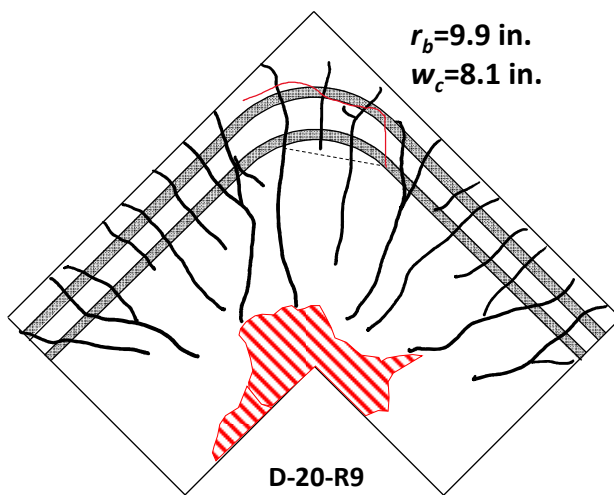
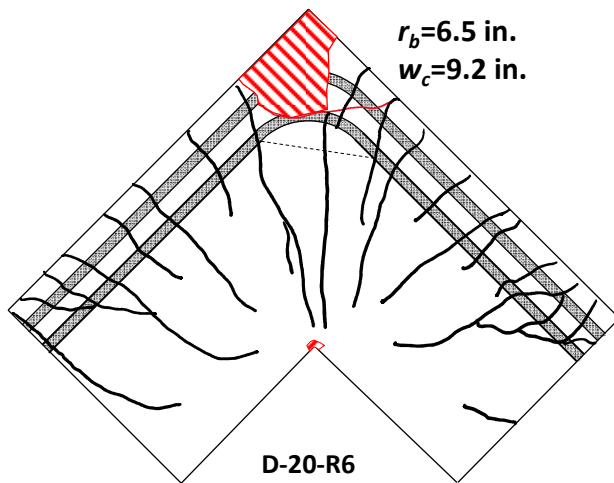
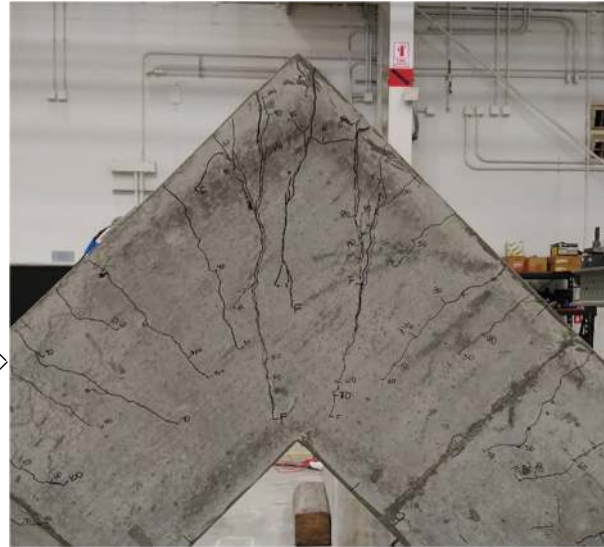
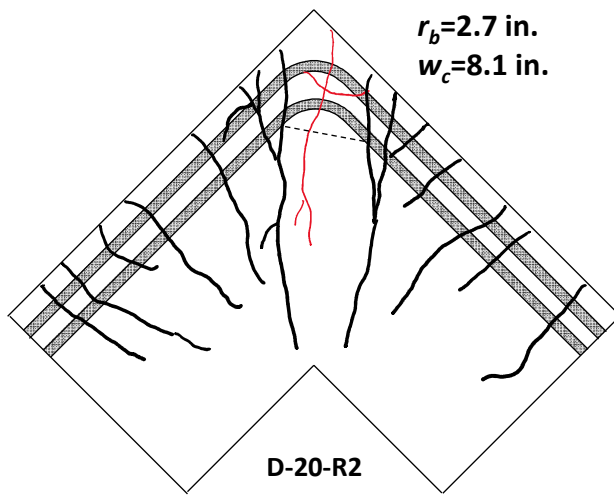


Figure 4-12 Crack maps and photos of Group D-1 specimens

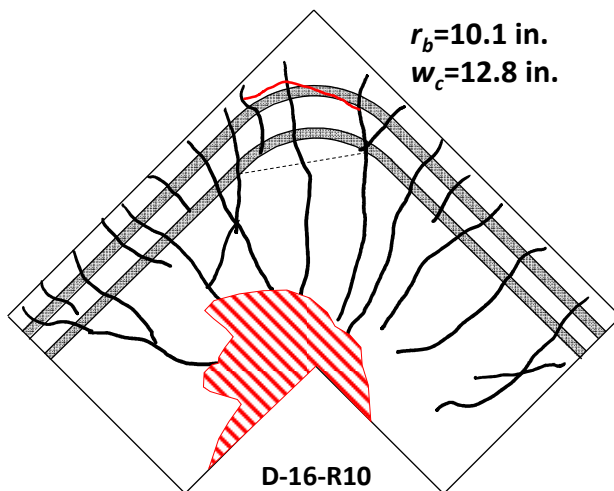
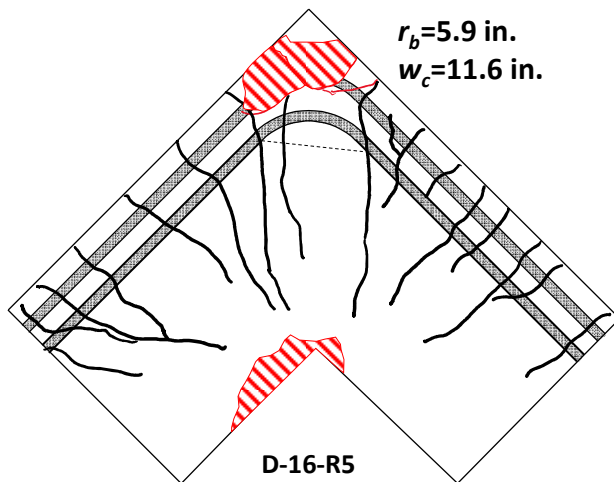
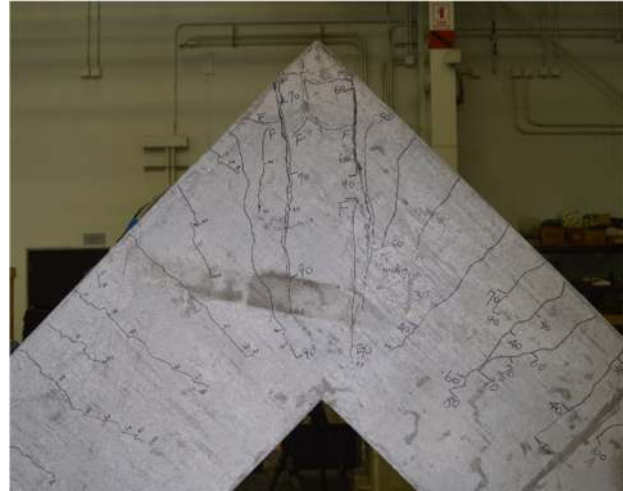
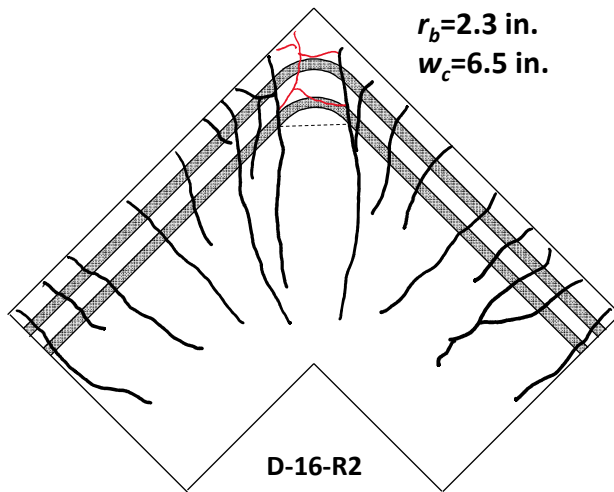


Figure 4-13 Crack maps and photos of Group D-2 specimens

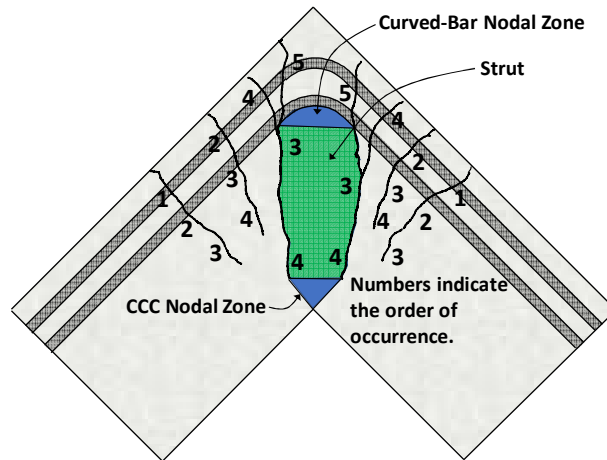


Figure 4-14 Typical crack formation and propagation in joints of D-Series specimens

The formation and propagation of cracks observed during the D-Series tests were similar to those observed for the S-Series tests. Regardless of the sizes of the bend radii, the first two cracks observed developed at the joint faces at approximately 30 kip. As the applied load increased, the cracks at the joint faces extended while new cracks formed within the joint. It should be noted that cracks that formed within the joint did not necessarily initiate from the extreme tension fiber; instead, some initiated away from the edges. Upon increasing the load further, the cracks then propagated toward the re-entrant corner. In the meantime, cracks that initiated away from the edges extended toward the edges of the specimen. At an applied load between 70 kip and 100 kip, the region enclosed by the two innermost cracks indicated the strut extending across the joint. After a load of 100 kip, new cracks were seldom found in the diagonal strut region until cracks were no longer marked due to safety concerns.

After the basic crack patterns formed (see Figure 4-14) and the ultimate failure conditions were approached, the development of damage in the joint as the load increased varied in an evident relationship with the sizes of the bend radii. For specimens with the bend radius of a standard hook (Specimens D-20-R2 and D-16-R2), the ultimate failure condition occurred not long after the basic crack pattern illustrated in Figure 4-14 developed. A vertical crack along the center of the diagonal strut suddenly formed and corresponded to the significant drop in the load-carrying capacity. The crack extended downward to the re-entrant corner for Specimen D-20-R2, while a horizontal crack between the two layers of the longitudinal reinforcement appeared simultaneously (see Figure 4-12). Specimen D-16-R2 also experienced the vertical crack, but the vertical crack did not extend

as far as that of Specimen D-20-R2 (see Figure 4-13). The vertical crack was connected to a nearly horizontal crack at the level of the inner layer of the longitudinal bars. At the same time, the two innermost cracks that enclosed the diagonal strut widened significantly. Both specimens did not exhibit signs of concrete crushing at the re-entrant corner.

Unlike specimens with the bend radius of a standard hook, specimens with a bend radius in between that of a standard hook and Eq. 2-20 (Specimens D-20-R6 and D-16-R5) experienced some concrete crushing at the re-entrant corner, but the spreading of the crushed concrete exhibited by the two specimens was different. After the peak load was reached, Specimen D-16-R5 sustained greater displacement than Specimen D-20-R6, exhibiting a large area of crushed concrete at the re-entrant corner as shown in Figure 4-13. Moreover, a horizontal crack located approximately between the two layers of longitudinal bars developed. Above the horizontal crack, concrete spalled from the joint. Specimen D-20-R6, on the other hand, did not exhibit much concrete crushing at the re-entrant corner. Only a small area of concrete at the re-entrant corner crushed and dropped off the specimen. At the ultimate failure condition, a horizontal crack also formed above the inner layer of the longitudinal bars, triggering concrete above the crack to spall.

Specimens with a bend radius satisfying the requirement by Eq. 2-20 (Specimens D-20-R9 and D-16-R10) experienced extensive concrete crushing before the ultimate failure condition. For Specimen D-20-R9, when the load-carrying capacity significantly dropped, cracks marked with the number “2” that extended from the edge of the specimens in Figure 4-14 suddenly widened, and a large amount of concrete on the bottom face of the re-entrant corner fell from the specimen. Specimen D-16-R10 also demonstrated a similar damage pattern. At the ultimate failure condition of Specimen D-16-R10, a horizontal crack formed approximately under the bar bend of the outer layer of the longitudinal bars (see Figure 4-13).

A line that connected the intersections of the inner most cracks and the inner longitudinal bar can be considered the width of the diagonal strut (see Figure 4-14), which is denoted as w_c and shown in each figure. Except for Specimens D-20-R9, the trend that a larger bend radii r_b leads to a greater measured value of w_c can be observed. The exception indicates that a limit might exist on the strut width at the interface with the curved-bar node. In other words, it may not be effective to further enlarge the bend radius if the required width of the strut is able to be achieved.

In addition to the side face, the damage pattern on the top face was affected by the bend radius as shown in Figure 4-15. Specimens with the bend radius of a standard bend (Specimens D-

20-R2 and D-16-R2) and specimens with a bend radius in between that of a standard hook and Eq. 2-20 had somewhat similar damage patterns. Concrete side cover spalled off the joint. In addition, concrete above the bar bend was no longer attached to the knee joint and could be easily removed without the assistance of hand tools. For specimens with a bend radius satisfying Eq. 2-20 (Specimens D-20-R9 and D-16-R10), a wide crack formed approximately along the centerline of the top face. Specimen D-16-R10 showed no indication of the detachment of top concrete. Specimen D-20-R9 had some cover concrete on one side that spalled off, but the concrete on the other side was not fully detached from the specimen.



Specimen D-20-R2



Specimen D-16-R2



Specimen D-20-R6



Specimen D-16-R5



Specimen D-20-R9



Specimen D-16-R10

Figure 4-15 Damage on the top face of each D-Series specimen

4.3.3 Strain in the Reinforcing Bars

In Figure 4-16 and Figure 4-17, the applied load is plotted against the strain readings measured at three points along the longitudinal bars as explained in Section 3.5.3. The plots show the strain readings up to the ultimate failure condition for each specimen.

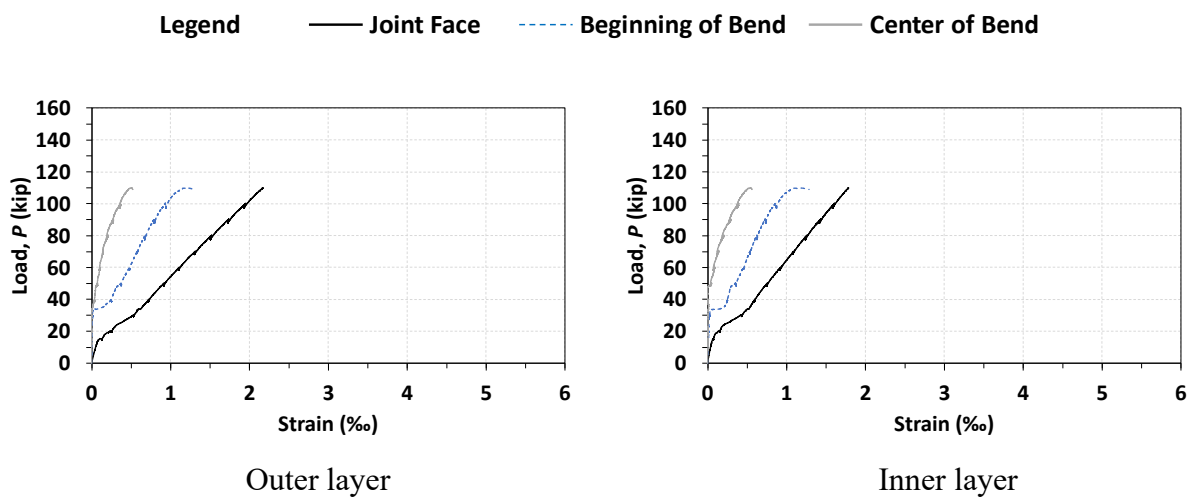
Generally, for specimens in Group D-1 and Group D-2, only the strain gauges at the position corresponding to the joint face had noticeable readings on both the outer layer and inner layer of the longitudinal reinforcing bars early in the test. At a load between approximately 20 kip and 30 kip, the slope of the curve for the strain at the joint face decreased suddenly, indicating that the specimen cracked at this load level. Upon the load increasing to between approximately 40 kip and 50 kip, strain readings at the other two strain gauge positions along the bars for both the outer and inner layers began to increase. This corresponds to the formation of cracks in the joint region. Before yielding of the bars at the joint face, the strain readings at the joint face were higher than the readings at the other two locations along the bars, indicating that bond stress existed within the joint region for both the outer and inner layers of longitudinal bars.

The comparison of strain readings measured along the outer layer to the readings measured along the inner layer gives information about the tensile stress distribution within the joint. For example, the strain readings at the location of the joint face increased more rapidly with the applied load for the outer layer compared to the inner layer prior to yielding, indicating that higher tensile strains occurred at points farther from the compression zone at the joint face. For the other two positions (that is, at the beginning and center of the bar bend), the strain readings indicate a different trend. In general, strain readings for the inner layer were higher than those for the outer layer, revealing that tensile stress was higher toward the center of the joint.

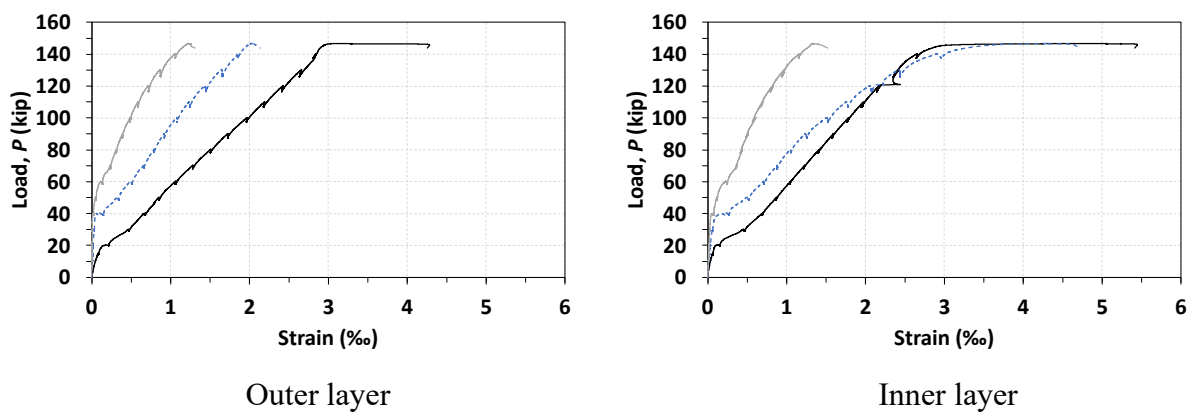
The data from the strain gauges also indicate that the bend radius affected the extent of yielding of the reinforcement within the joint prior to ultimate failure of the specimens. This observation was the same for the S-Series specimens. For specimens with the bend radius of a standard hook (Specimens D-20-R2 and D-16-R2), the strain at neither the beginning of the bar bend nor at the center of the bar bend reached the yield strain, only attaining a value of approximately 1.0‰ and 0.5‰, respectively. It should be noted that the yield strain was based on the measured yield stress divided by the modulus of elasticity of steel (29,000 ksi). Unfortunately, the strain reading at the center of the bar bend of the outer layer for Specimen D-16-R2 was lost. The strain readings at the joint face for Specimens D-20-R2 and D-16-R2 exhibited an important

difference. For Specimen D-20-R2, the strain in the outer layer barely reached the yield strain, while the inner layer did not reach the yield strain prior to failure of the specimen. However, both the inner and outer layers of the bars in Specimen D-16-R2, which had a lower mechanical reinforcement ratio, reached the yield strain at the joint face, resulting in a higher joint efficiency. Yielding was not experienced in the bend region. This observation indicates that the effective compressive strength of the concrete f_{ce} within the joint was reached before the yielding of the longitudinal bars extended into the bend region.

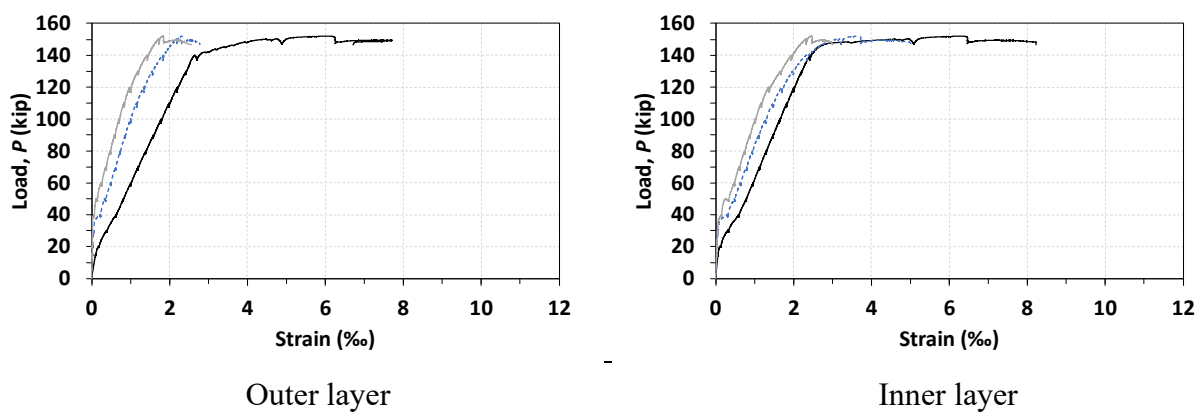
For specimens with a bend radius satisfying the requirement of Eq. 2-20 (Specimens D-20-R9 and D-16-R10), the strain readings at all three locations reached the yield strain prior to the ultimate failure condition. In other words, the yielded region extended entirely through the reinforcing bars whether in the outer layer or the inner layer, indicating that the stress distribution assumed by the strut-and-tie model was achieved. This phenomenon was the same as observed for the S-Series specimens. Specimens D-20-R6 and D-16-R5, which had a bend radius in between that of a standard bend and Eq. 2-20, did not experience yielding at the center of the bar bend, but the yield strain was reached at the joint face and the beginning of the bar bend. This is an indication that circumferential bond stress still existed prior to the ultimate failure condition.



Specimen D-20-R2

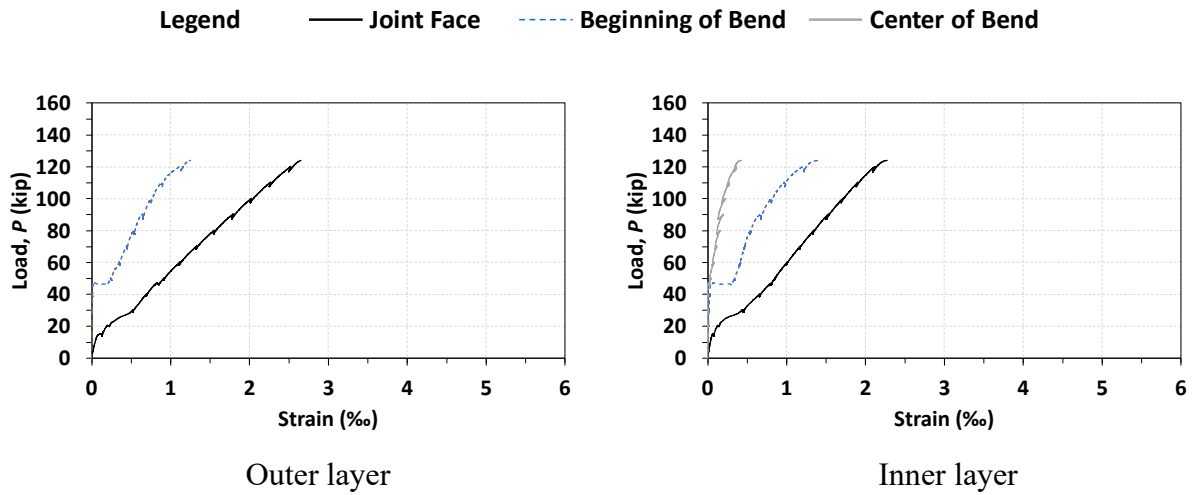


Specimen D-20-R6

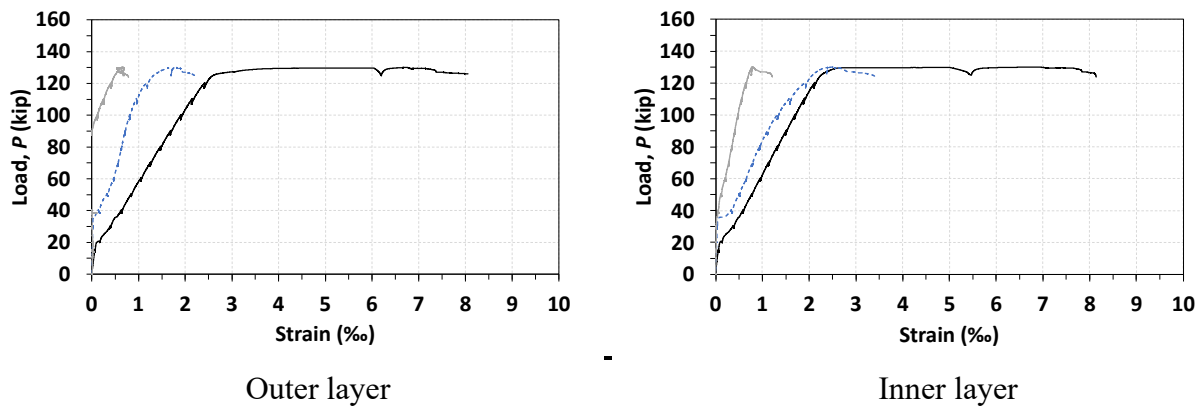


Specimen D-20-R9

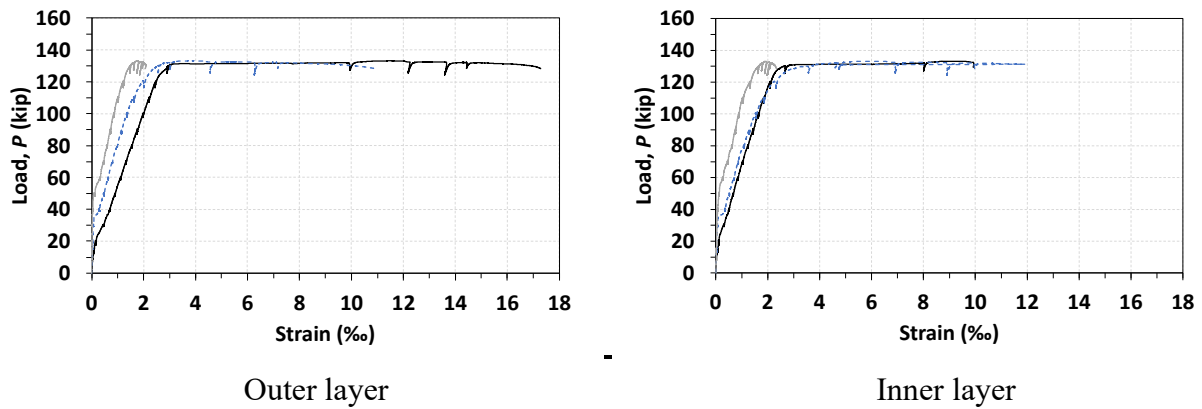
Figure 4-16 Measured strains in the reinforcing bars of Group D-1



Specimen D-16-R2



Specimen D-16-R5



Specimen D-16-R10

Figure 4-17 Measured strains in the reinforcing bars of Group D-2

4.3.4 Summary

To investigate the effect of the bend radius on knee joints reinforced with multiple layers of longitudinal reinforcement under closing moments, six specimens were fabricated and tested. In addition, the test results were also used to examine the validity of the requirement for the bend radius (Eq. 2-20) as suggested in ACI 318-19.¹ The primary observations are summarized as follows:

1. The bend radius of the longitudinal reinforcing bars significantly affected the joint efficiency (M_{test}/M_{calc}) and the displacement ductility factor. For specimens with a greater value of the mechanical longitudinal reinforcement ratio (approximately 20% greater), enlarging the bend radius from a radius that resulted in premature failure provided an increase in strength. If the joint efficiency was higher than 1.0 already, enlarging the bend radius resulted in an increase in the displacement ductility factor.
2. Different bend radii altered the behavior of the specimens in terms of damage patterns. For specimens with the bend radius of a standard hook, a premature failure caused by splitting of the diagonal strut was observed. For specimens with a bend radius in between that of a standard hook and Eq. 2-20, prior to the ultimate failure condition, some crushing of concrete at the re-entrant corner was observed. The specimens then failed due to a horizontal splitting crack approximately between the two layers of the longitudinal reinforcing bars. For specimens with a bend radius satisfying the requirement by Eq. 2-20, failure was characterized by crushing at the re-entrant corner (that is, at the CCC node).
3. The extension of the yielded region along the longitudinal reinforcing bars was influenced by the bend radius. Yielding did to extend to the bend region of the bars for the specimens with the bend radius of a standard hook. In fact, for the specimen with a relatively high longitudinal reinforcement ratio, the reinforcing bars in the inner layer did not yield at the joint face. For specimens with a bend radius in between that of a standard hook and Eq. 2-20, the yielded region was able to extend to the bar bend, allowing the specimen to exhibit some ductility. For specimens with a bend radius satisfying the requirement by Eq. 2-20, the longitudinal reinforcing bars yielded through the entire joint region, resulting in the greatest ductility. Furthermore, the stress distribution assumed by the strut-and-tie model for knee joints under closing moments was achieved for these specimens.

4. The test results indicate that the behavior of knee joints reinforced with two layers of longitudinal reinforcement were affected by the bend radii in a similar manner as specimens with a single layer of longitudinal reinforcement in terms of joint efficiency, damage patterns, and the yielding of reinforcing bars.

4.4 Series III: Reduced Clear Side Cover (C-Series)

This section describes the test results of the C-Series specimens. The four C-Series specimens were developed to investigate the effect of reduced clear side cover on the behavior of knee joints. As suggested in ACI 318-19,¹ for a curved-bar node with a clear side cover less than twice the bar diameter of the longitudinal reinforcement, the required bend radius should be further enlarged to prevent potential splitting of the side cover. To validate this, specimens in the series had the same cross-sectional dimensions and the same amount of longitudinal reinforcement as used in Group S-2 of the S-Series specimens. The clear side cover, however, was less than that used for the S-Series specimens (side cover of 1.25 in. measured to the longitudinal bars).

4.4.1 Overall Behavior

A plot of the load-displacement relationship of each C-Series specimen is presented in Figure 4-18. The dashed red line in the figure indicates the calculated load-carrying capacity, P_{calc} . Because the value of P_{calc} varied due to slightly different material properties as explained previously, only the maximum value is shown in the figure. The test results are summarized in Table 4-3. It should be noted that the two hydraulic cylinders were replaced with those with longer stroke limit to prevent early stop of tests after the tests of specimens in D-Series.

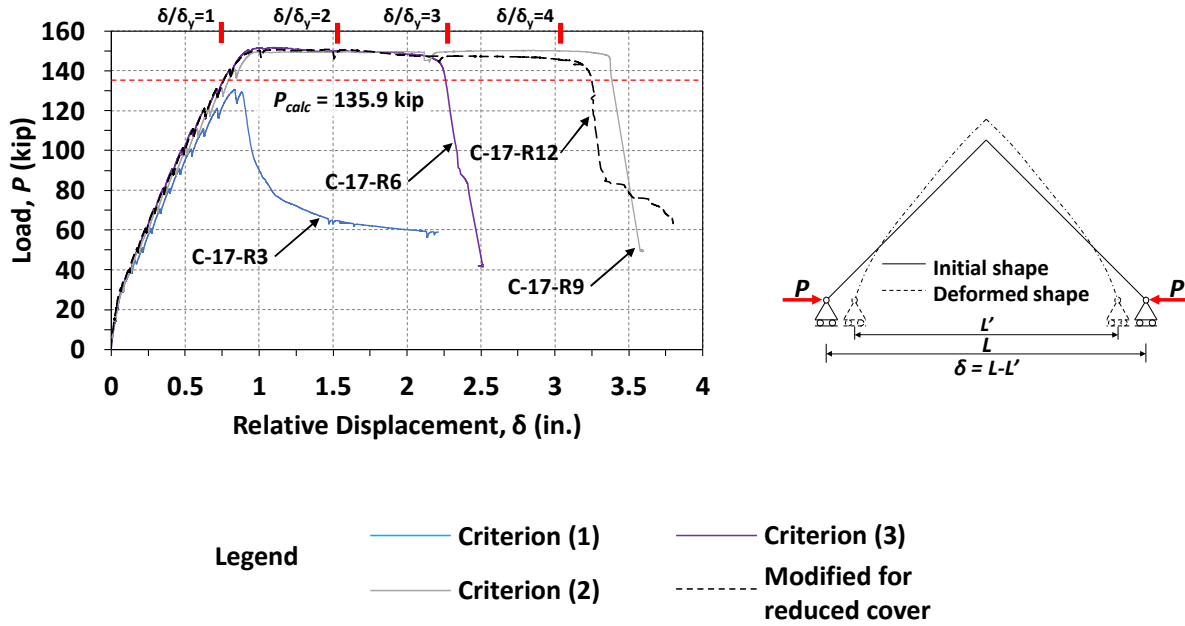


Figure 4-18 Load-displacement curves of C-Series knee joint specimens

Table 4-3 Summary of test results, joint efficiency, and ductility of C-Series specimens

| Specimen ID | P_{test} (kip) | M_{test} (kip-in.) | P_{calc} (kip) | M_{calc} (kip-in.) | M_{test}/M_{calc} | δ_{max} (in.) | δ_y (in.) | μ |
|-------------|------------------|----------------------|------------------|----------------------|---------------------|----------------------|------------------|-------|
| C-17-R3 | 130 | 6464 | 136.7 | 6766 | 0.96 | 0.89 | - | - |
| C-17-R6 | 151 | 7474 | 137.3 | 6796 | 1.10 | 2.24 | 0.76 | 2.93 |
| C-17-R9 | 150 | 7434 | 135.9 | 6728 | 1.10 | 3.37 | 0.81 | 4.18 |
| C-17-R12 | 151 | 7465 | 136.5 | 6757 | 1.10 | 3.21 | 0.77 | 4.20 |

Specimen C-17-R3, which had the bend radius of a standard hook, failed after attaining a peak load of 130 kip. As expected, the load-carrying capacity was lower than the calculated value, corresponding to a joint efficiency of 0.96. It should be noted that a slight load drop appears at 130 kip in the plot of Figure 4-18 because the test was paused to examine the test frame as was typically performed between load steps. After a sudden load drop, the rate at which the applied load decreased gradually slowed as shown in the plot.

Unlike Specimen C-17-R3, the other C-Series specimens exhibited some ductility. After Specimen C-17-R6 was loaded to a peak load of 151 kip, the specimen achieved a relative displacement of 2.24 in. before failure, which corresponds to a μ -value of 2.93. With a larger bend

radius, Specimen C-17-R9 sustained an even higher displacement of 3.37 in., corresponding to a μ -value of 4.18. It is obvious that increasing the bend radius from that of a standard hook improved joint efficiency. Once premature failure was avoided, enlarging the bend radius further improved ductility.

Both Specimens C-17-R9 and C-17-R12 had a reduced clear side cover of 1.25 in. measured to the longitudinal bars. The bend radius of Specimen C-17-R9 satisfied Eq. 2-20 without any modification for side cover. The bend radius of Specimen C-17-R12 was increased in accordance with the factor $2d_b/c_c$, as stated in Section 3.2.3.1. No notable improvement in ductility compared to Specimen C-17-R9, however, was exhibited by Specimen C-17-R12. The μ -value of 4.20 corresponding to Specimen C-17-R12 just exceeded the value for Specimen C-17-R9. In addition, the maximum relative displacement of Specimen C-17-R12 (3.21 in.) was less than that of Specimen C-17-R9 (3.37 in.). This observation implies that the further enlargement of the bend radius had no effect on the load-displacement behavior of the knee joints. In other words, the modification factor for the reduced clear side cover was not necessary in this case.

4.4.2 Visual Observations

The damage pattern and a photograph after the test conducted on each C-Series specimen are presented in Figure 4-19 and Figure 4-20. Red lines indicate cracks that occurred after the failure of the specimen and cracks that appeared at the ultimate failure condition. Shaded areas and hatched areas indicate spalled and crushed concrete, respectively. The measured bend radius of the longitudinal reinforcing bars and the measured width of the diagonal strut for each specimen are provided in the figure. It should be noted that the measured widths of the diagonal struts were taken as the distance between the points along the bars that were intercepted with cracks related to the failure.

The basic propagation of cracks was similar to that of the S-Series specimens, as presented in Figure 4-21. The first cracks formed at the joint faces (that is, the critical sections for flexure) at an applied load of approximately 30 kip. As the load increased, more cracks appeared within the joint region, and the cracks at the joint faces extended toward the re-entrant corner. It should be noted that cracks in the joint did not necessarily initiate from the edge of the specimen. As the load continued to increase, new cracks formed at locations closer to the center of the joint, enclosing an area corresponding with the zone of concentrated compressive stress.

After the basic crack patterns formed, the bend radius altered the damage patterns at the ultimate failure condition as presented in Figure 4-19 and Figure 4-20. For Specimen C-17-R3, significant splitting cracks formed along the strut at the moment when a substantial load drop occurred and was followed by the spalling of a large area of concrete cover under the bar bend. The area of spalled concrete was enclosed by the two innermost cracks and the bar bend, which was considered the region of concentrated compressive stress as previously stated. The spalling occurred gradually along with the decrease in load. The thinner clear side cover likely influenced the spalling of cover concrete. Moreover, concrete at the top corner of the joint was detached from the specimen. There was no concrete crushing at the re-entrant corner.

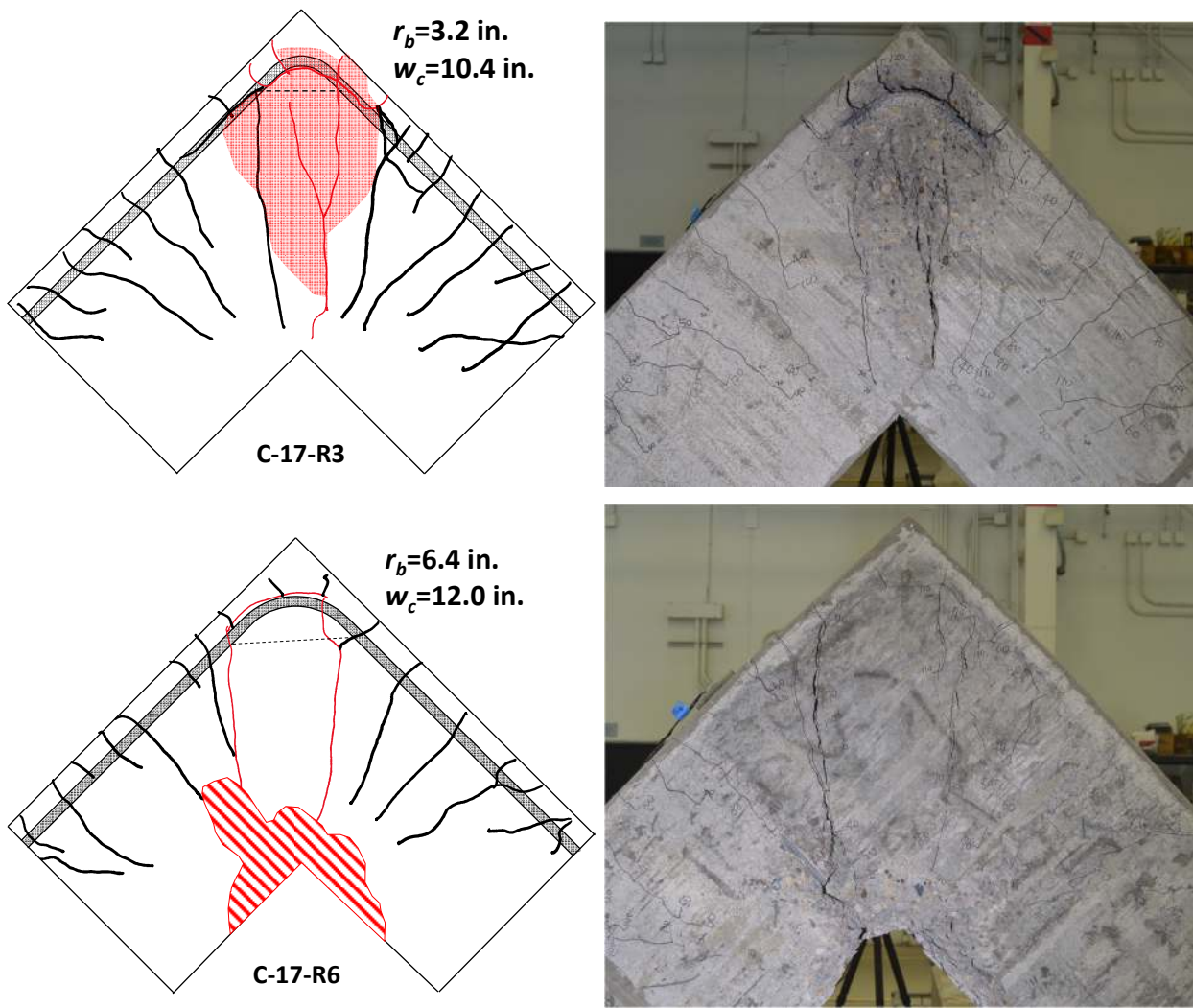


Figure 4-19 Crack maps and photos of C-Series specimens (Part 1)

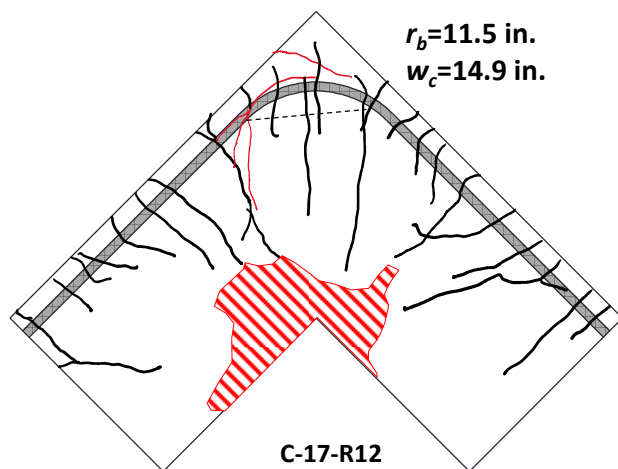
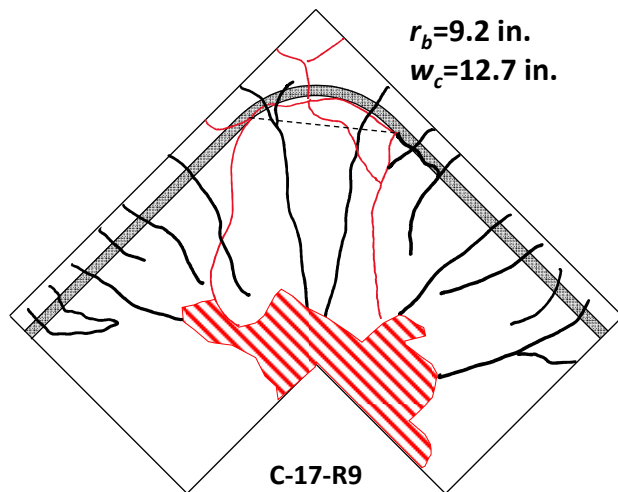


Figure 4-20 Crack maps and photos of C-Series specimens (Part 2)

With a bend radius in between that of a standard hook and Eq. 2-20, Specimen C-17-R6 failed when a horizontal crack located approximately along the bar bend developed as shown in Figure 4-19. Simultaneously, cracks that enclosed the region of the diagonal strut became wider. Prior to this stage, concrete at the re-entrant corner began to crush, and some of the concrete on the bottom surface dropped off. Above the bar bend, concrete was detached from the specimen. Unlike Specimen C-17-R3, however, cover concrete below the bar bend did not spall from the specimen.

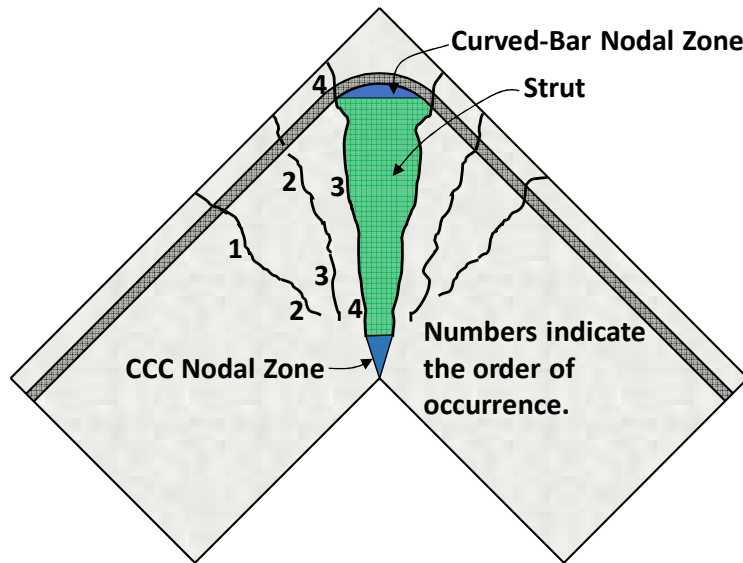


Figure 4-21 Typical crack formation and propagation in joints of C-Series specimens

Compared to Specimen C-17-R6, Specimen C-17-R9, which had a bend radius satisfying the requirement of Eq. 2-20 without the modification factor for the reduced cover, failed in a similar manner. A crack approximately along the bar bend formed when the load-carrying capacity substantially dropped. In addition, a crack that initiated at a load of 50 kip and propagated toward the re-entrant corner significantly widened. Along with the crack along the bar bend and the crack that developed at 50 kip, a new crack on the right side that developed at the ultimate failure condition defined the zone of compressive stress concentration (that is, the strut). At the re-entrant corner, Specimen C-17-R9 experienced a larger area of concrete crushing than that of Specimen C-17-R6. Furthermore, no effects resulting from the reduced cover concrete were observed.

Specimen C-17-R12, which had a further enlarged bend radius to account for the reduced clear side cover, exhibited almost the same damage patterns as Specimen C-17-R9 at the ultimate failure condition as shown in Figure 4-20. The area of crushed concrete had a similar size to that of Specimen C-17-R9. In the area corresponding with the strut extending across the joint, a few cracks, which were not considered to be significant to the failure behavior, formed at a load of approximately 100 kip. Moreover, no effects of the reduced cover concrete were observed.

In addition to the crack patterns on the side surface of each specimen, damage on the top surface after failure varied based on the bend radius, as presented in Figure 4-22. Generally, all four specimens exhibited indications that concrete above the bar bend was detached. Specimen C-

17-R3, however, had concrete near one of the side surfaces spalling off. Longitudinal cracks had propagated along the top surface of the specimen as shown in Figure 4-22(a). Specimen C-17-R6 also had similar longitudinal cracks, but the cracks were closer to the center of the specimen. In this case, the side spalling of concrete was not as significant. Instead, the detachment of top concrete was more evident. Specimens C-17-R9 and C-17-R12 demonstrated the least spalling of concrete. The observations indicate that the spalling of concrete may have been mitigated by a larger bend radius. However, it should again be noted that the enlarged bend radius did not result in improved load-displacement behavior.

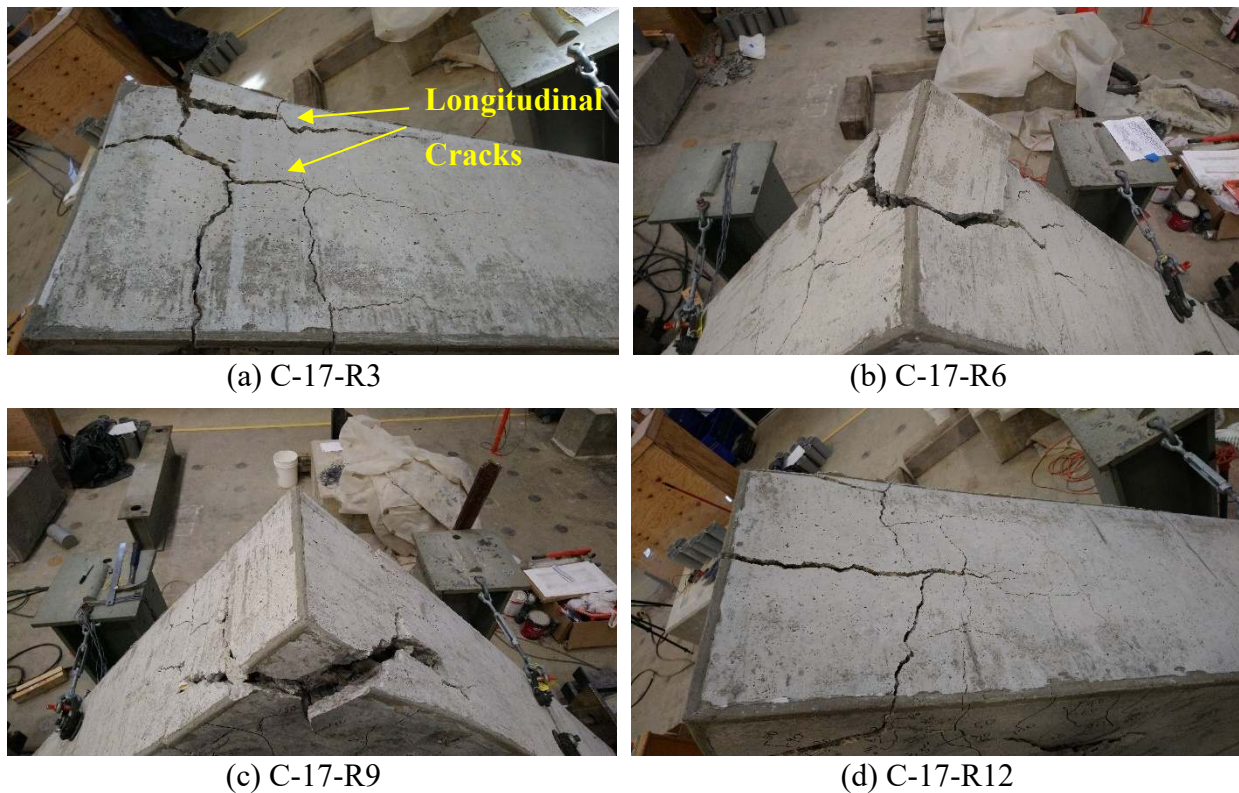


Figure 4-22 Damage patterns on top surfaces of C-Series specimens

4.4.3 Strain in the Reinforcing Bars

The relationship between load acting on the specimen and measured strain readings at the three location along the bars (that is, at the joint face, at the beginning of the bar bend, and at the center of the bar bend) is presented in Figure 4-23. It should be noted that the plots extend to just prior to the substantial drop in the load-carrying capacity of the specimens (that is, the ultimate failure condition).

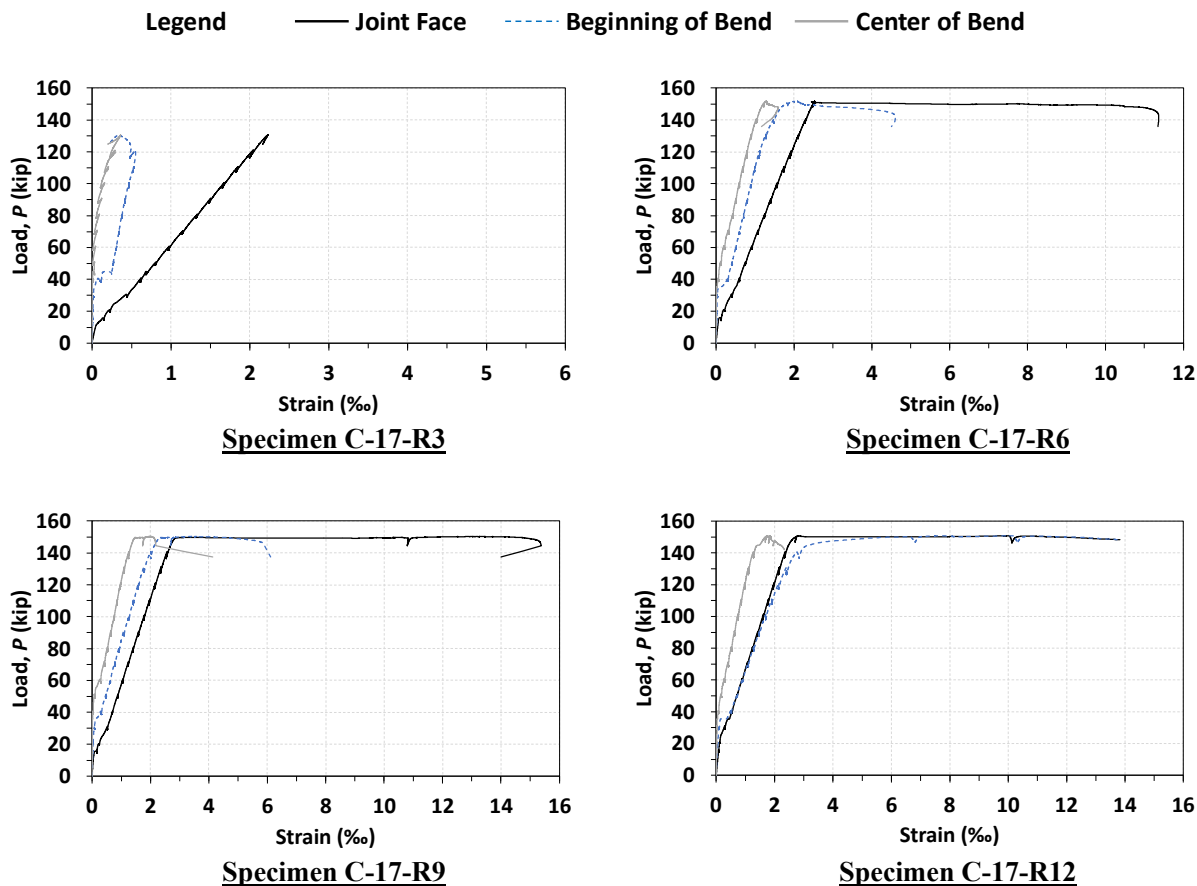


Figure 4-23 Measured strains in the reinforcing bars of C-Series specimens

In general, at the beginning of each test, only strain gauges at the joint face had noticeable readings, while those at the other two locations remained approximately zero. At a load between approximately 15 kip and 20 kip, the slope of the plotted strain data at the joint face decreased, indicating that cracks were forming at this stage. Between an applied load of approximately 30 kip and 40 kip, strain readings at the beginning of the bar bend suddenly increased, corresponding to the initiation of cracks within the joint region. Without a sudden increase, the strain readings at the center of the bend appeared at a load between approximately 40 kip and 50 kip, corresponding to the formation of the two innermost cracks through the joint region.

Unsurprisingly, the strain distribution along the longitudinal bars was affected by the bend radius. For Specimen C-17-R3 with the bend radius of a standard hook, only the strain at the joint face reached the yield strain of the longitudinal bars prior to the ultimate failure condition. The strain at the other two locations did not reach the yield strain. Again, it should be noted that the

yield strain was based on the value of the measured yield stress of the bar divided by the modulus of elasticity of steel (29,000 ksi). With an increased bend radius, the strain readings indicate that the bars in Specimen C-17-R6 reached the yield strain at both the joint face and the beginning of the bar bend as observed for companion specimens in the other test series.

With larger bend radii, all strain gauge readings for Specimens C-17-R9 and C-17-R12 reached the yield strain. In other words, the yielded region extended through the entire bar bend for these two specimens. This observation indicates that a bend radius satisfying the requirement of Eq. 2-20, but not increased in accordance with the modification factor for reduced side cover, still resulted in yielding throughout the entire bar bend. In other words, application of the modification factor was not required to achieve the stress distribution of the assumed strut-and-tie model (see Figure 2-3(a)). Nevertheless, Specimen C-17-R12 generally had a higher strain reading at the beginning of the bar bend than that of Specimen C-17-R9. In addition, the strain gauge readings of Specimen C-17-R12 at the beginning of the bar bend and at the joint face prior to a load of approximately 120 kip were similar. After that, the strain reading at the beginning of the bar bend exceeded the reading at the joint face. The magnitude of the strain at the beginning of the bar bend may have been influenced by the relatively large bend radius of Specimen C-17-R12.

4.4.4 Summary

The test results of four specimens that were developed to investigate the effect of reduced concrete clear side cover were described in this section. The concrete clear side cover of specimens in this series was 1.25 in., which is less than twice the diameter of the longitudinal reinforcing bars. According to ACI 318-19,¹ the bend radius should therefore be increased by the ratio $2d_b/c_c$. The primary observations from the tests are summarized as follows:

1. Similar to the S-Series and D-Series specimens, the bend radius had an obvious effect on the behavior of curved-bar nodes, altering the performance of the knee joints in terms of strength and displacement ductility. The specimen with the bend radius of a standard hook exhibited compromised strength compared to the other C-Series specimens. Specimen C-17-R6, which had a bend radius in between that of a standard hook and the requirement of Eq. 2-20, reached a joint efficiency that exceeded 1.0 and a displacement ductility factor of 2.94. Moreover, having a bend radius satisfying the requirement of Eq. 2-20 without the modification factor for reduced side cover, Specimen C-17-R9 reached a greater

displacement ductility ($\mu=4.18$). In this case, a larger bend radius improved the displacement ductility factor. Nevertheless, Specimen C-17-R12, which had a further enlarged bend radius to account for the thin concrete clear side cover, exhibited similar ductility to that of Specimen C-17-R9.

2. The damage patterns at the ultimate failure condition were affected by the bend radii. The failure of Specimen C-17-R3 occurred along with splitting of the strut followed by extensive spalling of concrete below the bar bend. No crushing of concrete was observed at the re-entrant corner. For the other C-Series specimens, extensive crushing of concrete at the re-entrant corner occurred prior to a significant drop in load-carrying capacity. At the load drop, a crack along the bar bend suddenly formed. Little or no spalling of concrete below the bar bend was observed.
3. The extension of the yielded region along the longitudinal reinforcing bars was also affected by the bend radii. For the specimen with the bend radius of a standard hook (Specimen C-17-R3), only strain gauges installed at the location of the joint face indicated that the yield strain was reached. For the specimen with a bend radius in between that of a standard hook and the requirement of Eq. 2-20, the yielded region extended to the beginning of the bar bend. With the largest bend radii, the other two specimens had strain gauge readings at all three locations reach the yield strain. That is, the bars yielded throughout the bend region. It seems that application of the modification factor for thinner concrete side cover was not needed to achieve the assumed strut-and-tie model for knee joints subjected to closing moments.

4.5 Series IV: Different Cross-Sections (B-Series)

The test results of the two B-Series specimens are discussed in this section. The B-Series specimens were developed to investigate the effect of a diagonal strut angle that is not equal to 45 degrees on the behavior of closing knee joints. To create a diagonal strut angle other than 45 degrees, two specimens with legs of different depths were tested. For the curved-bar nodes in the joints, ACI 318-19¹ requires that the bend radius satisfy Eq. 2-24 to develop the difference in the two tie forces through circumferential bond stress.

4.5.1 Overall Behavior

The relationship between the applied load and the relative displacement for the two B-Series specimens is presented in Figure 4-24. The red line represents the calculated load-carrying capacity based on the flexural strength at the joint face of the shallower leg calculated in accordance with ACI 318-19.¹ Integer values of the ratio δ/δ_y are also shown in the figure. It should be noted that both tests reached the stroke limit of the hydraulic cylinders so that the ultimate failure condition was not reached. The test results are summarized in Table 4-4. All notation used in the figure and the table is consistent with the definitions introduced previously.

Table 4-4 Summary of test results, joint efficiency, and ductility of B-Series specimens

| Specimen ID | P_{test} (kip) | M_{test} (kip-in.) | P_{calc} (kip) | M_{calc} (kip-in.) | M_{test}/M_{calc} | δ_{max} (in.) | δ_y (in.) | μ |
|-------------|---------------------|-------------------------|---------------------|-------------------------|---------------------|-------------------------|---------------------|-------|
| B-16-R3 | 75.6 | 3743 | 68.0 | 3212 | 1.11 | 5.320 | 0.664 | 8.00 |
| B-16-R6 | 76.1 | 3769 | 68.0 | 3212 | 1.12 | 5.847 | 0.664 | 8.80 |

It can be seen in Figure 4-24 that both specimens had a load-carrying capacity greater than the calculated value, P_{calc} , reaching joint efficiencies of 1.11 and of 1.12. Furthermore, both specimens exhibited excellent ductility. The maximum relative displacements of the specimens were 5.32 in. and 5.85 in. when the stroke limit of the hydraulic cylinders was reached. The displacement ductility factor, μ , of each specimen was relatively high compared to other specimens of the test program.

Although both specimens had similar peak loads and exhausted the stroke limit of the hydraulic cylinders, differences in the post-peak behavior were observed. Specimen B-16-R3, which was detailed with the bend radius of a standard hook, experienced a sudden drop in load-carrying capacity from approximately 65 kip to 55 kip at a displacement of 5.32 in, which was used to calculate the ductility factor. Prior to this load drop, the load-carrying capacity slowly decreased starting at a displacement of approximately 2.67 in. For Specimen B-16-R6, which had a bend radius satisfying the requirement of Eq. 2-20, a sudden load drop did not occur. Instead, the load began to decrease at a displacement of approximately 2.67 in. The rate of the decrease in load was faster than that of Specimen B-16-R3, but the rate gradually slowed as the displacement was further increased.

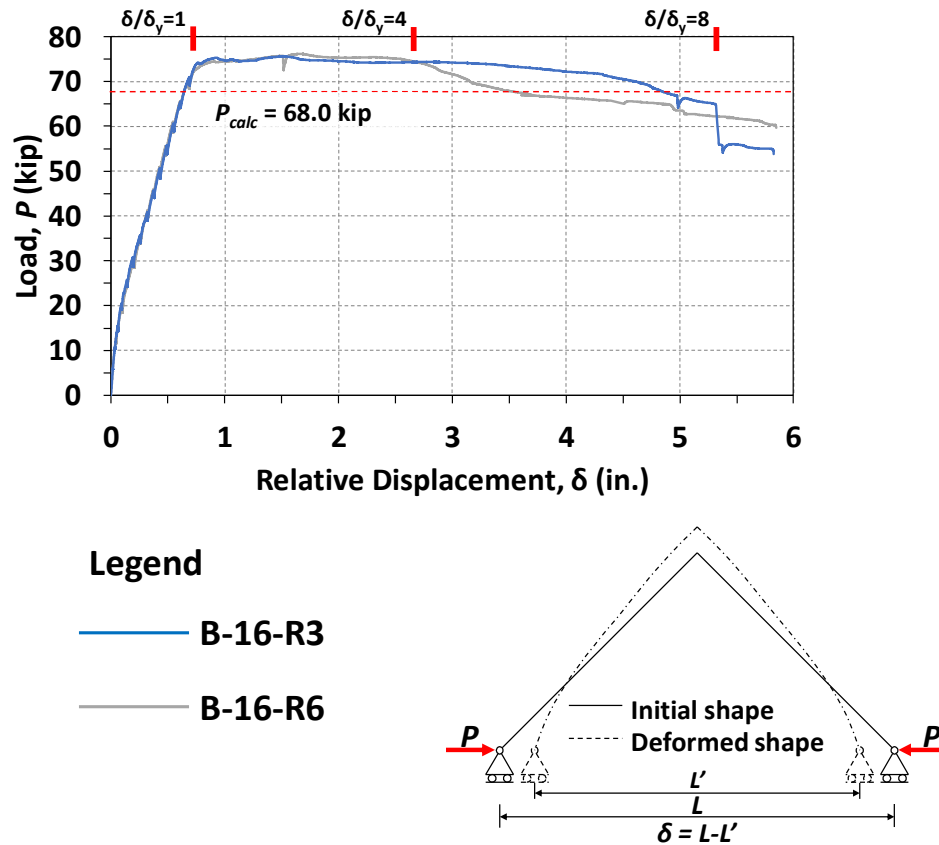


Figure 4-24 Load-displacement curves of B-Series knee joint specimens

4.5.2 Visual Observations

Damage patterns and photographs of the B-Series specimens after the end of the tests are presented in Figure 4-25. The hatched regions indicate the areas of crushed concrete. The general trend of crack formation and propagation observed during the tests is illustrated in Figure 4-26.

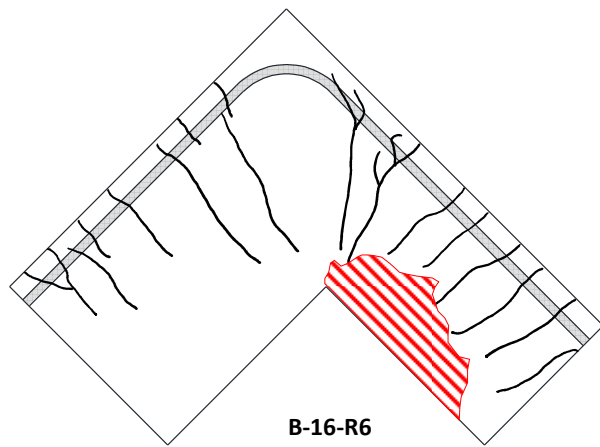
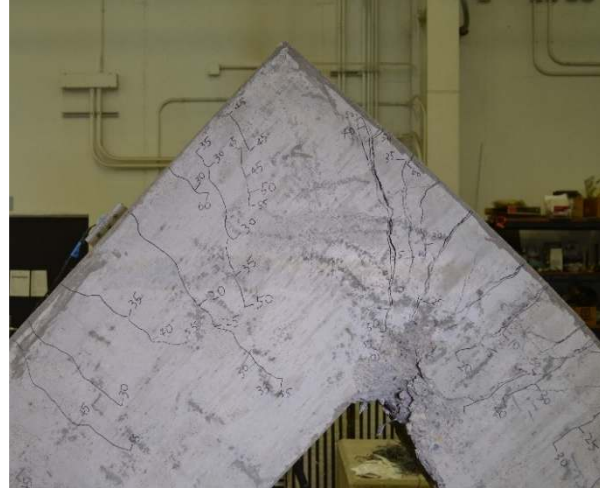
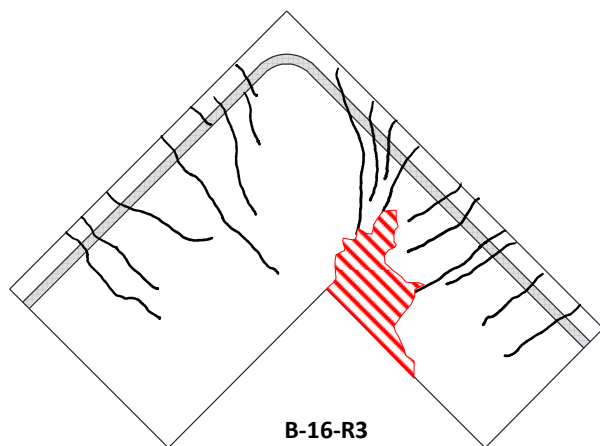


Figure 4-25 Crack maps and photos of B-Series specimens

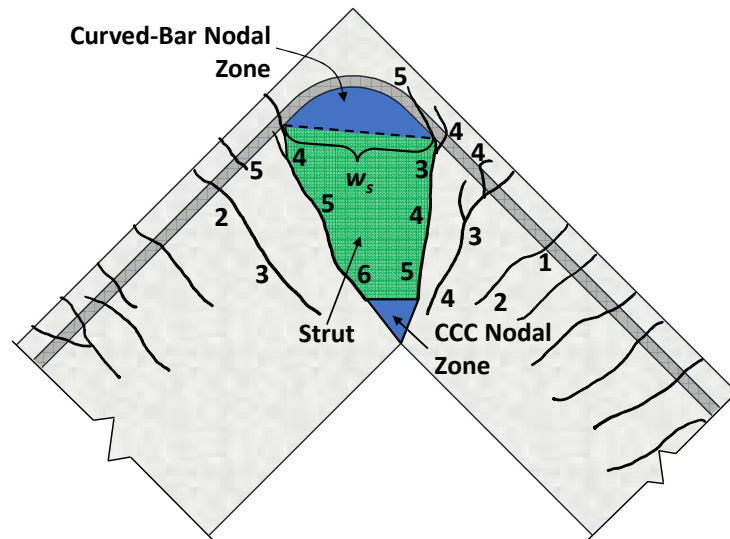


Figure 4-26 Typical crack formation and propagation in joints of B-Series specimens

Compared to specimens in the other test series, the crack propagation was somewhat different for the B-series specimens with unequal leg depths, as indicated in Figure 4-26. The first crack formed at the joint face of the shallower leg at a load of approximately 10 kip. At a load of approximately 20 kip, a crack formed at the joint face of the deeper leg as the first crack extended toward the re-entrant corner. As the applied load increased, cracks developed within the joint. At an applied load between 40 kip and 60 kip, a denser crack pattern within the joint near the shallower leg compared to the cracking near the deeper leg became apparent. Moreover, cracks near the shallower leg extended farther toward the re-entrant corner compared to cracks near the deeper leg.

Regardless of the bend radius, specimens in this series demonstrated similar damage patterns at the end of the tests as shown in Figure 4-25. The region enclosed by the two innermost cracks in the joint generally remained intact. Again, this region represents the zone of concentrated compressive stress (that is, the strut extending across the joint). Moreover, large crushing of concrete concentrated in the shallower leg side near the re-entrant corner. Although the ultimate failure condition was not reached, the behavior of the specimens indicate that a flexural failure at the joint face of the shallower leg was occurring.

Damage patterns on the top faces, however, were different between Specimen B-16-R3 and Specimen B-16-R6 as shown in Figure 4-27. On the top surface of Specimen B-16-R3, a longitudinal splitting crack was observed near the side where the speckle pattern was applied for the DIC system. The splitting crack caused concrete to separate from the specimen. It was also observed that the splitting crack formed at the same time the specimen experienced the sudden drop in the load-carrying capacity as previously described. Unlike Specimen B-16-R3, Specimen B-16-R6 showed no cracks on the top surface.

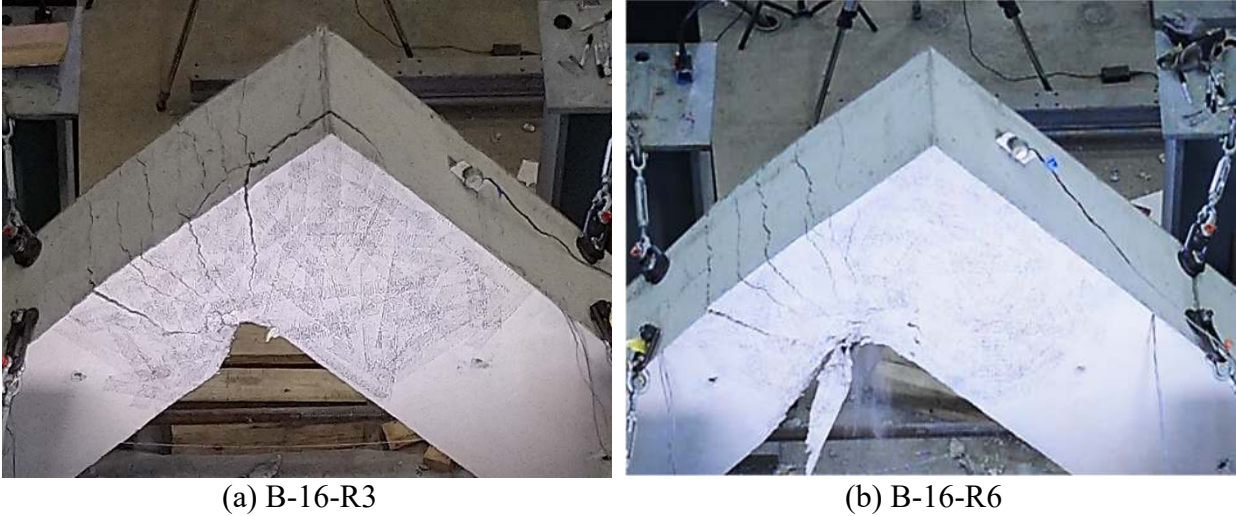


Figure 4-27 Damage patterns on top surfaces of B-Series specimens

4.5.3 Strain in the Reinforcing Bars

The strain distribution along the longitudinal reinforcing bars of each specimen at several load steps is presented in. The vertical axis shows the strain readings. For the horizontal axis, the number “18” indicates the strain gauges installed on the longitudinal reinforcing bars near the shallower leg, and the number “24” indicates the strain gauges installed on the longitudinal reinforcing bars near the deeper leg. The letters “JF” indicates the gauges were located at the joint face, while “BB” indicates the gauges installed at the beginning of the bar bend.

As shown in Figure 4-28, the strain in the longitudinal bars at the locations corresponding to the leg with a depth of 24 in. remained relatively constant after the initiation of the development of a plastic hinge near the joint face of the 18-in. deep leg. Upon further displacement of the specimen, the increase in bar strain was concentrated in this hinging region. As the end of test was approached, the bars exceeded the yield strain at the joint face and the beginning of the bend corresponding to the shallower leg of the specimen. The strains are consistent with the observed flexural failure at the joint face.

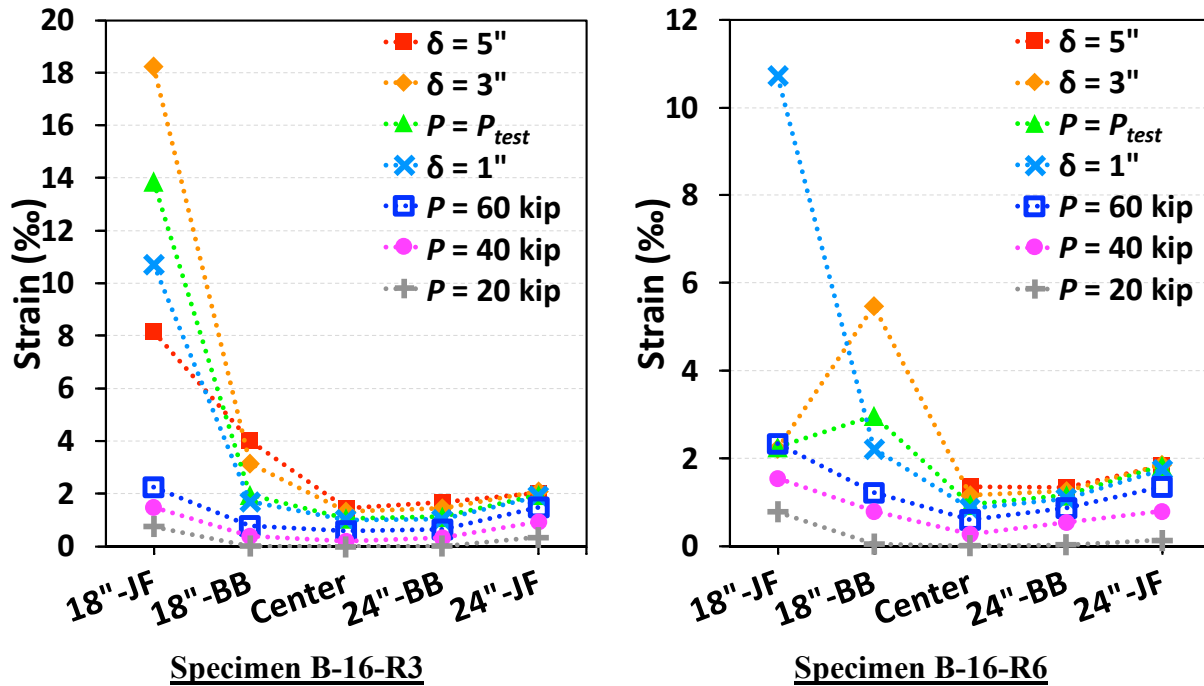


Figure 4-28 Strain readings along reinforcing bars of B-Series specimens

4.5.4 Summary

These B-Series specimens were developed to investigate the behavior resulting from a diagonal strut with an angle other than 45 degrees. The main purpose was to evaluate the requirement that the bar bend be sized to develop the difference in forces of the two ties intersecting at the curved-bar node. Two specimens with adjoining members detailed with different depths were tested. The primary observations are summarized as follows:

1. Both specimens were able to reach joint efficiencies greater than 1.0 regardless of the bend radii. Both bend radii were smaller than the size required to satisfy the current provision in ACI 318-19¹ in consideration of circumferential bond stress, indicating the requirement may be overconservative.
2. Both specimens did not reach the ultimate failure condition because of the stroke limit of the hydraulic cylinders. Prior to the end of the tests, both specimens experienced extensive crushing of concrete near the re-entrant corner.
3. The strain in the longitudinal bars at the location corresponding to the joint face of the deeper leg remained relatively constant, while that corresponding to the joint face of the

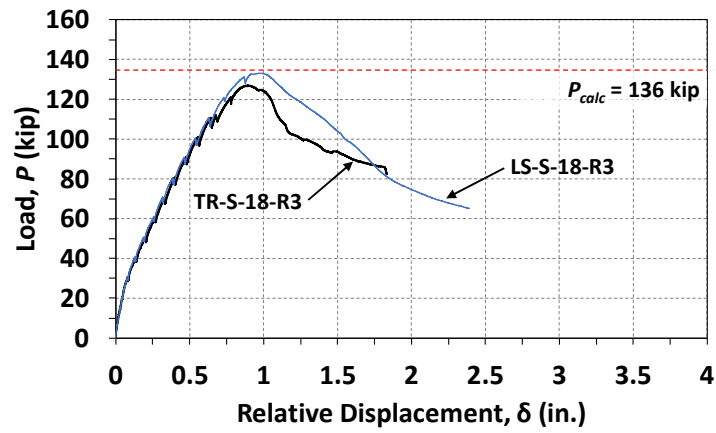
shallower leg kept increasing. The yielded region on the bars reached the beginning of the bar bend corresponding to the shallower adjoining member.

4.6 Series V: Multiple Purposes (M-Series)

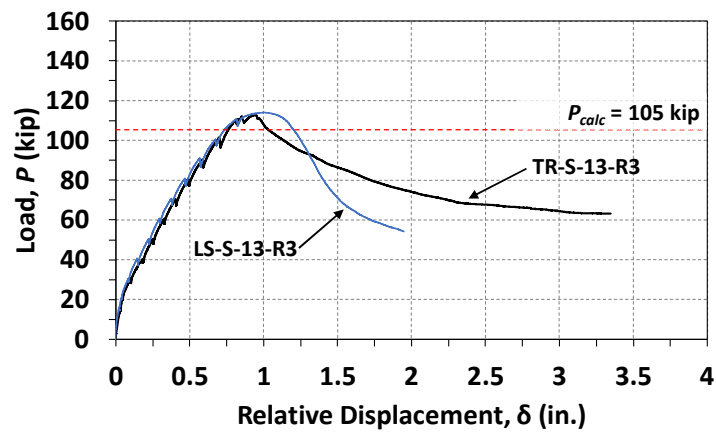
The test results of the four M-Series specimens are discussed in this section. One purpose of the M-Series specimens was to investigate the effect of the required minimum amount of distributed transverse reinforcement in knee joints. It has been widely accepted that distributed transverse reinforcement is needed to prevent premature failure of struts.^{1,73,74} The other purpose of the test series was to investigate a widely used detail in knee joints: longitudinal reinforcement in the beam and in the column spliced within the joint region. Transverse reinforcement was also provided within the joint of these specimens. All specimens in this series had the bend radius of a standard hook.

4.6.1 Overall Behavior

Plots that show the load-displacement relationship of each M-Series specimen are presented in Figure 4-29. The specimens with the same size of longitudinal bars (that is, the same value of A_{ts}) are shown together. Again, the red dashed lines indicate calculated load-carrying capacities, P_{calc} . Because slightly different material properties led to different values of P_{calc} , only the greater value of P_{calc} within each pair of specimens is shown in the figure to improve readability. The test results are summarized in Table 4-5. The parameters have the same definitions as those used in previous sections.



(a) Load-displacement curves of specimens with No. 8 longitudinal reinforcement



(b) Load-displacement curves of specimens with No. 7 longitudinal reinforcement

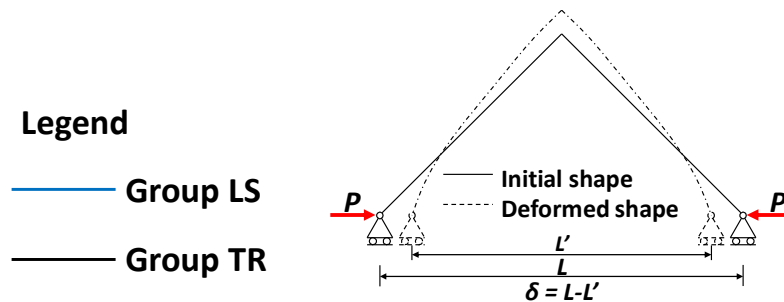


Figure 4-29 Load-displacement curves of M-Series knee joint specimens

Table 4-5 Summary of test results and joint efficiency of M-Series specimens

| Specimen ID | P_{test} (kip) | M_{test} (kip-in.) | P_{calc} (kip) | M_{calc} (kip-in.) | M_{test}/M_{calc} | C |
|-------------|---------------------|-------------------------|---------------------|-------------------------|---------------------|------|
| TR-S-18-R3 | 126 | 6237 | 134.9 | 6677 | 0.93 | 0.80 |
| LS-S-18-R3 | 133 | 6583 | 135.8 | 6723 | 0.98 | 0.85 |
| TR-S-13-R3 | 112 | 5544 | 105.0 | 5199 | 1.07 | 0.87 |
| LS-S-13-R3 | 114 | 5643 | 105.4 | 5216 | 1.08 | 0.90 |

The load-relative displacement curves of the specimens reinforced with No. 8 bars are presented in Figure 4-29(a). With the bend radius of a standard hook, both specimens failed prematurely before reaching the calculated load-carrying capacities. Although the joints were transversely reinforced, the load-carrying capacity started to drop after reaching the peak load (that is, the specimens did not experience a load plateau). The peak loads were slightly different between the knee joint with continuous reinforcing bars and the joint with lap-spliced reinforcing bars. Specimen TR-S-18-R3, which had continuous reinforcing bars, reached a joint efficiency of 0.93, while Specimen LS-S-18-R3 reached an efficiency of 0.98. The difference is small and cannot be attributed to the bar details.

Different from the specimens reinforced with No. 8 bars, Specimens TR-S-13-R3 and LS-S-13-R3 had a joint efficiency greater than 1.0. Nevertheless, both specimens demonstrated no ductility; the specimens did not experience a load plateau after reaching the peak loads, as shown in Figure 4-29(b). Different bar details (that is, continuous reinforcing bars and lap-spliced reinforcing bars) resulted in essentially the same load-carrying capacity.

The post-peak behaviors, however, were somewhat different between knee joints with continuous reinforcing bars and those with lap-spliced reinforcing bars. For specimens with lap-spliced reinforcing bars (Specimens LS-S-18-R3 and LS-S-13-R3), after reaching the peak load, the residual post-peak strength was lower than that of the specimens with continuous reinforcing bars. It should be noted that the test on Specimen TR-S-18-R3 was stopped early due to leakage of the hydraulic cylinders. However, the trend in the curve seems to imply that its residual strength was greater than that of Specimen LS-S-18-R3.

The C -values were also calculated for the M-Series specimens and are summarized in Table 4-5. It can be seen that a C -value greater than or equal to 0.87 corresponding to a joint efficiency greater than 1.0. Furthermore, the positive correlation between the C -values and the joint efficiency for C -values less than 0.87 seems to imply that continuous longitudinal reinforcing bars resulted

in the same response in terms of strength as lap-spliced reinforcing bars when transverse reinforcement was provided.

4.6.2 Visual Observations

The damage patterns and photographs of the M-Series specimens after the tests are presented in Figure 4-30 and Figure 4-31. The red lines indicate cracks that were related to failure, and the shaded regions indicate spalling of concrete or crushing of concrete.

The damage patterns observed after each test were affected by details of the longitudinal reinforcement. For specimens with continuous reinforcing bars (Specimens TR-S-18-R3 and TR-S-13-R3), the failure began with a splitting crack along the strut, followed by the separation of cover concrete from the side surface of the joint as the load-carrying capacity gradually decreased. The cover concrete did not fully detach from the knee joint. Instead, the concrete was held on by transverse reinforcement until the end of the test.

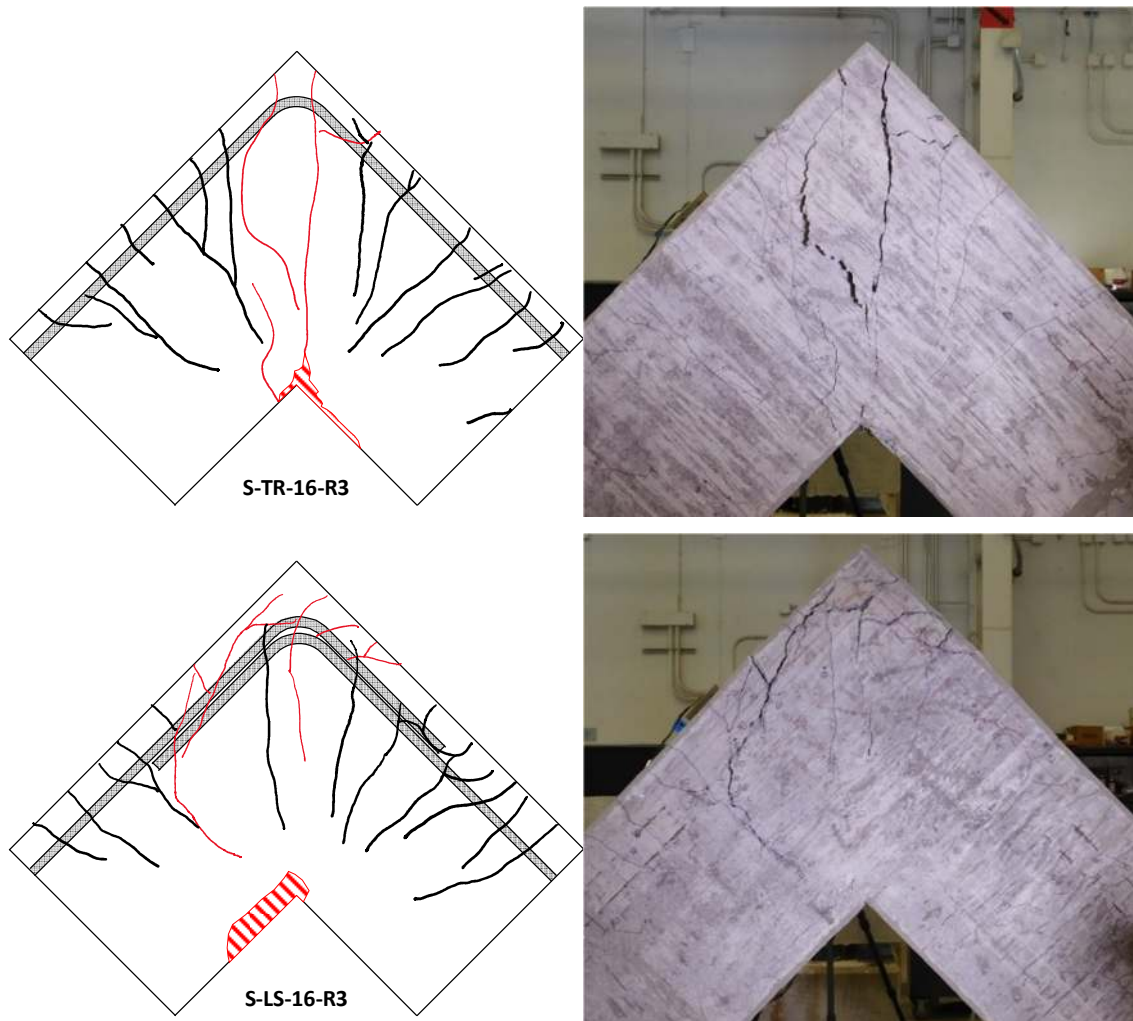


Figure 4-30 Damage patterns of specimens in M-Series (No.8 reinforcement)

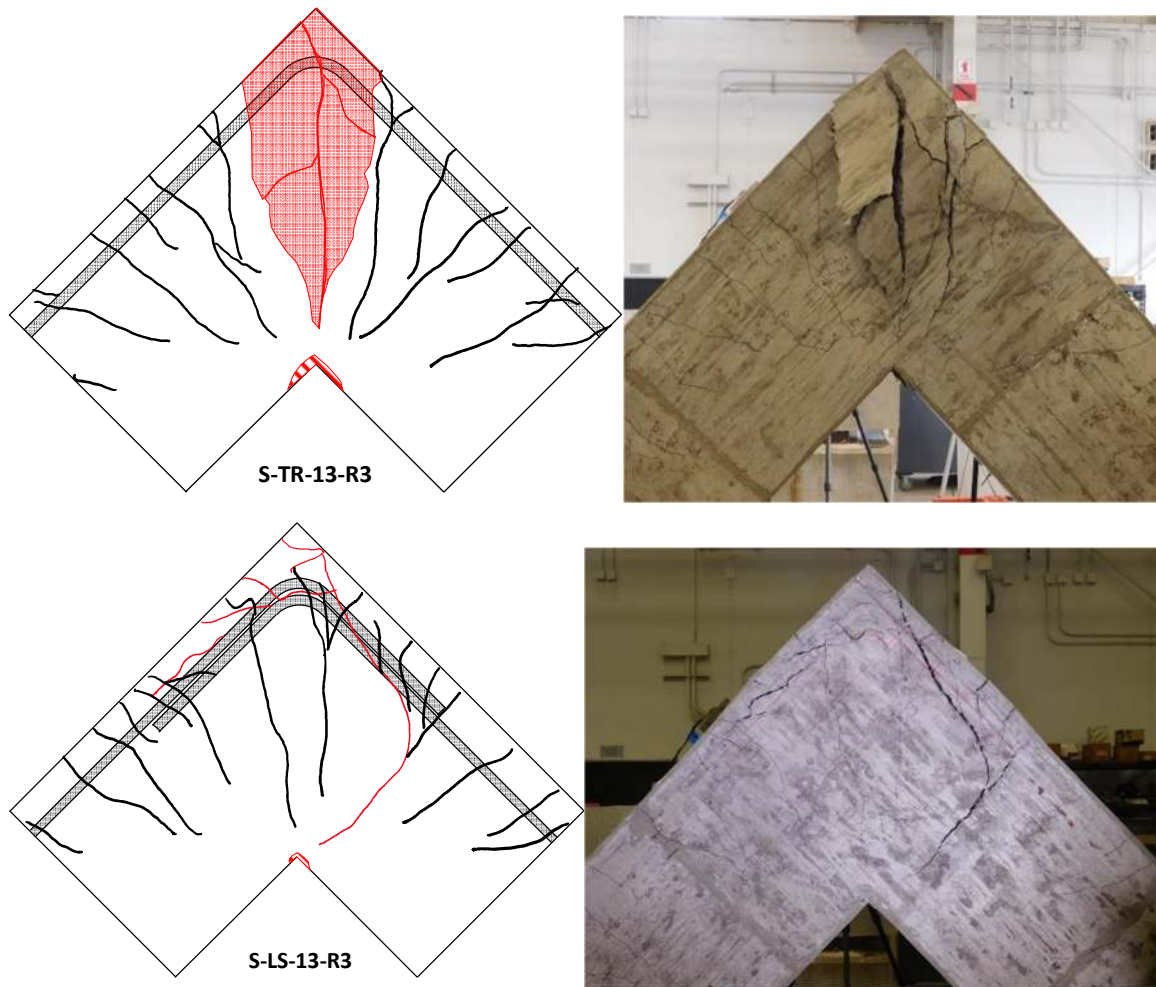


Figure 4-31 Damage patterns of specimens in M-Series (No.7 reinforcement)

Unlike the specimens with continuous reinforcing bars through the outer corner, specimens with lap-spliced reinforcing bars (Specimens LS-S-18-R3 and LS-S-13-R3) did not have similar separation of cover concrete nor significant splitting cracks along the strut. Instead, the specimens in this group failed when a splitting crack developed along one side of the lap splice. The splitting crack then connected to the flexural crack at the joint face on the same side.

Crack patterns on the top surface of each specimen varied depending on the details of the longitudinal reinforcing bars as shown in Figure 4-32. Specimens TR-S-18-R3 and TR-S-13-R3 had concrete at the outside corner that detached from the specimens. Two transverse cracks developed near the outside corner, causing concrete to separate from the specimen. On the other hand, Specimens LS-S-18-R3 and LS-S-13-R3 exhibited a longitudinal splitting crack located roughly along the center of the specimen width.



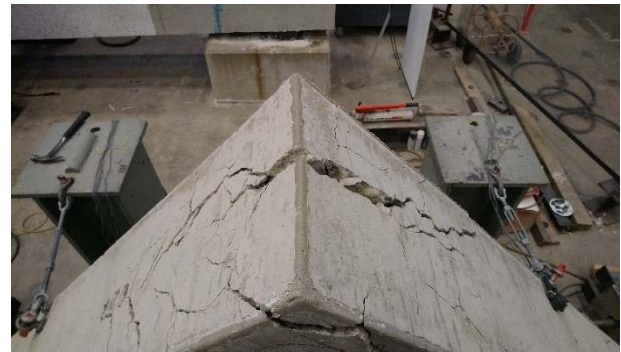
TR-S-16-R3



TR-S-13-R3



LS-S-16-R3

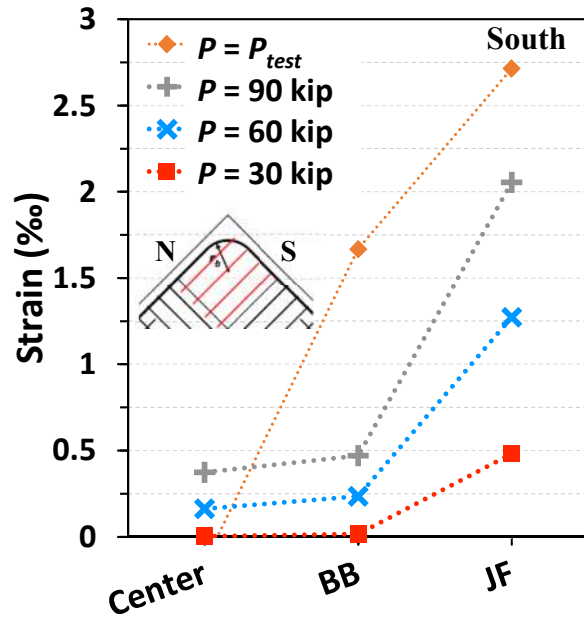
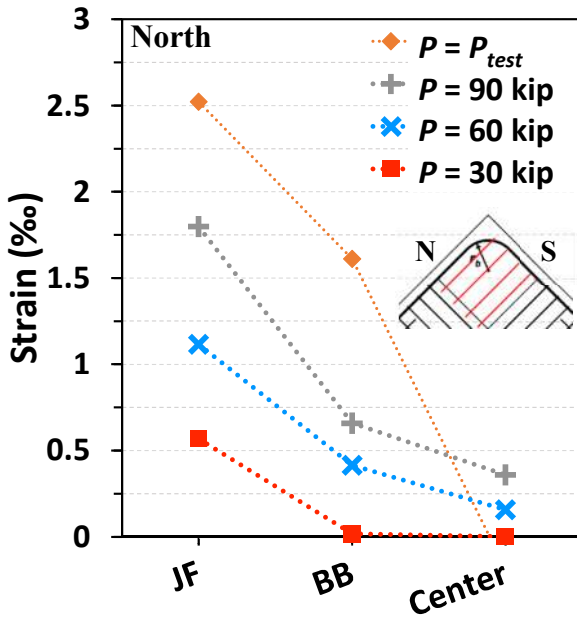


LS-S-13-R3

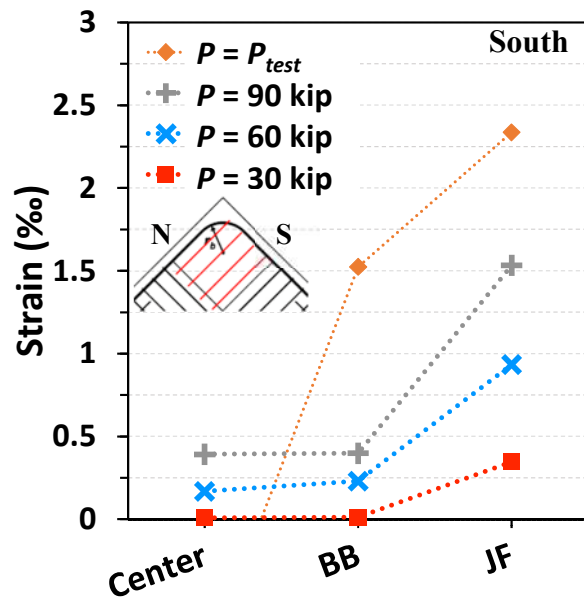
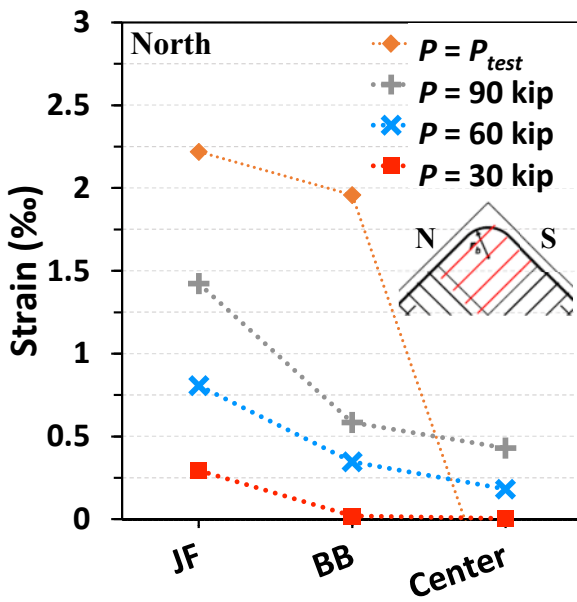
Figure 4-32 Damage patterns on top surfaces of M-Series specimens

4.6.3 Strain in the Reinforcing Bars

Strain readings along the longitudinal reinforcement of each specimen is presented in Figure 4-33 and Figure 4-34. For the figures showing strain readings from specimens in Group TR (see Figure 4-33), the plot on the left presents data from strain gauges distributed along the longitudinal reinforcement on the north portion of the joint, while the plot on the right presents data from strain gauges distributed on the south side of the joint. Labels on the horizontal axis indicate the positions where strain gauges were installed. Referring to Figure 3-26(c), letters “JF” indicates the joint face, “BB” indicates the beginning of the bar bend, and “Center” indicates the center of the bar bend. The strain readings from specimens in Group LS are provided in Figure 4-34. Because the longitudinal bars were lap spliced in the joint, two strain readings correspond to each of the positions along the bar bend (refer to Figure 3-26(d)). It should be noted that readings from two strain gauges in Specimen LS-S-13-R3 were lost.

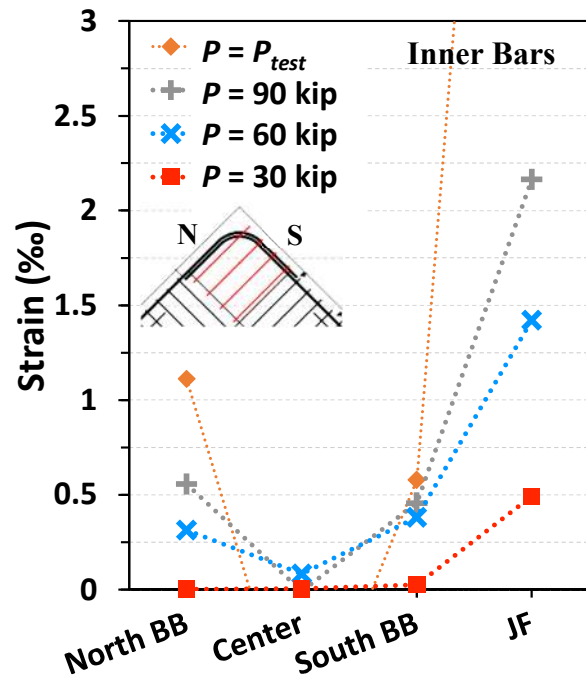
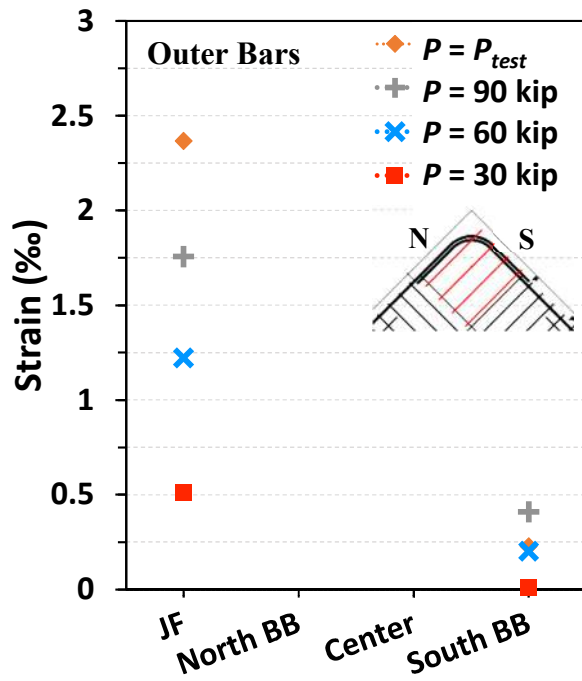


TR-S-13-R3

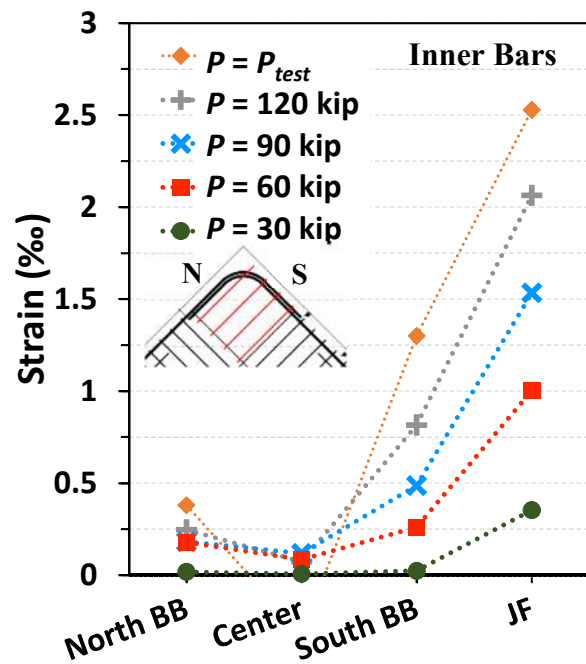
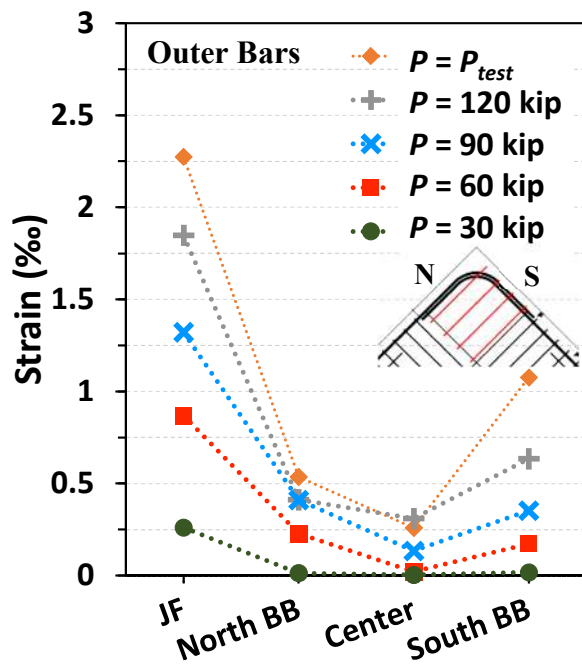


TR-S-16-R3

Figure 4-33 Strain readings along reinforcing bars of Group TR specimens



LS-S-13-R3



LS-S-16-R3

Figure 4-34 Strain readings along reinforcing bars of Group LS specimens

For specimens in Group TR (see Figure 4-33), regardless of the mechanical reinforcement ratio, strain readings from both the north side and south side display similar trends. Up to an applied load of 30 kip, measured strain was only indicated by the strain gauge at each joint face. Strains at the beginning of the bar bend for each side appeared at a load of approximately 40 kip, while the strain at the center of the bend appeared at approximately 50 kip. As load increased further, strain at each position increased, with the strain readings at the joint face being greatest. Strains at the positions corresponding to the beginning of the bend were the second greatest, and the smallest strains were measured at the center of the bend. At the peak load, only the strains measured at both joint faces reached the yield strain. The same trend was also observed for specimens in Group LS as shown in Figure 4-34. That is, strain readings appeared first at the joint faces followed by the locations corresponding with the beginnings of the bar bends, and then the strain readings at the centers of the bends began to increase slightly. Furthermore, at the peak load, only the strain at the joint faces reached the yield strain.

4.6.4 Summary

The test results of the four M-Series specimens were introduced in this section. The M-Series specimens were developed to investigate the effect of transverse reinforcement on knee joints. In addition, knee joints detailed with a common reinforcement detail (that is, lap splices in the joint) were investigated. All specimens had the bend radius of a standard hook in the joint. Observations are summarized as follows:

1. The M-Series specimens with a lower mechanical reinforcement ratio (Specimens TR-S-13-R3 and LS-S-13-R3) had a higher joint efficiency than those with a greater mechanical reinforcement ratio (Specimens TR-S-18-R3 and LS-S-18-R3). This trend is consistent with the results of the S-Series specimens. In addition, no significant difference in terms of strength was found between specimens in Group TR and their companion specimens in Group LS.
2. The joint efficiency of Specimens TR-S-18-R3 and LS-S-18-R3 was lower than 1.0, and all M-Series specimens lacked a load plateau. The phenomenon indicated that the bend radius still governed the strength and behavior regardless of the presence of transverse reinforcement or lap splices.

3. The failure patterns were different between specimens in Group TR and those in Group LS. Specimens in Group TR exhibited splitting of the strut combined with separation of cover concrete from the specimen. Specimens in Group LS failed due to splitting along the lap splices.
4. Trends in the strain distributions along the longitudinal reinforcement in the joint showed no significant difference between the specimens with continuous reinforcing bars and those with lap-spliced bars.

4.7 Closing Remarks

Twenty-four specimens were tested to investigate the behavior of closing knee joints that results from various parameters including the bend radius of longitudinal bars, the mechanical reinforcement ratio, the thickness of clear side cover, the angle of the diagonal strut extending across the joint, and the incorporation of commonly used details (that is, transverse reinforcement and lap splices). The test results reveal that the bend radius significantly affected the strength and the ductility of the knee joint specimens regardless of whether the longitudinal reinforcement was arranged in one or two layers. Moreover, the presence of transverse reinforcement in the knee joints was not observed to have a significant impact on the specimens. Instead, the bend radius was still the crucial factor affecting the joint efficiency and overall ductility (that is, lack of a load plateau) when comparing specimens with similar mechanical reinforcement ratios. This observation is true whether continuous longitudinal reinforcement or lap-spliced longitudinal reinforcement was used. Additional discussion is provided in Section 5.6.

With a limited number of specimens, the test results of the C-Series specimens demonstrate that the bend radius that was enlarged to account for the thin side cover did not improve overall behavior. In addition, the test results of the B-Series specimens indicate that, although the bend radii used for the specimens were much smaller than what would be required by current ACI 318-19¹ provisions to account for circumferential bond stress, no compromised strengths were observed. Rather, the specimens exhibited ductile behavior.

5. ANALYSIS OF THE EXPERIMENTAL RESULTS

5.1 Overview

This chapter includes the evaluation of each variable under investigation in the experimental program based on the test results. A method of categorization was proposed for the specimens tested in the experimental program based on behavior. The categorization facilitates the evaluation of experimental variables. First, the effect of the bend radius on the behavior of knee joints with various mechanical reinforcement ratios and one or two layers of reinforcement is evaluated. Secondly, the effect of thin clear side cover is assessed. Then, the requirement for bar bends to develop the stress difference on each side of curved-bar nodes (Eq. 2-24) is evaluated. Furthermore, performance of specimens detailed with transverse reinforcement and/or lap splices is assessed by comparing M-Series specimens to their companion S-Series specimens. Lastly, the current strength coefficient incorporated into the curved-bar node provisions of ACI 318-19¹ is evaluated based on the experimental results.

5.2 Categorization of Specimens

A summary of the 24 specimens of the experimental program and the test variables is presented in Table 5-1. The notation used in the table has been previously introduced, except for $w_{s,calc}$, which is the calculated strut width and is further discussed in Section 5.7. A method to categorize knee joint specimens based on the observed behaviors is needed to aid with the evaluation of the specimens resulting from the test variables. Considering failure modes, strength, ductility, and strain along the longitudinal bars, three primary categories are specified: 1) Strength Compromised (Lacking Ductility), 2) Transition (Ductility Compromised), and 3) Ductile Behavior. The three categories are summarized in Figure 5-1. Specimens that exhibited the characteristics described in the figure were placed into the corresponding category.

Specimens that were placed into the Strength Compromised category experienced failure governed by the CTT node or the diagonal strut. Specifically, at the ultimate failure condition, the specimen experienced splitting of the diagonal strut or splitting along the bar bend but little or no crushing of concrete at the re-entrant corner. In addition to the failure mode, the load-carrying capacity of these specimens was lower than the calculated strength P_{calc} , or lower than that of other

specimens with the same mechanical longitudinal reinforcement ratio but different bend radii. Furthermore, the load-carrying capacity dropped after reaching the peak on the load-relative displacement plot. In this case, ductility was not exhibited, and the yielded region along the longitudinal bars did not extend to the beginning of the bar bend.

Table 5-1 Summary of specimens and test variables

| Series | Specimen ID | f'_c (ksi) | A_{ls} (in. ²) | f_y (ksi) | ω (%) | c_c (in.) | Actual r_b (in.) | $w_{s,calc}$ (in.) | $w_{s,meas}$ (in.) | ACI ¹ r_b (in.) | FIP ⁵⁸ r_b (in.) | Criteria* |
|----------|-------------|-----------------|---------------------------------|----------------|--------------------|----------------|-----------------------|-----------------------|-----------------------|---------------------------------|----------------------------------|-----------|
| S-Series | S-27-R3-L | 3.45 | 4.74 | 68.6 | 27.40 | 2.0 | 3.9 | 5.5 | 8.9 | 11.8 | 11.8 | (1) |
| | S-27-R11-L | 3.49 | 4.74 | 68.6 | 27.08 | 2.0 | 10.8 | 15.3 | 13.2 | 11.6 | 11.6 | (2) |
| | S-18-R3 | 5.17 | 4.74 | 67.1 | 17.88 | 2.0 | 3.3 | 4.7 | 10.4 | 7.7 | 7.7 | (1) |
| | S-18-R6 | 5.02 | 4.74 | 67.1 | 18.42 | 2.0 | 6.5 | 9.2 | 11.5 | 7.9 | 7.9 | (3) |
| | S-18-R9 | 5.08 | 4.74 | 67.1 | 18.20 | 2.0 | 9.8 | 13.9 | 14.9 | 7.8 | 7.8 | (2) |
| | S-13-R3 | 5.15 | 3.60 | 66.1 | 13.39 | 2.0 | 3.3 | 4.7 | 10.3 | 5.8 | 5.8 | (1) |
| | S-13-R5 | 5.28 | 3.60 | 66.1 | 13.06 | 2.0 | 4.7 | 6.6 | 11.4 | 5.6 | 5.6 | (3) |
| | S-13-R8 | 5.35 | 3.60 | 66.1 | 12.89 | 2.0 | 8.1 | 11.5 | 14.2 | 5.6 | 5.6 | (2) |
| D-Series | D-20-R2 | 5.04 | 4.80 | 69.1 | 20.19 | 2.0 | 2.7 | 3.8 | 8.1 | 8.2 | 8.2 | (1) |
| | D-20-R6 | 5.14 | 4.80 | 69.1 | 19.79 | 2.0 | 6.5 | 9.2 | 11.9 | 8.1 | 8.1 | (3) |
| | D-20-R9 | 4.99 | 4.80 | 69.1 | 20.39 | 2.0 | 9.9 | 14.0 | 7.6 | 8.3 | 8.3 | (2) |
| | D-16-R2 | 5.38 | 4.40 | 62.6 | 15.61 | 2.0 | 2.4 | 3.4 | 6.5 | 6.4 | 6.4 | (1) |
| | D-16-R5 | 4.94 | 4.40 | 62.6 | 17.00 | 2.0 | 5.9 | 8.3 | 11.8 | 7.0 | 7.0 | (3) |
| | D-16-R10 | 5.29 | 4.40 | 62.6 | 15.87 | 2.0 | 10.1 | 14.3 | 12.8 | 6.5 | 6.5 | (2) |
| C-Series | C-17-R3 | 5.29 | 4.74 | 66.3 | 17.27 | 1.25 | 3.3 | 4.7 | 10.4 | 11.8 | 11.8 | (1) |
| | C-17-R6 | 5.33 | 4.74 | 66.3 | 17.13 | 1.25 | 6.4 | 9.1 | 12.0 | 11.8 | 11.8 | (3) |
| | C-17-R9 | 5.04 | 4.74 | 66.3 | 18.12 | 1.25 | 9.2 | 13.0 | 12.7 | 12.5 | 12.5 | (2) |
| | C-17-R12 | 5.16 | 4.74 | 66.3 | 17.70 | 1.25 | 11.5 | 16.3 | 13.5 | 12.2 | 12.2 | (4) |
| B-Series | B-16-R3 | 5.20 | 3.16 | 66.3 | 16.24 [†] | 2.0 | 3.2 | - | - | 12.4 ^{**} | 5.2 | (1) |
| | B-16-R6 | 5.20 | 3.16 | 66.3 | 16.24 [†] | 2.0 | 6.5 | - | - | 12.4 ^{**} | 5.2 | (2) |
| M-Series | LS-S-18-R3 | 5.04 | 4.74 | 66.3 | 18.1 | 2.0 | 3.3 | 3.9 | - | 7.8 | 7.8 | (1) |
| | TR-S-18-R3 | 4.84 | 4.74 | 66.3 | 18.9 | 2.0 | 2.8 | 4.6 | - | 8.1 | 8.1 | (1) |
| | LS-S-13-R3 | 4.76 | 3.60 | 64.7 | 14.2 | 2.0 | 3.3 | 3.9 | - | 6.1 | 6.1 | (1) |
| | TR-S-13-R3 | 4.66 | 3.60 | 64.7 | 14.5 | 2.0 | 2.7 | 4.7 | - | 6.3 | 6.3 | (1) |

* (1) Bar bend satisfies ACI 318¹ minimum radius

(2) Bar bend satisfies Eq. 2-20

(3) Bar bend is between that of a standard hook and the radius based on Eq. 2-20

(4) Bar bend satisfies Eq. 2-20 multiplied by the ratio $2d_b/c_c$

[†] Calculated using the dimensions from the shallower adjoining member

^{**} Calculated using Eq. 2-24; the required r_b using Eq. 2-20 is 5.0 in.

| Characteristic | Category | | |
|----------------|--|--|---|
| | Strength Compromised (Lacking Ductility) | Transition (Ductility Compromised) | Ductile Behavior |
| Failure Mode | CTT Node or Strut | Combined Failure | Failure at CCC Node |
| Strength | $P_{test} < P_{calc}$ or less than other specimens | $P_{test} > P_{calc}$ | $P_{test} > P_{calc}$ |
| Ductility | None | Compromised | High |
| Strain Profile | No yield or only at joint face | Yielding reaches beginning of bar bend | Yielding through entire bar bend (Not applicable for B-Series) |

Figure 5-1 Categorization of specimens

Specimens placed within the Ductile Behavior category exhibited ductile behavior. That is, the load-relative displacement curve showed a displacement ductility factor greater than 2.8 after the peak load and prior to the ultimate failure condition. Furthermore, prior to the ultimate failure condition, the specimen experienced extensive crushing of concrete at the re-entrant corner (that is, the CCC node). The yielded region along the longitudinal bars extended through the entire bar bend if the two legs of the specimen had identical cross sections, which means that the stress distribution corresponding to the assumed strut-and-tie model was achieved. It should be noted that the criterion for the yielded region along the bars does not apply to the B-Series specimens because strain was concentrated at the joint face of the shallower leg. In this case, the stress distribution corresponding to the strut-and-tie model was considered as being achieved if yielding reached the beginning of the bar bend.

The Transition (or Ductility Compromised) category includes specimens with behaviors that fall between the behaviors of the specimens in the other two categories. To be specific, specimens in the Transition category had a combined failure mode characterized by both splitting of concrete along the bar bend and crushing of concrete at the re-entrant corner. The load-carrying capacity was greater than the calculated value and a μ -value between 1.5 to 2.8 was reached.

Furthermore, the yielded region along the longitudinal bars extended to the beginning of the bar bend but not to the center of the bend.

5.3 Evaluation of the Design Expression for Radial Stress at the Bar Bend

To evaluate the design expression for curved-bar nodes that considers the radial stress acting at the bar bend (given as Eq. 2-20), the S-Series and D-Series specimens were categorized based on the criteria presented in Figure 5-1. The resulting categorization is summarized in Table 5-2. It should be noted that Specimen S-27-R11-L was not included because the specimen experienced an anchorage failure. A plot that shows the relationship between the bend radius ratio, $r_b/r_{b,ACI}$, defined as the measured bend radius divided by the ACI-required bend radius expressed as Eq. 2-20, is presented in Figure 5-2. A red dashed line is provided to indicate $P_{test}/P_{calc} = 1.0$.

Table 5-2 Categorization of S-Series and D-Series specimens

| Category | Specimen ID | $r_b/r_{b,ACI}$ | P_{test}/P_{calc} |
|---|-------------|-----------------|---------------------|
| Strength Compromised (Lacking Ductility) | S-27-R3-L | 0.33 | 0.87 |
| | S-18-R3 | 0.43 | 1.05 |
| | D-20-R2 | 0.33 | 0.82 |
| | D-16-R2 | 0.37 | 1.06 |
| Transition (Ductility Compromised) | S-18-R6 | 0.82 | 1.08 |
| | S-13-R3 | 0.57 | 1.14 |
| | S-13-R5 | 0.83 | 1.15 |
| | D-20-R6 | 0.80 | 1.11 |
| | D-16-R5 | 0.84 | 1.13 |
| Ductile Behavior | S-18-R9 | 1.25 | 1.06 |
| | S-13-R8 | 1.46 | 1.17 |
| | D-20-R9 | 1.19 | 1.14 |
| | D-16-R10 | 1.56 | 1.14 |

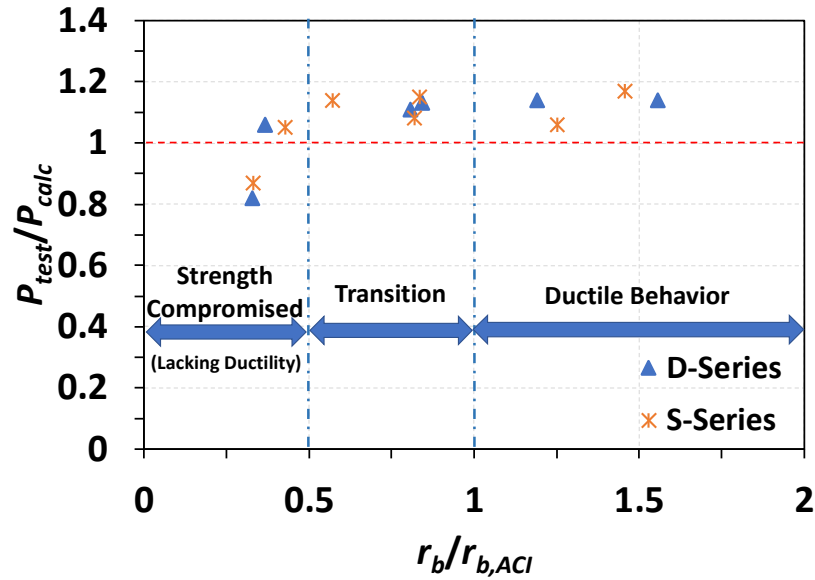


Figure 5-2 Relationship between joint efficiency and bend radius ratio for S-Series and D-Series specimens

As shown in Figure 5-2, the left four datapoints fell into the Strength Compromised (Lacking Ductility) category, the middle five specimens are in the Transition category, and the right four specimens are in the Ductile Behavior category. It can be seen that most specimens with a standard hook fell into the Strength Compromised (Lacking Ductility) category with an exception of Specimen S-13-R3. Although reinforced with a standard hook at the outer corner, Specimen S-13-R3 exhibited a behavior that was consistent with specimens in the Transition category. The three categories were correlated to the bend radius ratio as indicated by the two blue dashed lines in Figure 5-2. From the grouped datapoints, it is reasonable to state that specimens with a bend radius ratio less than 0.5 failed at least somewhat prematurely without exhibiting ductility, specimens with a bend radius ratio between 0.5 to 1.0 had a joint efficiency greater than 1.0 but exhibited compromised ductility, and specimens with a bend radius ratio greater than 1.0 (that is, satisfying the ACI requirement given as Eq. 2-20) displayed satisfying behavior. In other words, the ACI requirement considering radial stress at the bar bend is appropriate and conservative.

5.4 Evaluation of the Effect of Clear Side Cover

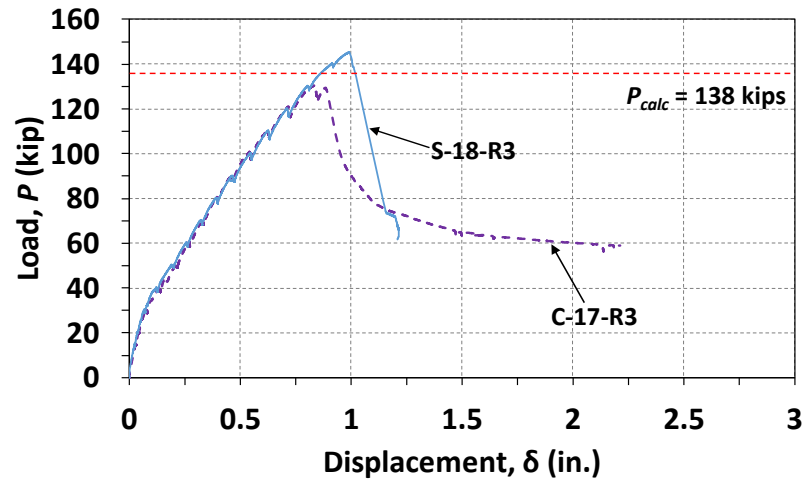
The interpretation of the test results of the C-Series specimens through a comparison with the S-Series specimens is discussed in this section. The method of categorization presented in Section 5.2 was also applied to the test results of the C-Series specimens for the purpose of evaluating the $2d_b/c_c$ factor required in ACI 318-19¹ when the clear side cover is less than 2 times the diameter of the longitudinal bars.

5.4.1 Comparison of Overall Behavior

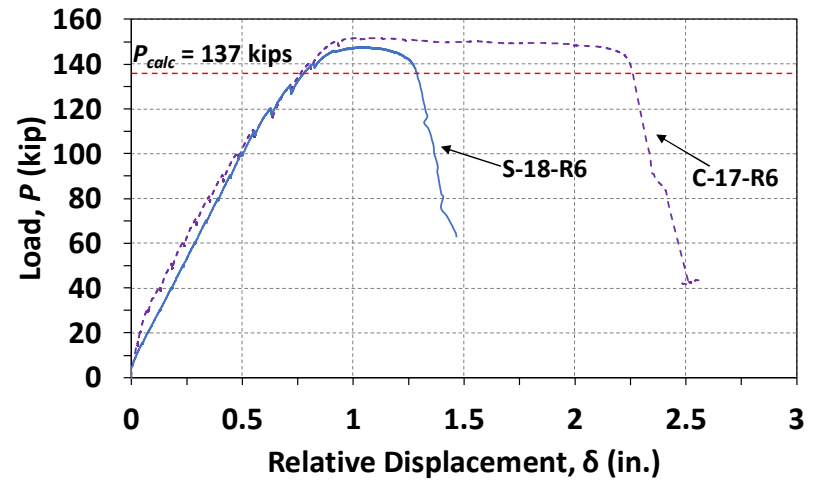
Plots that present a comparison between the load-relative displacement curves of the C-Series and S-Series specimens are shown in Figure 5-3. The red dashed line indicates the calculated load carrying capacity, P_{calc} , as defined previously. Again, the value of P_{calc} was slightly different among specimens shown in the same plot because of differences in the actual (measured) concrete compressive strengths. However, the same mixture design was used for the specimens. To improve readability, only the greatest value of P_{calc} for the specimens within a particular plot is shown. Moreover, a comparison of detailed test results is provided in Table 5-3.

The load-relative displacement curves of specimens with the bend radius of a standard hook (criterion (1)) are plotted together in Figure 5-3(a). Both specimens had nearly the same load-displacement behavior before reaching the ultimate failure condition. That is, the initial stiffness and cracked stiffness were nearly the same, and both specimens exhibit similar cracking loads of approximately 30 kip. Nevertheless, Specimen C-17-R3 had a lower load-carrying capacity than that of Specimen S-18-R3. Moreover, Specimen C-17-R3 did not reach the calculated strength of 138 kip, and only reached an applied load P_{test} of 130 kip. Specimen S-18-R3, however, exceeded the calculated strength. The ratio of the strength of Specimen C-17-R3 to that of Specimen S-18-R3 is 0.90 as presented in Table 5-3.

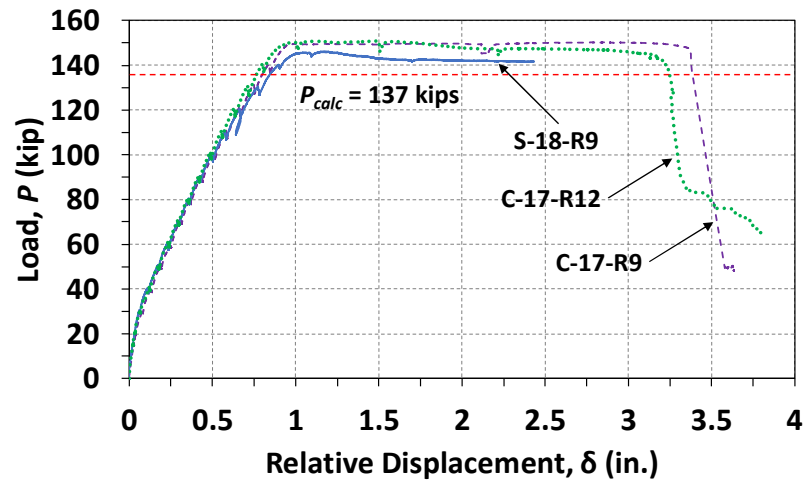
Unlike the specimens of criterion (1), Specimens C-17-R6 and S-17-R6 with a bend radius between that of a standard hook and the requirement of Eq. 2-20 (criterion (3)) reached the calculated load-carrying capacity with similar strengths of 151 kip and 148 kip, respectively. The displacement ductility factor of Specimen C-17-R6, however, was approximately 30% greater than that of Specimen S-18-R6, which means the thinner clear side cover of Specimen C-17-R6 actually did not compromise the behavior.



(a) Criterion (1)



(b) Criterion (3)



(c) Criterion (2) and Criterion (4)

Legend

- S-Series
- - - C-Series
- ... C-17-R12

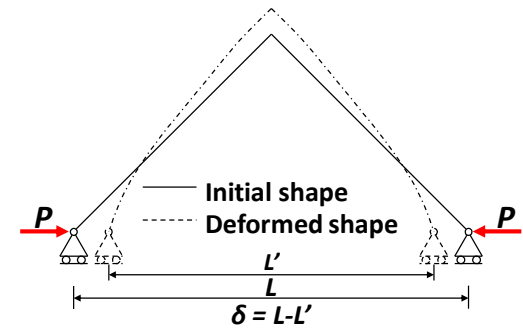


Figure 5-3 Comparison of load-displacement behaviors of S-Series and C-Series specimens

Table 5-3 Summary of test results of S-Series and C-Series specimens

| | ω (%) | | r_b (in.) | | c_c (in.) | | | P_{test} (kip) | | | μ | |
|----------------------|-----------------|------|----------------|------|----------------|------|-------|---------------------|------|-------|-------|-------------------|
| Radius Criterion* | C-17 | S-18 | C-17 | S-18 | C-17 | S-18 | Ratio | C-17 | S-18 | Ratio | C-17 | S-18 |
| Criterion (1) | 17.2 | 17.9 | 3.2 | 3.3 | 1.25 | 2.00 | 0.625 | 130 | 145 | 0.90 | - | - |
| Criterion (3) | 17.1 | 18.4 | 6.4 | 6.5 | 1.25 | 2.00 | 0.625 | 151 | 148 | 1.02 | 2.33 | 1.77 |
| Criterion (2) | 18.1 | 18.2 | 9.2 | 9.9 | 1.25 | 2.00 | 0.625 | 150 | 146 | 1.03 | 3.47 | 2.87 [†] |
| Criterion (4) | 17.7 | - | 11.5 | - | 1.25 | - | - | 151 | - | - | 3.31 | - |

* (1) Bar bend satisfies ACI 318-19¹ minimum radius

(2) Bar bend satisfies Eq. 2-20

(3) Bar bend is between that of a standard hook and the radius based on Eq. 2-20

(4) Bar bend satisfies Eq. 2-20 multiplied by the ratio $2d_b/c_c$

[†] The stroke limit of the hydraulic cylinder was exhausted

The phenomenon that reduced clear side cover did not compromise specimen behavior was also observed for the specimens with a bend radius satisfying criterion (2) (Specimens C-17-R9 and S-18-R9) as presented in Figure 5-3(c). It should be noted that the load-relative displacement curve for Specimen C-17-R12, which was designed based on criterion (4) (that is, with the $2d_b/c_c$ modification factor applied), is also plotted in the figure for comparison. Specimen C-17-R9 and Specimen S-18-R9 had similar load-relative displacement responses. Both specimens exhibited nearly the same initial stiffness and cracked stiffness. Moreover, both specimens were able to exceed the calculated strengths and achieved similar load-carrying capacities of 150 kip for Specimen C-17-R9 and 146 kip for Specimen S-18-R9. Considering the displacement ductility factor, Specimen C-17-R9 reached a μ -value of 3.47. Unfortunately, because the test on Specimen S-18-R9 was stopped due to the stroke limit of the hydraulic cylinders, the value of μ only reached 2.87 and the complete response of Specimen S-18-R9 is not known. Nevertheless, it can be seen that Specimen C-17-R9 exhibited satisfactory behavior. For Specimen C-17-R12, the bend radius satisfying criterion (4) did not result in a different behavior relative to that of Specimen C-17-R9 as previously stated in Section 4.4.1.

From the comparisons discussed above, it can be seen that the thin side cover may have only affected the strength of Specimen C-17-R3, which was detailed based on criterion (1). However, comparing the other C-Series and S-Series specimens in Table 5-3 with a bend radius

satisfying criteria (2) or (3), all of which achieved a P_{test}/P_{calc} value greater than 1.0, the shallow clear side cover did not compromise strength or ductility. Based on the results of these limited number of tests, the modification factor may be unnecessary if Eq. 2-20 is satisfied. The shallow clear side cover may have impacted strength of the specimen with a bend radius based on a standard hook. However, the lower strength may also be due to inherent scatter in the test results.

5.4.2 Evaluation of the Modification Factor for Reduced Clear Side Cover

The categorization described in Section 5.2 was also applied to the C-Series specimens based on behavior and ductility in order to evaluate the modification factor for reduced side cover ($2d_b/c_c$). The results are presented in Table 5-4. The value of $r_{b,ACI}$ is the required bend radius based on ACI 318-19¹ with the modification factor applied where applicable.

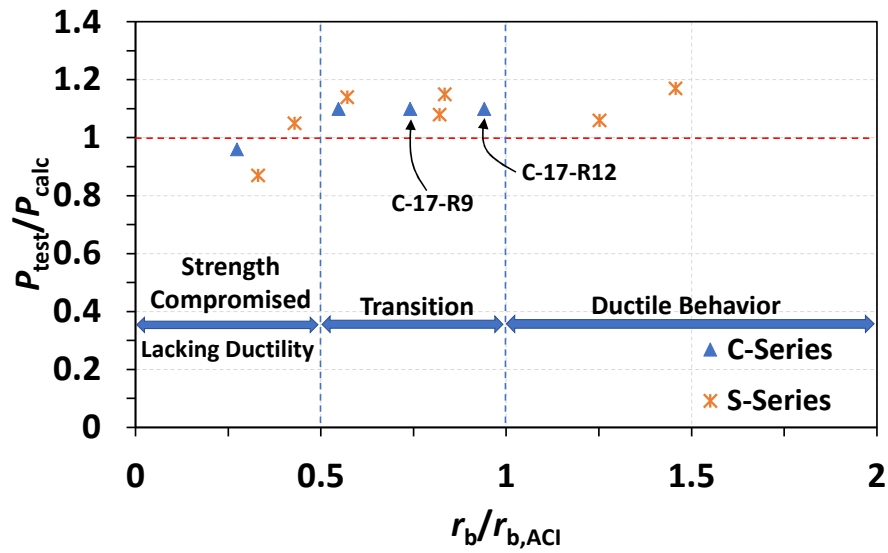
Table 5-4 Categorization of C-Series specimens

| Category | Specimen ID | $r_{b,ACI,modified}$ (in.) | $r_b/r_{b,ACI}$ | $r_b/r_{b,ACI,modified}$ | P_{test}/P_{calc} |
|--|-------------|----------------------------|-----------------|--------------------------|---------------------|
| Strength Compromised (Lacking Ductility) | C-17-R3 | 8.9 | 0.27 | 0.37 | 0.96 |
| Transition (Ductility Compromised) | C-17-R6 | 8.9 | 0.55 | 0.73 | 1.10 |
| Ductile Behavior | C-17-R9 | 9.4 | 0.74 | 0.98 | 1.10 |
| | C-17-R12 | 9.2 | 0.94 | 1.25 | 1.10 |

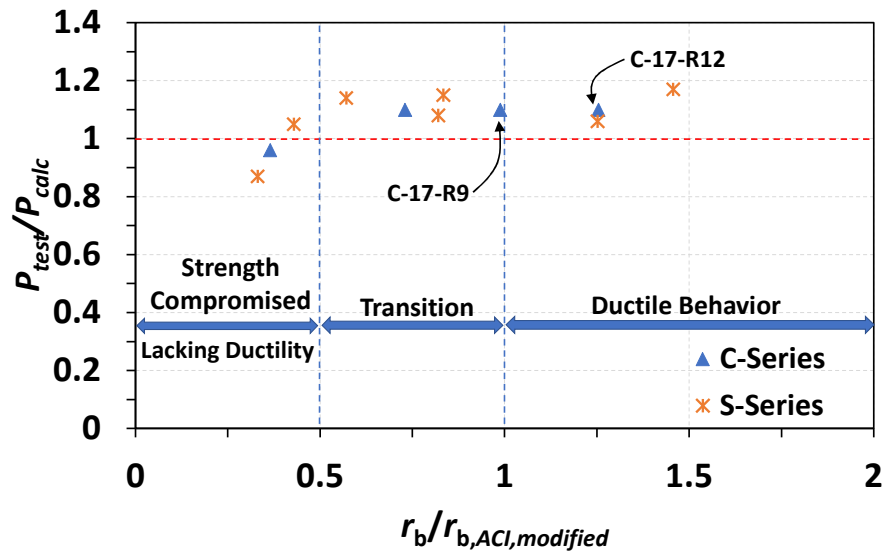
A comparison between the C-Series and S-Series specimens is provided in Figure 5-4, again with $r_{b,ACI}$ based on ACI 318-19.¹ When the same three-group categorization described in Section 5.3 is applied to the C-Series specimens (that is, divisions between the categories are assumed to correspond to bend radius ratios of 0.5 and 1.0 as shown in Figure 5-4), an inconsistency is observed. Three C-Series specimens with a bend radius larger than the bend radius of a standard hook fell into the Transition category as shown in Figure 5-4(a). Specimen C-17-R9 and C-17-R12, however, were observed to have a behavior belonging to the Ductile Behavior category. Therefore, based on these two specimens, the $2d_b/c_c$ factor suggested by ACI 318-19¹ for shallow clear side cover appears to be overly-conservative.

To make the categorization more consistent based on behavior, the modification factor can be reduced from $2d_b/c_c$ to $1.5d_b/c_c$. Using the new modification factor, the bend radius ratio was

updated as shown Table 5-4 (refer to column with the label $r_b/r_{b,ACI,modified}$). According to the new bend radius ratio, a comparison between the C-Series and S-Series specimens was again plotted as shown in Figure 5-4(b). It can be seen that application of the modified factor provides a more consistent categorization of specimens with regard to the expected behavior while maintaining conservativeness.



(a) C-Series and S-Series specimens with $r_{b,ACI}$ incorporating a cover factor of $2.0d_b/c_c$



(b) C-Series and S-Series specimens with $r_{b,ACI,modified}$ incorporating a cover factor of $1.5d_b/c_c$

Figure 5-4 Relationship between joint efficiency and bend radius ratio for C-Series and S-Series specimens

5.5 Evaluation of the Effect of a Strut Angle not Equal to 45 Degrees

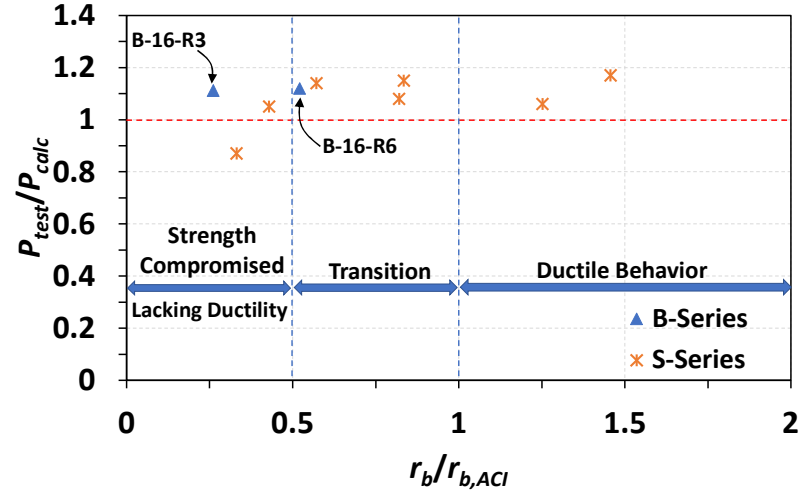
The evaluation of the design expressions for curved-bar nodes when the diagonal strut angle is not equal to 45 degrees is provided in this section. In this case, circumferential bond stress develops along the bar bend along with radial stress. In addition to providing sufficient bearing area for the diagonal strut, ACI 318-19¹ requires the length of the bar bend measured along the centerline of the bar to be long enough to develop the required bond stress. Different from ACI 318-19, FIP⁵⁸ considers only radial stress with the size of the bearing area being a function of the angle of the diagonal strut.

5.5.1 Evaluation

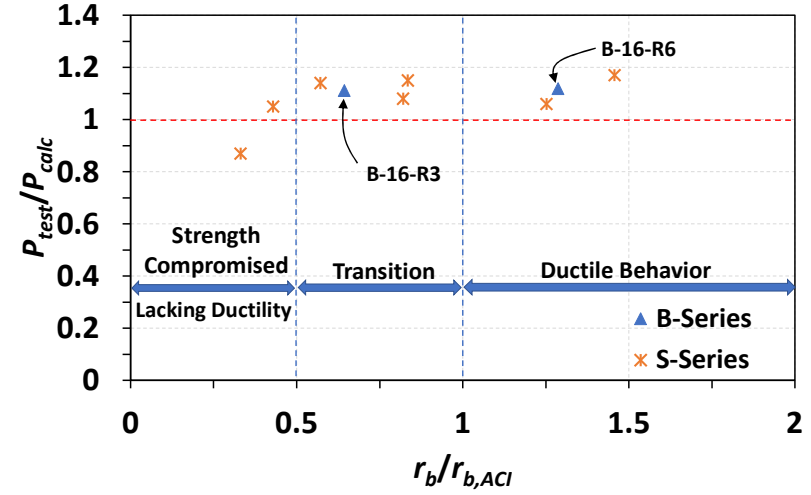
The B-Series specimens were categorized based on their behaviors as shown in Table 5-5. In the table, three bend radius ratios are provided: 1) the ratio of the measured bend radius to the requirement of Eq. 2-20 (from ACI 318-19¹), 2) the ratio of the measured bend radius to the requirement of Eq. 2-24 (from ACI 318-19¹), and 3) the ratio of the measured bend radius to the requirement of Eq. 2-26 (from FIP⁵⁸).

Table 5-5 Categorization of B-Series specimens

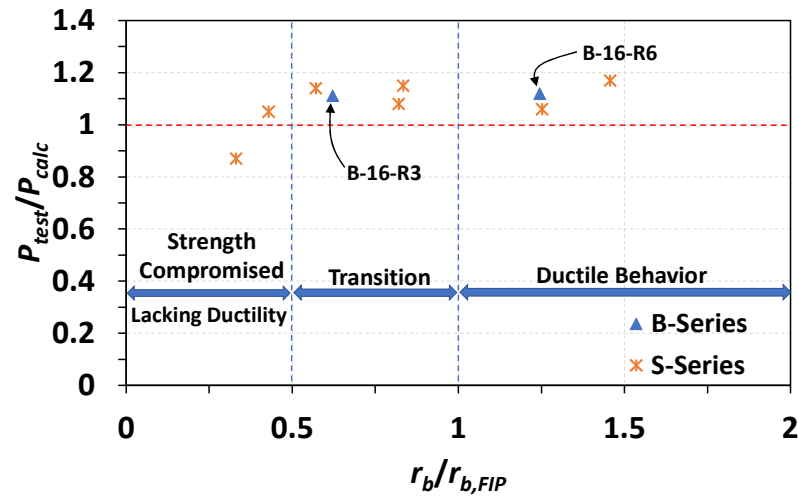
| Category | Specimen ID | $r_b/r_{b,ACI}$ Eq. 2-24 | $r_b/r_{b,ACI}$ Eq. 2-20 | $r_b/r_{b,FIP}$ Eq. 2-26 | P_{test}/P_{calc} |
|------------------|-------------|-----------------------------|-----------------------------|-----------------------------|---------------------|
| Ductile Behavior | B-16-R3 | 0.26 | 0.64 | 0.62 | 1.11 |
| Ductile Behavior | B-16-R6 | 0.52 | 1.29 | 1.24 | 1.12 |



(a) $r_{b,ACI}$ based on ACI 318 (Eq. 2-24)



(b) $r_{b,ACI}$ based on ACI 318 (Eq. 2-20)



(c) $r_{b,FIP}$ based on FIP (Eq. 2-26)

Figure 5-5 Relationship between joint efficiency and bend radius ratio for B-Series and S-Series specimens

The results from the B-Series specimens are presented in Figure 5-5 along with the results from the S-Series specimens. In the figure, the divisions between the categories are again assumed to correspond to bend radius ratios of 0.5 and 1.0. In Figure 5-5(a), the results from the B-Series specimens are plotted based on the requirement of Eq. 2-24 (that is, the required radius in consideration of circumferential bond stress). When applying Eq. 2-24, the development length l_d for No. 8 reinforcement was taken as 46.0 in. in accordance with Table 25.4.2.3 of ACI 318-19.¹ The diagonal strut angle θ_c was calculated using Eq. 5-1 as 35.8° , which is based on the assumption that the CCC node lies on the line that connects the CTT node and the re-entrant corner as shown in Figure 5-6. Both of the B-Series specimens contained bend radii that were less than or equal to 0.52 times the bend radius required by Eq. 2-24. One of the specimens therefore fell into the Strength Compromised (Lacking Ductility) category, and the other fell into the Transition category, as shown in Figure 5-5(a). Both specimens, however, did not experience compromised strength nor premature failure. Rather, the specimens exhibited ductile behavior ($\mu = 8.00$ and 8.80). Thus, the merit of the ACI 318-19¹ requirement given in Eq. 2-24 in consideration of circumferential bond stresses is questionable.

$$\theta_c = \tan^{-1} \frac{d_1}{d_2}$$

5-1

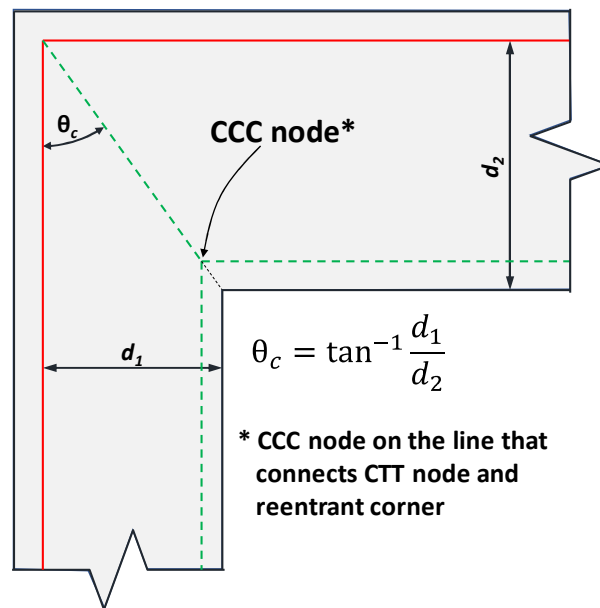


Figure 5-6 Calculation of θ_c for B-Series specimens

In Figure 5-5(b), the value of $r_{b,ACI}$ is based on the ACI 318-19¹ requirement given in Eq. 2-20 (that is, the required radius in consideration of radial stress at the bar bend). In this case, Specimen B-16-R3 fell into the division for the Transition category, while Specimen B-16-R6 fell into the division for the Ductile Behavior category. Compared to the method based on Eq 2-24, the results show a pattern that is more consistent with the observed behavior. Although Specimen B-16-R3 was placed in the Ductile Behavior category, it did demonstrate a bond splitting crack and slightly reduced ductility compared to Specimen B-16-R6. Therefore, in spite of not considering the diagonal strut angle, Eq. 2-20 was still conservative and provided reasonable results.

Unlike the other specimens of the test program, Eq. 2-24 from ACI 318-19¹ provides a different value for the required bend radius of the B-Series specimens compared to the design equation based on FIP⁵⁸ (Eq. 2-26). To evaluate the two B-Series specimens using Eq. 2-26, the angle θ_c was also taken as 35.8 using Eq. 5-1. As shown in Figure 5-5(c), when the design expression based on FIP⁵⁸ (Eq. 2-26) is used, Specimens B-16-R3 and B-16-R6 fall within the Transition and Ductile Behavior categories, respectively. Therefore, Eq. 2-26 provides a more consistent categorization of the specimens with regard to the expected behavior compared to Eq. 2-24. Although both specimens exhibited excellent ductility, the conservatism of the resulting categorization in Figure 5-5(c) is acceptable considering the limited number of B-Series specimens.

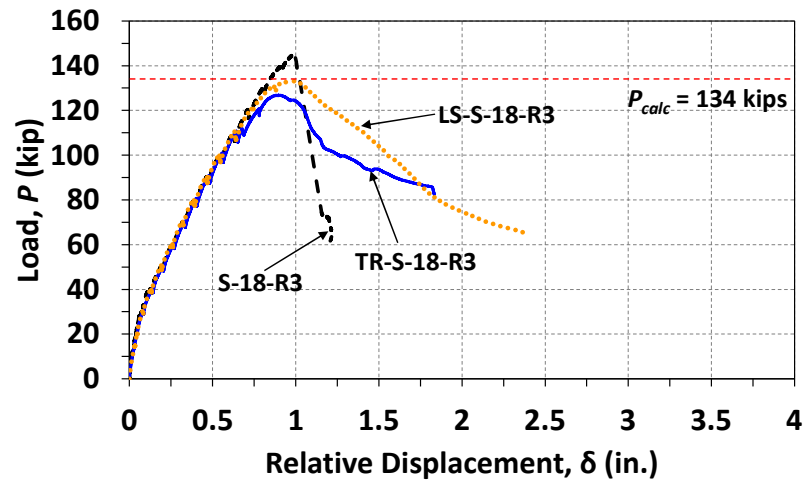
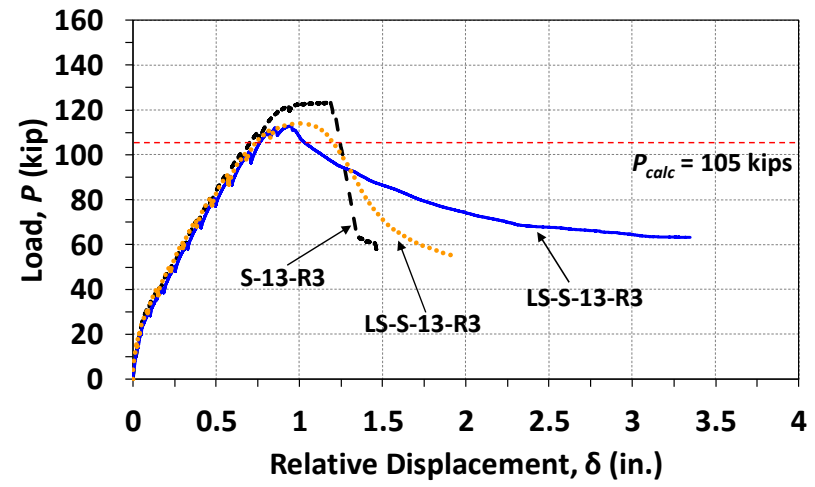
5.6 Performance of Knee Joints with Transverse Reinforcement

The behavior of knee joint with common reinforcement details is evaluated in this section by comparing the M-Series and S-Series specimens. ACI 318-19¹ specifies a minimum amount of distributed reinforcement to be provided across struts. The primary interest was to evaluate whether distributed reinforcement through a joint detailed with longitudinal bars with the bend radius of a standard hook would aid in delaying the failure of the joint. The effect of longitudinal bars lap-spliced within the joint was also evaluated.

5.6.1 Comparison of Overall Behavior

The load-relative displacement curves of the M-Series specimens (Group LS and Group TR) and their companion S-Series specimens are presented in Figure 5-7. The red dashed lines indicate the calculated load-carrying capacity, P_{calc} , which was based on measured material properties. Due to small variations in materials properties, the value of P_{calc} varied among the specimens, and only the lowest value for the specimens represented in each plot is shown to improve readability.

As shown in Figure 5-8(a) and (b), regardless of whether transverse reinforcement was present, a loss in load-carrying capacity occurred after reaching the peak load. That is, all specimens lacked ductility. However, the rate at which load decreased was slower for the M-Series specimens compared to their companion S-Series specimens. Considering previously described test specimens with longitudinal bars detailed with larger bend radii, the slight improvement in behavior by providing transverse reinforcement does not compare to the significant increase in ductility resulting from larger bend radii. The test results reveal that the traditional method of detailing knee joints could potentially lead to premature failures. Furthermore, the results imply that adding transverse reinforcement in the joint region had little to no effect on the load-carrying capacity of the specimens.

(a) Specimens with $\omega \approx 18\%$ (b) Specimens with $\omega \approx 13\%$

Legend

- S-Series
- Group LS
- Group TR

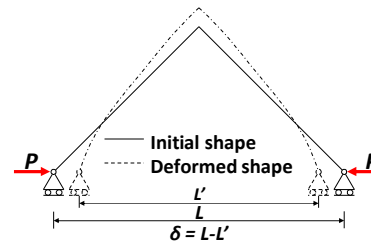


Figure 5-7 Comparison of load-relative displacement behaviors of S-Series, Group LS, and Group TR specimens

5.6.2 Evaluation of Commonly Used Joint Details

The categorization scheme presented in Figure 5-1 was again applied to the M-Series specimens. As indicated in Table 5-6, all specimens fell into the Strength Compromised (Lacking Ductility) category based on the behaviors observed during the tests. It should be noted that the parameter $r_{b,ACI}$ in the table is defined as the requirement of Eq. 2-20 (that is, the required radius in consideration of radial stress at the bar bend). Considering the results of previous tests (namely, the S-Series specimens), Eq. 2-20 is applicable to the specimens in Group TR with continuous longitudinal bars. Applicability of Eq. 2-20 to Group LS, however, is not clear although the lap splices shared similar characteristics as the continuous reinforcing bars. Nevertheless, it is interesting to compare specimens in Group TR and Group LS with S-Series and D-Series specimens, as shown in Figure 5-8. Again, $r_{b,ACI}$ is defined as the requirement of Eq. 2-20 in the figure.

Table 5-6 Categorization of M-Series specimens

| Category | Specimen ID | $r_b/r_{b,ACI}$ | P_{test}/P_{calc} |
|---|-------------|-----------------|---------------------|
| Strength Compromised (Lacking Ductility) | LS-S-18-R3 | 0.42 | 0.98 |
| | TR-S-18-R3 | 0.40 | 0.93 |
| | LS-S-13-R3 | 0.45 | 1.08 |
| | TR-S-13-R3 | 0.44 | 1.07 |

It can be observed from Figure 5-8 that the datapoints representing the M-Series specimens, regardless of whether the specimens are from Group LS or Group TR, seem to follow the trend of datapoints representing the S-Series and D-Series specimens. The results again imply that regardless of whether transverse reinforcement was present, the bend radius governed the strength of the knee joints. Moreover, specimens with longitudinal reinforcing bars lap-spliced in the joint were also affected by the bend radius. In addition, based on the limited data shown in Figure 5-8, values of the joint efficiency, P_{test}/P_{calc} , had a seemingly linear relationship with the bend radius ratio, $r_b/r_{b,ACI}$, for specimens in the Strength Compromised category.

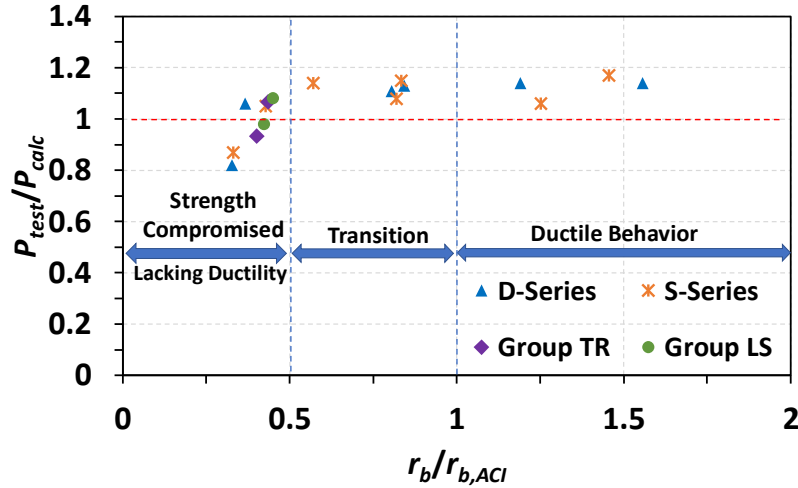


Figure 5-8 Relationship between joint efficiency and bend radius ratio for Group LS, Group TR, D-Series, and S-Series specimens

5.7 Stress Analysis of Diagonal Strut and Curved-Bar Node

The nodal zone coefficient for CTT nodes was evaluated by considering the force acting at the curved-bar node, which can be inferred from the measured strain along the longitudinal reinforcing bars. As stated previously, considering specimens with adjoining members with identical cross sections (S-Series, D-Series, C-Series, and M-Series), specimens within the Ductile Behavior category were able to achieve the stress distribution assumed by the strut-and-tie model (see Figure 2-36). That is, the longitudinal reinforcing bars yielded along their entire length (that is, from the joint face to the center of the bar bend). In addition, although yielding did not extend to the center of the bar bend, the yielded region of the longitudinal reinforcing bars of specimens that fell into the Transition category also had a constant bar stress from the beginning of the bar bend to the joint face. Therefore, the constant tie force for specimens in the Transition category and the Ductile Behavior category is equal to $A_{ts}f_y$.

By enforcing equilibrium at the curved-bar node, the force in the diagonal strut is expressed as $\sqrt{2}A_s f_y$. The stress acting on the concrete at the interface of the diagonal strut and the curved-bar node was calculated by dividing the force transmitted through the diagonal strut by the bearing area under the bar bend ($b\sqrt{2}r_b$). It should be noted that the value of $\sqrt{2}r_b$ is given as the calculated strut width, $w_{s,calc}$, in Table 5-1. Cancelling out the $\sqrt{2}$, the stress acting on the bearing area can be expressed as Eq. 5-2. Results of the stress analysis are summarized in Table 5-7 for specimens in

the Transition and Ductile Behavior categories (with the exception of the B-Series specimens). It should be noted that because Specimen S-13-R3 had a strain reading at the beginning of the bar bend close to the yield strain and the behavior was consistent with specimens in the Transition category, Eq. 5-2 was also applied to this specimen. For the C-Series specimens, the factor for reduced side cover was not included.

$$f_c = \frac{A_{ts}f_y}{br_b} \quad 5-2$$

Table 5-7 Stress acting on concrete under bar bend for specimens in the Transition and Ductile Behavior categories

| Category | Specimen ID | f_c (ksi) | f'_c (ksi) | $f_c/0.85f'_c$ |
|------------------|-------------|----------------|-----------------|----------------|
| Transition | S-18-R6 | 3.06 | 5.02 | 0.72 |
| | S-13-R3 | 4.51 | 5.15 | 1.03 |
| | S-13-R5 | 3.16 | 5.28 | 0.71 |
| | D-20-R6 | 3.19 | 5.14 | 0.73 |
| | D-16-R5 | 2.92 | 4.94 | 0.69 |
| | C-17-R6 | 3.02 | 5.33 | 0.67 |
| Ductile Behavior | S-18-R9 | 2.03 | 5.08 | 0.47 |
| | S-13-R8 | 1.84 | 5.35 | 0.40 |
| | D-20-R9 | 2.09 | 4.99 | 0.49 |
| | D-16-R10 | 1.69 | 5.29 | 0.38 |
| | C-17-R9 | 2.13 | 5.04 | 0.50 |
| | C-17-R12 | 1.71 | 5.16 | 0.39 |

The stress acting on the interface between the curved-bar node and the diagonal strut, f_c , was divided by 0.85 times the measured compressive strength of concrete to evaluate the nodal zone coefficient corresponding to the curved-bar node. Considering specimens in the Transition category, which had a failure related to the CTT node, the greatest value of the ratio $f_c/0.85f'_c$ is 1.03, which implies that the nodal zone coefficient could be as large as 1.03 in some cases. For this specimen (Specimen S-13-R3), the effective compressive strength of concrete at the curved-bar node does not need to be reduced. Considering the other specimens for which splitting at the bar bend was observed, the value of $f_c/0.85f'_c$ ranges from 0.67 to 0.73. On the other hand, for specimens in Ductile Behavior category, it can be seen that if the value of $f_c/0.85f'_c$ is less than or equal to 0.50, no failure related to the diagonal strut or the curved-bar node occurred.

It may not be appropriate to use the assumed strut-and-tie model for closing knee joints to predict the strength of specimens categorized in the Strength Compromised category. The strut-and-tie model assumes a constant tie force, which means that the bar stress at the joint face and at the beginning of the bar bend are assumed to be the same. However, as explained in the Section 4.2.4, a fan shaped strut existed in the joint of the specimens in the Strength Compromised category, and bond stress developed along the longitudinal reinforcing bars between the yielded region of the bars and the beginning of the bar bend. In other words, the bar force increased from the bar bend to the joint face. Although a relatively small bend radius results in failure of the strut prior to yielding of the longitudinal bars at the bar bend, it is possible that the reinforcement may yield at the joint face, allowing the joint to reach its calculated capacity based on flexure at the joint face and to exceed its calculated capacity based on the strut-and-tie method. Further discussion is presented in Chapter 6.

Another factor that may contribute to the specimens achieving strengths that surpass those based on a strut-and-tie model is that the bearing area induced by the bar bend is larger than expected. The widths of the diagonal struts measured after each test, $w_{s,meas}$, are summarized in Table 5-1. The measured strut widths were typically larger than the calculated strut widths, $w_{s,calc}$. The ratio of the measured strut width to the calculated strut width, $w_{s,meas}/w_{s,calc}$, is plotted in Figure 5-9 against the actual (that is, measured) bend radii of the longitudinal bars. The data indicate that a bend radius based on a standard hook resulted in strut widths, and therefore bearing areas, that were approximately 1.5 to 2.3 times the calculated strut widths.

The two reasons mentioned above (that is, variation of force along the bars and actual versus calculated strut widths) may result in underestimations of the strength of knee joints when using the strut-and-tie method. Quantitatively, as an example, Specimen S-18-R3 had a bend radius of 3.3 in. For a certain bend radius, the bearing area under the curved-bar node can be calculated using $b\sqrt{2}r_b$ as explained. Therefore the corresponding bearing area is $(16 \text{ in.})(\sqrt{2})(3.3 \text{ in.})$, which is equal to 74.7 in.^2 . According to the model upon which the design provisions for curved-bar nodes is based, this bearing area allows the bar bend to develop a bar stress of 34.6 ksi when the concrete stress reaches the effective strength of $0.60f'_c = 3.1 \text{ ksi}$. Because the typically assumed strut-and-tie model (see Figure 2-3(a)) had a constant force along the tie corresponding to the longitudinal reinforcement, the bar stress at the joint is assumed to be the same as that at the bar bend. That is, the bar stress at the joint face is also 34.6 ksi under this assumption. The measured

bar strain at the joint face, however, was greater than the yield strain, and the specimen had a joint efficiency higher than 1.0. Moreover, if the nodal zone coefficient is assumed to be equal to 1.0 instead of 0.60, the bar stress at the bar bend could be as high as 57.6 ksi, which is still less than the yield stress. To further understand the cause of the underestimated strengths, the bar stress calculated based on the effective compressive strength was compared to the actual bar stress at the joint face for specimens in the Strength Compromised category. The calculated bar stress was determined by enforcing equilibrium at the curved-bar node as shown in Eq. 5-3 and Eq. 5-4. It should be noted that the effective compressive strength was taken as $0.60f'_c$. The actual bar stress was determined by multiplying 29,000 ksi by the measured bar strain. The results are presented in Table 5-8.

$$f_{ce}\sqrt{2}r_b b \sin 45^\circ = A_{ts}f_s \quad 5-3$$

$$f_s = \frac{f_{ce}r_b b}{A_{ts}} \quad 5-4$$

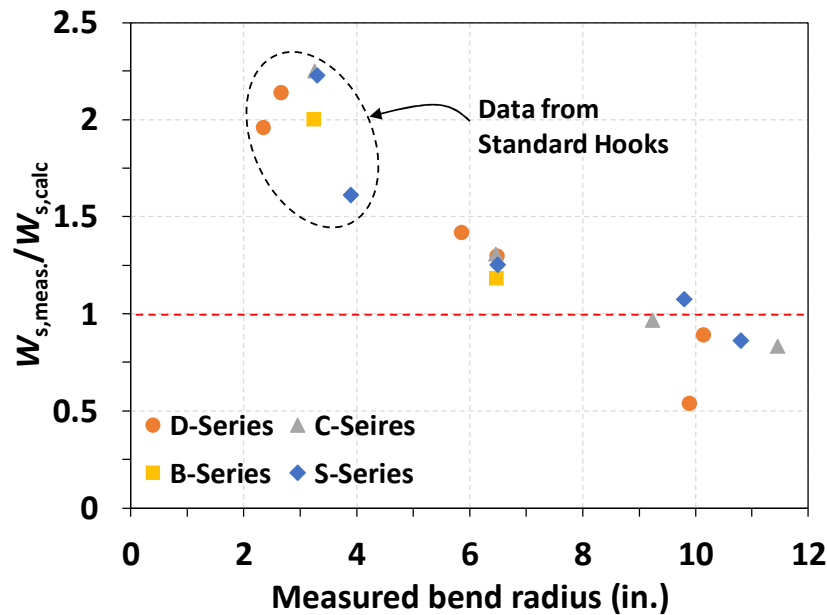


Figure 5-9 Relationship between measured bend radius and strut width

Table 5-8 Stress analysis of bars for specimens in the Strength Compromised category

| Specimen ID | Measured ϵ_s (‰) | f'_c (ksi) | Actual f_s (ksi) | f_y (ksi) | Calculated f_s (ksi) | $\frac{\text{Actual } f_s}{\text{Calculated } f_s}$ |
|-------------|---------------------------------|-----------------|--------------------------|----------------|------------------------------|---|
| S-27-R3-L | 1.99 | 3.45 | 57.7 | 68.6 | 27.3 | 2.11 |
| S-18-R3 | 2.70 | 5.17 | 67.1 | 67.1 | 34.5 | 1.94 |
| D-20-R2 | 1.78 | 5.04 | 51.6 | 69.1 | 27.2 | 1.90 |
| D-16-R2 | 2.27 | 5.38 | 62.6 | 62.6 | 28.2 | 2.22 |
| C-17-R3 | 2.28 | 5.29 | 66.1 | 66.3 | 35.3 | 1.87 |
| LS-S-18-R3 | 2.27 | 5.04 | 65.8 | 66.3 | 33.6 | 1.96 |
| TR-S-18-R3 | 2.22 | 4.76 | 64.4 | 66.3 | 27.0 | 2.39 |
| LS-S-13-R3 | 2.37 | 4.84 | 64.7 | 64.7 | 42.5 | 1.52 |
| TR-S-13-R3 | 2.52 | 4.66 | 64.7 | 64.7 | 33.6 | 1.93 |

As shown in the Table 5-8, all values of the ratio of the actual bar stress to the calculated bar stress at the joint face range from 1.52 to 2.39. The results indicate that if a nodal zone coefficient of 0.60 is applied, the tie force at the joint face can be underestimated. The stress analysis implies that the nodal zone coefficient of 0.60 was not necessary to determine the required bend radius for curved-bar nodes in order to achieve expected strengths. Even a nodal factor greater than 1.0 would lead to underestimated strengths. This phenomenon can be attributed to that the analysis neglected stress development along the straight portion of the longitudinal reinforcement between the bar bend and the joint face, which contradicts the strain readings in the tests. Nevertheless, as observed during the test program, if both adequate strength and ductility are desired, the bend radius required by ACI 318-19¹ (Eq. 2-20) is still needed.

5.8 Summary

In this chapter, the adequacy of the design expressions in ACI 318-19¹ for curved-bar nodes were evaluated using the results from tests on the 24 knee joint specimens under closing moments. The primary observations and conclusions based on the analysis are as follows:

1. Overall, the equation for the required bend radius, r_b , in ACI 318-19¹ based on radial compressive stress at a curved-bar node resulted in satisfactory strength and ductility regardless of whether the specimen was reinforced with a single layer of reinforcing bars or double layers of reinforcing bars.

2. Based on the results of the C-Series specimens, the current factor of $2d_b/c_c$ required by ACI 318-19¹ to be applied to the required bend radius for curved-bar nodes with shallow clear side cover may be overly-conservative. Applying a factor of $1.5d_b/c_c$ resulted in improved results.
3. Based on the two specimens with curved-bar nodes at which the angle of the strut was other than 45° , the merits of the design expression included in ACI 318-19¹ in consideration of circumferential bond stresses is questionable. Application of the design expression based on the ACI-required bend radius in consideration of radial stress or the expression based on FIP⁵⁷ delivered satisfactory results when applied to the specimens.
4. When only strength is considered, the ACI nodal zone coefficient for CTT nodes (0.60) used to calculate the effective compressive strength of concrete provided conservative results when used to determine the required bend radius at curved-bar nodes. Nevertheless, application of the current coefficient is recommended for satisfactory strength and ductility.

6. STRUT-AND-TIE MODEL AND DATABASE ANALYSIS

6.1 Overview

Closing knee joint tests in the literature were collected and filtered to develop an evaluation database consisting of 116 specimens. The evaluation database was used to verify a procedure that was developed for constructing strut-and-tie models for closing knee joints. To evaluate the accuracy and the conservativeness of the method, strength coefficients specified in ACI 318-19¹ and alternative coefficients were considered. Moreover, sectional analysis and joint shear analysis were assessed using the evaluation database.

As discussed in the previous chapters, the behavior of reinforced concrete knee joints under closing moment is affected by the bend radius at the outer corner and by the clear side cover. In other words, consideration of the CTT node, or the curved-bar node, plays an important role in determining the behavior of closing knee joints.

In spite of the understanding gained in regard to curved-bar nodes, knowledge gaps still exist when the strut-and-tie method is used to design and detail closing knee joints. The specific stress conditions for the strut within knee joints and its appropriate strut coefficient deserve attention. Moreover, different factors^{60,75,76} for the nodal zone coefficient for CTT nodes have been proposed. As discussed in this chapter, current design provisions result in overconservative results for knee joint specimens within the evaluation database. Furthermore, the current modification factor for reduced clear side cover for curved-bar nodes was found to be somewhat overly conservative. It is important to develop a consistent procedure for appropriately constructing strut-and-tie models for closing knee joints, and an evaluation of the strength coefficients for the strut and nodes in the joint region is also warranted.

In this chapter, a procedure is introduced that includes guidance for the selection of a permissible strut-and-tie model, the proportioning of elements of the model, and the optimization of the selected model. Strength coefficients based on both the current design code and the experimental program are considered and evaluated using the evaluation database. The database includes tests from the literature and the experimental results of the current study. Moreover, the results generated by the STM are compared to those generated by sectional analysis. The strength of closing knee joints based on joint shear capacity (see Eq. 2-5) is also considered. It should be

noted that discussion about the predictive methods in this chapter focuses on only strength. Ductility behavior of closing knee joints is not incorporated.

6.2 Database

Data from 12 past studies^{2-8,10,14,16,23,77} that include 154 knee joint specimens tested under closing moments were collected as presented in Table 6-1. Twenty-three tests conducted in this experimental program introduced in previous chapters are also included in the table, resulting in a total of 177 tests. Some tests, however, could not be included in a database evaluation due to missing details or were not suitable for the current study and were therefore filtered out. Firstly, 21 tests were filtered out because of incomplete information. Out of these 21 tests, 15 tests from Mayfield⁵ did not properly include the experimental capacities. The documents describing the other seven tests from Zouzou et al.⁷ and Ostund³ did not report the yield strength of the reinforcing bars. Secondly, 32 tests from Richart² were filtered out because the specimens had tapered adjoining members and the study was focused on chamfer and fillet details in the joint region, which was not the primary focus of the current study. After being filtered, 116 specimens remained in the resulting evaluation database, indicated by the shaded rows in Table 6-1.

Testing methods (that is, loading configurations used to create closing moments in the joint) varied among the studies in the evaluation database. In general, five different methods were identified as illustrated in Figure 6-1. The loading systems were given the following titles: Horizontal, U-Type, Cantilever, Vertical, and Portal. The Horizontal loading configuration was used in the current study. For the U-Type loading system, loads were applied in opposite directions to both legs to test the two knee joints simultaneously. The system was further subdivided into U-Type 1 and U-Type 2 based on the lengths of the parallel legs of the specimens. For U-Type 1, the load point is within the D-region near the knee joint due to the short length of the legs. Contrary to U-Type 1, U-Type 2 had longer legs, and the load point was outside of the D-region. The Cantilever configuration developed closing moments at the knee joint by applying a downward load near the end of a cantilevered beam. The Vertical configuration, shown in Figure 6-1(d), was subdivided into Vertical 1 and Vertical 2 according to the aspect ratio of the adjoining members (that is, leg length divided by depth of the cross section). The specimens in the Vertical 1 subset had a greater aspect ratio compared to the specimens in the Vertical 2 subset and therefore the load point was outside the D-region of the knee joint. For Vertical 2, the whole test specimen was

considered a D-region. The aspect ratio affected the layout of the strut-and-tie model as described in Section 6.4.1. Lastly, the Portal configuration consisted of a statically indeterminate system in which the specimens were pin-supported portal frames. Two concentrated loads were applied at the third points along the horizontal beam to create closing moments in the two joints. The number of specimens in the evaluation database that correspond to each loading configuration is presented in Figure 6-2.

Table 6-1 Collected knee joints tested with closing moments from the literature

| Source | Number of tests | b (in.) | | d (in.) | | c (in.) | | A_{ts} (in. ²) | | r_b^* (in.) | | d_b (in.) | | f_c (ksi) | | f_y (ksi) | |
|-------------------------|-----------------|--------------|-------|--------------|-------|--------------|------|---------------------------------|-------|------------------|-------|----------------|------|----------------|------|----------------|-------|
| | | Min. | Max. | Min. | Max. | Min. | Max. | Min. | Max. | Min. | Max. | Min. | Max. | Min. | Max. | Min. | Max. |
| Richart et al. (1938) | 32 | 12 | 12 | 14.5 | 14.5 | 1.13 | 1.13 | 1.76 | 4.84 | 10.5 | 10.5 | 0.75 | 0.75 | 2.76 | 4.25 | 44.2 | 56.8 |
| Ostlund (1963) | 12 | 7.87 | 7.87 | 10.5 | 10.5 | 0.94 | 1.30 | 0.62 | 1.20 | 4.72 | 9.45 | 0.63 | 0.88 | 1.74 | 6.38 | - | - |
| Swann (1969) | 5 | 5.98 | 5.98 | 4.86 | 4.86 | 0.75 | 0.75 | 0.88 | 0.88 | 2.24 | 2.24 | 0.75 | 0.75 | 3.39 | 3.97 | 42.79 | 42.79 |
| Mayfield (1971) | 15 | 5.91 | 7.87 | 5.78 | 5.78 | 1.57 | 1.57 | 0.35 | 0.35 | 1.42 | 1.42 | 0.47 | 0.47 | 2.50 | 3.5 | 65.12 | 65.12 |
| Stroband et al. (1981) | 33 | 2.76 | 2.76 | 4.25 | 4.25 | 0.35 | 0.35 | 0.088 | 0.088 | 0.59 | 1.77 | 0.24 | 0.24 | 1.74 | 4.10 | 65.27 | 65.27 |
| Yuan et al. (1982) | 3 | 12 | 12 | 3.11 | 4.15 | 1.42 | 1.42 | 0.22 | 0.22 | 1.13 | 1.13 | 0.38 | 0.38 | 3.05 | 3.05 | 60.05 | 60.05 |
| Zouzou et al. (1993) | 2 | 7.87 | 7.87 | 11.81 | 11.81 | - | - | 1.46 | 1.46 | 2.36 | 2.36 | 0.79 | 0.79 | 6.67 | 7.11 | - | - |
| Luo et al. (1994) | 27 | 7.87 | 11.81 | 15.75 | 19.69 | 1.00 | 1.00 | 1.18 | 3.57 | 1.42 | 11.02 | 0.71 | 1.10 | 2.23 | 5.16 | 53.1 | 69.18 |
| Johansson (2001) | 8 | 23.62 | 23.62 | 10.55 | 11.02 | 1.57 | 1.57 | 0.49 | 1.87 | 0.79 | 1.26 | 0.39 | 0.63 | 4.16 | 4.31 | 68.60 | 73.10 |
| Scott (2010) | 4 | 24 | 24 | 36 | 36 | 2.25 | 2.25 | 7.9 | 7.9 | 4 | 4 | 1.00 | 1.00 | 4 | 5.4 | 65 | 65 |
| H. Hotta et al. (2012) | 5 | 1.97 | 3.15 | 7.34 | 7.34 | 0.53 | 0.89 | 0.22 | 0.22 | 0.79 | 3.15 | 0.38 | 0.38 | 5.06 | 5.70 | 66.28 | 66.28 |
| Marchetto et al. (2016) | 8 | 16.73 | 16.73 | 29.33 | 30.71 | 2.26 | 3.15 | 0.94 | 2.28 | 1.26 | 3.44 | 0.63 | 0.98 | 3.29 | 7.41 | 79.77 | 79.77 |
| Current study | 23** | 16 | 16 | 20.5 | 21.56 | 1.25 | 2.00 | 3.60 | 4.80 | 2.35 | 11.46 | 0.75 | 1.00 | 3.45 | 5.38 | 62.6 | 69.8 |

* The bend radii are taken as the radius of a standard hook if not reported in the literature.

** One specimen that experienced an anchorage failure is not included.

Note: Shaded rows indicate specimens included in the evaluation database.

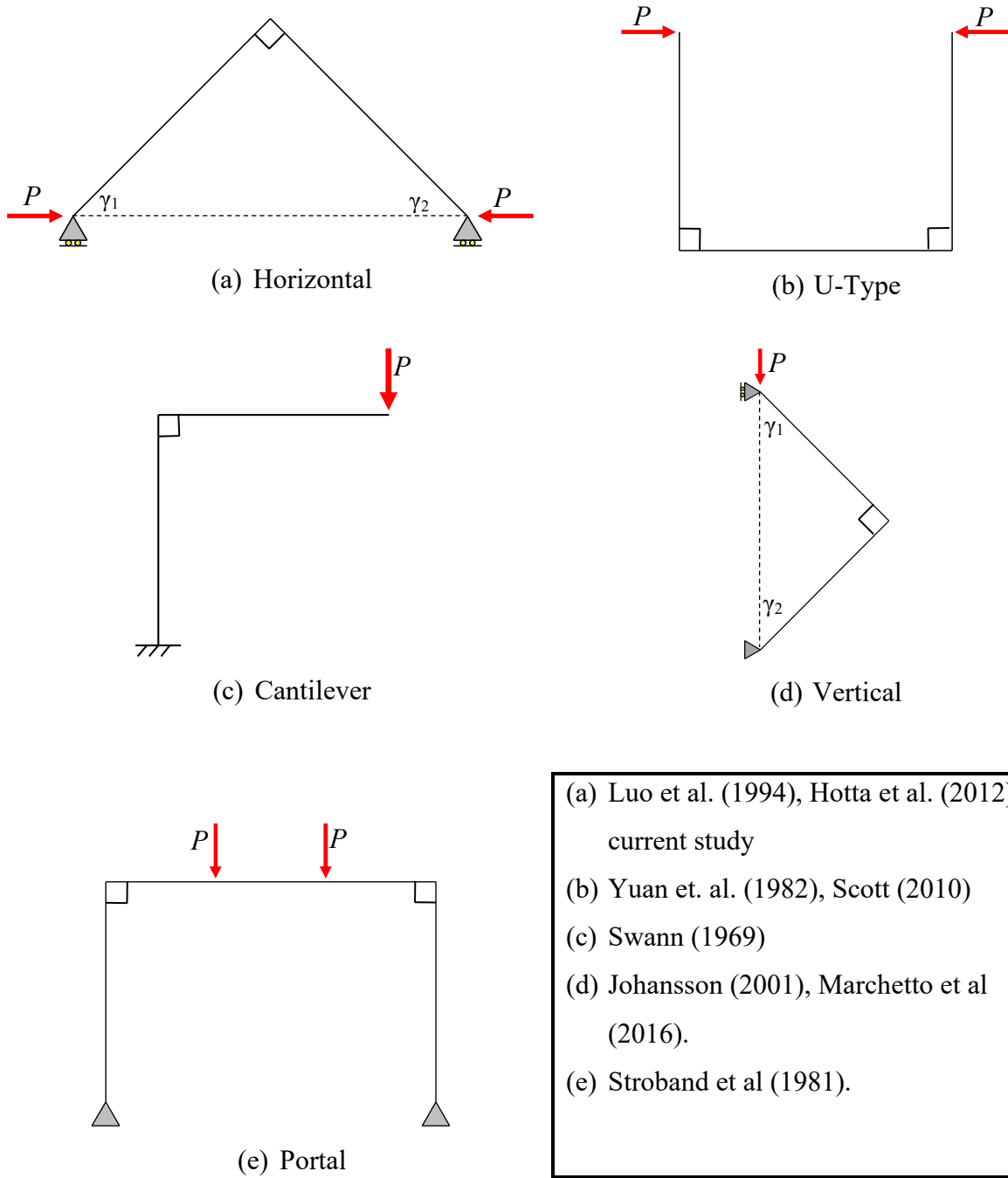


Figure 6-1 Schematics of loading configurations for specimens in the evaluation database

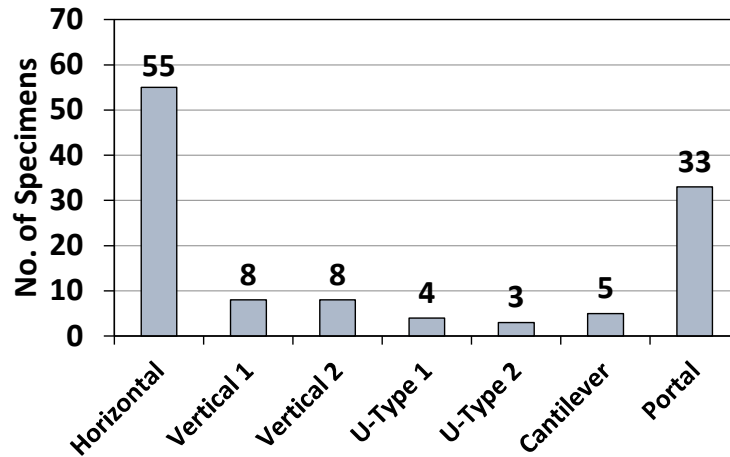


Figure 6-2 Number of specimens with each loading configuration in the evaluation database

A difficulty that had to be addressed was unifying the reported concrete compressive strengths from various testing methods. Reported concrete strengths in the evaluation database were from both cube tests and cylinder tests with varying sample sizes. It was necessary to convert the reported concrete compressive strengths to the same baseline to facilitate comparisons. Here, if cube strengths were used, the reported compressive strengths of concrete were converted to the corresponding cylinder strengths. Based on Reineck et al.,⁷⁸ for 4-in. cube specimens, the reported cube strengths, $f_{c,cube,100}$, were multiplied by 0.9 to obtain the equivalent cube strengths, $f_{c,cube}$. For 6-in. cube specimens, the reported strengths were directly taken as the cube strengths, $f_{c,cube}$. The obtained cube strengths were then multiplied by 0.75 to obtain the corresponding cube uniaxial strengths, $f_{1c,cube}$. The corresponding cylinder strengths f'_c were then taken as $f_{1c,cube}$ divided by 0.95.

When the strut-and-tie method is applied to the specimens in the database, a curved-bar node^{1,22} develops at the outer corner of closing knee joints. However, the bend radii of the longitudinal reinforcing bars were often not reported and needed to be assumed in most cases. When the bend radii were not reported, the radius of a standard hook was assumed. Among the evaluation database, the bend radius was assumed for 24 out of the 116 tests.

The distribution of primary variables in the evaluation database is presented in Figure 6-3. It can be seen in Figure 6-3(a) that the evaluation database included a wide range of mechanical longitudinal reinforcement ratios. Furthermore, 57 specimens had transverse reinforcement in the joint region while 59 specimens did not have transverse joint reinforcement. Some specimens,

however, were relatively small, having a joint width under 8 in. and a joint height under 12 in. Sixteen cases had a concrete compressive strength less than 2.5 ksi, while seventy-two cases had concrete compressive strengths suitable for general use (that is, minimum 2.5 ksi for general application) as required in Section 19.2.1.1 of ACI 318-19.¹ The details of the specimens in the evaluation database are included in Appendix C.

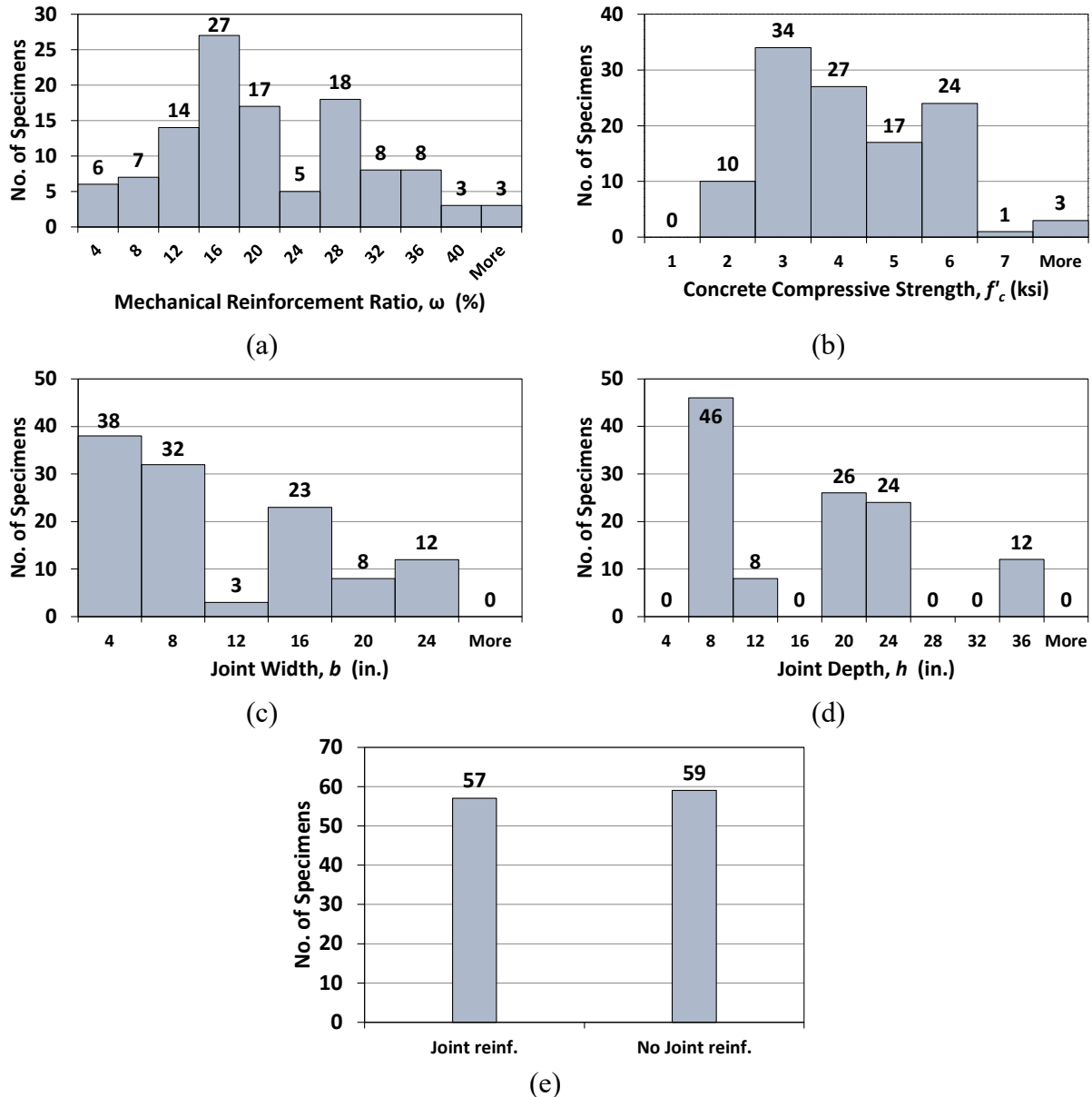


Figure 6-3 Histograms of primary variables in the evaluation database

6.3 Sectional Analysis and Joint Shear Capacity

Each specimen in the evaluation database was analyzed using conventional sectional methods based on joint shear capacity. More specifically, it was first determined if the joint shear capacity of a specimen was sufficient for the longitudinal reinforcement to develop its yield stress at the cross section corresponding to the face of the joint. If the joint shear strength was sufficient, the nominal flexural strength at the joint face was calculated and considered to be the moment capacity of the specimen in accordance with sectional methods. If the joint shear strength was not adequate to allow the longitudinal reinforcement to yield, the moment acting at the joint face that corresponds to the joint shear capacity (that is, the moment acting at the joint face when the joint shear strength is reached) was calculated and considered to be the capacity of the specimen using sectional methods. The calculations for determining the specimen capacities based on this approach are detailed in the following paragraphs.

In accordance with Section 15.4 of ACI 318-19,¹ the joint shear capacity of a closing knee joint can be expressed as Eq. 2-5. The shear demand is the total force in the longitudinal reinforcing bars as shown in Figure 2-19. With a known shear capacity (unfactored), the allowable bar stress carried by the knee joint can be calculated using Eq. 6-1.

$$f_s = \frac{V_n}{A_s} = \frac{\gamma \sqrt{f'_c} b_j h_j}{A_s} \leq f_y \quad 6-1$$

where b_j and h_j are the width and height of the effective joint cross section.

If the joint shear capacity of a knee joint is sufficient for the reinforcement to develop the yield stress of the bars, the flexural strength at the joint face can be calculated in accordance Section 22.3 of ACI 318-19.¹⁶ That is, the equivalent rectangular stress block is used as shown in Figure 6-4. The flexural strength is determined by solving Eq. 6-2 and Eq. 6-3 simultaneously. The relationship between a and f'_s is established by considering a linear strain profile, which is expressed as Eq. 6-4. In Eq. 6-4, E_s is the elasticity modulus of steel, taken as 29,000 ksi, ϵ_u is usable concrete strain, taken as 0.003, and β_1 is the ratio of the depth of the stress block to the depth of the neutral axis as required in Section 22.2.2.4.3 of ACI 318-19.¹

$$P_n + A_s f_y = 0.85 f'_c a b + A'_s (f'_s - 0.85 f'_c) \quad 6-2$$

$$M_n = A_s f_y \left(d - \frac{h}{2} \right) + 0.85 f'_c ab \left(\frac{h}{2} - \frac{a}{2} \right) + A'_s (f'_s - 0.85 f'_c) \left(\frac{h}{2} - d' \right) \quad 6-3$$

$$f'_s = E_s \epsilon_u \frac{a/\beta_1 - d'}{a/\beta_1} \quad 6-4$$

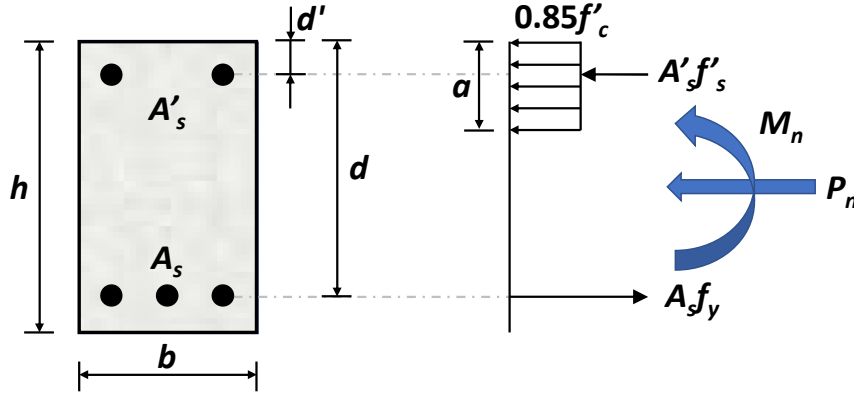


Figure 6-4 Notation for sectional analysis at nominal flexural strength

The axial force P_n and moment M_n in Figure 6-4 are acting on the cross section corresponding with the joint face. For the different test setups shown in Figure 6-1, both values are related to the external load, P , applied to the specimen. Except for the Portal loading configuration, all other cases are statically determinate, and the relationship between P , P_n , and M_n is determined directly by equilibrium. For the Portal system, , an elastic structural analysis can be conducted to determine the reactions, and therefore the internal forces, as shown in Figure 6-5. The relationships among P , P_n , and M_n for each test setup are summarized in Table 6-2. The angles represented by γ_1 and γ_2 are labeled in Figure 6-1.

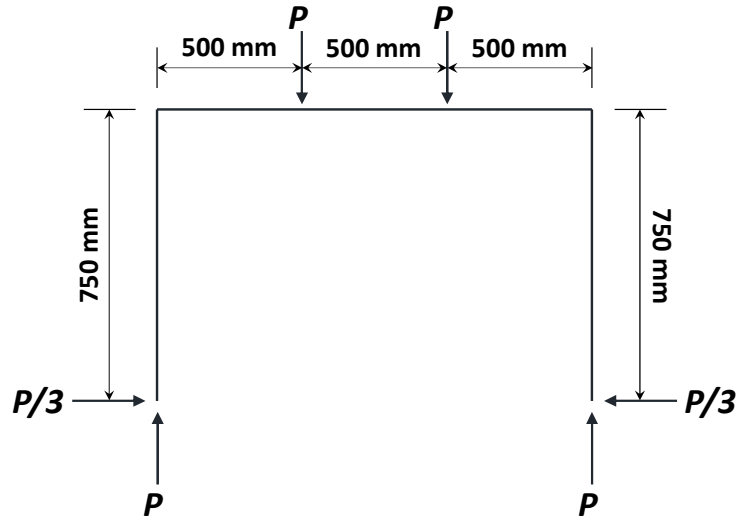


Figure 6-5 Structural analysis for Portal system

Table 6-2 Relationship between applied load, internal axial force, and bending moment at the joint face

| Frame Type | P_n | M_n^* |
|------------|--|--|
| Horizontal | $P \cos \gamma_1$ or $P \cos \gamma_2$ | $l_n P \sin \gamma_1$ or $l_n P \sin \gamma_2$ |
| Vertical | $P \cos \gamma_1$ | $l_n P \sin \gamma_1$ |
| U-Type | 0 | $P l_n$ |
| Cantilever | 0 | $P l_n$ |
| Portal** | $\frac{1}{3} P$ | $7.48 P$ (kip-in.) $190 P$ (N-mm) |

* l_n represents the distance between the applied load and the joint face.

** For detailed calculations, refer to Appendix B.

If the joint shear capacity of a knee joint is not sufficient for the reinforcement to develop the yield stress of the bars, the flexural strength is then determined assuming a bar stress calculated using Eq. 6-1. In this case, the compressive stress distribution in the concrete on the compression side of the neutral axis (see Figure 6-6) is based on the modified Hognestad stress-strain model^{17,79,80} as shown in Figure 6-7, in which the value of E_c was taken as $57,000\sqrt{f'_c}$ psi for simplicity. The capacity based on joint shear analysis was determined by solving Eq. 6-5 and Eq.

6-6 simultaneously. The relationship between c and f'_s is established by considering a linear strain profile.

$$P_n + A_s f_s = \int_0^c f_c b dy - f_c|_{y=c-d'} A'_s + A'_s f'_s \quad 6-5$$

$$M_n = \left(\frac{h}{2} - c + \bar{y} \right) \left[\int_0^c f_c b dy \right] + A_s f_s \left(d - \frac{h}{2} \right) + A'_s (f'_s - f_c|_{y=c-d'}) \left(\frac{h}{2} - d' \right) \quad 6-6$$

where \bar{y} is the location of the resultant of the compressive stress measured from the neutral axis and is calculated using Eq. 6-7.

$$\bar{y} = \frac{\int_0^c f_c b y dy}{\int_0^c f_c b dy} \quad 6-7$$

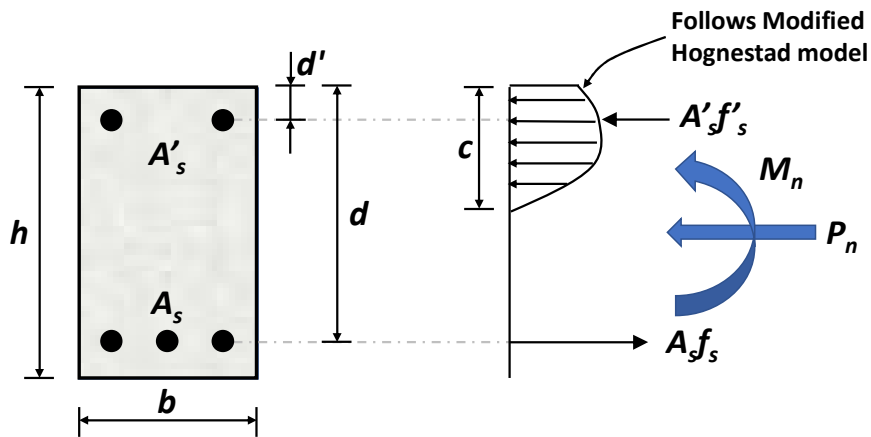


Figure 6-6 Notation for sectional analysis if longitudinal reinforcement has not yielded

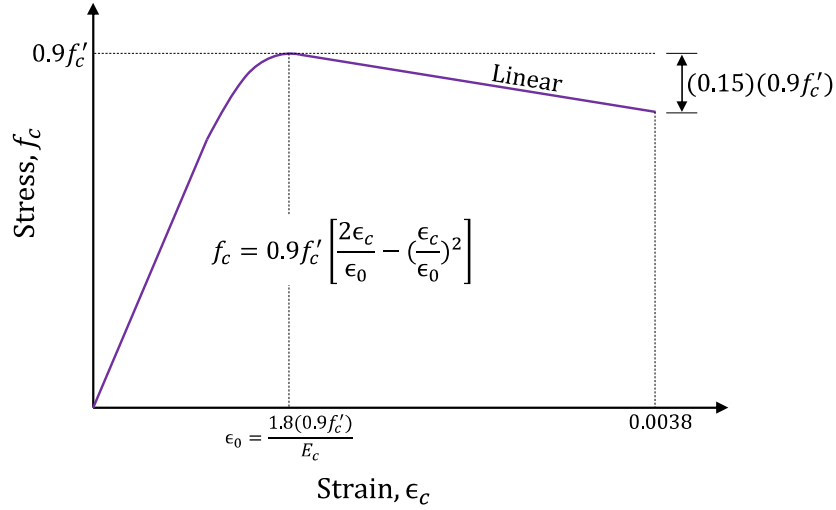


Figure 6-7 Modified Hognestad model (adapted from Hognestad^{80,79} and Wight et al.¹⁷)

6.4 Development of the Strut-and-Tie Model

6.4.1 Strut-and-Tie Models for Various Loading Configurations

To properly reflect the stress flow in the specimens of the evaluation database, the strut-and-tie model for each specimen should be constructed in a manner consistent with the applied loads acting on the specimen. Therefore, the various loading configurations illustrated in Figure 6-1 require different strut-and-tie models. Four different patterns for the strut-and-tie models within the D-region near the joint were selected and are illustrated in Figure 6-8. In the figure, solid red lines represent ties, green dashed lines represent struts, and black dots represent nodes. The corresponding tie forces and strut forces within each model are denoted symbolically.

For the Horizontal, Vertical 1, and Portal loading configurations, because the applied loads were outside the D-region a strut-and-tie model was only developed for the D-region as illustrated in Figure 6-8(a). In the D-region, longitudinal ties were arranged at the top (denoted as T_2 and T'_2) and the left side (denoted as T_1 and T'_1) to reflect tension resulting from the closing moments. Struts were placed along the compression zone of both legs (denoted as C_{H1} , C'_{H1} , C_{H2} , and C'_{H2}) to model the flexural compressive stress. The diagonal strut that extends across the joint (denoted as C_{st}) connects the CTT node located at the intersection of the ties at the outer corner and the CCC node at the intersection of the struts at the re-entrant corner. The strut angle θ_c is measured from the tie T_1 and is less than or equal to 45 degrees. Inclined struts and transverse ties were used to

carry the shear force in the legs. The orientation of the inclined struts in the horizontal member (denoted as C_{I2} and C'_{I2}) shown in

Figure 6-8(a) is defined by angle α . Similarly, the inclined struts in the vertical member (denoted as C_{I1} and C'_{I1}) were oriented at an angle β from the longitudinal strut. A transverse tie (denoted as T_{1s} and T_{2s}) was positioned in each member as appropriate. The values of α and β are not important because the struts from each member that intersect at the CCC node located at the reentrant corner will be resolved together when analyzing the node as detailed in Section 6.4.2.

The adjoining members of the Vertical 2 configuration, which was used by Marchetto et al.,^{15,16} had smaller aspect ratios compared to the specimens loaded in the Horizontal and Vertical 1 configurations, and the entire specimen was categorized as a D-region because the leg length was short compared to the cross-sectional depth. All specimens loaded in the Vertical 2 configuration were symmetrical. The strut-and-tie model developed for the Vertical 2 configuration is shown in Figure 6-8(b). In this case, only one inclined strut was needed within each leg (denoted as C_I). A transverse tie in each leg (denoted as T_s) resisted the shear force in the members. A single strut extended from the end of this tie to the applied load point and carried a compressive force equal to the applied load P . Moreover, because of symmetry, the two longitudinal ties extending from the CTT node at the outer corner of the joint force (denoted as T) resisted equal forces as did the longitudinal struts intersecting at the CCC node (denoted as C_H). The strut that extended across the joint region (denoted by C_{st}) is oriented at an angle of 45 degrees with the ties.

The strut-and-tie model for the Cantilever and U-Type 2 configurations is shown in Figure 6-8(c). For the two specimen types, the applied point loads were relatively far from the joint and therefore not shown in the figure. Using the same concepts applied for the other strut-and-tie models, longitudinal ties were arranged along the adjoining members (denoted as T_1 and T_2 as shown in Figure 6-8(c)). Longitudinal struts were also positioned along the members. A single longitudinal strut (denoted as C_{H1}) is located along the vertical member in Figure 6-8(c) due to the constant moment within the member. With varying moment, two longitudinal struts (denoted as C_{H2} and C'_{H2}) were positioned along the horizontal member in the figure. Inclined struts and a transverse tie were used to carry the shear force in the horizontal member. The vertical member carried no shear and therefore contained no inclined struts or transverse ties. Again, the strut extending across the joint (denoted as C_{st}) connected the CTT node near the outer corner and the

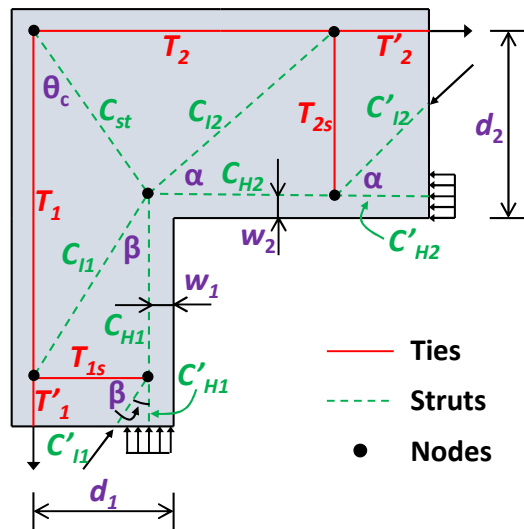
CCC node near the re-entrant corner. The diagonal strut has an acute angle of θ_c measured from the longitudinal tie in the vertical member (that is, the member carrying no shear).

Unlike the Cantilever and U-Type 2 configurations, the external applied load of the U-Type 1 loading system was located relatively close to the joint, and therefore the D-region extended to this point load as shown in Figure 6-8(d). In this case, a single inclined strut (denoted as C_{I2}) connected the CCC node near the re-entrant corner and the node at which the applied load was introduced to the specimen. This inclined strut was oriented at an angle α with the longitudinal axis of the adjoining member. Other details of the strut-and-tie model are similar to those of the model used for the Cantilever and U-Type 2 configurations.

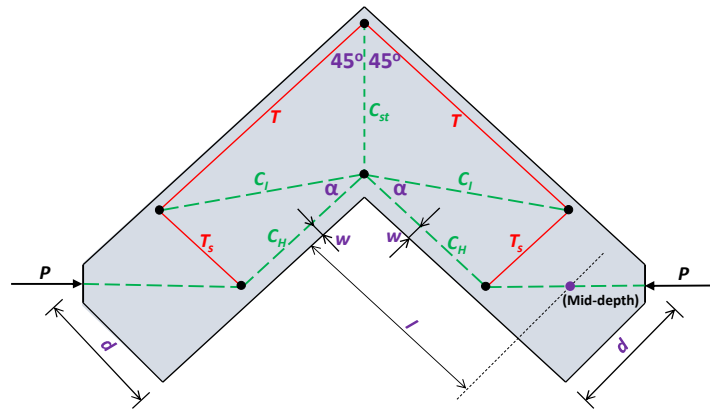
The position of the CCC node near the re-entrant corner was defined using the dimensions w_1 and w_2 , as shown in Figure 6-8. Furthermore, the longitudinal ties were aligned with the centroid of the longitudinal reinforcing bars, and the position of the CTT node was defined by the intersection of the ties. Therefore, the diagonal strut angle θ_c can be calculated using Eq. 6-8. It should be noted that for all specimens loaded in the Vertical 2 configuration, both values of θ_c are equal to 45 degrees due to symmetry.

$$\theta_c = \tan^{-1} \frac{d_1 - w_1}{d_2 - w_2} = \frac{l_{p1}}{l_{p2}} \quad 6-8$$

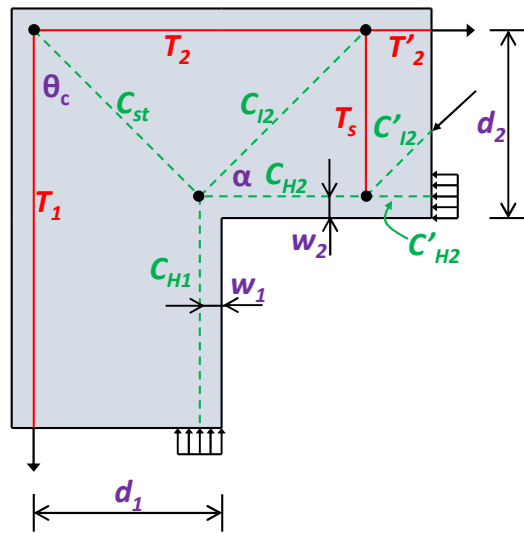
Here, l_{p1} and l_{p2} are the distances between the longitudinal tie and the longitudinal strut in the adjoining members (that is, legs) of the specimen.



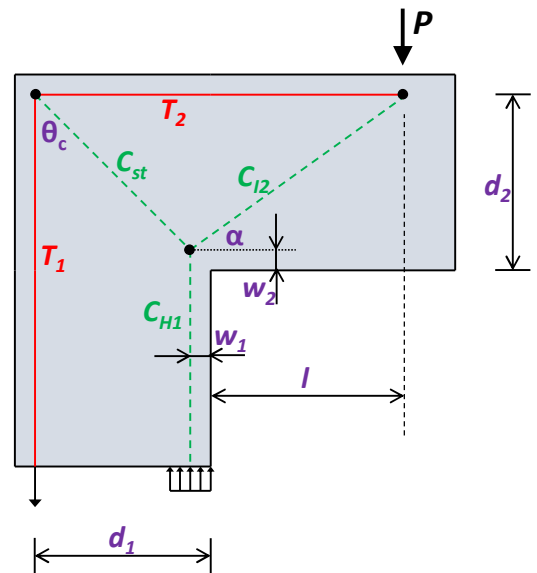
(a) Horizontal, Vertical 1, or Portal



(b) Vertical 2



(c) Cantilever and U-Type 2



(d) U-Type 1

Figure 6-8 Selected strut-and-tie models for different loading configurations

6.4.2 Calculation of Internal Forces

After the geometry of the strut-and-tie model was determined, the forces in the struts and ties could be determined and expressed in terms of the external load, P . The calculated longitudinal tie forces T_1 and T_2 (see Figure 6-8) in terms of P are summarized in Table 6-3 for each study included in the evaluation database. Detailed calculations and other forces are provided in Appendix B.

For the purpose of sizing the CCC node near the re-entrant corner, the inclined strut and the horizontal strut coming from each adjoining member were resolved together, where applicable, to create a node with only three concurrent struts. In other words, the struts C_{H2} and C_{I2} were resolved to create F_b , and the struts C_{H1} and C_{I1} were resolved to create F_c , as shown in Figure 6-9. The strut C_{st} that extends across the joint remained unchanged and has a force denoted as F_a . For strut-and-tie model type (b) in Figure 6-8, F_b is equal to F_c , both of which were resolved from C_H and C_I due to symmetry. The procedure of resolving the struts was not applied to strut-and-tie model type (d) because only three struts frame into the CCC node.

In Figure 6-9, θ_1 and θ_2 are the angles between the resolved struts (with forces F_b and F_c) and the longitudinal axis of the applicable member (this is, leg). It should be noted that θ_1 is equal to zero for strut-and-tie model types (c) and (d) in Figure 6-8. Moreover, strut-and-tie model type (d) has a value of θ_2 equal to α . The formulas developed for the forces F_b and F_c of the resolved struts and the orientations θ_1 and θ_2 of these struts are summarized in Table 6-4 and Table 6-5, respectively. It can be observed that for strut-and-tie model types (a) and (c), the angles α and β introduced in Section 6.4.1 were not included in the results. The values of these angles can be arbitrarily chosen without affecting the results. In this database analysis, α and β were selected as 45 degrees. For strut-and-tie model types (b) and (d), the angle α is a function of the specimen geometry and loading. The angle α for model types (b) and (d) are expressed in Eq. 6-9 and Eq. 6-10, respectively. In Eq. 6-9, h represents the total depth of the cross-section.

$$\alpha = \tan^{-1} \frac{d - w}{l + w - (h - w) \sin 45^\circ} \quad 6-9$$

$$\alpha = \tan^{-1} \left(\frac{d_2 - w_2}{l + w_1} \right) \quad 6-10$$

Table 6-3 Magnitudes of tie forces

| STM Type* | Study | T_1 | T_2 |
|-----------|-------------------------|--|--|
| (a) | Current study | $\frac{P}{l_{p1}} \left[\sin \gamma_1 (l_1 + w_2) - \cos \gamma_1 \left(\frac{h_1}{2} - w_1 \right) \right]$ | $\frac{P}{l_{p2}} \left[\sin \gamma_2 (l_2 + w_1) - \cos \gamma_2 \left(\frac{h_2}{2} - w_2 \right) \right]$ |
| | Johansson (2001) | | |
| | H. Hotta et al. (2012) | | |
| | Luo et al. (1994) | | |
| | Stroband et al. (1981) | $\frac{P}{l_{p1}} \left(\frac{l}{2} - \frac{2}{3}h + w_1 + \frac{1}{3}w_2 \right)$ | $\frac{P}{l_{p2}} \left(\frac{l}{2} - \frac{2}{3}h + w_1 + \frac{1}{3}w_2 \right)$ |
| (b) | Marchetto et al. (2016) | $\frac{\sqrt{2}}{2} P \frac{l + w - \frac{\sqrt{2}}{2}(h - w)}{d - w} = \frac{\sqrt{2}}{2} P \cot \alpha$ | $\frac{\sqrt{2}}{2} P \frac{l + w - \frac{\sqrt{2}}{2}(h - w)}{d - w} = \frac{\sqrt{2}}{2} P \cot \alpha$ |
| (c) | Swann (1969) | $P \frac{l + w_1}{l_{p2}} \cot \theta_c$ | $P \frac{l + w_1}{l_{p2}}$ |
| | Yuan et al. (1982) | | |
| (d) | Scott (2011) | $P \cot \alpha \cot \theta_c$ | $P \cot \alpha$ |

* Refer to Figure 6-8.

Note:

1. l_1 and l_2 represent the distance from the intersection of the extension of the load and the centerline of the cross section to the joint face, where the subscript numbers correspond to the side with the load angle γ_1 and γ_2 .
2. Except for Marchetto et al., the parameter l represents the distance between the load and the joint face.
3. h_1 and h_2 represent the cross-sectional depth, where the subscript numbers correspond to the side with the load angle γ_1 and γ_2 .

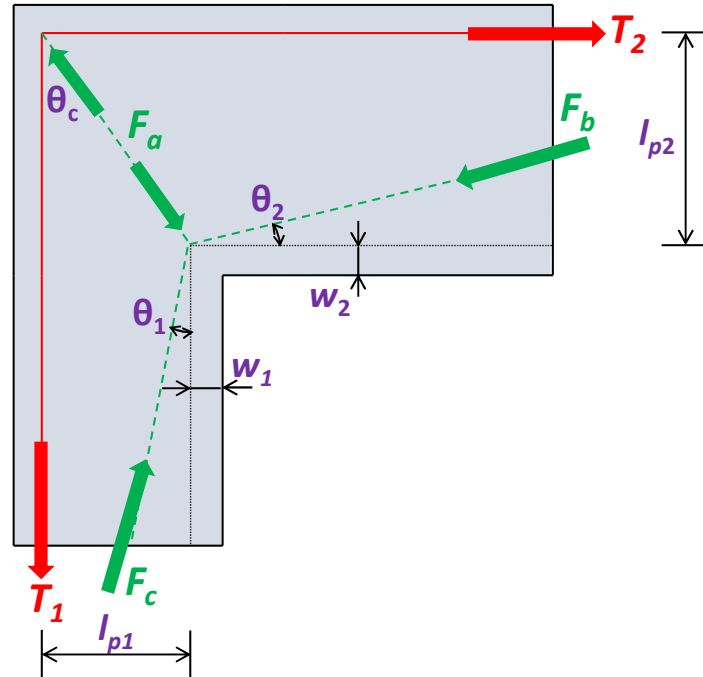


Figure 6-9 Resolved struts and resulting orientations

Table 6-4 Magnitudes of resultant strut forces

| STM Type | Study | F_a | F_b | F_c |
|----------|-------------------------|------------------------|--|--|
| (a) | Current study | $\sqrt{T_1^2 + T_2^2}$ | $P \sqrt{\left[\frac{\sin \gamma_2 (l_2 + w_1) + \cos \gamma_2 (d_2 - \frac{h_2}{2})}{l_{p2}} \right]^2 + \sin^2 \gamma_2}$ | $P \sqrt{\left[\frac{\sin \gamma_1 (l_1 + w_2) + \cos \gamma_1 (d_1 - \frac{h_1}{2})}{l_{p1}} \right]^2 + \sin^2 \gamma_1}$ |
| | Johansson (2001) | | | |
| | H. Hotta et al. (2012) | | | |
| | Luo et al. (1994) | | | |
| | Stroband et al. (1981) | | | |
| (b) | Marchetto et al. (2016) | $\sqrt{T_1^2 + T_2^2}$ | $\frac{\sqrt{2}}{2} P \sqrt{1 + (1 + \cot \alpha)^2}$ | $\frac{\sqrt{2}}{2} P \sqrt{1 + (1 + \cot \alpha)^2}$ |
| (c) | Swann (1969) | | $P \sqrt{\left(\frac{l + w_1}{d_2 - w_2} \right)^2 + 1}$ | $P \left(1 + \frac{l + w_1}{l_{p2}} \cot \theta_c \right)$ |
| | Yuan et al. (1982) | | | |
| (d) | Scott (2011) | | $P \csc \alpha$ | $P (1 + \cot \alpha \cot \theta_c)$ |

Note: notation used in this table follows the same definitions as previously defined.

Table 6-5 Orientations of resolved struts

| STM Type | Study | θ_1 | θ_2 |
|----------|-------------------------|--|--|
| (a) | Current study | $\tan^{-1} \left(\frac{l_{p1} \sin \gamma_1}{(l_1 + w_2) \sin \gamma_1 - \left(\frac{h_1}{2} - d_1 \right) \cos \gamma_1} \right)$ | $\tan^{-1} \left(\frac{l_{p2} \sin \gamma_2}{(l_2 + w_1) \sin \gamma_2 - \left(\frac{h_2}{2} - d_2 \right) \cos \gamma_2} \right)$ |
| | Johansson (2001) | | |
| | H. Hotta et al. (2012) | | |
| | Luo et al. (1994) | | |
| | Stroband et al. (1981) | $\cot^{-1} \left[\frac{3}{l_{p1}} \left(l_{p1} + \frac{L}{2} - \frac{2h}{3} + w_1 + \frac{w_2}{3} \right) \right]$ | $\cot^{-1} \left[\frac{1}{l_{p2}} \left(\frac{l_{p2}}{3} + \frac{L}{2} - \frac{2h}{3} + w_1 + \frac{w_2}{3} \right) \right]$ |
| (b) | Marchetto et al. (2016) | $\tan^{-1} \frac{1}{1 + \cot \alpha}$ | $\tan^{-1} \frac{1}{1 + \cot \alpha}$ |
| (c) | Swann (1969) | 0 | $\tan^{-1} \left(\frac{d_2 - w_2}{l + w_1} \right)$ |
| | Yuan et al. (1982) | | |
| (d) | Scott (2011) | 0 | α |

Note: notation used in this table follows the same definitions as previously defined.

6.4.3 Sizing the CTT node and the CCC node

The CCC node near the re-entrant corner was modeled as a hydrostatic node. That is, all faces of the CCC node are subjected to a stress with the same magnitude, and each of the three struts framing into the node are perpendicular to the corresponding nodal face as shown in Figure 6-10. Restricted by the re-entrant corner, the widths of the two faces perpendicular to the resolved struts with forces of F_b and F_c can be geometrically expressed as Eq. 6-11 and Eq. 6-12, respectively:

$$w_b = 2\sqrt{w_1^2 + w_2^2} \cos(\theta^* - \theta_2) \quad 6-11$$

$$w_c = 2\sqrt{w_1^2 + w_2^2} \cos\left(\frac{\pi}{2} - \theta^* - \theta_1\right) \quad 6-12$$

where the dimensions w_b and w_c are shown in Figure 6-10, and θ^* is expressed as Eq.

$$\theta^* = \tan^{-1} \frac{w_1}{w_2}$$

Because the CCC node is a hydrostatic node, Eq. 6-13 can be used to determine the width w_a labeled in Figure 6-10 (that is, the width of the diagonal strut where it intersects with the CCC node) using the known strut forces. Therefore, the widths of the three faces of the CCC node are related to w_1 and w_2 .

$$w_a : w_b : w_c = F_a : F_b : F_c \quad 6-13$$

The CTT node at the outer corner was modeled as a curved-bar node if continuous longitudinal reinforcing bars passed through the outer corner or if the bars were individually anchored with a 90-degree hook (see Figure 2-5). In this case, the width of the nodal face perpendicular to the diagonal strut, w_s , is $\sqrt{2}r_b$ according to Klein.²² It should be noted that the effect of circumferential bond stress along the bar bend was not considered for sizing the curved-bar node. If the longitudinal reinforcing bars were headed and anchored at the outer corner, which is the case for two specimens in the evaluation database, the width of the node at the interface with the diagonal strut, w_s , was related to the width of the heads, w_{h1} and w_{h2} , and taken as $w_{h1} \sin \theta_c + w_{h2} \cos \theta_c$ as indicated in Figure 6-11.^{47,56}

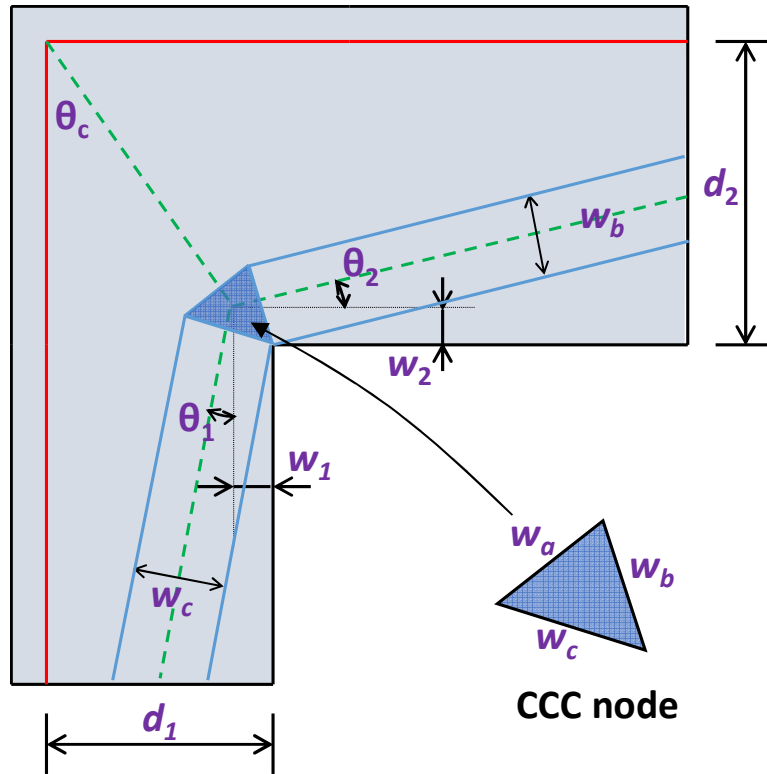


Figure 6-10 Geometry of the CCC node as a hydrostatic node

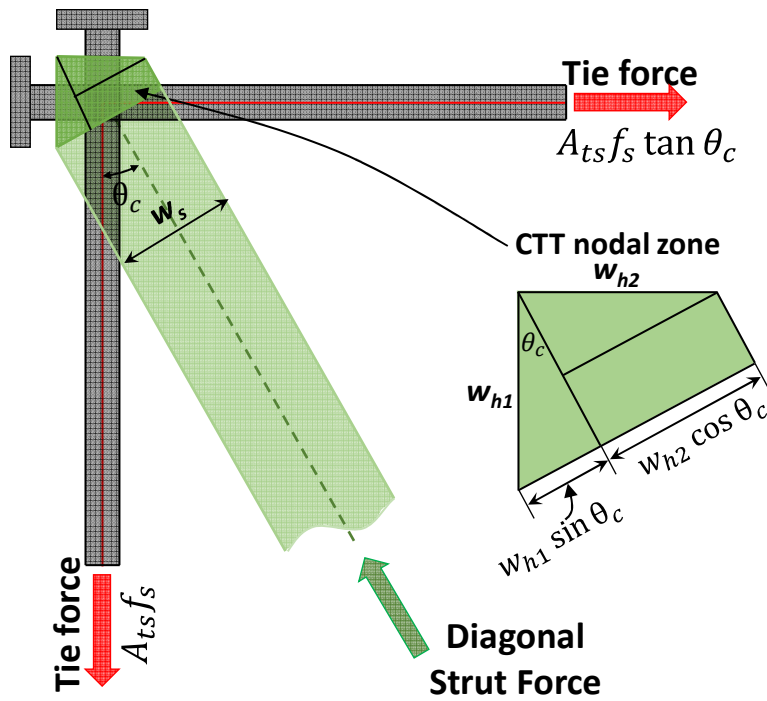


Figure 6-11 Geometry of the CTT node when headed bars were used

6.4.4 Determination of Load Capacity

The calculated load-carrying capacity, P_{STM} , of a specimen was taken as the magnitude of the applied load P when the most critical component of the strut-and-tie model reached its calculated strength. For the strut-and-tie models shown in Figure 6-8, the CTT node at the outer corner, the CCC node at the re-entrant corner, and the three struts (including the strut that extends across the joint) framing into the CCC node were considered as potential critical components. Tie forces T_1 and T_2 were also limited by the yield strength of the longitudinal reinforcement.

The strength of the face of the CTT node can be expressed as Eq. 6-14 in accordance with Section 23.9 of ACI 318-19.¹ It should be noted that the confinement modification factor, β_c , was not applied here because no bearing surface was associated with the node. In addition, b_s was taken as the cross-sectional width of the specimen as was done in Chapter 4.

$$F_{nn,CTT} = 0.85\beta_n f'_c b_s w_s \quad 6-14$$

If the CTT node was modeled as a curved-bar node, a modification factor for clear side cover was applied to reflect the potential reduction in strength due to insufficient clear side cover. As suggested in the current design code¹ and by Klein,²² the required bend radius (and thus the bearing area under the bar bend) should be enlarged by a factor of $2d_b/c_c$ if the clear side cover is less than twice the longitudinal bar diameter. The modification implies that the strength of curved-bar nodes is proportionally reduced as the clear side cover decreases when the side cover is thinner than $2d_b$. Therefore, the strength of the face of the curved-bar node can be expressed as

$$F_{nn,CTT} = 0.85\beta_n f'_c b_s w_s \left(\frac{c_c}{C_f d_b} \right) \quad 6-15$$

where the factor C_f was named as the clear side cover parameter, which is equal to 2 in ACI 318-19.¹ It should be noted that the factor $\left(\frac{c_c}{C_f d_b} \right)$ should not be taken greater than 1.0.

The strength of the ties with forces T_1 and in T_2 that intersect at the CTT node was taken as the product of the area of reinforcing bars and the yield strength in accordance with Section 23.7.2 of ACI 318-19.¹ The strength of the ties is expressed as

$$F_y = A_{ts} f_y \quad 6-16$$

If the yield strength or the area of reinforcing bars in the two adjoining members of the specimen were different, the tie strengths were denoted as F_{y1} and F_{y2} for the ties with forces T_1 and T_2 , respectively.

The strength of the strut that extends across the joint was calculated based on the width of the interface with the CTT node near the outer corner, as presented in Eq. 6-17. This equation is written in accordance with Section 23.4 of ACI 318-19.¹ Again, the confinement modification factor, β_c , was not applied.

$$F_{ns} = 0.85\beta_s f'_c b_s w_s \quad 6-17$$

With the constraints of Eq. 6-14 to Eq. 6-17 and under the condition of equilibrium at the CTT node, the allowable force transmitted through the strut that extends across the joint can be expressed as

$$F_{na} = \min \left\{ F_{nn,CTT}, F_{ns}, \frac{F_{y1}}{\cos \theta_c}, \frac{F_{y2}}{\sin \theta_c} \right\} \quad 6-18$$

After determining the allowable force transmitted through the strut that extends across the joint, the load-carrying capacity P can be expressed as a function of w_1 and w_2 by first equating Eq. 6-18 to the internal force (that is, the demand) of the strut (see F_a in Table 6-4) as stated in Eq. 6-19.

$$F_{na} = F_a = \sqrt{[T_1(P, w_1, w_2)]^2 + [T_2(P, w_1, w_2)]^2} \quad 6-19$$

It should be noted that T_1 and T_2 given in Table 6-3 can be written in terms of P , w_1 , and w_2 , as indicated in Eq. 6-19, by inputting known values based on specimen geometry, reinforcement location, and writing all other variables in terms of w_1 and w_2 .

If Eq. 6-19 is rearranged to solve for the load-carrying capacity P , the value of P can be maximized by adjusting the values of w_1 and w_2 under the condition that sufficient strength is provided to the CCC node near the re-entrant corner and the ends of the three struts that intersect at the CCC node. In other words, w_1 and w_2 can be defined so that the width of three interfaces, w_a , w_b , and w_c (see Figure 6-10), are just large enough to resist the forces acting at the interfaces. The width of the three faces, as mentioned previously, are determined by geometry as shown in Eq. 6-11 to Eq. 6-13. Because the nodal zone coefficient for CCC nodes is equal to 1.0 in ACI 318-19,¹ the strengths at the interfaces between the struts and the node are assumed to be governed by the struts. The appropriate strut coefficient will be evaluated later and is assumed not to be

greater than 1.0. Therefore, only the strengths of the three struts intersecting at the CCC node, as expressed in Eq. 6-20 to Eq. 6-22, were used as constraints to solve for the values of w_1 and w_2 .

$$F_a \leq 0.85\beta_s f'_c b_s w_a \quad 6-20$$

$$F_b \leq 0.85\beta_s f'_c b_s w_b \quad 6-21$$

$$F_c \leq 0.85\beta_s f'_c b_s w_c \quad 6-22$$

6.4.5 Parameters for the Strut-and-Tie Model

The equations previously introduced that are used to determine the strengths of the critical elements of the strut-and-tie models include the following parameters that can be evaluated based on experimental results: the nodal zone coefficient β_n , the strut coefficient β_s , and the clear side cover parameter C_f . For the purpose of evaluating the ACI-based strut-and-tie method, two sets of parameters were used to calculate the load-carrying capacity, P , as summarized in Table 6-6. The first set is in accordance with Sections 23.4.3, 23.9.2, and 23.10.3 of ACI 318-19.¹ The second set of parameters is based on the experimental results of the current study. The CTT nodal zone coefficient was specified as 1.0 because it was observed that only half the required bend radius given by Eq. 2-20 was needed to reach an uncompromised strength for closing knee joints based on the results of the current study. Moreover, the strut coefficients were specified as 1.0. It was not necessary to take a lower strut coefficient than the CTT nodal zone coefficient. Otherwise, the diagonal strut would control the strength of the interface. In addition, it was also observed that a C_f -value of 1.5 led to improved results as explained in Section 5.4.2. It should be noted that the modified coefficients are considered for strength assessment only. The current factors in ACI 318-19 are still deemed appropriate for design. For curved-bar nodes, it has been shown that the current code-defined nodal zone coefficient for CTT results in ductile behavior.

Table 6-6 Coefficients for the strut-and-tie model

| Coefficient | Based on ACI 318-19 ¹ | Modified |
|--|-------------------------------------|----------|
| CTT nodal zone coefficient, β_n | 0.6 | 1.0 |
| CCC nodal zone coefficient, β_n | 1.0 | 1.0 |
| Coefficient for strut in beam-column joint, β_s | 0.75 | 1.0 |
| Coefficient for interior strut, β_s | 0.75 | 1.0 |
| Clear side cover parameter, C_f | 2.0 | 1.5 |

6.5 Results and Discussion

The specimens of the current study and in the evaluation database were evaluated based on (1) sectional analysis and joint shear capacity as outlined in Section 6.3 and (2) the strut-and-tie method as described in Section 6.4. Prior to presenting the results of the evaluation, it is convenient to introduce a parameter, the diagonal strut width ratio η , to facilitate the evaluation of the strength-predicting methods. Expressed as Eq. 6-23, the value of η is defined as the ratio of the width of the interface between the diagonal strut and the CTT node, w_s , to the required width of this interface, based on strength calculations, that would allow the ties intersecting at the CTT node to yield at the moment the compressive strength at the interface is reached. This interface width is denoted as w_{sb} and can be expressed as Eq. 6-24. In other words, if a specimen has a value of η greater than 1.0, the stress acting on the interface would not exceed the effective compressive strength of concrete, and theoretically no failure should occur at the CTT node or at the intersecting strut. It should be noted that the nodal zone coefficient, β_n , in Eq. 6-24 is taken as 0.6, and the clear side cover parameter C_f is taken as 2.0 based on ACI 318-19.¹

$$\eta = \frac{w_s}{w_{sb}} \quad 6-23$$

$$w_{sb} = \frac{\min\left\{\frac{F_{y1}}{\cos \theta_c}, \frac{F_{y2}}{\sin \theta_c}\right\}}{0.85\beta_n f'_c b_s \left(\frac{C_f d_b}{c_c}\right)} \quad 6-24$$

6.5.1 Evaluation of ACI Sectional Analysis and Joint Shear Capacity

6.5.1.1 Data from the experimental program of the current study

The test results of the knee joint specimens described in Chapters 4 and 5 were used as part of the evaluation database. The strength ratio P_{test}/P_{calc} based on the sectional analysis and joint shear capacity approach described in Section 6.3 is plotted against the diagonal strut width ratio η in Figure 6-12 for the specimens of the current research program. In the figures, datapoints shown as blue triangles indicate specimens with sufficient joint shear capacity according to Eq. 2-5, allowing the yield stress of the longitudinal reinforcing bars to develop (refer to Eq. 6-1). On the other hand, datapoints shown as orange asterisks indicate specimens with insufficient joint shear capacity. The experimental and analytical results are summarized in Table 6-7.

Figure 6-12(a) shows the results for the strength ratio if the calculated joint shear capacity is neglected. That is, all specimens were analyzed under the assumption that the longitudinal reinforcement yields before the concrete crushes. The red dashed line indicates a strength ratio of 1.0, separating conservative predictions and unconservative predictions. As shown in the figure, all specimens achieved P_{calc} when the value of η was greater than 0.5, which is the same observation described in Chapter 5. There are five unconservative predictions for values of η less than 0.5, including two specimens without sufficient shear capacity. However, two specimens achieved their calculated flexural strength even though strength calculations indicate that the specimens do not have an adequate joint shear area to allow the yield stress of the bars to develop at the joint face.

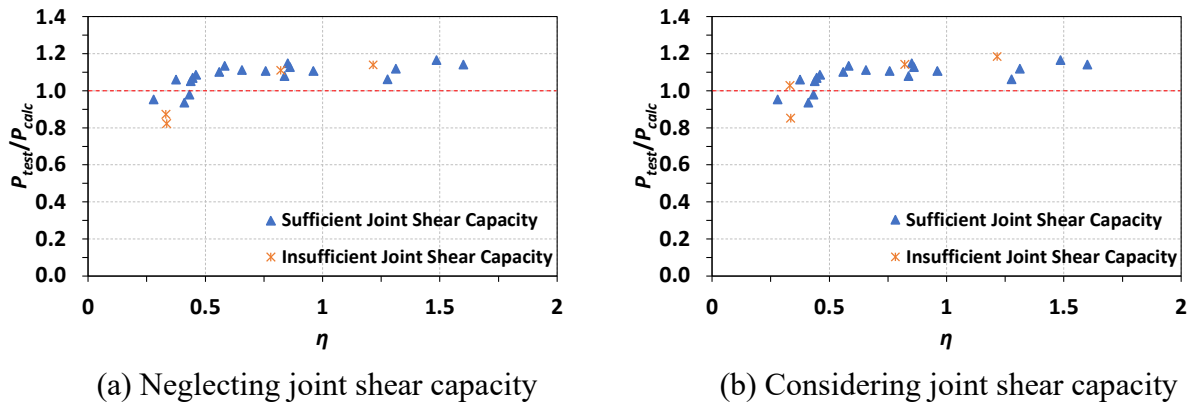


Figure 6-12 Strength ratio based on sectional analysis versus diagonal strut width ratio for specimens in the current study

Table 6-7 Summary of analysis results using sectional analysis for specimens in the current study

| Series | Specimen ID | η | P_{test} (kip) | P_{calc}^{**} (kip) | P_{test}/P_{calc} | P_{calc}^{***} (Joint shear) (kip) | P_{test}/P_{calc} (Joint shear) |
|-----------|-------------|--------|---------------------|--------------------------|---------------------|--|--------------------------------------|
| S-Series* | S-27-R3-L | 0.33 | 113 | 129.4 | 0.87 | 109.9 | 1.03 |
| | S-18-R3 | 0.44 | 145 | 138.1 | 1.05 | 137.2 | 1.08 |
| | S-18-R6 | 0.84 | 148 | 137.3 | 1.08 | 137.5 | 1.06 |
| | S-18-R9 | 1.28 | 146 | 137.6 | 1.06 | 108.4 | 1.13 |
| | S-13-R3 | 0.58 | 123 | 108.3 | 1.14 | 108.8 | 1.15 |
| | S-13-R5 | 0.85 | 125 | 108.7 | 1.15 | 109.0 | 1.17 |
| | S-13-R8 | 1.49 | 127 | 108.8 | 1.17 | 129.1 | 0.85 |
| D-Series | D-20-R2 | 0.33 | 110 | 133.7 | 0.82 | 130.4 | 1.14 |
| | D-20-R6 | 0.82 | 149 | 134.2 | 1.11 | 128.4 | 1.18 |
| | D-20-R9 | 1.22 | 152 | 133.4 | 1.14 | 117.0 | 1.06 |
| | D-16-R2 | 0.37 | 124 | 117.0 | 1.06 | 115.4 | 1.13 |
| | D-16-R5 | 0.86 | 130 | 114.9 | 1.13 | 116.7 | 1.14 |
| | D-16-R10 | 1.60 | 133 | 116.7 | 1.14 | 137.0 | 0.95 |
| C-Series | C-17-R3 | 0.28 | 131 | 136.7 | 0.96 | 137.1 | 1.10 |
| | C-17-R6 | 0.56 | 151 | 137.3 | 1.10 | 135.8 | 1.11 |
| | C-17-R9 | 0.76 | 150 | 135.9 | 1.10 | 136.4 | 1.11 |
| | C-17-R12 | 0.96 | 151 | 136.5 | 1.10 | 109.9 | 1.03 |
| B-Series | B-16-R3 | 0.66 | 75.6 | 68.0 | 1.12 | 68.0 | 1.11 |
| | B-16-R6 | 1.31 | 76.1 | 68.0 | 1.12 | 68.0 | 1.12 |
| M-Series | TR-S-13-R3 | 0.45 | 112 | 105.0 | 1.07 | 104.7 | 1.07 |
| | TR-S-18-R3 | 0.41 | 126 | 134.9 | 0.93 | 134.7 | 0.94 |
| | LS-S-13-R3 | 0.46 | 114 | 105.4 | 1.08 | 105.0 | 1.09 |
| | LS-S-18-R3 | 0.43 | 133 | 135.8 | 0.98 | 135.8 | 0.98 |

* Specimen S-27-R11-L was not included because an anchorage failure occurred during the test.

** The calculated capacity using sectional analysis without considering joint shear capacity.

*** The calculated capacity using sectional analysis with consideration of joint shear capacity.

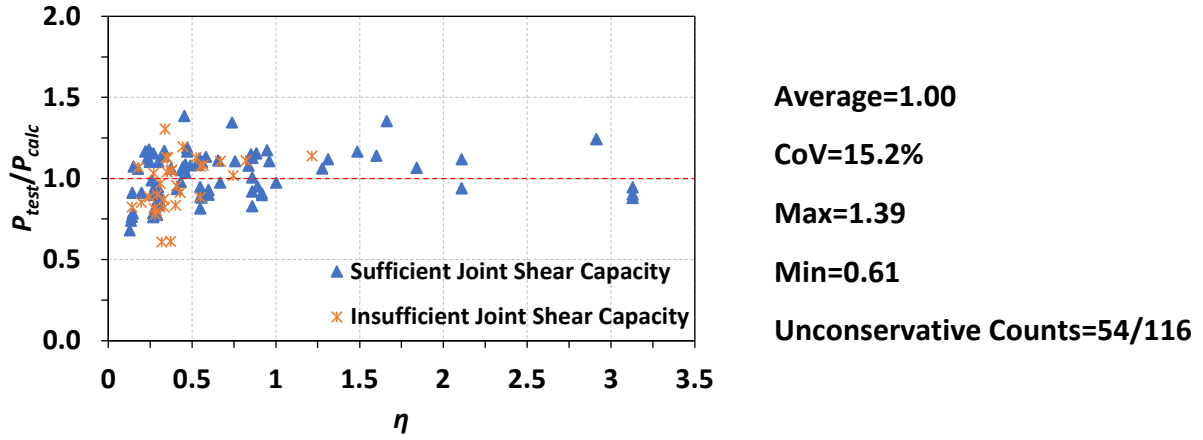
If the joint shear capacity is considered as a limit state, most datapoints were not affected because the corresponding specimens had sufficient joint shear capacities. There are four datapoints affected. One of these datapoints is for Specimen S-27-R3-L, and the other three are from Group D-1 (Specimens D-20-R2, D-20-R6, and D-20-R9). These three specimens had similar calculated joint shear strengths but achieved different experimental capacities. It is reasonable to state that, based on the results shown in Figure 6-12, the effect of the value of η should be considered in design to prevent unconservative results and that consideration of joint shear strength does not capture premature failures related to small bar bend radii. Application of the sectional analysis approach described in Section 6.3, even with consideration of calculated joint shear strength, is shown to be inappropriate for closing knee joints with an η -value less than 0.5.

6.5.1.2 Data from the evaluation database

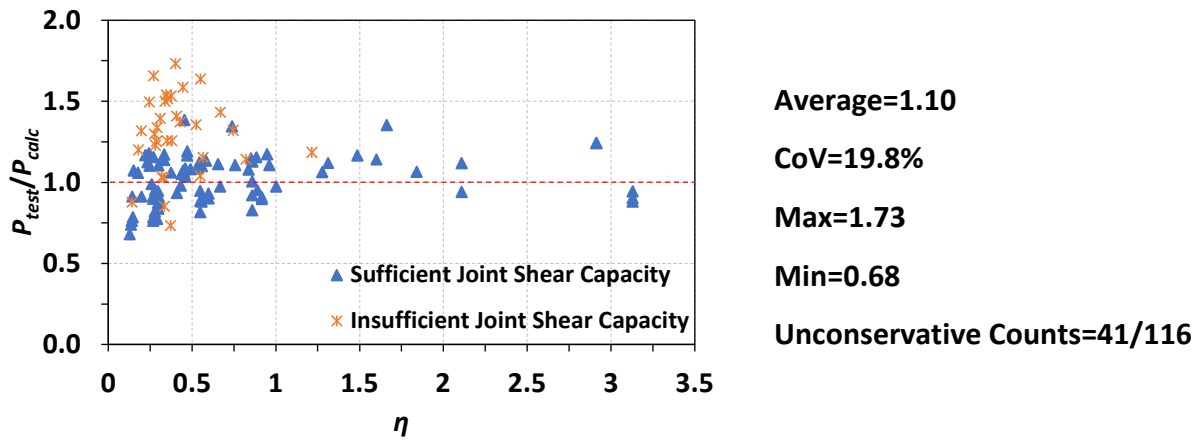
Based on data from the experimental program of the current study, the sectional analysis and joint shear capacity approach was proven to be ineffective when the value of η is less than 0.5. In this section, the results from the analysis of all specimens in the evaluation database are discussed. The strength ratio P_{test}/P_{calc} based on the sectional analysis and joint shear capacity approach is plotted against the diagonal strut width ratio η in Figure 6-13. The figure also includes basic statistics based on the results.

The analysis results in Figure 6-13(a) are based on the sectional analysis procedure while neglecting the calculated joint shear capacity. Again, the red dashed line indicates a strength ratio of 1.0, separating conservative predictions and unconservative predictions. Generally, it can be argued that the predictions are accurate, having an average strength ratio of 1.0 and a coefficient of variation of 15.2%. However, strength estimates for 54 out of the 116 tests are unconservative. Moreover, the minimum value for the strength ratio is quite low at 0.61. The corresponding specimen had an η -value of 0.45.

Although the number of unconservative predictions decrease when the calculated joint shear capacity is considered, the predictive ability of the sectional analysis procedure is still not satisfactory. As shown in Figure 6-13(b), the strength ratios that are affected by considering joint shear capacity generally increased, which resulted in the number of unconservative counts reducing to 41 out of 116 specimens, and the average strength ratio increased to 1.10. Nevertheless, more than half of the datapoints were not affected by the consideration of calculated joint shear strength, and therefore many remain unconservative. The lowest P_{test}/P_{calc} value is still quite low at 0.68. Considering the number of unconservative predictions and the overall scatter in the results, it is obvious that the sectional analysis and joint shear capacity approach does not appropriately capture all factors related to joint capacity. The data indicate that the other factors that affect the strength of closing knee joint should be considered.



(a) Neglecting joint shear capacity



(b) Considering joint shear capacity

Figure 6-13 Strength ratio based on sectional analysis versus diagonal strut width ratio for specimens in the evaluation database

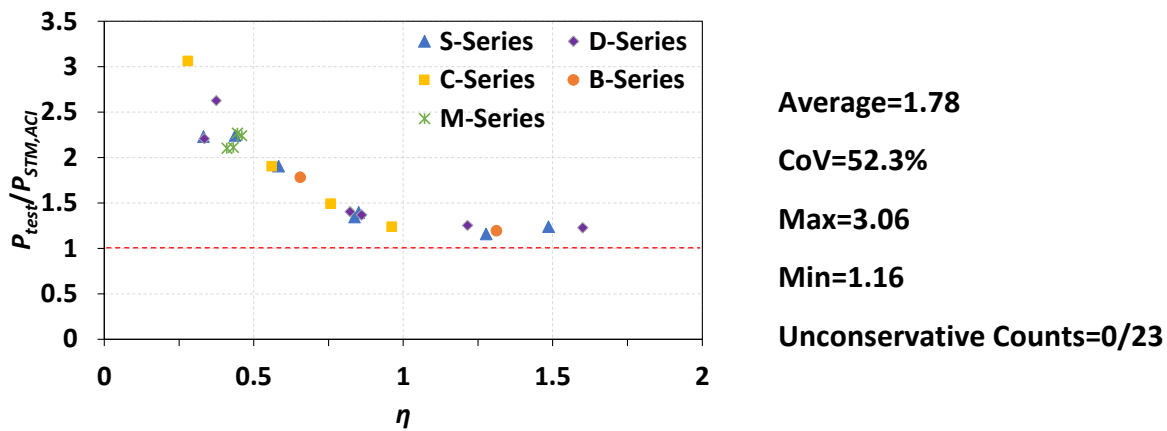
Four unconservative predictions out of the 13 specimens with η -values greater than 2.0 are indicated in Figure 6-13. The lowest strength ratio of these four specimens is 0.88. This indicates that specimens with an exceedingly large interface between the diagonal strut and the CTT node near the outer corner may still have strength ratios less than 1.0. Nevertheless, examining the reported descriptions about the failures of these specimens gives a better understanding. Unlike tests with η -values less than 0.5, many of which were reported to have experienced failures within the joint region, the four specimens failed in flexure at the joint face. For the three cases with η -values greater than 3.0, the researchers⁶ reported that all failures were due to yielding of the longitudinal reinforcement. Furthermore, the fourth specimen experienced failure due to fracture of longitudinal reinforcing bars.¹³ Therefore, based on these observations, it is believed that

sectional analysis is appropriate to apply to closing knee joints with η -values greater than 1.0. This also implies that the requirement of Eq. 2-20 for the bend radius of curved-bar nodes is appropriate.

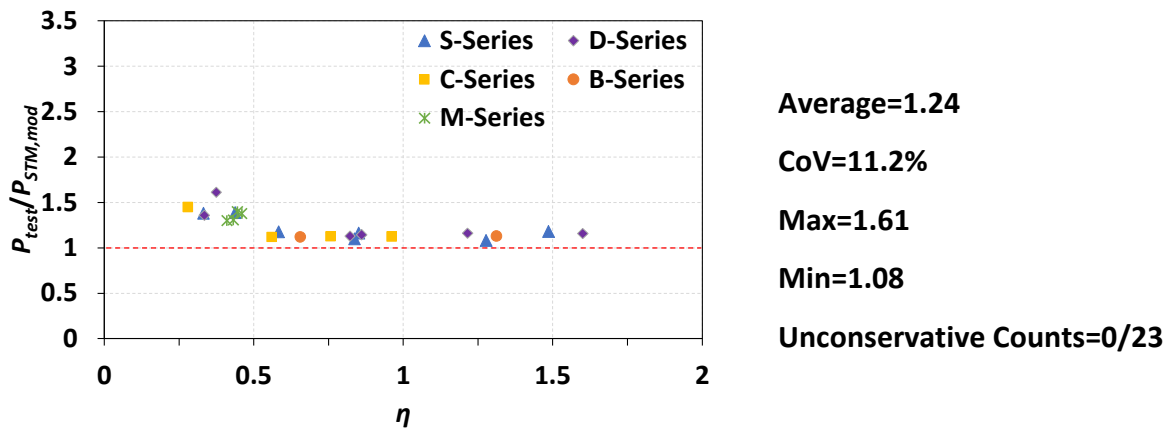
6.5.2 Evaluation of the Strut-and-Tie Method

6.5.2.1 Data from the experimental program of the current study

The strength ratio P_{test}/P_{calc} based on the strut-and-tie method approach presented in Section 6.4 is plotted against the value of η -value in Figure 6-14 for the specimens of the current research program. The red dashed line in each figure separates conservative predictions and unconservative predictions. The datapoints from different test series are differentiated within the plots. The analysis results are summarized numerically in Table 6-8.



(a) Incorporating ACI 318-19¹ coefficients



(b) Incorporating modified coefficients

Figure 6-14 Strength ratio based on the strut-and-tie method versus diagonal strut width ratio for specimens in the current study

Table 6-8 Summary of analysis results using the strut-and-tie method for specimens in the current study

| Series | Specimen ID | η | P_{test} (kip) | $P_{STM,ACI}^{**}$ (kip) | $P_{test}/P_{STM,ACI}$ | $P_{STM,mod}^{***}$ (kip) | $P_{test}/P_{STM,mod}$ |
|-----------|-------------|--------|---------------------|-----------------------------|------------------------|------------------------------|------------------------|
| S-Series* | S-27-R3-L | 0.33 | 113 | 50.6 | 2.23 | 81.8 | 1.38 |
| | S-18-R3 | 0.44 | 145 | 64.6 | 2.24 | 104.5 | 1.39 |
| | S-18-R6 | 0.84 | 148 | 110.0 | 1.35 | 134.6 | 1.10 |
| | S-18-R9 | 1.28 | 146 | 125.9 | 1.16 | 135.0 | 1.08 |
| | S-13-R3 | 0.58 | 123 | 64.5 | 1.91 | 104.4 | 1.18 |
| | S-13-R5 | 0.85 | 125 | 89.6 | 1.40 | 107.4 | 1.16 |
| | S-13-R8 | 1.49 | 127 | 102.4 | 1.24 | 107.6 | 1.18 |
| D-Series | D-20-R2 | 0.33 | 110 | 49.8 | 2.21 | 80.9 | 1.36 |
| | D-20-R6 | 0.82 | 149 | 106.0 | 1.41 | 131.8 | 1.13 |
| | D-20-R9 | 1.22 | 152 | 121.3 | 1.25 | 130.9 | 1.16 |
| | D-16-R2 | 0.37 | 124 | 47.2 | 2.63 | 76.9 | 1.61 |
| | D-16-R5 | 0.86 | 130 | 95.0 | 1.37 | 113.5 | 1.15 |
| | D-16-R10 | 1.60 | 133 | 108.3 | 1.23 | 115.0 | 1.16 |
| C-Series | C-17-R3 | 0.28 | 131 | 42.6 | 3.06 | 90.1 | 1.45 |
| | C-17-R6 | 0.56 | 151 | 79.3 | 1.90 | 134.8 | 1.12 |
| | C-17-R9 | 0.76 | 150 | 100.7 | 1.49 | 133.3 | 1.13 |
| | C-17-R12 | 0.96 | 151 | 121.6 | 1.24 | 133.9 | 1.13 |
| B-Series | B-16-R3 | 0.66 | 75.6 | 42.4 | 1.78 | 67.4 | 1.12 |
| | B-16-R6 | 1.31 | 76.1 | 63.8 | 1.19 | 67.4 | 1.13 |
| M-Series | TR-S-13-R3 | 0.45 | 112 | 49.3 | 2.27 | 80.1 | 1.40 |
| | TR-S-18-R3 | 0.41 | 126 | 59.9 | 2.10 | 96.9 | 1.30 |
| | LS-S-13-R3 | 0.46 | 114 | 50.9 | 2.24 | 82.7 | 1.38 |
| | LS-S-18-R3 | 0.43 | 133 | 63.0 | 2.11 | 101.8 | 1.31 |

* Specimen S-27-R11-L was not included because an anchorage failure occurred during the test.

** The calculated capacity using the STM based on ACI coefficients.

*** The calculated capacity using the STM with modified coefficients.

Incorporating the consideration of the CTT node (or curved-bar node) and the diagonal strut in the joint, the strut-and-tie model based on both sets of coefficients eliminated the unconservative predictions generated by the sectional analysis and joint shear capacity approach. The strut-and-tie model with coefficients based on ACI 318-19,¹ however, provides results that trend toward increased overconservativeness as the value of η decreases below a value of 1.0, as shown in Figure 6-14(a). The highest strength ratio P_{test}/P_{calc} is 3.06, which corresponds to an η -value of 0.28. This phenomenon could be attributed to the inappropriate reduction of concrete compressive strength at the CTT node. Another possible reason for this observation is that the strut-and-tie model ignores the development of bar stress along the straight portion of the bars

between the joint face and the bar bend, causing the development of a fan-shaped strut (see Chapter 4).

Still ignoring the development of bar stress within the joint but incorporating a greater nodal coefficient for the CTT node, the strut-and-tie model with the modified coefficients significantly mitigated the overconservative results for low values of η . Overall, the predictions are more accurate and strength ratios present less scatter, resulting in an average strength ratio of 1.24 and a coefficient of variation of 11.2%. Although the strength predictions for some specimens with η -values less than 0.5 may still be considered as being overly-conservative, the highest strength ratio was reduced from 3.06 to 1.61. The results reveal that even though the nodal zone and strut coefficients were taken as 1.0 (see Table 6-6), the strut-and-tie model with the modified coefficients generated more accurate but still conservative predictions for closing knee joints. Moreover, based on the limited number of tests from the current research program, in order to avoid overcomplicating the strut-and-tie model, it seems reasonable to ignore the development of bar stress within the joint (that is, to assume the ties within the joint carry a constant force along their lengths) in order to obtain conservative results for closing knee joints with η -values between 0.25 to 0.5.

6.5.2.2 Data from the evaluation database

Strength ratios calculated using the strut-and-tie model with coefficients based on ACI 318-19¹ are plotted for the specimens in the evaluation database against the diagonal strut width ratio as shown in Figure 6-15(a). In the plot, specimens with adjoining members with identical cross sections are differentiated from specimens with legs that had different cross sections. Again, the red dashed line corresponds to a strength ratio of 1.0. Compared to the sectional analysis and joint shear capacity approach (see Section 6.5.1.2), the strut-and-tie model with ACI coefficients was able to mitigate the occurrence of unconservative strength predictions. The strengths of only four out of the 116 specimens were overestimated. All four specimens for which strengths were overestimated experienced a flexural failure as described previously in Section 6.5.1.2. However, significant underestimations of strength are observed, especially for η -values less than 0.5. The highest predicted strength ratio is 8.96, which corresponds to a specimen with an η -value of 0.18. Moreover, many strength ratios exceed 2.0 when the η -value is less than 1.0. Results with significant overconservativeness are shown for the specimens with legs having different cross

sections that were tested by Luo et al.⁸ Due to thin clear side cover, the clear side cover parameter, C_f , of 2.0 was also incorporated into the strength calculations.

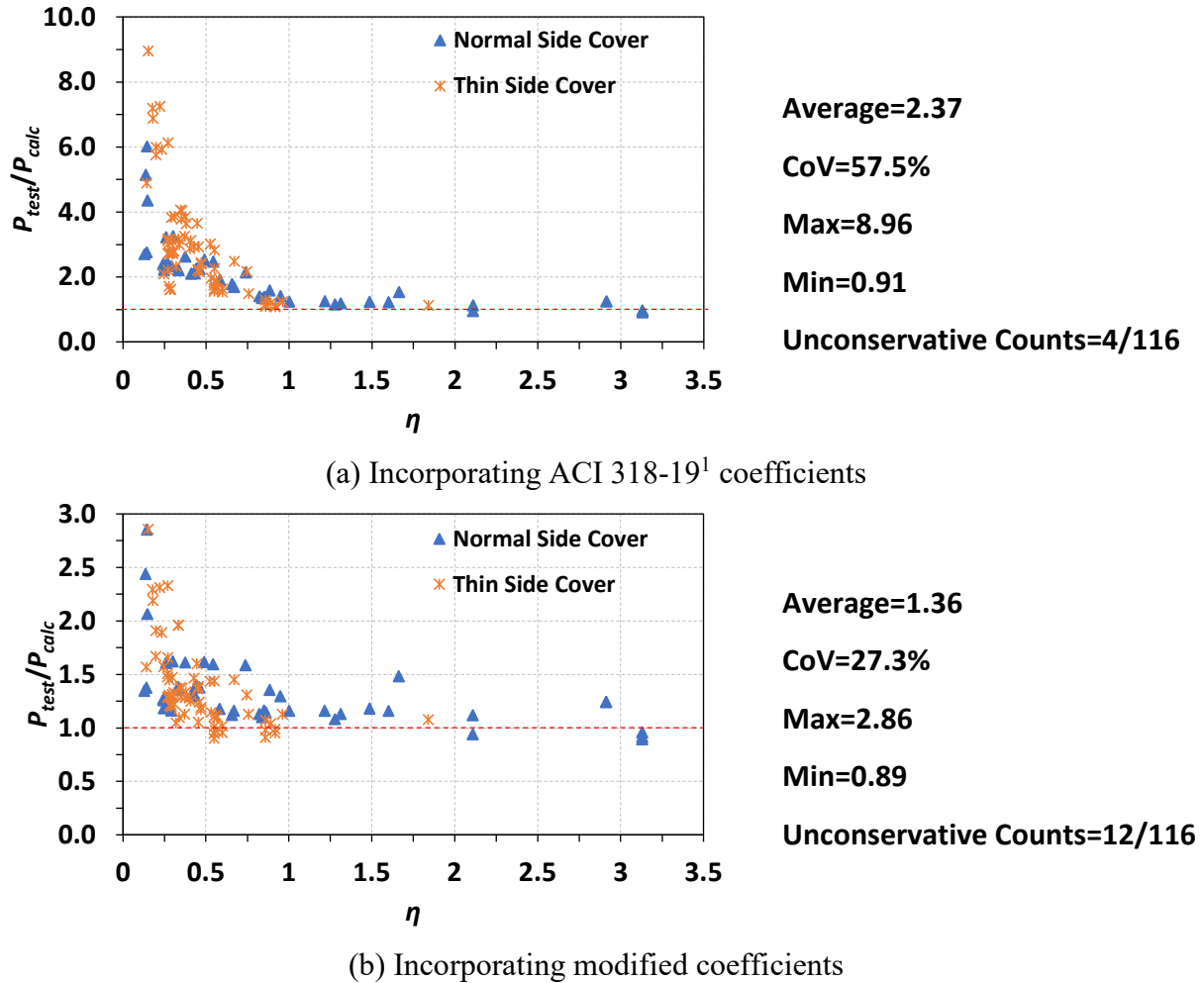


Figure 6-15 Strength ratio based on the strut-and-tie method versus diagonal strut width ratio for specimens in the evaluation database

The strut-and-tie model with the modified coefficients mitigated the level of overconservativeness as shown in Figure 6-15(b). Although some level of overconservativeness remains, especially for low values of η , the average value of the strength ratios is 1.36, indicating significantly increased accuracy compared to the results from the strut-and-tie model with coefficients based on ACI 318-19.¹ However, strengths of 12 out of the 116 specimens were overestimated, which is a greater than the number of unconservative results from the strut-and-tie method with ACI-based coefficients. Among the 12 unconservative cases, the four cases

corresponding to η -values greater than 2.0 experienced flexural failures as explained above, and the other eight specimens tested by Stroband et al.²³ had a diagonal strut width ratio between 0.5 to 1.0. Nevertheless, most specimens in the evaluation database correspond to strength ratios between 1.0 and 1.5.

The trend that small η -values led to greater underestimation of strength was also observed, especially for η -values less than 0.25. Eight cases resulted in strength ratios greater than 2.0. Overall, this observation reflects that reducing the nodal zone and strut coefficients to values less than 1.0 (see Table 6-6) may not be appropriate for closing knee joints if only strength is considered. Moreover, consideration of the development of bar stress within the joint may help to further mitigate the overconservativeness for low η -values.

Furthermore, when the modified coefficients were applied, the largest strength ratios for specimens with thin clear side cover were reduced from 8.96 to less than 3.0, which is more consistent with the results for the specimens with similar η -values and a thicker clear side cover, as shown in Figure 6-15(b). The results indicate the modified C_f -value is appropriate. In general, the modified coefficients resulted in improved strength predictions without losing too much conservativeness.

In sum, the strut-and-tie method with the modified coefficients generated more accurate and still conservative predictions in terms of strength when compared to that based on ACI-required coefficients. Therefore, the modified coefficients are particularly suitable for assessing the strength of closing knee joints.

6.6 Summary

To evaluate the applicability of different methods for the design of knee joints subjected to closing moments, a database analysis was conducted. The database included 177 tests on knee joint specimens. A filtering criterion was applied to the database in order to screen out incomplete reports and specimens not suitable for the current study, and therefore 116 specimens were left in the evaluation database. The strength of each specimen was then calculated using (1) a sectional analysis and joint shear capacity approach based on ACI 318-19,¹ (2) the strut-and-tie method with strength coefficients from ACI 318-19,¹ and (3) the strut-and-tie method with the modified coefficients. Furthermore, a procedure for developing a strut-and-tie model for knee joints under closing moments was introduced. Several observations can be made from the database evaluation as follows:

1. Application of the ACI sectional analysis approach while neglecting the calculated joint shear capacity resulted in strength predictions for which the average P_{test}/P_{calc} value is equal to 1.00 and the coefficient of variation is 15.2%. However, for diagonal strut width ratios, η , less than 1.0, the experimental capacity could be as low as 61% of the calculated capacity. The result reveals the inadequacy of the sectional analysis for closing knee joints.
2. Application of the ACI sectional analysis approach with consideration of the calculated joint shear capacity did not effectively resolve the issue of unconservative results for η -values less than 1.0. However, the method decreased the predicted strengths of specimen for which the bar stress at the joint face was limited by the calculated joint shear capacity. Even with consideration of calculated joint shear strength, the results indicate the presence of other factors affecting the strength of the specimens not considered within the approach.
3. The strut-and-tie model with coefficients based on ACI 318-19,¹ which considered the size of the CTT node based on the bar bend radius, mitigated the unconservativeness that resulted from the sectional analysis approach. Many predictions, however, greatly underestimated specimen strengths, especially for specimens with adjoining members with different cross sections and specimens with η -values less than 1.0. The ACI coefficients used to reduce the compressive strength of concrete were found to provide overly conservative results in many cases. Neglecting the development of bar stress

along the straight portion of the bars within the joint region also likely contributed to the underestimations.

4. The strut-and-tie model with the modified coefficients generally reduced the level of overconservativeness resulting from the strut-and-tie model with coefficients based on ACI 318-19.¹ However, more unconservative estimates also resulted. Nevertheless, the modified coefficients, in general, delivered improved results compared to the ACI coefficients. The trend that smaller η -values result in underestimated strength predictions was still observed, but the most overly conservative estimates resulting from the ACI coefficients were improved. The modified coefficients are particularly suitable for assessing strength of knee joints subjected to closing moments.

7. FINITE ELEMENT ANALYSIS

This chapter describes the analytical investigation conducted through the non-linear finite element analysis (FEA) of knee joints under closing moments. The finite element analysis software ATENA 3D^{81,82} was used for all of the computational modeling. The purpose of conducting FEA is first presented, followed by details of the computational modeling parameters and techniques. Then, the validation of finite element model is described. Lastly, a parametric analysis using the validated finite element model is presented and used as a supplement to the experimental program in order to further evaluate the code-specified design expressions for the bend radius of curved-bar nodes.

7.1 Overview

Non-linear finite element analysis is an important tool widely used in solid mechanics. In the field of reinforced concrete structures, non-linear FEA is also utilized to model and predict stress distribution and crack propagation. In this study, the non-linear FEA software ATENA 3D was used to develop an effective modeling technique. ATENA 3D, a program specialized in the analysis of reinforced concrete components, features a variety of non-linear concrete material models, including damage-plasticity, bond behavior between reinforcement and concrete, and others. Because of its versatility, ATENA 3D was employed to provide supplemental data to further investigate the design expressions related to closing knee joints using the strut-and-tie method.

As previously introduced, the experimental program and the database analysis validated the design expression considering radial stresses near the bar bend presented in Eq. 2-20. Applying the strut-and-tie method to closing knee joints was also proven effective. However, the validation of equations incorporating the effect of a diagonal strut angle not equal to 45 degrees (that is, Eq. 2-24 from ACI 318-19¹ and Eq. 2-26 from FIP⁵⁸) was based on limited data. Although Eq. 2-24 and Eq. 2-26 were assessed to be conservative based on the limited test results, further investigation into the effects of the diagonal strut angle is warranted. In lieu of conducting additional experiments, non-linear FEA is a quick and economic solution that can be verified using existing experimental data.

The non-linear FEA model in this study was calibrated/validated using selected results from the experimental program. Benchmark specimens from the experimental program were selected for this purpose. The FEA model was then used to simulate more cases in order to conduct a parametric analysis. The main purpose of the parametric analysis was to compare the calculated strengths using FEA to the predictions given by both the STM and sectional analysis. The numerical analysis included 72 numerical specimens. The configurations were the same as specimens in the experimental program. The numerical knee joint specimens consisted of two adjoining legs, and the loads were applied horizontally to create closing moments, as introduced in later sections.

7.2 Modeling Parameters

The procedure for modeling knee joint specimens subjected to closing moments is introduced in this section. First, material models used for calibration are presented. Following the material models, configuration, boundary conditions, and mesh sizes are explained. The solver for the finite element models is then described. Lastly, the comparison of numerical results to corresponding experiments is provided.

7.2.1 Material

7.2.1.1 Concrete

The concrete material model used in the software is named “CC3DNonLinCementitious2.” The material model includes constitutive relationships based on concrete fracturing and plastic behavior as well as a biaxial failure criterion. The tensile behavior, or fracture model, is described using an orthotropic smeared crack model. It includes strength failure criterion, exponential softening. Furthermore, tension stiffening can be specified, and cracks can be modeled as rotated or fixed. For compressive behavior, the plasticity is based on the Menetrey-Willam⁸³ failure surface. The compressive behavior is subjected to strain softening and the compressive strength is reduced due to transverse tensile strain. More information can be found in ATENA Program Documentation Part 1: Theory.⁸⁴

Parameters used for the concrete model “CC3DNonLinCementitious2,” are summarized in Table 7-1. The parameters are subdivided into five primary subsets: “Basic,” “Tensile,”

“Compressive,” and “Miscellaneous.” Under the “Basic” subset, uniaxial properties can be specified, including the elastic modulus, Poisson’s ratio, tensile strength, and compressive strength. The values in the “Used Value” column represent the inputs that were used in order to validate numerical models using physical specimens. For this validation process, measured concrete properties corresponding to benchmark specimens were input for the “Basic” subset. The tensile strength in ATENA is based on the direct tensile strength of concrete. The splitting tensile strength of concrete, however, was measured during the experimental program. To determine the direct tensile strength, a conversion was used. Because the direct tensile strength is approximately $3\sqrt{f'_c}$ to $5\sqrt{f'_c}$ and the splitting tensile strength is approximately $6\sqrt{f'_c}$ to $8\sqrt{f'_c}$, it is legitimate to use 0.7 times the measured splitting tensile strength for the calibration.

Table 7-1 Concrete material model

| Subset | Parameter | Default Value | Used Value |
|---------------|--|--------------------------------|--------------------------------|
| Basic | Elastic modulus, E_c | - | Measured |
| | Poisson’s ratio, ν | - | Measured |
| | Tensile strength, f'_t | - | $0.7f'_{sp}$ |
| | Compressive strength, f'_c | - | Measured |
| Tensile | Specific Fracture Energy, G_f | $0.000025f'_t$ | $0.000025f'_t$ |
| | Crack spacing, s_{max} | Deactivated | Deactivated |
| | Tension stiffening, c_{ts} | Deactivated | Deactivated |
| | Unloading | Deactivated | Deactivated |
| Compressive | Critical compressive displacement, w_d | 5 mm | 5mm and 10 mm |
| | Plastic strain at compressive strength, ε_{cp} | f'_c/E_c | f'_c/E_c |
| | Reduction of comp. strength due to cracks, r_c^{lim} | 0.8 | 0.8 and 1.0 |
| Shear | Crack shear stiffness factor, s_F | 20 | 20 |
| | Aggregate size | 0.020 m | 0.020 m |
| | Aggregate interlock | Activated | Activated |
| Miscellaneous | Failure surface eccentricity | 0.52 | 0.52 |
| | Multiplier for the plastic flow direction, β | 0 | 0 |
| | Specific material weight, ρ | $2.3\text{e-}2 \text{ MN/m}^3$ | $2.3\text{e-}2 \text{ MN/m}^3$ |
| | Coefficient of thermal expansion, α | $1.2\text{e-}5 \text{ 1/K}$ | $1.2\text{e-}5 \text{ 1/K}$ |
| | Fixed crack model coefficient | 1.0 | 1.0 |

Describing the formation and the propagation of cracks, the “Tensile” subset includes four parameters related to the tensile behavior of concrete. The crack opening process in ATENA 3D⁸⁴ can be illustrated as shown in Figure 7-1. The specific fracture energy G_f represents the area under the curve indicated in the figure, or the minimum required energy to create a unit area of a stress-free crack.⁸⁴ The default value of G_f is $0.000025f'_t$ (in MPa), which was used for the calibration of

numerical models. In addition to the specific fracture energy, the other three parameters, crack spacing, tension stiffening, and unloading, were deactivated. Specifying crack spacing limits the maximum space between two cracks, and the tension stiffening parameter sets a minimum tensile stress. That is, the tensile stress stops decreasing with the increase of the crack opening at this point. The unloading parameter specifies the closure stiffness of cracks, which was not applicable because unloading was not included in the analyses.

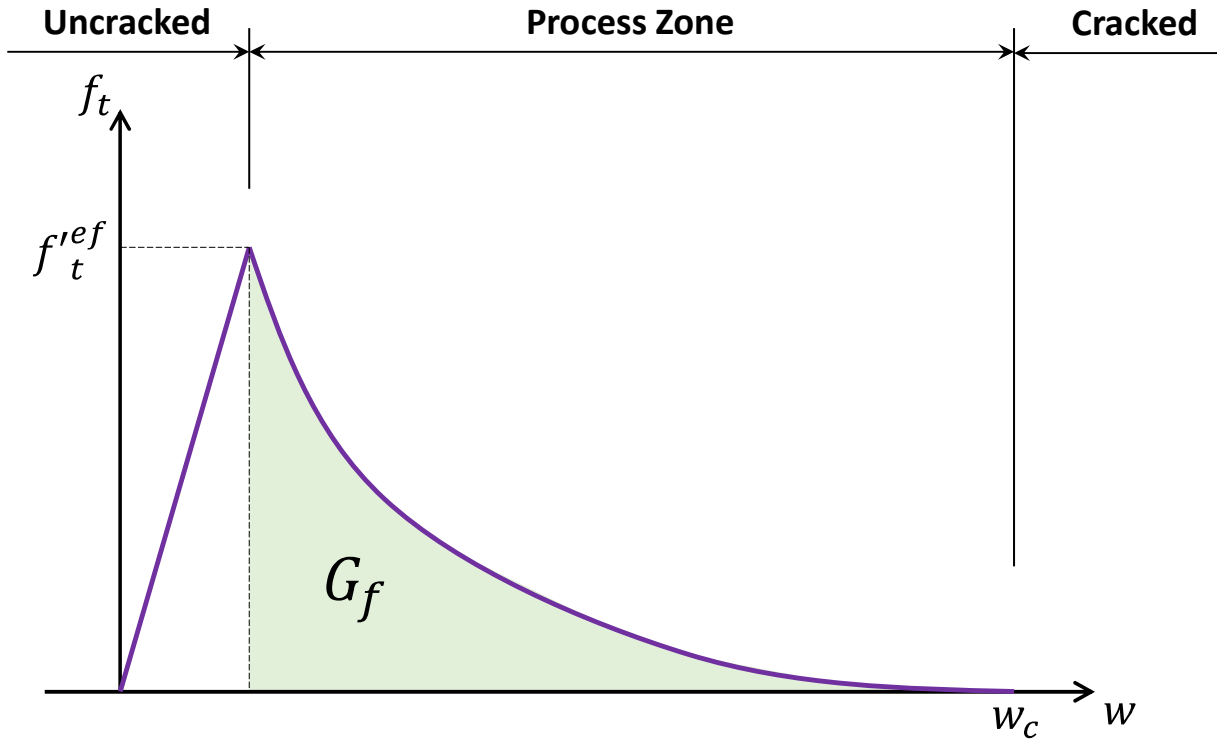


Figure 7-1 Crack opening (adapted from Cervenka et al.⁶⁷)

Parameters related to compressive plasticity are under the “Compressive” subset, in which four values are entered: critical compressive displacement, w_d ; plastic strain at compressive strength, ϵ_{cp} ; and reduction of compressive strength due to cracks, r_c^{lim} . As shown in Figure 7-2, the default value of ϵ_{cp} is simply defined as f'_c/E_c ; therefore, actual concrete properties were used. This strain value defines where the ascending curve stops as shown in Figure 7-2. It should be noted that the ascending portion is a parabola. In Figure 7-3, the value of w_d represents the displacement over which the concrete stress descends to zero. It should be noted that the value has units of millimeters instead of being dimensionless. That is, the critical compressive displacement

is independent of the size of concrete elements based on the study by Van.⁸⁵ The value of w_d is set to 5 mm by default. However, for the purpose of calibration, the value was specified as 10 mm assuming the concrete had an ultimate strain of approximately 4‰ for concrete cylinder samples with a height of 4 in. Furthermore, to reflect the property that the compressive strength of concrete decreases as the transverse strain ε_1 increases, ATENA 3D incorporates the strain softening of concrete based on Vecchio and Collins.⁸⁶ The strength decrease has a lower limit, which is represented by the variable r_c^{lim} as shown in Figure 7-4. The value of r_c^{lim} should not be taken less than 0.8 as suggested in the study by Dyngeland.⁸⁷ ATENA incorporates a default value of 0.8. Here, the values considered for the calibration of the model were 0.8 and 1.0.

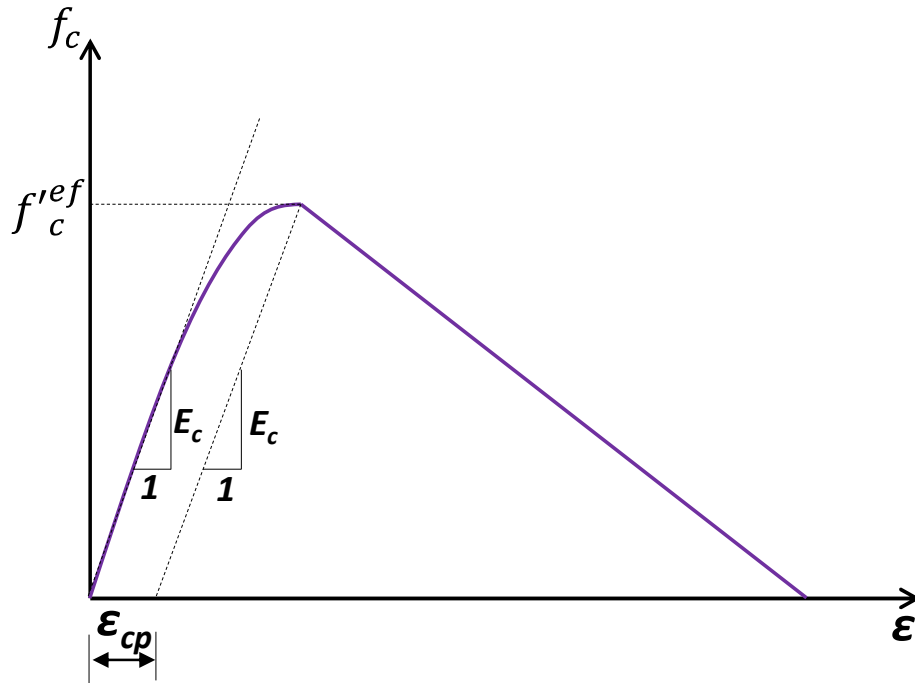


Figure 7-2 Stress-strain curve of concrete (adapted from Cervenka et al.⁸⁴)

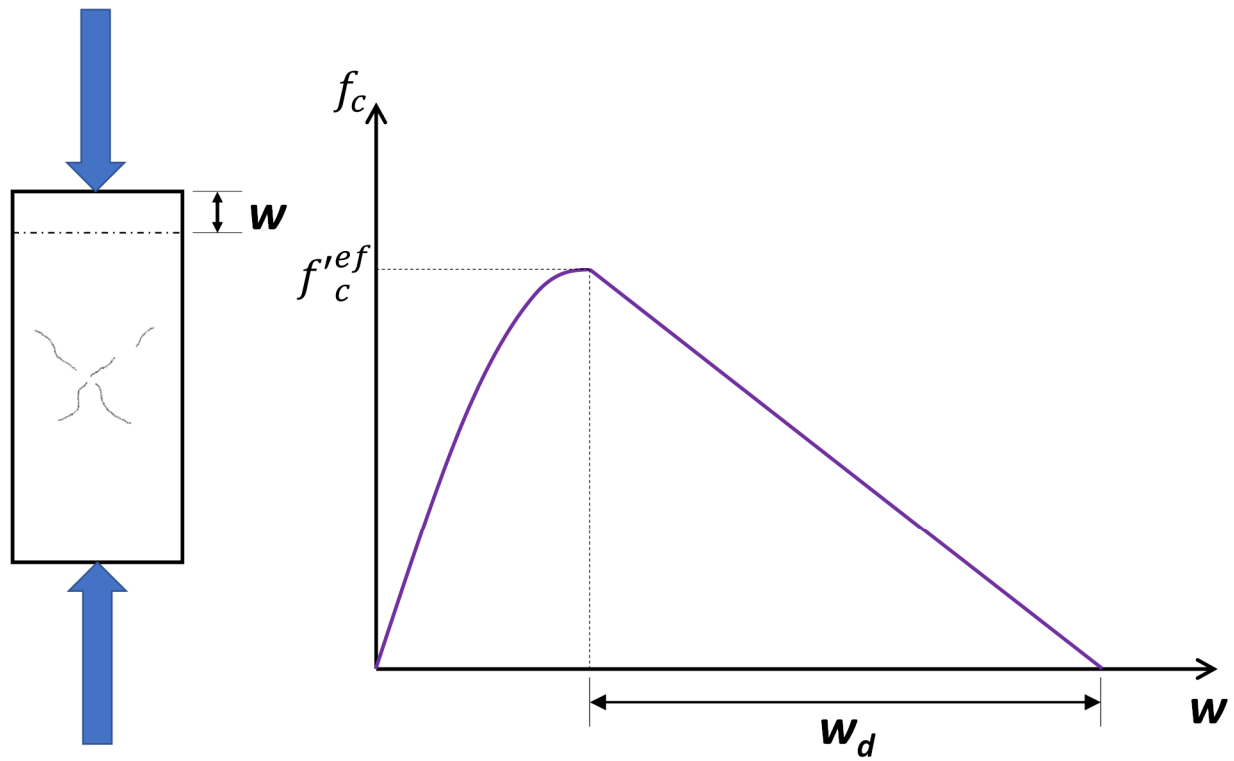


Figure 7-3 Critical compressive displacement (adapted from Cervenka et al.⁸⁴)

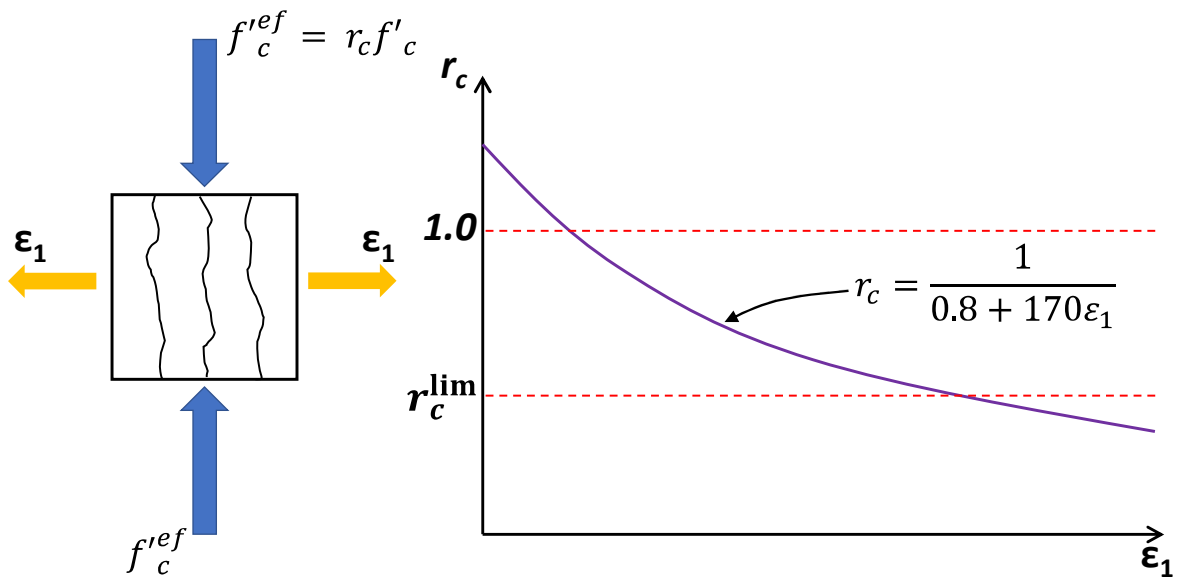


Figure 7-4 Reduction of compressive strength of concrete due to cracks (adapted from Cervenka et al.⁸⁴)

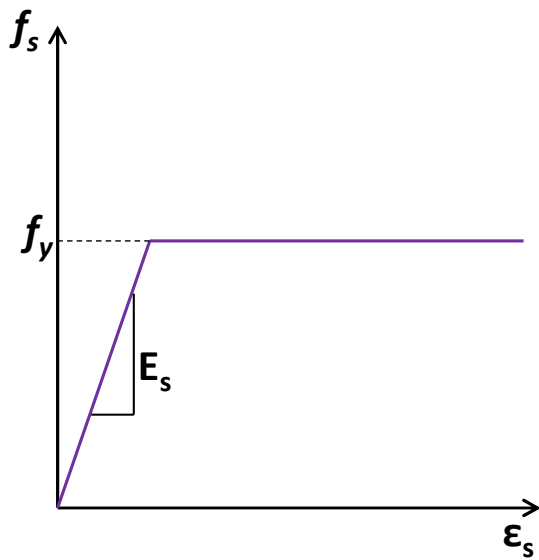
Parameters related to shear behavior belong to the “Shear” subset. Under this subset, users can specify the crack shear stiffness factor and activate aggregate interlock. The crack shear stiffness factor, s_F , is used to define normal crack stiffness and shear crack stiffness. The default value of the shear factor coefficient is 20 based on the study by Walraven.⁸⁸ In addition, it is possible to activate aggregate interlock and specify the aggregate size, which determines the shear strength of cracked concrete based on the modified compression field theory.⁸⁶ For validation of the computational models, the value for the shear factor coefficient was kept at the default value. Aggregate interlock was activated, and the size of the aggregates was equivalent to 0.75 in. as used in the experimental program.

The last subset, “Miscellaneous,” includes parameters related to concrete plasticity, the crack model, and concrete material properties. The first value to specify is the failure surface eccentricity, which defines the multi-axial failure criterion for concrete based on the study by Menetrey et al.⁸³ The eccentricity determines the shape of the triaxial failure envelope and is recommended to be 0.52 as Menetrey et al.⁸³ suggest. The value of the multiplier for the plastic flow direction, β , reflects the volume change during concrete crushing. Considering concrete plasticity, plastic deformation is accompanied by volume increase, known as dilatancy.⁸⁹ In the software, positive numbers of β denote that the material is dilating. The default value of zero was used for β . The troubleshooting manual for the software⁹⁰ suggests that the default value results in conservative results, but values up to between 0.5 and 0.9 are also recommended. The fixed crack model coefficient is also specified under the “Miscellaneous” subset. The value defines the residual tensile stress level (as a fraction of the tensile strength) at which the crack direction is fixed. The default number 1.0 represents “the fixed crack model,” meaning cracks do not change direction once they form. The last two parameters are related to concrete material and include the unit weight and thermal expansion. These parameters were kept as the default values.

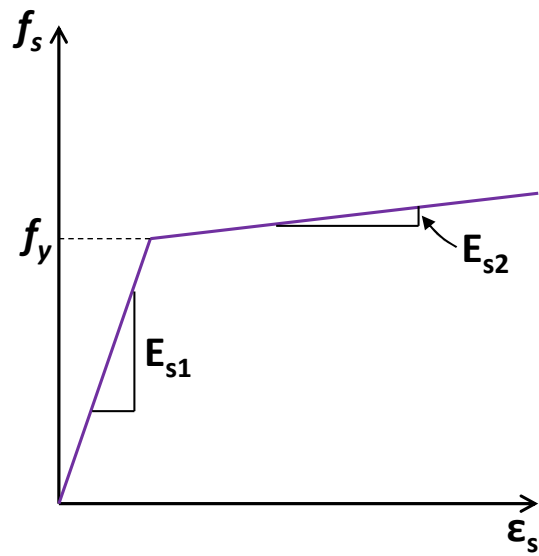
7.2.1.2 Reinforcement and steel

ATENA 3D provides various elastic-plastic models for reinforcing bars and steel, including the elastic-perfectly plastic model, the elastic-strain hardening plastic model, the multi-linear model, and the linear elastic model as illustrated in Figure 7-5. In this study, because the reinforcement in the test specimens of the experimental program (see Chapter 3) did not reach the strain-hardening range, the elastic-perfectly plastic model was used. The yield strength was

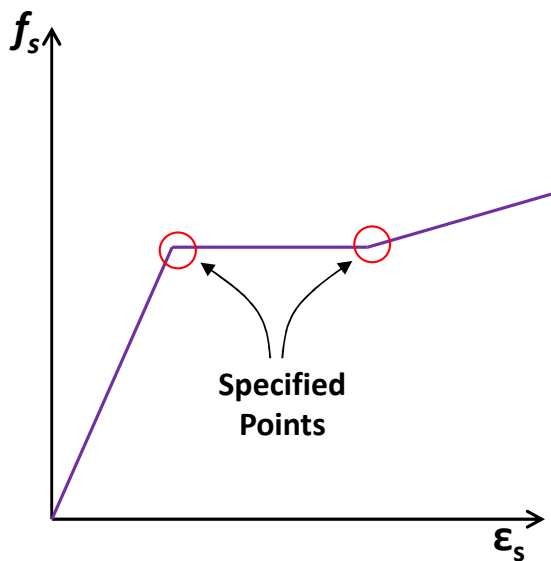
specified as the measured yield strength (see Section 3.2) and the elastic modulus was 200,000 MPa, equivalent to 29,000 ksi. The Poisson's ratio was 0.3 by default. For the bearing and support plates, the linear elastic model named "3D Elastic Isotropic" was used. This model assumes linear elastic behavior such that the relationship between stress and strain is linearly proportional with a fixed elastic modulus. The assumed elastic modulus was again 200,000 MPa as widely used for steel.



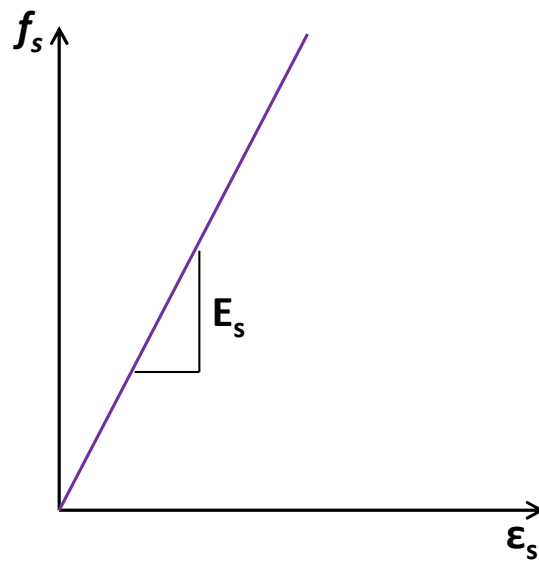
(a) Elastic-perfectly plastic



(b) Elastic-strain hardening



(c) Multi-linear



(d) Elastic

Figure 7-5 Material models for reinforcement and steel plates

7.2.2 Configuration

7.2.2.1 Parts and Topology

Concrete and steel plates, classified as 3D solid elements, program were modeled using “Macroelements” in ATENA 3D as shown in Figure 7-6(a). To layout the three-dimensional model, the origin was located at one side of the re-entrant corner. From the origin, the locations of all other vertices of the joint and the adjoining members were specified as well as the edges. The load and support plates were generated using the same method. Between the concrete and the each of the steel plates, a partial contact connection was automatically established as shown in Figure 7-6(c).

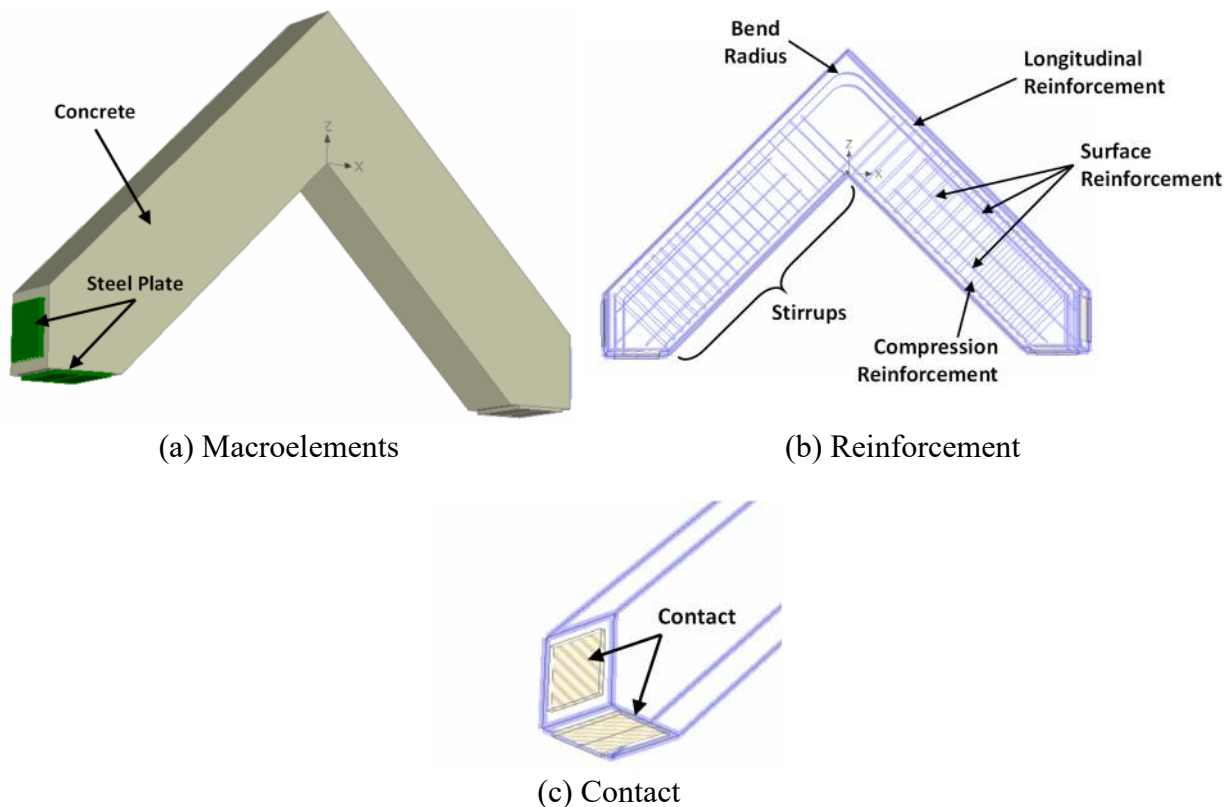


Figure 7-6 Modeling specimen components in ATENA

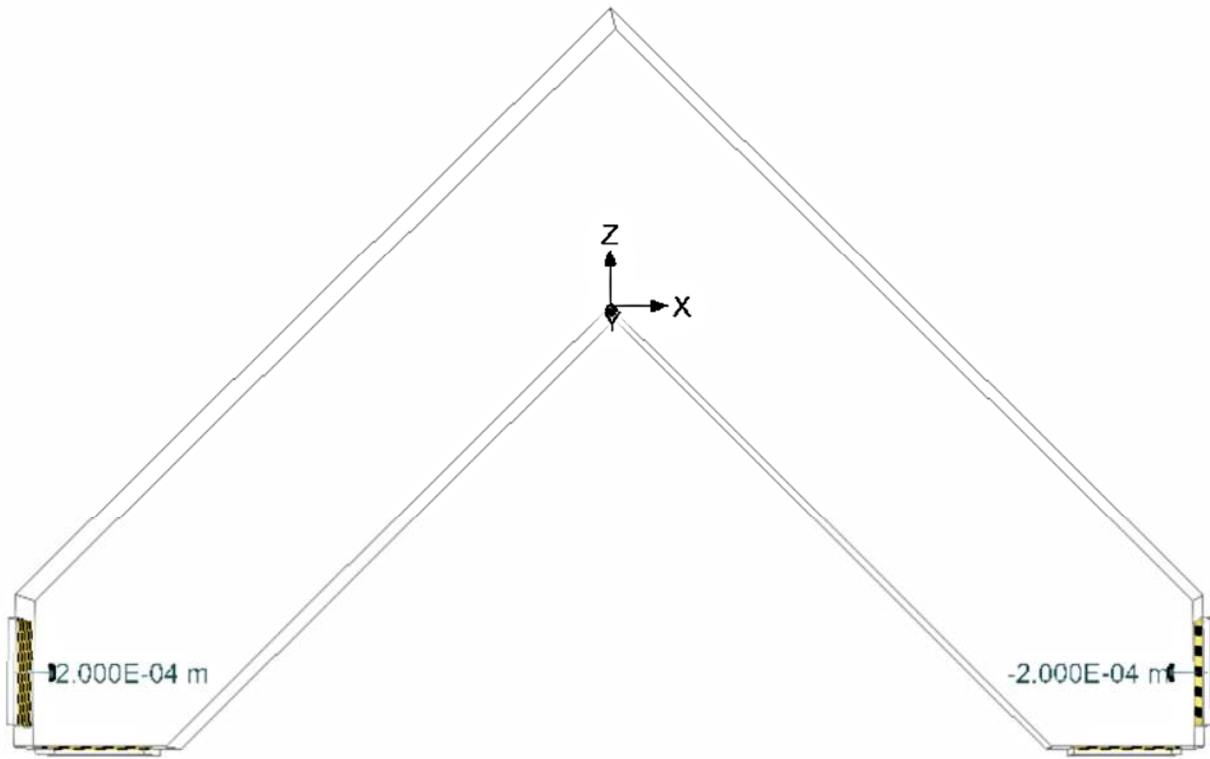
The coordinates of the reinforcement were located with reference to the same origin. One-dimensional truss elements were used to model the reinforcement (see Figure 7-6(b)). For the longitudinal tension reinforcing bars, straight segments began at the end of each leg (that is, near the load points) and extended along the leg toward the joint. No bar bend was detailed at the end

of the leg near the load point because of its negligible effect on overall behavior. In the joint, however, the bend radius was the primary variable and, for validation, was modeled to match the actual measured bend radius of the corresponding benchmark specimen. In the software, arcs are composed of several straight segments, and the bar bend in the model was divided every ten degrees along the bend. In addition, for the numerical specimens used for validating the model, the size as well as the distribution of the stirrups and the surface reinforcement were, of course, the same as the benchmark specimens. The bar bends of the stirrups and the surface reinforcement were not modeled for simplicity. The compression reinforcement was also modeled to match that of the benchmark specimens. The additional smaller stirrups near the end of each leg (that is, near the load points), however, were not included due to their negligible influence on behavior.

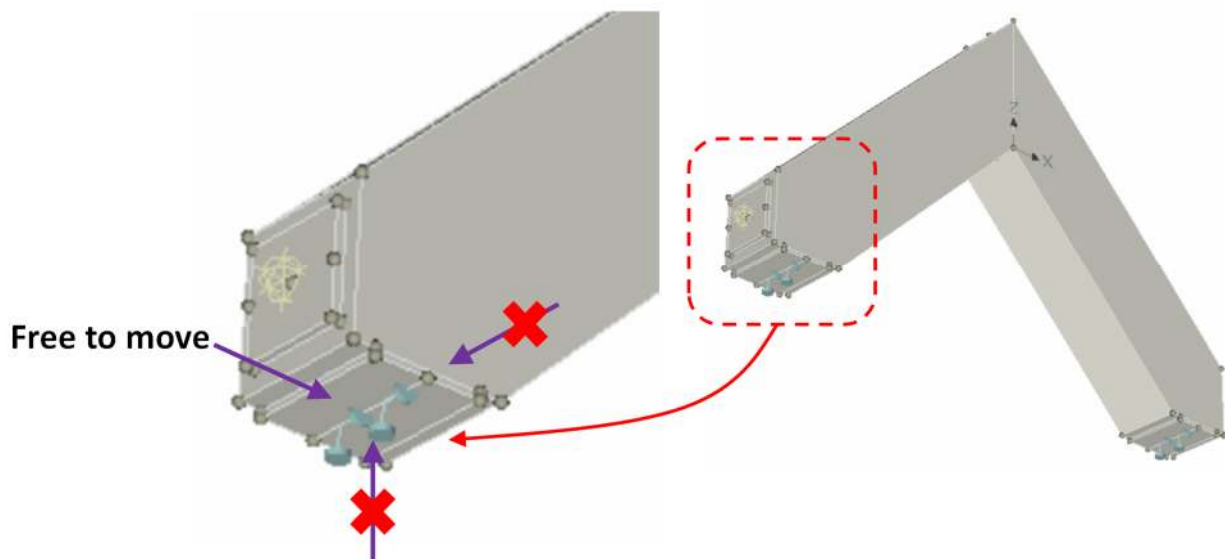
For calibration, all reinforcement was assigned the same material properties as introduced in Section 7.2.1. Any differences in the yield strengths of the longitudinal reinforcement and the other bars in the benchmark specimens was neglected as the difference was thought to have negligible effect on overall behavior. All reinforcement was therefore assigned a yield strength based on the measured yield strength of the longitudinal bars. Moreover, bond between the reinforcement and the concrete was not included. According to the troubleshooting manual for ATENA 3D,⁹⁰ in many cases, the actual response is captured well without modeling bond if the mesh is fine enough relative to the bar diameter and the bars are ribbed.

7.2.2.2 Loads and boundary conditions

In ATENA 3D, both loads and boundary conditions fall into the category of load cases. As shown in Figure 7-7(a), loads were applied to numerical specimens through prescribed displacements at the center point of each steel loading plate. For each step, the displacement induced to each point was 0.2 mm inward (that is, toward the opposite load point). In other words, the increment of relative displacement between the legs was 0.4 mm for each step. The increment was expected to result in the anticipated maximum displacement being reached after approximately 200 steps. Moreover, as shown in Figure 7-7(b), the rollers underneath the steel plates were modeled to be free to move along the x-axis but were fixed along the y-axis and the z-axis at the centerlines of the steel plates.



(a) Prescribed displacements



(b) Supports

Figure 7-7 Load cases

7.2.3 Mesh

The macroelement for concrete was meshed using the function “Extrude” in ATENA 3D, which generates brick (hexahedral) meshes. Brick elements can be linear or quadratic. A linear brick element has eight nodes, and a quadratic element has 20 nodes as shown in Figure 7-8(a). To save computational resources, eight-node linear brick elements were used. For the purpose of comparison and to ensure the appropriate mesh was selected, tetrahedral meshes were also considered during the validation process. Tetrahedral elements can also be linear (four-node) or quadratic (nine-node) as shown in Figure 7-8(b).

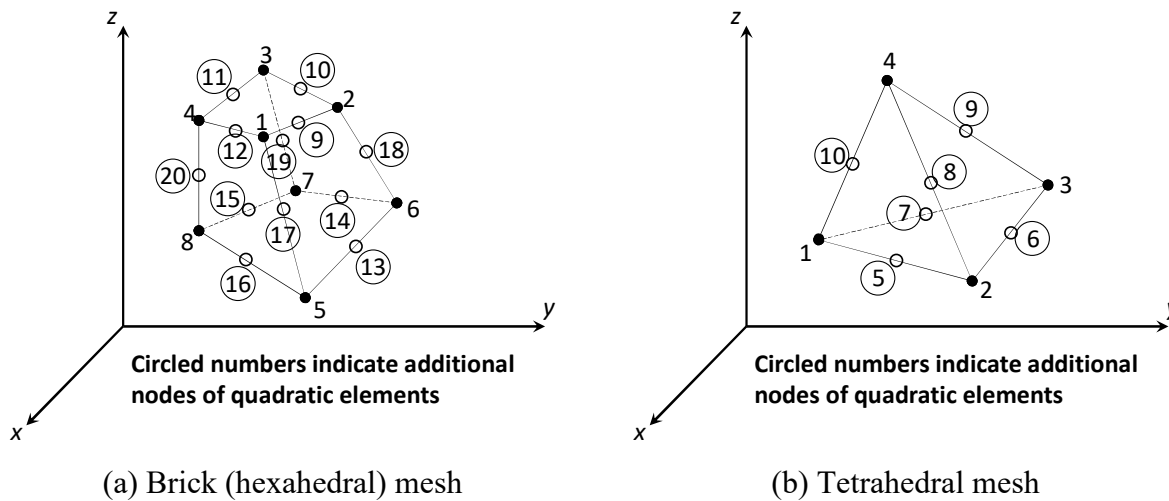


Figure 7-8 Mesh types (adapted from Cervenka et al.⁸⁴)

To guarantee the quality of the calculated results, two different sizes of mesh were considered. According to the ATENA Engineering Example Manual,⁹¹ at least four elements over the thickness of the model are needed for qualitative results and six to ten elements over the thickness for quantitative results. During the validation process, for the brick elements, a mesh size of 0.1 m, corresponding to four elements through the width, was used as coarse mesh. A mesh size of 0.05 m, corresponding to eight elements through the width, was used as fine mesh. In addition, a mesh size of 0.075 m was used for the models meshed with tetrahedral elements. The meshing results for each scenario are shown in Figure 7-9. It should be noted that for all cases, the steel load and support plates were meshed using tetrahedral elements.

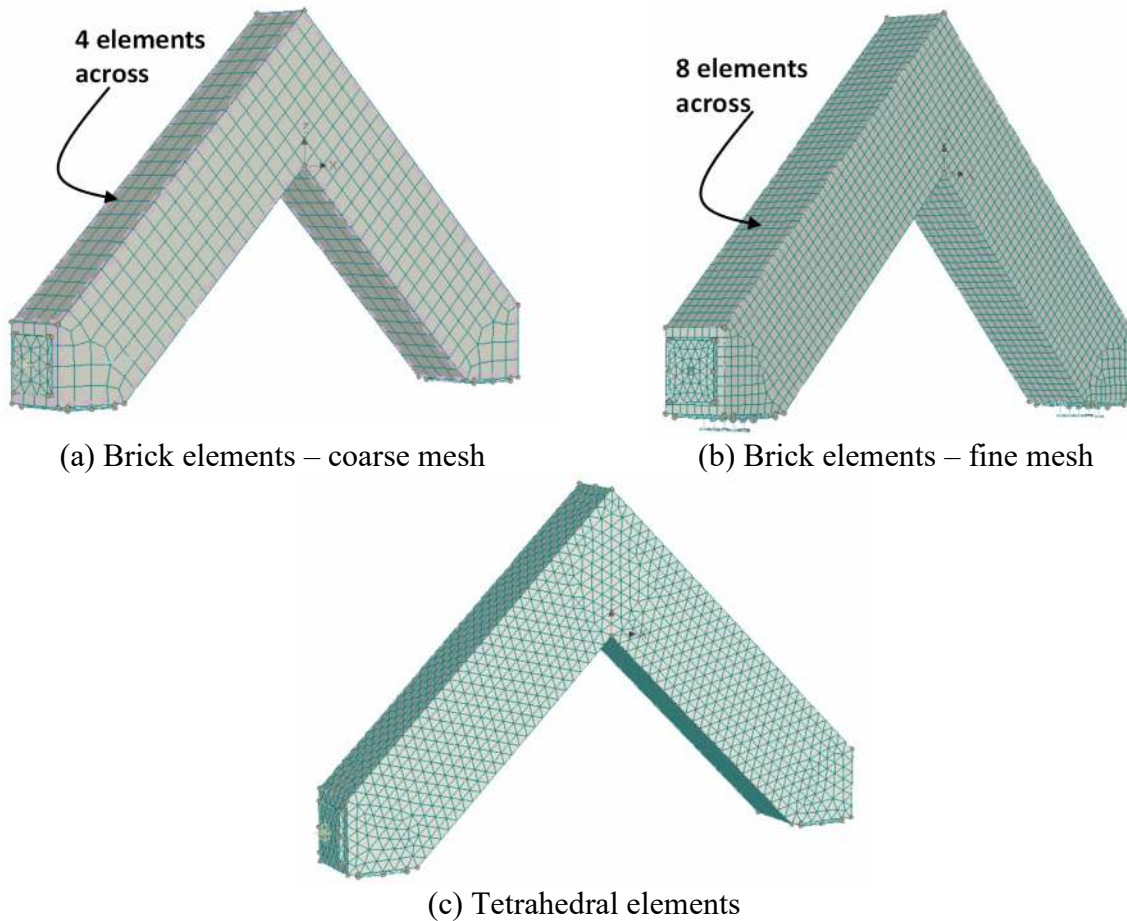


Figure 7-9 Mesh types and sizes used for validation

7.2.4 Solver Parameters

ATENA 3D provides the Newton-Raphson method and the modified Newton-Raphson method to derive solutions. For the analytical investigation, the Newton-Raphson method was used, in which the stiffness matrix is updated in each iteration and the load increment is based on tangent stiffness.⁸⁴ All the convergence criteria were by default. The iteration limitation for one step was set at 30. The line search method, which stabilizes the solving process⁸⁴ was activated, and the iteration limit was set at three.

7.3 Model Calibration

The selected benchmark specimens were from Group S-2 of the experimental program. More specifically, Specimens S-18-R3, S-18-R6, and S-18-R9 were used to calibrate the FEA model parameters because the three specimens were treated as a reference group in the

experimental program for comparison to other specimens. Furthermore, the tests on these three specimens demonstrated how the bend radius affects the behavior of closing knee joints in terms of failure mode, strength, and ductility. The calibration was based on the load-relative displacement curves, with special attention placed on the peak strength. Furthermore, the crack patterns from the FEA were compared to observations during the tests on the specimens.

7.3.1 Effect of various material parameters

Plots that show the load-relative displacement relationships of the three benchmark specimens are presented in Figure 7-10. The results from three different sets of parameters for concrete material were compared to the experimental load-relative displacement curves. The parameters that were varied are r_c^{lim} and w_d as noted in Table 7-1. A brick mesh with an element size of 0.05 m (that is, a fine brick mesh as introduced previously) was used. Other mesh options are evaluated later in Section 7.3.2. Generally, all three sets led to results that accurately capture the pre-peak behavior. The calculated stiffness and the calculated cracking load were obtained, and the curves are in good agreement with the experimental results. It should again be noted that Specimen S-18-R6 was unloaded and later reloaded during the test (see Section 4.2.1), causing the experimental response to not exhibit an uncracked stiffness. Furthermore, for Specimens S-18-R6 and S-18-R9, the load-carrying capacity was successfully captured, and the trend that larger bend radii lead to improved behavior was reflected by the FEA.

However, as indicated by the dashed green line in Figure 7-10(a), the default values for r_c^{lim} and w_d resulted in a peak load 19.3% less than the experimental value for Specimen S-18-R3. Moreover, the default values also resulted in an early loss in load-carrying capacity for Specimen S-18-R9 as shown in Figure 7-10(c). For Specimen S-18-R6, on the other hand, the FEA results generally matched the experimental curves.

A slight improvement was made when the value of r_c^{lim} was changed to 1.0. The calculated peak load for Specimen S-18-R3 increased to 125 kip, which was still 13.8% less than the experimental value. The analytical results for the other two specimens still demonstrate post-peak behavior, and the ultimate displacements are in agreement with the experimental results. Further increasing the value of w_d from 5 mm to 10 mm resulted in an improved estimate of the peak load for Specimen S-18-R3. The calculated peak load was 8.3% less than the experiment value. For the models mimicking Specimen S-18-R6, the adjustment resulted in the ductility indicated by the

FEA to be 11.5% greater than the experimental result, as indicated by the solid blue curve in Figure 7-10(b). Nevertheless, the results for Specimen S-18-R9 were not significantly affected.

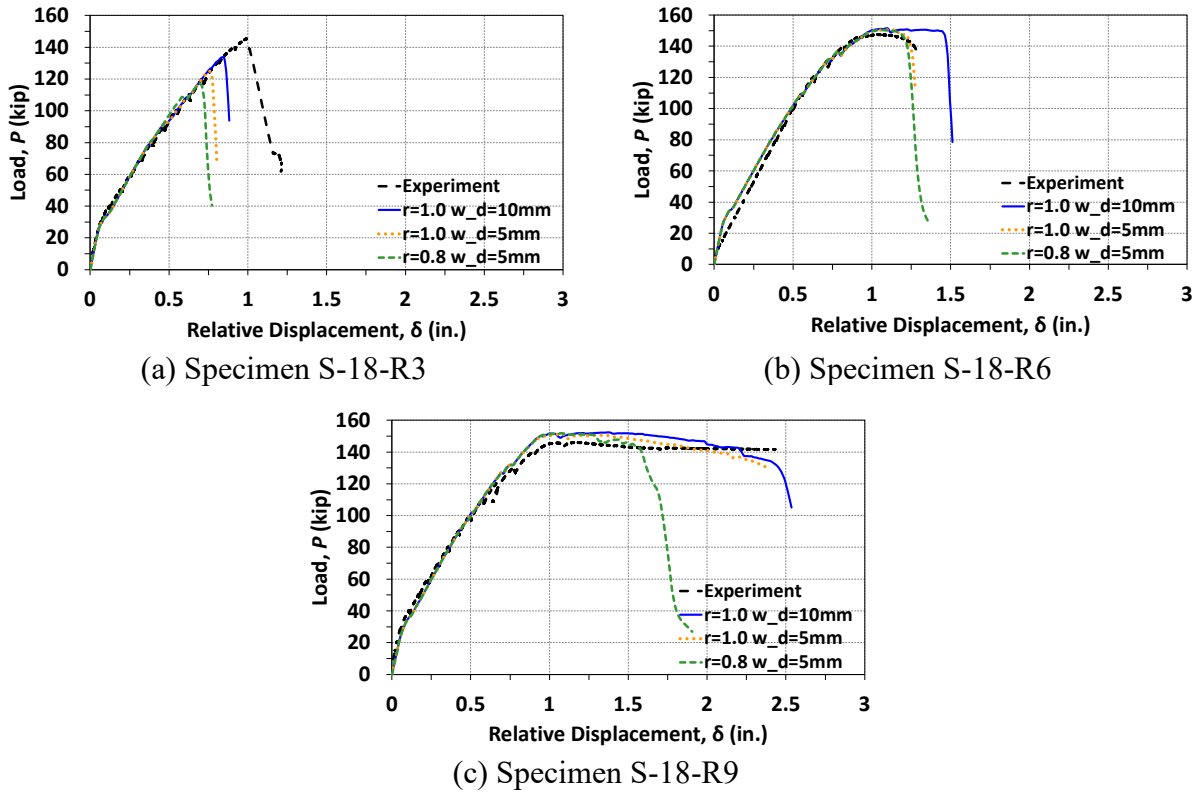


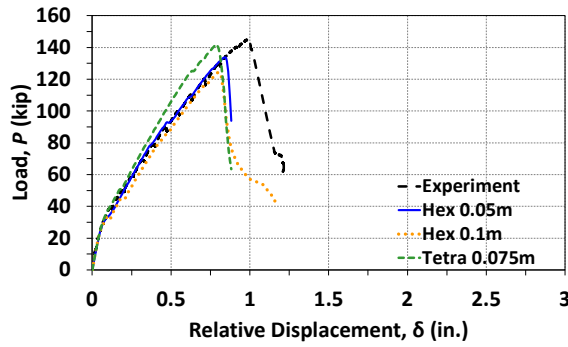
Figure 7-10 Calibration of FE models with various material parameters

7.3.2 Results from different mesh types

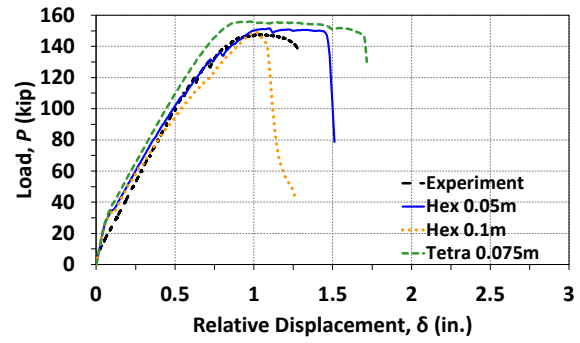
As the material parameters (r_c^{lim} equal to 1.0 and w_d equal to 10 mm) were proven to be effective, the mesh types and sizes shown in Figure 7-9 (fine brick, coarse brick, and tetrahedral elements) were evaluated. The fine brick (hexahedral) mesh used an element size of 0.05 m, which corresponds to eight elements across the width of the member cross section. The coarse brick mesh used an element size of 0.1 m, corresponding to four elements across the member width. Lastly, the tetrahedral mesh had an element size of 0.075 m. Plots that show the experimental and analytical load-relative displacement relationships of the three benchmark specimens are shown in Figure 7-11.

Generally, the tetrahedral elements delivered a stiffer post-cracking behavior compared to the hexahedral elements as shown in Figure 7-11. The tetrahedral elements also resulted in relatively greater peak load-carrying capacities for Specimens S-18-R6 and S-18-R9. For these specimens, the tetrahedral elements led to an overestimation of the experimental strengths, but a closer prediction resulted for Specimen S-18-R3 compared to the hexahedral elements. In spite of the overestimation of strength for two specimens, the results were, in general, still close to the experimental results. Moreover, the trend that larger bend radii leads to improved ductility was also captured. However, the maximum displacement of Specimen S-18-R6 was overestimated.

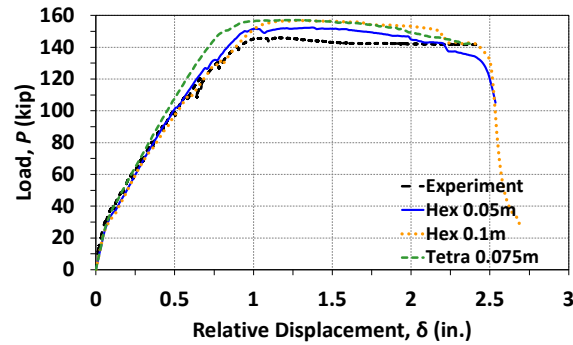
As shown in Figure 7-11, the pre-peak stiffnesses resulting from the use of fine brick mesh and coarse brick mesh are in good agreement with the experimental results. Nevertheless, the coarse elements resulted in an underestimation for the strength of Specimen S-18-R3 and an overestimation for the strength of Specimen S-18-R9. For Specimen S-18-R6, although the coarse elements led to the experimental capacity being accurately captured, the displacement was somewhat lower than the experimental result. The fine brick mesh resulted in slightly improved strength estimations for Specimens S-18-R3 and S-18-R9. For Specimen S-18-R6, the fine mesh resulted in the display of some ductility for the specimen, unlike the coarse mesh.



(a) Specimen S-18-R3



(b) Specimen S-18-R6

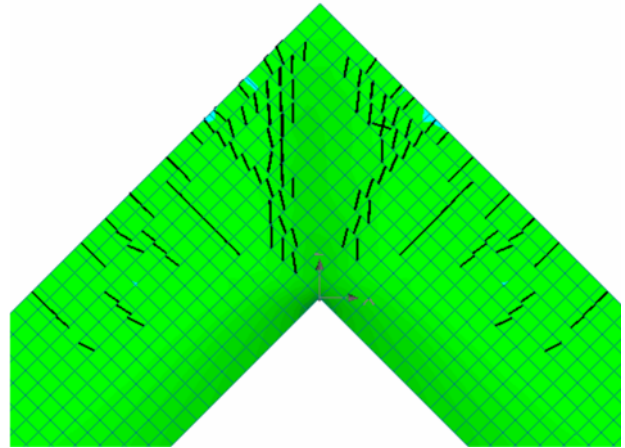


(c) Specimen S-18-R9

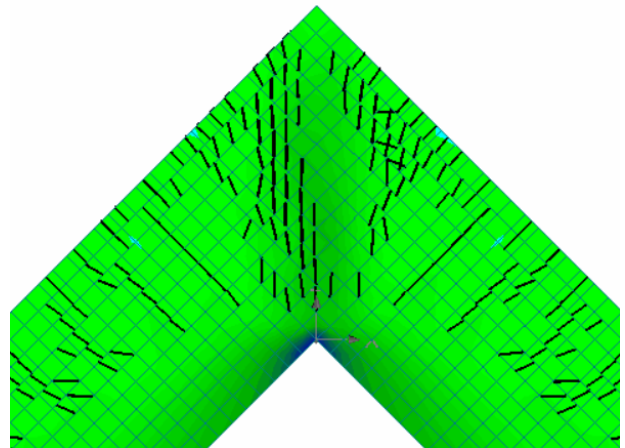
Figure 7-11 Calibration of FE models with various element types and sizes

7.3.3 Comparison of damage patterns at different load steps

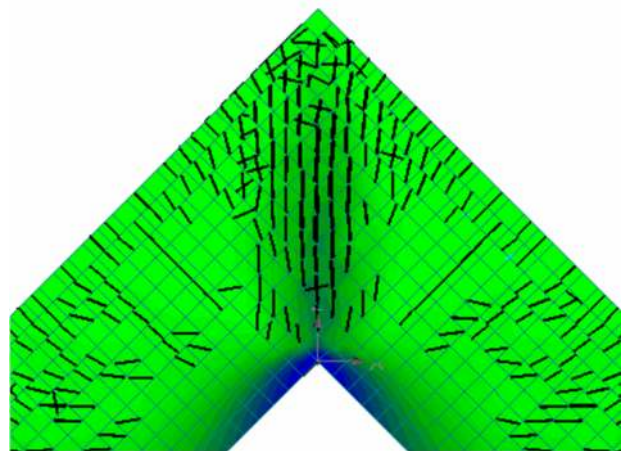
The comparison between the observed crack patterns and those indicated by ATENA 3D for the specimens used for validation is presented in Figure 7-12, Figure 7-13, and Figure 7-14 for different load steps. The damage patterns at various load steps and the propagation of cracks suggest that the software was able to accurately capture the actual cracking behavior of the specimen of the experimental program. As shown in the figures, the analytical results are in good agreement with the actual crack patterns observed during the experiments.



At $P = 60$ kip

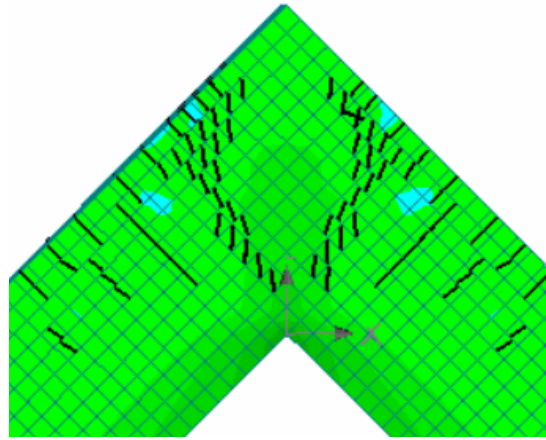


At $P = 90$ kip

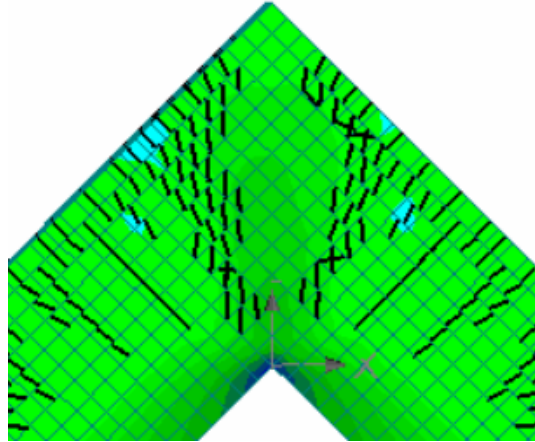


After failure

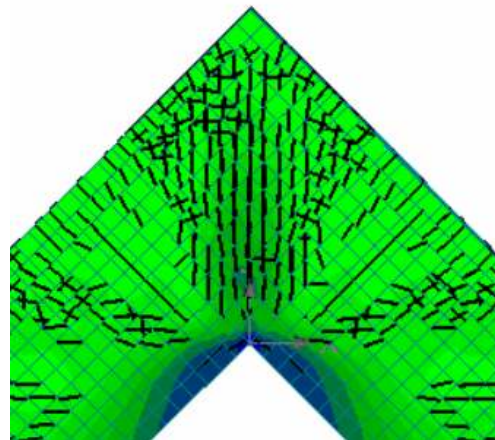
Figure 7-12 Comparison between actual and predicted damage patterns for Specimen S-18-R3



At $P = 60$ kip

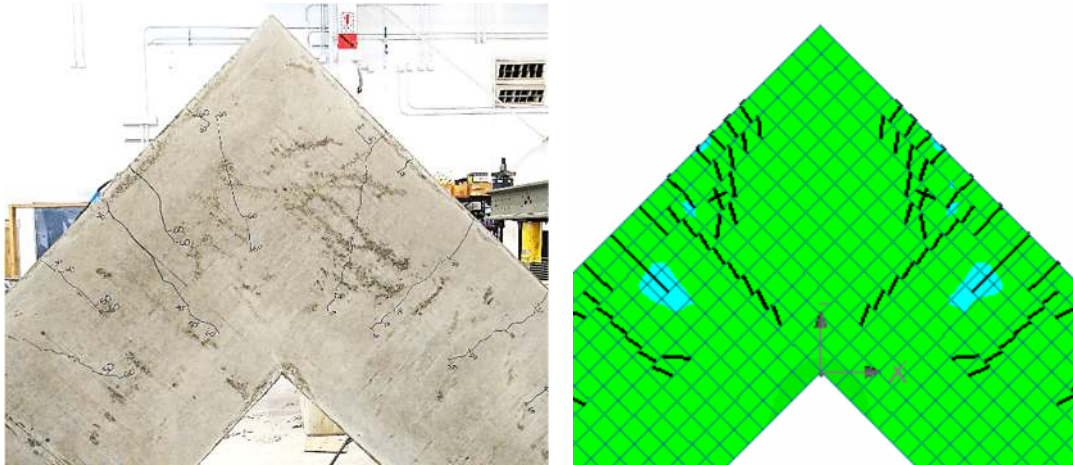


At $P = 90$ kip

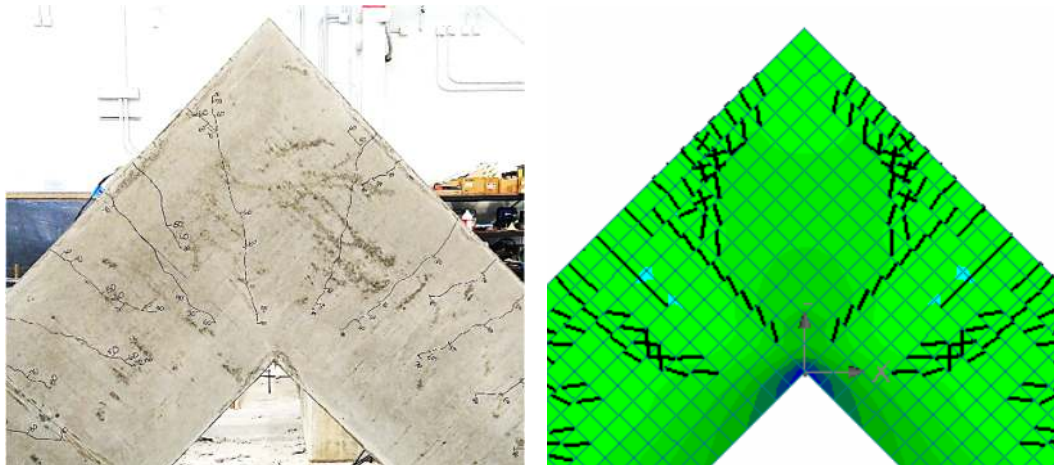


After failure

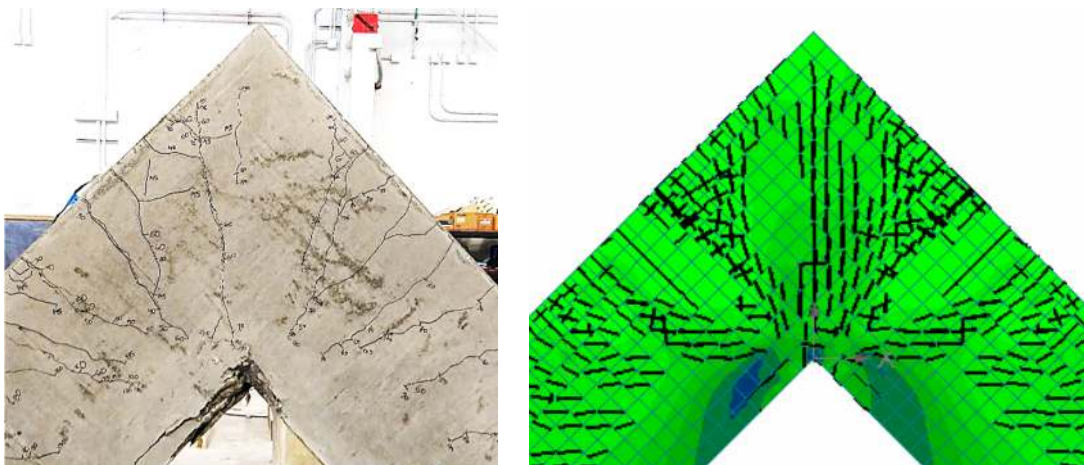
Figure 7-13 Comparison between actual and predicted damage patterns for Specimen S-18-R6



At $P = 60$ kip



At $P = 90$ kip



After the end of the test

Figure 7-14 Comparison between actual and predicted damage patterns for Specimen S-18-R9

7.3.4 Summary of Model Calibration

In sum, the software ATENA 3D was able to accurately predict the behavior of specimens in Group S-2 of the experimental program in terms of strength and stiffness. Furthermore, the effect of the bend radius was also captured. Based on the previous discussions, it was determined that FEA results best matched the experimental results when the fine brick mesh (element size of 0.05 m) was used, the parameter r_c^{lim} was set at 1.0, and the parameter w_d was set at 10 mm. These settings were therefore applied for the analytical investigation described in the following sections.

7.4 Analytical Investigation

A parametric analysis using the calibrated finite element model is presented in this section and used as a supplement to the experimental program in order to further evaluate the code-specified design expressions for the bend radius of curved-bar nodes. The primary variables for this analytical investigation are as follows: (a) bend radius, (b) mechanical longitudinal reinforcement ratio, (c) clear side cover, (d) presence of transverse reinforcement, and (e) diagonal strut angle. A total of 72 numerical specimens were analyzed. These specimens were divided into five series named to match specimen series of the experimental program: FEM-S-Series, FEM-D-Series, FEM-C-Series, FEM-TR-Series, and FEM-B-Series. The first four series consist of specimens with adjoining members with matching cross sections and are summarized in Table 7-2. The fifth series, FEM-B-Series, consists of specimens with adjoining members with different cross sections and is summarized in Table 7-3. The nomenclature for identifying the numerical specimens is shown in Figure 7-15. The mechanical reinforcement ratios within the specimen IDs are approximate. Most of the numbers were taken as the integer number of the mechanical reinforcement ratios with some exceptions in Series FEM-TR. The series resembled specimens in Group TR of the experimental program, and therefore, the number in the specimen IDs for the mechanical reinforcement ratios are also “13” to ease comparisons between numerical and experimental specimens. Exact values for the mechanical reinforcement ratios are provided in Table 7-2 and Table 7-3.

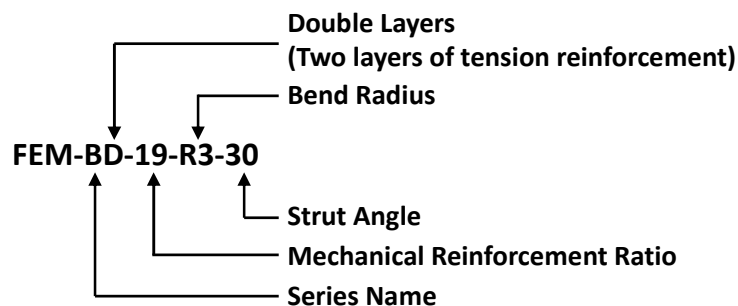


Figure 7-15 Nomenclature for numerical specimens

The configuration of the numerical specimens resembled the specimens of the experimental program as illustrated in Figure 7-16. That is, each of the numerical specimens consisted of a joint into which two 70-in. long adjoining members framed. Both legs were reinforced with No. 4 stirrups with a spacing of 4 in. to prevent the occurrence of a shear failure. The reduced stirrup spacing of 3 in. that was used near the end of each leg in the experimental program was not included. No surface reinforcement was assigned for simplicity. On each of the two surfaces at the end of each leg, a steel plate was modeled and connected.

Table 7-2 FEA numerical specimens with identical adjoining members

| Series | Specimen ID | f'_c (ksi) | Long. Reinf. | A_{ts} (in. ²) | f_y (ksi) | ω (%) | c_c (in.) | d_b (in.) | r_b (in.) | b (in.) | h (in.) | d (in.) | Criteria* |
|-----------------|---------------|-----------------|-----------------|---------------------------------|----------------|-----------------|----------------|----------------|----------------|--------------|--------------|--------------|-----------|
| FEM S-Series | FEM-S-19-R4 | 5.00 | 5-No. 9 | 5.00 | 67.00 | 19.53 | 2.00 | 1.13 | 4.51 | 16 | 24 | 21.44 | (1) |
| | FEM-S-19-R6 | 5.00 | 5-No. 9 | 5.00 | 67.00 | 19.53 | 2.00 | 1.13 | 6.50 | 16 | 24 | 21.44 | (3) |
| | FEM-S-19-R8 | 5.00 | 5-No. 9 | 5.00 | 67.00 | 19.53 | 2.00 | 1.13 | 8.50 | 16 | 24 | 21.44 | (2) |
| | FEM-S-19-R12 | 5.00 | 5-No. 9 | 5.00 | 67.00 | 19.53 | 2.00 | 1.13 | 12.75 | 16 | 24 | 21.44 | (4) |
| FEM D-Series | FEM-DD-21-R2 | 5.00 | 12-No. 6 | 5.28 | 67.00 | 21.57 | 2.00 | 0.75 | 2.25 | 16 | 24 | 20.50 | (1) |
| | FEM-DD-21-R5 | 5.00 | 12-No. 6 | 5.28 | 67.00 | 21.57 | 2.00 | 0.75 | 5.88 | 16 | 24 | 20.50 | (3) |
| | FEM-DD-21-R9 | 5.00 | 12-No. 6 | 5.28 | 67.00 | 21.57 | 2.00 | 0.75 | 9.50 | 16 | 24 | 20.50 | (2) |
| | FEM-DD-21-R14 | 5.00 | 12-No. 6 | 5.28 | 67.00 | 21.57 | 2.00 | 0.75 | 14.25 | 16 | 24 | 20.50 | (4) |
| | FEM-DD-26-R3 | 5.00 | 8-No. 8 | 6.32 | 67.00 | 26.14 | 2.00 | 1.00 | 3.00 | 16 | 24 | 20.25 | (1) |
| | FEM-DD-26-R7 | 5.00 | 8-No. 8 | 6.32 | 67.00 | 26.14 | 2.00 | 1.00 | 7.25 | 16 | 24 | 20.25 | (3) |
| | FEM-DD-26-R11 | 5.00 | 8-No. 8 | 6.32 | 67.00 | 26.14 | 2.00 | 1.00 | 11.50 | 16 | 24 | 20.25 | (2) |
| | FEM-DD-26-R17 | 5.00 | 8-No. 8 | 6.32 | 67.00 | 26.14 | 2.00 | 1.00 | 17.25 | 16 | 24 | 20.25 | (4) |
| FEM C-Series | FEM-C-19-R4 | 5.00 | 5-No. 9 | 5.00 | 67.00 | 19.53 | 1.25 | 1.13 | 4.51 | 16 | 24 | 21.44 | (1) |
| | FEM-C-19-R6 | 5.00 | 5-No. 9 | 5.00 | 67.00 | 19.53 | 1.25 | 1.13 | 6.50 | 16 | 24 | 21.44 | (3) |
| | FEM-C-19-R8 | 5.00 | 5-No. 9 | 5.00 | 67.00 | 19.53 | 1.25 | 1.13 | 8.50 | 16 | 24 | 21.44 | (2) |
| | FEM-C-19-R12 | 5.00 | 5-No. 9 | 5.00 | 67.00 | 19.53 | 1.25 | 1.13 | 12.75 | 16 | 24 | 21.44 | (4) |
| | FEM-C-13-R3 | 5.15 | 6-No. 7 | 3.60 | 66.10 | 13.43 | 1.25 | 0.88 | 3.30 | 16 | 24 | 21.56 | (1) |
| | FEM-C-13-R4 | 5.28 | 6-No. 7 | 3.60 | 66.10 | 13.10 | 1.25 | 0.88 | 4.70 | 16 | 24 | 21.56 | (3) |
| | FEM-C-13-R8 | 5.35 | 6-No. 7 | 3.60 | 66.10 | 12.93 | 1.25 | 0.88 | 8.10 | 16 | 24 | 21.56 | (2) |
| | FEM-C-13-R12 | 5.35 | 6-No. 7 | 3.60 | 66.10 | 12.93 | 1.25 | 0.88 | 12.00 | 16 | 24 | 21.56 | (4) |
| | FEM-CD-21-R2 | 5.00 | 12-No. 6 | 5.28 | 67.00 | 21.57 | 1.25 | 0.75 | 2.25 | 16 | 24 | 20.50 | (1) |
| | FEM-CD-21-R6 | 5.00 | 12-No. 6 | 5.28 | 67.00 | 21.57 | 1.25 | 0.75 | 6.50 | 16 | 24 | 20.50 | (3) |
| | FEM-CD-21-R10 | 5.00 | 12-No. 6 | 5.28 | 67.00 | 21.57 | 1.25 | 0.75 | 10.75 | 16 | 24 | 20.50 | (2) |
| | FEM-CD-21-R16 | 5.00 | 12-No. 6 | 5.28 | 67.00 | 21.57 | 1.25 | 0.75 | 16.13 | 16 | 24 | 20.50 | (4) |
| | FEM-CD-26-R3 | 5.00 | 8-No. 8 | 6.32 | 67.00 | 26.14 | 1.25 | 1.00 | 3.00 | 16 | 24 | 20.25 | (1) |
| | FEM-CD-26-R7 | 5.00 | 8-No. 8 | 6.32 | 67.00 | 26.14 | 1.25 | 1.00 | 7.25 | 16 | 24 | 20.25 | (3) |
| | FEM-CD-26-R10 | 5.00 | 8-No. 8 | 6.32 | 67.00 | 26.14 | 1.25 | 1.00 | 11.50 | 16 | 24 | 20.25 | (2) |
| | FEM-CD-26-R17 | 5.00 | 8-No. 8 | 6.32 | 67.00 | 26.14 | 1.25 | 1.00 | 17.25 | 16 | 24 | 20.25 | (4) |

Table 7-2 FEA numerical specimens with identical adjoining members (cont'd)

| Series | Specimen ID | f'_c (ksi) | Long. Reinf. | A_{ts} (in. ²) | f_y (ksi) | ω (%) | c_c (in.) | d_b (in.) | r_b (in.) | b (in.) | h (in.) | d (in.) | Criteria* |
|------------------|---------------|-----------------|-----------------|---------------------------------|----------------|-----------------|----------------|----------------|----------------|--------------|--------------|--------------|-----------|
| FEM TR-Series | FEM-TR-18-R6 | 4.84 | 6-No. 8 | 4.74 | 66.30 | 18.85 | 2.00 | 1.00 | 6.50 | 16 | 24 | 21.50 | (3) |
| | FEM-TR-18-R9 | 4.84 | 6-No. 8 | 4.74 | 66.30 | 18.85 | 2.00 | 4.84 | 9.80 | 16 | 24 | 21.50 | (2) |
| | FEM-TR-18-R14 | 4.84 | 6-No. 8 | 4.74 | 66.30 | 18.85 | 2.00 | 4.84 | 11.50 | 16 | 24 | 21.50 | (4) |
| | FEM-TR-13-R4 | 4.66 | 6-No. 7 | 3.60 | 64.72 | 14.49 | 2.00 | 0.88 | 4.70 | 16 | 24 | 21.56 | (3) |
| | FEM-TR-13-R8 | 4.66 | 6-No. 7 | 3.60 | 64.72 | 14.49 | 2.00 | 0.88 | 8.10 | 16 | 24 | 21.56 | (2) |
| | FEM-TR-13-R14 | 4.66 | 6-No. 7 | 3.60 | 64.72 | 14.49 | 2.00 | 0.88 | 12.00 | 16 | 24 | 21.56 | (4) |
| | FEM-TR-19-R4 | 5.00 | 5-No. 9 | 5.00 | 67.00 | 19.53 | 2.00 | 1.13 | 4.51 | 16 | 24 | 21.44 | (1) |
| | FEM-TR-19-R6 | 5.00 | 5-No. 9 | 5.00 | 67.00 | 19.53 | 2.00 | 1.13 | 6.50 | 16 | 24 | 21.44 | (3) |
| | FEM-TR-19-R8 | 5.00 | 5-No. 9 | 5.00 | 67.00 | 19.53 | 2.00 | 1.13 | 8.50 | 16 | 24 | 21.44 | (2) |
| | FEM-TR-19-R12 | 5.00 | 5-No. 9 | 5.00 | 67.00 | 19.53 | 2.00 | 1.13 | 12.75 | 16 | 24 | 21.44 | (4) |

Note: * (1) Bar bend satisfies ACI 318¹ minimum radius.

(2) Bar bend satisfies Eq. 2-20.

(3) Bar bend is between that of a standard hook and the radius based on Eq. 2-20.

(4) Bar bend approximately satisfies Eq. 2-20 multiplied by 1.5.

Table 7-3 FEA numerical specimens with different adjoining members (FEM-B-Series)

| Specimen ID | f'_c (ksi) | Long. Reinf. | A_{ts} (in. ²) | f_y (ksi) | ω (%) | c_c (in.) | r_b (in.) | b (in.) | h_1 (in.) | d_1 (in.) | h_2 (in.) | d_2 (in.) | θ_c (Degree) | Criteria* |
|-----------------|-----------------|-----------------|---------------------------------|----------------|-----------------|----------------|----------------|--------------|----------------|----------------|----------------|----------------|------------------------|-----------|
| FEM-B-17-R3-30 | 5.00 | 4-No. 8 | 3.16 | 67.00 | 17.07 | 2.00 | 3.00 | 16.00 | 18.00 | 15.50 | 29.00 | 26.50 | 30.32 | (1) |
| FEM-B-17-R5-30 | 5.00 | 4-No. 8 | 3.16 | 67.00 | 17.07 | 2.00 | 4.50 | 16.00 | 18.00 | 15.50 | 29.00 | 26.50 | 30.32 | (3) |
| FEM-B-17-R7-30 | 5.00 | 4-No. 8 | 3.16 | 67.00 | 17.07 | 2.00 | 6.00 | 16.00 | 18.00 | 15.50 | 29.00 | 26.50 | 30.32 | (2) |
| FEM-B-17-R10-30 | 5.00 | 4-No. 8 | 3.16 | 67.00 | 17.07 | 2.00 | 9.00 | 16.00 | 18.00 | 15.50 | 29.00 | 26.50 | 30.32 | (4) |
| FEM-B-17-R3-35 | 5.00 | 4-No. 8 | 3.16 | 67.00 | 17.07 | 2.00 | 3.00 | 16.00 | 18.00 | 15.50 | 25.00 | 22.50 | 34.56 | (1) |
| FEM-B-17-R4-35 | 5.00 | 4-No. 8 | 3.16 | 67.00 | 17.07 | 2.00 | 4.50 | 16.00 | 18.00 | 15.50 | 25.00 | 22.50 | 34.56 | (3) |
| FEM-B-17-R6-35 | 5.00 | 4-No. 8 | 3.16 | 67.00 | 17.07 | 2.00 | 6.00 | 16.00 | 18.00 | 15.50 | 25.00 | 22.50 | 34.56 | (2) |
| FEM-B-17-R9-35 | 5.00 | 4-No. 8 | 3.16 | 67.00 | 17.07 | 2.00 | 9.00 | 16.00 | 18.00 | 15.50 | 25.00 | 22.50 | 34.56 | (4) |
| FEM-B-17-R3-40 | 5.00 | 4-No. 8 | 3.16 | 67.00 | 17.07 | 2.00 | 3.00 | 16.00 | 18.00 | 15.50 | 21.00 | 18.50 | 39.96 | (1) |

Table 7-3 FEA numerical specimens with different adjoining members (FEM-B-Series) (cont'd)

| Specimen ID | f'_c (ksi) | Long. Reinf. | A_{ts} (in. ²) | f_y (ksi) | ω (%) | c_c (in.) | r_b (in.) | b (in.) | h_1 (in.) | d_1 (in.) | h_2 (in.) | d_2 (in.) | θ_c (Degree) | Criteria* |
|------------------|-----------------|-----------------|---------------------------------|----------------|-----------------|----------------|----------------|--------------|----------------|----------------|----------------|----------------|------------------------|-----------|
| FEM-B-17-R4-40 | 5.00 | 4-No. 8 | 3.16 | 67.00 | 17.07 | 2.00 | 4.50 | 16.00 | 18.00 | 15.50 | 21.00 | 18.50 | 39.96 | (3) |
| FEM-B-17-R6-40 | 5.00 | 4-No. 8 | 3.16 | 67.00 | 17.07 | 2.00 | 6.00 | 16.00 | 18.00 | 15.50 | 21.00 | 18.50 | 39.96 | (2) |
| FEM-B-17-R9-40 | 5.00 | 4-No. 8 | 3.16 | 67.00 | 17.07 | 2.00 | 9.00 | 16.00 | 18.00 | 15.50 | 21.00 | 18.50 | 39.96 | (4) |
| FEM-B-17-R3-45 | 5.00 | 4-No. 8 | 3.16 | 67.00 | 17.07 | 2.00 | 3.00 | 16.00 | 18.00 | 15.50 | 18.00 | 15.50 | 45.00 | (1) |
| FEM-B-17-R6-45 | 5.00 | 4-No. 8 | 3.16 | 67.00 | 17.07 | 2.00 | 4.50 | 16.00 | 18.00 | 15.50 | 18.00 | 15.50 | 45.00 | (3) |
| FEM-B-17-R9-45 | 5.00 | 4-No. 8 | 3.16 | 67.00 | 17.07 | 2.00 | 6.00 | 16.00 | 18.00 | 15.50 | 18.00 | 15.50 | 45.00 | (2) |
| FEM-B-17-R12-45 | 5.00 | 4-No. 8 | 3.16 | 67.00 | 17.07 | 2.00 | 9.00 | 16.00 | 18.00 | 15.50 | 18.00 | 15.50 | 45.00 | (4) |
| FEM-BD-18-R2-30 | 5.00 | 8-No. 6 | 3.52 | 67.00 | 18.87 | 2.00 | 2.25 | 16.00 | 18.00 | 15.63 | 29.00 | 26.63 | 30.41 | (1) |
| FEM-BD-18-R6-30 | 5.00 | 8-No. 6 | 3.52 | 67.00 | 18.87 | 2.00 | 4.63 | 16.00 | 18.00 | 15.63 | 29.00 | 26.63 | 30.41 | (3) |
| FEM-BD-18-R10-30 | 5.00 | 8-No. 6 | 3.52 | 67.00 | 18.87 | 2.00 | 7.00 | 16.00 | 18.00 | 15.63 | 29.00 | 26.63 | 30.41 | (2) |
| FEM-BD-18-R16-30 | 5.00 | 8-No. 6 | 3.52 | 67.00 | 18.87 | 2.00 | 10.50 | 16.00 | 18.00 | 15.63 | 29.00 | 26.63 | 30.41 | (4) |
| FEM-BD-18-R2-35 | 5.00 | 8-No. 6 | 3.52 | 67.00 | 18.87 | 2.00 | 2.25 | 16.00 | 18.00 | 15.63 | 25.00 | 22.63 | 34.63 | (1) |
| FEM-BD-18-R5-35 | 5.00 | 8-No. 6 | 3.52 | 67.00 | 18.87 | 2.00 | 4.63 | 16.00 | 18.00 | 15.63 | 25.00 | 22.63 | 34.63 | (3) |
| FEM-BD-18-R9-35 | 5.00 | 8-No. 6 | 3.52 | 67.00 | 18.87 | 2.00 | 7.00 | 16.00 | 18.00 | 15.63 | 25.00 | 22.63 | 34.63 | (2) |
| FEM-BD-18-R13-35 | 5.00 | 8-No. 6 | 3.52 | 67.00 | 18.87 | 2.00 | 10.50 | 16.00 | 18.00 | 15.63 | 25.00 | 22.63 | 34.63 | (4) |
| FEM-BD-18-R2-40 | 5.00 | 8-No. 6 | 3.52 | 67.00 | 18.87 | 2.00 | 2.25 | 16.00 | 18.00 | 15.63 | 21.00 | 18.63 | 39.99 | (1) |
| FEM-BD-18-R5-40 | 5.00 | 8-No. 6 | 3.52 | 67.00 | 18.87 | 2.00 | 4.63 | 16.00 | 18.00 | 15.63 | 21.00 | 18.63 | 39.99 | (3) |
| FEM-BD-18-R8-40 | 5.00 | 8-No. 6 | 3.52 | 67.00 | 18.87 | 2.00 | 7.00 | 16.00 | 18.00 | 15.63 | 21.00 | 18.63 | 39.99 | (2) |
| FEM-BD-18-R12-40 | 5.00 | 8-No. 6 | 3.52 | 67.00 | 18.87 | 2.00 | 10.50 | 16.00 | 18.00 | 15.63 | 21.00 | 18.63 | 39.99 | (4) |
| FEM-BD-18-R2-45 | 5.00 | 8-No. 6 | 3.52 | 67.00 | 18.87 | 2.00 | 2.25 | 16.00 | 18.00 | 15.63 | 18.00 | 15.63 | 45.00 | (1) |
| FEM-BD-18-R5-45 | 5.00 | 8-No. 6 | 3.52 | 67.00 | 18.87 | 2.00 | 4.63 | 16.00 | 18.00 | 15.63 | 18.00 | 15.63 | 45.00 | (3) |
| FEM-BD-18-R8-45 | 5.00 | 8-No. 6 | 3.52 | 67.00 | 18.87 | 2.00 | 7.00 | 16.00 | 18.00 | 15.63 | 18.00 | 15.63 | 45.00 | (2) |
| FEM-BD-18-R12-45 | 5.00 | 8-No. 6 | 3.52 | 67.00 | 18.87 | 2.00 | 10.50 | 16.00 | 18.00 | 15.63 | 18.00 | 15.63 | 45.00 | (4) |

Note: * (1) Bar bend satisfies ACI 318¹ minimum radius.

(2) Bar bend satisfies Eq. 2-20.

(3) Bar bend is between that of a standard hook and the radius based on Eq. 2-20.

(4) Bar bend approximately satisfies Eq. 2-20 multiplied by 1.5.

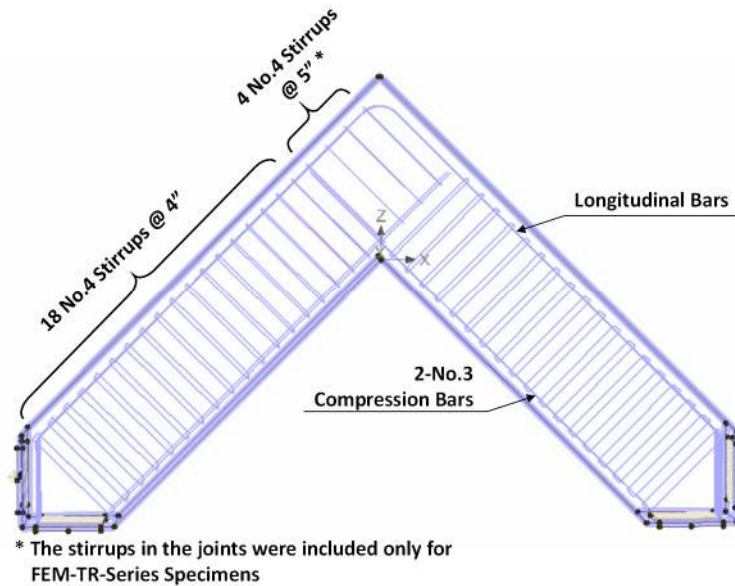


Figure 7-16 Configuration of numerical specimens (with identical adjoining members)

The FEM-S-Series and FEM-D-Series correspond to specimens with a single layer of longitudinal tension reinforcement and specimens with two layers of longitudinal tension reinforcement, respectively. Based on the area of longitudinal reinforcement, cross-sectional dimensions, and material properties, three different mechanical longitudinal reinforcement ratios, ω , were generated: 19.53%, 21.57%, and 26.14%. For each value of ω , specimens with four different bend radii were modeled: 1) the minimum inside bend diameter for standard hooks required by ACI 318-19¹, 2) the bend radius satisfying the ACI requirement for limiting radial stress at the curved-bar node (Eq. 2-20) without the factor for thin side cover, 3) a bend radius between that of criterion (1) and criterion (2), and 4) approximately 1.5 times the bend radius of criterion (2). The FEM-C-Series, on the other hand, repeated all FEM-S-Series and FEM-D-Series specimens, but the clear side cover, c_c , was thinner (see Table 7-2). In addition, four more specimens with six No. 7 bars as the longitudinal tension reinforcement were included. These numerical specimens had the same mechanical longitudinal reinforcement ratios as the physical specimens in Group S-3 of the S-Series specimens but were given thinner clear side cover. The values of f'_c and f_y are different for these numerical specimens compared to other numerical specimens to provide values of ω that match those of the Group S-3 specimens in the experimental program.

Specimens with transverse reinforcement in the joint are in the FEM-TR-Series. Ten specimens with values of ω equal to 14.49%, 18.85%, and 19.53% were included in this series. The mechanical longitudinal reinforcement ratios were chosen to match the values of ω of the specimens in Group TR of the experimental program or be equal to the value of ω of the FEM-S-Series specimens. The amount of transverse reinforcement in the joint was chosen in accordance with the minimum amount required by Section 23.5.1 in ACI 318-19,¹ which corresponds to No. 4 stirrups at 5-in. spacing. This matches the transverse reinforcement provided in the joints of the Group TR specimens of the experimental program (see Section 3.2.5).

To study the effect of varying strut angles within the joint, the FEM-B-Series specimens listed in Table 7-3 had one adjoining member equal to or shallower than the other member to create four different strut angles. More specifically, one leg had a depth of 18 in., while the other had a depth ranging from 18 in. to 29 in. as shown in Figure 7-17. Therefore, some numerical specimens had adjoining members with matching cross sections for comparison purposes. It should be noted that the diagonal strut angles listed in Table 7-3 were calculated based on Eq. 5-1. Two different mechanical longitudinal reinforcement ratios were selected (17.07% and 18.87%). For each combination of strut angle and mechanical reinforcement ratio, numerical specimens with four different bend radii based on the four criteria previously described were analyzed, resulting in a total of 32 specimens.

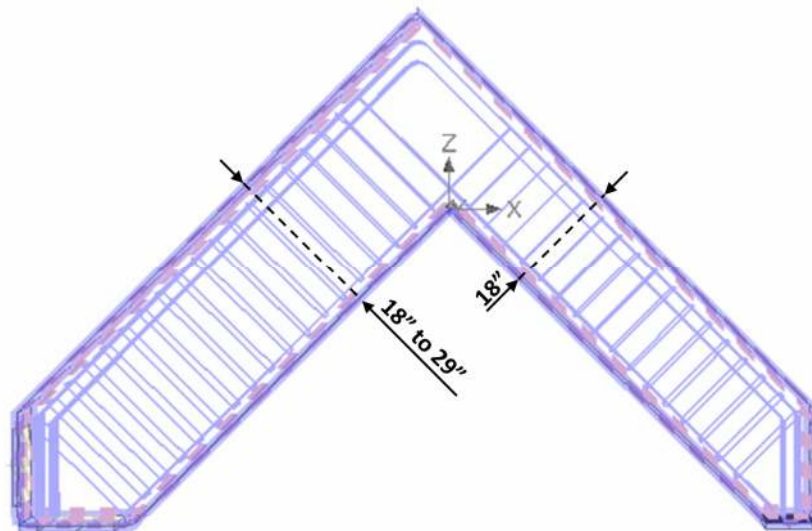


Figure 7-17 Different adjoining member depths of numerical specimens in FEM-B-Series

The parameters used for the concrete model are summarized in Table 7-4. Under the “Basic” subset, the compressive strength of concrete was specified as 34.5 MPa (equivalent to 5.0 ksi). The elastic modulus was taken as $57,000\sqrt{f'_c}$ psi ($4731\sqrt{f'_c}$ MPa) and the Poisson’s ratio was taken as 0.2 as widely used in practice. The tensile strength was taken as $0.33\sqrt{f'_c}$ MPa by default. Under the “Tensile” subset, the specific fracture energy was taken as $0.000025f'_t$ by default and the other parameters remained deactivated. Under the “Compressive” subset, the critical compressive displacement, w_d , was taken as 10 mm, and the reduction of compressive strength due to cracks, r_c^{lim} , was taken as 1.0 as determined during the validation process for the numerical model. The rest of the parameters were all taken by default.

Table 7-4 Concrete material model used in the analytical investigation

| Subset | Parameter | Used Value |
|---------------|---|--------------------------|
| Basic | Elastic modulus, E_c | 27,789 MPa |
| | Poisson’s ratio, ν | 0.2 |
| | Tensile strength, f'_t | 1.9375 MPa |
| | Compressive strength, f'_c | 34.5 MPa |
| Tensile | Specific Fracture Energy, G_f | 4.844e-5 MN/m |
| | Crack spacing, s_{max} | Deactivated |
| | Tension stiffening, c_{ts} | Deactivated |
| | Unloading | Deactivated |
| Compressive | Critical compressive displacement, w_d | 10 mm |
| | Plastic strain at compressive strength, ϵ_{cp} | 1.241e-3 |
| | Reduction of comp. strength due to cracks, r_c^{lim} | 1.0 |
| Shear | Crack shear stiffness factor, s_F | 20 |
| | Aggregate size | 0.020 m |
| | Aggregate interlock | Activated |
| Miscellaneous | Failure surface eccentricity | 0.52 |
| | Multiplier for the plastic flow direction, β | 0 |
| | Specific material weight, ρ | 2.3e-2 MN/m ³ |
| | Coefficient of thermal expansion, α | 1.2e-5 1/K |
| | Fixed crack model coefficient | 1.0 |

As incorporated into the models used for validation, the reinforcement was modeled as elastic-perfectly plastic. A yield strength of 67 ksi was input as a realistic value for Grade 60 reinforcement with some exceptions in order to match specimens in the experimental program, as mentioned above and shown in Table 7-2. The modulus of elasticity was taken as 200,000 MPa, as widely used for reinforcement. The steel plates for bearing and supports were assigned an elastic material model with a modulus of elasticity of 200,000 MPa.

For the FEM-B-Series specimens, bond stress was expected to develop along the bar bend at the outer corner. To capture any effect of the bond stress on the failure behavior of the specimens, the bond-slip model between reinforcement and concrete was activated for this series. The bond-slip model used in ATENA 3D is based on CEP-FIB model code 1990²⁵ and describes the bond strength between reinforcement and the surrounded concrete with regard to the magnitude of slip as shown in Figure 7-18. Parameters shown in the figure that define the bond-slip relationship depend on concrete compressive strength, confinement of concrete, the type of reinforcement, and bond condition. In this case, unconfined concrete was used because no reinforcement was provided in the joint, and good bond condition was used.^{25,84} For the type of reinforcement, ribbed bars were selected. The selections automatically generated a set of parameters shown in Table 7-5.

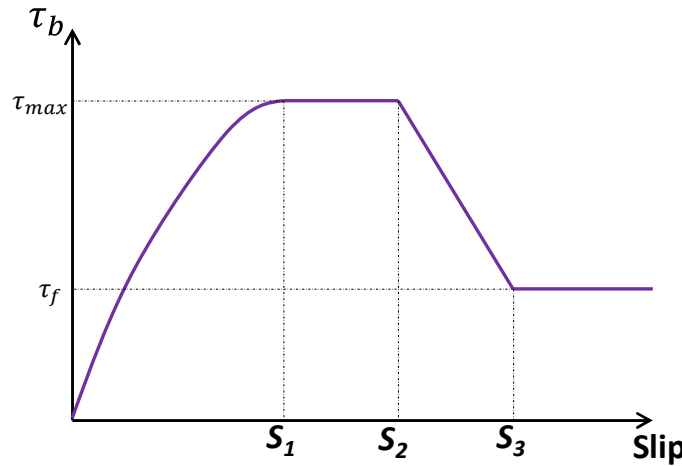


Figure 7-18 Bond-slip relationship used in ATENA 3D (adapted from ATENA 3D⁸⁴ and CEB-FIP model code²⁵)

Table 7-5 Parameters defining bond-slip relationship

| Parameter | Value |
|--------------|---|
| S_1 | 0.6 mm (0.023 in.) |
| S_2 | 0.6 mm (0.023 in.) |
| S_3 | 1.0 mm (0.023 in.) |
| α | 0.4 |
| τ_{max} | $2.0\sqrt{f'_c}$ MPa ($0.76\sqrt{f'_c}$ ksi) |
| τ_f | $0.15\tau_{max}$ |
| τ_b | $\tau_{max}\left(\frac{s}{s_1}\right)^\alpha$ $0 \leq s \leq S_1$ |

The typical finite element model is shown in Figure 7-9(b). For concrete, brick mesh with an element size of 0.05 m was used, which was determined to provide the best results during the validation process using benchmark specimens. The steel plates were meshed using tetrahedral elements, and the reinforcement was modeled using 1D elements, matching the models used for validation. For each step of the analysis, loads were again modeled as prescribed displacements of 0.2 mm at the center of each load plate. Boundary conditions were applied along the centerline of each support plate to allow displacement only along the x-axis as shown in Figure 7-7.

7.5 Results and Discussion of the Numerical Investigation

The results of the analytical investigation are introduced in this section. The effect of the bend radius and of the mechanical reinforcement ratio on the strength of closing knee joints is first discussed. Then, the effects of thin clear side cover and transverse reinforcement are evaluated. Lastly, the influence of the diagonal strut angle is studied. Methods for predicting the strengths of specimens are also compared to the finite element results.

7.5.1 Evaluation of the Strength of Numerical Specimens with Identical Adjoining Members

7.5.1.1 FEM-S-Series and FEM-D-Series

Plots that show the load-relative displacement relationships of the FEM-S-Series and FEM-D-Series specimens are presented in Figure 7-19. Each plot includes results from specimens with the same area of longitudinal reinforcement. Therefore, specimens with different bend radii are arranged in the same plot. In the plots, horizontal dashed red lines indicate the calculated load-carrying capacity based on the nominal flexural capacity at the joint face, P_{calc} , and the load-carrying capacity based on the joint shear capacity, P_{shear} . The methods used to determine the values of P_{calc} and P_{shear} are detailed in Section 6.3. The corresponding results of the analytical investigation are summarized in Table 7-6, in which P_{FEA} is the peak strength indicated by the finite element analysis. Two required bend radii were shown in Table 7-6: $r_{b,ACI}$ and $r_{b,modified}$. The former radius is based on the ACI 318-19¹ requirement in consideration of radial stresses at the bar bend with the factor for clear side cover ($2d_b/c_c$) included. The latter radius is based on the same ACI requirement but with the reduced factor discussed in Chapter 5 ($1.5d_b/c_c$) applied. The

factor was applied when the clear side cover was less than 1.5 multiplied by the bar diameter. The factors should be taken as 1.0 if the calculated value is less than 1.0. Among specimens considered in this section, specimens in Group FEM-S-19 were affected because these specimens had a clear side cover of 2 in., which is less than twice the diameter of No. 9 bars (2.256 in.). In addition, the modified thin clear side cover factor for these specimens was not applied because the clear side cover was thicker than 1.5 multiplied by the bar diameter (1.692 in.). Corresponding to these two values, bend radius ratios are included in Table 7-6.

Table 7-6 FEA results and calculated strengths of FEM-S-Series and FEM-D-Series specimens

| Specimen ID | $r_{b,ACI}$ (in.) | $r_{b,mod.}$ (in.) | $r_b/r_{b,ACI}$ | $r_b/r_{b,mod}$ | P_{calc} (kip) | P_{shear} (kip) | P_{FEA} (kip) | P_{FEA}/P_{calc} | P_{FEA}/P_{shear} |
|---------------|----------------------|-----------------------|-----------------|-----------------|---------------------|----------------------|--------------------|--------------------|---------------------|
| FEM-S-19-R4 | 9.45 | 8.38 | 0.48 | 0.54 | 142.38 | 135.23 | 145.20 | 1.02 | 1.07 |
| FEM-S-19-R6 | 9.45 | 8.38 | 0.69 | 0.78 | 142.38 | 135.23 | 159.00 | 1.12 | 1.17 |
| FEM-S-19-R8 | 9.45 | 8.38 | 0.90 | 1.01 | 142.38 | 135.23 | 159.10 | 1.12 | 1.17 |
| FEM-S-19-R12 | 9.45 | 8.38 | 1.35 | 1.52 | 142.38 | 135.23 | 159.20 | 1.12 | 1.17 |
| FEM-DD-21-R2 | 8.84 | 8.84 | 0.25 | 0.25 | 141.34 | 128.54 | 107.72 | 0.76 | 0.84 |
| FEM-DD-21-R5 | 8.84 | 8.84 | 0.66 | 0.66 | 141.34 | 128.54 | 153.97 | 1.09 | 1.20 |
| FEM-DD-21-R9 | 8.84 | 8.84 | 1.07 | 1.07 | 141.34 | 128.54 | 159.11 | 1.13 | 1.24 |
| FEM-DD-21-R14 | 8.84 | 8.84 | 1.61 | 1.61 | 141.34 | 128.54 | 160.04 | 1.13 | 1.24 |
| FEM-DD-26-R3 | 10.59 | 10.59 | 0.28 | 0.28 | 159.45 | 125.55 | 134.00 | 0.84 | 1.07 |
| FEM-DD-26-R7 | 10.59 | 10.59 | 0.68 | 0.68 | 159.45 | 125.55 | 179.77 | 1.13 | 1.43 |
| FEM-DD-26-R11 | 10.59 | 10.59 | 1.09 | 1.09 | 159.45 | 125.55 | 182.00 | 1.14 | 1.45 |
| FEM-DD-26-R17 | 10.59 | 10.59 | 1.63 | 1.63 | 159.45 | 125.55 | 182.69 | 1.15 | 1.46 |

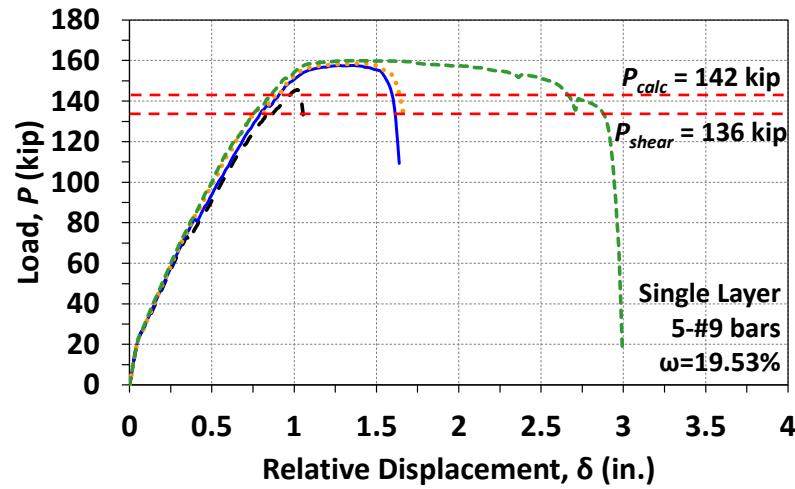
It can be observed that the value of P_{calc} for all of the FEM-S-Series and FEM-D-Series specimens is greater than the value of P_{shear} . The calculations therefore imply that the nominal joint shear capacity of the numerical specimens should not allow the longitudinal reinforcement to yield at the joint face. Nevertheless, considering the specimens represented in Table 7-6, the numerical specimen attained a load-carrying capacity greater than P_{calc} as long as the bend radius was at least large enough to satisfy criterion (3). The yielded region almost extended throughout the bar bend for specimens detailed with a bend radius larger than criterion (2). Indeed, the manner the bend radius affected the distribution of the stress along the bars was in good agreement with the observations from the experimental program (see Section 4.2.3). An example of the distribution of stress along the bars at one step before the end of the analysis is given for the Group FEM-DD-21 specimens in Figure 7-20. For specimens with the bend radius of a standard hook (Specimens FEM-S-19-R4, FEM-DD-21-R2 and FEM-DD-26-R3), the strength indicated by FEA did not

attain P_{calc} nor P_{shear} , and the longitudinal reinforcing bars did not yield at the position corresponding to the joint face. The FEA results reveal that the bend radius in the joint significantly affects joint strength. Larger bend radii were needed to fully develop the strength of the closing knee joints. Moreover, the joint shear capacity did not appropriately reflect the load-carrying capacity. Specimens in the same group (that is, with the same amount of longitudinal reinforcement) had the same value of P_{shear} based on calculated joint shear strength (see Section 6.3). The FEA results, however, demonstrate that the capacity was not sensitive to the effective shear area but was impacted by the size of the bend radius (or the CTT node) at the outer corner.

To evaluate the ACI requirement for the bend radius, strength ratios P_{FEA}/P_{calc} are plotted against the bend radius ratio in Figure 7-21. In Figure 7-21(a), the bend radius ratio, $r_{b,ACI}$, is based on the ACI requirement with the factor $2d_b/c_c$ for clear side cover included when applicable. In the figure, the vertical dashed blue line located at a bend radius ratio of 1.0 separates datapoints for numerical specimens that satisfy the ACI requirement from those that violate the ACI requirement. It can be seen in the figure that when the bend radius ratio is greater than 1.0, none of the numerical specimens exhibited a compromised load-carrying capacity. These numerical specimens also generally demonstrated greater ductility than the other specimens with a smaller bend radius ratio. The observation strengthens the importance of satisfying the ACI requirement. On the other hand, three numerical specimens had a bend radius ratio less than 0.5. Among the three numerical specimens, two fell below the strength ratio of 1.0, and the other (Specimen FEM-S-19-R4) had a lower strength than other specimens with larger bend radii. Disadvantages of using small bend radii are evident.

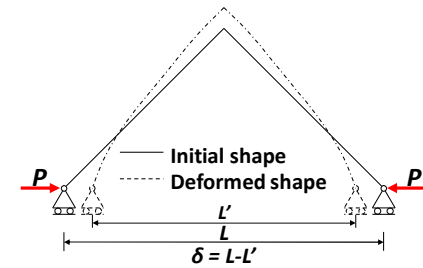
If the bend radius ratio was based on the modified requirement (clear cover factor of $1.5d_b/c_c$ applied when applicable), the points representing the Group FEM-S-19 specimens shifted slightly right, causing the point for Specimen FEM-S-19-R4 to fall into the division for a bend radius ratio greater than 0.5. However, relative to the numerical specimens with larger bend radii, Specimen FEM-S-19-R4 exhibited compromised strength. In addition, Specimen FEM-S-19-R8 fell into the division for a bend radius ratio greater than 1.0 but its ductility was not as high as that of Specimen FEM-S-19-R12. This observation seems somewhat inconsistent with the experimental program. Nevertheless, the bend radius ratio of Specimen FEM-S-19-R4 is very close to a value of 0.5, and that of FEM-S-19-R8 is very close to a value of 1.0. The results are generally in agreement with the experimental program, and the modified cover factor, $1.5d_b/c_c$,

presents no clear disadvantages, especially considering that all numerical specimens with a ratio $r_b/r_{b,modified}$ greater than 1.0 exhibited acceptable strengths.

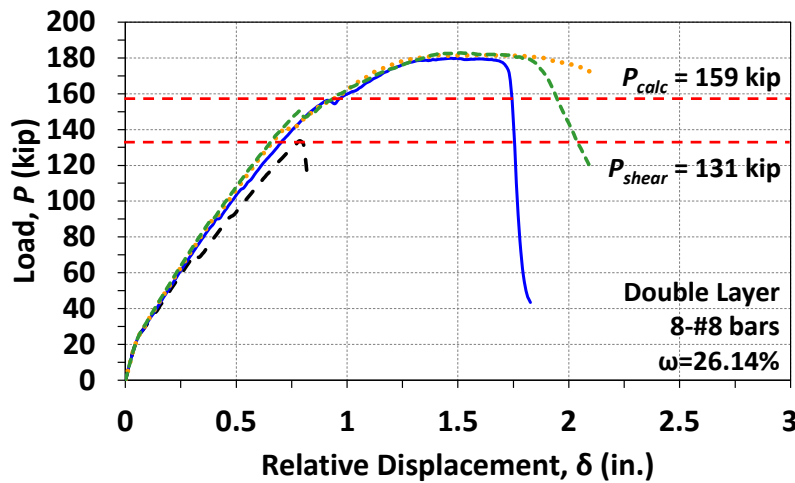


(a) Group FEM-S-19

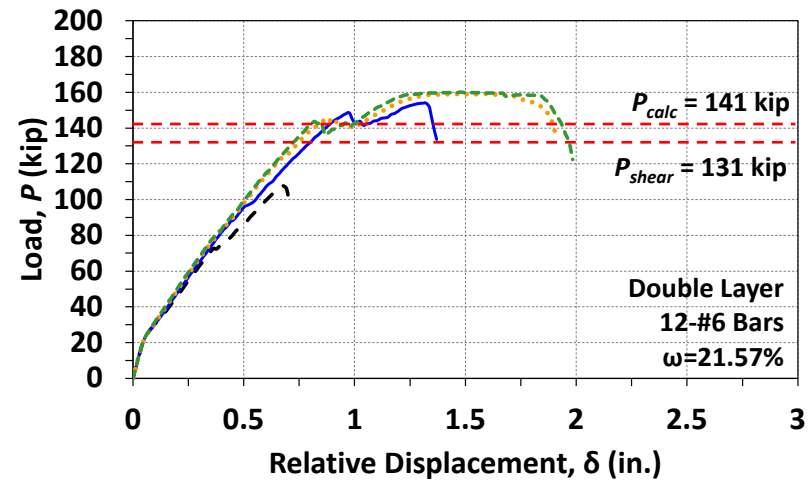
- Criterion (1)
- ... Criterion (2)
- Criterion (3)
- - - Criterion (4)



18.



(b) Group FEM-DD-26



(b) Group FEM-DD-21

Figure 7-19 Load-displacement curves of FEM-S-Series and FEM-D-Series specimens

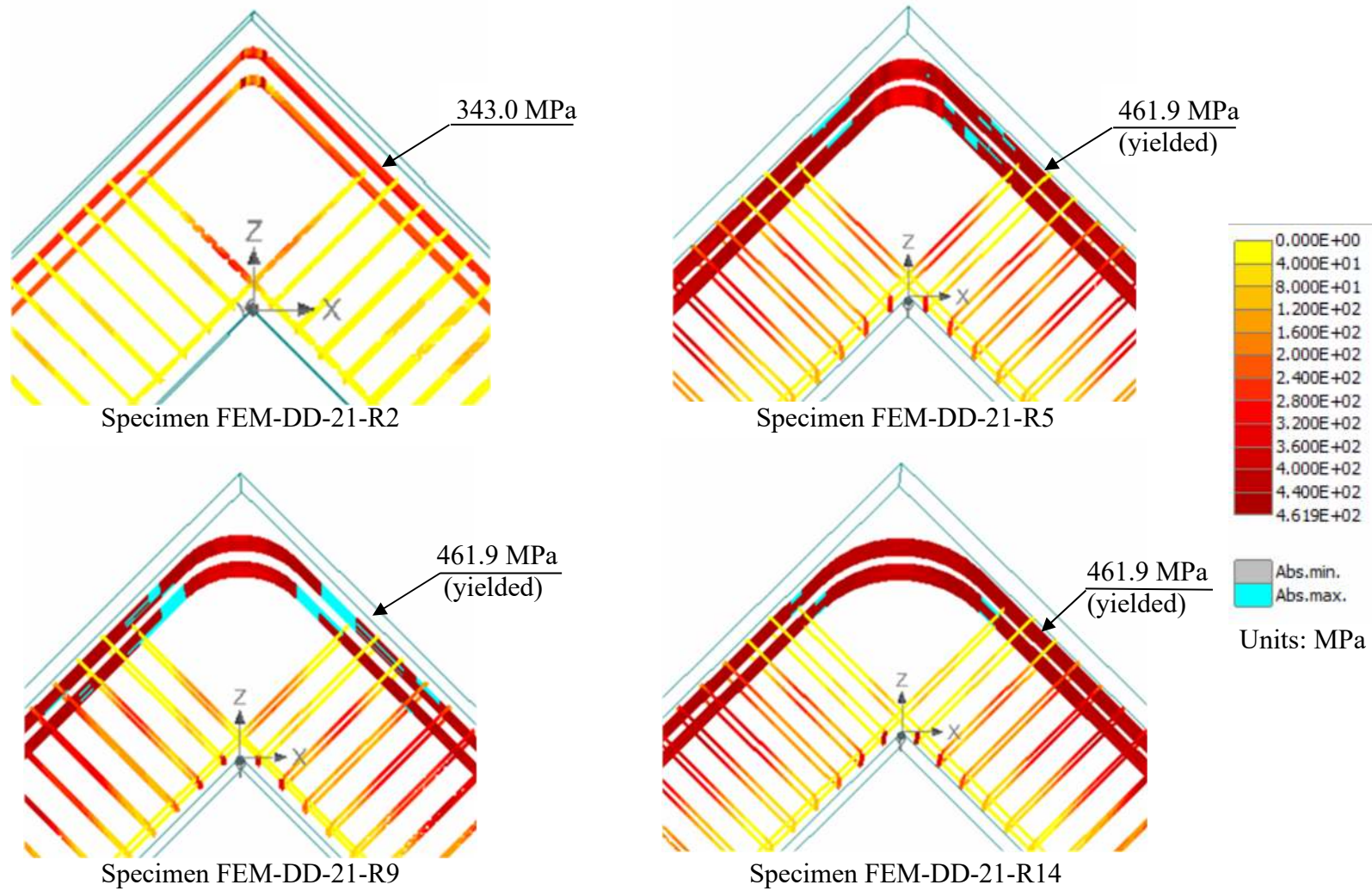
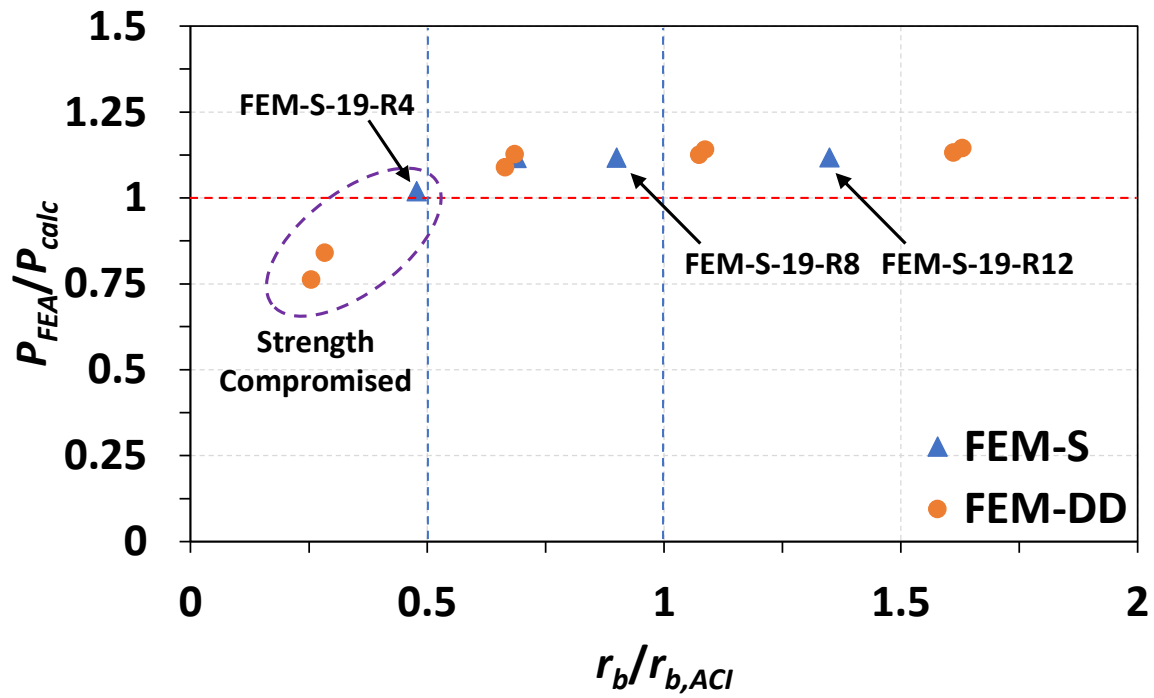
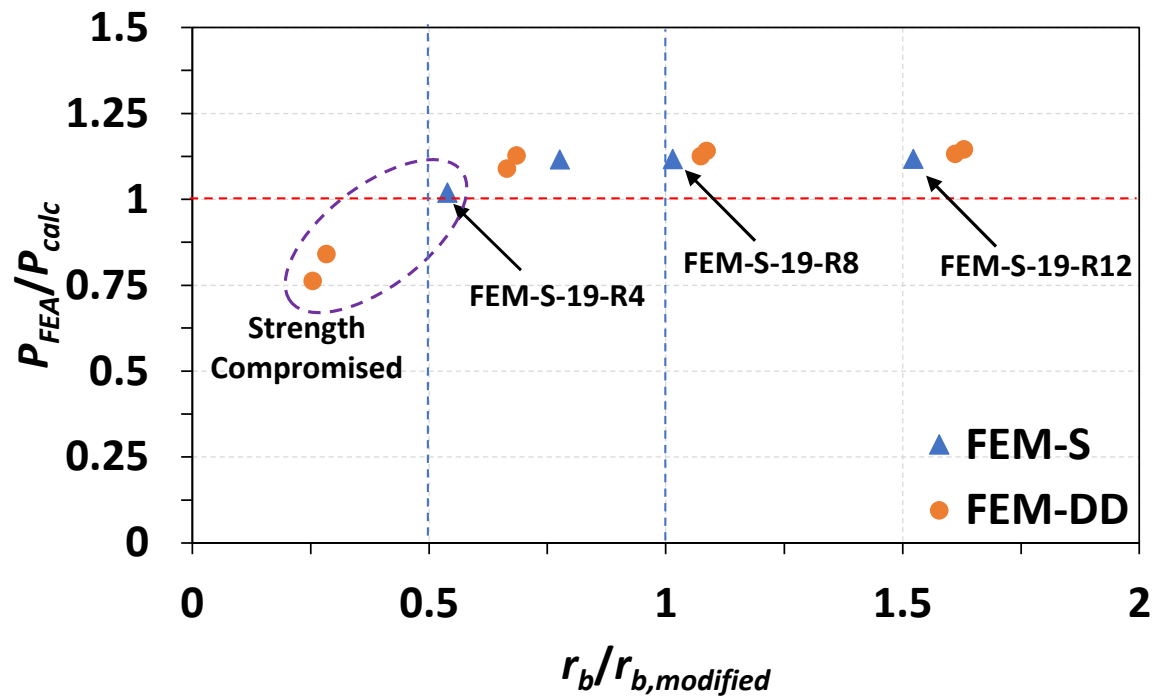


Figure 7-20 Stress along longitudinal reinforcement from analytical results for Group FEM-DD-21 specimens before failure



(a) Bend radius ratio based on ACI requirement



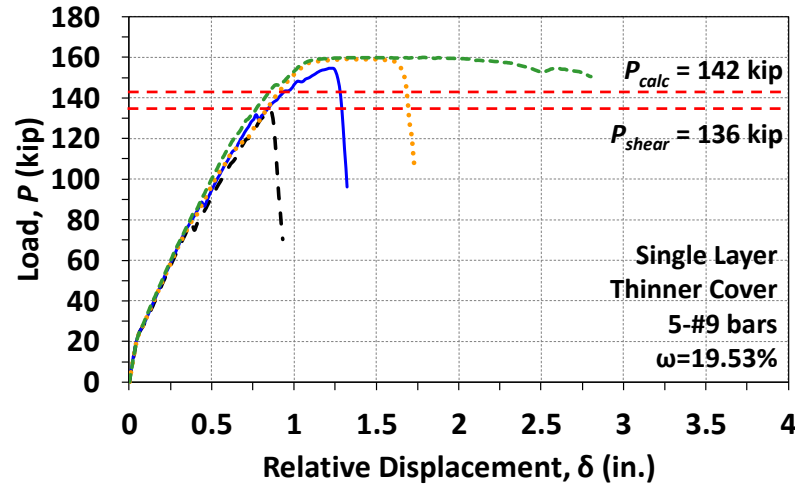
(b) Bend radius ratio based on modified requirement

Figure 7-21 Relationship between P_{FEA}/P_{calc} and bend radius ratio for FEM-S-Series and FEM-D-Series specimens

7.5.1.2 FEM-C-Series and effect of reduced clear side cover

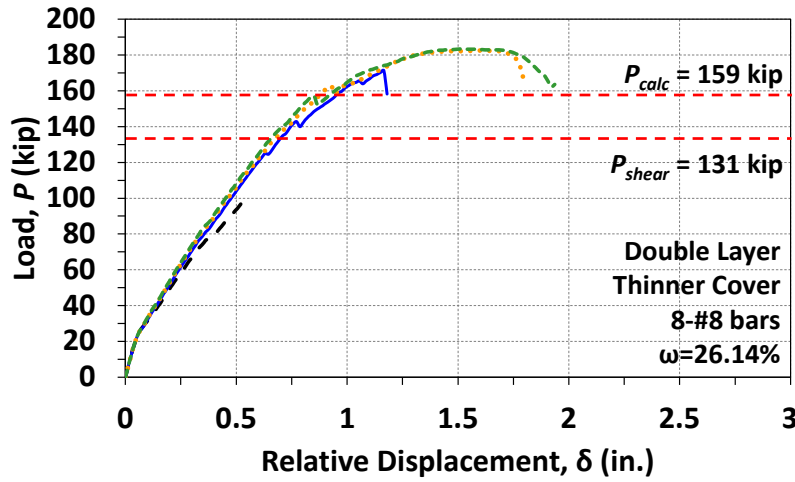
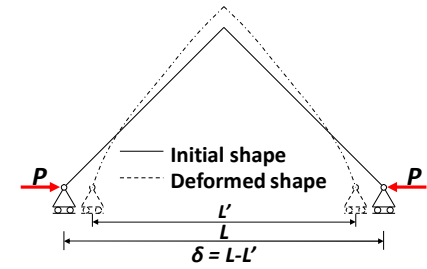
Plots of the load-relative displacement relationships of the FEM-C-Series specimens that had companion specimens in the FEM-S-Series or FEM-D-Series are presented in Figure 7-22. Similar plots for the remaining FEM-C-Series specimens (FEM-C-13 specimens) are shown in Figure 7-23. Plots that do not show an obvious loss in load-carrying capacity failed to converge to a solution beyond the last point that is plotted. Again, the dashed red lines indicate the calculated load carrying capacity based on flexural strength P_{calc} and based on joint shear strength P_{shear} . These calculated values and the FEA results are summarized in Table 7-7. Because flexural analysis at the joint face and joint shear analysis do not incorporate the factor for thin clear side cover, the value of P_{calc} and the value of P_{shear} are the same as those for the companion specimens in the FEM-S-Series and FEM-D-Series.

It can once again be observed from the FEA results that the bend radius significantly affected the behavior of the numerical specimens. The phenomenon, however, was not considered by the sectional analysis or joint shear analysis, resulting in some unconservative strength predictions for bend radii based on the radius of a standard hook. The trend that larger bend radii lead to improved behavior in terms of strength and ductility can be seen from Figure 7-22 and Figure 7-23. It should be noted that the analysis of Specimen FEM-C-13-R12 (that is, the specimen in Figure 7-23 meeting criterion (4)) failed to converge to a solution prior to exhibiting a notable loss in load-carrying capacity. Nevertheless, for the three groups, the modified ACI requirement for thin clear side cover does not seem to be necessary. Considering the Group FEM-C-19 specimens, the specimen detailed with a bend radius satisfying criterion (4) (Specimen FEM-C-19-R12) had an improved ductility compared to Specimen FEM-C-19-R8, which had a lower bend radius ratio than specimens satisfying criterion (2) in the other groups.

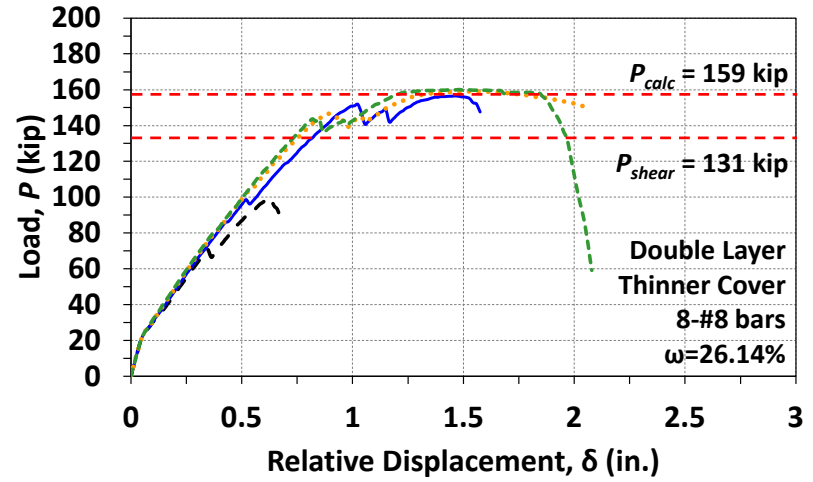


(a) Group FEM-C-19

- — — Criterion (1)
- Criterion (2)
- Criterion (3)
- - - Criterion (4)



(b) Group FEM-CD-26



(c) Group FEM-CD-21

Figure 7-22 Load-displacement curves of FEM-C-Series specimens

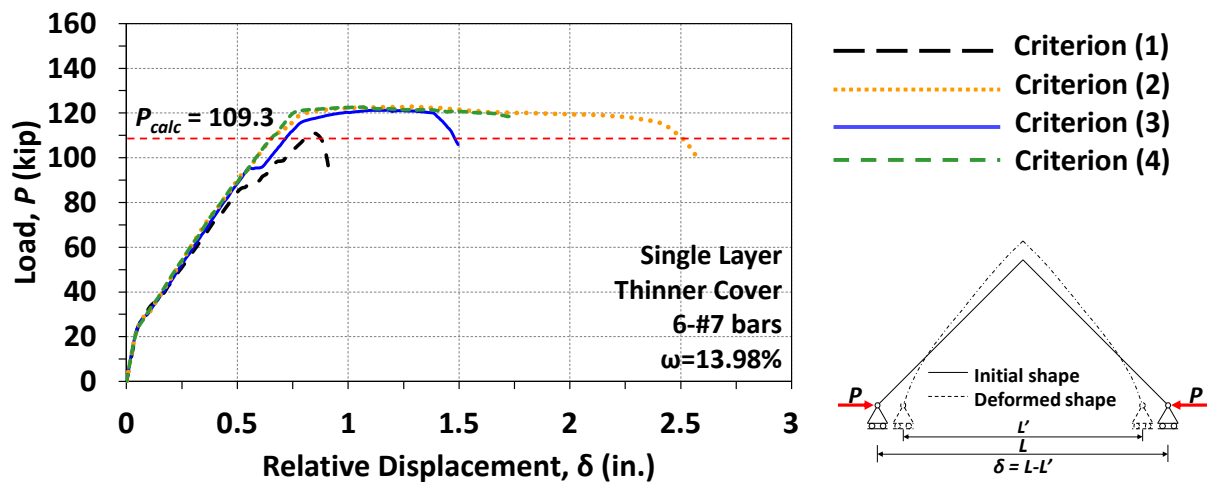


Figure 7-23 Load-displacement curves of Group FEM-C-13 specimens

Table 7-7 FEA results and calculated strengths of FEM-C-Series specimens

| Specimen ID | $r_{b,ACI}$ (in.) | $r_{b,mod.}$ (in.) | $r_b/r_{b,ACI}$ | $r_b/r_{b,mod}$ | P_{calc} (kip) | P_{shear} (kip) | P_{FEA} (kip) | P_{FEA}/P_{calc} | P_{FEA}/P_{shear} |
|---------------|----------------------|-----------------------|-----------------|-----------------|---------------------|----------------------|--------------------|--------------------|---------------------|
| FEM-C-19-R4 | 15.12 | 11.34 | 0.30 | 0.40 | 142.38 | 135.23 | 134.30 | 0.94 | 0.99 |
| FEM-C-19-R6 | 15.12 | 11.34 | 0.43 | 0.57 | 142.38 | 135.23 | 154.60 | 1.09 | 1.14 |
| FEM-C-19-R8 | 15.12 | 11.34 | 0.56 | 0.75 | 142.38 | 135.23 | 159.30 | 1.12 | 1.18 |
| FEM-C-19-R12 | 15.12 | 11.34 | 0.84 | 1.12 | 142.38 | 135.23 | 159.90 | 1.12 | 1.18 |
| FEM-CD-21-R2 | 10.61 | 8.84 | 0.21 | 0.25 | 141.34 | 128.54 | 99.41 | 0.70 | 1.02 |
| FEM-CD-21-R5 | 10.61 | 8.84 | 0.61 | 0.73 | 141.34 | 128.54 | 156.50 | 1.11 | 1.12 |
| FEM-CD-21-R9 | 10.61 | 8.84 | 1.01 | 1.22 | 141.34 | 128.54 | 159.11 | 1.13 | 1.13 |
| FEM-CD-21-R14 | 10.61 | 8.84 | 1.52 | 1.82 | 141.34 | 128.54 | 159.97 | 1.13 | 1.12 |
| FEM-CD-26-R3 | 16.94 | 12.70 | 0.18 | 0.24 | 159.45 | 125.55 | 98.64 | 0.62 | 0.77 |
| FEM-CD-26-R7 | 16.94 | 12.70 | 0.43 | 0.57 | 159.45 | 125.55 | 171.34 | 1.07 | 1.22 |
| FEM-CD-26-R11 | 16.94 | 12.70 | 0.68 | 0.91 | 159.45 | 125.55 | 182.58 | 1.15 | 1.24 |
| FEM-CD-26-R17 | 16.94 | 12.70 | 1.02 | 1.36 | 159.45 | 125.55 | 183.50 | 1.15 | 1.24 |
| FEM-C-13-R2 | 8.11 | 6.08 | 0.41 | 0.54 | 108.59 | - | 110.89 | 1.02 | - |
| FEM-C-13-R6 | 7.91 | 5.93 | 0.59 | 0.79 | 108.95 | - | 121.28 | 1.11 | - |
| FEM-C-13-R9 | 7.81 | 5.86 | 1.04 | 1.38 | 109.14 | - | 122.92 | 1.13 | - |
| FEM-C-13-R12 | 8.44 | 6.33 | 1.42 | 1.90 | 109.14 | - | 122.63 | 1.12 | - |

The analytical strengths of FEM-C-Series specimens and their companion specimens of FEM-S-Series and FEM-D-Series are summarized in Table 7-8. The ratio $c_c/2d_b$ corresponding to the specimens is also included. The last column provides the ratio of P_{FEA} for the FEM-C-Series specimen to the P_{FEA} of the companion specimen in the FEM-S-Series. It should be noted that the clear side cover measured to the longitudinal reinforcement for FEM-S-Series and FEM-D-Series specimens is typical of members in the field: 1.5 in. cover to the stirrups plus the diameter of No. 4 stirrups. From Table 7-8, the effect of thin clear side cover is noted when small bend radii

(criterion (1)) were used. For specimens detailed with the bend radius of a standard hook, the strengths of the FEM-C-Series specimens were less than their companion specimens with thicker clear side cover. The analytical strength ratio was as low as 0.73, corresponding to Specimen FEM-CD-26-R3. For specimens with bend radii based on criterion (3), although the strengths of specimens with thin clear side cover were close to those of the companion specimens with thicker clear side cover, ductility was lost (see Figure 7-22), except for Specimen FEM-CD-21-R6, which had a greater value of $c_c/2d_b$ compared to the specimens in Groups FEM-C-19 and FEM-CD-26 in Table 7-8.

Table 7-8 Evaluation of cover effect based on FEA results

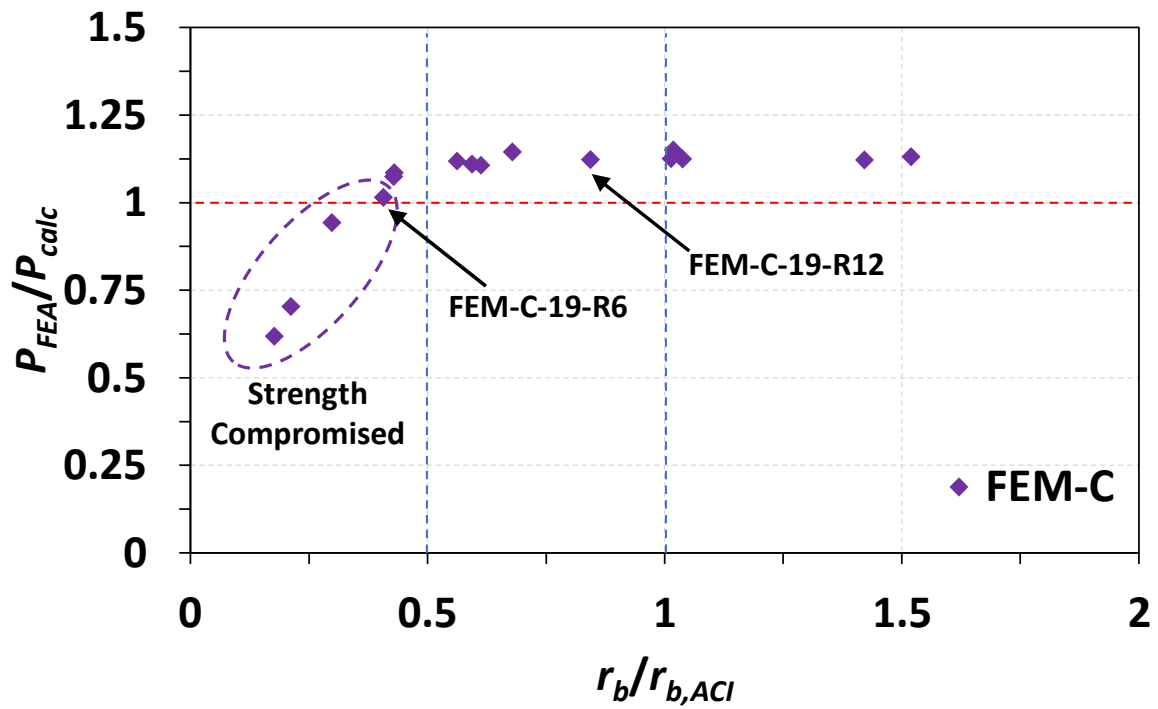
| Criterion | $\frac{c_c}{2d_b}$ | | P_{FEA} (kip) | | Ratio |
|-----------|--------------------|-----------|-----------------|-----------|-------|
| | FEM-S-19 | FEM-C-19 | FEM-S-19 | FEM-C-19 | |
| (1) | 0.89 | 0.55 | 145.2 | 134.3 | 0.93 |
| (3) | 0.89 | 0.55 | 159.0 | 154.6 | 0.97 |
| (2) | 0.89 | 0.55 | 159.1 | 159.3 | 1.00 |
| (4) | 0.89 | 0.55 | 159.2 | 159.9 | 1.00 |
| | FEM-DD-21 | FEM-CD-21 | FEM-DD-21 | FEM-CD-21 | Ratio |
| (1) | 1.33 | 0.83 | 107.7 | 99.4 | 0.93 |
| (3) | 1.33 | 0.83 | 154.0 | 156.5 | 1.02 |
| (2) | 1.33 | 0.83 | 159.1 | 159.1 | 1.00 |
| (4) | 1.33 | 0.83 | 160.0 | 160.0 | 1.00 |
| | FEM-DD-26 | FEM-CD-26 | FEM-DD-26 | FEM-CD-26 | Ratio |
| (1) | 1.0 | 0.63 | 134.0 | 98.6 | 0.73 |
| (3) | 1.0 | 0.63 | 179.8 | 171.3 | 0.95 |
| (2) | 1.0 | 0.63 | 182.0 | 182.6 | 1.00 |
| (4) | 1.0 | 0.63 | 182.7 | 183.5 | 1.00 |

Table 7-9 shows a similar comparison for numerical specimens in Group FEM-C-13 and companion specimens in Group S-3 of the experimental program (see Section 3.2.1). The last column presents the ratio of P_{FEA} of the specimen from Group FEM-C-13 to the value of P_{test} for the companion specimen from Group S-3. From the comparison, a similar trend as described above is observed. The numerical specimen with the bend radius of a standard hook (Specimen FEM-C-13-R3) had a lower strength than its companion specimen, while numerical specimens based on criteria (2) and (3) had a similar strength as their companions. It can be seen that a difference in the ratio $c_c/2d_b$ did affect the strength of closing knee joints when small bend radii were used.

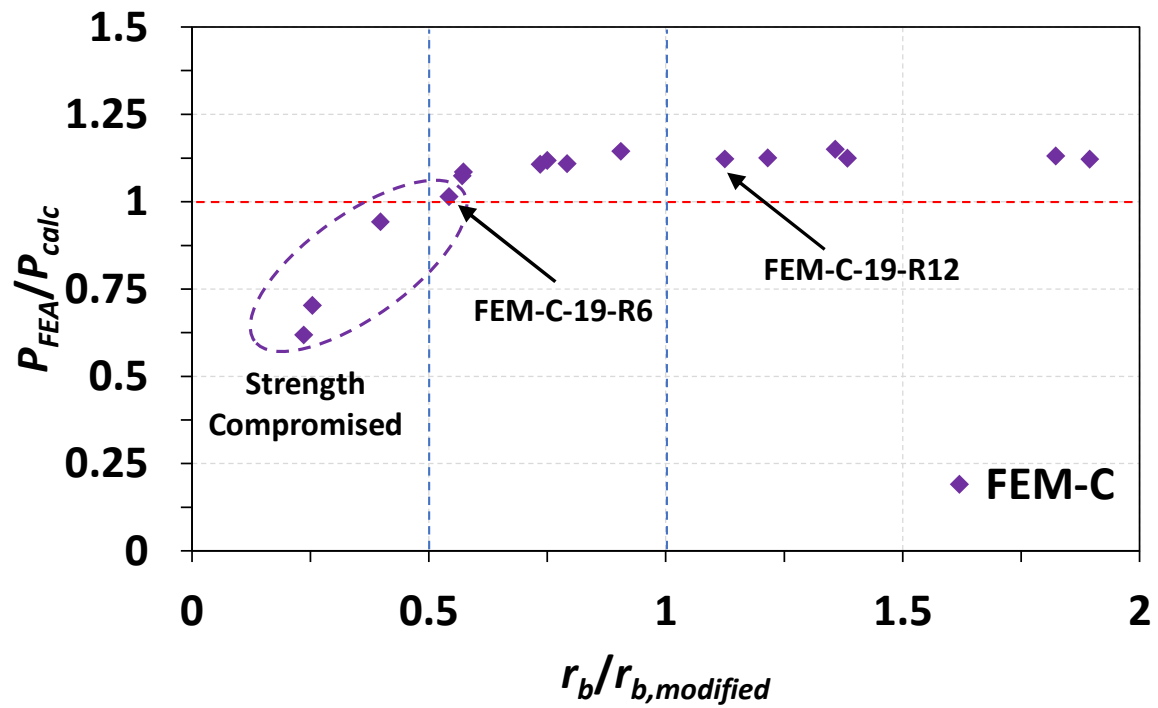
Table 7-9 Evaluation of cover effect based on both FEA and experimental results

| Criterion | $\frac{c_c}{2d_b}$ | | Strength | | Ratio |
|-----------|--------------------|----------|------------------|-----------------|-------|
| | S-13 | FEM-C-13 | P_{test} (kip) | P_{FEA} (kip) | |
| | | | S-13 | FEM-C-13 | |
| (1) | 1.14 | 0.71 | 123 | 110.9 | 0.90 |
| (3) | 1.14 | 0.71 | 125 | 121.3 | 0.97 |
| (2) | 1.14 | 0.71 | 127 | 122.9 | 0.97 |
| (4) | - | 0.71 | - | 122.6 | - |

It is more evident that the modification factor $2d_b/c_c$ provides conservative results by plotting the strength ratio P_{FEA}/P_{calc} against the bend radius ratio based on both the ACI modification factor ($2d_b/c_c$) and the proposed modification factor ($1.5d_b/c_c$), as shown in Figure 7-24. It should be noted that the proposed modification factor ($1.5d_b/c_c$) was 1.0 for Group FEM-CD-21 because the clear side cover (1.25 in.) was thicker than 1.5 multiplied by the bar diameter (1.125 in.). When the ACI-based modification factor is applied (Figure 7-24(a)), all datapoints for specimens with a bend radius ratio greater than 1.0 correspond to a strength greater than P_{calc} based on nominal flexural capacity at the joint and exhibited ductility, indicating that the requirement is conservative. However, the datapoint Specimen FEM-C-19-R12, which also had similar behavior, fell left of the division representing a bend radius ratio of 1.0. When the proposed modification factor for thin side cover is used, the datapoint for Specimen FEM-C-19-R12 falls right of the division, leading to a more consistent result with the other specimens. In addition, some specimens with a bend radius ratio less than 0.5 have a strength ratio lower than 1.0. It should be noted that Specimen FEM-C-19-R6 exhibited compromised strength compared to other FEM-C-Series specimens with larger bend radii although the specimen corresponds to a bend radius ratio greater than 0.5 when the proposed modification factor is used. However, its bend radius ratio is very close to 0.5. Overall, the results here generally agree with the experimental results and the database analysis introduced in the previous chapters. The numerical results indicate that applying the proposed modification factor for reduced side cover provides satisfactory results. It should be noted that the lowest value of $c_c/2d_b$ included in the study was 0.55. Application of the findings from the study should be limited to knee joints with $c_c/2d_b$ values within the range considered.



(a) Bend radius ratio based on ACI requirement



(b) Bend radius ratio based on modified requirement

Figure 7-24 Relationship between P_{FEA}/P_{calc} and bend radius ratio for FEM-C-Series

7.5.1.3 FEM-TR-Series and effect of minimum distributed reinforcement

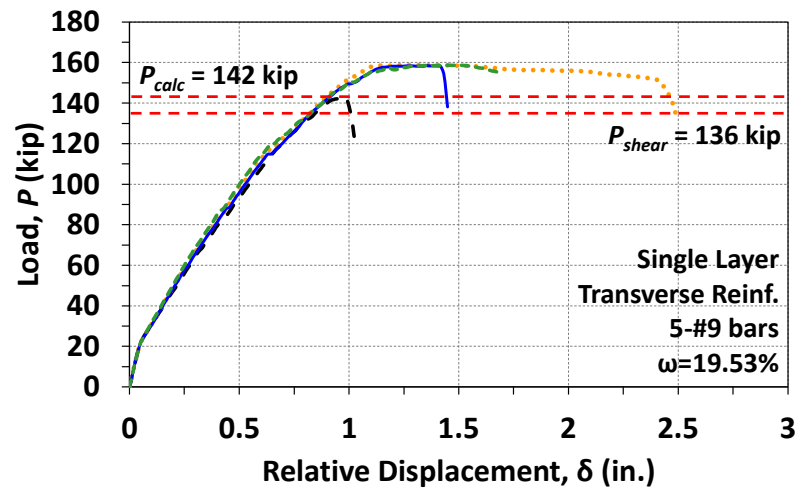
The load-relative displacement relationships of the FEM-TR-Series specimens are presented in Figure 7-25. The dashed red lines again indicate the calculated load-carrying capacities based on sectional analysis, P_{calc} , and joint shear capacity, P_{shear} . The value of P_{shear} is not shown in Figure 7-25(b) and (c) because the joint shear strength does not govern the calculated load-carrying capacity for these cases. In other words, the joint shear demand based on yielded longitudinal reinforcement is less than the calculated joint shear strength. No numerical specimens based on criterion (1) were analyzed for Groups FEM-TR-17 and FEM-TR-13 (see Figure 7-25(b) and (c)). Therefore, the results from the tests on similar specimens detailed with the bend radius of a standard hook that were testing during the experimental program (Specimens TR-S-18-R3 and TR-S-13-R3) are plotted for the purpose of comparison. These specimens had the same longitudinal reinforcement as the numerical specimens represented in the plots. The analysis results are summarized in Table 7-10.

As shown in Figure 7-25(a), the numerical specimens with a mechanical reinforcement ratio of 19.53% behaved with the same pattern as the companion numerical specimens without transverse reinforcement in the FEM-S-Series (see Figure 7-19). The specimen with the bend radius of a standard hook failed prematurely after reaching the peak load, and further enlarging the bend radius increased the strength and ductility. The presence of transverse reinforcement in the joint of the specimen detailed based on criterion (1) did not prevent a premature failure from occurring. On the other hand, the deformation ability of the specimen satisfying criterion (2) (Specimen FEM-TR-19-R8) improved when compared to its companion specimens in the FEM-S-Series (Specimen FEM-S-19-R8, see Figure 7-19), while the specimen satisfying criterion (3) (Specimen FEM-TR-19-R6) did not exhibit an obviously different behavior from Specimen FEM-S-19-R6. It should be noted that Specimen FEM-TR-19-R12 failed to converge to a solution prior to a significant loss in load-carrying capacity, and therefore, a meaningful comparison to its companion specimens is not possible. Moreover, when comparing numerical specimens of Group FEM-TR-18 to the companion specimens of Group S-2 of the experimental program (that is, the benchmark specimens used for validation of the analytical model), which had almost the same mechanical reinforcement ratio, it can be seen that Specimen FEM-TR-18-R6 detailed based on criterion (3) had much improved ductility compared to Specimen S-18-R6 (see Figure 7-10).

Specimens in Group FEM-TR-13 do not have companion specimens without transverse reinforcement for comparison, but the specimens in this group demonstrated a similar pattern as those in Group FEM-TR-19. When the bend radius satisfied criterion (2) or (4) (Specimens FEM-TR-13-R8 and FEM-TR-13-R14), ductility was observed. However, the presence of transverse reinforcement did not improve the ductility of the specimen detailed based on criterion (3) (Specimen FEM-TR-13-R6) to a level similar to specimens in the research program with larger bend radii. Therefore, the observation seems to indicate that the size of the bend radius is more important than the presence of transverse reinforcement in the joint.

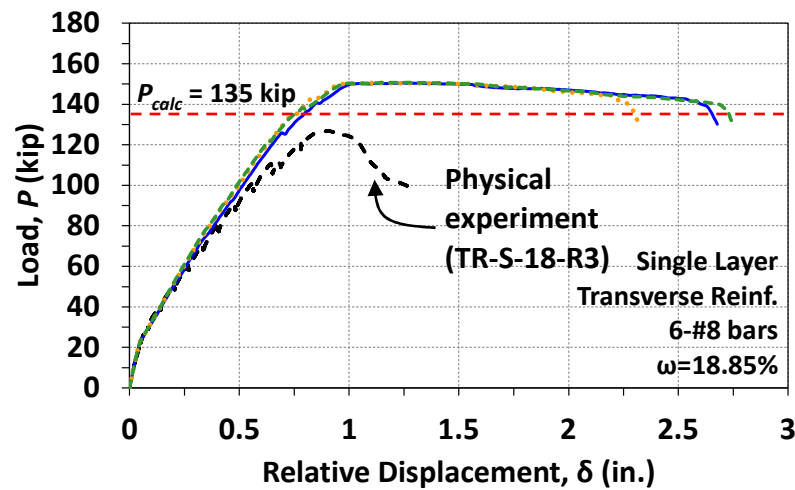
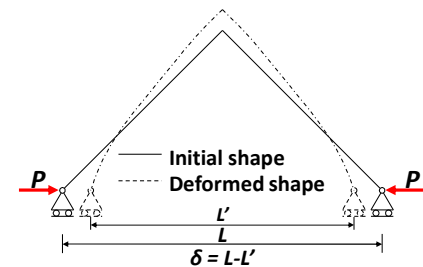
Table 7-10 FEA results and calculated strengths of FEM-TR-Series specimens

| Specimen ID | $r_{b,ACI}$ (in.) | $r_{b,mod}$ (in.) | $r_b/r_{b,ACI}$ | $r_b/r_{b,mod}$ | P_{calc} (kip) | P_{shear} (kip) | P_{FEA} (kip) | P_{FEA}/P_{calc} | P_{FEA}/P_{shear} |
|---------------|----------------------|----------------------|-----------------|-----------------|---------------------|----------------------|--------------------|--------------------|---------------------|
| FEM-TR-18-R6 | 8.12 | 8.12 | 0.74 | 0.74 | 134.73 | - | 150.50 | 1.12 | 1.12 |
| FEM-TR-18-R9 | 8.12 | 8.12 | 1.11 | 1.11 | 134.73 | - | 150.57 | 1.12 | 1.12 |
| FEM-TR-18-R14 | 8.12 | 8.12 | 1.66 | 1.66 | 134.73 | - | 150.75 | 1.12 | 1.12 |
| FEM-TR-13-R4 | 6.25 | 6.25 | 0.80 | 0.80 | 105.03 | - | 115.68 | 1.10 | 1.10 |
| FEM-TR-13-R8 | 6.25 | 6.25 | 1.44 | 1.44 | 105.03 | - | 115.77 | 1.10 | 1.10 |
| FEM-TR-13-R14 | 6.25 | 6.25 | 2.16 | 2.16 | 105.03 | - | 115.77 | 1.10 | 1.10 |
| FEM-TR-19-R4 | 9.45 | 8.38 | 0.48 | 0.54 | 142.38 | 135.23 | 143.36 | 1.01 | 1.06 |
| FEM-TR-19-R6 | 9.45 | 8.38 | 0.69 | 0.78 | 142.38 | 135.23 | 158.40 | 1.11 | 1.17 |
| FEM-TR-19-R8 | 9.45 | 8.38 | 0.90 | 1.01 | 142.38 | 135.23 | 158.90 | 1.12 | 1.17 |
| FEM-TR-19-R12 | 9.45 | 8.38 | 1.35 | 1.52 | 142.38 | 135.23 | 158.60 | 1.11 | 1.17 |

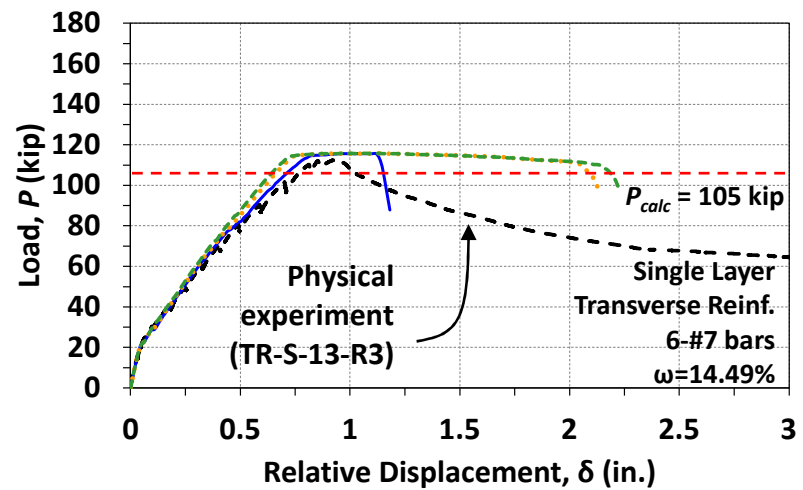


(a) Group FEM-TR-19

- Criterion (1)
- Criterion (2)
- Criterion (3)
- Criterion (4)



(b) Group FEM-TR-18



(c) Group FEM-TR-13

Figure 7-25 Load-displacement curves of FEM-TR-Series specimens

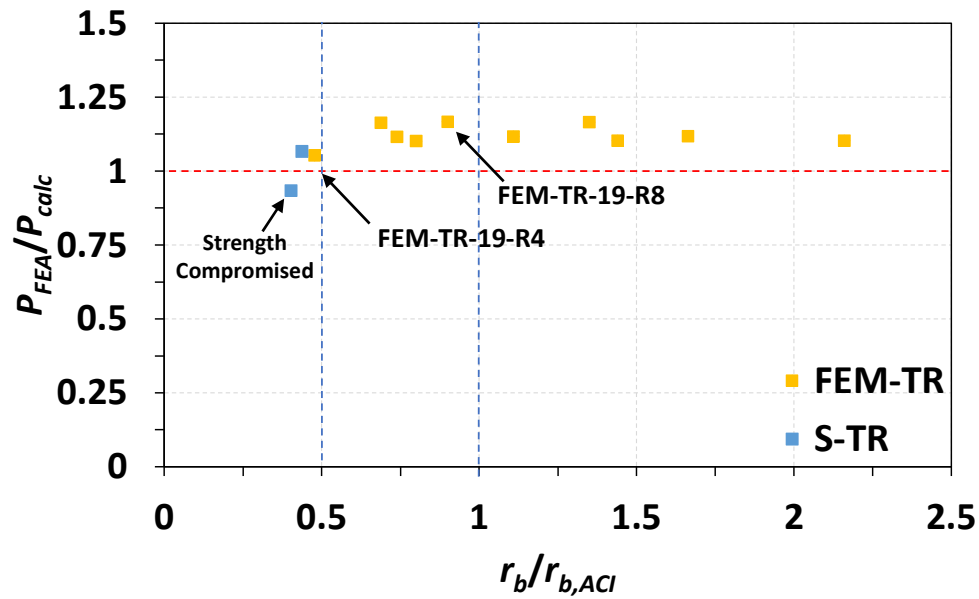
The effect of transverse reinforcement on the load-carrying capacity can be evaluated by comparing the value of P_{FEA} of specimens in Group FEM-TR-19 to those in Group FEM-S-19 as shown in Table 7-11. In the table, the last column provides the ratio of P_{FEA} of the specimen in Group FEM-TR-19 to P_{FEA} of its companion specimen in Group FEM-S-19. It can be seen that all the ratios are equal to or nearly equal to 1.00, indicating that the peak loads were approximately the same for all cases. It is not surprising for specimens detailed with large bend radii (criteria (2), (3), and (4)) to have similar strengths because they all exhibited a load plateau in the load-relative displacement plots. However, the peak load was also approximately the same for the specimens with the bend radius of a standard hook (criterion (1)). The strength was obviously more dependent on the bend radius than the presence of transverse reinforcement.

Table 7-11 Evaluation of the effect of transverse reinforcement based on both FEA and experimental results

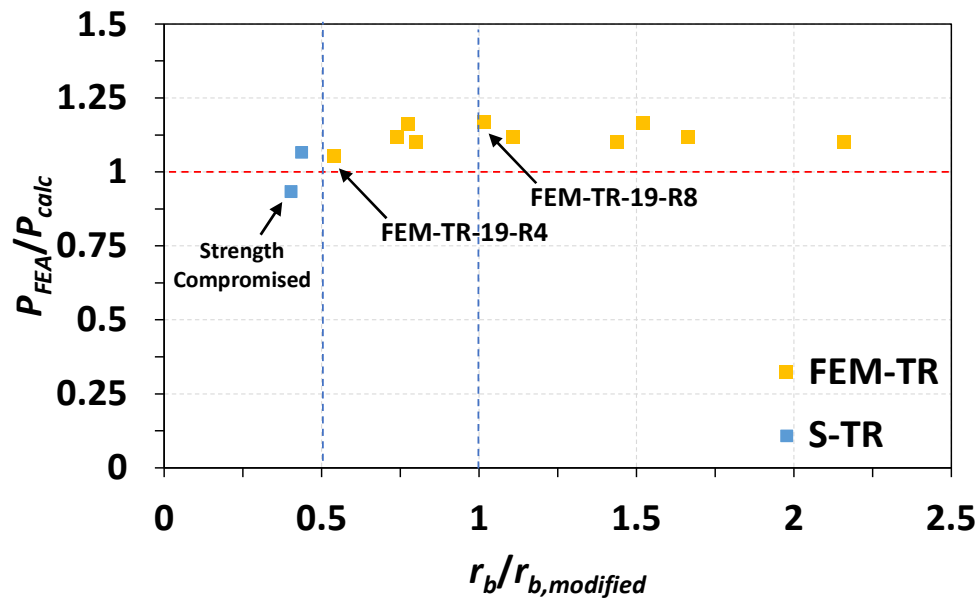
| Criterion | P_{FEA} (kip) | | |
|-----------|-----------------|-----------|-------|
| | FEM-S-19 | FEM-TR-19 | Ratio |
| (1) | 145.2 | 143.4 | 0.99 |
| (3) | 159.0 | 158.4 | 1.00 |
| (2) | 159.1 | 158.9 | 1.00 |
| (4) | 159.2 | 158.6 | 1.00 |

The observation that the specimen strength is independent of the presence of transverse reinforcement in the joint is made clearer by plotting the strength ratio P_{FEA}/P_{calc} against the bend radius ratio based on both the ACI modification factor ($2d_b/c_c$) and the proposed modification factor ($1.5d_b/c_c$), as shown in Figure 7-26. Specimens in Group FEM-TR-19 were affected by the ACI modification factor. In the figure, the datapoints representing the numerical specimens are colored yellow, and those representing specimens from the experimental program are colored blue. It can be seen that when the bend radius ratio based on the modified factor is used, one datapoint, the datapoint for Specimen FEM-TR-19-R4, shifted slightly right, crossing the border representing a bend radius ratio of 0.5, and the datapoint for Specimen FEM-TR-19-8 shifted across the border representing a bend radius ratio of 1.0. Both plots in Figure 7-26 provide a consistent pattern relative to what was observed for the relationship between the strength ratio P_{FEA}/P_{calc} and the bend radius ratio for the FEM-S-Series specimens without transverse reinforcement in the joint, as introduced in Section 7.5.1.1 (see Figure 7-21). Nevertheless, based on the results, it is appropriate to conclude that whether or not transverse reinforcement is provided in the joint, a bend radius

ratio greater than 0.5 is needed to avoid premature failure, and using a bend radius ratio greater than 1.0 (that is, satisfying ACI requirement) is recommended.



(a) Bend radius ratio based on ACI requirement



(b) Bend radius ratio based on modified requirement

Figure 7-26 Relationship between P_{FEA}/P_{calc} and bend radius ratio for specimens with minimum distributed reinforcement in the joint

7.5.1.4 Evaluation of the Strut-and-Tie method Using the FEA results

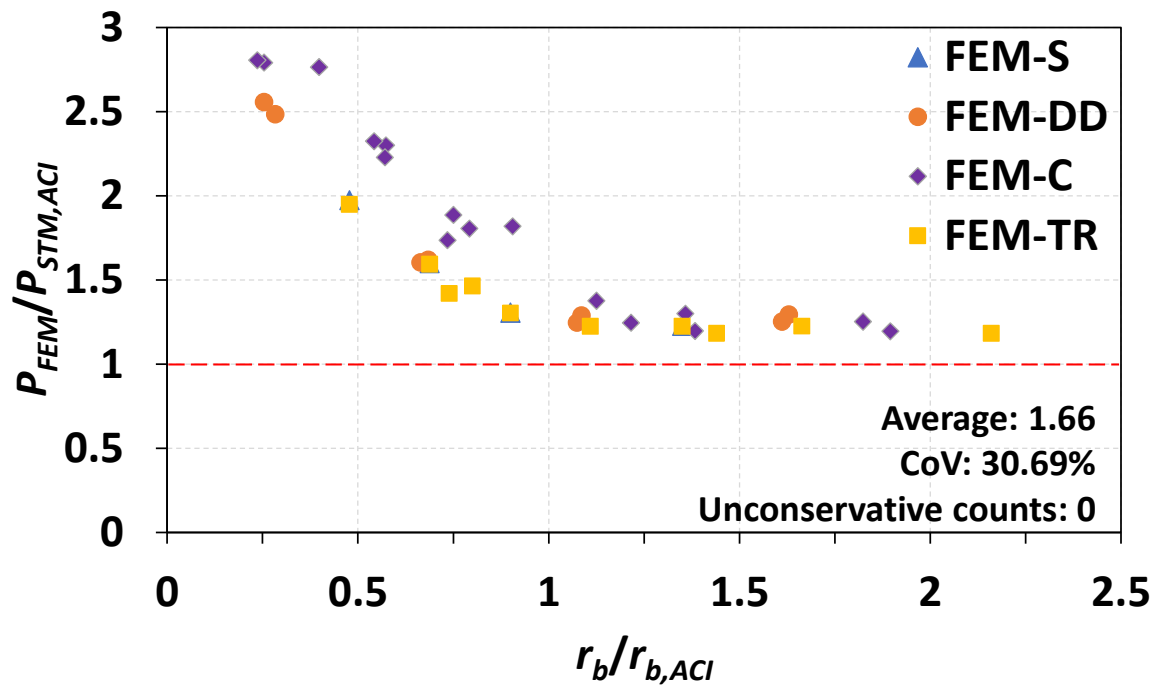
The procedure developed to assess the capacity of knee joints using strut-and-tie model type (a) as introduced in Chapter 6 was applied to the numerical specimens, and the results are summarized in Table 7-12. In the table, the value of $P_{STM,ACI}$ is the capacity based on the nodal zone coefficients and strut coefficients specified in ACI 318-19.¹ The value of $P_{STM,mod.}$ is based on the modified coefficients (see Table 6-6).

The ratio of the strength indicated by the finite element analyses, P_{FEA} , to the capacity determined using the STM was plotted against the bend radius ratio as shown in Figure 7-27. It can be seen in Figure 7-27(a) that the prediction from the strut-and-tie model with coefficients based on ACI 318-19¹ was conservative. The results had an average strength ratio of 1.66, and no datapoints fell below the red dashed line indicating a strength ratio of 1.0. However, for bend radius ratios less than 1.0, overconservativeness occurred. Moreover, the trend that smaller bend radius ratios correspond to higher degrees of overconservativeness is evident. For bend radius ratios less than 0.5, the strength ratio ranged from 1.95 to 2.80. The largest strength ratio (2.80) corresponds to a bend radius ratio of 0.25. The phenomenon resulted in a relatively large value for the coefficient of variation of 30.69%.

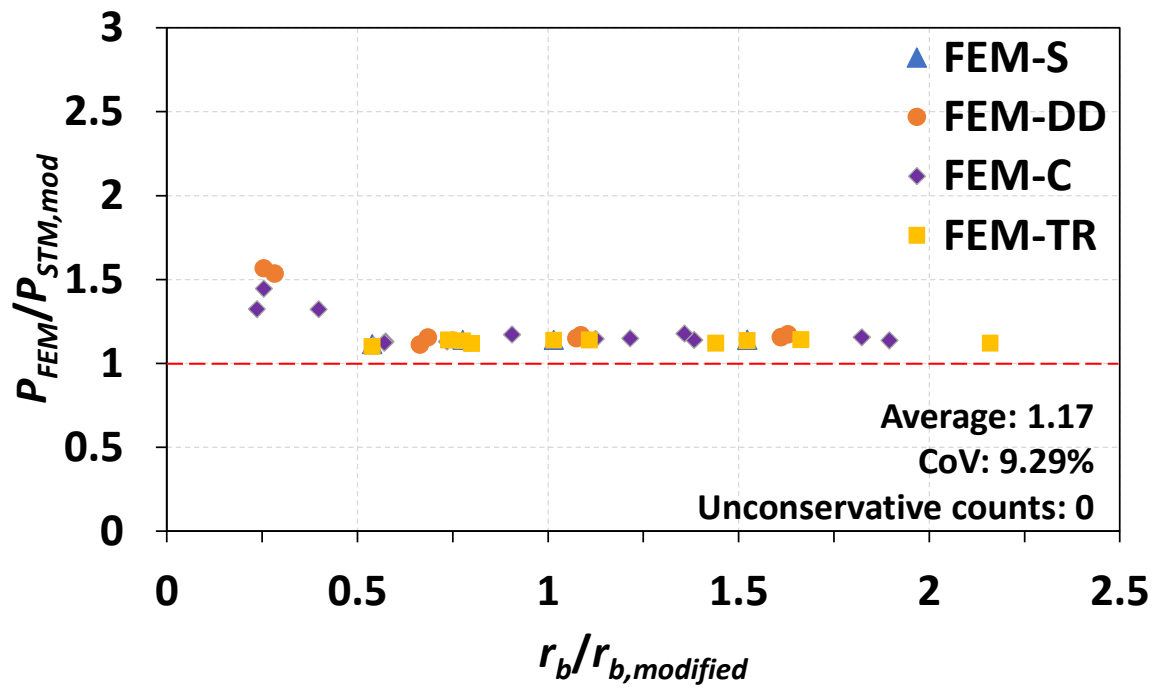
The overly-conservative predictions resulting from the strut-and-tie model with coefficients based on ACI 318-19¹ is consistent with the results of the database analysis introduced in Chapter 6 (see Section 6.5.2). The significant underestimations of strength for bend radius ratios less than 1.0 can be partially attributed to the ACI-required bend radius (Eq. 2-20) and the factor for thin clear side cover ($2d_b/c_c$). The current provisions prohibit using bend radii smaller than the requirement. Taking this into consideration, the strength of curved-bar nodes was reduced within the strut-and-tie model used for the evaluation (see Section 6.5.2.1) if the bend radius of the numerical specimen did not satisfy the requirement. Clearly, the reduction in strength based on the current code provisions was too severe. Moreover, it can be observed in Figure 7-27(a) that the level of overconservatism is greatest for FEM-C-Series specimens, which had thin clear side cover, proving that the reduction in calculated strength due to thin clear side cover based on the factor of $2d_b/c_c$ is also too strict if only strength is considered.

Table 7-12 Comparison of FEA results and STM results

| Specimen ID | $P_{STM,ACI}$ (kip) | $P_{STM,mod.}$ (kip) | P_{FEA} (kip) | $P_{FEA}/P_{STM,ACI}$ | $P_{FEA}/P_{STM,mod.}$ |
|---------------|------------------------|-------------------------|--------------------|-----------------------|------------------------|
| FEM-S-19-R4 | 73.58 | 130.31 | 145.20 | 1.97 | 1.11 |
| FEM-S-19-R6 | 99.41 | 139.62 | 159.00 | 1.60 | 1.14 |
| FEM-S-19-R8 | 121.88 | 139.62 | 159.10 | 1.31 | 1.14 |
| FEM-S-19-R12 | 129.58 | 139.62 | 159.20 | 1.23 | 1.14 |
| FEM-DD-21-R2 | 42.14 | 68.76 | 107.72 | 2.56 | 1.57 |
| FEM-DD-21-R5 | 96.09 | 138.52 | 153.97 | 1.60 | 1.11 |
| FEM-DD-21-R9 | 127.73 | 138.52 | 159.11 | 1.25 | 1.15 |
| FEM-DD-21-R14 | 127.73 | 138.52 | 160.04 | 1.25 | 1.16 |
| FEM-DD-26-R3 | 53.93 | 87.38 | 134.00 | 2.48 | 1.53 |
| FEM-DD-26-R7 | 111.08 | 155.84 | 179.77 | 1.62 | 1.15 |
| FEM-DD-26-R11 | 141.23 | 155.84 | 182.00 | 1.29 | 1.17 |
| FEM-DD-26-R17 | 141.23 | 155.84 | 182.69 | 1.29 | 1.17 |
| FEM-C-19-R4 | 48.59 | 101.57 | 134.30 | 2.76 | 1.32 |
| FEM-C-19-R6 | 67.22 | 136.87 | 154.60 | 2.30 | 1.13 |
| FEM-C-19-R8 | 84.42 | 139.62 | 159.30 | 1.89 | 1.14 |
| FEM-C-19-R12 | 116.24 | 139.62 | 159.90 | 1.38 | 1.15 |
| FEM-CD-21-R2 | 35.62 | 68.76 | 99.41 | 2.79 | 1.45 |
| FEM-CD-21-R5 | 90.12 | 138.52 | 156.50 | 1.74 | 1.13 |
| FEM-CD-21-R9 | 127.73 | 138.52 | 159.11 | 1.25 | 1.15 |
| FEM-CD-21-R14 | 127.73 | 138.52 | 159.97 | 1.25 | 1.15 |
| FEM-CD-26-R3 | 35.17 | 74.55 | 98.64 | 2.80 | 1.32 |
| FEM-CD-26-R7 | 76.89 | 152.53 | 171.34 | 2.23 | 1.12 |
| FEM-CD-26-R11 | 100.38 | 155.84 | 182.58 | 1.82 | 1.17 |
| FEM-CD-26-R17 | 141.23 | 155.84 | 183.50 | 1.30 | 1.18 |
| FEM-C-13-R3 | 47.72 | 100.13 | 110.89 | 2.32 | 1.11 |
| FEM-C-13-R6 | 67.18 | 107.68 | 121.28 | 1.81 | 1.13 |
| FEM-C-13-R9 | 102.66 | 107.89 | 122.92 | 1.20 | 1.14 |
| FEM-C-13-R12 | 102.66 | 107.89 | 122.63 | 1.19 | 1.14 |
| FEM-TR-19-R4 | 73.58 | 130.31 | 143.36 | 1.95 | 1.10 |
| FEM-TR-19-R6 | 99.41 | 139.62 | 158.40 | 1.59 | 1.13 |
| FEM-TR-19-R8 | 121.88 | 139.62 | 158.90 | 1.30 | 1.14 |
| FEM-TR-19-R12 | 129.58 | 139.62 | 158.60 | 1.22 | 1.14 |
| FEM-TR-18-R6 | 106.02 | 132.16 | 150.50 | 1.42 | 1.14 |
| FEM-TR-18-R9 | 122.97 | 132.16 | 150.57 | 1.22 | 1.14 |
| FEM-TR-18-R14 | 122.97 | 132.16 | 150.75 | 1.22 | 1.14 |
| FEM-TR-13-R6 | 79.04 | 103.44 | 112.00 | 1.46 | 1.12 |
| FEM-TR-13-R9 | 97.85 | 103.44 | 115.68 | 1.18 | 1.12 |
| FEM-TR-13-R14 | 97.85 | 103.44 | 115.77 | 1.18 | 1.12 |



(a) Incorporating ACI 318-19¹ coefficients



(b) Incorporating modified coefficients

Figure 7-27 Strength ratio P_{FEA}/P_{STM} versus the bend radius ratio

Being generally greater in magnitude compared to the ACI nodal zone and strut coefficients, the modified coefficients were based on the experimental results while incorporating ideas from past studies in the literature. To be specific, the effective compressive strength of concrete was taken as $0.85f'_c$ and the factor for thin clear side cover was taken as $1.5d_b/c_c$ (see Section 6.4.5). As shown in Figure 7-27(b), the underestimations of strength that occur with the incorporation of parameters based on the current code were mitigated when the modified factors were used, and the strength predictions are overall closer to the strengths indicated by finite element analysis. Although the factors within the STM were increased, there were still no unconservative results. With an average strength ratio of 1.17 and a coefficient of variation of 9.29%, the strut-and-tie model with the modified coefficients provided improved results compared to the strut-and-tie model with coefficients based on ACI 318-19.¹

In spite of the satisfactory predictive ability, the model with the modified coefficients still displays a trend toward overconservativeness for bend radius ratios less than 0.5. This can be partially attributed to the fact that the strut-and-tie model applied to closing knee joint neglects the development of bar stress along the straight portion of the bars in the joint. Considering the strut-and-tie model, when the force carried by the diagonal strut within the joint is equal to the effective strength of concrete under the bar bend, the forces in the ties extending from the CTT node at the outer corner are assumed to be constant along their length. Therefore, the strength at the CTT node governs the maximum force in the tie at the joint faces. In reality, even though the stress in the longitudinal reinforcement at the bar bend may not reach the yield stress due to the limited concrete strength at the CTT node, the bar at the joint face might experience yielding. Nevertheless, the level of overconservativeness is much improved with the incorporation of the proposal factors, which results in the greatest strength ratio being 1.57 for a bend radius ratio of 0.25.

Reflecting the effect of the bend radius and clear side cover, both the strut-and-tie model with coefficients based on ACI 318-19¹ and the model with the modified coefficients eliminated the unconservative results generated by both the nominal flexural strength based on sectional analysis and the calculated joint shear strength. Therefore, it is recommended to assess knee joint under closing moments using the STM.

7.5.2 Evaluation of the Strength of Numerical Specimens with Various Strut Angles

The results of finite element analysis on the FEM-B-Series specimens is discussed in this section. The strength determined by FEA is compared to those determined by both sectional analysis and the strut-and-tie method to evaluate the effect of the diagonal strut angle in combination with various bend radii. In the following sections, specimens with a bend radius larger than the bend radius of a standard hook are discussed separately from those with a standard bend radius to provide a more effective comparison of the results. The results are summarized in Table 7-13.

Table 7-13 FEA results and calculated strengths of FEM-B-Series specimens

| Specimen ID | $r_{b,ACI}$ Eq. 2-20 (in.) | $r_{b,ACI}$ Eq. 2-24 (in.) | $r_{b,FIP}$ Eq. 2-26 (in.) | $r_b/r_{b,ACI}$ Eq. 2-20 | $r_b/r_{b,ACI}$ Eq. 2-24 | $r_b/r_{b,FIP}$ Eq. 2-26 | P_{calc} (kip) | $P_{STM,ACI}$ (kip) | $P_{STM,mod.}$ (kip) | P_{FEA} (kip) | $P_{FEA}/$ P_{calc} | $P_{FEA}/$ $P_{STM,ACI}$ | $P_{FEA}/$ $P_{STM,mod}$ | Criterion* |
|------------------|----------------------------------|----------------------------------|----------------------------------|-----------------------------|-----------------------------|-----------------------------|---------------------|------------------------|-------------------------|--------------------|--------------------------|-----------------------------|-----------------------------|------------|
| FEM-B-17-R3-30 | 5.29 | 12.02 | 6.07 | 0.57 | 0.25 | 0.49 | 65.11 | 51.11 | 70.35 | 71.10 | 1.09 | 1.39 | 1.01 | (1) |
| FEM-B-17-R5-30 | 5.29 | 8.88 | 6.07 | 0.85 | 0.37 | 0.74 | 65.11 | 66.36 | 70.35 | 79.33 | 1.22 | 1.20 | 1.13 | (3) |
| FEM-B-17-R7-30 | 5.29 | 8.88 | 6.07 | 1.13 | 0.50 | 0.99 | 65.11 | 66.36 | 70.35 | 79.35 | 1.22 | 1.20 | 1.13 | (2) |
| FEM-B-17-R10-30 | 5.29 | 8.88 | 6.07 | 1.70 | 0.75 | 1.48 | 65.11 | 66.36 | 70.35 | 79.33 | 1.22 | 1.20 | 1.13 | (4) |
| FEM-B-17-R3-35 | 5.29 | 8.88 | 5.66 | 0.57 | 0.34 | 0.53 | 65.11 | 47.53 | 68.08 | 76.79 | 1.18 | 1.62 | 1.13 | (1) |
| FEM-B-17-R4-35 | 5.29 | 4.39 | 5.66 | 0.85 | 0.51 | 0.79 | 65.11 | 64.27 | 68.08 | 76.72 | 1.18 | 1.19 | 1.13 | (3) |
| FEM-B-17-R6-35 | 5.29 | 4.39 | 5.66 | 1.13 | 0.68 | 1.06 | 65.11 | 64.27 | 68.08 | 76.95 | 1.18 | 1.20 | 1.13 | (2) |
| FEM-B-17-R9-35 | 5.29 | 4.39 | 5.66 | 1.70 | 1.01 | 1.59 | 65.11 | 64.27 | 68.08 | 76.95 | 1.18 | 1.20 | 1.13 | (4) |
| FEM-B-17-R3-40 | 5.29 | 4.39 | 5.38 | 0.57 | 0.68 | 0.56 | 65.11 | 43.06 | 65.95 | 69.15 | 1.06 | 1.61 | 1.05 | (1) |
| FEM-B-17-R4-40 | 5.29 | 12.02 | 5.38 | 0.85 | 1.02 | 0.84 | 65.11 | 60.54 | 65.95 | 73.76 | 1.13 | 1.22 | 1.12 | (3) |
| FEM-B-17-R6-40 | 5.29 | 8.88 | 5.38 | 1.13 | 1.37 | 1.12 | 65.11 | 62.30 | 65.95 | 73.64 | 1.13 | 1.18 | 1.12 | (2) |
| FEM-B-17-R9-40 | 5.29 | 8.88 | 5.38 | 1.70 | 2.05 | 1.67 | 65.11 | 62.30 | 65.95 | 73.62 | 1.13 | 1.18 | 1.12 | (4) |
| FEM-B-17-R3-45 | 5.29 | - | 5.29 | 0.57 | - | 0.57 | 65.11 | 38.72 | 62.48 | 69.69 | 1.07 | 1.80 | 1.12 | (1) |
| FEM-B-17-R6-45 | 5.29 | - | 5.29 | 0.85 | - | 0.85 | 65.11 | 54.43 | 64.44 | 71.67 | 1.10 | 1.32 | 1.11 | (3) |
| FEM-B-17-R9-45 | 5.29 | - | 5.29 | 1.13 | - | 1.13 | 65.11 | 60.90 | 64.44 | 71.53 | 1.10 | 1.17 | 1.11 | (2) |
| FEM-B-17-R12-45 | 5.29 | - | 5.29 | 1.70 | - | 1.70 | 65.11 | 60.90 | 64.44 | 71.44 | 1.10 | 1.17 | 1.11 | (4) |
| FEM-BD-18-R2-30 | 5.90 | 7.10 | 6.75 | 0.38 | 0.32 | 0.33 | 71.91 | 40.08 | 65.00 | 79.17 | 1.10 | 1.98 | 1.22 | (1) |
| FEM-BD-18-R6-30 | 5.90 | 7.10 | 6.75 | 0.78 | 0.65 | 0.68 | 71.91 | 72.63 | 77.51 | 79.26 | 1.10 | 1.09 | 1.02 | (3) |
| FEM-BD-18-R10-30 | 5.90 | 7.10 | 6.75 | 1.19 | 0.99 | 1.04 | 71.91 | 72.63 | 77.51 | 79.24 | 1.10 | 1.09 | 1.02 | (2) |
| FEM-BD-18-R16-30 | 5.90 | 7.10 | 6.75 | 1.78 | 1.48 | 1.55 | 71.91 | 72.63 | 77.51 | 79.26 | 1.10 | 1.09 | 1.02 | (4) |
| FEM-BD-18-R2-35 | 5.90 | 5.22 | 6.30 | 0.38 | 0.43 | 0.36 | 71.91 | 37.17 | 60.39 | 78.30 | 1.09 | 2.11 | 1.30 | (1) |
| FEM-BD-18-R5-35 | 5.90 | 5.22 | 6.30 | 0.78 | 0.89 | 0.73 | 71.91 | 68.51 | 75.03 | 78.41 | 1.09 | 1.14 | 1.05 | (3) |
| FEM-BD-18-R9-35 | 5.90 | 5.22 | 6.30 | 1.19 | 1.34 | 1.11 | 71.91 | 70.37 | 75.03 | 78.46 | 1.09 | 1.11 | 1.05 | (2) |
| FEM-BD-18-R13-35 | 5.90 | 5.22 | 6.30 | 1.78 | 2.01 | 1.67 | 71.91 | 70.37 | 75.03 | 78.41 | 1.09 | 1.11 | 1.05 | (4) |
| FEM-BD-18-R2-40 | 5.90 | 2.54 | 5.99 | 0.38 | 0.89 | 0.38 | 71.91 | 33.61 | 54.70 | 66.92 | 0.93 | 1.99 | 1.22 | (1) |
| FEM-BD-18-R5-40 | 5.90 | 2.54 | 5.99 | 0.78 | 1.82 | 0.77 | 71.91 | 62.41 | 72.70 | 76.21 | 1.06 | 1.22 | 1.05 | (3) |
| FEM-BD-18-R8-40 | 5.90 | 2.54 | 5.99 | 1.19 | 2.76 | 1.17 | 71.91 | 68.24 | 72.70 | 76.03 | 1.06 | 1.11 | 1.05 | (2) |
| FEM-BD-18-R12-40 | 5.90 | 2.54 | 5.99 | 1.78 | 4.13 | 1.75 | 71.91 | 68.24 | 72.70 | 75.96 | 1.06 | 1.11 | 1.04 | (4) |
| FEM-BD-18-R2-45 | 5.90 | - | 5.90 | 0.38 | - | 0.38 | 71.91 | 30.24 | 49.21 | 63.82 | 0.89 | 2.11 | 1.30 | (1) |
| FEM-BD-18-R5-45 | 5.90 | - | 5.90 | 0.78 | - | 0.78 | 71.91 | 56.14 | 71.05 | 73.53 | 1.02 | 1.31 | 1.03 | (3) |
| FEM-BD-18-R8-45 | 5.90 | - | 5.90 | 1.19 | - | 1.19 | 71.91 | 66.72 | 71.05 | 73.60 | 1.02 | 1.10 | 1.04 | (2) |
| FEM-BD-18-R12-45 | 5.90 | - | 5.90 | 1.78 | - | 1.78 | 71.91 | 66.72 | 71.05 | 73.60 | 1.02 | 1.10 | 1.04 | (4) |

Note: *(1) Bar bend satisfies ACI 318¹ minimum radius

(2) Bar bend satisfies Eq. 2-20

(3) Bar bend is between that of a standard hook and the radius based on Eq. 2-20

(4) Bar bend approximately satisfies Eq. 2-20 multiplied by 1.5.

7.4.2.1 Specimens with a bend radius larger than a standard bend

Numerical specimens with a bend radius larger than that of a standard hook are discussed in this section. All such specimens exhibited post-yield behavior. That is, no strength reductions due to small bend radii were observed in the analyses. Plots that show the load-relative displacement curves of specimens in Groups FEM-B-17 and FEM-BD-18 are presented in Figure 7-28 and Figure 7-29, respectively. The numerical specimens represented in the plots were detailed based on criteria (2) through (4). The dashed red lines in the plots indicate the calculated strengths based on the nominal moment capacity at the joint face in accordance with ACI sectional analysis provisions, denoted as P_{calc} , and the calculated strength based on the strut-and-tie model with the modified coefficients, denoted as P_{STM} in the figure. It should be noted that the value of P_{calc} was calculated using the depth of the shallow adjoining member, which had a lower flexural capacity than the deeper member. The calculated strength based on joint shear capacity is not presented because it was not critical for the specimens.

As shown in Figure 7-28 and Figure 7-29, all specimens surpassed the calculated strength P_{calc} and exhibited ductile behavior after reaching the peak load. Because all specimens under consideration here had a value of $r_b/r_{b,ACI}$ based on Eq. 2-20 (that is, the ACI 318-19¹ equation based on limiting compressive stresses at the bend region) of at least 0.78, it can be concluded that if Eq. 2-20 is satisfied, the strength will reach the calculated strength P_{calc} based on nominal moment capacity at the joint face of the shallower member.

Because the shallower adjoining member of all the specimens in a particular group (Group FEM-B-17 and Group FEM-BD-18) had the same cross-sectional dimensions (see Table 7-3), the value of the calculated strength P_{calc} was the same (65.1 kip for Group FEM-B-17 and 71.9 kip for Group FEM-BD-18). However, the peak load from the finite element analyses, P_{FEA} , varied and was affected by the diagonal strut angle resulting from the different depths of the deeper adjoining member as presented in Table 7-13. Quantitatively, considering the specimens represented in Figure 7-28 and Figure 7-29, the largest value for the ratio of the strength prediction from FEA analysis to that based on sectional analysis, P_{FEA}/P_{calc} , is 1.22, while the largest value for the ratio of the strength prediction from FEA analysis to that from the strut-and-tie model with the modified coefficients, $P_{FEA}/P_{STM,mod.}$, is 1.13. This observation indicates a limitation of using flexural analysis at the joint face to determine the strength of closing knee joints.

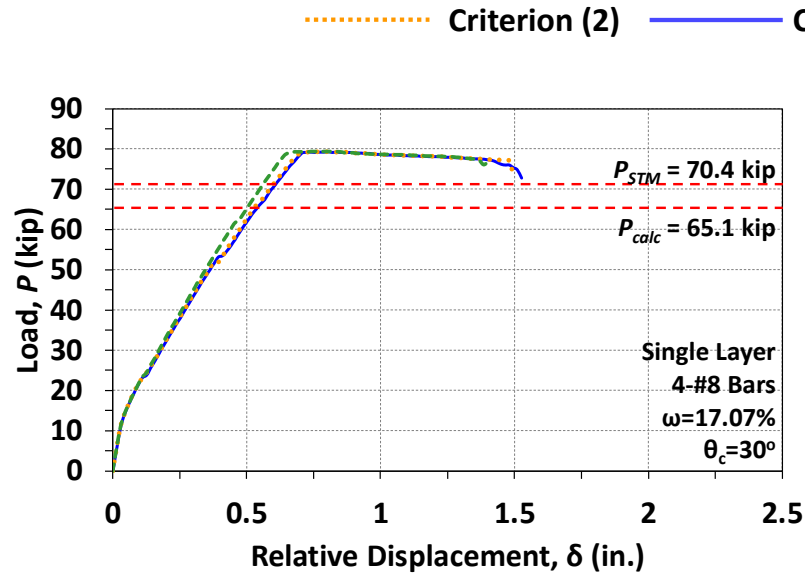
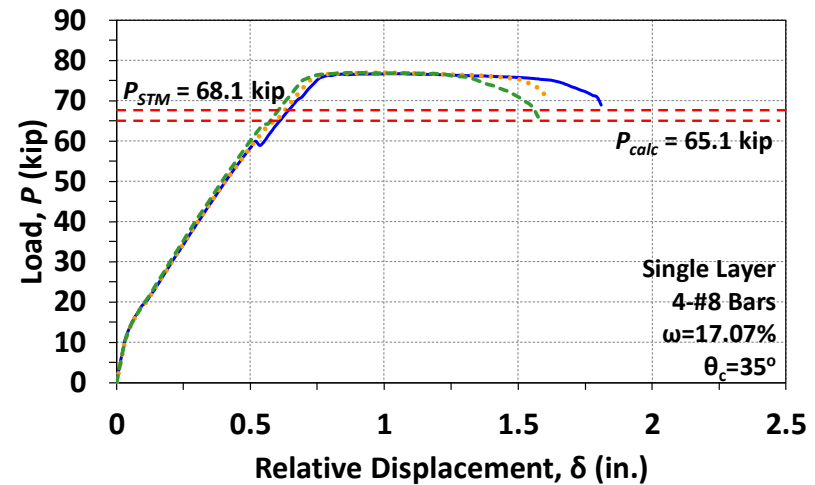
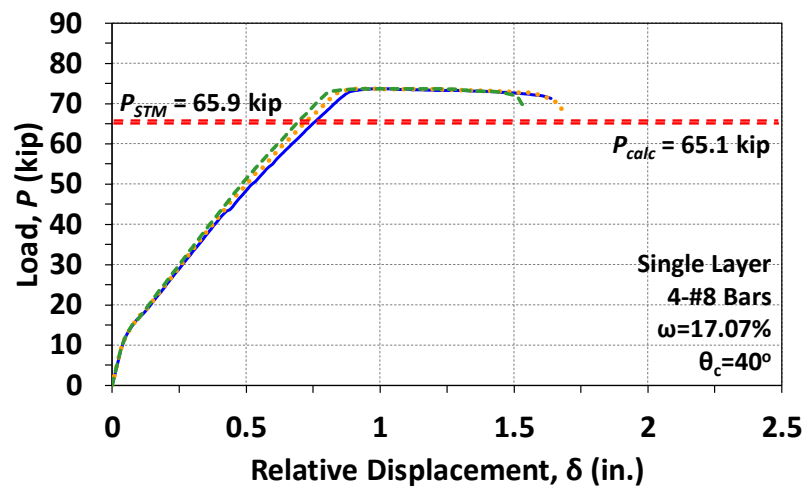
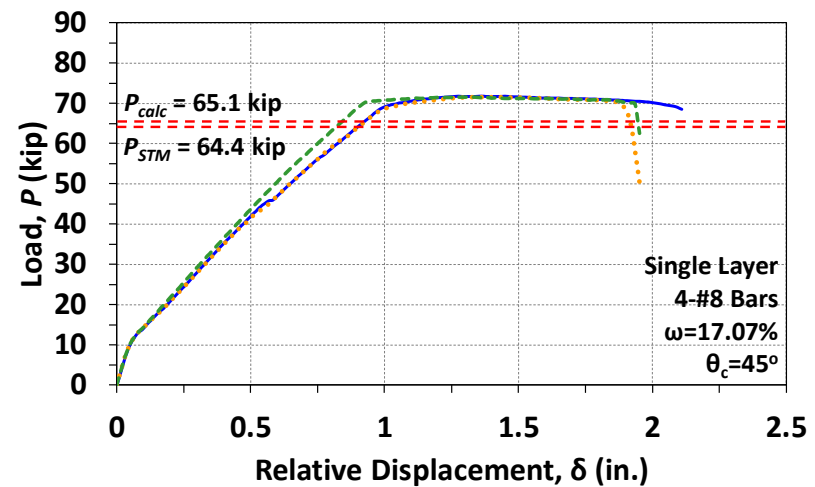
(a) Diagonal strut angle θ_c equal to 30 degrees(b) Diagonal strut angle θ_c equal to 35 degrees(c) Diagonal strut angle θ_c equal to 40 degrees(d) Diagonal strut angle θ_c equal to 45 degrees

Figure 7-28 Load-displacement curves of Group FEM-B-17 specimens

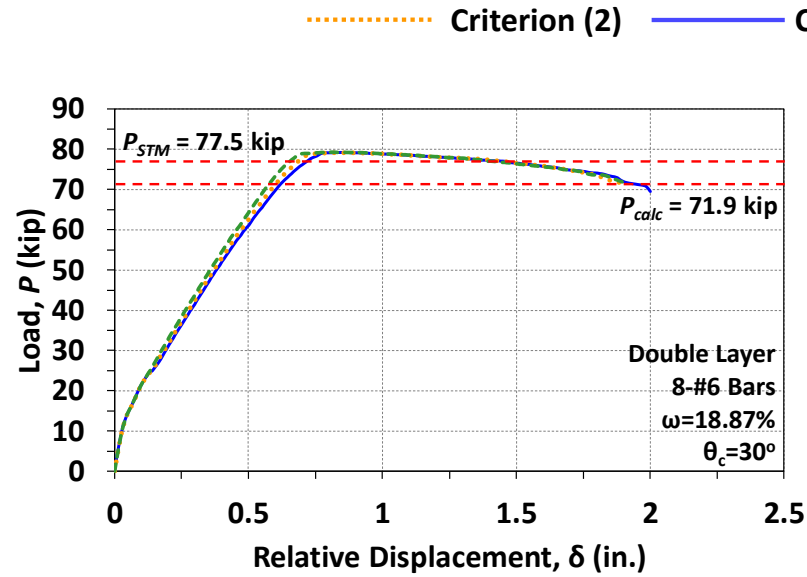
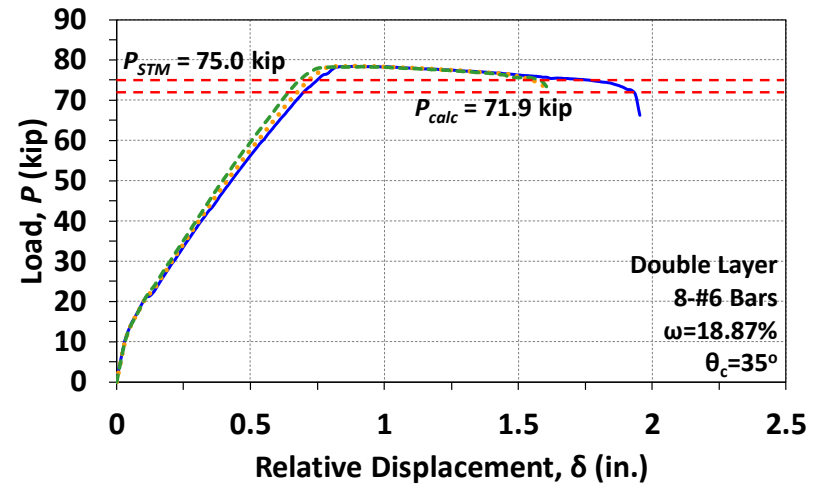
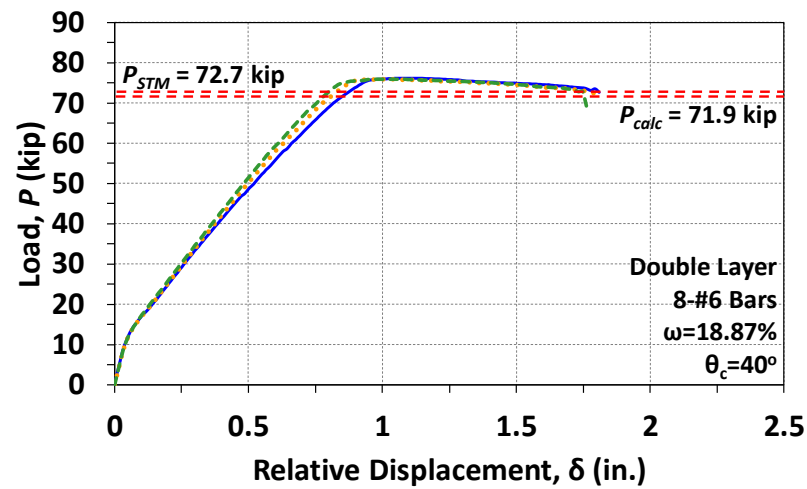
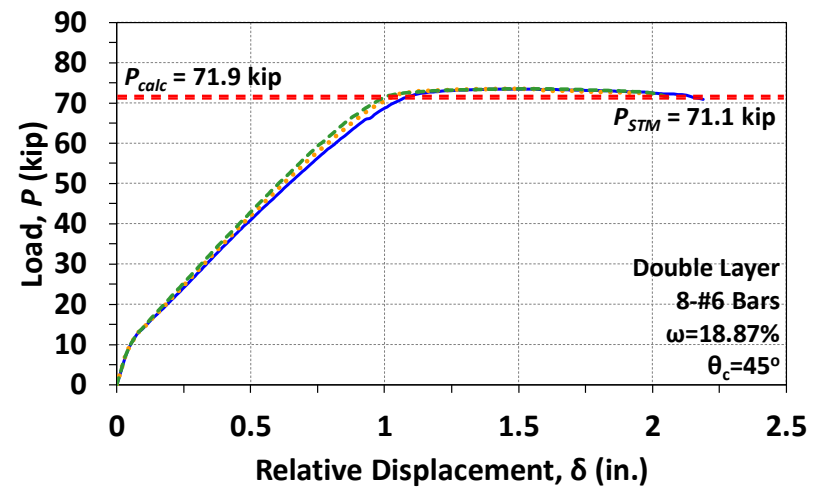
(a) Diagonal strut angle θ_c equal to 30 degrees(b) Diagonal strut angle θ_c equal to 35 degrees(c) Diagonal strut angle θ_c equal to 40 degrees(d) Diagonal strut angle θ_c equal to 45 degrees

Figure 7-29 Load-displacement curves of Group FEM-BD-18 specimens

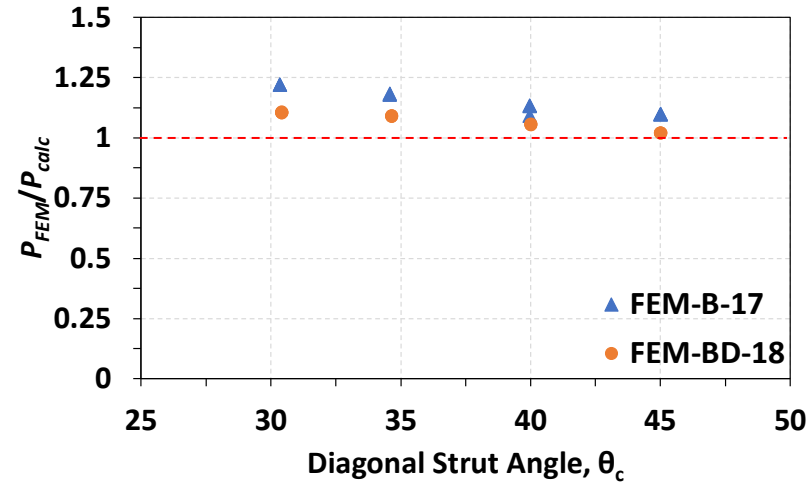
Unlike the strength predictions based on flexural analysis at the joint face, the calculated strengths from the application of strut-and-tie model type (a) (see Section 6.4.1) varied based on the diagonal strut angle, θ_c , (see Table 7-13) because the diagonal strut angle was an important factor in the construction of the strut-and-tie model. To be specific, the diagonal strut angle affected the size of the CCC node at the re-entrant corner for the specimens under consideration. (see 6.4.3) The strut-and-tie model with either the ACI-based coefficients or the modified coefficients reflect the effect of the diagonal strut angle. Plots of the relationship between the strength ratio of specimens under consideration in this section based on the various strength-predictive models versus the diagonal strut angle are presented in Figure 7-30. As shown in Figure 7-30(a), the strength ratio based on nominal flexural strength demonstrates a downward trend as the value of θ_c increases. This trend is eliminated when the strut-and-tie method is used.

Considering the three approaches for predicting strength represented in Figure 7-30, the strut-and-tie model with ACI-based coefficients resulted in the datapoints corresponding to the lowest level of accuracy. The strut-and-tie model with the modified coefficients delivered results with greater accuracy compared to the strut-and-tie model with coefficients from ACI 318-19,¹ while also successfully reflecting the effect of the diagonal strut angle. Moreover, the results using the modified coefficients remained conservative. Therefore, the advantages to using the strut-and-tie model with the modified parameters are clear. It should be noted that the above observations are limited to the values of the mechanical longitudinal reinforcement ratio, ω , considered for the FEM-B-Series.

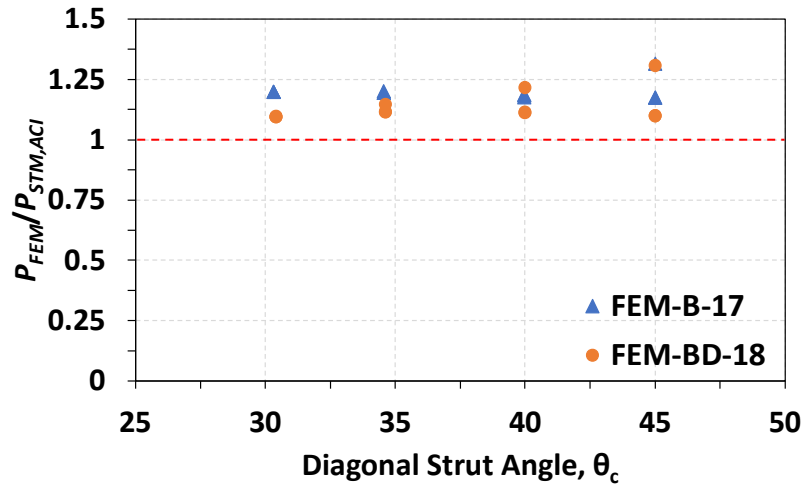
The overall similarities between the three plots shown in Figure 7-30 should also be discussed. For example, a majority of the datapoints fall within a strength ratio between 1.0 and 1.25. For the sectional analysis, the strength of all specimens was governed by the yielding of the longitudinal reinforcing bars at the joint face because the specimens were designed to have tension-controlled sections. For the strut-and-tie model with the modified coefficients, longitudinal reinforcing bars were also able to develop the yield stress because the CTT node was strong enough with application of the modified nodal zone coefficient. The strut-and-tie model with ACI-based coefficients, however, assumed a lower strength for the CTT node, leading to two predicted strengths governed by the CTT node (Specimens FEM-B-17-R3-45 and FEM-BD-18-R2-45).

From the data presented in Table 7-13, it can be also observed that the requirement of Eq. 2-24 (that is, the ACI 318-19¹ requirement in consideration of bond stress along the bar bend) does

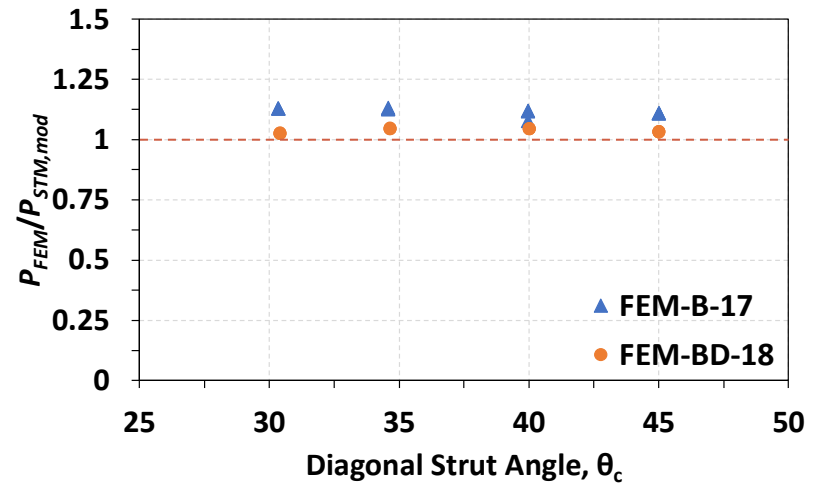
not correlate with the strengths indicated by the finite element analyses. In this series, 10 out of 33 numerical specimens had a bend radius satisfying the requirement by Eq. 2-24. However, all specimens were able to reach acceptable strengths if Eq. 2-20 was satisfied.



(a) Based on nominal flexural capacity at joint face (sectional analysis)



(b) Based on STM incorporating ACI 318-19¹ coefficients



(c) Based on STM incorporating modified coefficients

Figure 7-30 Relationship between strength ratio based on various strength predictions and diagonal strut angle for FEM-B-Series specimens with a bend radius larger than a standard bend

7.5.2.1 Specimens with the bend radius of a standard bend

Plots that show the load-relative displacement curves of specimens in Groups FEM-B-17 and FEM-BD-18 with a standard bend are presented in Figure 7-31. More specifically, these specimens have IDs that include “FEM-BD-17-R3” or “FEM-BD-18-R2.” The dashed red lines in the plots indicate the calculated strength of the shallow adjoining member based on the nominal flexural capacity using sectional analysis. The calculated strengths derived from the STM are not presented on the plots to improve readability because different bend radii result in different strength predictions. Detailed FEA results and the calculated strengths are summarized in Table 7-13.

Unsurprisingly, the finite element analyses indicated that some FEM-BD-18-R2 specimens had a strength that is less than the calculated values based on the nominal flexural capacity due to the small bend radius. However, the strength of the specimen with the diagonal strut angle of 30 degrees (Specimen FEM-BD-18-R2-30) not only exceeded P_{calc} , but the numerical specimen also exhibited ductile behavior. Furthermore, the specimen with a diagonal strut angle of 35 degrees (Specimen FEM-BD-18-R2-35) also exhibited some post-peak ductility. This phenomenon is not in agreement with the ACI 318-19¹ required bend radius in consideration of radial stress at the bar bend. Specimens FEM-BD-18-R2-30 and FEM-BD-18-R2-35 have a bend radius ratio of 0.38 based on Eq. 2-20. Therefore, the behavior of the specimens indicated by the analyses is inconsistent with other specimens of the research program with such a small bend radius ratio based on Eq. 2-20. Moreover, the required bend radius based on Eq. 2-24 also does not properly reflect the specimen behaviors. According to Eq. 2-24, smaller diagonal strut angles (that is, smaller values of θ_c) should lead to the need for larger bend radii. However, the observation contradicts this trend: the smallest diagonal strut angle resulted in the best behavior. The diagonal strut angle is not in positive correlation with strength as expected based on Eq. 2-24.

Considering the FEM-B-17-R3 specimens, a sudden decrease in load-carrying capacity was exhibited by the specimens after reaching the peak load with the exception of Specimen FEM-BD-17-R3-35, which demonstrated ductile behavior. For the three specimens that lacked ductility, the diagonal strut angle did not correspond with a change in strength. Furthermore, it is not surprising that all four specimens were able to reach the calculated strength based on nominal flexural capacity because the bend radius ratio based on Eq. 2-20 was 0.57.

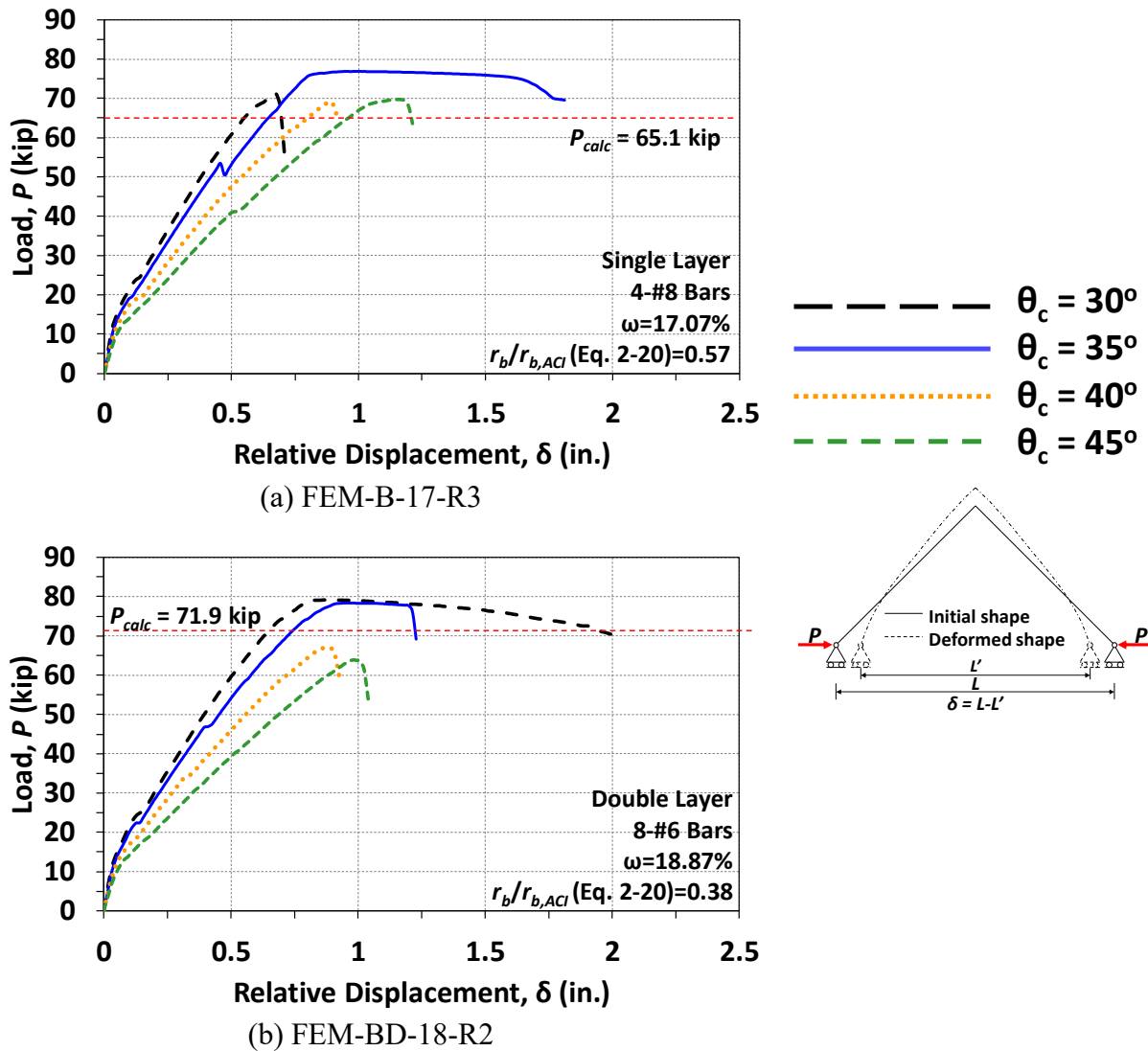


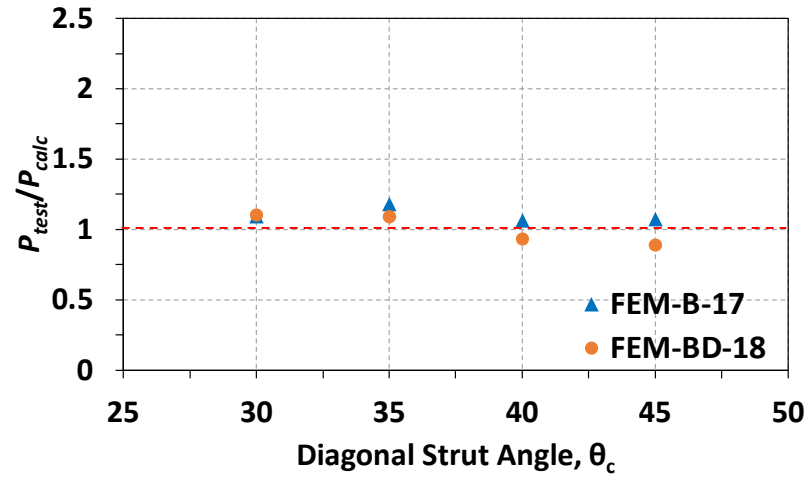
Figure 7-31 Load-displacement curves of FEM-B-Series specimens with a standard bend

The specimens under consideration in this section were also analyzed using the strut-and-tie method with both ACI-based coefficients and the modified coefficients. The strength ratios based on the nominal flexural capacity and the STM are plotted against the diagonal strut angle in Figure 7-32. Among the three methods represented in the figure, the strut-and-tie model with the ACI-based coefficients delivered the most conservative predictions as shown in Figure 7-32(b) and can be considered to have resulted in overconservative results. The greatest strength ratio is 2.11, corresponding to Specimen FEM-BD-18-R2-45.

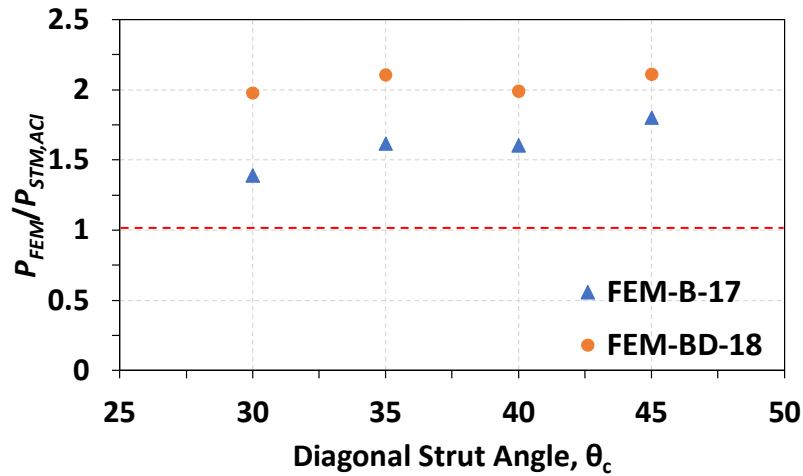
The nominal moment capacity based on sectional analysis delivered the most accurate results as shown in Figure 7-32(a). Nevertheless, two unconservative predictions are observed.

Both datapoints represent numerical specimens with a bend radius ratio of 0.38 based on Eq. 2-20, again implying that assuming the nominal moment capacity based on sectional analysis is not suitable for specimens with small bend radii.

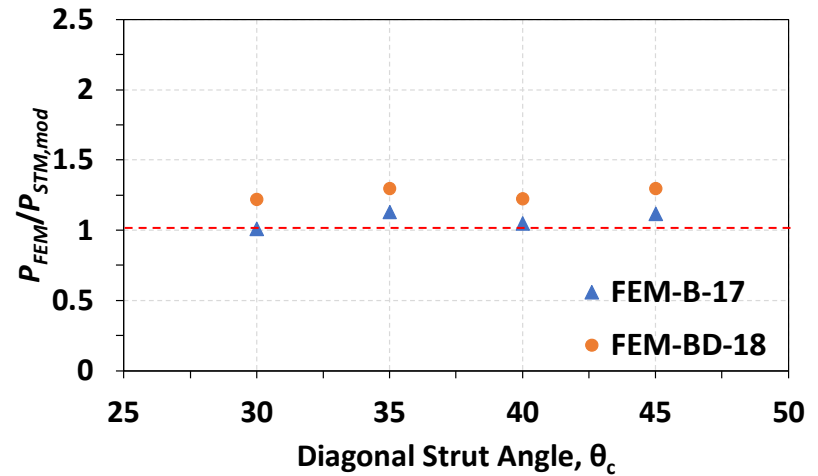
The strut-and-tie model with the modified coefficients also resulted in more accuracy compared to the use of the ACI-based coefficients as shown in Figure 7-32(c). Here, the greatest value of the strength ratio is 1.22, and all predictions resulted in a strength ratio greater than 1.0. In addition, the strut-and-tie model with the modified coefficients showed no bias relative to the diagonal strut angle.



(a) Based on nominal flexural capacity at joint face (sectional analysis)



(b) Based on STM incorporating ACI 318-19¹ coefficients



(c) Based on STM incorporating modified coefficients

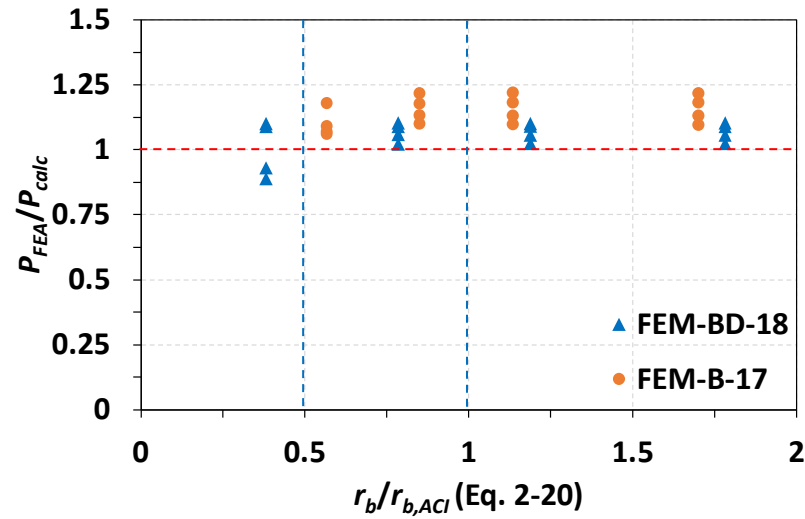
Figure 7-32 Relationship between strength ratio based on various strength predictions and diagonal strut angle for FEM-B-Series specimens with a bend radius of a standard bend

7.5.2.2 General evaluation of various requirements for the bend radius using FEM-B-Series specimens

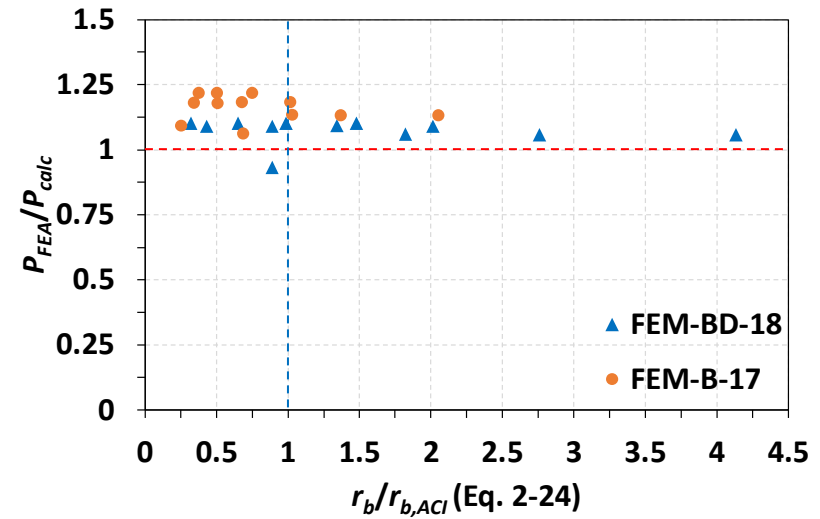
The design expressions for the bend radius (Eq. 2-20, Eq. 2-24, and Eq. 2-26) can be evaluated using all the specimens in the FEM-B-Series by studying plots displaying the relationship between the strength ratio P_{FEA}/P_{calc} and bend radius ratios based on the three expressions, as presented in Figure 7-33. Here, P_{calc} is based on the nominal flexural strength at the joint face. As shown in Figure 7-33(a), when the bend radius ratio based on the equation from ACI 318-19¹ in consideration of radial stresses at the bar bend (Eq. 2-20) was greater than 0.5, all numerical specimens were able to reach a strength ratio greater than 1.0. This observation is consistent with the experimental program as well as numerical specimens with adjoining members with identical cross sections. Of course, if Eq. 2-20 was satisfied, no specimens with compromised strengths were observed. Therefore, it is recommended that bend radii satisfying the requirement of Eq. 2-20 be used although the equation does not incorporate the diagonal strut angle.

When the bend radius based on FIP⁵⁸ (Eq. 2-26) was used, the results are similar to those from the application of Eq. 2-20, as shown in Figure 7-33(c), although the effect of the diagonal strut angle on the size of the bearing area under the bar bend was considered. For bend radius ratios greater than 0.50, the value of P_{FEA}/P_{calc} for all numerical specimens is greater than 1.0. Like Eq. 2-20, the FIP expression also seems to be suitable for evaluating the curved-bar node of closing knee joints.

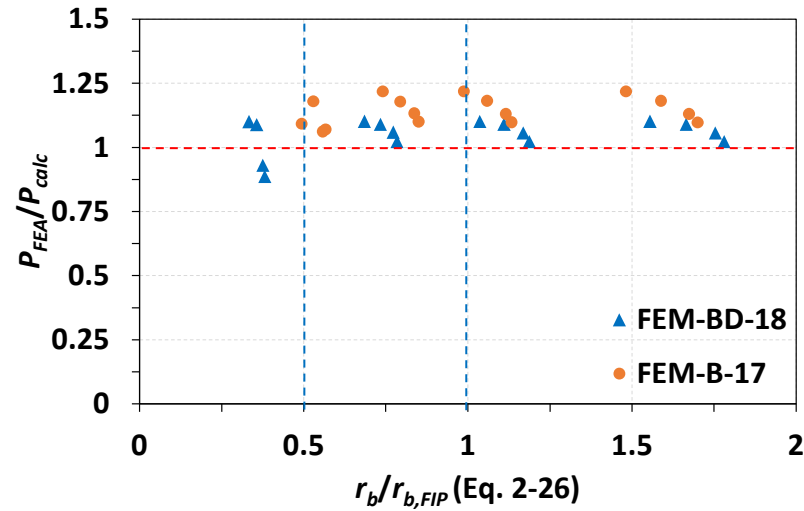
Different from the previous requirements, Eq. 2-24 considers circumferential bond stress along the bar bend. The equation was evaluated using the plot shown in Figure 7-33(b). The equation does not apply to specimens in the FEM-B-Series with a diagonal strut angle of 45 degrees, and these specimens are therefore not represented in the plot. It should be noted that the development length used to calculate the required bend radius using Eq. 2-24 was 47.4 in. for No. 8 bars and 28.4 in. for No. 6 bars in accordance with Section 25.4.3.3 of ACI 318-19.¹ It can be observed from Figure 7-33(b) that there is no obvious correlation between the strength ratio and the bend radius ratio based on Eq. 2-24. Most specimens fell into the region corresponding to a bend radius ratio less than 1.0, but the strength ratio was greater than 1.0 for most cases. Although it incorporates different diagonal strut angles, applying Eq. 2-24, developed in consideration of circumferential bond stress, appears to be unnecessary.



(a) Based on requirement of Eq. 2-20



(b) Based on requirement of Eq. 2-24



(c) Based on requirement of Eq. 2-26

Figure 7-33 Relationship between strength ratio P_{FEA}/P_{calc} and bend radius ratio for FEM-B-Series specimens

7.6 Summary

Finite element analysis on knee joints subjected to closing moments using the software ATENA 3D was presented in this chapter. Finite element models were developed and calibrated/validated using benchmark specimens from the experimental program. Comparing the results of load-relative displacement curves generated by ATENA to the experimental results showed that the finite element models were able to accurately predict the peak load-carrying capacity of closing knee joints. ATENA was therefore used to conduct a parametric analysis to investigate factors that might affect the behavior of curved-bar nodes and closing knee joints. The factors were similar to those considered in the experimental program, including the bend radius, mechanical reinforcement ratio, clear side cover, and presence of transverse reinforcement in the joint. Moreover, the diagonal strut angle was the most important factor to investigate through the analytical study because limited results were obtained from the experimental program. The primary observations and conclusions resulting from the analysis of seventy-two numerical specimens using ATENA are as follows:

1. The finite element analyses on numerical specimens with a wider range of mechanical reinforcement ratios and bend radii than what was possible through the experimental program again revealed that the requirement for the bend radius given by Eq. 2-20 is appropriate for achieving satisfactory behavior. This observation is independent of whether a single layer or two layers of longitudinal reinforcement is provided. If strength is the only concern, bend radii with a value half of the requirement given by Eq. 2-20 may be acceptable.
2. Thin clear side cover caused a reduction in strength for specimens with a bend radius ratio less than 0.5 based on Eq. 2-20 modified by the factor $2d_b/c_c$. The effect, however, was not obvious for other specimens. A reduced factor of $1.5d_b/c_c$ as introduced based on the experimental program can be applied to provide results that are more consistent with other specimens with thicker cover. That is, bend radius ratios based on Eq. 2-20 with the modified factor that are greater than 0.5 resulted in specimens with satisfactory strength.
3. The presence of transverse reinforcement in the joint did not necessarily increase the load-carrying capacity. The bend radius still governed the behavior of closing knee joints.

4. Calculated joint shear strength did not properly reflect the capacity of closing knee joints. That is, closing knee joints with a calculated joint shear capacity less than the shear demand corresponding to the yielding of the longitudinal reinforcing bars at the joint face still reached the calculated nominal flexural strength if the bend radius was large enough. Both flexural analysis and the joint shear analysis could not appropriately reflect the effect of the bend radius.
5. For specimens with different adjoining members, if the requirement for the bend radius based on radial stress (Eq. 2-20) was satisfied, compromised strengths were not observed regardless of the angles of the diagonal strut. Indeed, a bend radius ratio based on Eq. 2-20 of 0.50 was sufficient if only strength was considered. When the bend radius ratio was not greater than 0.57, the diagonal strut angle affected the joint behavior. However, joint strength did not demonstrate a positive correlation with the diagonal strut angle.
6. The expression for the bend radius based on circumferential bond stress (Eq. 2-24) did not show a clear correlation with the strength ratio of closing knee joints. It is suggested that the requirement imposed by this equation be revisited.
7. The strut-and-tie method with ACI-based coefficients and the modified coefficients delivered conservative predictions for closing knee joints. However, the strut-and-tie model with ACI-based coefficients resulted in overconservative strength estimates in many cases, especially when the bend radius ratio based on Eq. 2-20 was less than 0.5. The underestimations were mitigated with the use of the modified STM coefficients.

The software ATENA 3D demonstrated satisfactory performance in predicting the behavior of knee joints under closing moments. Moreover, the comprehensive finite element analyses provided greater confidence in the use of the equations for the bend radius as well as the use of the strut-and-tie method.

8. CONCLUSIONS

The research described in this dissertation was focused on reinforced concrete frame corners (that is, knee joints) subjected to closing moments. The design of such joints has commonly relied on “good practice.” Classified as a D-region, the strut-and-tie method is an appropriate approach for the design of closing knee joints. In the 2019 edition of ACI 318,¹ curved-bar nodes were first introduced in the strut-and-tie method provisions included in the building code. A curved-bar node models the stresses at the outer corner of closing knee joints detailed with continuous longitudinal bars that pass through the joint. Although the curved-bar node provisions are consistent with other STM code provisions, the design expressions for curved-bar nodes have not been experimentally verified through a comprehensive research program focused on evaluating design methodologies for curved-bar nodes. A research program was therefore developed to verify and/or refined the existing curved-bar node design provisions and better understand the behavior of reinforced concrete knee joints under closing moments. Considering the proper application of the strut-and-tie method to closing knee joints was also desired. To achieve these goals, the research program included an experimental program, a database analysis, and finite element analysis.

The experimental program consisted of load tests on 24 specimens that were used to thoroughly investigate factors affecting the behavior of closing knee joints. The factors evaluated through the test program included the bend radius of the longitudinal reinforcement, the mechanical longitudinal reinforcement ratio, multiple layers of longitudinal reinforcement, reduced clear side cover, the diagonal strut angle, lap-spliced longitudinal reinforcement, and transverse reinforcement in the joint. The strengths and behaviors of the specimens were used to evaluate the suitability of current code provisions. Including the 24 specimens of the test program, an evaluation database consisting of 116 tests on closing knee joint was established and used to corroborate a procedure that was developed for constructing a strut-and-tie model for closing knee joints. Furthermore, the database was used to evaluate strength predictions calculated with the strut and nodal zone coefficients specified in ACI 318-19.¹ Modified coefficients that result in improved strength predictions were also introduced. Lastly, finite element analysis using the software ATENA 3D was conducted to supplement the test data in order to further verify the strut-and-tie

method with the modified coefficients. The primary observations and conclusions from the research program are summarized as follows:

1. Based on the results from tests on knee joint specimens with either a single layer or two layers of longitudinal reinforcement, the ratio of the actual bend radius of the longitudinal bars to the bend radius required by ACI 318-19¹ in consideration of radial stresses at the bar bend, $r_b/r_{b,ACI}$, significantly affects the behavior of closing knee joints in terms of the strength ratio P_{test}/P_{calc} , the failure mode, and the extent of yielding of the longitudinal reinforcement. For closing knee joints with a bend radius ratio, $r_b/r_{b,ACI}$, less than 0.5, the experimental capacity was often less than the calculated capacity based on ACI sectional analysis; the failure mode was related to splitting of the diagonal strut in the joint, showing no ductility; and the yielding of the reinforcing bars did not extend to the bar bend. When the bend radius ratio was greater than 1.0, satisfying the ACI-required bend radius in consideration of radial stresses at the bar bend, the closing knee joints exhibited significant ductility and yielding of the longitudinal reinforcement extended through the entire bar bend, achieving the stress distribution assumed by the strut-and-tie model. When the bend radius ratio was between 0.5 to 1.0, strength was not compromised but the ductility exhibited by the specimens was inferior to that of the specimens that satisfied the ACI-required bend radius. It is therefore recommended that the current bend radius required by ACI 318-19¹ in consideration of radial stresses at the bar bend be satisfied to achieve satisfactory behavior.
2. The specimen detailed with the bend radius of a standard hook and reduced clear side cover at the location of curved-bar node exhibited lower strength compared to its companion specimen without reduced side cover. At the same time, if the unmodified ACI requirement in consideration of radial stresses was satisfied, further enlarging the bend radius did not improve the ductility. The modification factor $2d_b/c_c$ specified in ACI 318-19¹ to account for the effects of thin side cover provides conservative results. The test data suggest, however, that using a reduced factor of $1.5d_b/c_c$ to calculate $r_{b,ACI}$ within the bend radius ratio, $r_b/r_{b,ACI}$, for specimens with thin side clear cover results in a more consistent categorization based on behavior relative to other specimens in the test program that have adjoining members with matching cross sections.

3. The requirement in ACI 318-19¹ that the bend radius of the longitudinal bars be sufficient to allow the difference in tie forces to develop along the bar bend was shown to be overly conservative according to the limited test results, giving reason to revisit the current requirement. Based on the tests in the experimental program for which the ties intersecting at the curved-bar node carried different forces (that is, the diagonal strut angle was not equal to 45 degrees), a bend radius greater than 50% of that required by either the ACI requirement in consideration of radial stresses or the FIP⁵⁸ requirement resulted in a strength ratio P_{test}/P_{calc} greater than 1.0.
4. Transverse reinforcement in the joint was not effective in increasing the strength ratio for specimens with bend radius ratios $r_b/r_{b,ACI}$ less than 0.5. The transverse reinforcement only slowed the loss in load-carrying capacity after the peak load was reached. This observation applies whether continuous longitudinal reinforcement passed through the joint or the reinforcement was lap-spliced in the joint.
5. In general, the results of the database evaluation suggest that sectional analysis based on ACI 318-19¹ can be used to predict the strength of closing knee joints when the diagonal strut width ratio is greater than 1.0. Otherwise, the prediction may be unconservative.
6. With the consideration of the bar stress at the joint face limited by the calculated joint shear capacity, the sectional analysis approach gave improved strength predictions for the specimens in the evaluation database for which the bar stress was limited by the calculated shear strength, as expected. Nevertheless, considering all specimens in the database, many unconservative cases remained for diagonal strut width ratios less than 1.0 because the calculated joint shear capacity does not incorporate the effect of small bend radii. Although specimens may have the same effective joint shear area and similar concrete compressive strengths, the bar stress at the joint face (or moment at the joint face) can be governed by a small bend radius.
7. In general, the strut-and-tie method delivers conservative predictions for the strengths of specimens in the evaluation database. The strut-and-tie model with coefficients based on ACI 318-19¹ can be overly conservative, especially for diagonal strut width ratios less than 1.0. This observation can be attributed to the nodal zone coefficient applied to the CTT node and the fact that the strut-and-tie method neglects the development of bar stress along

the straight portion of the bars within the joint region. Furthermore, the strength reduction due to thin clear side cover contributed to the underestimated strengths.

8. Compared to the strut-and-tie model with coefficients based on ACI 318-19¹, the strut-and-tie model with the modified coefficients provides increased accuracy but is still conservative. Some overconservativeness was also still observed. This is again partially attributed to the development of the bar stress within the joint being neglected.
9. Finite element models of knee joints under closing moments were created using the software ATENA 3D. The models were calibrated with selected specimens from the experimental program that acted as benchmarks, and the finite element analyses were proven to be able to accurately capture the load-relative displacement relationships of the specimens.
10. Seventy-two numerical specimens were modeled and analyzed to provide supplemental data, especially for closing knee joints with different adjoining members (that is, a diagonal strut angle not equal to 45 degrees). In general, the numerical results were in good agreement with the experimental results. In other words, the bend radius was again shown to significantly affect the behavior of closing knee joints. The bend radius required by ACI 318-19¹ in consideration of radial stresses and the modification factor for thin clear side cover were verified to be appropriate for numerical specimens with legs that have matching cross sections. The ACI-required bend radius in consideration of circumferential bond stress, however, showed no correlation with strength. Furthermore, the strut-and-tie model with modified coefficients delivered more accurate but still conservative strength predictions when compared to the strut-and-tie model with coefficients based on ACI 318-19.¹ This observation strengthens the viability of applying the STM with the modified coefficients for the strength assessment of closing knee joints.

APPENDIX A. MEASUREMENT OF BEND RADII

The bend radius of a bar bend could not be measured directly because the bend was not a perfect arc with 90 degrees. An indirect method of measurement was used to calculate the average bend radius using geometry as follows:

1. As shown in Figure A.1, take two arbitrary points A and B on the arc of the inner bar bend and the distance between point A and point B is measured and denoted as \overline{AB} .
2. Make the bisection of line AB as line CD. Line CD intersects line AB at point E and the inner bar bend at point F.
3. Measure the distance of line FE, denoted as \overline{FE} .

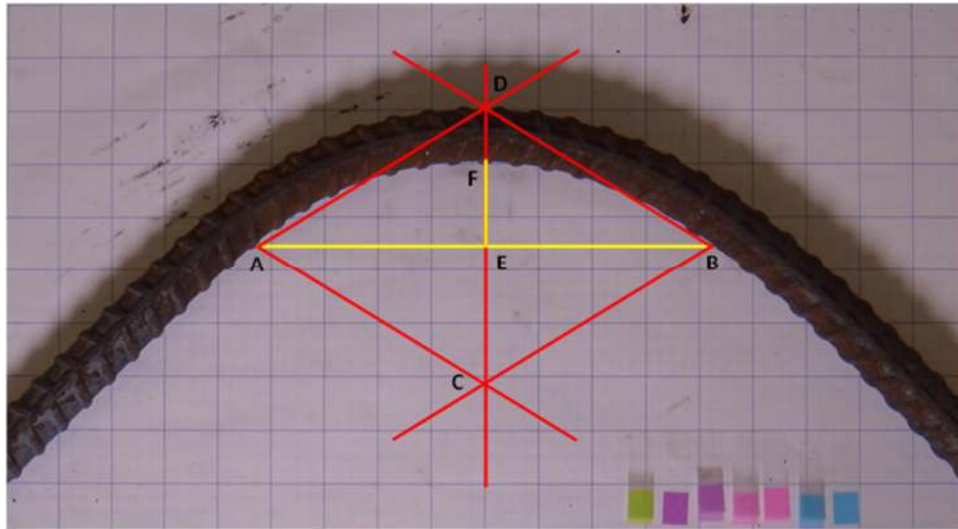


Figure A.1 Measurement of bend radius

4. For an arc with known distance \overline{AB} and \overline{FE} , the radius of the arc, namely inner bend radius r_b , is calculated using Eq. A-1.

$$r_b = \frac{\overline{AB}^2 + 4\overline{FE}^2}{8\overline{FE}} \quad \text{A-1}$$

5. Repeat the steps above for three times and take the average of the three calculated values of the inner bend radius as the final measurement.

APPENDIX B. DETERMINATION OF INTERNAL FORCES FOR STRUT-AND-TIE MODELS

In Chapter 6, several strut-and-tie models were constructed on the basis of types of knee joint specimens and loading method. The internal force of each element was then determined by equilibrium. Detailed procedures are introduced in this appendix.

B.1 Strut-and-Tie Model Type (a) (Not Including Specimen Type Portal)

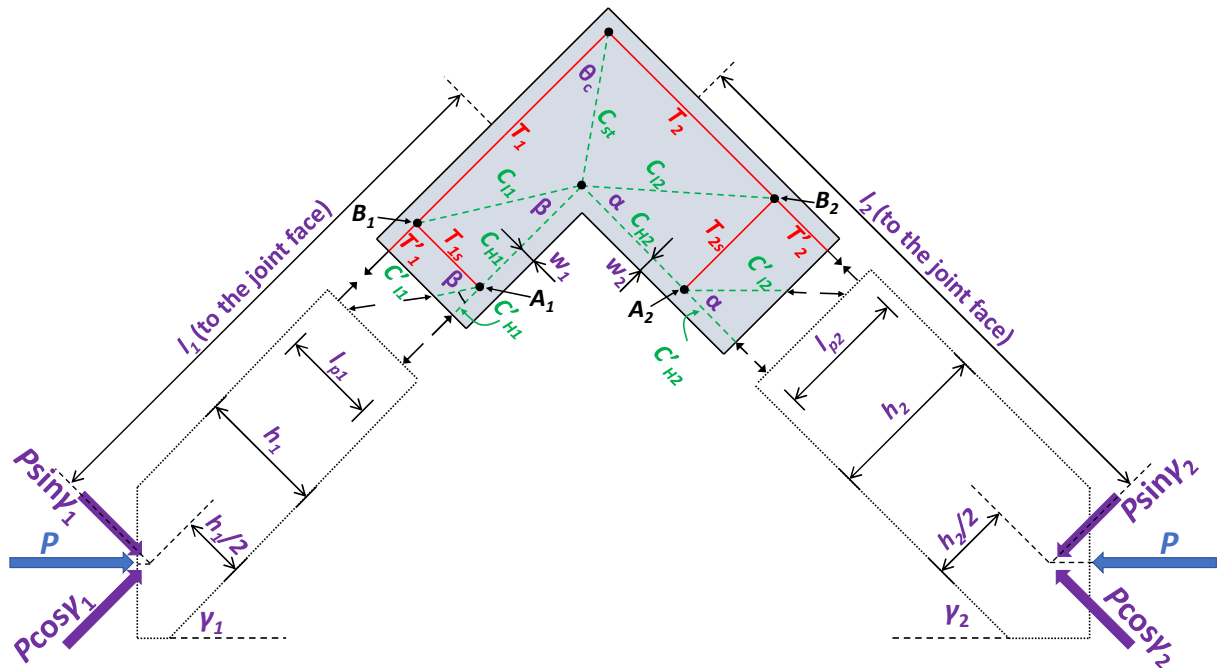


Figure B-1 Free body diagram of strut-and-tie model type(a)

1. For the free body diagram of the right leg shown in Figure B.1, taking moment equal to zero about node A_2 and taking equilibrium of the forces deliver the following equations:

$$T'_2 l_{p2} - P \sin \gamma_2 (l_2 + w_1 - l_{p2} \cot \alpha) + P \cos \gamma_2 \left(\frac{h_2}{2} - w_2 \right) = 0 \quad \text{B-1}$$

$$C'_{12} \sin \alpha - P \sin \gamma_2 = 0 \quad \text{B-1}$$

$$T'_2 + P \cos \gamma_2 - C'_{12} \cos \alpha - C'_{H2} = 0 \quad \text{B-2}$$

2. Take equilibrium of the forces at node A_2 , and Eq. B-4 and Eq. B-5 can be derived.

$$T_{2s} - C'_{I2} = 0 \quad \text{B-4}$$

$$C_{H2} - C'_{I2} \cos \alpha - C'_{H2} = 0 \quad \text{B-5}$$

3. Take equilibrium of the forces at node B_2 , and Eq. B-6 and Eq. B-7 can be derived.

$$T_{2s} - C_{I2} = 0 \quad \text{B-6}$$

$$T_2 - C_{I2} \cos \alpha - T'_2 = 0 \quad \text{B-7}$$

4. Solving Eq. B-1 to Eq. B-7 simultaneously obtains the internal forces T_2 , C_{I2} and C_{H2} as follows:

$$T_2 = \frac{P}{l_{p2}} \left[\sin \gamma_2 (l_2 + w_1) - \cos \gamma_2 \left(\frac{h_2}{2} - w_2 \right) \right] \quad \text{B-8}$$

$$C_{I2} = \frac{P \sin \gamma_2}{\sin \alpha} \quad \text{B-9}$$

$$C_{H2} = \frac{P}{l_{p2}} \left[\sin \gamma_2 (l_2 + w_1 - l_{p2} \cot \alpha) - \cos \gamma_2 \left(\frac{h_2}{2} - w_2 - l_{p2} \right) \right] \quad \text{B-10}$$

5. Resolving the forces C_{I2} and C_{H2} obtains the resultant F_b and the orientation θ_2 as follows:

$$F_b = P \sqrt{\left[\frac{\sin \gamma_2 (l_2 + w_1) + \cos \gamma_2 \left(d_2 - \frac{h_2}{2} \right)}{l_{p2}} \right]^2 + \sin^2 \gamma_2} \quad \text{B-11}$$

$$\theta_2 = \tan^{-1} \left(\frac{l_{p2} \sin \gamma_2}{(l_2 + w_1) \sin \gamma_2 - \left(\frac{h_2}{2} - d_2 \right) \cos \gamma_2} \right) \quad \text{B-12}$$

6. Repeat the procedure through taking the free body diagram of the left leg and equilibrium of node A_1 and B_1 to obtain T_1 , F_c and θ_1 as follows:

$$T_1 = \frac{P}{l_{p1}} \left[\sin \gamma_1 (l_1 + w_2) - \cos \gamma_1 \left(\frac{h_1}{2} - w_1 \right) \right] \quad \text{B-13}$$

$$F_c = P \sqrt{\left[\frac{\sin \gamma_1 (l_1 + w_2) + \cos \gamma_1 \left(d_1 - \frac{h_1}{2} \right)}{l_{p1}} \right]^2 + \sin^2 \gamma_1} \quad \text{B-14}$$

$$\theta_1 = \tan^{-1} \left(\frac{l_{p1} \sin \gamma_1}{(l_1 + w_2) \sin \gamma_1 - \left(\frac{h_1}{2} - d_1 \right) \cos \gamma_1} \right) \quad \text{B-15}$$

B.2 Strut-and-Tie Model Type (a) (Specimen Type Portal)

The specimens tested in the study by Stroband et al. were shaped portal supported by a pin at each column, which was a statically indeterminate structure. To determine the reactions and internal shear and moment in the structure, elastic structural analysis was used. Therefore, the internal forces of elements of the strut-and-tie model were calculated. Detailed procedure is introduced in this section.

B.2.1 Internal Forces for Sectional Analysis

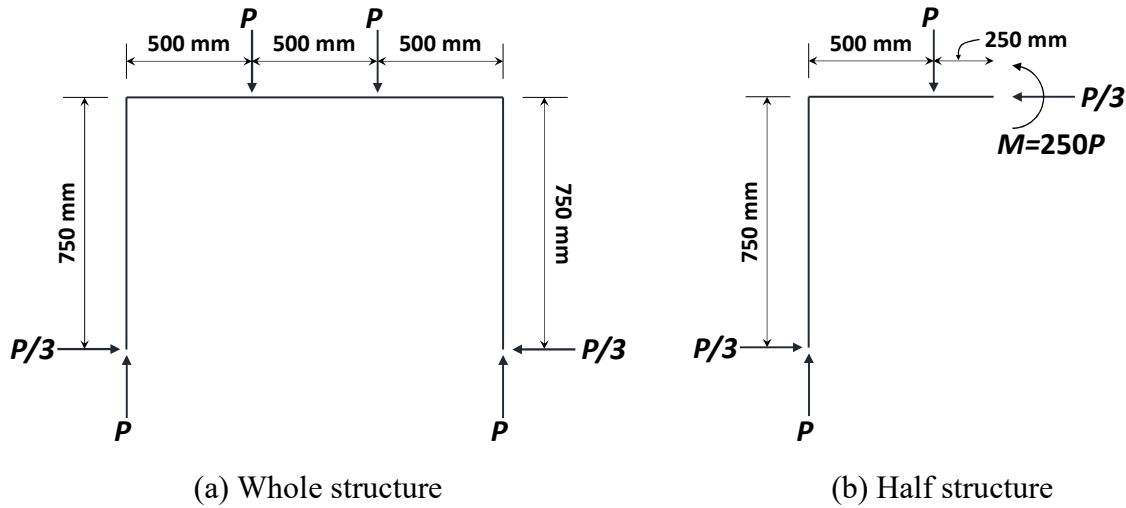


Figure B-2 Structural analysis of portal specimen used by Stroband et al.

Consider a structure shown in Figure B-2(a) and the horizontal reaction can be determined by structural analysis as $P/3$. The vertical reaction under each column is P , equal to the external force due to symmetry. Also, the structure can be solved considering only the half as shown in Figure B-2(b). For the free body diagram, no shear is needed at the cut of the section because of symmetry. By equilibrium, the moment and the axial force can be determined as shown in Figure B-2(b).

Forces acting on the knee joint are also determined simply by equilibrium as the detailed shown in Figure B-3. The sectional moment at the joint face of the beam M_{j2} was $190P$ with a unit of N-mm. And the axial force acting on the joint face of the beam was $P/3$. The two values were then used to determine the nominal flexural capacity of the beam at the joint face.

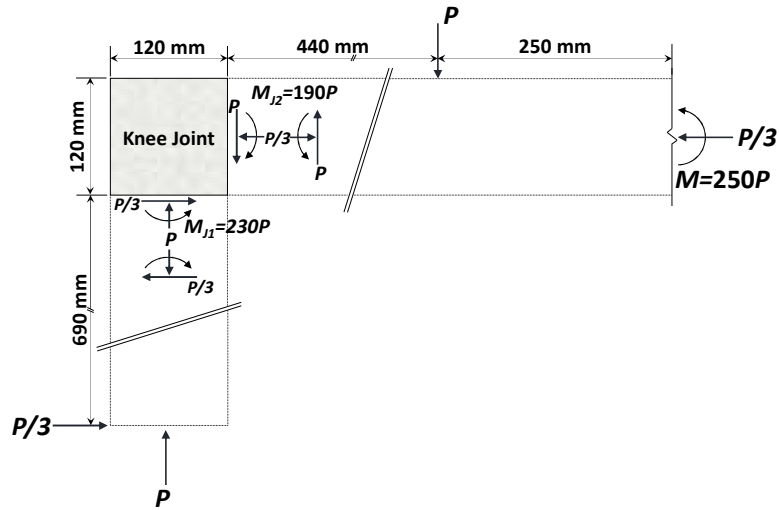


Figure B-3 Forces acting on knee joint of type Portal

B.2.2 Internal Forces for Strut-and-Tie Model

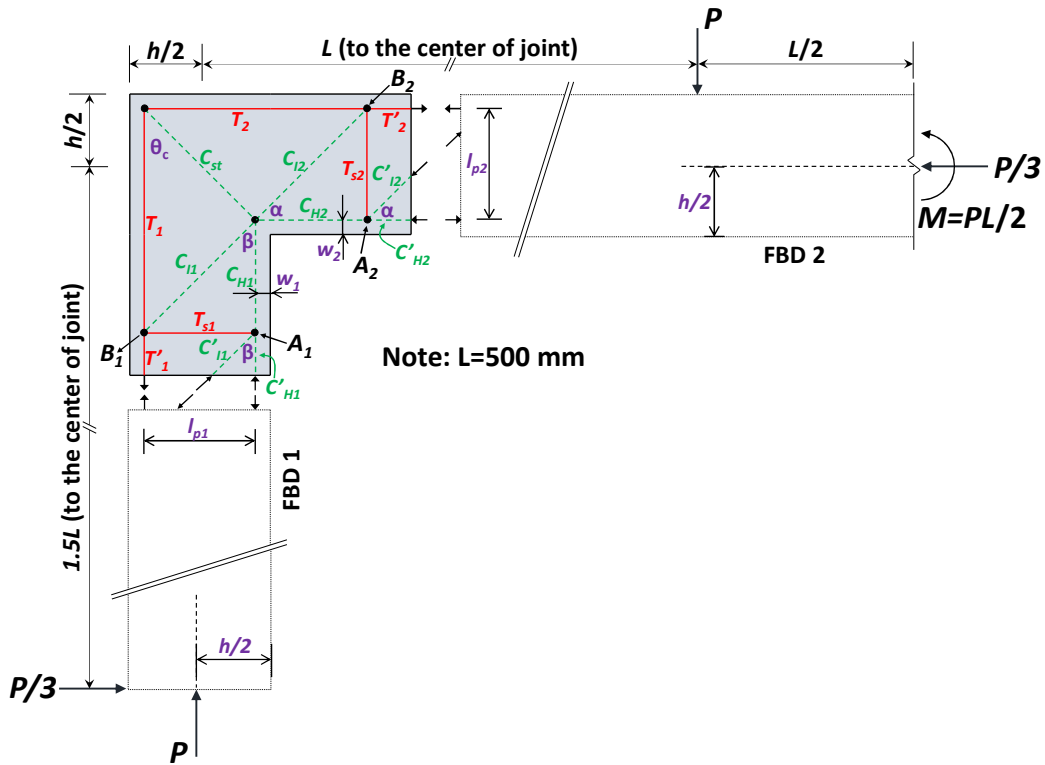


Figure B-4 Free body diagram of strut-and-tie model type(a) for Portal

1. For the free body diagram FBD 2 shown in Figure B-4, taking moment equal to zero about node A_2 and taking equilibrium of forces gives

$$T'_2 l_{p2} + \frac{1}{2} PL + \frac{1}{3} P \left(\frac{h}{2} - w_2 \right) - P \left(L - \frac{h}{2} + w_1 - l_{p2} \cot \alpha \right) = 0 \quad \text{B-16}$$

$$C'_{I2} \sin \alpha - P = 0 \quad \text{B-17}$$

$$T'_2 + \frac{P}{3} - C'_{I2} \cos \alpha - C'_{H2} = 0 \quad \text{B-18}$$

2. Taking equilibrium of the forces at node A_2 gives

$$T_{2s} - C'_{I2} = 0 \quad \text{B-19}$$

$$C_{H2} - C'_{I2} \cos \alpha - C'_{H2} = 0 \quad \text{B-20}$$

3. Again, taking equilibrium of the forces at node B_2 gives

$$T_{2s} - C_{I2} = 0 \quad \text{B-21}$$

$$T_2 - C_{I2} \cos \alpha - T'_2 = 0 \quad \text{B-22}$$

4. Solving Eq. B-16 to B-22 simultaneously obtains the internal forces T_2 , C_{I2} and C_{H2} as follows:

$$T_2 = \frac{P}{l_{p2}} \left(\frac{L}{2} - \frac{2}{3} h + w_1 + \frac{1}{3} w_2 \right) \quad \text{B-23}$$

$$C_{I2} = \frac{P}{\sin \alpha} \quad \text{B-24}$$

$$C_{H2} = \frac{P}{l_{p2}} \left(\frac{L}{2} - \frac{2}{3} h + w_1 + \frac{1}{3} w_2 - l_{p2} \cot \alpha + \frac{l_{p2}}{3} \right) \quad \text{B-25}$$

5. Resolving the forces C_{I2} and C_{H2} obtains the resultant F_b and the orientation θ_2 as follows:

$$F_b = P \sqrt{1 + \left[\frac{1}{l_{p2}} \left(\frac{l_{p2}}{3} + \frac{L}{2} - \frac{2h}{3} + w_1 + \frac{w_2}{3} \right) \right]^2} \quad \text{B-26}$$

$$\theta_2 = \cot^{-1} \left[\frac{1}{l_{p2}} \left(\frac{l_{p2}}{3} + \frac{L}{2} - \frac{2h}{3} + w_1 + \frac{w_2}{3} \right) \right] \quad \text{B-27}$$

6. Again, repeat the steps through taking equilibrium of the free body diagram FBD 1, node A_1 , and node B_1 , then T_1 , F_c , and θ_2 can be obtained

$$T_1 = \frac{P}{l_{p1}} \left(\frac{l}{2} - \frac{2}{3} h + w_1 + \frac{1}{3} w_2 \right) \quad \text{B-28}$$

$$F_c = P \sqrt{\left(\frac{1}{3}\right)^2 + \left[\frac{1}{l_{p1}} \left(l_{p1} + \frac{l}{2} - \frac{2h}{3} + w_1 + \frac{w_2}{3}\right)\right]^2} \quad \text{B-29}$$

$$\theta_1 = \cot^{-1} \left[\frac{3}{l_{p1}} \left(l_{p1} + \frac{l}{2} - \frac{2h}{3} + \frac{2w_2}{3}\right) \right] \quad \text{B-30}$$

B.2 Strut-and-Tie Model Type (b)

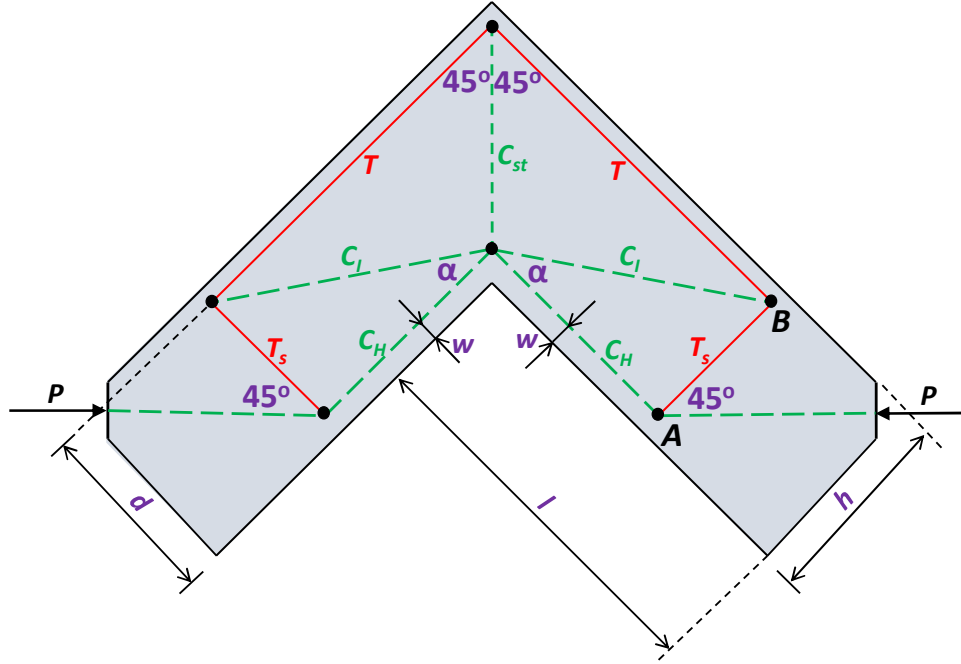


Figure B-5 Free body diagram of strut-and-tie model type(b)

1. Taking equilibrium of node A delivers

$$T_s - P \cos 45^\circ = 0 \quad \text{B-31}$$

$$C_H - P \sin 45^\circ = 0 \quad \text{B-32}$$

2. Taking equilibrium of node B delivers

$$C_I \cos \alpha - T = 0 \quad \text{B-33}$$

$$C_I \sin \alpha - T_s = 0 \quad \text{B-34}$$

where α can be expressed as

$$\alpha = \tan^{-1} \frac{d - w}{l + w - (h - w) \sin 45^\circ} \quad \text{B-35}$$

3. Therefore, the force T , C_I and C_H can be determined through solving Eq. B-31 to Eq. B-34 as

$$T = \frac{\sqrt{2}}{2} P \frac{l + w - \frac{\sqrt{2}}{2}(h - w)}{d - w} = \frac{\sqrt{2}}{2} P \cot \alpha \quad \text{B-36}$$

$$C_I = \frac{\sqrt{2}}{2} P \csc \alpha \quad \text{B-37}$$

$$C_H = \frac{\sqrt{2}}{2} P \quad \text{B-38}$$

4. Resolving the force C_I and the force C_H obtains the resultant F_b and the orientation θ_2 . The resultant F_c and the orientation θ_1 are also determined by symmetry as follows:

$$F_b = F_c = \frac{\sqrt{2}}{2} P \sqrt{1 + (1 + \cot \alpha)^2} \quad \text{B-39}$$

$$\theta_1 = \theta_2 = \tan^{-1} \frac{1}{1 + \cot \alpha} \quad \text{B-40}$$

B.3 Strut-and-Tie Model Type (c)

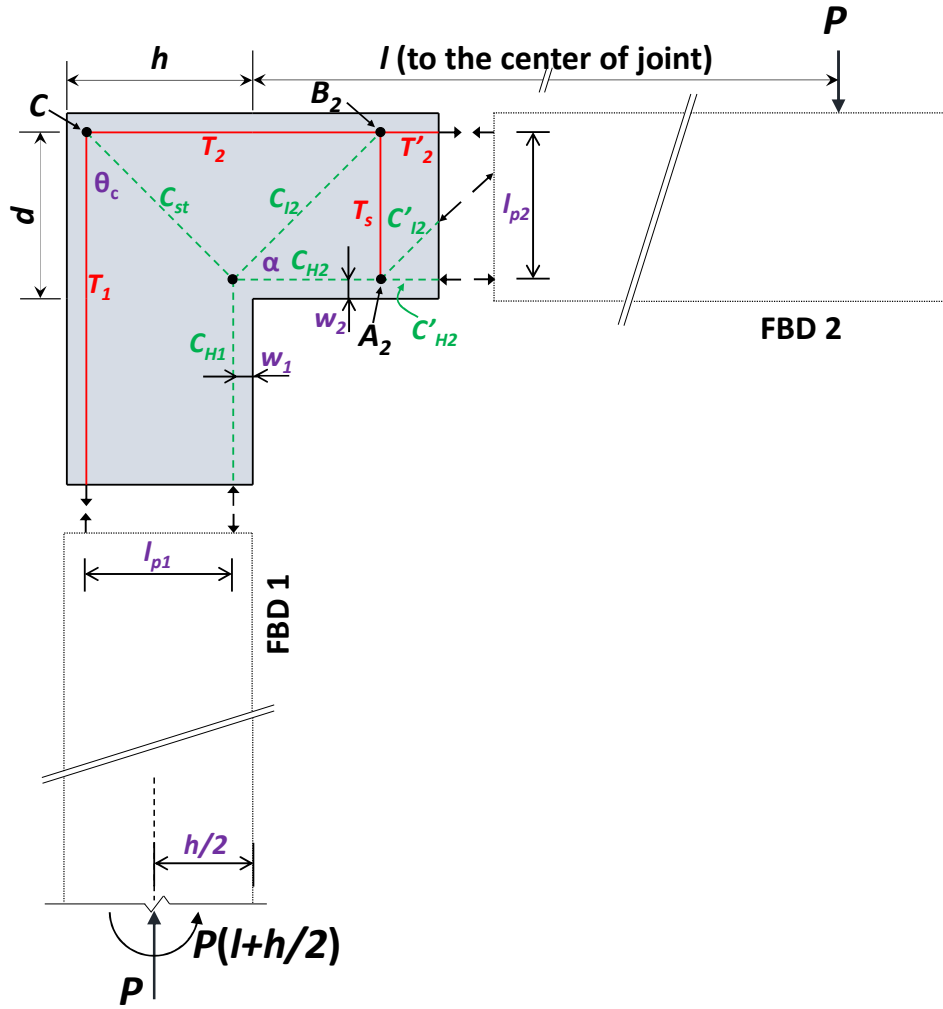


Figure B-6 Free body diagram of strut-and-tie model type(c)

1. For the free body diagram FBD 2 shown in Figure B-6, taking moment equal to zero about node A_2 and taking equilibrium of forces obtains

$$T'_2 l_{p2} - P(l + w_1 - l_{p2} \cot \alpha) = 0 \quad \text{B-41}$$

$$C'_{I2} \sin \alpha - P = 0 \quad \text{B-42}$$

$$C'_{H2} + C'_{I2} \cos \alpha - T'_2 = 0 \quad \text{B-43}$$

2. Taking equilibrium of the forces at node A_2 gives

$$T_{2s} - C'_{I2} = 0 \quad \text{B-44}$$

$$C_{H2} - C'_{I2} \cos \alpha - C'_{H2} = 0 \quad \text{B-45}$$

3. Again, taking equilibrium of the forces at node B_2 gives

$$T_{2s} - C_{I2} = 0 \quad \text{B-46}$$

$$T_2 - C_{I2} \cos \alpha - T'_2 = 0 \quad \text{B-47}$$

4. solving Eq. B-41 to B-47 simultaneously obtains the internal forces T_2 , C_{I2} and C_{H2} as follows:

$$T_2 = P \frac{l + w_1}{l_{p2}} \quad \text{B-48}$$

$$C_{I2} = \frac{P}{\sin \alpha} \quad \text{B-49}$$

$$C_{H2} = \frac{P}{l_{p2}} (l + w_1 - l_{p2} \cot \alpha) \quad \text{B-50}$$

5. Considering the equilibrium of node C and the free body diagram, T_1 and C_{H1} can be expressed as

$$T_1 = T_2 = P \frac{l + w_1}{l_{p2}} \cot \alpha \quad \text{B-51}$$

$$C_{H1} = P + T_1 = P \left(1 + \frac{l + w_1}{l_{p2}} \cot \theta_c \right) \quad \text{B-52}$$

6. Resolving the forces C_{I2} and C_{H2} obtains the resultant F_b and the orientation θ_2 as follows:

$$F_b = P \sqrt{\left(\frac{l + w_1}{d_2 - w_2} \right)^2 + 1} \quad \text{B-53}$$

$$\theta_2 = \tan^{-1} \left(\frac{d_2 - w_2}{l + w_1} \right) \quad \text{B-54}$$

7. In this case, the resultant F_c is equal to C_{H1} and the orientation is zero degree.

B.4 Strut-and-Tie Model Type (d)

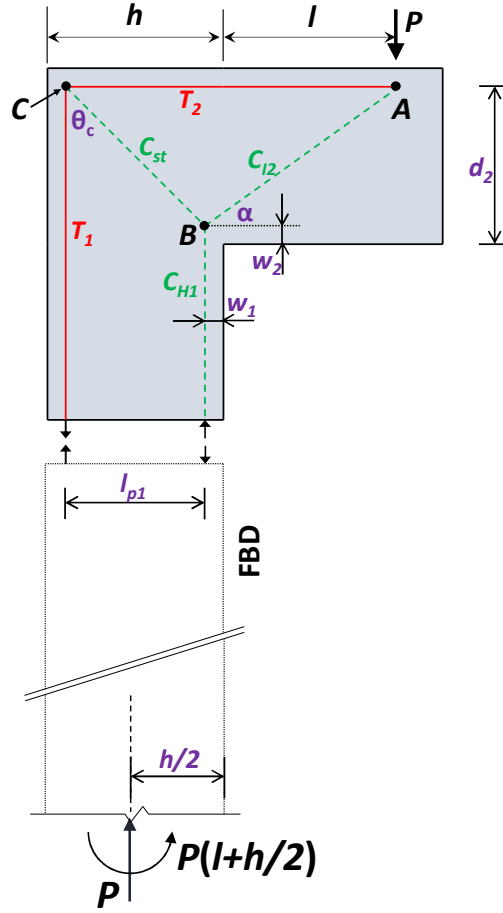


Figure B-7 Free body diagram of strut-and-tie model type(d)

1. Taking equilibrium of node A, node C, and the free body diagram FBD delivers the following equations:

$$C_{I2} \sin \alpha - P = 0 \quad \text{B-55}$$

$$T_2 - C_{I2} \cos \alpha = 0 \quad \text{B-56}$$

$$T_1 = T_2 \cot \theta_c \quad \text{B-57}$$

$$T_1 + P - C_{H1} = 0 \quad \text{B-58}$$

2. Solving Eq. B-55 to Eq. B-58 gives

$$T_2 = P \cot \alpha \quad \text{B-59}$$

$$T_1 = \cot \alpha \cot \theta_c \quad \text{B-60}$$

$$C_{I2} = P \csc \theta_c \quad \text{B-61}$$

$$C_{H1} = P(1 + \cot \alpha \cot \theta_c) \quad \text{B-62}$$

3. In this case, no resolving is needed to determine the force F_b , F_c and their orientations as

$$F_b = C_{I2} = P \csc \theta_c \quad \text{B-63}$$

$$F_c = P(1 + \cot \alpha \cot \theta_c) \quad \text{B-64}$$

$$\theta_1 = 0 \quad \text{B-65}$$

$$\theta_2 = \alpha \quad \text{B-66}$$

APPENDIX C. LIST OF EVALUATION DATABASE

For strut-and-tie model type (a) (not including specimens from Stroband et al.)

| Specimen ID | Material | | Section 1 | | | | | | | | Section 2 | | | | | | | | | |
|---------------------------|-----------------|----------------|--------------------------------|--------------|--------------|--------------|----------------|-----------------|----------------|----------------|--------------------------------|--------------|--------------|--------------|----------------|-----------------|----------------|-----------------|--------------|----------------|
| | f'_c (ksi) | f_y (ksi) | A_{ls} (in ²) | b (in.) | h (in.) | d (in.) | d_b (in.) | γ (°) | c_c (in.) | β (°) | A_{ls} (in ²) | b (in.) | h (in.) | d (in.) | d_b (in.) | γ (°) | c_c (in.) | α (°) | l (in.) | r_b (in.) |
| Specimens from this study | | | | | | | | | | | | | | | | | | | | |
| S-27-R3 | 3.45 | 69.8 | 4.74 | 18 | 24 | 21.5 | 1.00 | 45 | 2.0 | 45 | 4.74 | 16 | 24 | 21.5 | 1.00 | 45 | 2.0 | 45 | 70 | 3.9 |
| S-18-R3 | 5.17 | 67.1 | 4.74 | 16 | 24 | 21.50 | 1.00 | 45 | 2 | 45 | 4.74 | 16 | 24 | 21.50 | 1.00 | 45 | 2 | 45 | 70 | 3.3 |
| S-18-R6 | 5.02 | 67.1 | 4.74 | 16 | 24 | 21.50 | 1.00 | 45 | 2 | 45 | 4.74 | 16 | 24 | 21.50 | 1.00 | 45 | 2 | 45 | 70 | 6.5 |
| S-18-R9 | 5.08 | 67.1 | 4.74 | 16 | 24 | 21.50 | 1.00 | 45 | 2 | 45 | 4.74 | 16 | 24 | 21.50 | 1.00 | 45 | 2 | 45 | 70 | 9.8 |
| S-13-R3 | 5.15 | 66.1 | 3.6 | 16 | 24 | 21.56 | 0.88 | 45 | 2 | 45 | 3.6 | 16 | 24 | 21.56 | 0.88 | 45 | 2 | 45 | 70 | 3.3 |
| S-13-R5 | 5.28 | 66.1 | 3.6 | 16 | 24 | 21.56 | 0.88 | 45 | 2 | 45 | 3.6 | 16 | 24 | 21.56 | 0.88 | 45 | 2 | 45 | 70 | 4.7 |
| S-13-R8 | 5.35 | 66.1 | 3.6 | 16 | 24 | 21.56 | 0.88 | 45 | 2 | 45 | 3.6 | 16 | 24 | 21.56 | 0.88 | 45 | 2 | 45 | 70 | 8.1 |
| D-20-R2 | 5.04 | 69.1 | 4.8 | 16 | 24 | 20.38 | 0.88 | 45 | 2 | 45 | 4.8 | 16 | 24 | 20.38 | 0.88 | 45 | 2 | 45 | 70 | 2.7 |
| D-20-R6 | 5.14 | 69.1 | 4.8 | 16 | 24 | 20.38 | 0.88 | 45 | 2 | 45 | 4.8 | 16 | 24 | 20.38 | 0.88 | 45 | 2 | 45 | 70 | 6.5 |
| D-20-R9 | 4.99 | 69.1 | 4.8 | 16 | 24 | 20.38 | 0.88 | 45 | 2 | 45 | 4.8 | 16 | 24 | 20.38 | 0.88 | 45 | 2 | 45 | 70 | 9.9 |
| D-16-R2 | 5.38 | 62.6 | 4.4 | 16 | 24 | 20.50 | 0.75 | 45 | 2 | 45 | 4.4 | 16 | 24 | 20.50 | 0.75 | 45 | 2 | 45 | 70 | 2.4 |
| D-16-R5 | 4.94 | 62.6 | 4.4 | 16 | 24 | 20.50 | 0.75 | 45 | 2 | 45 | 4.4 | 16 | 24 | 20.50 | 0.75 | 45 | 2 | 45 | 70 | 5.9 |
| D-16-R10 | 5.29 | 62.6 | 4.4 | 16 | 24 | 20.50 | 0.75 | 45 | 2 | 45 | 4.4 | 16 | 24 | 20.50 | 0.75 | 45 | 2 | 45 | 70 | 10.2 |
| C-17-R3 | 5.29 | 66.2 | 4.74 | 16 | 24 | 21.50 | 1.00 | 45 | 1.25 | 45 | 4.74 | 16 | 24 | 21.50 | 1.00 | 45 | 1.25 | 45 | 70 | 3.3 |
| C-17-R6 | 5.33 | 66.2 | 4.74 | 16 | 24 | 21.50 | 1.00 | 45 | 1.25 | 45 | 4.74 | 16 | 24 | 21.50 | 1.00 | 45 | 1.25 | 45 | 70 | 6.5 |
| C-17-R9 | 5.04 | 66.2 | 4.74 | 16 | 24 | 21.50 | 1.00 | 45 | 1.25 | 45 | 4.74 | 16 | 24 | 21.50 | 1.00 | 45 | 1.25 | 45 | 70 | 9.2 |
| C-17-R12 | 5.16 | 66.2 | 4.74 | 16 | 24 | 21.50 | 1.00 | 45 | 1.25 | 45 | 4.74 | 16 | 24 | 21.50 | 1.00 | 45 | 1.25 | 45 | 70 | 11.5 |
| B-16-R3 | 5.2 | 66.3 | 3.16 | 16 | 24 | 21.50 | 1.00 | 45 | 2 | 45 | 3.16 | 16 | 18 | 15.50 | 1.00 | 45 | 2 | 45 | 70 | 3.2 |
| B-16-R6 | 5.2 | 66.3 | 3.16 | 16 | 24 | 21.50 | 1.00 | 45 | 2 | 45 | 3.16 | 16 | 18 | 15.50 | 1.00 | 45 | 2 | 45 | 70 | 6.5 |
| TR-S-13-R3 | 4.66 | 64.7 | 3.6 | 16 | 24 | 21.56 | 0.88 | 45 | 2 | 45 | 3.6 | 16 | 24 | 21.56 | 0.88 | 45 | 2 | 45 | 70 | 2.7 |
| TR-S-18-R3 | 4.84 | 66.3 | 4.74 | 16 | 24 | 21.50 | 1.00 | 45 | 2 | 45 | 4.74 | 16 | 24 | 21.50 | 1.00 | 45 | 2 | 45 | 70 | 3.3 |
| LS-S-13-R3 | 4.76 | 64.7 | 3.6 | 16 | 24 | 21.56 | 0.88 | 45 | 2 | 45 | 3.6 | 16 | 24 | 21.56 | 0.88 | 45 | 2 | 45 | 70 | 2.8 |
| LS-S-18-R3 | 5.04 | 66.3 | 4.74 | 16 | 24 | 21.50 | 1.00 | 45 | 2 | 45 | 4.74 | 16 | 24 | 21.50 | 1.00 | 45 | 2 | 45 | 70 | 3.3 |
| Specimens from Luo et al. | | | | | | | | | | | | | | | | | | | | |
| CJSa-1 | 2.8 | 58.5 | 1.58 | 7.87 | 19.69 | 18.27 | 0.87 | 60 | 1.43 | 45 | 2.07 | 11.81 | 15.75 | 14.33 | 0.87 | 30 | 1.43 | 50 | 31.50 | 1.7 |
| CJSa-2 | 2.6 | 63.1 | 1.77 | 7.87 | 19.69 | 18.27 | 0.87 | 60 | 1.43 | 45 | 2.23 | 11.81 | 15.75 | 14.33 | 0.87 | 30 | 1.43 | 50 | 31.50 | 8.7 |
| CJSa-5 | 2.0 | 63.1 | 1.18 | 7.87 | 19.69 | 18.27 | 0.87 | 60 | 1.43 | 45 | 1.64 | 11.81 | 15.75 | 14.33 | 0.87 | 30 | 1.43 | 50 | 31.50 | 1.7 |
| CJSa-7 | 2.3 | 58.9 | 0.79 | 7.87 | 19.69 | 18.35 | 0.71 | 60 | 1.35 | 45 | 1.29 | 11.81 | 15.75 | 14.41 | 0.71 | 30 | 1.35 | 50 | 31.50 | 1.4 |
| CJSa-8 | 2.5 | 63.1 | 1.77 | 7.87 | 19.69 | 18.27 | 0.87 | 60 | 1.43 | 45 | 2.23 | 11.81 | 15.75 | 14.33 | 0.87 | 30 | 1.43 | 50 | 31.50 | 6.1 |
| CJSa-9 | 2.4 | 59.1 | 1.18 | 7.87 | 19.69 | 18.27 | 0.87 | 60 | 1.43 | 45 | 1.67 | 11.81 | 15.75 | 14.33 | 0.87 | 30 | 1.43 | 50 | 31.50 | 1.7 |
| CJSa-10 | 2.6 | 59.1 | 1.69 | 7.87 | 19.69 | 18.27 | 0.87 | 60 | 1.43 | 45 | 2.18 | 11.81 | 15.75 | 14.33 | 0.87 | 30 | 1.43 | 50 | 31.50 | 4.3 |
| CJSa-11 | 3.1 | 59.2 | 2.21 | 7.87 | 19.69 | 18.21 | 0.98 | 60 | 1.49 | 45 | 2.70 | 11.81 | 15.75 | 14.27 | 0.98 | 30 | 1.49 | 50 | 46.06 | 4.9 |
| CJSa-12 | 2.5 | 59.2 | 2.21 | 7.87 | 19.69 | 18.21 | 0.98 | 60 | 1.49 | 45 | 2.70 | 11.81 | 15.75 | 14.27 | 0.98 | 30 | 1.49 | 50 | 46.06 | 6.9 |
| CJSa-13 | 2.4 | 59.2 | 2.21 | 7.87 | 19.69 | 18.21 | 0.98 | 60 | 1.49 | 45 | 2.70 | 11.81 | 15.75 | 14.27 | 0.98 | 30 | 1.49 | 50 | 46.06 | 9.8 |
| CJSa-14 | 3.0 | 69.3 | 2.79 | 7.87 | 19.69 | 18.15 | 1.10 | 60 | 1.55 | 45 | 3.21 | 11.81 | 15.75 | 14.21 | 1.10 | 30 | 1.55 | 50 | 46.06 | 7.7 |
| CJSa-15 | 2.6 | 69.3 | 2.86 | 7.87 | 19.69 | 18.15 | 1.10 | 60 | 1.55 | 45 | 3.29 | 11.81 | 15.75 | 14.21 | 1.10 | 30 | 1.55 | 50 | 46.06 | 11.0 |

| Specimen ID | Material | | Section 1 | | | | | | | | Section 2 | | | | | | | | | |
|-----------------------------|-----------------|----------------|--------------------------------|--------------|--------------|--------------|----------------|-----------------|----------------|----------------|--------------------------------|--------------|--------------|--------------|----------------|-----------------|----------------|-----------------|--------------|----------------|
| | f'_c (ksi) | f_y (ksi) | A_{fs} (in ²) | b (in.) | h (in.) | d (in.) | d_b (in.) | γ (°) | c_c (in.) | β (°) | A_{fs} (in ²) | b (in.) | h (in.) | d (in.) | d_b (in.) | γ (°) | c_c (in.) | α (°) | l (in.) | r_b (in.) |
| CJSa-16 | 2.5 | 53.1 | 2.85 | 7.87 | 19.69 | 18.31 | 0.79 | 60 | 1.39 | 45 | 3.40 | 11.81 | 15.75 | 14.37 | 0.79 | 30 | 1.39 | 50 | 46.06 | 5.5 |
| CJSb-2 | 3.5 | 63.1 | 1.77 | 7.87 | 19.69 | 18.27 | 0.87 | 60 | 1.43 | 45 | 2.23 | 11.81 | 15.75 | 14.33 | 0.87 | 30 | 1.43 | 50 | 31.50 | 1.7 |
| CJSa-4 | 2.9 | 63.1 | 1.77 | 7.87 | 19.69 | 18.27 | 0.87 | 60 | 1.43 | 45 | 2.36 | 11.81 | 15.75 | 14.33 | 0.87 | 30 | 1.43 | 50 | 31.50 | 8.7 |
| CJSa-6 | 2.9 | 63.1 | 1.18 | 7.87 | 19.69 | 18.27 | 0.87 | 60 | 1.43 | 45 | 1.77 | 11.81 | 15.75 | 14.33 | 0.87 | 30 | 1.43 | 50 | 31.50 | 1.7 |
| CJSb-1 | 4.5 | 63.1 | 1.77 | 7.87 | 19.69 | 18.27 | 0.87 | 60 | 1.43 | 45 | 2.36 | 11.81 | 15.75 | 14.33 | 0.87 | 30 | 1.43 | 50 | 31.50 | 1.7 |
| CJSa-17 | 2.8 | 59.1 | 1.71 | 7.87 | 19.69 | 18.27 | 0.87 | 60 | 1.43 | 45 | 2.21 | 11.81 | 15.75 | 14.33 | 0.87 | 30 | 1.43 | 50 | 31.50 | 6.1 |
| CJSa-18 | 2.6 | 59.1 | 1.71 | 7.87 | 19.69 | 18.27 | 0.87 | 60 | 1.43 | 45 | 2.21 | 11.81 | 15.75 | 14.33 | 0.87 | 30 | 1.43 | 50 | 31.50 | 6.1 |
| CJSa-19 | 2.6 | 57.9 | 1.71 | 7.87 | 19.69 | 18.27 | 0.87 | 60 | 1.43 | 45 | 2.21 | 11.81 | 15.75 | 14.33 | 0.87 | 30 | 1.43 | 50 | 46.06 | 4.3 |
| CJSa-20 | 2.9 | 60.9 | 2.28 | 7.87 | 19.69 | 18.21 | 0.98 | 60 | 1.49 | 45 | 2.74 | 11.81 | 15.75 | 14.27 | 0.98 | 30 | 1.49 | 50 | 46.06 | 4.9 |
| CJSa-21 | 2.7 | 60.9 | 2.28 | 7.87 | 19.69 | 18.21 | 0.98 | 60 | 1.49 | 45 | 2.74 | 11.81 | 15.75 | 14.27 | 0.98 | 30 | 1.49 | 50 | 46.06 | 4.9 |
| CJSa-22 | 2.4 | 58.2 | 1.71 | 7.87 | 19.69 | 18.27 | 0.87 | 60 | 1.43 | 45 | 2.18 | 11.81 | 15.75 | 14.33 | 0.87 | 30 | 1.43 | 50 | 46.06 | 4.3 |
| CJSa-23 | 3.4 | 60.3 | 2.28 | 7.87 | 19.69 | 18.21 | 0.98 | 60 | 1.49 | 45 | 3.04 | 11.81 | 15.75 | 14.27 | 0.98 | 30 | 1.49 | 50 | 46.06 | 4.9 |
| CJSa-24 | 3.5 | 53.8 | 2.86 | 7.87 | 19.69 | 18.15 | 1.10 | 60 | 1.55 | 45 | 3.57 | 11.81 | 15.75 | 14.21 | 1.10 | 30 | 1.55 | 50 | 46.06 | 6.6 |
| CJSa-25 | 2.9 | 58.7 | 2.23 | 7.87 | 19.69 | 18.21 | 0.98 | 60 | 1.49 | 45 | 3.04 | 11.81 | 15.75 | 14.27 | 0.98 | 30 | 1.49 | 50 | 46.06 | 3.0 |
| CJSa-26 | 3.2 | 60.3 | 2.28 | 7.87 | 19.69 | 18.21 | 0.98 | 60 | 1.49 | 45 | 2.74 | 11.81 | 15.75 | 14.27 | 0.98 | 30 | 1.49 | 50 | 46.06 | 4.9 |
| Specimens from Hotta et al. | | | | | | | | | | | | | | | | | | | | |
| LA-50-20 | 5.7 | 66.3 | 0.22 | 1.97 | 7.87 | 7.34 | 0.38 | 45 | 0.34 | 45 | 0.22 | 1.97 | 7.87 | 7.34 | 0.38 | 45 | 0.34 | 45 | 19.69 | 0.79 |
| LA-50-80 | 5.7 | 66.3 | 0.22 | 1.97 | 7.87 | 7.34 | 0.38 | 45 | 0.34 | 45 | 0.22 | 1.97 | 7.87 | 7.34 | 0.38 | 45 | 0.34 | 45 | 19.69 | 3.15 |
| LA-80-20 | 5.7 | 66.3 | 0.22 | 3.15 | 7.87 | 7.34 | 0.38 | 45 | 0.70 | 45 | 0.22 | 3.15 | 7.87 | 7.34 | 0.38 | 45 | 0.70 | 45 | 19.69 | 0.79 |
| LA-80-26 | 5.1 | 66.3 | 0.22 | 3.15 | 7.87 | 7.34 | 0.38 | 45 | 0.70 | 45 | 0.22 | 3.15 | 7.87 | 7.34 | 0.38 | 45 | 0.70 | 45 | 19.69 | 1.02 |
| LA-80-80 | 5.7 | 66.3 | 0.22 | 3.15 | 7.87 | 7.34 | 0.38 | 45 | 0.70 | 45 | 0.22 | 3.15 | 7.87 | 7.34 | 0.38 | 45 | 0.70 | 45 | 19.69 | 3.15 |
| Specimens from Johansson | | | | | | | | | | | | | | | | | | | | |
| RV1 | 4.3 | 68.6 | 1.87 | 23.62 | 11.81 | 10.55 | 0.63 | 45 | 0.94 | 45 | 1.87 | 23.62 | 11.81 | 10.55 | 0.63 | 45 | 0.94 | 45 | 66.93 | 1.50 |
| RV2 | 4.3 | 68.6 | 1.87 | 23.62 | 11.81 | 10.55 | 0.63 | 45 | 0.94 | 45 | 1.87 | 23.62 | 11.81 | 10.55 | 0.63 | 45 | 0.94 | 45 | 66.93 | 1.50 |
| RV3 | 4.2 | 73.1 | 0.49 | 23.62 | 11.81 | 11.02 | 0.39 | 45 | 1.06 | 45 | 0.49 | 23.62 | 11.81 | 11.02 | 0.39 | 45 | 1.06 | 45 | 66.93 | 1.50 |
| RV4 | 4.2 | 73.1 | 0.49 | 23.62 | 11.81 | 11.02 | 0.39 | 45 | 1.06 | 45 | 0.49 | 23.62 | 11.81 | 11.02 | 0.39 | 45 | 1.06 | 45 | 66.93 | 1.50 |
| RV5 | 4.4 | 82.2 | 1.55 | 23.62 | 11.81 | 10.55 | 0.63 | 45 | 0.94 | 45 | 1.55 | 23.62 | 11.81 | 10.55 | 0.63 | 45 | 0.94 | 45 | 66.93 | 1.50 |
| RV6 | 4.4 | 82.2 | 1.55 | 23.62 | 11.81 | 10.55 | 0.63 | 45 | 0.94 | 45 | 1.55 | 23.62 | 11.81 | 10.55 | 0.63 | 45 | 0.94 | 45 | 66.93 | 1.50 |
| RV7 | 4.9 | 83.1 | 0.37 | 23.62 | 11.81 | 11.02 | 0.39 | 45 | 1.06 | 45 | 0.37 | 23.62 | 11.81 | 11.02 | 0.39 | 45 | 1.06 | 45 | 66.93 | 1.50 |
| RV8 | 4.9 | 83.1 | 0.37 | 23.62 | 11.81 | 11.02 | 0.39 | 45 | 1.06 | 45 | 0.37 | 23.62 | 11.81 | 11.02 | 0.39 | 45 | 1.06 | 45 | 66.93 | 1.50 |

For strut-and-tie model type (a) for portal specimens from Stroband et al.

| Specimen ID | Material | | Sectional and strut-and-tie model parameters | | | | | | | | | |
|-------------|-----------------|----------------|--|--------------|--------------|--------------|----------------|--------------|----------------|-----------------|----------------|----------------|
| | f'_c (ksi) | f_y (ksi) | A_{ts} (in. ²) | b (in.) | h (in.) | d (in.) | d_b (in.) | L (in.) | c_c (in.) | α (°) | β (°) | r_b (in.) |
| A1 | 3.0 | 65.3 | 0.088 | 2.76 | 4.72 | 4.25 | 0.24 | 19.69 | 0.307 | 45 | 50 | 0.59 |
| A2 | 3.2 | 65.3 | 0.088 | 2.76 | 4.72 | 4.25 | 0.24 | 19.69 | 0.307 | 45 | 50 | 0.59 |
| A3 | 3.1 | 65.3 | 0.088 | 2.76 | 4.72 | 4.25 | 0.24 | 19.69 | 0.307 | 45 | 50 | 0.59 |
| A4 | 2.9 | 65.3 | 0.088 | 2.76 | 4.72 | 4.25 | 0.24 | 19.69 | 0.307 | 45 | 50 | 1.18 |
| A5 | 3.2 | 65.3 | 0.088 | 2.76 | 4.72 | 4.25 | 0.24 | 19.69 | 0.307 | 45 | 50 | 1.18 |
| A6 | 2.9 | 65.3 | 0.088 | 2.76 | 4.72 | 4.25 | 0.24 | 19.69 | 0.307 | 45 | 50 | 1.18 |
| A7 | 3.0 | 65.3 | 0.088 | 2.76 | 4.72 | 4.25 | 0.24 | 19.69 | 0.307 | 45 | 50 | 1.77 |
| A8 | 3.2 | 65.3 | 0.088 | 2.76 | 4.72 | 4.25 | 0.24 | 19.69 | 0.307 | 45 | 50 | 1.77 |
| A9 | 3.1 | 65.3 | 0.088 | 2.76 | 4.72 | 4.25 | 0.24 | 19.69 | 0.307 | 45 | 50 | 1.77 |
| A10 | 3.0 | 65.3 | 0.088 | 2.76 | 4.72 | 4.25 | 0.24 | 19.69 | 0.307 | 45 | 50 | 0.59 |
| A11 | 3.2 | 65.3 | 0.088 | 2.76 | 4.72 | 4.25 | 0.24 | 19.69 | 0.307 | 45 | 50 | 0.59 |
| A12 | 3.1 | 65.3 | 0.088 | 2.76 | 4.72 | 4.25 | 0.24 | 19.69 | 0.307 | 45 | 50 | 0.59 |
| A13 | 2.9 | 65.3 | 0.088 | 2.76 | 4.72 | 4.25 | 0.24 | 19.69 | 0.307 | 45 | 50 | 1.18 |
| A14 | 3.0 | 65.3 | 0.088 | 2.76 | 4.72 | 4.25 | 0.24 | 19.69 | 0.307 | 45 | 50 | 1.18 |
| A15 | 3.2 | 65.3 | 0.088 | 2.76 | 4.72 | 4.25 | 0.24 | 19.69 | 0.307 | 45 | 50 | 1.18 |
| A16 | 3.0 | 65.3 | 0.088 | 2.76 | 4.72 | 4.25 | 0.24 | 19.69 | 0.307 | 45 | 50 | 1.77 |
| A17 | 3.2 | 65.3 | 0.088 | 2.76 | 4.72 | 4.25 | 0.24 | 19.69 | 0.307 | 45 | 50 | 1.77 |
| A18 | 3.0 | 65.3 | 0.088 | 2.76 | 4.72 | 4.25 | 0.24 | 19.69 | 0.307 | 45 | 50 | 1.77 |
| A19 | 2.9 | 65.3 | 0.088 | 2.76 | 4.72 | 4.25 | 0.24 | 19.69 | 0.307 | 45 | 50 | 0.59 |
| A20 | 2.9 | 65.3 | 0.088 | 2.76 | 4.72 | 4.25 | 0.24 | 19.69 | 0.307 | 45 | 50 | 0.59 |
| A21 | 2.9 | 65.3 | 0.088 | 2.76 | 4.72 | 4.25 | 0.24 | 19.69 | 0.307 | 45 | 50 | 0.59 |
| A22 | 2.6 | 65.3 | 0.088 | 2.76 | 4.72 | 4.25 | 0.24 | 19.69 | 0.307 | 45 | 50 | 1.18 |
| A23 | 2.6 | 65.3 | 0.088 | 2.76 | 4.72 | 4.25 | 0.24 | 19.69 | 0.307 | 45 | 50 | 1.18 |
| A24 | 2.6 | 65.3 | 0.088 | 2.76 | 4.72 | 4.25 | 0.24 | 19.69 | 0.307 | 45 | 50 | 1.18 |
| A25 | 1.5 | 65.3 | 0.088 | 2.76 | 4.72 | 4.25 | 0.24 | 19.69 | 0.307 | 45 | 50 | 1.18 |
| A26 | 1.4 | 65.3 | 0.088 | 2.76 | 4.72 | 4.25 | 0.24 | 19.69 | 0.307 | 45 | 50 | 1.18 |
| A27 | 1.6 | 65.3 | 0.088 | 2.76 | 4.72 | 4.25 | 0.24 | 19.69 | 0.307 | 45 | 50 | 0.59 |
| A28 | 1.4 | 65.3 | 0.088 | 2.76 | 4.72 | 4.25 | 0.24 | 19.69 | 0.307 | 45 | 50 | 1.18 |
| A29 | 1.5 | 65.3 | 0.088 | 2.76 | 4.72 | 4.25 | 0.24 | 19.69 | 0.307 | 45 | 50 | 1.18 |
| A30 | 1.4 | 65.3 | 0.088 | 2.76 | 4.72 | 4.25 | 0.24 | 19.69 | 0.307 | 45 | 50 | 0.59 |
| A31 | 1.5 | 65.3 | 0.088 | 2.76 | 4.72 | 4.25 | 0.24 | 19.69 | 0.307 | 45 | 50 | 0.59 |
| A32 | 1.4 | 65.3 | 0.088 | 2.76 | 4.72 | 4.25 | 0.24 | 19.69 | 0.307 | 45 | 50 | 1.18 |
| A33 | 1.6 | 65.3 | 0.088 | 2.76 | 4.72 | 4.25 | 0.24 | 19.69 | 0.307 | 45 | 50 | 1.18 |

For strut-and-tie model type (b)

| Specimen ID | Material | | Sectional and strut-and-tie model parameters | | | | | | | |
|-------------|-----------------|----------------|--|--------------|--------------|--------------|----------------|--------------|----------------|----------------|
| | f'_c (ksi) | f_y (ksi) | A_{ts} (in.2) | b (in.) | h (in.) | d (in.) | d_b (in.) | l (in.) | c_c (in.) | r_b (in.) |
| 25-CV-25 | 3.5 | 79.8 | 2.28 | 16.73 | 33.46 | 29.33 | 0.98 | 64.96 | 3.15 | 2.95 |
| 45-CV-25 | 7.2 | 79.8 | 2.28 | 16.73 | 33.46 | 29.33 | 0.98 | 64.96 | 3.15 | 2.95 |
| 25-CV-16 | 3.3 | 76.9 | 0.94 | 16.73 | 33.46 | 30.71 | 0.63 | 64.96 | 3.15 | 1.89 |
| 45-CV-16 | 7.4 | 76.9 | 0.94 | 16.73 | 33.46 | 30.71 | 0.63 | 64.96 | 3.15 | 1.89 |
| 25-TH-25 | 2.9 | 79.8 | 2.28 | 16.73 | 33.46 | 29.33 | 0.98 | 64.96 | 3.15 | 3.94 |
| 45-TH-25 | 7.2 | 79.8 | 2.28 | 16.73 | 33.46 | 29.33 | 0.98 | 64.96 | 3.15 | 1.97 |
| 25-TH-16 | 3.5 | 77.1 | 0.94 | 16.73 | 33.46 | 30.71 | 0.63 | 64.96 | 3.15 | 2.17 |
| 45-TH-16 | 6.8 | 77.1 | 0.94 | 16.73 | 33.46 | 30.71 | 0.63 | 64.96 | 3.15 | 1.18 |

For strut-and-tie model type (c)

| Specimen ID | Material | | Sectional and strut-and-tie model parameters | | | | | | | | |
|----------------------------|-----------------|----------------|--|--------------|--------------|--------------|----------------|--------------|----------------|-----------------|----------------|
| | f'_c (ksi) | f_y (ksi) | A_{ts} (in.2) | b (in.) | h (in.) | d (in.) | d_b (in.) | l (in.) | c_c (in.) | α (°) | r_b (in.) |
| Specimens from Swann | | | | | | | | | | | |
| 103 | 3.1 | 42.8 | 0.88 | 5.98 | 5.98 | 4.86 | 0.75 | 44.02 | 0.75 | 45 | 2.24 |
| 104 | 3.1 | 42.8 | 0.88 | 5.98 | 5.98 | 4.86 | 0.75 | 44.02 | 0.75 | 45 | 2.24 |
| 106 | 3.0 | 42.8 | 0.88 | 5.98 | 5.98 | 4.86 | 0.75 | 44.02 | 0.75 | 45 | 2.24 |
| 109 | 2.7 | 42.8 | 0.88 | 5.98 | 5.98 | 4.86 | 0.75 | 44.02 | 0.75 | 45 | 2.24 |
| 110 | 3.0 | 42.8 | 0.88 | 5.98 | 5.98 | 4.86 | 0.75 | 44.02 | 0.75 | 45 | 2.24 |
| Specimens from Yuan et al. | | | | | | | | | | | |
| IA1 | 4.5 | 60 | 0.22 | 12 | 5 | 3.11 | 0.375 | 10 | 2.8125 | 45 | 1.5 |
| IA2 | 4.5 | 60 | 0.22 | 12 | 5 | 3.5 | 0.375 | 10 | 2.8125 | 45 | 1.5 |
| IA3 | 4.5 | 60 | 0.22 | 12 | 5 | 3.5 | 0.375 | 10 | 2.8125 | 45 | 1.5 |

For strut-and-tie model type (d)

| Specimen ID | Material | | Sectional and strut-and-tie model parameters | | | | | | | |
|-------------------|-----------------|----------------|--|--------------|--------------|--------------|----------------|--------------|----------------|----------------|
| | f'_c (ksi) | f_y (ksi) | A_{ts} (in.2) | b (in.) | h (in.) | d (in.) | d_b (in.) | l (in.) | c_c (in.) | r_b (in.) |
| Specimen 1 Singly | 5.4 | 65 | 7.9 | 24 | 36 | 33.25 | 1 | 36 | 1.75 | 4 |
| Specimen 1 Doubly | 5.4 | 65 | 7.9 | 24 | 36 | 33.25 | 1 | 36 | 1.75 | 4 |
| Specimen 4 Singly | 4 | 65 | 7.9 | 24 | 36 | 33.25 | 1 | 36 | 1.75 | 4 |
| Specimen 4 Doubly | 4 | 65 | 7.9 | 24 | 36 | 33.25 | 1 | 36 | 1.75 | 4 |

APPENDIX D. LIST OF NUMERICAL SPECIMENS

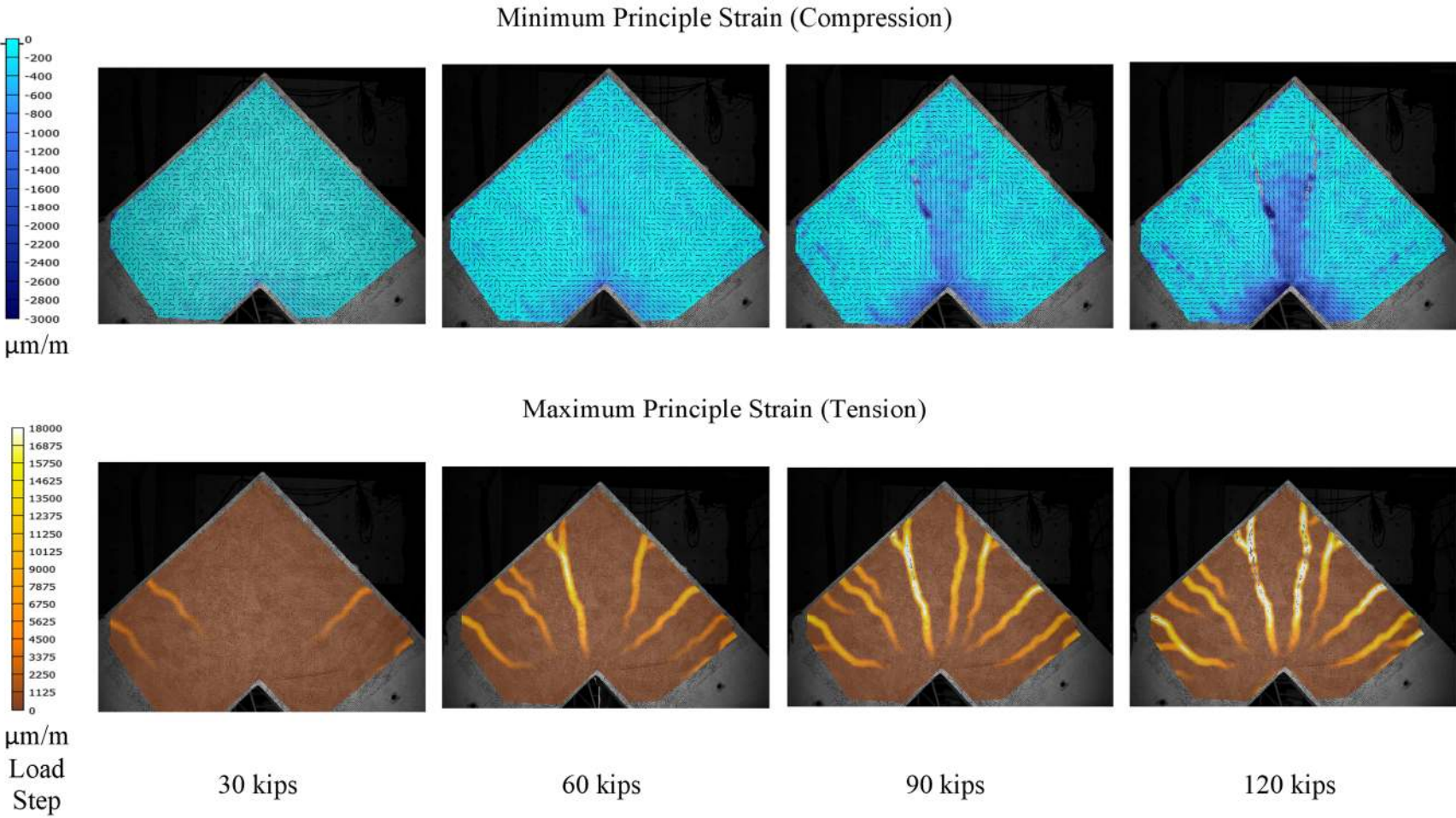
| Specimen ID | Material | | Section 1 | | | | | | | | | Section 2 | | | | | | | | | | |
|----------------|-----------------|----------------|--------------------------------|--------------|--------------|--------------|----------------|-----------------|----------------|----------------|--------------------------------|--------------|--------------|--------------|----------------|-----------------|----------------|-----------------|--------------|----------------|--|--|
| | f'_c (ksi) | f_y (ksi) | A_{ts} (in ²) | b (in.) | h (in.) | d (in.) | d_b (in.) | γ (°) | c_c (in.) | β (°) | A_{ts} (in ²) | b (in.) | h (in.) | d (in.) | d_b (in.) | γ (°) | c_c (in.) | α (°) | l (in.) | r_b (in.) | | |
| FEM-S-19-R4 | 5.0 | 67.0 | 5.00 | 16.0 | 24.0 | 21.44 | 1.13 | 45 | 2.00 | 45 | 5.00 | 16.0 | 24.0 | 21.44 | 1.13 | 45 | 2.00 | 45 | 70 | 45 | | |
| FEM-S-19-R6 | 5.0 | 67.0 | 5.00 | 16.0 | 24.0 | 21.44 | 1.13 | 45 | 2.00 | 45 | 5.00 | 16.0 | 24.0 | 21.44 | 1.13 | 45 | 2.00 | 45 | 70 | 45 | | |
| FEM-S-19-R8 | 5.0 | 67.0 | 5.00 | 16.0 | 24.0 | 21.44 | 1.13 | 45 | 2.00 | 45 | 5.00 | 16.0 | 24.0 | 21.44 | 1.13 | 45 | 2.00 | 45 | 70 | 45 | | |
| FEM-S-19-R12 | 5.0 | 67.0 | 5.00 | 16.0 | 24.0 | 21.44 | 1.13 | 45 | 2.00 | 45 | 5.00 | 16.0 | 24.0 | 21.44 | 1.13 | 45 | 2.00 | 45 | 70 | 45 | | |
| FEM-DD-21-R2 | 5.0 | 67.0 | 5.28 | 16.0 | 24.0 | 20.50 | 0.75 | 45 | 2.00 | 45 | 5.28 | 16.0 | 24.0 | 20.50 | 0.75 | 45 | 2.00 | 45 | 70 | 45 | | |
| FEM-DD-21-R5 | 5.0 | 67.0 | 5.28 | 16.0 | 24.0 | 20.50 | 0.75 | 45 | 2.00 | 45 | 5.28 | 16.0 | 24.0 | 20.50 | 0.75 | 45 | 2.00 | 45 | 70 | 45 | | |
| FEM-DD-21-R9 | 5.0 | 67.0 | 5.28 | 16.0 | 24.0 | 20.50 | 0.75 | 45 | 2.00 | 45 | 5.28 | 16.0 | 24.0 | 20.50 | 0.75 | 45 | 2.00 | 45 | 70 | 45 | | |
| FEM-DD-21-R14 | 5.0 | 67.0 | 5.28 | 16.0 | 24.0 | 20.50 | 0.75 | 45 | 2.00 | 45 | 5.28 | 16.0 | 24.0 | 20.50 | 0.75 | 45 | 2.00 | 45 | 70 | 45 | | |
| FEM-DD-26-R3 | 5.0 | 67.0 | 6.32 | 16.0 | 24.0 | 20.25 | 1.00 | 45 | 2.00 | 45 | 6.32 | 16.0 | 24.0 | 20.25 | 1.00 | 45 | 2.00 | 45 | 70 | 45 | | |
| FEM-DD-26-R7 | 5.0 | 67.0 | 6.32 | 16.0 | 24.0 | 20.25 | 1.00 | 45 | 2.00 | 45 | 6.32 | 16.0 | 24.0 | 20.25 | 1.00 | 45 | 2.00 | 45 | 70 | 45 | | |
| FEM-DD-26-R11 | 5.0 | 67.0 | 6.32 | 16.0 | 24.0 | 20.25 | 1.00 | 45 | 2.00 | 45 | 6.32 | 16.0 | 24.0 | 20.25 | 1.00 | 45 | 2.00 | 45 | 70 | 45 | | |
| FEM-DD-26-R17 | 5.0 | 67.0 | 6.32 | 16.0 | 24.0 | 20.25 | 1.00 | 45 | 2.00 | 45 | 6.32 | 16.0 | 24.0 | 20.25 | 1.00 | 45 | 2.00 | 45 | 70 | 45 | | |
| FEM-C-19-R4 | 5.0 | 67.0 | 5.00 | 16.0 | 24.0 | 21.44 | 1.13 | 45 | 1.25 | 45 | 5.00 | 16.0 | 24.0 | 21.44 | 1.13 | 45 | 1.25 | 45 | 70 | 45 | | |
| FEM-C-19-R6 | 5.0 | 67.0 | 5.00 | 16.0 | 24.0 | 21.44 | 1.13 | 45 | 1.25 | 45 | 5.00 | 16.0 | 24.0 | 21.44 | 1.13 | 45 | 1.25 | 45 | 70 | 45 | | |
| FEM-C-19-R8 | 5.0 | 67.0 | 5.00 | 16.0 | 24.0 | 21.44 | 1.13 | 45 | 1.25 | 45 | 5.00 | 16.0 | 24.0 | 21.44 | 1.13 | 45 | 1.25 | 45 | 70 | 45 | | |
| FEM-C-19-R12 | 5.0 | 67.0 | 5.00 | 16.0 | 24.0 | 21.44 | 1.13 | 45 | 1.25 | 45 | 5.00 | 16.0 | 24.0 | 21.44 | 1.13 | 45 | 1.25 | 45 | 70 | 45 | | |
| FEM-C-13-R3 | 5.2 | 66.3 | 3.60 | 16.0 | 24.0 | 21.56 | 0.88 | 45 | 1.25 | 45 | 3.60 | 16.0 | 24.0 | 21.56 | 0.88 | 45 | 1.25 | 45 | 70 | 45 | | |
| FEM-C-13-R4 | 5.3 | 66.3 | 3.60 | 16.0 | 24.0 | 21.56 | 0.88 | 45 | 1.25 | 45 | 3.60 | 16.0 | 24.0 | 21.56 | 0.88 | 45 | 1.25 | 45 | 70 | 45 | | |
| FEM-C-13-R8 | 5.4 | 66.3 | 3.60 | 16.0 | 24.0 | 21.56 | 0.88 | 45 | 1.25 | 45 | 3.60 | 16.0 | 24.0 | 21.56 | 0.88 | 45 | 1.25 | 45 | 70 | 45 | | |
| FEM-C-13-R12 | 5.4 | 66.3 | 3.60 | 16.0 | 24.0 | 21.56 | 0.88 | 45 | 1.25 | 45 | 3.60 | 16.0 | 24.0 | 21.56 | 0.88 | 45 | 1.25 | 45 | 70 | 45 | | |
| FEM-CD-21-R2 | 5.0 | 67.0 | 5.28 | 16.0 | 24.0 | 20.50 | 0.75 | 45 | 1.25 | 45 | 5.28 | 16.0 | 24.0 | 20.50 | 0.75 | 45 | 1.25 | 45 | 70 | 45 | | |
| FEM-CD-21-R6 | 5.0 | 67.0 | 5.28 | 16.0 | 24.0 | 20.50 | 0.75 | 45 | 1.25 | 45 | 5.28 | 16.0 | 24.0 | 20.50 | 0.75 | 45 | 1.25 | 45 | 70 | 45 | | |
| FEM-CD-21-R10 | 5.0 | 67.0 | 5.28 | 16.0 | 24.0 | 20.50 | 0.75 | 45 | 1.25 | 45 | 5.28 | 16.0 | 24.0 | 20.50 | 0.75 | 45 | 1.25 | 45 | 70 | 45 | | |
| FEM-CD-21-R16 | 5.0 | 67.0 | 5.28 | 16.0 | 24.0 | 20.50 | 0.75 | 45 | 1.25 | 45 | 5.28 | 16.0 | 24.0 | 20.50 | 0.75 | 45 | 1.25 | 45 | 70 | 45 | | |
| FEM-CD-26-R3 | 5.0 | 67.0 | 6.32 | 16.0 | 24.0 | 20.25 | 1.00 | 45 | 1.25 | 45 | 6.32 | 16.0 | 24.0 | 20.25 | 1.00 | 45 | 1.25 | 45 | 70 | 45 | | |
| FEM-CD-26-R7 | 5.0 | 67.0 | 6.32 | 16.0 | 24.0 | 20.25 | 1.00 | 45 | 1.25 | 45 | 6.32 | 16.0 | 24.0 | 20.25 | 1.00 | 45 | 1.25 | 45 | 70 | 45 | | |
| FEM-CD-26-R10 | 5.0 | 67.0 | 6.32 | 16.0 | 24.0 | 20.25 | 1.00 | 45 | 1.25 | 45 | 6.32 | 16.0 | 24.0 | 20.25 | 1.00 | 45 | 1.25 | 45 | 70 | 45 | | |
| FEM-CD-26-R17 | 4.8 | 66.2 | 4.74 | 16.0 | 24.0 | 21.50 | 1.00 | 45 | 2.00 | 45 | 4.74 | 16.0 | 24.0 | 21.50 | 1.00 | 45 | 2.00 | 45 | 70 | 45 | | |
| FEM-TR-18-R6 | 4.8 | 66.2 | 4.74 | 16.0 | 24.0 | 21.50 | 1.00 | 45 | 2.00 | 45 | 4.74 | 16.0 | 24.0 | 21.50 | 1.00 | 45 | 2.00 | 45 | 70 | 45 | | |
| FEM-TR-18-R9 | 4.8 | 66.2 | 4.74 | 16.0 | 24.0 | 21.50 | 1.00 | 45 | 2.00 | 45 | 4.74 | 16.0 | 24.0 | 21.50 | 1.00 | 45 | 2.00 | 45 | 70 | 45 | | |
| FEM-TR-18-R14 | 4.7 | 64.7 | 3.60 | 16.0 | 24.0 | 21.56 | 0.88 | 45 | 2.00 | 45 | 3.60 | 16.0 | 24.0 | 21.56 | 0.88 | 45 | 2.00 | 45 | 70 | 45 | | |
| FEM-TR-13-R4 | 4.7 | 64.7 | 3.60 | 16.0 | 24.0 | 21.56 | 0.88 | 45 | 2.00 | 45 | 3.60 | 16.0 | 24.0 | 21.56 | 0.88 | 45 | 2.00 | 45 | 70 | 45 | | |
| FEM-TR-13-R8 | 4.7 | 64.7 | 3.60 | 16.0 | 24.0 | 21.56 | 0.88 | 45 | 2.00 | 45 | 3.60 | 16.0 | 24.0 | 21.56 | 0.88 | 45 | 2.00 | 45 | 70 | 45 | | |
| FEM-TR-13-R14 | 5.0 | 67.0 | 5.00 | 16.0 | 24.0 | 21.44 | 1.13 | 45 | 2.00 | 45 | 5.00 | 16.0 | 24.0 | 21.44 | 1.13 | 45 | 2.00 | 45 | 70 | 45 | | |
| FEM-TR-19-R4 | 5.0 | 67.0 | 5.00 | 16.0 | 24.0 | 21.44 | 1.13 | 45 | 2.00 | 45 | 5.00 | 16.0 | 24.0 | 21.44 | 1.13 | 45 | 2.00 | 45 | 70 | 45 | | |
| FEM-TR-19-R6 | 5.0 | 67.0 | 5.00 | 16.0 | 24.0 | 21.44 | 1.13 | 45 | 2.00 | 45 | 5.00 | 16.0 | 24.0 | 21.44 | 1.13 | 45 | 2.00 | 45 | 70 | 45 | | |
| FEM-TR-19-R8 | 5.0 | 67.0 | 5.00 | 16.0 | 24.0 | 21.44 | 1.13 | 45 | 2.00 | 45 | 5.00 | 16.0 | 24.0 | 21.44 | 1.13 | 45 | 2.00 | 45 | 70 | 45 | | |
| FEM-TR-19-R12 | 5.0 | 67.0 | 5.00 | 16.0 | 24.0 | 21.44 | 1.13 | 45 | 2.00 | 45 | 5.00 | 16.0 | 24.0 | 21.44 | 1.13 | 45 | 2.00 | 45 | 70 | 45 | | |
| FEM-B-17-R3-30 | 5.0 | 67.0 | 3.16 | 16.0 | 29.0 | 21.44 | 1.00 | 45 | 2.00 | 45 | 3.16 | 16.0 | 18.0 | 15.50 | 1.00 | 45 | 2.00 | 45 | 70 | 45 | | |

| Specimen ID | Material | | Section 1 | | | | | | | | | Section 2 | | | | | | | | |
|------------------|-----------------|----------------|--------------------------------|--------------|--------------|--------------|----------------|-----------------|----------------|----------------|--------------------------------|--------------|--------------|--------------|----------------|-----------------|----------------|-----------------|--------------|----------------|
| | f'_c (ksi) | f_y (ksi) | A_{tr} (in ²) | b (in.) | h (in.) | d (in.) | d_b (in.) | γ (°) | c_c (in.) | β (°) | A_{tr} (in ²) | b (in.) | h (in.) | d (in.) | d_b (in.) | γ (°) | c_c (in.) | α (°) | l (in.) | r_b (in.) |
| FEM-B-17-R5-30 | 5.0 | 67.0 | 3.16 | 16.0 | 29.0 | 21.44 | 1.00 | 45 | 2.00 | 45 | 3.16 | 16.0 | 18.0 | 15.50 | 1.00 | 45 | 2.00 | 45 | 70 | 45 |
| FEM-B-17-R7-30 | 5.0 | 67.0 | 3.16 | 16.0 | 29.0 | 21.44 | 1.00 | 45 | 2.00 | 45 | 3.16 | 16.0 | 18.0 | 15.50 | 1.00 | 45 | 2.00 | 45 | 70 | 45 |
| FEM-B-17-R10-30 | 5.0 | 67.0 | 3.16 | 16.0 | 29.0 | 21.44 | 1.00 | 45 | 2.00 | 45 | 3.16 | 16.0 | 18.0 | 15.50 | 1.00 | 45 | 2.00 | 45 | 70 | 45 |
| FEM-B-17-R3-35 | 5.0 | 67.0 | 3.16 | 16.0 | 25.0 | 20.50 | 1.00 | 45 | 2.00 | 45 | 3.16 | 16.0 | 18.0 | 15.50 | 1.00 | 45 | 2.00 | 45 | 70 | 45 |
| FEM-B-17-R4-35 | 5.0 | 67.0 | 3.16 | 16.0 | 25.0 | 20.50 | 1.00 | 45 | 2.00 | 45 | 3.16 | 16.0 | 18.0 | 15.50 | 1.00 | 45 | 2.00 | 45 | 70 | 45 |
| FEM-B-17-R6-35 | 5.0 | 67.0 | 3.16 | 16.0 | 25.0 | 20.50 | 1.00 | 45 | 2.00 | 45 | 3.16 | 16.0 | 18.0 | 15.50 | 1.00 | 45 | 2.00 | 45 | 70 | 45 |
| FEM-B-17-R9-35 | 5.0 | 67.0 | 3.16 | 16.0 | 25.0 | 20.50 | 1.00 | 45 | 2.00 | 45 | 3.16 | 16.0 | 18.0 | 15.50 | 1.00 | 45 | 2.00 | 45 | 70 | 45 |
| FEM-B-17-R3-40 | 5.0 | 67.0 | 3.16 | 16.0 | 21.0 | 20.25 | 1.00 | 45 | 2.00 | 45 | 3.16 | 16.0 | 18.0 | 15.50 | 1.00 | 45 | 2.00 | 45 | 70 | 45 |
| FEM-B-17-R4-40 | 5.0 | 67.0 | 3.16 | 16.0 | 21.0 | 20.25 | 1.00 | 45 | 2.00 | 45 | 3.16 | 16.0 | 18.0 | 15.50 | 1.00 | 45 | 2.00 | 45 | 70 | 45 |
| FEM-B-17-R6-40 | 5.0 | 67.0 | 3.16 | 16.0 | 21.0 | 20.25 | 1.00 | 45 | 2.00 | 45 | 3.16 | 16.0 | 18.0 | 15.50 | 1.00 | 45 | 2.00 | 45 | 70 | 45 |
| FEM-B-17-R9-40 | 5.0 | 67.0 | 3.16 | 16.0 | 21.0 | 20.25 | 1.00 | 45 | 2.00 | 45 | 3.16 | 16.0 | 18.0 | 15.50 | 1.00 | 45 | 2.00 | 45 | 70 | 45 |
| FEM-B-17-R3-45 | 5.0 | 67.0 | 3.16 | 16.0 | 18.0 | 21.44 | 1.00 | 45 | 2.00 | 45 | 3.16 | 16.0 | 18.0 | 15.50 | 1.00 | 45 | 2.00 | 45 | 70 | 45 |
| FEM-B-17-R6-45 | 5.0 | 67.0 | 3.16 | 16.0 | 18.0 | 21.44 | 1.00 | 45 | 2.00 | 45 | 3.16 | 16.0 | 18.0 | 15.50 | 1.00 | 45 | 2.00 | 45 | 70 | 45 |
| FEM-B-17-R9-45 | 5.0 | 67.0 | 3.16 | 16.0 | 18.0 | 21.44 | 1.00 | 45 | 2.00 | 45 | 3.16 | 16.0 | 18.0 | 15.50 | 1.00 | 45 | 2.00 | 45 | 70 | 45 |
| FEM-B-17-R12-45 | 5.0 | 67.0 | 3.16 | 16.0 | 18.0 | 21.44 | 1.00 | 45 | 2.00 | 45 | 3.16 | 16.0 | 18.0 | 15.50 | 1.00 | 45 | 2.00 | 45 | 70 | 45 |
| FEM-BD-18-R2-30 | 5.0 | 67.0 | 3.52 | 16.0 | 29.0 | 21.56 | 0.75 | 45 | 2.00 | 45 | 3.52 | 16.0 | 18.0 | 15.63 | 0.75 | 45 | 2.00 | 45 | 70 | 45 |
| FEM-BD-18-R6-30 | 5.0 | 67.0 | 3.52 | 16.0 | 29.0 | 21.56 | 0.75 | 45 | 2.00 | 45 | 3.52 | 16.0 | 18.0 | 15.63 | 0.75 | 45 | 2.00 | 45 | 70 | 45 |
| FEM-BD-18-R10-30 | 5.0 | 67.0 | 3.52 | 16.0 | 29.0 | 21.56 | 0.75 | 45 | 2.00 | 45 | 3.52 | 16.0 | 18.0 | 15.63 | 0.75 | 45 | 2.00 | 45 | 70 | 45 |
| FEM-BD-18-R16-30 | 5.0 | 67.0 | 3.52 | 16.0 | 29.0 | 21.56 | 0.75 | 45 | 2.00 | 45 | 3.52 | 16.0 | 18.0 | 15.63 | 0.75 | 45 | 2.00 | 45 | 70 | 45 |
| FEM-BD-18-R2-35 | 5.0 | 67.0 | 3.52 | 16.0 | 25.0 | 20.50 | 0.75 | 45 | 2.00 | 45 | 3.52 | 16.0 | 18.0 | 15.63 | 0.75 | 45 | 2.00 | 45 | 70 | 45 |
| FEM-BD-18-R5-35 | 5.0 | 67.0 | 3.52 | 16.0 | 25.0 | 20.50 | 0.75 | 45 | 2.00 | 45 | 3.52 | 16.0 | 18.0 | 15.63 | 0.75 | 45 | 2.00 | 45 | 70 | 45 |
| FEM-BD-18-R9-35 | 5.0 | 67.0 | 3.52 | 16.0 | 25.0 | 20.50 | 0.75 | 45 | 2.00 | 45 | 3.52 | 16.0 | 18.0 | 15.63 | 0.75 | 45 | 2.00 | 45 | 70 | 45 |
| FEM-BD-18-R13-35 | 5.0 | 67.0 | 3.52 | 16.0 | 25.0 | 20.50 | 0.75 | 45 | 2.00 | 45 | 3.52 | 16.0 | 18.0 | 15.63 | 0.75 | 45 | 2.00 | 45 | 70 | 45 |
| FEM-BD-18-R2-40 | 5.0 | 67.0 | 3.52 | 16.0 | 21.0 | 20.25 | 0.75 | 45 | 2.00 | 45 | 3.52 | 16.0 | 18.0 | 15.63 | 0.75 | 45 | 2.00 | 45 | 70 | 45 |
| FEM-BD-18-R5-40 | 5.0 | 67.0 | 3.52 | 16.0 | 21.0 | 20.25 | 0.75 | 45 | 2.00 | 45 | 3.52 | 16.0 | 18.0 | 15.63 | 0.75 | 45 | 2.00 | 45 | 70 | 45 |
| FEM-BD-18-R8-40 | 5.0 | 67.0 | 3.52 | 16.0 | 21.0 | 20.25 | 0.75 | 45 | 2.00 | 45 | 3.52 | 16.0 | 18.0 | 15.63 | 0.75 | 45 | 2.00 | 45 | 70 | 45 |
| FEM-BD-18-R12-40 | 5.0 | 67.0 | 3.52 | 16.0 | 21.0 | 21.50 | 0.75 | 45 | 2.00 | 45 | 3.52 | 16.0 | 18.0 | 15.63 | 0.75 | 45 | 2.00 | 45 | 70 | 45 |
| FEM-BD-18-R2-45 | 5.0 | 67.0 | 3.52 | 16.0 | 18.0 | 21.50 | 0.75 | 45 | 2.00 | 45 | 3.52 | 16.0 | 18.0 | 15.63 | 0.75 | 45 | 2.00 | 45 | 70 | 45 |
| FEM-BD-18-R5-45 | 5.0 | 67.0 | 3.52 | 16.0 | 18.0 | 21.50 | 0.75 | 45 | 2.00 | 45 | 3.52 | 16.0 | 18.0 | 15.63 | 0.75 | 45 | 2.00 | 45 | 70 | 45 |
| FEM-BD-18-R8-45 | 5.0 | 67.0 | 3.52 | 16.0 | 18.0 | 21.56 | 0.75 | 45 | 2.00 | 45 | 3.52 | 16.0 | 18.0 | 15.63 | 0.75 | 45 | 2.00 | 45 | 70 | 45 |
| FEM-BD-18-R12-45 | 5.0 | 67.0 | 3.52 | 16.0 | 18.0 | 21.56 | 0.75 | 45 | 2.00 | 45 | 3.52 | 16.0 | 18.0 | 15.63 | 0.75 | 45 | 2.00 | 45 | 70 | 45 |

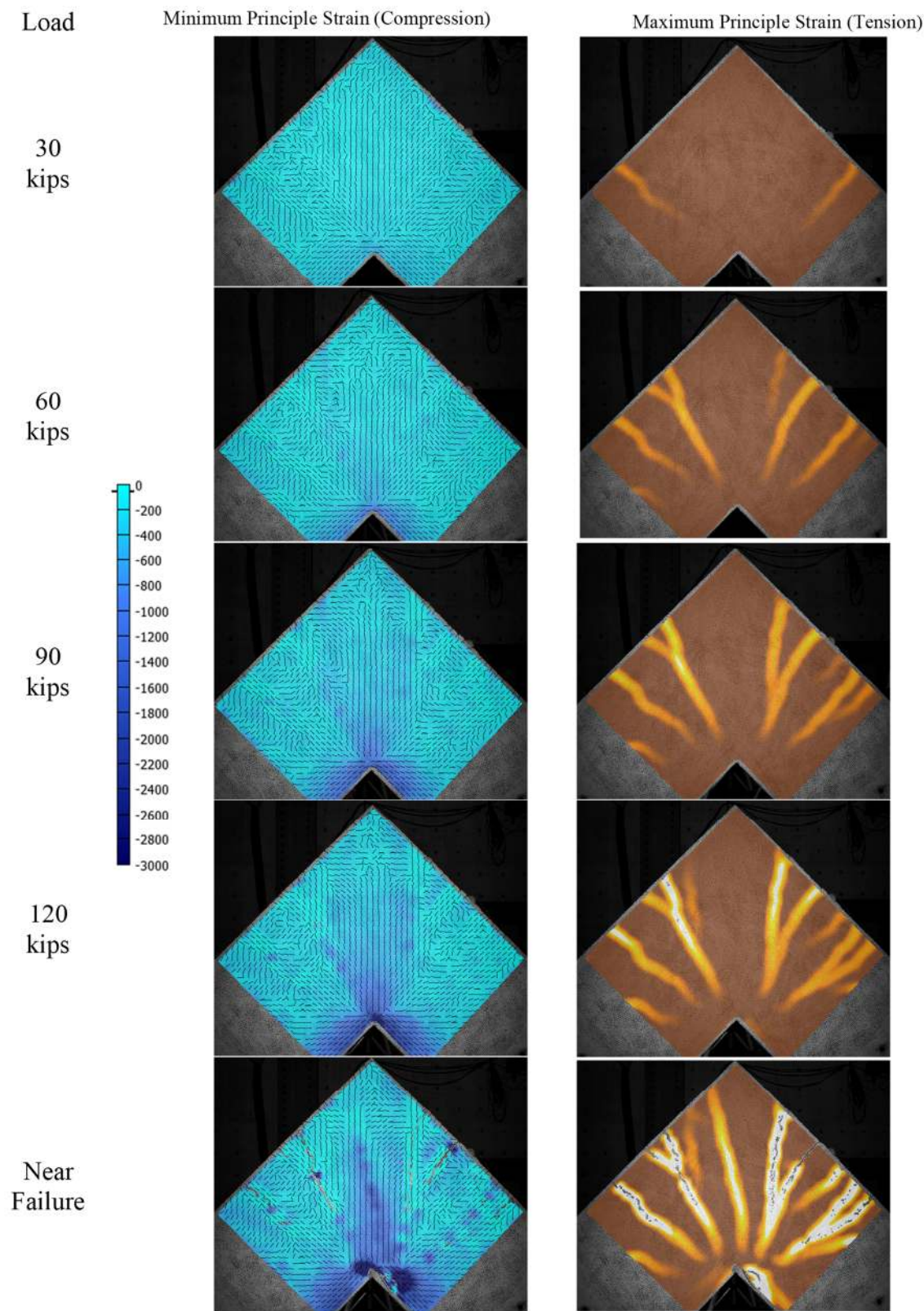
APPENDIX E. FULL-FIELD STRAIN MAP FROM DIGITAL IMAGE CORRELATION
MEASUREMENT

Specimen D-16-R2

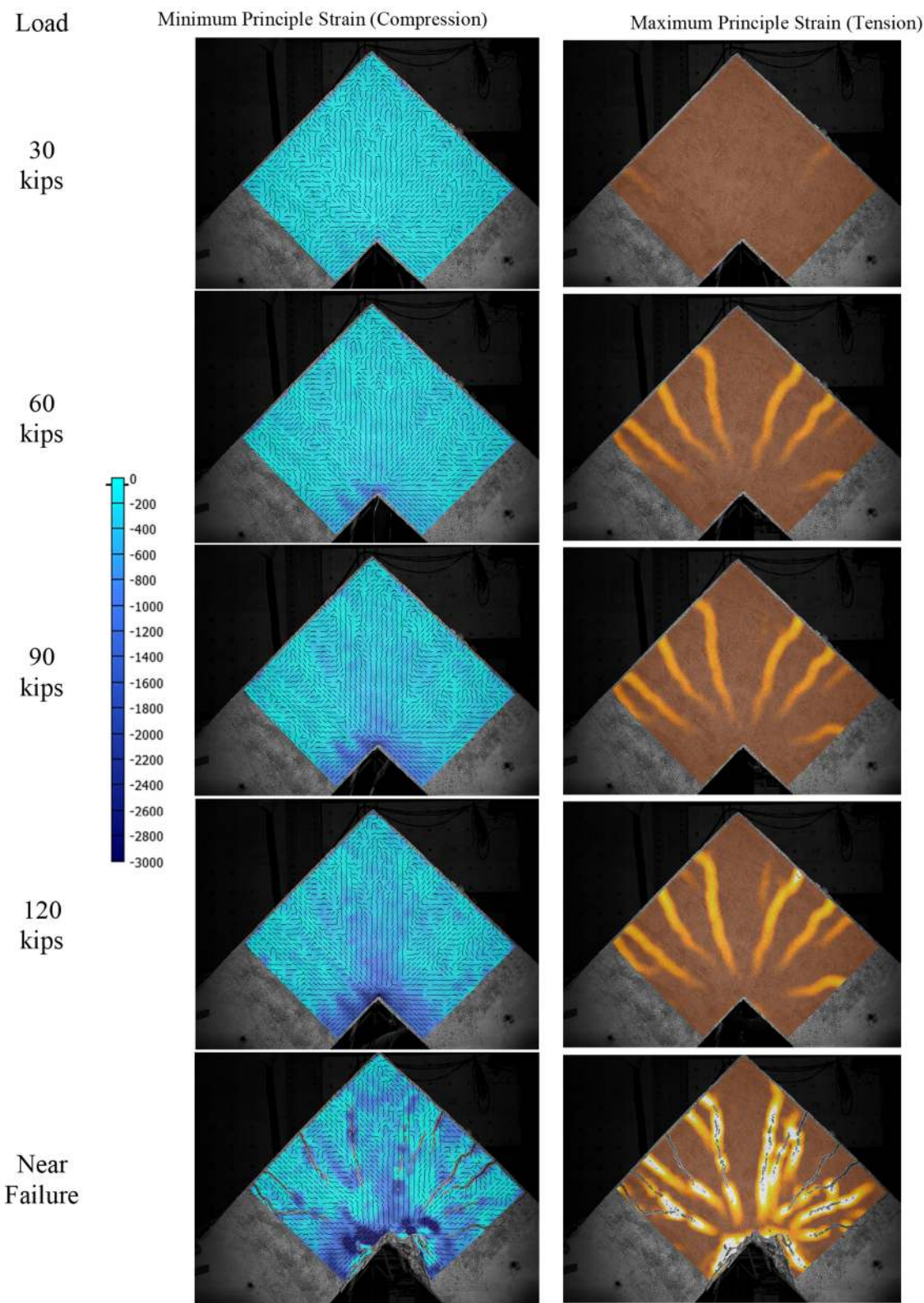
315



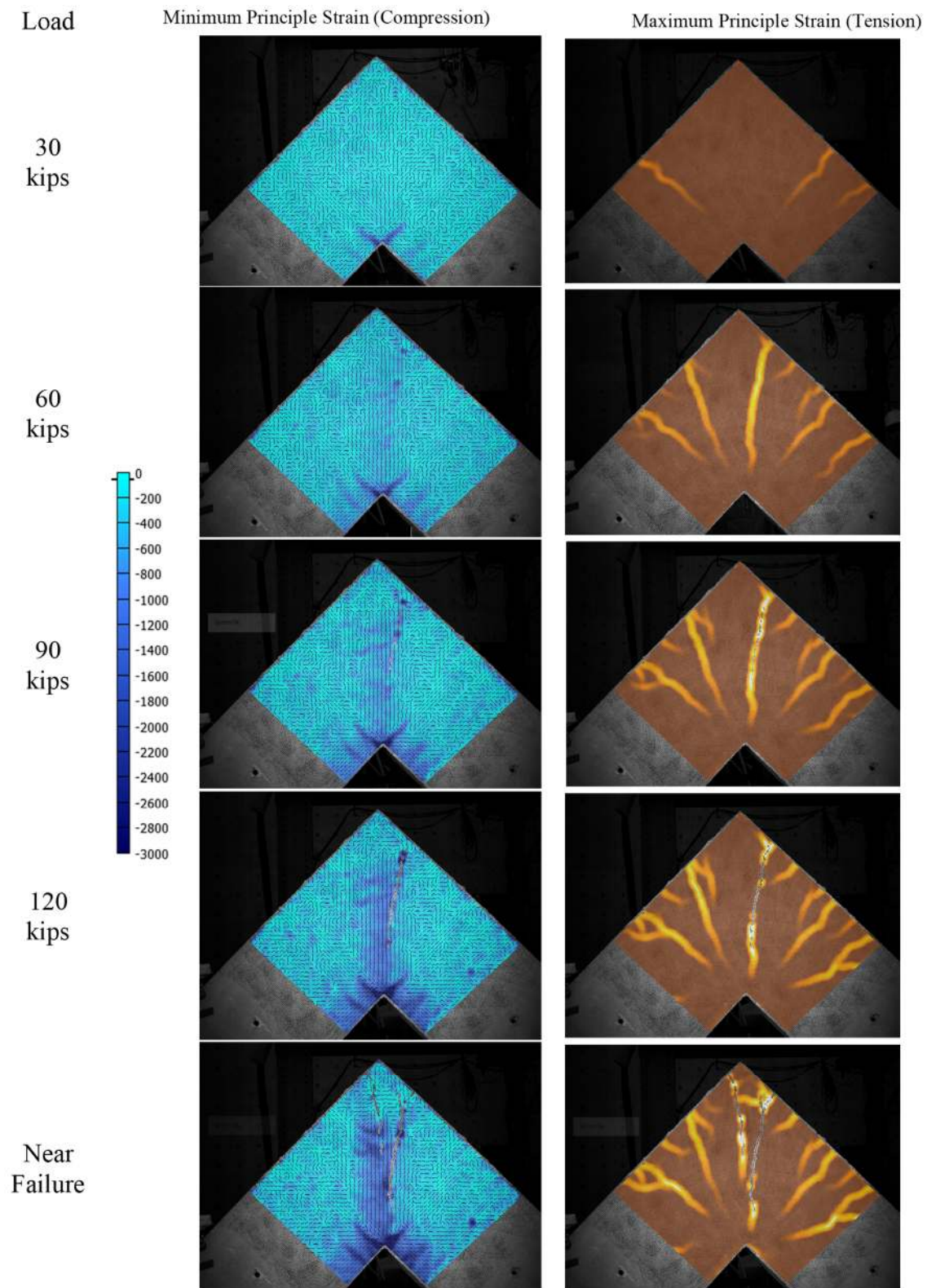
Specimen D-16-R5



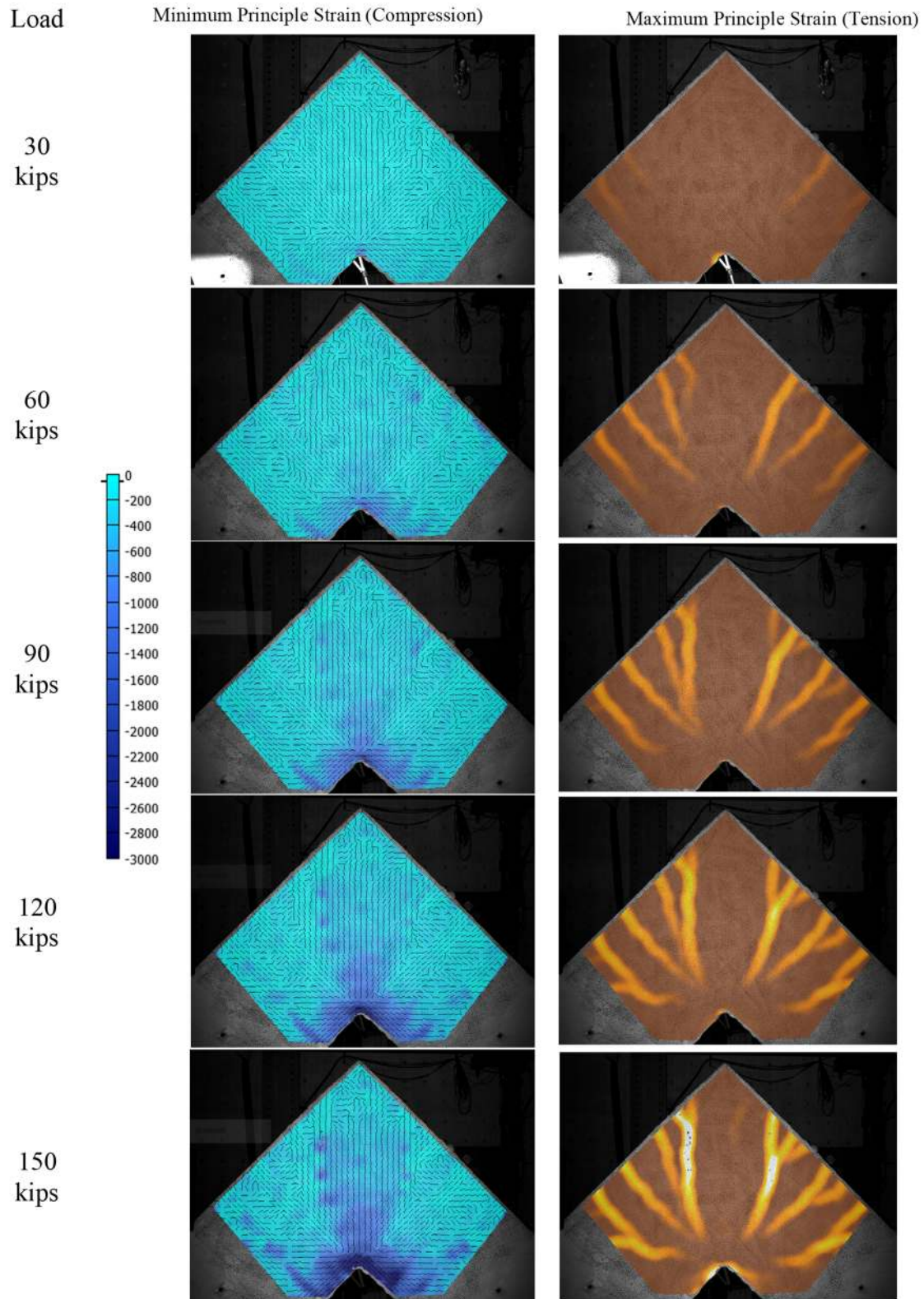
Specimen D-16-R10



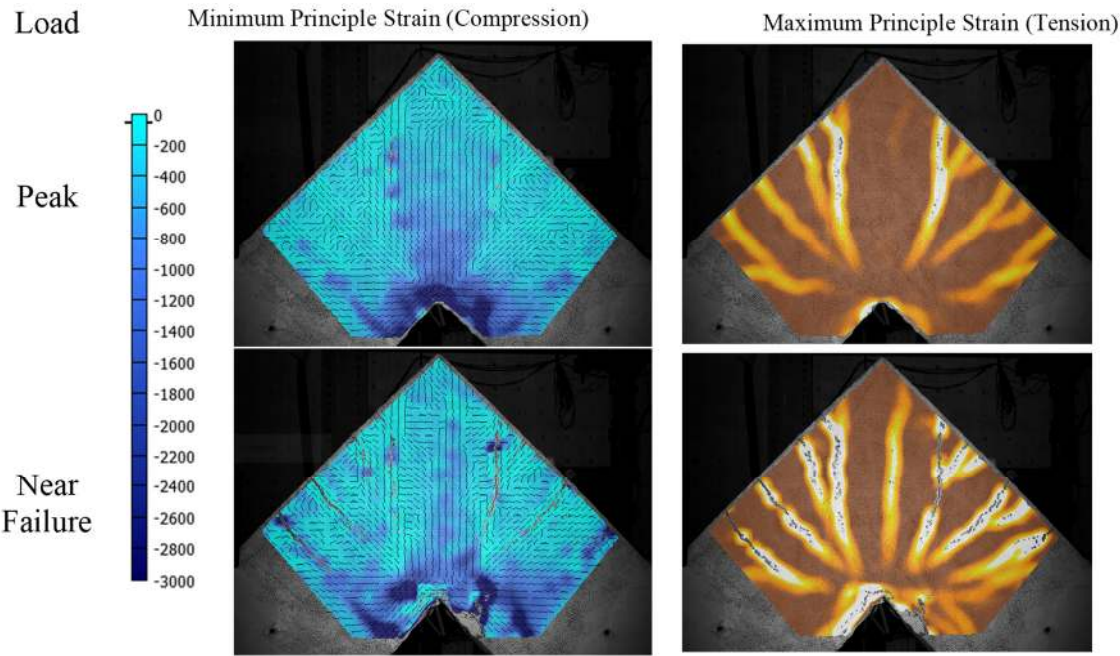
Specimen C-17-R3



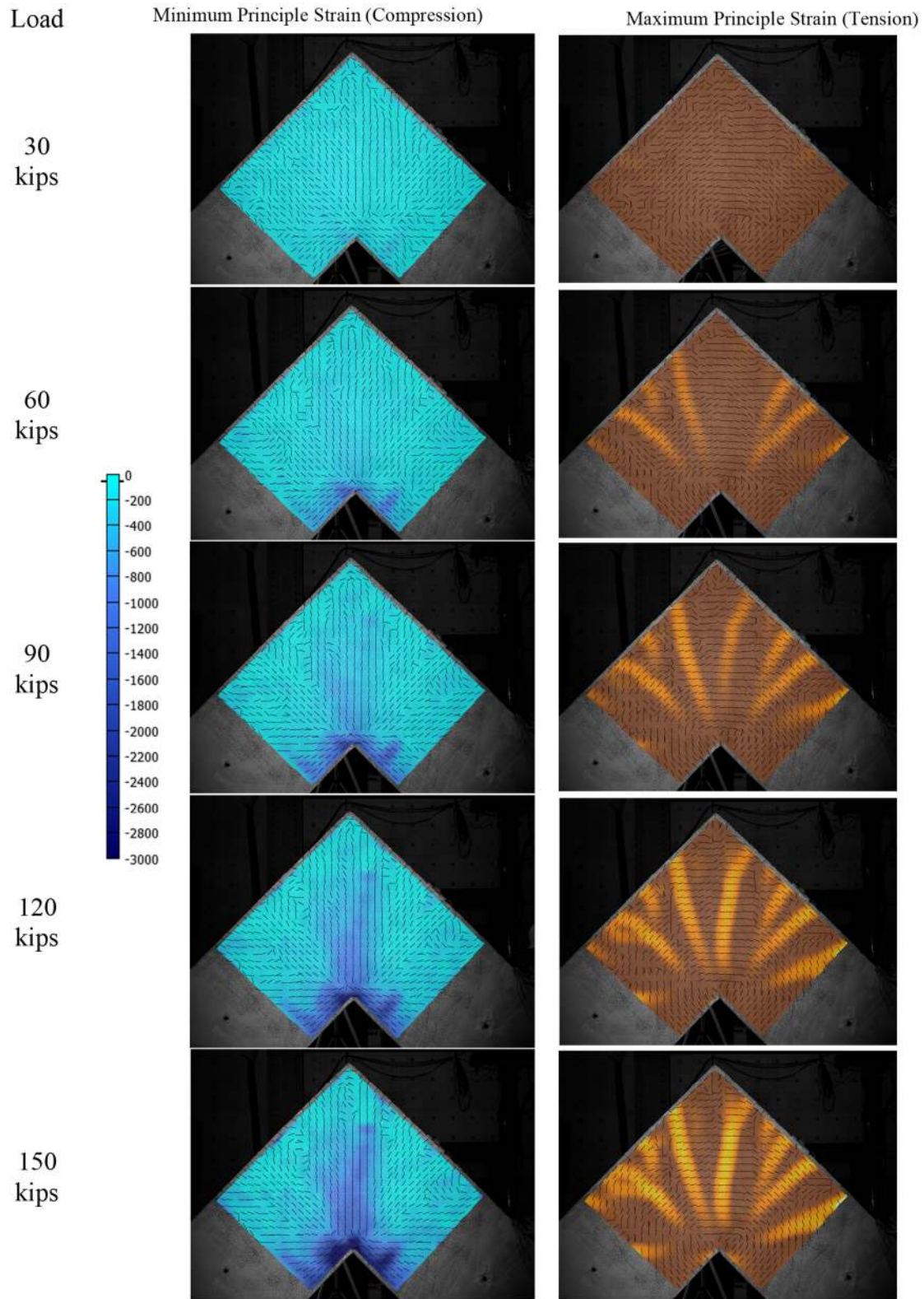
Specimen C-17-R6



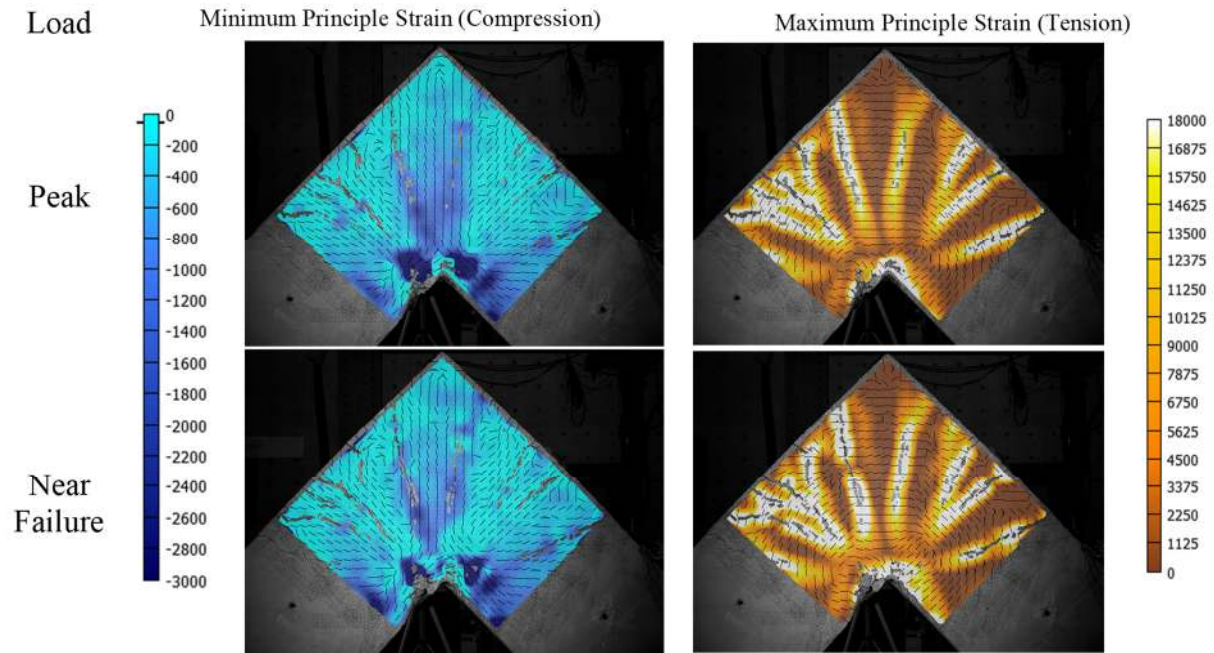
Specimen C-17-R6 (Continued)



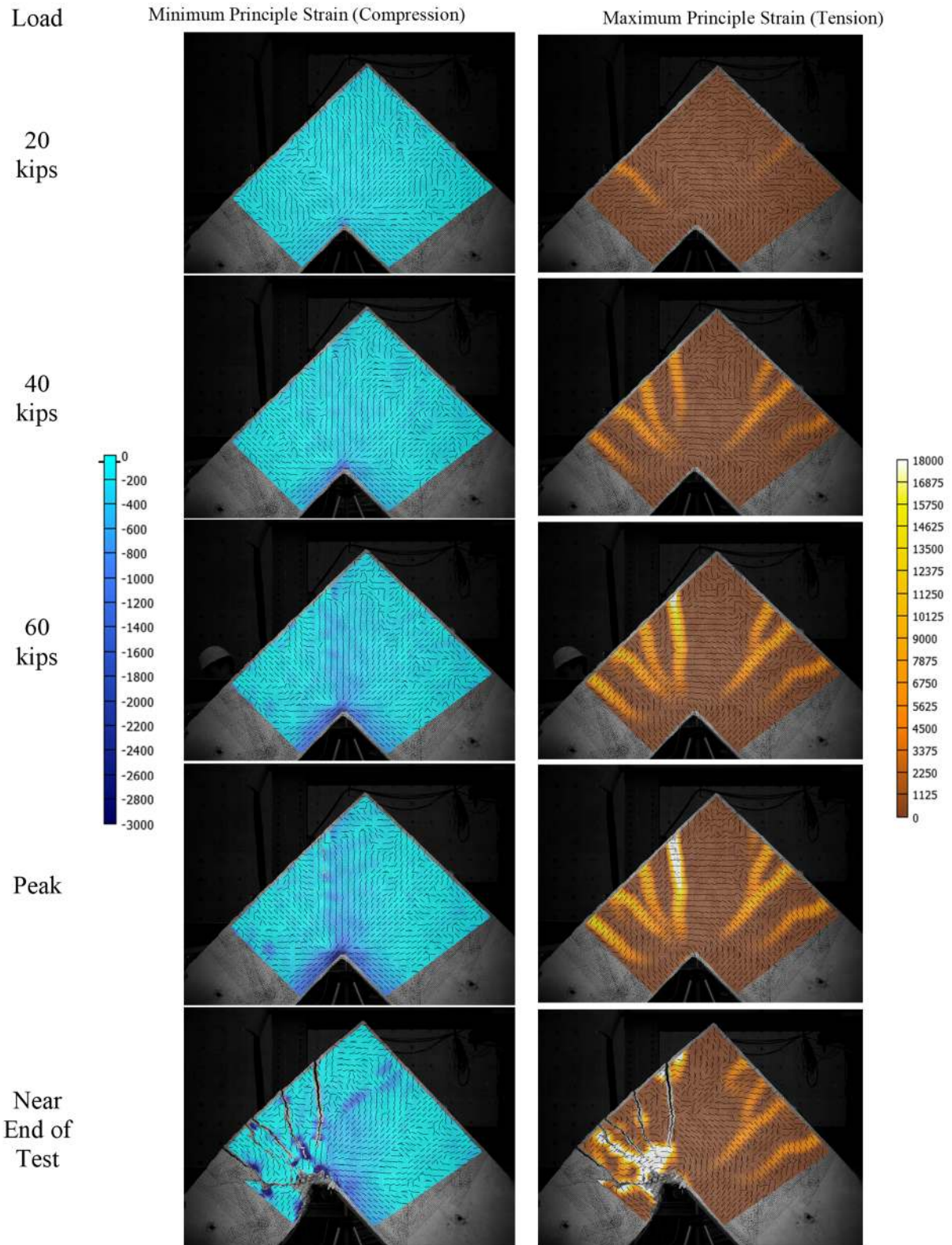
Specimen C-17-R9



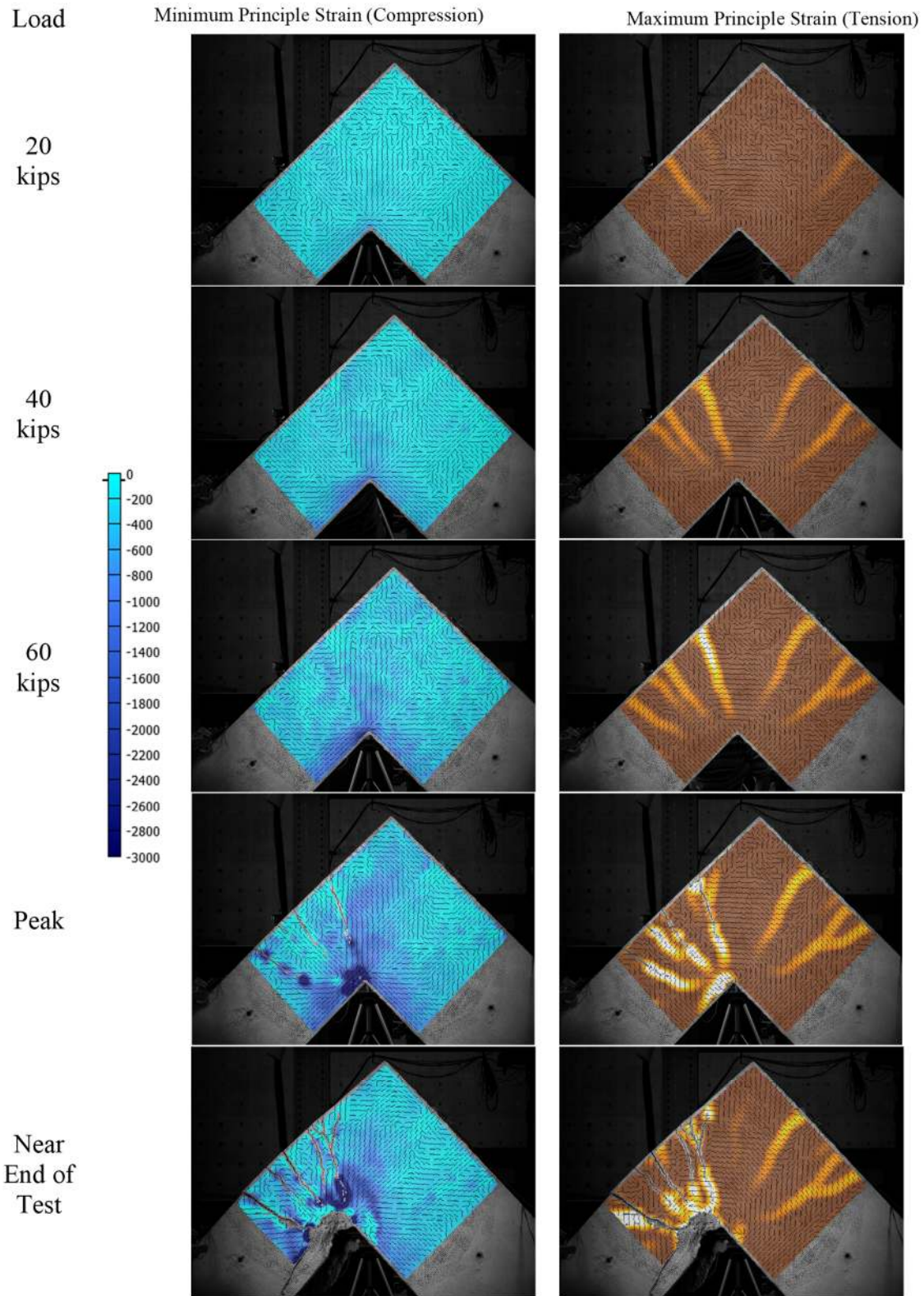
Specimen C-17-R9 (Continued)



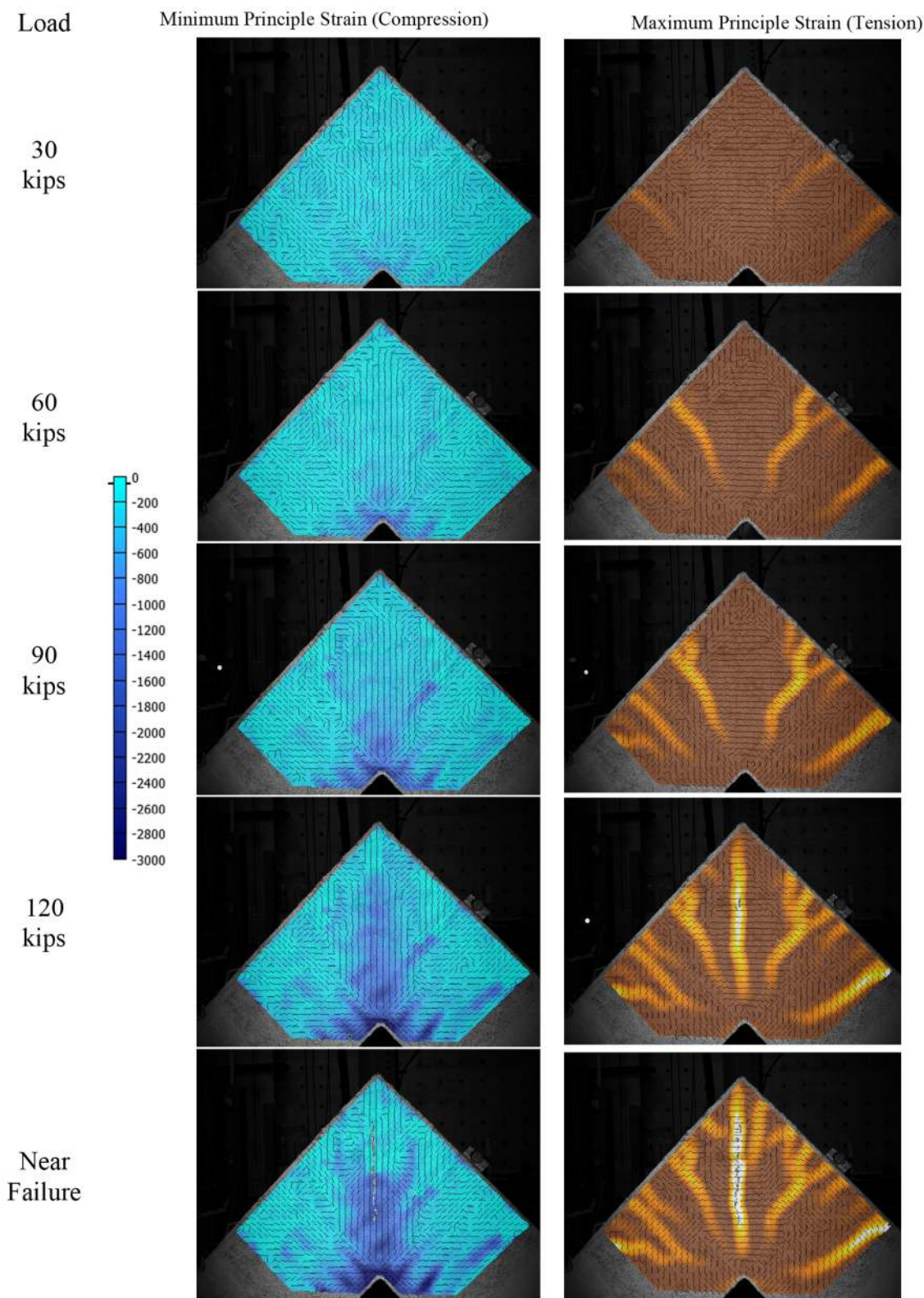
Specimen B-16-R3



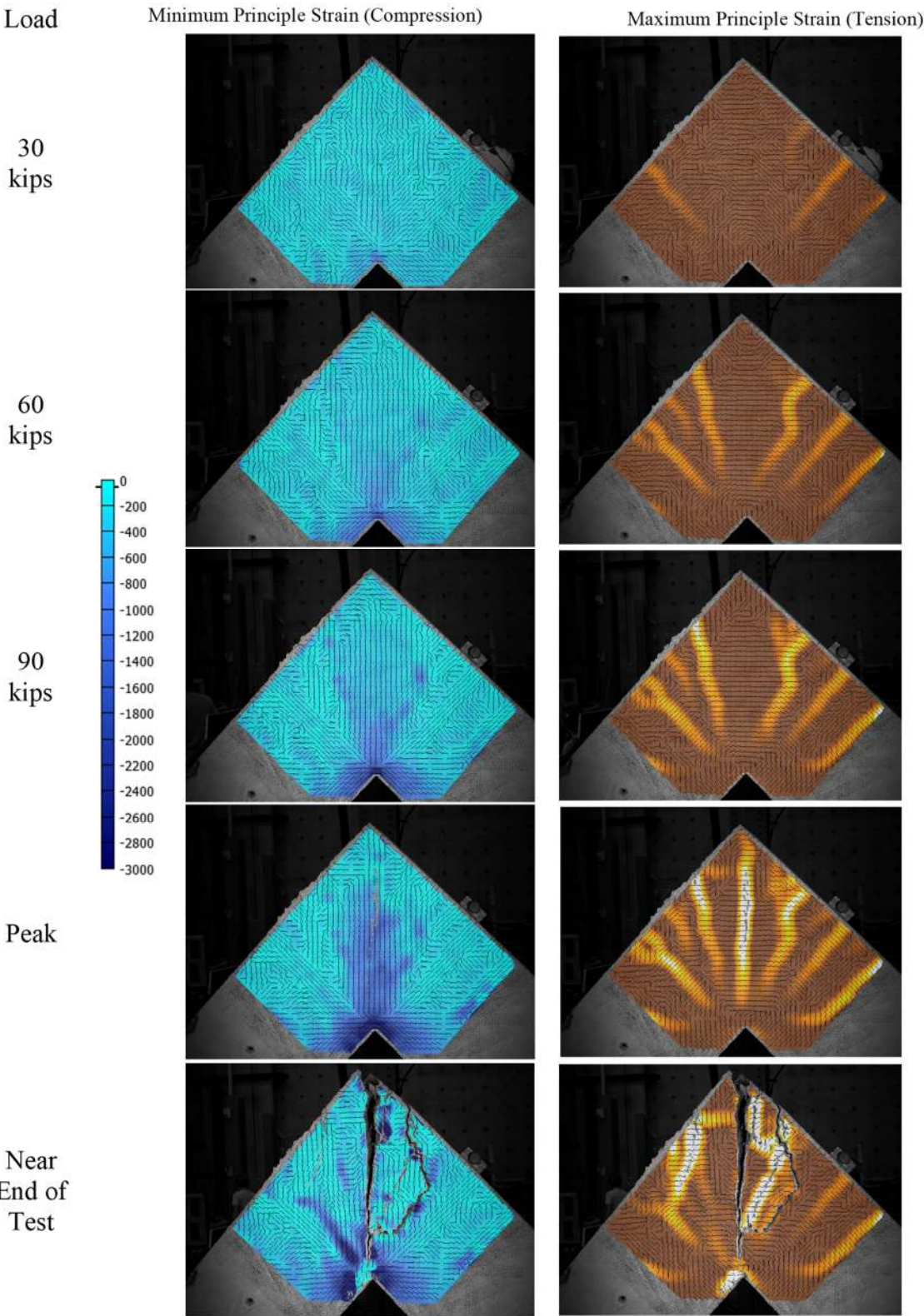
Specimen B-16-R6



Specimen TR-S-17-R3



Specimen TR-S-13-R3



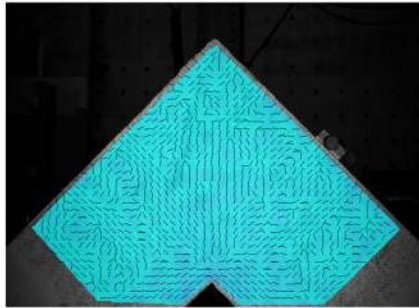
Specimen LS-S-18-R3

Load

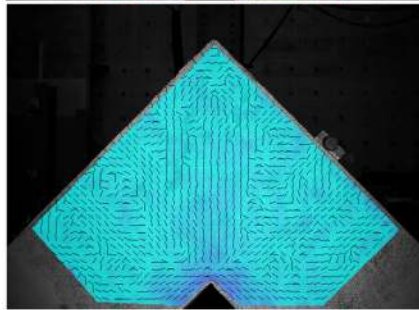
Minimum Principle Strain (Compression)

Maximum Principle Strain (Tension)

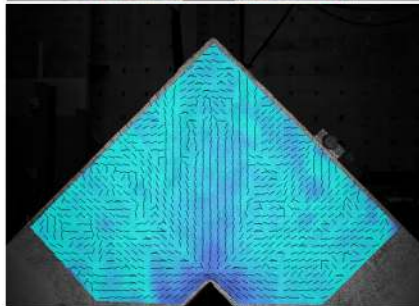
30
kips



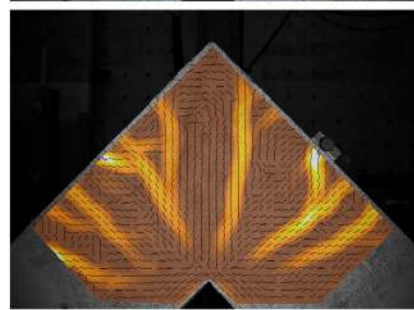
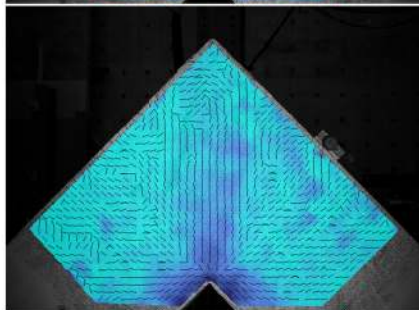
60
kips



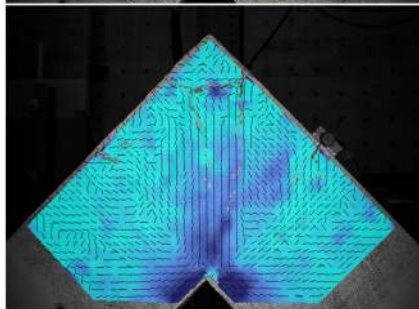
90
kips



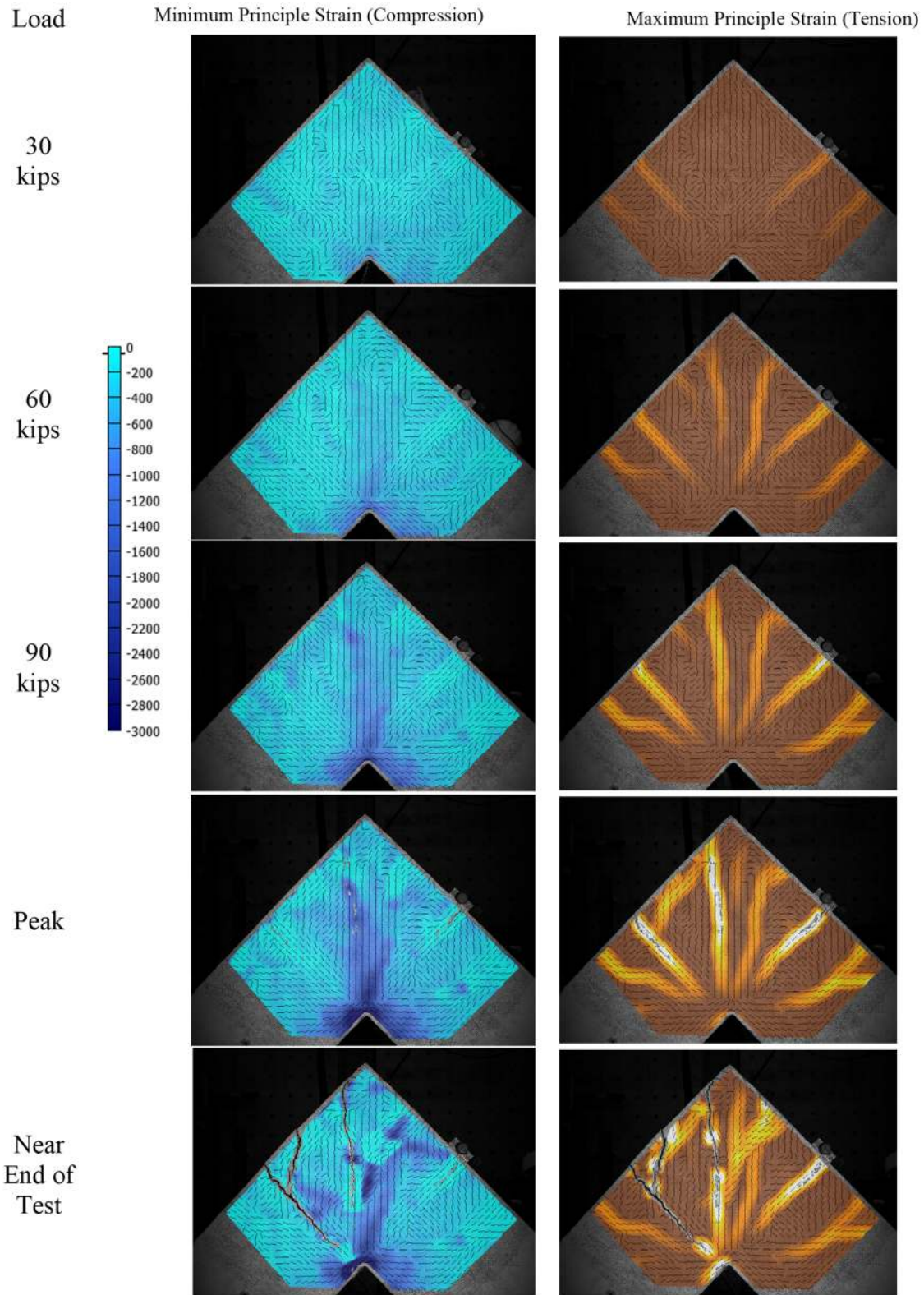
120
kips



Near
Failure



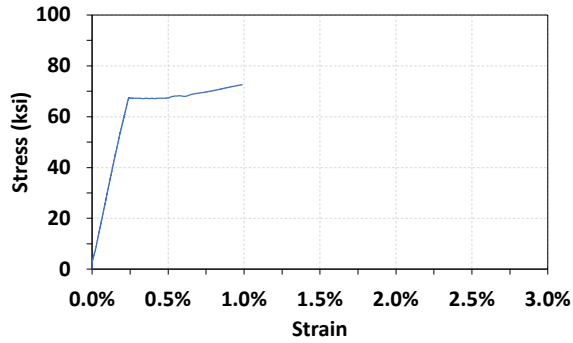
Specimen LS-S-13-R3



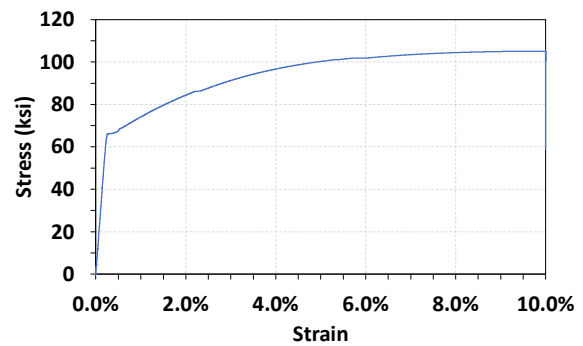
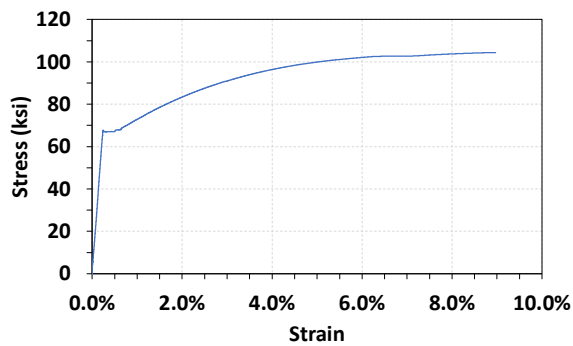
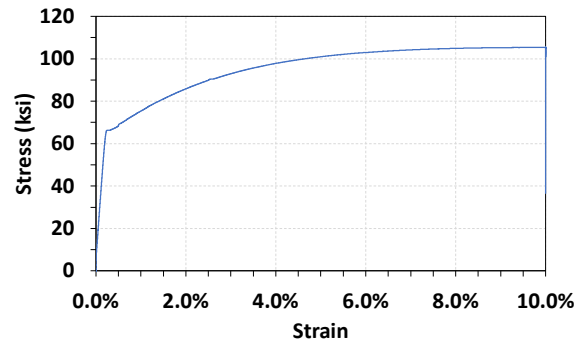
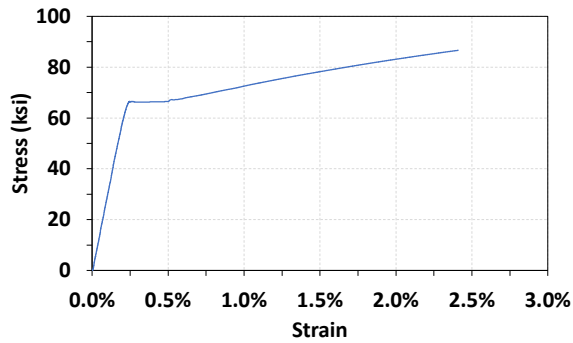
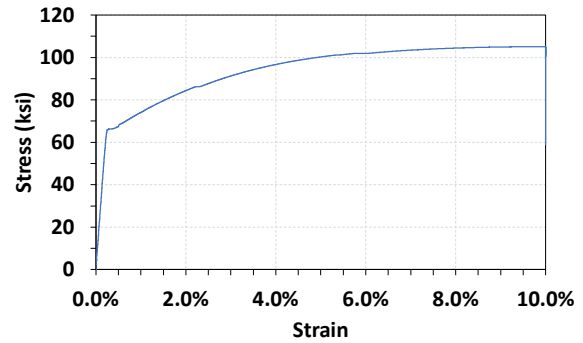
APPENDIX F. STRESS-STRAIN CURVES OF LONGITUDINAL REINFORCEMENT

S-Series

No. 8

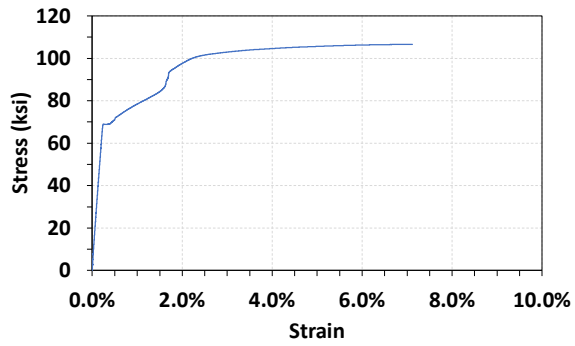


No. 7

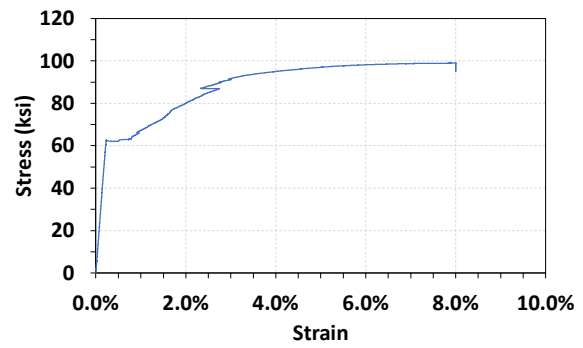
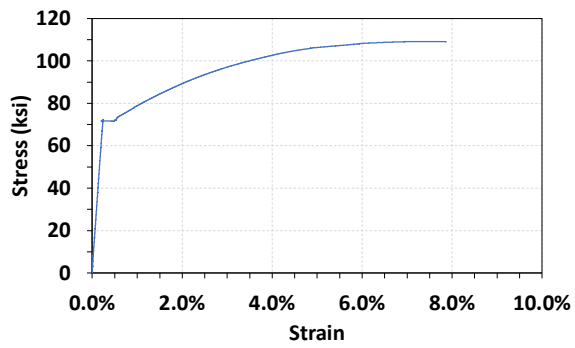
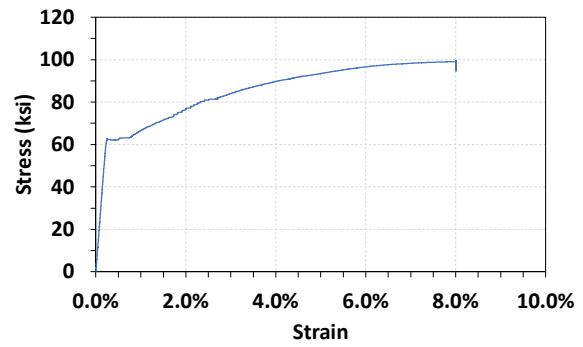
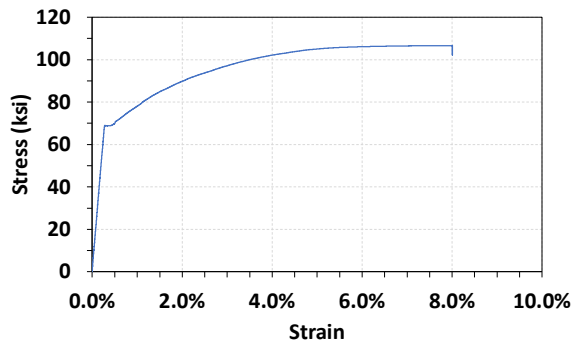
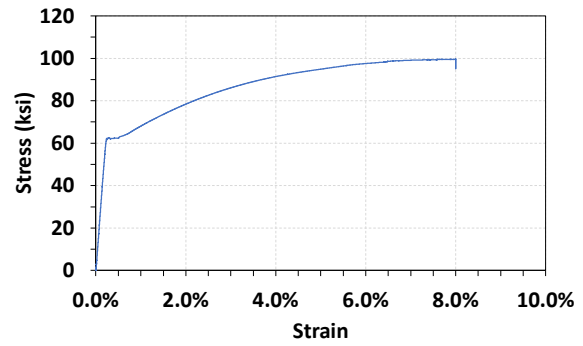


D-Series

No. 7

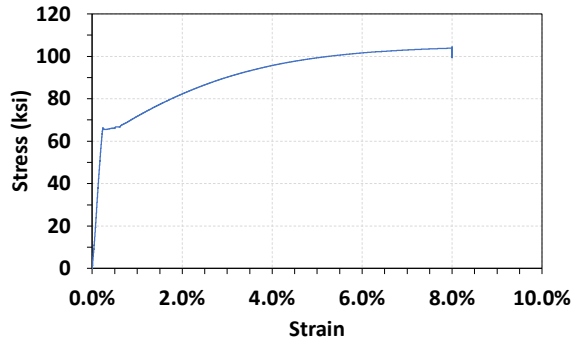


No. 6

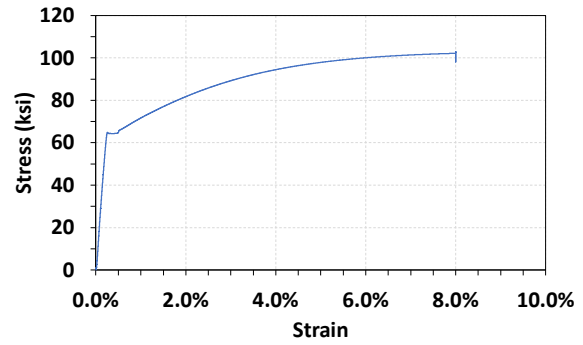
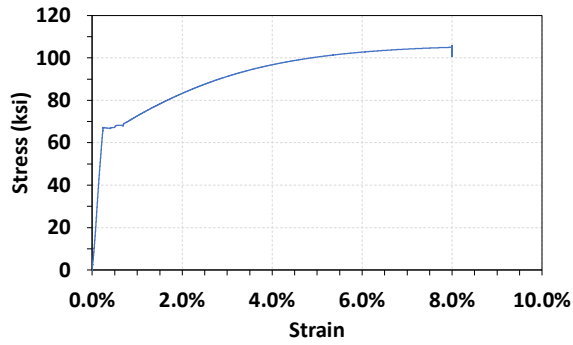
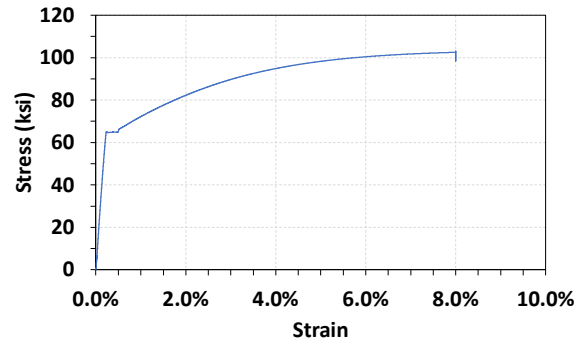
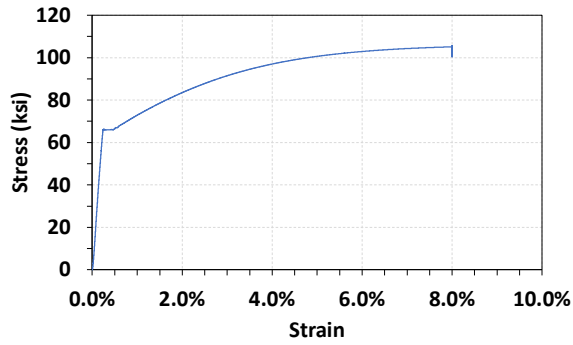
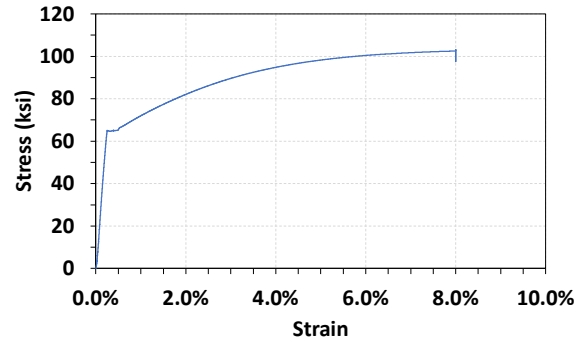


C-Series, B-Series, M-Series

No. 8



No. 7



REFERENCES

1. ACI Committee 318. "Building Code Requirements for Structural Concrete (ACI 318-19) and Commentary (ACI 318R-19)," Farmington Hills, MI, American Concrete Institute, 2019, 623 pp.
2. Richart, F. E., Dolan, T. J., and Olson, T. A. "An Investigation of Rigid Frame Bridges Part 1 - Test of Reinforced Concrete Knee Frames and Backlite Models," *University of Illinois Engineering Experiment Station*, V. 34, No. 23, 1938, p. 47.
3. Ostlund, L. "Inverkan av böckningsradier och täckande betongskikt hos kamstål på spjälkningsrisken för armerade betongkonstruktioner (The Influence of Bending Radius and Concrete Cover for Deformed Bars on the Risk of Splitting Failure in Reinforced Concrete Structures)," Stockholm, Sweden, The Royal Institute of Technology, 1963, 92 pp.
4. Swann, R. A. "Flexural Strength of Corners of RC Portal Frames," *Cement and Concrete Association*, V. Tech Rept TRA 434, 1969, p. 14.
5. Mayfield, B., Kong, F.-K., Bennison, A., et al. "Corner Joint Details in Structural Lightweight Concrete," *ACI Journal*, V. 68, No. 5, 1971, pp. 366–72.
6. Yuan, R. L., McLelland, G. R., and Chen, W. F. "Experiments on Closing Reinforced Concrete Corners," *Journal of the Structural Division*, V. 108, No. 4, 1982, pp. 771–9.
7. Zouzou, A., and Haldane, D. "Detailing reinforced concrete closing corner joints for ductility," *Proc. Instn Civ. Engrs Structs & Bids*, No. 99, 1993, pp. 43–8.
8. Luo, Y. H., Durrani, A. J., Bai, S., et al. "Study of Reinforcing Detail of Tension Bars in Frame Corner Connections," *ACI Structural Journal*, V. 91, No. 4, 1994, pp. 486–96.
9. Plos, M. "Splicing of Reinforcement in Frame Corners Experimental Studies," *Nordic Concrete Research*, V. 14, No. 1/1994, 1994, pp. 103–21.
10. Johansson, M. "Concrete frame corners in civil defence shelters subjected to negative moment," *AEDIFICATIO Publishers, Fracture Mechanics of Concrete Structures*, V. 3, 1998, pp. 1511–1522.
11. Lundgrn, K. "Three-dimensional modelling of bond in reinforced concrete: theoretical model, experiments and applications," Göteborg, Chalmers Univ. of Technology, 1999, 130 pp.

12. Johansson, M. "Structural behaviour in concrete frame corners of civil defence shelters: non-linear finite element analyses and experiments," Göteborg, Chalmers Univ. of Technology, 2000, 300 pp.
13. Johansson, M. "Reinforcement Detailing in Concrete Frame Corners," *ACI Structural Journal*, V. 98, No. 1, 2001, pp. 105–15.
14. H. Hotta., and N. Nishizawa. "Experimental Study on Influence of Arrangement of Main Bars on Stress Transmission in Reinforced Concrete Beam-column Knee Joints." Lisboa, 2012. p. 10.
15. Marchetto, F. "Use of Headed Reinforcement Bars in Construction - A Theoretical Approach to Determine The Dimensions of Anchorage Plates and Experimental Tests on Knee Joints Subjected to a Closing Moment." Technical University of Madrid, Spain, 2015.
16. Marchetto, F., Caldentey, A. P., and Peiretti, H. C. "Structural performance of corner joints subjected to a closing moment using mechanical anchorages an experimental study," *Structural Concrete*, V. 17, No. 6, 2016, pp. 987–1002.
17. Wight, J. K., and MacGregor, J. G. "Reinforced Concrete: Mechanics and Design," 6th edition, England, Pearson Education Limited, 2013, 1175 pp.
18. ACI Committee 352. "Recommendations for Design of Beam-Column Connections in Monolithic Reinforced Concrete Structures," Farmington Hills, MI, American Concrete Institute, 2002, 38 pp.
19. Schlaich, J., Schafer, K., and Jennewein, M. "Toward a Consistent Design of Structural Concrete," *PCI Journal*, V. 32, No. 3, 1987, pp. 74–150.
20. K. Schafer., and J. Schlaich. "Design and detailing of structural concrete using strut-and-tie models," *The Structural Engineer*, V. 69, No. 6, 1991, pp. 113–25.
21. El-Metwally, S. E.-D. E., and Chen, W.-F. "Structural concrete: strut-and-tie models for unified design," Boca Raton, CRC Press, Taylor & Francis Group, CRC Press is an imprint of the Taylor & Francis Group, an informa business, 2018, 230 pp.
22. Klein, G. J. "Curved-Bar Nodes: A detailing tool for strut-and-tie models," *Concrete International*, V. 30, No. 9, 2008, pp. 42–7.
23. Stroband, J., and Kolpa, J. J. "The behaviour of reinforced concrete column-to-beam joints. Part 1. Corner joints subjected to negative moments," Delft, Department of Civil Engineering, Delft University of Technology, 1983.

24. Ingham, J. "Seismic Performance of Bridge Knee Joints." University of California, San Diego, 1995.
25. CEB. "CEB-FIP Model Code 1990," Lausanne, CEB Bulletin d'Information No. 213/214, 1993.
26. Bai, S., and Luo, Y. "Concrete Frame Corners." New Zealand, 1988. pp. 157–68.
27. Bai, S., and Luo, Y. "RC Frame Corners Subjected to Closing Loads," *Journal of Chongqing Institute of Architecture and Engineering*, V. 11, No. 1, 1989, pp. 1–21.
28. Fujii, S., Kawakami, S., and Yamada, T. "Re-evaluation of test data on 90 degree bent bar anchorage," *Journal of Struct. Constr. Engng. AIJ*, No. 429, 1991.
29. Schlaich, M., and Anagnostou, G. "Stress fields for nodes of strut-and-tie models," *Journal of Structural Engineering*, V. 116, No. 1, 1990, pp. 13–23.
30. Ritter, W. "Die Bauweise Hennebique," *Schweizerische Bauzeitung*, V. 33, No. 7, 1899, pp. 59–61.
31. Morsch, E. "Der Eisenbetonbar," 3rd (English Transl. by E. P. Goodrich), New York, McGraw-Hill Book Company, 1909, 368 pp.
32. Ramirez, J. A., and Breen, J. E. "Review of Design Procedures for Shear and Torsion in Reinforced and Prestressed Concrete," The Center, 1983.
33. Marti, P. "Basic Tools of Reinforced Concrete Beam Design," *ACI Journal Proceedings*, V. 82, No. 1, 1985, pp. 46–56.
34. Marti, P. "Truss Models in Detailing," *Concrete International*, V. 7, No. 12, 1985, pp. 66–73.
35. D. Cook, W., and Mitchell, D. "Studies of Disturbed Regions near Discontinuities in Reinforced Concrete Members," *ACI Structural Journal*, V. 85, No. 2, 1988, pp. 206–16.
36. Chen, B. S., Hagenberger, M. J., and Breen, J. E. "Evaluation of Strut-and-Tie Modeling Applied to Dapped Beam with Opening," *ACI Structural Journal*, 2002, p. 6.
37. Kuchma, D., Yindeesuk, S., Nagle, T., et al. "Experimental validation of strut-and-tie method for complex regions," *ACI Structural Journal*, V. 105, No. 5, 2008, p. 578.
38. Alshegeir, A., and Ramirez, J. A. "Strut-Tie Approach in Pretensioned Deep Beams," *ACI Structural Journal*, V. 89, No. 3, 1992, pp. 296–304.
39. Vollum, R. L., and Newman, J. B. "Strut and tie models for analysis/design of external beam—column joints," *Magazine of Concrete Research*, V. 51, No. 6, 1999, pp. 415–25.

40. Hwang, S.-J., Lu, W.-Y., and Lee, H.-J. "Shear Strength Prediction for Reinforced Concrete Corbels," *ACI Structural Journal*, V. 97, No. 4, 2000, pp. 543–52.
41. Maxwell, B. S., and Breen, J. E. "Experimental Evaluation of Strut-and-Tie Model Applied to Deep Beam with Opening," *ACI Structural Journal*, 2000, p. 7.
42. Sritharan, S., Ingham, J. M., and Priestley, M. N. "Strut-and-tie model concepts for seismic design and assessment of concrete bridge joints." 12th World Conference on Earthquake Engineering, Auckland, New Zealand, January, CD-Rom Paper, vol. 1448. 2000.
43. Zechmann, R., and Matamoros, A. B. "Use of Strut-and-Tie Models to Calculate the Strength of Deep Beams with Openings," Lawrence, Kansas, University of Kansas Center for Research, Inc., 2002.
44. Park, J., Kuchma, D., and Souza, R. "Strength predictions of pile caps by a strut-and-tie model approach," *Canadian Journal of Civil Engineering*, V. 35, No. 12, 2008, pp. 1399–413.
45. Tuchscherer, R. G. "Strut-and-tie modeling of reinforced concrete deep beams: Experiments and design provisions," The University of Texas at Austin, 2008.
46. Souza, R., Kuchma, D., Park, J., et al. "Adaptable strut-and-tie model for design and verification of four-pile caps," *ACI Structural Journal*, V. 106, No. 2, 2009, p. 142.
47. Williams, C. S., Deschenes, D., and Bayrak, O. "Strut-and-Tie Model Design Examples for Bridges Final Report," Center for Transportation Research at The University of Texas at Austin, 2012.
48. Kassem, W. "Strength Prediction of Corbels Using Strut-and-Tie Model Analysis," *International Journal of Concrete Structures and Materials*, V. 9, No. 2, 2015, pp. 255–66.
49. ACI Committee 318. "Building code requirements for structural concrete (ACI 318-14): an ACI standard : commentary on building code requirements for structural concrete (ACI 318R-14), an ACI report," Farmington Hills, MI, American Concrete Institute, 2014, 520 pp.
50. Vecchio, F. J., and Collins, M. P. "Compression Response of Cracked Reinforced Concrete," *Journal of Structural Engineering*, V. 119, No. 12, 1993, pp. 3590–610.
51. Guyon, Y. "Prestressed Concrete," London, Contractor's Record LTD, 1953, 543 pp.
52. Brown, M. D., Sankovich, C. L., Bayrak, O., et al. "Behavior and Efficiency of Bottle-Shaped Struts," *ACI Structural Journal*, V. 103, No. 3, 2006, pp. 348–54.
53. Rezaei, N. "Study on Strut and Node Behavior in Strut-and-Tie Modeling." Doctor of Philosophy Civil Engineering, Florida International University, 2018.

54. Sahoo, D. K., Gautam, R. K., Singh, B., et al. "Strength and deformation characteristics of bottle-shaped struts," *Magazine of Concrete Research*, V. 60, No. 2, 2008, pp. 137–44.
55. Birrcher, D. B. "Design of reinforced concrete deep beams for strength and serviceability," The University of Texas at Austin, 2009.
56. Brown, M. D., Sankovich, C. L., Bayrak, O., et al. "Design for Shear in Reinforced Concrete Using Strut-and-Tie Models," Center for Transportation Research, The University of Texas at Austin, 2006.
57. ACI SP-273. "Further Examples for the Design of Structural Concrete with Strut-and-Tie Models," Farmington Hills, MI, American Concrete Institute, 2010, 288 pp.
58. FIP Commission 3. "Practical Design of Structural Concrete," FIP Recommendation 1996, Fédération Internationale de la Précontrainte, n.d.
59. Rogowsky, D. M., and MacGregor, J. G. "Design Of Reinforced Concrete Deep Beams," *Concrete International*, V. 8, No. 8, 1986, pp. 49–58.
60. Jirsa, J. O., Breen, J. E., and Bergmeister, K. "Experimental studies of nodes in strut-and-tie models." IABSE reports, vol. 62. 1991. pp. 525–32.
61. Sahoo, D. K., Singh, B., and Bhargava, P. "An appraisal of the ACI strut efficiency factors," *Magazine of Concrete Research*, V. 61, No. 6, 2009, pp. 445–56.
62. Laughery, L., and Pujol, S. "Compressive Strength of Unreinforced Struts," *ACI Structural Journal*, V. 112, No. 5, 2015.
63. Pujol, S., Rautenberg, J. M., and Sozen, M. A. "Compressive Strength of Concrete in Nonprismatic Elements," n.d., p. 8.
64. ASTM A615/A615M-16. "Standard Specification for Deformed and Plain Carbon-Steel Bars for Concrete Reinforcement," West Conshohocken, PA, ASTM International, 2016, 6 pp.
65. ASTM C143 / C143M - 15a. "Standard Test Method for Slump of Hydraulic-Cement Concrete," West Conshohocken, PA, ASTM International, 2015, 4 pp.
66. ASTM C94 / C94M-17. "Standard Specification for Ready-Mixed Concrete," West Conshohocken, PA, ASTM International, 2017.
67. ASTM C39 / C39M-17. "Standard Test Method for Compressive Strength of Cylindrical Concrete Specimens," West Conshohocken, PA, ASTM International, 2017.
68. ASTM C31 / C31M - 17. "Standard Practice for Making and Curing Concrete Test Specimens in the Field," West Conshohocken, PA, ASTM International, 2017.

69. ASTM C469 / C469M - 14. "Standard Test Method for Static Modulus of Elasticity and Poisson's Ratio of Concrete in Compression," West Conshohocken, PA, ASTM International, 2014.
70. ASTM C496 / C496M - 17. "Standard Test Method for Splitting Tensile Strength of Cylindrical Concrete Specimens," West Conshohocken, PA, ASTM International, 2017.
71. ASTM C78 / C78M - 16. "Standard Test Method for Flexural Strength of Concrete (Using Simple Beam with Third-Point Loading)," West Conshohocken, PA, ASTM International, 2016.
72. ASTM A370 - 17. "Standard Test Methods and Definitions for Mechanical Testing of Steel Products," West Conshohocken, PA, STM International, 2017.
73. Bayrak, O., and Brown, M. "Minimum Transverse Reinforcement for Bottle-Shaped Struts," *ACI Structural Journal*, V. 103, No. 6, 2006, pp. 813–22.
74. Sahoo, D. K., Singh, B., and Bhargava, P. "Minimum Reinforcement for Preventing Splitting Failure in Bottle-Shaped Struts," *ACI Structural Journal*, V. 108, No. 2, 2011, pp. 206–16.
75. Anderson, R. B. "Behavior of CTT-Nodes in Reinforced Concrete Strut-and-Tie Models." The Universtiy of Texas at Austin, 1988.
76. Yun, Y. M., and Ramirez, J. A. "Strength of struts and nodes in strut-tie model," *Journal of Structural Engineering*, V. 122, No. 1, 1996, pp. 20–29.
77. Scott, R. M. "Experimentally Validated Compatibility Strut and Tie Modeling of Reinforced Concrete Bridge Piers." Texas A & M University, 2010.
78. Reineck, K.-H., Kuchma, D. A., Kim, K. S., et al. "Shear Database for Reinforced Concrete Members without Shear Reinforcement," *ACI Structural Journal*, V. 100, No. 2, 2003, pp. 240–9.
79. Hognestad, E. "Fundamental Concepts in Ultimate Load Design of Reinforced Concrete Members," *ACI Journal Proceedings*, V. 48, No. 6, 1952.
80. Hognestad, E. "A study of combined bending and axial load in reinforced concrete members," Urbana Illinois, University of Illinois Engineering Experiment Station, 1951, 128 pp.
81. Cervenka, V., Cervenka, J., and Pukl, R. "ATENA — A tool for engineering analysis of fracture in concrete," *Sadhana*, V. 27, No. 4, 2002, pp. 485–92.
82. Cervenka, V., Cervenka, J., and Pukl, R. "ATENA — an Advanced Tool for Engineering Analysis of Connections," *RILEM Publications Ens France*, 2001, pp. 658–67.

83. Menetrey, P., and Willam, K. J. "Triaxial Failure Criterion for Concrete and its Generalization," *ACI Structural Journal*, V. 92, No. 3, 1995, pp. 311–8.
84. Červenka, V., Jendele, L., and Červenka, J. "ATENA Program Documentation Part 1: Theory," Prague, Czech Republic, Červenka Consulting s.r.o., 2018, 319 pp.
85. Van, M. J. G. M. "Multiaxial strain-softening of concrete. Part I: fracture," *Materials and structures, RILEM*, V. 19, No. 111, 1986.
86. Vecchio, F. J., and Collins, M. P. "Modified Compression-Field Theory for Reinforced Concrete Beams Subjected to Shear," *ACI JOURNAL*, V. 83, No. 2, 1986, pp. 219–23.
87. Dyngeland, T. "Behavior of Reinforced Concrete Panels, Dissertation." Trondheim University, Norway, 1989.
88. Walraven, J. C. "Fundamental Analysis of Aggregate Interlock," *Journal of the Structural Division*, V. 107, No. 11, 1981, pp. 2245–70.
89. Chen, W.-F. "Plasticity in Reinforced Concrete," McGraw-Hill Book Company, 1982, 474 pp.
90. Pryl, D., and Červenka, J. "ATENA Program Documentation Part 11: Troubleshooting Manual," Prague, Czech Republic, Červenka Consulting s.r.o., 2018, 319 pp.
91. Kabele, P., Červenka, V., and Červenka, J. "ATENA Program Documentation Part 3-1: ATENA Engineering Example Manual," Prague, Czech Republic, Červenka Consulting s.r.o., 2010, 86 pp.